MODELLING AGGREGATE INTERLOCK LOAD TRANSFER AT CONCRETE PAVEMENT JOINTS

ANNA CATHARINA BRINK

A thesis submitted in fulfilment of the requirements for the degree of

PHILOSOPHIAE DOCTOR (ENGINEERING)

In the

FACULTY OF ENGINEERING

UNIVERSITY OF PRETORIA

July 2003

THESIS SUMMARY

MODELLING AGGREGATE INTERLOCK LOAD TRANSFER AT CONCRETE PAVEMENT JOINTS

AC BRINK

Supervisor: Prof Emile Horak

Co-Supervisor: Prof Alex Visser

Department: Civil Engineering

University: University of Pretoria

Degree: Philosophiae Doctor (Engineering)

The South African concrete pavement community recognized the need to upgrade the South African Concrete Pavement Design and Construction Manual, to a manual based on mechanistic design principles. During a re-evaluation of factors affecting riding quality, structural service life, maintenance and rehabilitation needs, the prominent influence of joint performance in jointed concrete pavements (JCP) was re-confirmed. It was identified that the analytical equation used in the manual to predict relative movement at joints was only applicable to a small range of aggregate sizes. Further research was therefore needed, which resulted in the study presented in this thesis.

The primary objective of this research was to evaluate pavement response in terms of deflections, to static and moving impulse or dynamic loads (equivalent to traffic loads), and to take into account existing methods for modelling aggregate interlock shear transfer. This was in order to develop a fundamental model that reflects variations in joint load transfer with joint opening, load magnitude and concrete properties to replace an existing equation in the new South African mechanistic concrete pavement design manual. In the context of this thesis, modelling can be defined as the execution of pre-planned tests in a laboratory under controlled conditions using materials commonly used in the construction of concrete pavements in South Africa in order to develop an equation simulating performance in the field.

Theoretical analyses of concrete pavement models were first done by the author using the three-dimensional finite element computer software programme EverFE. This was in order to determine the ranges for the

different input variables that could be expected during modelling in the laboratory. Both aggregate interlock and dowel/concrete interaction were evaluated using EverFE.

The focus of subsequent laboratory testing was to measure relevant responses during testing of instrumented concrete pavement models. Instrumentation included load cells, actuators, linear variable displacement transducers, as well as horizontal strain displacement transducers to collect fast responses induced by dynamic loads. Thermocouples collected further information on the influence of environmental temperature. The preliminary testing also included determining the relevant engineering properties for the typical South African aggregates used in the study.

The laboratory concrete pavement test sections were constructed on rubber mats to simulate a Winkler foundation. Constructing the models on rubber mats made it possible to repeat experiments with the same founding conditions, which reduced the number of variables that had to be taken into consideration during analysis of the data.

Conclusions reached from the study were inter alia that there was no significant deterioration of the crack face during the application of up to two million dynamic load cycles, which indicated that little abrasion took place at the initial crack width. It also indicated that fatigue of the aggregates at the joint face did not play a significant role, which could be attributed to the high quality of the crushed stone used in South Africa, as well as to the fact that testing was conducted inside the controlled environment of a laboratory. Moment and inertia in the slab contributed to greater load transfer efficiency under dynamic loading, than under static loading.

A specific relationship determined from laboratory results was used to refine the aggregate interlock load transfer model in the software developed for the new mechanistic design manual. Data from field investigations of in service concrete pavements in southern Africa was used to calibrate the laboratory data.

ABSTRACT

Title: Modelling Aggregate Interlock Load Transfer at Concrete Pavement Joints

Author: Anna-Carin Brink

Supervisor: Prof Emile Horak

Co-Supervisor: Prof Alex Visser

Department: Civil Engineering

University: University of Pretoria

Degree: Philosophiae Doctor (Engineering)

Keywords: Aggregate interlock, Load transfer efficiency, Jointed concrete pavement, Winkler foundation, Dynamic and static loading, Relative movement.

The South African concrete pavement fraternity recognized the need to upgrade the South African Concrete Pavement Design and Construction Manual, to a manual based on mechanistic design principles. During a re-evaluation of factors affecting riding quality, structural service life, maintenance and rehabilitation needs, the prominent influence of joint performance was re-confirmed. Further research was needed to enable modelling of aggregate interlock load transfer at concrete pavement joints, which resulted in the study presented in this thesis.

The primary objective of this research was to evaluate pavement response in terms of deflections, to static and moving impulse or dynamic loads (equivalent to traffic loads), and to take into account existing methods for modelling aggregate interlock shear transfer (In the context of this thesis, modelling can be defined as the execution of pre-planned tests in a laboratory under controlled conditions using materials commonly used in the construction of concrete pavements in South Africa in order to develop an equation simulating performance in the field). This was in order to develop a fundamental model that reflects variations in joint load transfer with joint opening, load magnitude and concrete properties to replace an existing equation in the new South African mechanistic concrete pavement design manual.

During modelling the focus was to measure relevant responses during testing of instrumented concrete pavement models. Instrumentation included load cells, actuators, linear variable displacement transducers, as well as horizontal strain displacement transducers to collect fast responses induced by dynamic loads. Thermocouples collected further information on environmental influences. The preliminary testing also

included determining the relevant engineering properties for South African materials. The concrete pavement models were constructed on rubber mats to simulate a Winkler foundation with or without inter-layers.

Conclusions reached from the study were inter alia that there was no significant deterioration of the crack face during dynamic loading, which indicated that little abrasion took place at the initial crack width. It also indicated that in this instance fatigue of the aggregates at the joint face did not play a role, which could be attributed to the high quality of the crushed stone used in South Africa. Moment and inertia in the slab contributed to the greater load transfer efficiency under dynamic loading, than under static loading.

A specific relationship determined from laboratory results was used to refine the aggregate interlock load transfer model in the software developed for the new mechanistic design manual. Data from field investigations of in service concrete pavements in southern Africa was used to calibrate the laboratory data.

To my children

Annica and Dawid

and my parents

Danie and Annetjie Brink

ACKNOWLEDGEMENTS

I wish to express my gratitude to God, my Father, that I have had the opportunity to do this research and that He has kept my mother alive to pray for me, despite being seriously ill.

Further, I wish to express my appreciation to the following organisations and persons who made this thesis possible:

a) BKS (Pty) Ltd for allowing me two years' study leave, and for paying my salary while doing so.

b) The Cement and Concrete Institute (C&CI) for financial support and the use of their library facilities during the course of the research.

c) The Technology and Human Resources for Industry Program (THRIP) and the Centre for Transport Development for financial support.

d) Professor Emile Horak and Professor Alex Visser, my supervisors, for their guidance and support.

e) Prof Christo van As for assistance with the development of the mathematical equation used in the CncRisk software.

f) Investmech for the use of their laboratory facilities and their mechanical engineering input to assist in sorting out testing procedures and for generating data for analysis of the experimental concrete slabs.

g) Alpha Stone, Lyttleton (Pty) Ltd, and Lafarge Readymix for supplying materials for casting the concrete slabs.

h) My daughter, Annica and my son, Dawid for their love and enthusiasm to see their mother complete this study.

CONTENTS

CHAPTER 1: INTRODUCTION

TABLE OF CONTENTS

LIST OF FIGURES

1 INTRODUCTION

1.1 BACKGROUND

Prior to 1968 concrete pavements were used only in exceptional cases in the Republic of South Africa. They were constructed using hand methods and rudimentary plant, which did not produce the longitudinal profile needed for modern traffic. As a result, the utilisation of concrete pavements was discontinued during the 1950's and 1960's. However, the results of the AASHO road test and studies and observations of modern concrete pavement performance, notably in the USA, stimulated interest in modern concrete pavements as a means of accommodating the rapidly growing traffic loading on South African highways. The high traffic densities not only made it expensive to rehabilitate existing national routes, but also dangerous, and the need for a relatively maintenance free pavement surface arose. Construction of modern concrete pavements in the RSA, therefore, commenced in 1968, where both jointed un-reinforced and continuously reinforced concrete pavements were constructed on a few selected routes for new construction and for rehabilitation purposes. Amongst others, the following routes were provided with concrete pavements (see Figure 1.1):

N2 from Cape Town to Somerset West (1968)
N4 between Witbank and Middelburg (1971)
N1 from the Vaal River to Johannesburg (1979)
N3 between Estcourt and Frere (1978)
R22 between Witbank and Springs (Experimental, 1973)
N1 between Johannesburg and Pretoria (1987/8)

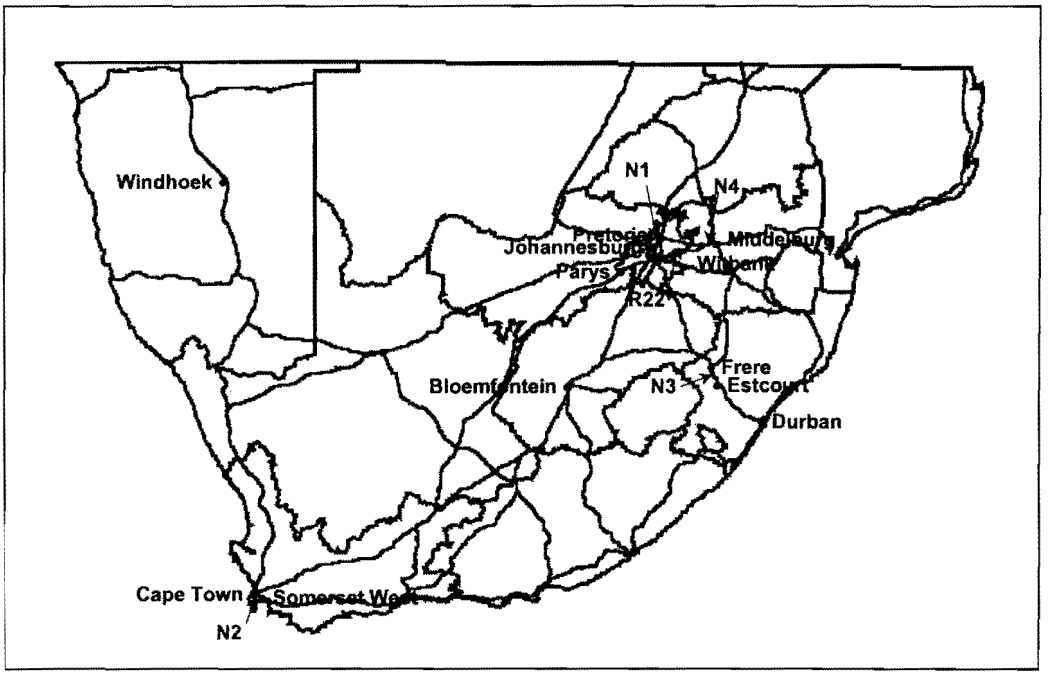

Figure 1.1 Concrete pavements in South Africa

The technology previously applied in South Africa was initially based on empirical methods developed from observations during the AASHO road test, the Alconbury Hill Experiment in the UK and also local Heavy Vehicle Simulator (HVS) tests (Du Plessis and Freeme, 1989). This was followed by designers using procedures developed by the US Portland Cement Association, Road Note 29 (Developed by the UK Transport and Road Research Laboratory), the US Army Corps of Engineers method and also procedures developed by the California State Highway Department (Mitchell et al, 1988). Local application of these design methods resulted in the construction of mostly jointed concrete pavements, without dowels at the joints, relying on aggregate interlock load transfer. Slab thicknesses of between 200 and 235 mm with 100 mm thick cement stabilised subbases were typically used to decrease the risk of subbase erosion, pumping and subsequent differential settlement or faulting at joints.

In most industrialised countries, road authorities specify that certain proportions of their highway networks be constructed in concrete. In England and Wales, for example, at least 20 percent of the major highways are required to be concrete pavement. In the USA, more than 50 percent of interstate highways and 15 percent of arterial roads are constructed of concrete. Yet, concrete pavements have in the past, (and still today according to many road engineers) been regarded as a pavement solution which is out of the ordinary and which requires greater attention than the more common asphalt pavement types. This myth, as well as resistance to the high initial construction costs has to some extent been prejudicial to the more extensive use of concrete pavements in South Africa. Less than 400 km (0,75 %) of the surfaced national road network is built as concrete pavements (Du Plessis and Freeme, 1989).

In Europe, jointed concrete pavements (JCPs) with doweled joints are commonly used. In the USA a variety of concrete pavement types are used, which include JCPs, jointed reinforced concrete pavements (JRCPs), continuously reinforced concrete pavements (CRCPs) and even pre-stressed (experimentally only) pavements.

In an attempt to introduce a degree of rationality into the design process, the South African Department of Transport issued a publication during 1980 in which the economics of the pavement type selection process for major roads was analysed, and all relevant factors were considered. This document, prepared by the Committee on Pavement Type Selection for the National Transport Commission, held that for pavements carrying 12 to 50 million equivalent standard axles over its design life: ".. there is no significant difference in present worth of cost between bituminous and concrete pavements based on 1978/79 unit costs. The cheapest alternative will depend on the local factors prevailing at the time." (Mitchell, 1988).

In 1985 the situation changed, due to a better understanding of road-user delay costs. It was shown that for heavy-duty pavements to carry up to 75 million equivalent axle loads over a 30-year analysis

period, a concrete pavement is more economical than a bituminous pavement on a present worth of cost basis (Mitchell, 1988).

The Department of Transport commissioned a research project aimed at providing a manual for the design and construction of concrete pavements in South Africa, during 1986. This study covered subjects such as the performance of existing concrete pavements, simulation of pavement response under laboratory conditions, mathematical analysis, mechanistic design and construction. At the initial stages of this study (which resulted in the Concrete Pavement Design and Construction, Manual M10, 1995) it was found that the performance of concrete pavements is influenced to a large extent by quality control during the construction phase. But, even more important, it was stated that the *behaviour of* joints was found to be significant in pavement behaviour as a whole. The *load transfer efficiency of the joint* not only influences the stresses in the pavement, but also has more importantly a direct effect on the possible erosion of the subbase material (Malan et al, 1988).

During the upgrading of the South African Concrete Pavement Design and Construction Manual M10 (Manual M10, 1995), to a concrete pavement design manual based on mechanistic design principles, a re-evaluation of factors affecting riding quality, structural service life, maintenance and rehabilitation needs re-confirmed the prominent effect of joint performance. It was identified that the current relationship modelling the mechanism of concrete joints in shear (aggregate interlock) was not accurate, especially for the smaller sized coarse aggregates used in the construction of concrete. Further research was therefore needed, which prompted the study presented in this thesis.

It has already been stated that most of the concrete pavements constructed in South Africa are JCPs, without dowels at the joints, relying on aggregate interlock load transfer. There are three primary types of joints in JCPs: contraction, isolation, and construction. Contraction joints are usually spaced every 3-5 m on average to permit contraction of the slabs, to control cracking in the concrete and to limit curling and warping stresses in the slab. They are typically formed by saw-cutting $^1/_4$ to $^1/_3$ the pavement thickness after curing, forcing a crack to occur at the joint through the pavement thickness. Aggregate interlock arising from the interaction of the two rough joint surfaces is an important load transfer mechanism at contraction joints. Isolation joints are used at the intersection of pavements with structures, and in some cases, within pavements. Construction joints are required between paving lanes, and at the end of a pour. In contrast to contraction joints, construction joints have formed joint surfaces with load transfer taking place through keys and tie bars.

The statement made by Du Plessis and Freeme (1989) that mechanistic models capable of evaluating the behaviour of concrete pavements with respect to the separate and combined influences of dowels, drainage, subbase, shoulder configurations, etc. have yet to be developed, is still true. Analysis models of this type, emphasizing the need for effective load transfer mechanisms are required especially for pavements carrying low- to medium volume traffic, if these are to be considered competitive with flexible pavements.

1.2 OBJECTIVE OF THE STUDY

The primary objectives of this research were:

a) To take into account existing methods for modelling aggregate interlock shear transfer to develop a model applicable to South African conditions that reflects variations in joint load transfer with joint opening, load magnitude, subbase support, aggregate size and concrete properties. This was in order to provide an improved aggregate interlock load transfer equation for the new South African mechanistic concrete pavement design method and application software, cncRisk.

b) To evaluate jointed concrete pavement response in terms of deflections, to static and moving impulse or dynamic loads (equivalent to traffic loads).

In the context of this thesis, modelling can be defined as the execution of pre-planned tests in a laboratory under controlled conditions using materials commonly used in the construction of concrete pavements in South Africa in order to develop an equation simulating performance in the field.

The secondary objectives were:

a) To obtain field measurements of crack widths and load transfer efficiency of existing jointed concrete pavements to calibrate the laboratory results.

b) To investigate existing methods for modelling steel dowel/concrete interaction at joints in jointed concrete pavements to determine a universal design model.

1.3 SCOPE OF THE STUDY

The scope of this study mainly involved the following:

a) Defining the rigid pavement system.

b) A detailed literature review of the main jointed concrete pavement load transfer mechanisms, namely, aggregate interlock and steel dowels.

c) Theoretical three-dimensional finite element (3D FE) modelling using the computer software programme EverFE (Davids et al, 1998) to determine ranges for input variables that could be expected during studies on part-slab sections in the laboratory. Both aggregate interlock and steel dowel load transfer mechanisms were modelled theoretically, as well as the combined effect of aggregate interlock and steel dowel load transfer mechanisms

d) Determining aggregate interlock load transfer efficiency through laboratory studies on part-slab sections.

e) Comparison of theoretical and laboratory modelling results with crack width and load transfer efficiency results obtained from testing actual in-service jointed concrete pavements in the field.

The scope of this study did not include laboratory modelling of steel dowel load transfer devices. This was only done theoretically. Voids beneath the concrete due to erosion of the subbase were also not investigated.

1.4 METHODOLOGY

In order to obtain a sound foundation for modelling load transfer at a joint in a concrete pavement a review of historical developments of rigid pavement design procedures had to be performed, together with a literature review of available rigid pavement response models, including two- and three-dimensional finite element techniques.

Theoretical analyses of full-scale concrete pavement models were first analysed using the 3D FE computer software programme EverFE (Davids et al, 1998). This was in order to determine the ranges for the different input variables that could be expected during experimental studies in the laboratory. Both aggregate interlock and dowel/concrete interaction was evaluated using EverFE.

In the laboratory, however, the scope of the investigation had to be narrowed down to what could be achieved practically within the scope of the project. Instead of full-scale models, so-called part-slab studies were conducted, and only the aggregate interlock load transfer aspect was investigated in detail. The change in deflection, and shear stiffness with variations in aggregate size, and joint opening were monitored. Instrumentation included thermocouples to collect slow responses due to environmental temperature influences. Linear variable displacement transducers (LVDT's) and strain displacement transducers collected fast responses induced by dynamic and static loads. The testing also included determining the relevant engineering properties for South African concrete aggregates.

The concrete pavement part-slab sections were constructed on rubber mats to simulate a liquid (Winkler) foundation. Constructing the slabs on rubber mats, made it possible to repeat experiments with the same founding conditions, which reduced the number of variables that had to be taken into consideration during calculations.

The success of the studies has laid the foundation for future testing involving dowel bars, as well as different subbase types to study the effect of erosion.

The software package, EverFE, which permits 3D FE models to be run on desktop computers, was recently developed in the USA. This package still needed 'field data" to validate the theoretically

calculated stresses and strains at the joint in the concrete pavement using South African materials and under our local environmental conditions.

As it was identified that the current relationship used in the South African concrete pavement design manual (Manual M10, 1995) modelling the mechanism of concrete joints in shear (aggregate interlock) was not accurate, especially for the smaller sized coarse aggregates used in the construction of concrete, the focus of this study was therefore to develop a more accurate formula through laboratory testing.

1.5 ORGANISATION OF THE THESIS

This thesis is organised as follows:

a) Chapter 1 serves as introduction to the thesis.

b) Chapter 2 contains the literature review. The literature review includes a definition of the rigid pavement system and a survey of the historical developments of rigid pavement design procedures, including two- and three-dimensional finite element techniques. It explains the mechanics of aggregate interlock and provides an overview of past attempts to model this phenomenon. It also covers the modelling of dowels and dowel-slab interaction as presented in the literature. The main aim of the literature review was to obtain guidance for laboratory modelling.

c) Chapter 3 presents a summary of the results obtained during laboratory modelling and also summarizes results obtained from field investigations on in-service concrete pavements in South Africa.

d) Chapter 4 describes how the laboratory and field data was analysed in the development of an improved modelling equation.

e) Chapter 5 describes the application of the model developed in this study.

f) Chapter 6 presents conclusions and recommendations for future research.

CHAPTER 2: LITERATURE REVIEW AND GUIDANCE FOR MODELLING

TABLE OF CONTENTS

LIST OF TABLES

LIST OF FIGURES

LIST OF SYMBOLS

a	Radius of applied load
agg	Nominal size of 20% biggest particles in concrete mix
AGG	Aggregate interlock joint shear stiffness per unit length of crack/joint
A_d	Cross-sectional area of dowel
A_z	Cross-sectional area of dowel effective in shear
AIF	Aggregate interlock factor
β	Relative stiffness of dowel/concrete system
C	Load transfer coefficient
c	Dowel bar radius
$[C]$	Damping matrix
D	Slab stiffness
Δ_L	Maximum edge deflection of the loaded slab
Δ_s	Aggregate interlock wear out
Δ_U	Maximum edge deflection of the adjacent unloaded slab
Δ_f	Maximum edge deflection with no joint
Δ_{di}	Deflection of any given dowel relative to the concrete
Δ_0	Deflection of the dowel relative to the concrete at the face of the joint
dia	Diameter of steel bar (dowel)
Δ	Deflection of the plate / shear displacement
EI	Endurance index
E_c	Modulus of elasticity of concrete
E_d	Modulus of elasticity of dowel
E_e	Equivalent subgrade support stiffness
E_s	Modulus of elasticity of soil
e	Effective length
$\{F\}$	Vector of nodal point forces
FE	Finite element

FWD	Falling Weight Deflectometer
F_x	Total force in X-plane
F_y	Total force in Y-plane
f_{cu}	Concrete cube crushing strength
Gd	Shear modulus of dowel bar
h	Concrete slab thickness
I_d	Moment of inertia of the dowel
J	Total stiffness ratio
J_{AI}	Dimensionless aggregate interlock stiffness ratio
J_D	Dimensionless dowel stiffness ratio
h_e	Effective concrete slab thickness
J	Corner stress coefficient (load transfer coefficient) Joint stiffness computed on transverse crack
JE	Joint effectiveness
K	Slab support modulus / dowel support modulus
$[K]$	Stiffness matrix
k	Modulus of subgrade reaction
L	Length of the slab
l	Radius of relative stiffness
LTE	Load transfer efficiency
LTE_Δ	Deflection load transfer efficiency
LTE_σ	Stress load transfer efficiency
$[M]$	Mass matrix
μ	Poisson's ratio for concrete / coefficient of friction between paste and aggregate
μ_d	Poisson's ratio of dowel
μ_s	Poisson's ratio for steel / soil
n	Number of load applications
n_{ij}	Number of axle load applications for current sub increment i and load group j
p	Pressure on plate loading test plate
P	Load, representing wheel load
P_d	Load on a dowel
P_i	Shear force acting on any particular dowel, transferred across the joint
P_L	Portion of load supported by loaded slab
P_T	Total load transferred across entire length of joint
P_U	Portion of load supported by unloaded slab
ΣA_x	X-projection of the sum of the most probable contact areas
ΣA_y	Y-projection of the sum of the most probable contact areas
σ	Maximum tensile stress
σ_b	Bearing stress of concrete
σ_E	Edge stress
σ_L	Maximum bending stress in the loaded slab

σ_U	Maximum bending stress in the adjacent unloaded slab
σ_f	Maximum bending stress for the free edge loading condition
σ_{pu}	Stress normal to the contact area
S	Dowel spacing
τ	Shear stress
τ_{pu},	Stress tangential to the contact area
τ_{stress}	Shear stress on the transverse crack
τ_{ref}	Reference shear stress derived from Portland Cement Association test results
TLE	Total load efficiency
$\{u\}$	Vector of nodal point displacements
$\{\dot{u}\}$	Vector of nodal point velocities
$\{\ddot{u}\}$	Vector of nodal point accelerations
v	Speed of heavy vehicles
$Void$	Length of void below slab
w	Joint/crack opening
w_i	Crack width in sub-increment i
W	Width of the slab
x	Crack width
y	Relative vertical movement at joint

NOTE: Equations (2.29) and (2.32) contain constants a, b, c, d, e, f, and g which are defined together with the equations on p4-18 and p4-19.

2 LITERATURE REVIEW AND GUIDANCE FOR MODELLING

2.1 INTRODUCTION

An in depth literature review has been conducted to lend guidance to the laboratory modelling envisaged for this thesis. This chapter deals with the definition of the rigid pavement system, historical developments in the field of concrete pavement modelling, aggregate interlock and dowel modelling.

Each paragraph has a short introduction, as well as a summary at the end.

2.2 RIGID PAVEMENT SYSTEM

2.2.1 Introduction

In the following paragraphs the rigid pavement system is defined, definitions are presented for deflection load transfer and stress load transfer developed in practice. An explanation is given of the different load transfer mechanisms encountered, and rigid pavement foundations are also described.

2.2.2 Pavement system

A rigid pavement system may be defined as a pavement structure in which the primary load-supporting element comprises a rigid layer/slab constructed from relatively thin Portland cement concrete (Manual M10, 1995). Concrete slabs are finite in length and width and are constructed over one or more foundation layers (Hammons and Ioannides, 1996). Figure 2.1 shows a representation of a typical rigid pavement system subjected to static loading. When a slab-on-grade is subjected to a wheel load, it develops bending stresses and distributes the load over the foundation. However, the response of these finite slabs is controlled by joint or edge discontinuities. Edge loading can increase the stress in the slab by up to 50% and stress in the slab support by up to 150% compared to internal loading (Manual M10, 1995). By their nature, joints are structurally weakening components of the system. Almost any type of crack in a slab (or unsealed joint) eventually allows water to enter the sublayers. This may facilitate erosion of the subbase with a subsequent loss of slab support. This increases slab deflection and shear stress on the jointing system. Material is displaced by erosion, or the subgrade subsides and a void develops under the slab leading to a further increase in stress until the stress is high enough to cause additional cracking in the slab. Thus, the response and effectiveness of joints are primary concerns in rigid pavement analysis and design.

A conceptual view of the mechanism of load transfer is presented in Figure 2.2. The concept of load transfer is fairly simple: stresses and deflections in a loaded slab are reduced if a portion of the load is transferred across the joint. Load transfer is important and fundamental to rigid pavement design procedures. Load transfer can vary with concrete pavement temperature (see paragraph 2.4), age,

moisture content, construction quality, magnitude and repetition of load and type of joint (Hammons and Ioannides, 1996).

When a joint is capable of transferring load, statics dictate that the total load (P) must be equal to the sum of that portion of the load supported by the loaded slab (P_L) and the portion of the load supported by the unloaded slab (P_U), i.e.:

$$P_L + P_U = P \tag{2.1}$$

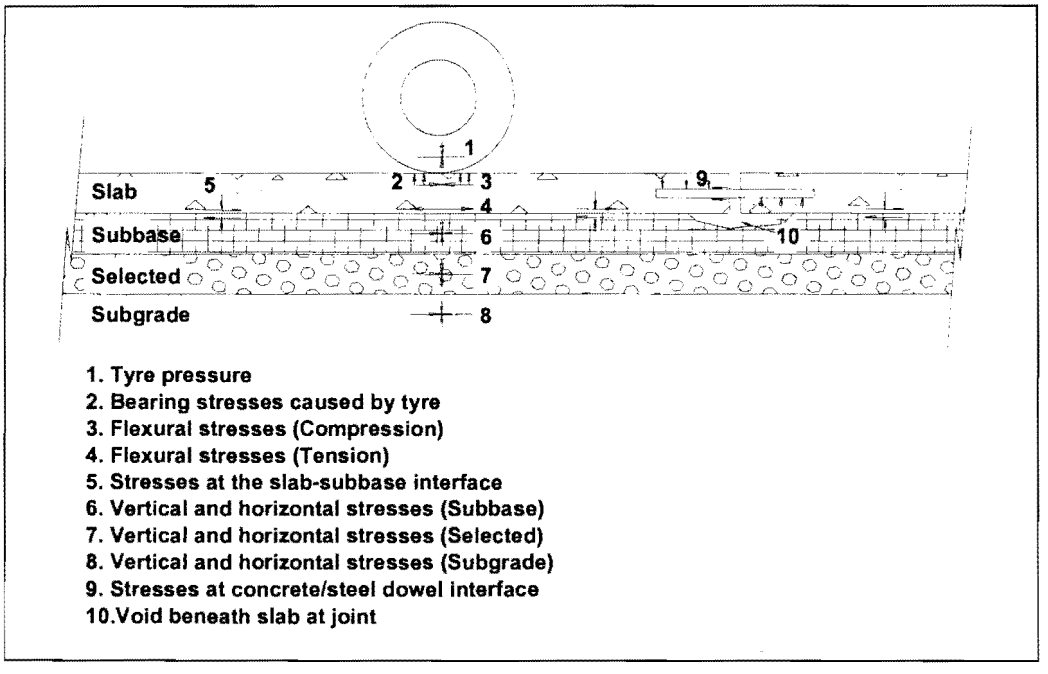

Figure 2.1: Typical rigid pavement system (Hammons and Ioannides, 1996)

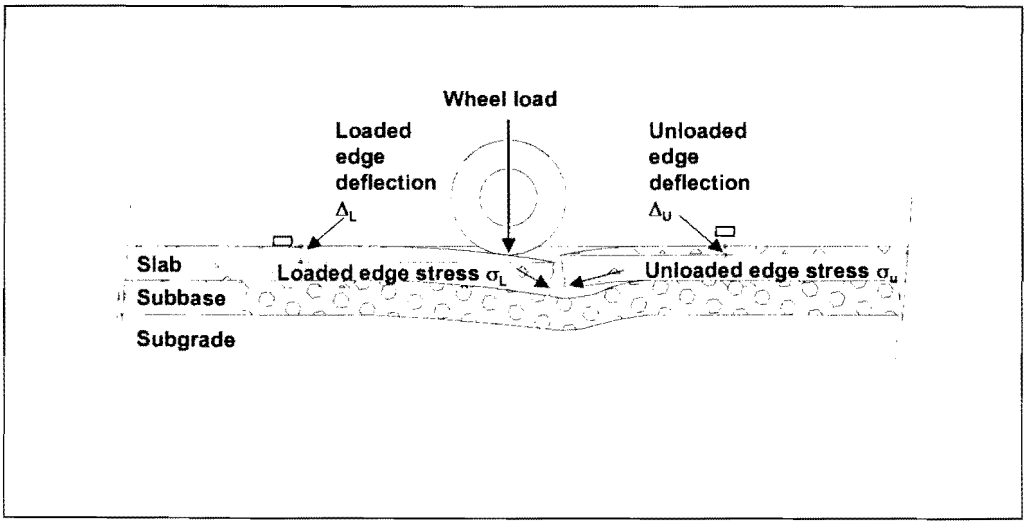

Figure 2.2: Concept of load transfer (Hammons and Ioannides, 1996)

Load may be transferred across a joint by shear or bending moments. However, it has been commonly argued that load transfer is primarily caused by vertical shear. In either case, the following relationship applies:

$$\sigma_L + \sigma_U = \sigma_f \tag{2.2}$$

Where:

σ_L = Maximum bending stress in the loaded slab;

σ_U = Maximum bending stress in the adjacent unloaded slab; and

σ_f = Maximum bending stress for the free edge loading condition.

Because maximum slab deflections are also directly proportional to applied load under the stated conditions, it follows from Equation (2.1) that

$$\Delta_L + \Delta_U = \Delta_f \tag{2.3}$$

Where:

Δ_L = Maximum edge deflection of the loaded slab;

Δ_U = Maximum edge deflection of the adjacent unloaded slab; and

Δ_f = Maximum edge deflection with no joint.

2.2.3 Load transfer definitions

Deflection load transfer efficiency (LTE_Δ) is defined as the ratio of the deflection of the unloaded slab (Δ_U) to the deflection of the loaded slab (Δ_L) as follows:

$$LTE_\Delta = \Delta_U/\Delta_L \; x \; 100 \; percent \tag{2.4}$$

The main load transfer mechanism in both doweled and un-doweled joints is shear (through dowel action and aggregate interlock), provided that the deflection load transfer efficiency (LTE_Δ), is in excess of about 80% (Ioannides, 1991).

Figure 2.3 illustrates load transfer efficiency in terms of deflection.

Stress load transfer efficiency (LTE_σ) is defined as the ratio of the edge stress in the unloaded slab to edge stress in the loaded slab as follows:

$$LTE_\sigma = \sigma_U/\sigma_L \; x \; 100 \; percent \tag{2.5}$$

Load transfer (LT) in the FAA rigid pavement design procedure is defined as that portion of the edge stress (σ_E) that is carried by the adjacent unloaded slab, as follows:

$$LT=\left[\frac{\sigma_U}{\sigma_f}\right]=\left[\frac{\sigma_E-\sigma_L}{\sigma_f}\right]=\left[1-\frac{\sigma_L}{\sigma_f}\right] \tag{2.6}$$

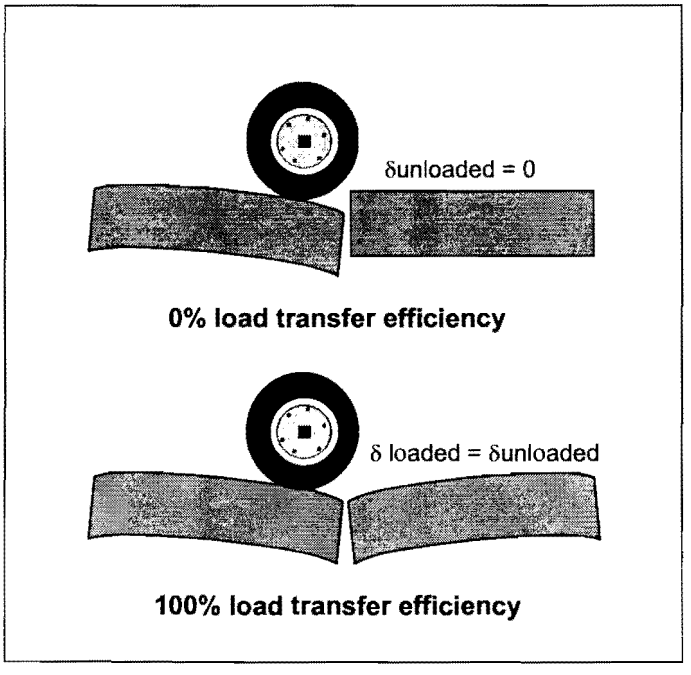

Figure 2.3: Illustration of 0% and 100% load transfer efficiency

The range of LTE_Δ and LTE_σ is from zero to one, while the range of LT is from zero to 0,5. Equation (2.6) can be related to Equation (2.5) as follows:

$$LT=\frac{LTE_\sigma}{1+LTE_\sigma} \tag{2.7}$$

The US Army Corps of Engineers' design criteria prescribe LT = 0,25, effectively reducing the design stress and allowing a reduced slab thickness. This accepted value is primarily based upon test sections trafficked from the mid-1940's to the mid-1950's (Hammons and Ioannides, 1996). If the load transfer assumption is violated through a degradation of the joint system, the pavement life can be significantly reduced.

2.2.4 Load transfer mechanisms

Load transfer at joints is accomplished by two primary load transfer mechanisms:

a) Dowel bars.
b) Aggregate interlock.

Dowel bars are often placed across a joint to provide load transfer through dowel action and to maintain slab alignment. Dowels are smooth, round bars with bond intentionally broken on one half to allow longitudinal movement of the slabs (see Figure 2.1).

Aggregate interlock is a load transfer mechanism that relies on shear forces developed at the rough vertical interface of a concrete pavement joint. These shear forces are caused by mechanical interlock between the rough vertical surfaces of the joint and by sliding friction (see Figure 2.4).

Deformed steel bars, often called *tie bars*, can be placed across the joint (normal to the plane of the joint) to hold slab faces in intimate contact. Bond between the concrete and bar develops in both slabs; thus movement normal to the joint is restrained. Diameter, length and spacing of tie bars are fixed by design criteria. However, load transfer due to dowel action of tie bars, is small in comparison to that provided by dowel bars.

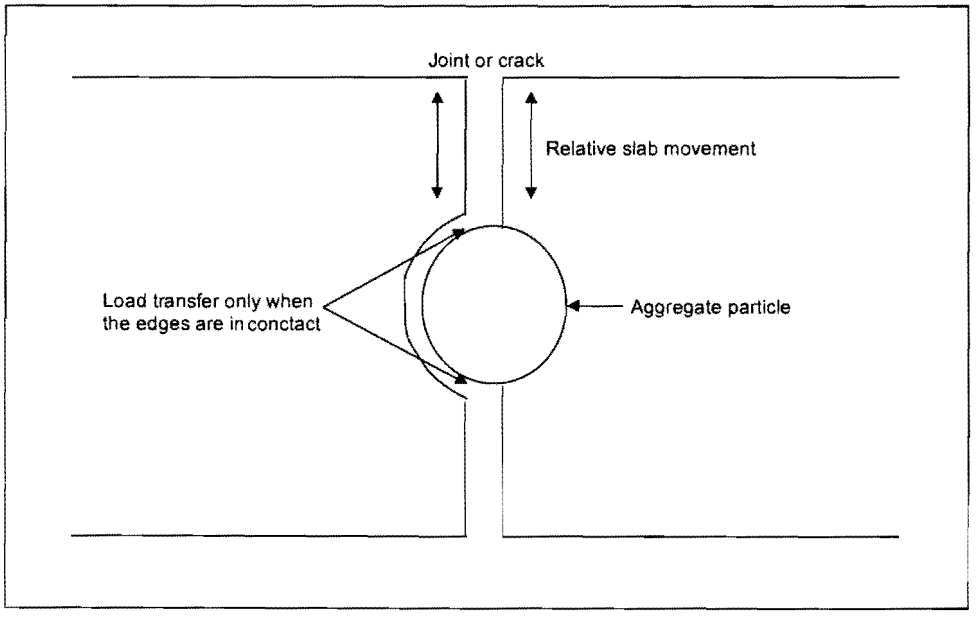

Figure 2.4: Effect of aggregate interlock at joints or cracks (Manual M10, 1995)

Figure 2.5 indicates the effect of different load transfer devices on relative movement, as determined for Manual M10: Concrete Pavement Design and Construction (1995). The top part of the figure shows the relative effect of dowel bars and the bottom part the relative effect of aggregate interlock.

The three major types of joints are:

a) Contraction joints.
b) Construction joints.
c) Isolation joints.

Contraction joints, used to control cracking in the concrete and to limit curling and warping stresses in the slab, are formed by introducing a weakened plane into the concrete and allowing a crack to form at the weakened plane. Typically, sawing a groove in the concrete while it is curing creates the weakened plane. Contraction joints may be plain (often called dummy joints), doweled, or tied (often called hinged joints).

Construction joints are required between lanes of paving and where it is necessary to stop construction within a paving lane. The two most common types of load transfer devices in construction joints are dowels and keyways.

Isolation joints are used at the intersections of pavements with structures, and in some cases, within pavements. Their primary purpose is to relieve compressive stresses induced by expansion of the concrete caused by temperature and moisture changes against relatively immovable objects such as foundations, drainage structures, and etcetera. Isolation joints may contain dowels or have thickened edges. To obtain load transfer at an isolation joint, a load transfer device is required (usually a dowel bar).

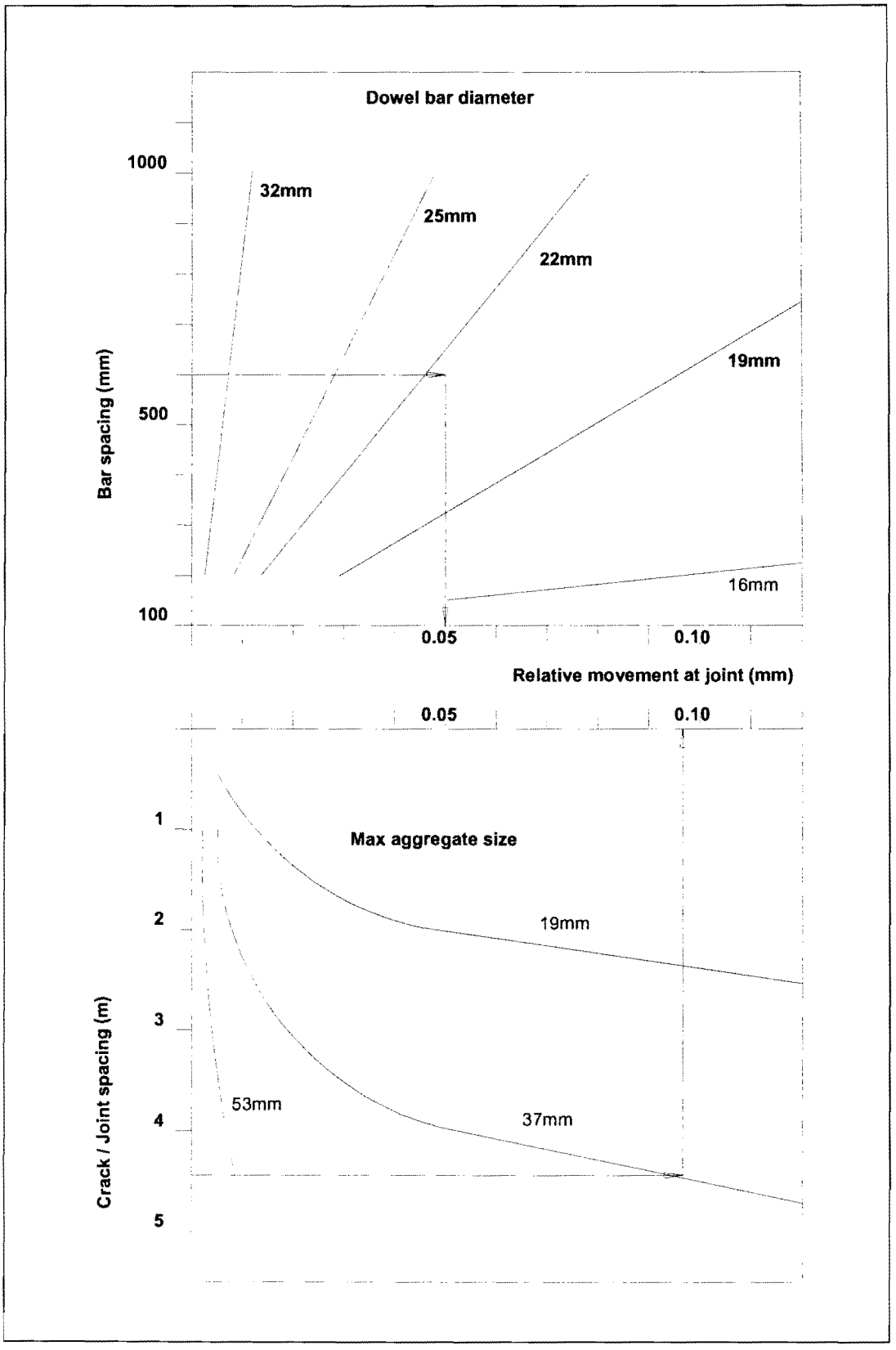

Figure 2.5: Effect of load transfer devices (Manual M10, 1995)

2.2.5 Rigid pavement foundations

The slab may be placed directly on the subgrade; however, most current practice has slabs placed on an unbound or bound subbase. Such subbase layers may be constructed to:

a) Provide uniform bearing support for the pavement slab.
b) Provide a construction platform.
c) Protect the subgrade from frost effects (not normally applicable to South African conditions).
d) Produce a suitable surface for operating construction equipment.
e) Improve foundation strength.
f) Prevent subgrade pumping.
g) Provide drainage of water from under the pavement.

An unbound subbase may be a densely graded granular material or an open-graded or free-draining granular material. The subbase may be bound with Portland cement, a lime-fly ash blend, bitumen, or other agent.

One or more subbases may be present in the pavement system. These subbases may be a lesser quality material and may be chemically stabilised. The subbase provides additional strength to the pavement system, provides more uniform support over variable soil conditions, and may provide protection against frost damage and swelling. Stabilised subbases need to be structurally considered as part of the concrete slab, rather than as part of the subgrade.

The subgrade is naturally occurring soil, compacted naturally occurring soil, or compacted fill. It may be subject to pumping, collapsing sands, frost damage, swelling (expansive soils/clays), or unstable (earth fills). Subgrade soils will have different values of strength depending on its soil classification, moisture conditions, and compaction.

2.2.6 Summary of rigid pavement system

In summary, the rigid pavement system has been defined as a pavement structure in which the primary load-supporting element comprises a rigid layer/slab constructed from relatively thin Portland cement concrete (Manual M10, 1995). Concrete slabs are finite in length and width and are constructed over one or more foundation layers (Hammons and Ioannides, 1996). Dowels bars or aggregate interlock at contraction, construction, or isolation joints accomplishes load transfer. The foundation layers or subbase primarily have to provide uniform bearing support for the pavement slab and as such need to be of high quality material.

2.3 OVERVIEW OF HISTORICAL DEVELOPMENTS

2.3.1 Introduction

A survey of past developments of rigid pavement design theory is presented, with specific reference to the work done by Westergaard, and the limitations of his theory, together with a literature review of available rigid pavement response models, including two- and three-dimensional finite element techniques. This provides insight into the current state-of–the-art of rigid pavement analysis tools.

This paragraph also presents a short overview of the development of the South African concrete pavement design manual (Manual M10), as well as the main reason for the motivation of the research presented in this thesis.

2.3.2 Westergaard theory

The design of rigid pavements and the name Westergaard have been synonymous for the past 80 years.

Professor Harald Malcolm Westergaard published a series of papers containing relationships for calculating stresses in rigid pavements based upon elastic theory. His pioneering work was first published in Danish in 1923 (Westergaard, 1926). However, this work was not widely read, and in 1926, he published a method in English for calculating stresses in rigid pavements (Westergaard 1926). He developed relationships for stresses *by assuming the slab to act as a homogeneous, isotropic, elastic solid in equilibrium, and by assuming that the reactions of the subgrade to be vertical only and to be proportional to the deflections of the slab* (Westergaard, 1926; Hammons and Ioannides, 1996).

Westergaard characterized the subgrade by the *modulus of subgrade reaction (k)*, which is a measure of the stiffness of the subgrade, and is defined as the reactive force (pressure) generated by unit displacement (deflection) of the subgrade surface. Subgrade reaction (k) is normally determined from a loading test on a circular plate, 762 mm (30 inch) in diameter (ASTM D1196-93, 1997). To minimize bending, a series of stacked plates should be used. The load is applied to the plates by a hydraulic jack. A steel beam tied to heavy mobile equipment can be used as the reaction for the load. Three dial gauges located at the outside edge, 120 degrees apart, measure deflections of the plate. The support for the deflection dials must be located as far from the loaded area as possible, usually not less than 4,5 m (15 feet). Figure 2.6 is a schematic layout of the plate-loading test. The load is applied at a predetermined rate until a pressure of 70 kPa (10 psi) is reached. The pressure is held constant until the deflection increases not more than 0,025 mm (0,001 inch) per minute for three consecutive minutes.

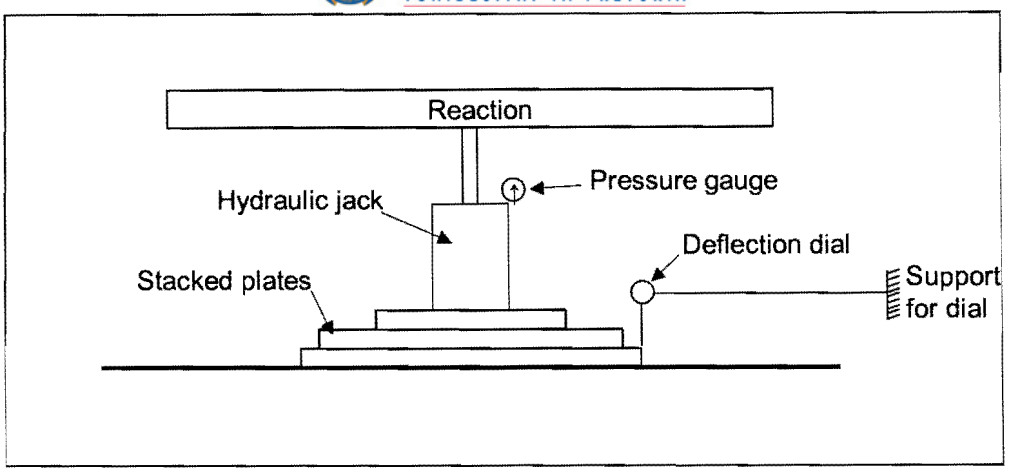

Figure 2.6: Schematic layout of plate loading test (Huang, 1993)

The average of the three dial readings is used to determine the deflection. The modulus of subgrade reaction is then given by:

$$k = \frac{p}{\Delta} \tag{2.8}$$

Where:

p = Pressure on the plate (kPa or psi); and

Δ = Deflection of the plate (mm or inch)

The principles of dimensional analysis were used in the interpretation of data pertaining to the response of rigid pavement systems, derived from either field measurements or from analytical studies (Ioannides, 1990). The governing principle was stated as follows: "The fundamental relationships in the physical world are essentially non-dimensional, existing between non-dimensional independent variables and non-dimensional dependent variables. This is self evident, since order in nature pre-existed the conventional definitions of units of measurement."

On the basis of this hypothesis Ioannides (1990) showed that the fundamental independent variable determining the response of a slab relative to the subgrade (analysed using plate theory), is the dimensionless load size ratio (a/l), where a is the radius of the loaded area and l is the radius of relative stiffness of the slab-subgrade system. This term in the Westergaard theory that quantifies stiffness of the slab relative to that of the subgrade, is expressed by the following relationship:

$$l = \sqrt[4]{\frac{E_c h^3}{12(1-\mu^2)k}} \tag{2.9}$$

Where:

E_c = Modulus of elasticity of concrete (MPa);

h = Concrete slab thickness (mm); and

μ = Poisson's ratio of concrete.

In Equation (2.9) it is assumed that the response of a slab can be compared to that of a plate on a bed of springs, the so-called Winkler foundation. Westergaard (1926) solved for the ratio $\sigma h^2/P$ as a function of ratio a/l where σ is the maximum stress, P is the magnitude of the applied load, and a is the radius of the circular area upon which the applied load acts for the following three cases:

a) Wheel load close to the corner of a semi-infinite slab (critical stress at the top of the slab, causing corner breaks).

b) Wheel load at the interior of an infinite slab (critical tension occurs at the bottom of the slab under the centre of the load circle).

c) Wheel load at the edge of a semi-infinite slab (critical stress is a tension at the bottom of the slab under the centre of the load circle).

Westergaard considered two cases for the edge load case:

a) The load distributed over the area of a full circle, or

b) The entire load distributed over the area of a semi-circle (the more severe case if the tyre was operating on the very edge of the pavement with no support under half of the tyre, as occurs on a severely faulted pavement).

During 1933 Westergaard modified his 1926 formulae to reflect the conditions of the Road Tests conducted at Arlington, VA, in 1932. Westergaard extended his procedures to airfield pavements in 1938, again revising his formulae to account for the larger contact area of aircraft tyres (Westergaard 1941).

Although Westergaard considered the interior, corner, and edge loading cases in his early works, he concentrated on interior loadings. Ioannides, Thompson and Barenberg (1985) found that several of the equations ascribed to Westergaard in the literature are incorrect due to typographical errors or misapplication. They also reported that the 1926 equation for edge loading was incorrect.

It was not until 1947 that Westergaard (1947) published relationships that were valid for computation of stresses caused by edge loading of large wheel loads on large contact areas. His revised formulas allowed the load to be characterised as an ellipse rather than being limited to a circular tyre print. Ioannides, Thompson and Barenberg (1985) recommended the use of these equations as being more accurate than the 1926 equations.

Still, several investigators noted repeatedly that although the Westergaard solutions agreed fairly well with their observations for the interior loading condition, it failed to give even a close estimate of the response of the edge and corner loading. Ioannides, Thompson and Barenberg (1985) felt that the time-honoured Westergaard solutions deserved a thorough re-examination, using the tool of finite element analysis (ILLI-SLAB). They developed improved expressions for maximum corner loading responses, as summarised in Appendix A.

During 1951 Pickett and Ray (Hammons and Ioannides, 1996) developed graphical solutions for the Westergaard theory in the form of response charts. These charts / nomograms were presented for four different load cases: interior loading assuming a dense liquid subgrade, interior loading assuming an elastic solid subgrade, edge loading assuming a dense liquid subgrade, and load placed at *l*/2 from an edge assuming a liquid subgrade.

2.3.2.1 Westergaard theory limitations

There are several limitations to the Westergaard theory, namely (Hammons and Ioannides, 1996):

a) All pavement layers below the slab must be represented by a single parameter, the modulus of subgrade reaction. In practice, however, a pavement normally has several layers of materials, including bound or unbound subbases and selected layers with each layer having an increase in quality and stiffness. This leads to a decrease in exactness of the analysis.

b) The foundation layer is assumed to respond linear-elastically. Most subgrade materials are non-linear, stress-dependant and change with time and environment.

c) It was assumed that the slab is in full contact with the subgrade at all points. It does not therefore take into account voids developed due to pumping, or slab/subgrade separation due to warping and curling.

d) Westergaard assumed the slabs were infinite (for the interior load case) or semi-infinite (for the edge and corner load cases); the slabs extend far enough from the loaded area that boundaries (discontinuities such as joints or cracks) have no effect on the solution. In practice this is not the case, because rigid pavement slabs tend to be relatively narrow and have many cracks and joints.

e) Load transfer cannot be directly modelled. Load transfer is assumed to be a constant 25 percent for airport pavement design. A more rational method of analysing load transfer is required for mechanistic evaluation of rigid pavements.

f) The thickness of the slab must be uniform, which makes it impossible to analyse thickened edge slabs or slabs of non-uniform thickness.

In a recent study conducted by Ioannides et al. (1999), they reconsidered the Westergaard solution to curling due to temperature differentials, and noted the following further limitations to the Westergaard theory:

a) The slab was assumed to have continuous contact with the subgrade (infinite slab self-weight).

b) It was assumed that the principle of superposition with regard to the summation of load-induced and thermal stresses could be applied.

c) Assuming a linear temperature variation through the slab thickness was considered adequate.

d) The slab response under night time conditions was assumed to be a mirror image of the corresponding behaviour under daytime conditions.

2.3.3 Elastic layer theory

The elastic layer theory was first formulated for a point load and one layer by Boussinesq and later generalised for a uniformly distributed load acting over a circular area and two or more layers, by others. Where manual solutions of one- or two-layer elastic systems to one circular load were cumbersome, computerised solutions have made it possible to analyse a system of many layers subjected to multiple loads. Among these programmes are BISAR, CHEVRON, ELSYM5, and JULEA.

The basic assumptions of the elastic layer theory are:

a) All materials in the system are assumed to be homogeneous, isotropic, and linear elastic; thus each pavement layer can be represented by three parameters: thickness, modulus of elasticity, and Poisson's ratio. Each layer may have different elastic properties.

b) Each layer is infinite in horizontal extent, and the bottom layer extends vertically to infinity.

c) The load is static and is uniformly distributed over one or more circular areas. Most programmes assume the load to be entirely vertical, although some can accommodate horizontal components.

d) The layers are continuously in contact. Also, the degree of restraint between adjacent layers must be assumed. Common assumptions are that the adjacent layers are fully bonded or that they are frictionless. Some programmes can allow any degree of restraint between these two extremes.

Because of the assumptions of the elastic layer models, it holds certain limitations for the analysis of rigid pavements:

a) Joint and cracks in rigid pavements are ignored, as the model assumes each layer to be infinite in horizontal extent. Cracks in stabilised layers are also ignored.

b) Each material is assumed to be linear elastic, leading to inconsistencies in stress calculations in the foundation layers.

For the case with an elastic solid foundation the radius of relative stiffness (l) is expressed as follows:

$$l = \sqrt[3]{\frac{E_c h^3 (1-\mu_s^2)}{6(1-\mu^2)E_s}} \qquad (2.10)$$

Where:

E_s = Modulus of elasticity of the soil (MPa); and

μ_s = Poisson's ratio of the soil.

The difference between a spring-supported Winkler foundation and an elastic solid foundation is illustrated in Figure 2.7. Although the elastic solid foundation is often considered as a more realistic soil representation, it has not been used extensively in concrete pavement analysis and design. This is probably because elastic solid is a continuum model, and sometimes fails to simulate the behaviour of real soils, which are particulate media, especially under conditions of edge and corner loading (Khazanovich and Ioannides, 1993).

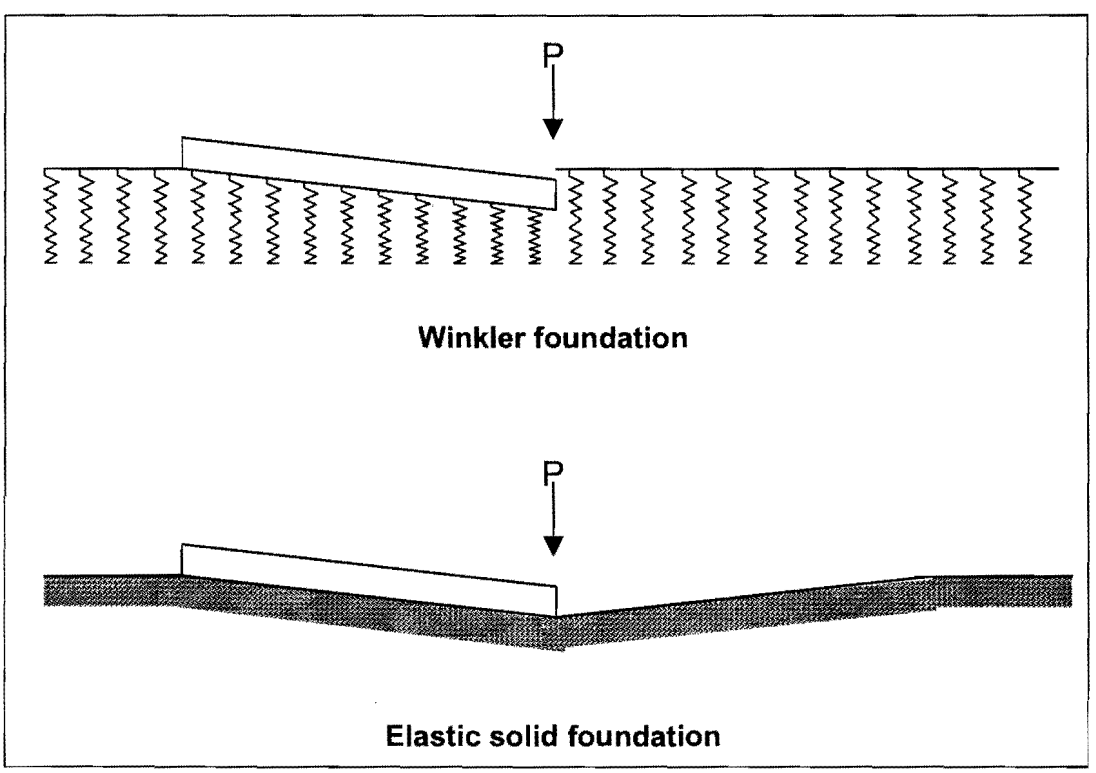

Figure 2.7: Foundation displacement under a loaded plate for Winkler and elastic solid foundations (Hammons and Ioannides, 1996)

2.3.4 Finite element model development

The finite element (FE) method is a powerful numerical analysis technique that has been successfully used to solve a broad class of boundary value problems in engineering. The FE method to model joint and edge discontinuities has led to its emergence as the analysis method of choice for rigid pavement research (Hammons and Ioannides, 1996). In line with this statement, it is remarkable to note that up to approximately 1994, most of the FE research studies conducted were two-dimensional (2D), whereas there are a relatively large number of three-dimensional (3D) studies that were published during the period 1994 to 1999.

Certain key attributes of the more common FE programmes as reported in the literature are summarised in Tables 2.1 (2D studies) and 2.2 (3D studies).

Table 2.1: Overview of 2D FE models for rigid pavements (Hammons and Ioannides, 1996, with modifications by author)

Programme name	Slab model	Load transfer	Foundation model(s)
ILLI-SLAB (Tabatabaie and Barenberg, 1980)	2D medium thick plate	Linear spring, beam element on spring foundation	Winkler, Boussinesq, non-linear, two- and three-parameter models
ILLI-SLAB (Ioannides et al. 1985b)	2D medium thick plate	Linear spring, beam element on spring foundation	Winkler, Boussinesq, two-parameter models
ILLI-SLAB (Ioannides and Korovesis, 1990)	2D medium thick plate	Linear spring, beam element on spring foundation	Winkler
ILLI-SLAB (Khazanovich and Ioannides, 1993)	2D medium thick plate	-	Winkler, Boussinesq, non-linear, two- and three-parameter models
WESLIQID (Chou, 1981) and KENSLABS (Huang, 1993)	2D medium thick plate	Linear springs	Winkler
FEACONS III (Wu et al., 1993)	2D medium thick plate	Linear and torsional springs	Winkler
GEOSYS (Ioannides et al., 1985b)	3D brick element	None	3-D brick elements with stress-dependent subgrade model
ABAQUS (Kuo, 1994)	2D shell element 3D brick element	Linear and non-linear springs, interface elements, gap elements, multipoint constraints, explicit models	Winkler, 3-D brick element with linear and non-linear elastic, plastic, and visco-elastic constitutive models, user-defined models
DYNA-SLAB (Chatti et al, 1994)	2D plate element	Linear spring, beam element on spring foundation	Winkler and layered visco-elastic solid
ILLI-SLAB and JSLAB (Masad et al, 1997)	2D medium thick plate	Friction	Linear solid
ILLI-SLAB (and HVS) (Coetzee, 1989)	2D medium thick plate	Linear springs	Winkler

Table 2.2: Summary of features of 3D FE studies

Programme name	Loading	Slab(s)	Subbase layer(s)	Foundation	Dowels	Aggr. interl.
GEOSYS (Ioannides and Donnelly, 1988)	Static	Linear 8-noded brick elements		Non linear solid		
(Channakeshawa et al., 1993)	Static and temperature	Multiple and non linear		Winkler	Beams	
ABAQUS (Zaghloul et al., 1994)	Dynamic	Multiple and non linear	Non linear solid	Non linear solid	Bars	Friction
ABAQUS (Uddin et al., 1996)	Dynamic (FWD)	Multiple and linear	Linear solid	Linear solid	Beams	Friction
ABAQUS (Kuo et al., 1996)	Static and temperature	Multiple and linear	Linear solid	Winkler	Beams	Springs
ABAQUS (Hammons, 1998)	Dynamic (FWD)	2D shell 3D hexahedral	3D hexahedral	Winkler		Springs
Various programmes (Zaman and Alvappillai, 1995)	Static and dynamic	Linear		Winkler		
NIKE3D (Brill and Lee, 1999a, 1999b)	Static	Linear	Linear solid	Linear solid		
EverFE (Davids et al., 1998a, 1998b)	Static and temperature	Linear elastic	Linear elastic	Winkler	Beams	Shear

It is widely accepted that 3D FE models are necessary to adequately capture the structural response of rigid pavement systems (Lourens and Strauss, 1988; Davids et al., 1998a). However, there are still areas that must be addressed if realistic 3D finite element models are to be routinely used for the evaluation, retrofit, and design of rigid pavements:

a) Beyond permitting dowel slip, dowel-slab interaction has not been considered, except by Channakeshawa et al. (1993), and more recently by Davids et al. (1998a). EverFE models the portion of the dowels within the slab using an embedded quadratic beam element. This ensures no loss in solution accuracy over a conventional formulation and permits the dowel to be de-bonded by releasing the dowel's axial degrees of freedom (Davids et al., 1998a). Paragraph 2.5 describes dowel modelling techniques in more detail.

b) Aggregate interlock has mostly been modelled using linear spring elements (Kuo et al., 1996), or assuming classical friction behaviour (Masad et al., 1997; Uddin et al., 1996; Zaghloul et al., 1994). In attempting to validate the use of ABAQUS for 3D FE modelling of joints in concrete airport pavements, Hammons (1998) also studied the aggregate interlock of joints in the *subbase* beneath the concrete slab. Both the joints in the concrete and in the subbase were modelled as springs across the crack. This approach did not capture the actual mechanism of aggregate interlock. In developing his aggregate interlock model for EverFE, Davids et al. (1998a) chose the two-phase constitutive model developed by Walraven (1981; 1994) to model aggregate interlock shear transfer (see paragraph 2.5). Laboratory studies are still required to determine optimal parameters for this model. *Load transfer across pavement joints due to aggregate interlock has to be determined under a variety of loadings, geometries, and joint openings for design purposes.*

c) Up till recently, the 3D FE models available could only be used in research applications due to computational requirements. During their research study, Lourens and Strauss (1988), made an attempt to develop nomograms for the mechanistic design of continuously reinforced concrete pavements, using finite element techniques. This was in an attempt to bridge the gap between sophisticated (first-world) design methods and the need for practical and directly applicable designs in remote (third-world) areas. This was also the method used to design the continuously reinforced concrete overlay during the rehabilitation of the N1 Ben Schoeman freeway between Buccleuch and Brakfontein Interchanges. Similarly, nomograms/response charts need to be developed (or existing response charts refined) for the mechanistic design of doweled jointed concrete pavements. Davids et al. (1998a), on the other hand, developed EverFE with the specific aim to make a 3D model available for implementation on desktop computers.

2.3.5 Rigid pavement joints

Early work by the US Corps of Engineers showed that design thickness of rigid pavement slabs was controlled relative to fatigue cracking, by the tensile stresses that occurred at the edges of the pavement slabs (Hammons and Ioannides, 1996). They conducted accelerated trafficking tests under controlled conditions during 1943. The tests were designed to permit a comprehensive evaluation of many of the factors influencing rigid pavement design. Each of the tests contained extensive strain and deflection measurements at slab interiors, edges and corners.

This work indicated that increasing the efficiency of joints through improved design methods reduced the edge stresses at both transverse and longitudinal joints. The transferral of loads across joints in a pavement is desirable to reduce the independent vertical movement of adjacent slabs and reduce the occurrence of distresses like spalling, faulting, and effects due to pumping (i.e. differential displacement).

The following ranking of joint types from the most to the least effective in terms of load transfer was made by Sale and Hutchinson (1959) based on the performance of test items in the Lockbourne No 2 Test Track:

a) Doweled contraction joint.
b) Doweled construction joint.
c) Keyed construction joint with tie bars.
d) Contraction joint.
e) Keyed construction joint.
f) Doweled expansion joint.
g) Free-edge expansion joint.

For doweled joints in thick concrete pavements, it was found that there was no apparent advantage in using structural shapes over conventional round bars (Hammons and Ioannides, 1996).

Observations at test tracks at Lockbourne and later at Sharonville, Ohio (Sale and Hutchinson, 1959), indicated that load transfer at doweled joints also varied with the methods of doweled joint construction. At both Lockbourne and Sharonville, the concrete slabs were cast against forms, and the dowels were locked into place in the forms. At Lockbourne, the dowels were installed by bonding one end in the concrete, pulling the forms off over the dowels, painting and greasing the exposed half of the dowel and then paving the adjacent lane. At Sharonville the dowels were installed by painting and greasing the end of the dowel in the first paving lane, turning and removing the dowel, removing the forms, reinserting the painted and greased end of the dowels into the same hole from which they were removed, and bonding the exposed end of the dowel into the adjacent lane. Strain gauges and deflection gauges were installed in the pavement on each side of the joints at both test tracks. A load cart with a twin tandem assembly was used to load the track in each case. The dowel installations at Lockbourne and Sharonville are shown graphically in Figure 2.8.

The most important result from these tests is that the construction method used at Lockbourne (in which the first end of the dowel was bonded) performed better (higher load transfer) than the construction method used at Sharonville. In both cases better load transfer was measured when the slab with the bonded end of the dowel was loaded, than when the slab with the un-bonded end of the dowel was loaded. Thus it was recommended that the dowels be installed with no manipulation of the dowel after concrete was placed to maximize the load transfer obtained by the doweled joint. Furthermore, load transfer across doweled joints resulted in an edge stress reduction of 25 percent. The load transfer computed from deflections was more than the load transfer computed from stresses. The load transfer across joints in multi-layer pavements is about the same as load transfer in single slab construction.

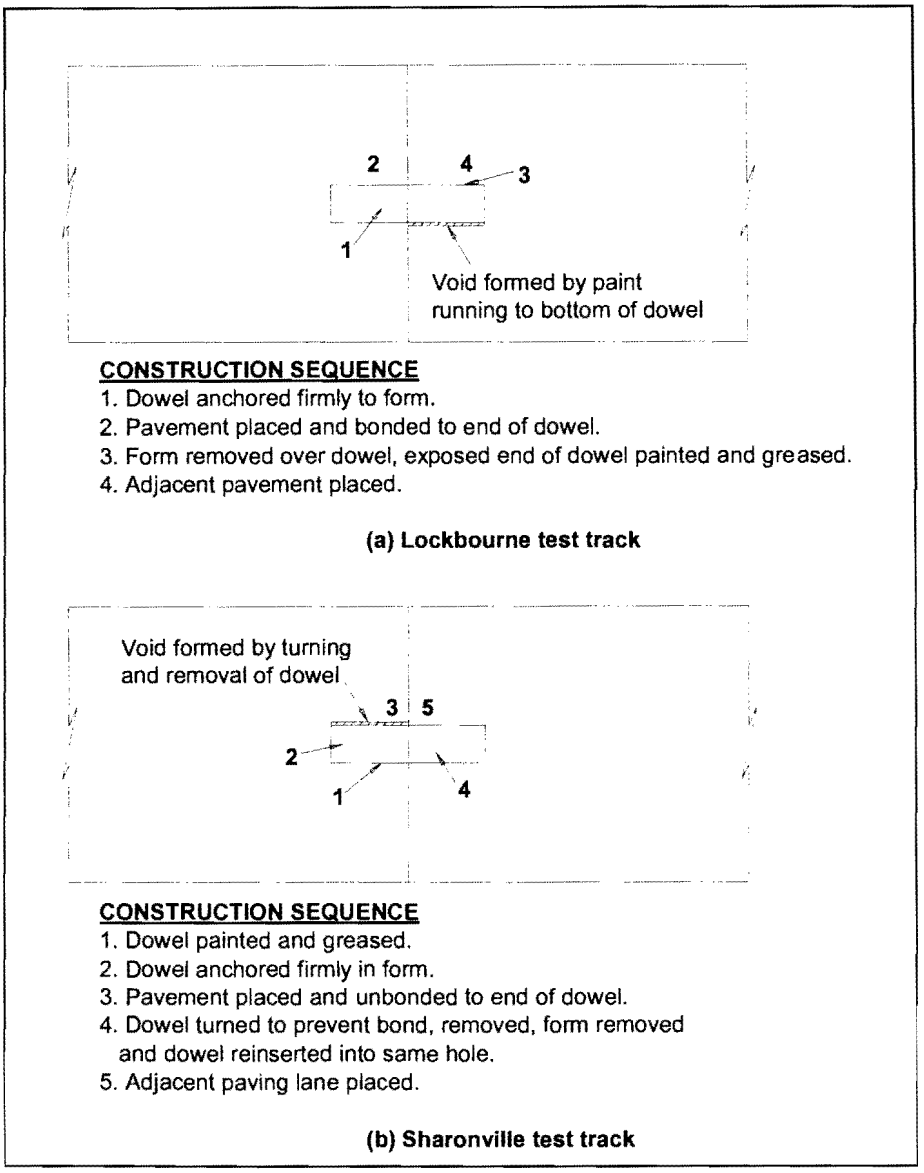

Figure 2.8: Dowel installations at Lockbourne and Sharonville Test Tracks (Sale and Hutchinson, 1959)

2.3.6 The effects of moment and inertia

The effects of moment and inertia were specifically investigated in order to gain an understanding of what the effect of a moving load could be on the load transferred across a crack/joint in a concrete pavement. One of the most common methods used in practice to determine deflection load transfer efficiency at a joint in a concrete pavement is by using a falling weight deflectometer (FWD). With the FWD, a static impulse load is applied by dropping a load onto the pavement on the one side of a crack/joint, and measuring the deflection at both sides. The deflection load transfer efficiency is then calculated using Equation (2.4). In practice, however, the loads applied to a pavement are not "one-

sided", but a dynamic load is transferred from one slab to the next. The response of the slabs therefore had to be captured under dynamic loading as well as under static loading to be able to capture real-life conditions and to compare the results.

The dynamic response of a pavement is fundamentally a function of the inertia and damping characteristics of the structure (Huang, 1993). These characteristics generally invalidate attempts to approach the problem with static or quasi-static analyses and experiments. In a study by Lourens (1991) the equation for motion was formulated as follows:

$$\{F\} = [K]\{u\} + [C]\{\dot{u}\} + [M]\{\ddot{u}\} \tag{2.11}$$

Where:

$\{F\}$	=	Vector of nodal point forces;
$[K]$	=	Stiffness matrix;
$\{u\}$	=	Vector of nodal point displacements;
$[C]$	=	Damping matrix;
$\{\dot{u}\}$	=	Vector of nodal point velocities;
$[M]$	=	Mass matrix; and
$\{\ddot{u}\}$	=	Vector of nodal point accelerations.

The last two quantities in Equation (2.11) are exclusive to dynamic analyses and need some clarification. The term $[C]$ is necessary to dampen the induced movement, as an un-dampened system will oscillate up to infinity in time after acceleration. Damping therefore defines the loss of energy due to friction and other effects. The mass term $[M]$ and acceleration $\{\ddot{u}\}$ is Newton's Second Law of Motion, and can be viewed as the inertial effect or "resistance to movement" which is experienced when an attempt is made to accelerate an object.

Measurements on pavements and vehicles have shown that the frequency of dynamic loads at a discontinuity in a pavement stay more or less constant at about 3 Hz, and is apparently not affected by the speed of the vehicle (Papagiannakis et al., 1988; Sousa et al., 1988, Steyn and Visser, 2001). The forces developed by the vehicles vary according to a host of factors, the most important being the road roughness and suspension type, although contradicting results have been reported on this aspect. The dynamic forces reported were nearly always substantially higher than the static forces (Papagiannakis et al., 1988; Sousa et al., 1988), and measured forces of up to 150% of the static values have been reported (Bergan and Papagiannakis, 1984).

On the other hand, it was found that deflection and strain values generally decreased with increased speeds (Steyn and Visser, 2001). Stress values generally remained constant with increased speeds. Load magnitude showed good relationships with stresses in the upper part of the pavement structure, while load speed showed good relationships with the strains in the pavement structure. The expected

pavement lives calculated using the response parameters from a moving constant load analysis caused higher expected lives than when doing the calculation using static load data. The analysis of data from all the pavement response analysis methods used by Steyn and Visser (2001) at all load and speed conditions, indicated that the calculated stresses were not affected by load speed to the same magnitude as the calculated strains in flexible pavements.

Despite the fact that there is a difference between the response of the pavement under dynamic loading to the response under static loading, the static loading testing method, using the FWD still takes precedence. The main reason is that the equipment used for the FWD is less expensive than for, for example Weigh in Motion (WIM) or Stress in Motion (SIM) stations. On the other hand back-calculation from FWD data is a two-dimensional problem, and therefore simpler and more commonly used, whereas back-calculation from WIM/SIM data is a three-dimensional problem, requiring more sophisticated and time consuming methods.

2.3.7 A mechanistically and risk based design method for concrete pavements in southern Africa (Strauss et al., 2001)

A study was initiated in 1988 to investigate the performance of rigid pavements in South Africa and to develop design techniques based on South African experience (Strauss, 1992). The research study involved a field evaluation, laboratory study (Malan et al., 1988) and the development of a modelling technique based on finite element analysis.

During modelling of the pavements under investigation, significant differences in behaviour occurred for loading at the interior and loading at an edge or corner of a slab, emphasising the fact that edge load transfer has a marked influence on the performance of the pavement.

Evaluating the effectiveness of aggregate interlock for different types of mixes, an increase in relative movement was obtained with an increase in crack width. For the same crack width, concrete that cracked at 28 days allow ten times more relative vertical movement before aggregate interlock is enacted than concrete cracked at 3 days of concrete age. The same applied for concrete mixes with 25 mm aggregate, which showed 30 times more relative vertical movement than 50 mm aggregate concrete.

From this study, Strauss (1992) compiled an equation to predict the relative movement that takes place at an aggregate interlock joint in a concrete pavement, as follows:

$$y(x) = 114000 \frac{x^3}{agg^{4,5}} \qquad (2.12)$$

Where:

$y(x)$	=	Relative vertical movement (mm);
x	=	Crack width (mm); and
agg	=	Nominal size of 20% biggest particles in concrete mix / maximum aggregate size (mm) in concrete mix.

Equation (2.12) accepts that the age of cracking cannot be controlled, and assumes all cracks developed within 7 days. The research done by Strauss (1992) evolved into the production of Manual M10 (1995). Most of the design curves used in this manual were developed using linear elastic layered theory together with finite element analysis and were confirmed against presently used design procedures. The manual essentially followed a "recipe-type" approach to design and used a series of nomograms. The design process consisted of the following basic steps:

a) Estimating traffic loads and volumes.
b) Assessment of slab support conditions.
c) Joint design and load transfer mechanism identification.
d) Determining slab properties.
e) Calculation of concrete slab thickness.

The structural design of concrete overlays on flexible pavements was also included in Manual M10 (1995). The same theoretical base as for new pavements was used. Due to the fact that it is easy to determine the deflections of the surface to be overlaid, and that most settlement was assumed to have taken place, it was considered that the overlay design could be done with a higher degree of certainty than the design of new pavements.

Specifically for joint design, it was stated that load transfer efficiency could be improved by:

a) Large (greater than 26,5 mm) durable coarse aggregate.
b) Dowels.
c) Reduced joint opening.
d) Stiff subbases.

Specific guidelines for dowel design were also given in the manual, together with guidelines for the functional design parameters such as skid resistance, noise, glare and roughness. The manual also contained typical specifications for the construction of the underlying pavement layers, as well as for the concrete pavement itself.

Equation (2.12) was incorporated as the aggregate interlock model of Manual M10 (1995). However, this equation was only accurate for concrete constructed with a maximum aggregate size of around 26,5 mm; the aggregate used in the concrete constructed for the laboratory studies (Malan et al., 1988).

This will be demonstrated in more detail in the chapter dealing with the laboratory studies conducted for this thesis (Chapter 3).

The South African concrete pavement fraternity recognized the need to upgrade the South African Concrete Pavement Design and Construction Manual (Manual M10, 1995), to a manual based on mechanistic design principles with the aim of increasing the market share for concrete roads. It became apparent from overseas research, performance of local pavements and some instrumented sections of a concrete inlay on the National Route 3, that current concrete design methods were inherently conservative and consequently resulted in expensive pavements.

A number of strategy sessions identified the need for a departure from existing practice. A new design method was needed that utilised a mechanistic approach and would result in more cost-effective pavements (for equivalent performance to asphalt pavements). This approach is fuelled by the fact that concrete pavements are increasingly utilised as overlays on old flexible pavements where characteristics are determined through linear elastic theory and software packages. An integration of flexible and rigid mechanistic design approaches is therefore becoming more and more important. The new method was, however, to be pragmatic and aimed at ordinary pavement design practitioners rather than researchers and academics.

Simultaneously it was also decided to develop a simple, user-friendly software programme as part of the manual. Among the critical input parameters that were identified at the outset of this whole process, was an aggregate interlock load transfer constant, Ca. The fact that the format of the aggregate interlock equation itself was still uncertain was emphasized and it was recognised that further research was required to ascertain a more accurate, mechanistic formula.

A survey of the South African road network indicated that the great majority of structural failures of road pavements could be attributed to construction and materials problems. Structural failures were thus caused by deficiencies built into the pavement, which were aggravated by traffic and environmental factors. It was also established that the traditional approach, using single values for input parameters, was not ideal as uncertainty in the input was not translated into uncertainty in the output and therefore in the inherent risk of the design.

The design package had therefore to incorporate variability of the different parameters. Its structure should also enable it to be used to assess the relative effects of poor construction, higher than planned for variation in properties and to develop a bonus/penalty scheme for contractual purposes.

The basic principles incorporated in the new manual and the software programme, as well as a description of input data and interpretation of the output is given below. The specific area where the research conducted for this thesis had to make a contribution to the design modelling is also pointed out in the following paragraph.

2.3.7.1 Modelling of performance

Based on the requirement that the design procedure should be user friendly and that the software needed to run on relatively inexpensive and readily available hardware, the use of sophisticated methods in calculating pavement response was precluded. However it was recognised that, in order to develop suitable pavement response and performance models, the latest technological tools had to be employed. The decision was therefore made to develop a database using finite element techniques, multi-layer analysis software packages, instrumented pavement sections measuring dynamic effects and the actual performance of the concrete road network to develop performance equations.

Maximum tensile stress in a concrete slab that is placed on an elastic support can be calculated using several methods (Hogg, 1938; Skarlatos and Ioannides, 1998), the most familiar being Westergaard (1926). The following relationship indicates the basic format of these theories:

$$\sigma = f\left(C, \frac{P}{h_1^{\,2}}, \sqrt[4]{\frac{D}{K}}\right) \qquad (2.13)$$

Where:

σ	=	Maximum tensile stress close to a joint or crack in the pavement (MPa);
C	=	A coefficient that primarily depends on load/slab configuration and load transfer at a crack or joint (mm);
D	=	Slab stiffness (MPa);
K	=	Slab support modulus (MPa);
P	=	Load (kN); and
h	=	Slab thickness (mm).

Tensile stress close to the joint or crack is calculated since structural failure affecting performance can usually be associated with it.

Coefficient C, the load transfer coefficient, depends on the extent of load transfer at a joint or crack through aggregate interlock or dowels (longitudinal reinforcement for continuously reinforced pavements).

The magnitude of slab loading, P, for a given load application can be defined in terms of wheel loading with due consideration for the effect of dynamic loading and speed of loading.

Slab stiffness, D, is a function of slab thickness and concrete stiffness.

Slab support modulus, K, is not only dependent on the stiffnesses and thicknesses of the supporting layers, but also on the uniformity of the support. Relative settlement of sub-layers and/or erosion under traffic loading and the presence of water creating voids will have an influence on slab support.

The ratio of slab tensile stress/slab tensile strength has always been used in calculating the number of load applications N of magnitude P to failure:

$$N = a\left(\frac{tensile\ stress}{tensile\ strength}\right)^{b} \tag{2.14}$$

Where:

N	=	Number of load applications to failure;
a	=	Damage constant; and
b	=	Damage factor.

Based on the discussion above the modelling can be subdivided into:

a) A load transfer component.
b) Slab loading through moving traffic.
c) Slab support including voids under the slab.
d) Slab characteristics and stress calculations.
e) Structural performance as a function of the stress/strength ratio.

2.3.7.1.1 Load Transfer at the Joint/Crack

Load transfer can be achieved in two ways namely aggregate interlock and dowel action of longitudinal steel bars. In order to isolate the effect of load transfer at a joint/crack on slab stress from the influence of slab support as far as possible, the relative vertical movement at the joint/crack due to a load moving across the joint/crack is taken as indicative of joint/crack shear stiffness.

Based on work by Walraven (1981) as well as a laboratory study of some typical South African concrete mixes using hard, crushed, granitic material (Strauss, 1992), the following was found for aggregate interlock:

$$y(x) = f\left(\sqrt{n}, \frac{1}{E_c}, \frac{x^{1,5}}{agg}\right) \tag{2.15}$$

Where:

$y(x)$, x, agg		As defined for Equation (2.12)
E_c	=	Modulus of elasticity of the concrete (MPa); and
n	=	Number of load applications.

By this stage the format of the relative movement equation already changed from the version published earlier by Strauss (1992). Note that the *agg* parameter has no exponent anymore, and that the *x* of the latter version is raised to the power 1,5, instead of 3, as previously. As mentioned in Chapter 1, the research conducted for this thesis was therefore primarily aimed at developing a new aggregate interlock load transfer equation, covering the normal range of maximum sized crushed aggregates (19,0 mm to 37,5 mm) used in the construction of concrete pavements in South Africa.

Applying the fundamental theory of dowel design (Yoder and Witczak, 1975) relative vertical movement at a joint/crack with steel bars through it can be written as a function:

$$y(x) = f\left(P_d, \left(\frac{1}{E_c}\right)^{0,75}, \left(\frac{1}{dia}\right)^{1,75}, \sqrt[4]{\frac{1}{E_d}}, \sqrt[4]{n}\right) \tag{2.16}$$

Where:

P_d	=	Load on a dowel (kN);
E_c	=	Modulus of elasticity of the concrete (MPa);
dia	=	Diameter of steel bar (dowel) (mm);
E_d	=	Modulus of elasticity of dowel / steel bar (MPa); and
n	=	Number of load applications.

In order to translate relative vertical movement at the joint/crack into a C value as depicted in Equation (2.13) above, the following relationship is used:

$$C = f\left(\sqrt{y(x)}\right) \tag{2.17}$$

Where C, the load transfer coefficient, is in the order of 0,16 for interior loading and 0,55 for free edge loading of a slab (no load transfer to the next slab). These values of C were determined for typical South African roads with slab thickness ranging from 150 to 250 mm, concrete cube strengths of about 40 MPa after 28 days and fairly stiff subgrade support.

2.3.7.1.2 Loading of the Pavement

External loading of the pavement is primarily through moving truck traffic. In order to determine amongst other factors, the influence of speed on stress in the slab, trial pavement sections were instrumented and tested under different speeds of a standard loaded dual-wheel single-back-axle truck. A typical plot of speed versus surface deflection for three different types of pavements is shown in Figure 2.9 for illustrative purposes (Lourens and Strauss, 2000). It is clear from the data that the un-dowelled jointed pavement is much more affected by speed (109% increase in deflection from static

loading) if compared with dowelled jointed (62%) and continuously reinforced concrete (31%). The simplified equation to depict this in terms of horizontal tensile stress in the concrete is:

$$\text{Stress} = f\left(\frac{P}{v^{0.2C}}\right) \tag{2.18}$$

Where:

v = Speed of loading (km/h); and

C = Load transfer coefficient.

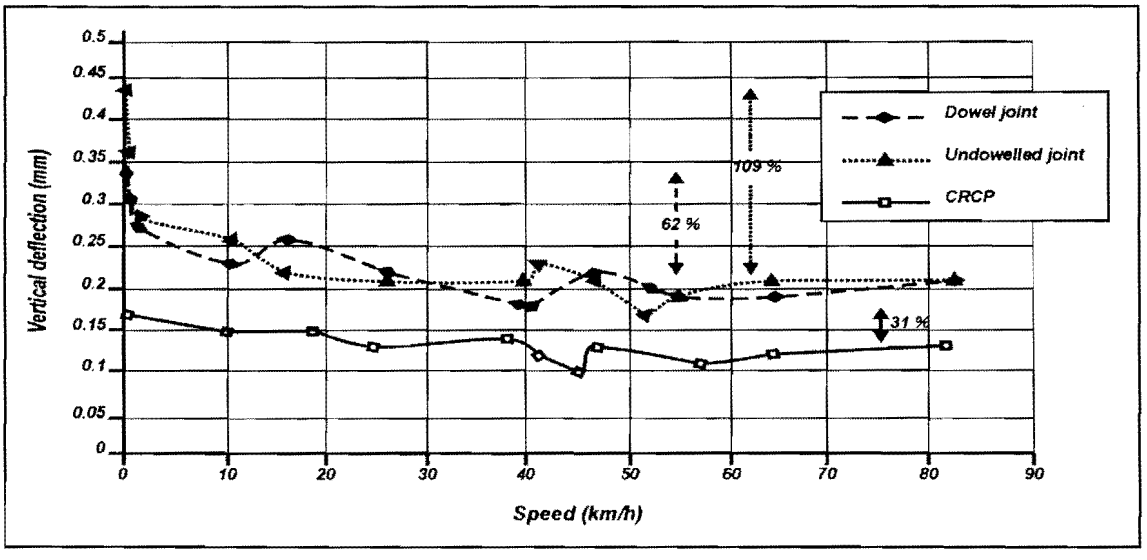

Figure 2.9: Measured surface deflection versus speed

2.3.7.1.3 Slab Support

Slab support is provided through several layers of natural materials, some of which are modified or stabilised and the top layer, the subbase, consisting of asphaltic, cemented or high quality granular material. Since concrete overlays on flexible pavements are also becoming more popular, the use of multi-layer linear elastic software programs to calculate not only residual life of the old pavement, but also its stiffness as an input into the design of overlays, is essential.

Although it is recognised that a stabilised subbase could structurally be considered as part of the concrete, during the development of cncRisk, slab support was simplified into a two-layer system, namely the subbase and an equivalent stiffness representing the contribution of lower layers. Using a multi-layer linear elastic program the equivalent stiffness of the layers below the subbase, which render the same tensile stress in the slab, could therefore be calculated

Voids below the slab, as a result of erosion or pumping of the subbase, or settlement in the lower layers, can increase tensile stress within the slab by up to 40% if compared to uniform slab support conditions (Dominichini and La Torre, 1998; Strauss and Lourens, 1998).

2.3.7.1.4 Slab Geometry and the Calculation of Stress

Recognising the need for simple equations, an attempt was made to utilise finite-element modelling together with actual measurement of strain on concrete roads under dynamic loading to develop models through regression techniques. A database was developed using a three-dimensional non-linear dynamic finite-element programme (STATAN), a three- dimensional linear elastic multi-layer programme (ELSYM5) and field measurements on pavements under traffic (Lourens and Strauss, 2000). Eight variables were introduced to develop the basic equation: load transfer constant C, void length, concrete stiffness E_c, slab thickness h_1, subbase stiffness E_2, subbase thickness h_2, subgrade stiffness E_e and speed of loading. Submodels for load transfer through aggregate interlock and dowel action of steel bars, the effect of different loads and surface pressures and the combination of sublayers to form an equivalent subgrade stiffness E_e were developed separately using different databases.

The equation for maximum tensile stress at a joint/crack under dynamic truck loading finally arrived through regression analyses is:

$$Stress = constant\left[\frac{(Void+1)^{0,80(C-0,1)}C^{0,45}\ E_c^{\ 0,60}}{h_1^{\ a}(h_2E_2)^{0,08}\left(3\sqrt{v+1}\right)^{0,40C}E_e^{\ 0,27}}\right] \quad (2.19)$$

Where:

$Void$	=	Length of void below slab (m);
C	=	Load transfer constant derived from Equations (2.15), (2.16) and (2.17);
$E_c h_1$	=	Slab stiffness and thickness (MPa, mm);
$E_2 h_2$	=	Subbase stiffness and thickness (MPa, mm);
E_e	=	Equivalent subgrade support stiffness (MPa);
v	=	Speed of heavy vehicles (km/h);
a	=	$1,95/(h_2 E_2)^{0,05}$; and
$constant$	=	Depends on wheel load and surface pressure.

The data on which the above equation is based was generated for 4,5 m joint spacing, a concrete shoulder 2,5 m wide, two travelling lanes each 3,7 m wide and the loading is by an 80 kN single axle with double wheels.

As mentioned, the load transfer constant, C in Equation (2.19) depends on the extent of load transferred through either aggregate interlock or dowels. The smaller of the values calculated with Equations

(2.15) and (2.16) is used. Furthermore, in Equation (2.19) C has a coefficient of 0,45. In the event of an interior loading condition where C is in the order of 0,16, the numerical value becomes 0,44 once the coefficient has been applied, which is nearly three times higher than the original value. Similarly for a free edge where C is in the order of 0,55, the calculated value becomes 0,76, which is less than twice the original value. Equation (2.19) therefore becomes less sensitive to a change in the load transfer constant, the larger the movement and the smaller the load transfer efficiency of the joint.

2.3.7.1.5 Structural Performance

Many different performance curves or transfer functions are being used by designers to convert stress to expected number of load applications to failure. Figure 2.10 shows some typical data obtained from the literature. Both the RISC (Majidzadeh and Ilves, 1983) and ARE (Treybig et al., 1977) curves are based on AASHTO data, the first assuming a terminal serviceability index of 2,0 and the second (ARE) a terminal serviceability of 2,5. Both these curves are based on the format of Equation (2.14) and thus the value of b for RISC is 4,29 and that of ARE 3,21. Darter (1977) used laboratory beam fatigue tests to produce the curve in Figure 2.10, which is similar to the findings of other laboratory studies (Hilsdorf and Kesler, 1966). The performance curve used by PCA (1984) is also illustrated in this figure and is used, in similar format, for design procedures in Australia and Canada.

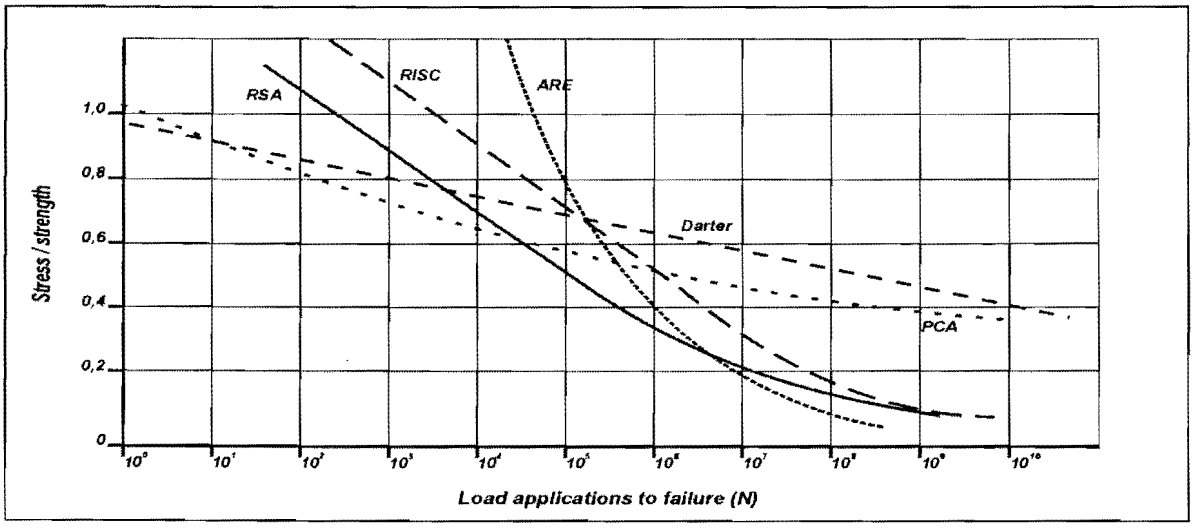

Figure 2.10: Performance curves used by various designers.

Using Equation (2.14) as a basis for the performance curve, as was done by Majidzadeh and Ilves (1983) and Treybig et al. (1977), the constant a leads to the situation that at high stress ratio e.g. 1,0, the number of load applications to failure is between 2 300 and 230 000. To overcome this problem, a can be defined as a function of the category of road in terms of the number of vehicles for which the pavement is designed. The curve depicted as *RSA* in Figure 2.10 is being used in the model until such

time that present research suggests an improvement. The value of b for this curve in Equation (2.14) is 4,2.

2.3.7.1.6 Deflection at a Joint

Using the same database that was developed for generating the equation for stress and supplementing with calculated field-measured information, the relationship for maximum deflection at a joint is:

$$Deflection = constant \left(\frac{C^{0,4} \left(void + 1\right)^{0,2}}{h_1 E_c^{0,25} \left(h_2 E_2\right)^{0,1} E_e^{0,4} \left(v + 1\right)^{0,02/C}} \right) \quad (2.20)$$

Where the constant depends on surface loading determined through. vehicle traffic or by falling weight deflectometer.

2.3.7.2 Design evaluation based on the view of consequences

2.3.7.2.1 Background

An effective but simple approach was adopted to evaluate the quality of design and thus facilitate competent decision-making. The approach is based on the evaluation of consequences. The consequences of a certain pavement design are expressed in terms of three output variables, namely risk of premature pavement failure, excessive deflection, and – in case of continuously reinforced concrete – excessive crack spacing.

Conceptually, pavement failure occurs when demand exceeds supply. In practice this happens when the number of load applications n a pavement is supposed to carry over the design period exceeds the number of load application N the pavement can carry at an acceptable level of structural and/or functional integrity. The ratio n / N is called cumulative damage CD. By definition $CD = n / N$. The risk R of premature pavement failure is defined as the probability of n being greater than N. In other words, R is the probability (P) of cumulative damage CD being greater than unity:

$$R = P\{CD > 1\} \quad (2.21)$$

One should mention that the complement of risk, i.e. $1 - R$, is called *reliability*.

2.3.7.2.2 Input

The proposed design method, cncRisk, requires five input constants, namely the Damage factor b, Damage constant a (as in Equation (2.14)), Ratio $k1 = E_c f$, Ratio $k2 = ITS / f$ (where f is the flexural

strength of the concrete and *ITS* the Indirect Tensile Strength), and Steel diameter *dia*. Apart from these, the method relies on nineteen input variables, such as aggregate size, crack width, slab thickness and others. For a concrete pavement with a concrete shoulder, traffic loading is considered as interior loading, whereas for a concrete pavement with no shoulder, traffic loading is considered as edge loading.

Due to uncertainty, the designer may find it difficult to determine appropriate values for these variables. Many designers realise the uncertainty about correct input and, consequently, try to avoid the use of single point-estimates. Instead, they prefer indicating a range of reasonable practical values. Triangular probability distribution was used to express the stochastic nature of input variables. A triangular distribution is defined by three parameters, namely a minimum practical value, the best estimate, and a maximum practical value (see Figure 2.11). The triangular distribution has been chosen in preference to the Normal, Lognormal, Gumbel or Weibull types of probability distribution, because the determination of its parameters appeals to intuition, and is conducive to a direct application of the designer's experience.

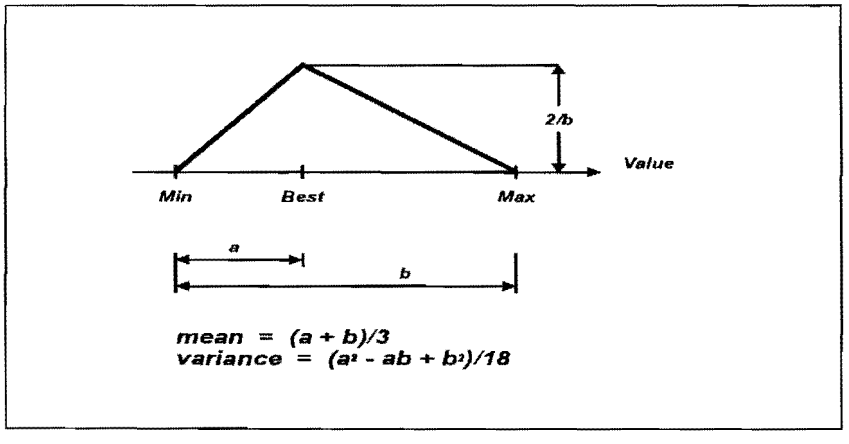

Figure 2.11: Triangular distribution of input variables.

Of the nineteen input variables eighteen have triangular distributions, whereas one – the dynamic axle load – follows an empirical distribution. A practical example of such an empirical distribution of axle loads, which was obtained from weigh-in-motion measurements, is shown in Figure 2.14.

2.3.7.2.3 Output

Because of the complexity of calculations, a Monte Carlo simulation technique was used to translate the uncertainty about the input into the uncertainty about the output. The magnitude of this uncertainty was established in terms of the probability distributions of the output variables, namely the cumulative

damage *CD*, pavement deflection *y*, and crack spacing *x*. The risk of premature failure *R* is then represented by the area of the *CD* distribution that lies right of the line for *CD* = *1*, outside the graph (see Figure 2.15).

The simplified flowchart on which the Monte Carlo simulation was based is shown in Figure 2.12.

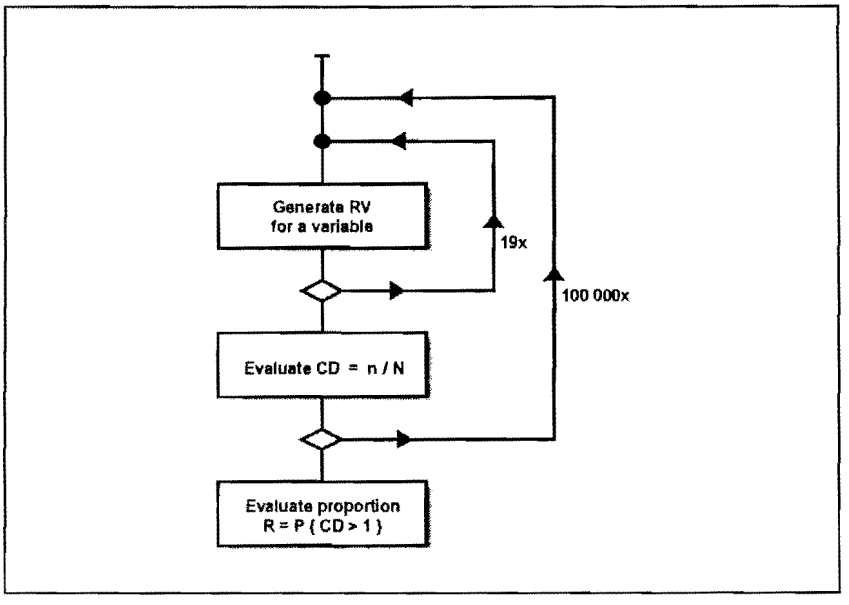

Figure 2.12: Simplified simulation flowchart.

2.3.7.2.4 Computer Simulation Program

A computer program was developed to perform the above simulation. The program is called CncRisk and runs on a PC under the Windows operating system. The user interface is divided into five panels, namely Main control, Statistics, Advanced input, Operating instructions and Manual highlights. A panel can be selected by clicking its tab.

Main control panel

Figure 2.13 shows the Main control panel of the program, together with default values of the input variables and constants. The values of main output variables – risk, deflection and crack spacing – are also shown on this panel. In addition, three dials are displayed. During a simulation run, the needles indicate the current level of cumulative damage, deflection and crack spacing, respectively, to continuously inform the user.

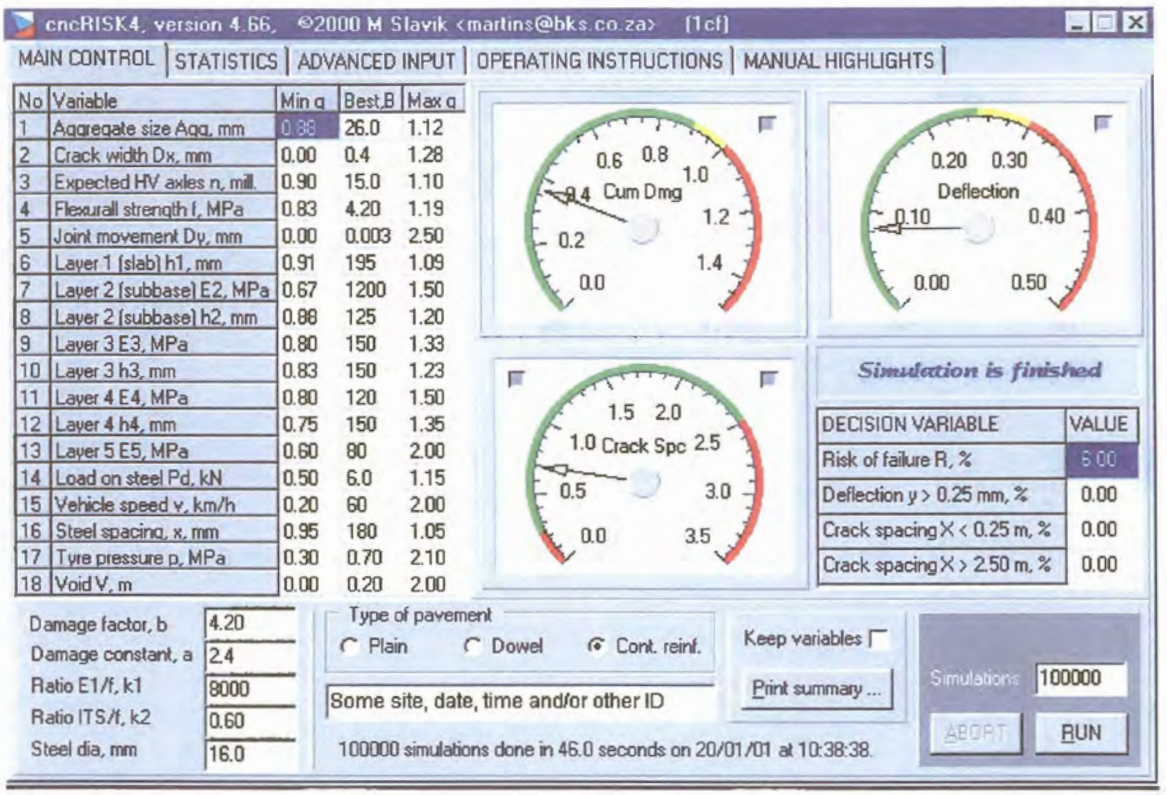

Figure 2.13: Example of the Main control panel.

The minimum and maximum practical values of the input variables are entered as factors q, by which the best value is multiplied to obtain the respective extreme. Three main types of concrete pavement – plain, dowelled and continuously reinforced – are selectable by means of 'radio' buttons. The number of simulations can be selected from 1 000 to 10 000 000.

Although a small number of simulations will be done very quickly, it may produce jagged output distribution curves and give dissimilar output figures for repeated simulation runs. In contrast to the above, a large number of simulations (say, over 100 000) will take more time to complete, but will yield relatively smooth probability distribution curves, and ensure good repeatability of output results.

Advanced input panel

The panel called Advanced input, which is shown in Figure 2.14, gives the user an opportunity to enter the distribution of dynamic axle loads that are applicable in his or her case. A typical distribution can be selected from a provided list. Alternatively, entering frequencies can create an individual distribution. In any case, a frequency plot is shown in a graph to guide the user. Also, the presence of a shoulder is selectable on this panel.

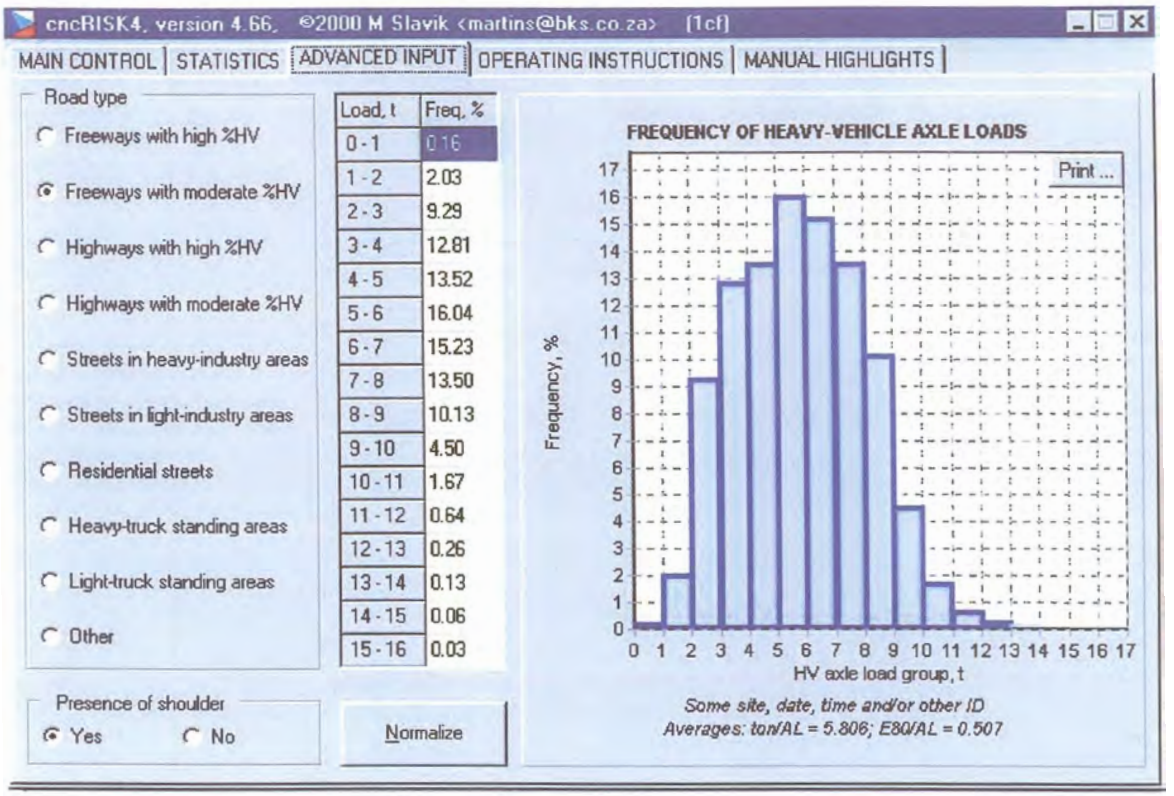

Figure 2.14: Example of the Advanced input panel.

Statistics panel

The probability distributions of the output variables, together with other figures of interest, are shown on the panel called Statistics – see an example in Figure 2.15. As mentioned earlier, the quality of design is reflected by the three main output variables, namely cumulative damage, deflection, and crack spacing in case of continuously reinforced concrete. To facilitate evaluation and competent decision-making, certain standards were laid down to guide the designer. As a rule of thumb, the risk R should not exceed 5% in case of national and strategic roads, 7% in case of provincial and less important roads, and 10% in case of low-standard roads. Similarly, the probability of deflection at a joint or crack exceeding 0,25 mm should also comply with the above standards. These percentages can also be applied to the probability of excessive crack spacing, which should never be less than 0,25 m and never more than 2,50 m. This deflection of 0,25 mm is associated with an 80 kN load on a single axle with double wheels; 40 kN on each side of the axle.

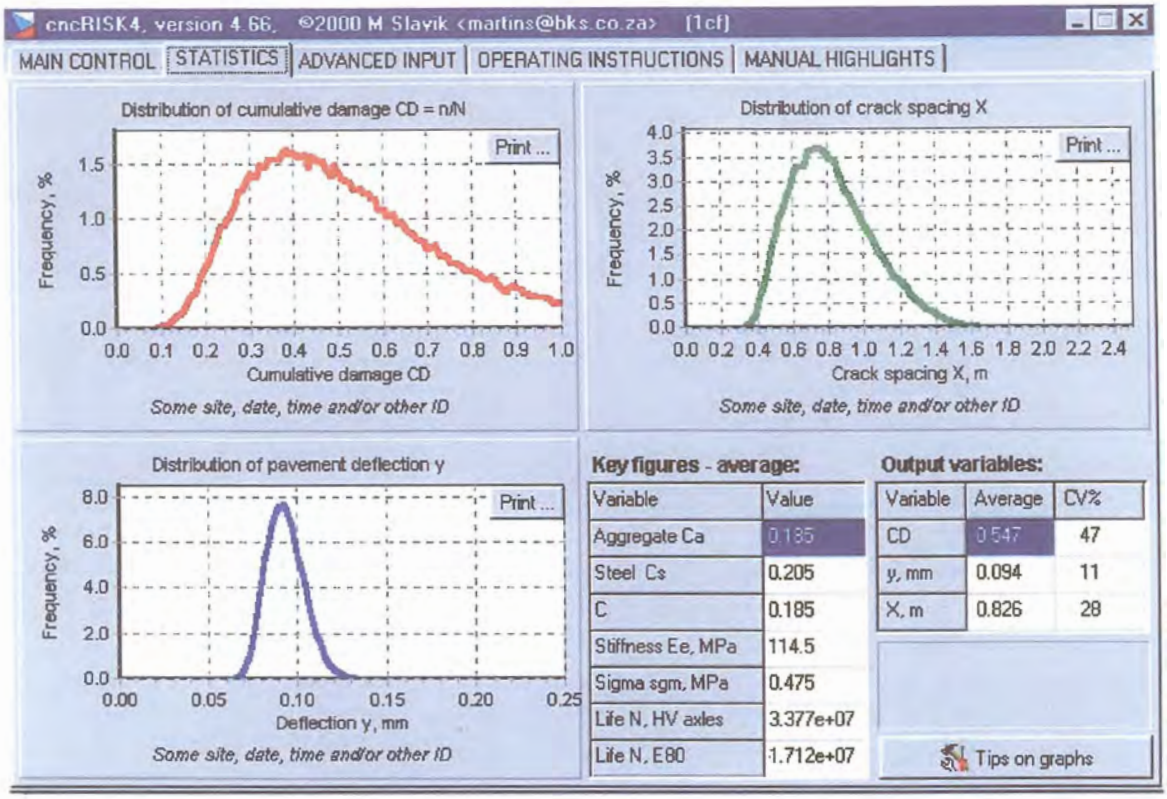

Figure 2.15: Example of the Statistics panel

One should consider the relation between the above figures and the uncertainty about the input. A conservative uninformed, or unsure designer would specify the respective triangular distributions with low minimum, and high maximum, practical values. This will result in "fat" distributions of the output variables, with probabilities exceeding the recommended figures. To bring the figures down to the standard, a stronger – and more expensive – design will have to be employed. The extra cost of such a design can then be viewed as a cost of imperfect knowledge of the input.

2.3.7.2.5 General

Apart from the research conducted for this thesis to develop the aggregate interlock load transfer function; research is also under way to further develop the load transfer function for dowels. This will increase the accuracy of the stress equation. However, the refinement of the performance curve is of the greatest importance and, in order to increase confidence in the prediction of performance, the program has been released for use by a selected group of practitioners. Feedback from them on the performance of pavement structures together with further research using the Heavy Vehicle Simulator (HVS) will be implemented during further development of the software.

2.3.8 Summary of historical developments

All design methods universally recognise the need to consider the subgrade, material characteristics, environmental effects, and the traffic anticipated in the design period. The concept of serviceability-performance, and a quantitative definition of "failure" are necessary. Stability or "balance" should be maintained throughout the various phases within the design period for repetitive permanent deformation, as well as repetitive fatigue of cemented layers. The pavement tends to reach a state of equilibrium during each of these phases within which a temporary imbalance may exist due to material changes (with time, water ingress, and changes in support).

Up till recently, the 3D FE models available could only be used in research applications due to computational requirements. Most researchers therefore tended to focus on developing empirical methods. These methods, however, were complicated as illustrated by the formulas and derivatives shown in Appendices A and B. Davids et al. (1998a), on the other hand, developed EverFE with the specific aim to make a 3D model available for implementation on desktop computers.

The "recipe-type" approach previously followed in Manual M10 (1995) for the design of concrete pavements in South Africa was conservative and resulted in expensive pavements. A new design method was needed that utilised a mechanistic approach and would result in more cost-effective pavements (for equivalent performance to asphalt pavements). An integration of flexible and rigid mechanistic design approaches was therefore becoming more and more important. The new method was, however, to be pragmatic and aimed at ordinary pavement design practitioners rather than researchers and academics (Strauss et al., 2001).

2.4 AGGREGATE INTERLOCK

2.4.1 Introduction

Aggregate interlock was first recognised as a beneficial load transfer mechanism in the early 1900s, when the popularity of Portland cement concrete as a paving material was beginning to increase. Aggregate interlock is a natural mechanism effective in transferring loads across discontinuities, such as joints and cracks in plain or reinforced concrete pavement systems. Only a shear action is operative in this mechanism. In contrast, load transfer devices such as dowel bars also involve bending, thus creating an interest to investigate load transfer by aggregate interlock (Ioannides and Korovesis, 1990).

Because of its questionable long-term endurance record in the United States of America (USA), aggregate interlock is not relied on as a primary load transfer mechanism in jointed concrete pavements, except perhaps in low volume roads. Abrasion and attrition of the aggregates coupled with temperature variations causing a fluctuation in the size of the opening at the discontinuity can result in

a significant decrease in the effectiveness of this mechanism over time (Ioannides and Korovesis, 1990).

The poor performance of joints/cracks relying on aggregate interlock only, and conclusions from the Bates Road Test, conducted near Bates in Illinois (Older, 1924), led to the conclusion that once cracks had formed in plain concrete, they tended to propagate rapidly and deteriorate badly under a small number of load repetitions. In contrast cracks developing in reinforced concrete pavement sections remained tight, deteriorated slowly, and exhibited overall much better behaviour. Therefore it was concluded that "when roughened edges of two slabs are held firmly together the aggregate interlock may be expected to function perfectly and permanently as a load-transfer medium" (Benkelman, 1933).

Various experimental studies on aggregate interlock shear transfer in concrete pavements demonstrated that joint shear transfer effectiveness and endurance depend on many factors including joint width, slab thickness, load magnitude, foundation type, subgrade modulus, and aggregate shape (Colley and Humphrey, 1967).

Research by Walraven (1981) into shear transfer across discrete cracks in concrete has shown the mechanics of aggregate interlock shear transfer to be highly complex. In addition to contact between sharp edges of aggregates on joint surfaces, there may be localised crushing of the cement paste and the aggregate, as well as entry of loose materials. The amount of crushing and the bearing area of the surfaces depends on the joint opening, normal restraint of the joint, the strength of the concrete (both the paste and the aggregate), and the size and distribution of the aggregate particles. Walraven (1981) stated that the modelling of aggregate interlock shear transfer in rigid pavements should take all these factors into account.

During finite element (FE) modelling of aggregate interlock shear transfer in rigid pavement systems, most researchers tend to use discrete linear spring elements (see paragraph 2.3). While this may be considered reasonable for an examination of the effect of aggregate interlock shear transfer effectiveness on the global slab response, it does not permit modelling of local response at the joint. Even when the use of linear springs is appropriate, the rational choice of a spring stiffness may be difficult, if not impossible, and the appropriate spring value is valid only for one model geometry, set of material properties, and loading. The need for the more realistic FE modelling of aggregate interlock shear transfer was recognised by Davids et el. (1998a). They chose the two-phase model developed by Walraven (1981) to model aggregate interlock shear transfer in the FE software EverFE.

A literature review, distinguishing between theoretical modelling, laboratory studies, and field investigations has been conducted to provide an overview of past attempts to model this phenomenon and to explain the mechanics of aggregate interlock. The focus of the literature review was to investigate methods used during previous studies, to assist in the design of the experiments, and the compilation of the test programme for the current study.

2.4.2 Theoretical aggregate interlock modelling

2.4.2.1 Micro-mechanics-based model

Probably the most important development in the theoretical modelling of aggregate interlock in concrete was the development of the two-phase model by Walraven (1981). This model is based on a statistical analysis of the crack structure and the associated contact areas between the crack faces as a function of the displacements, w (crack width), and Δ (shear displacement), and the composition of the concrete mix.

The fundamentals on which the study was based are that concrete can be represented as constituted by two distinct materials, the hardened cement paste, and a collection of embedded aggregate particles. Generally the strength and stiffness of the aggregate particles are greater than those of the matrix, however, the contact area between both materials, the bond zone, was assumed to be the weakest link of the system.

The micro-roughness of the crack, caused by the aggregate particles projecting from the crack plane, was assumed to dominate the macro-roughness, due to overall undulations of the crack faces. Because of the large plastic deformations of the cement paste due to pore-volume reduction, the cement paste was idealised as obeying a rigid-plastic stress-strain law. The aggregate was idealised as incompressible.

The aggregate particles were modelled as spheres of varying size, distributed according to a Fuller curve. The aggregate particles intersect the crack plane at various depths, depending on their statistical distribution within the concrete matrix as shown in Figure 2.16.

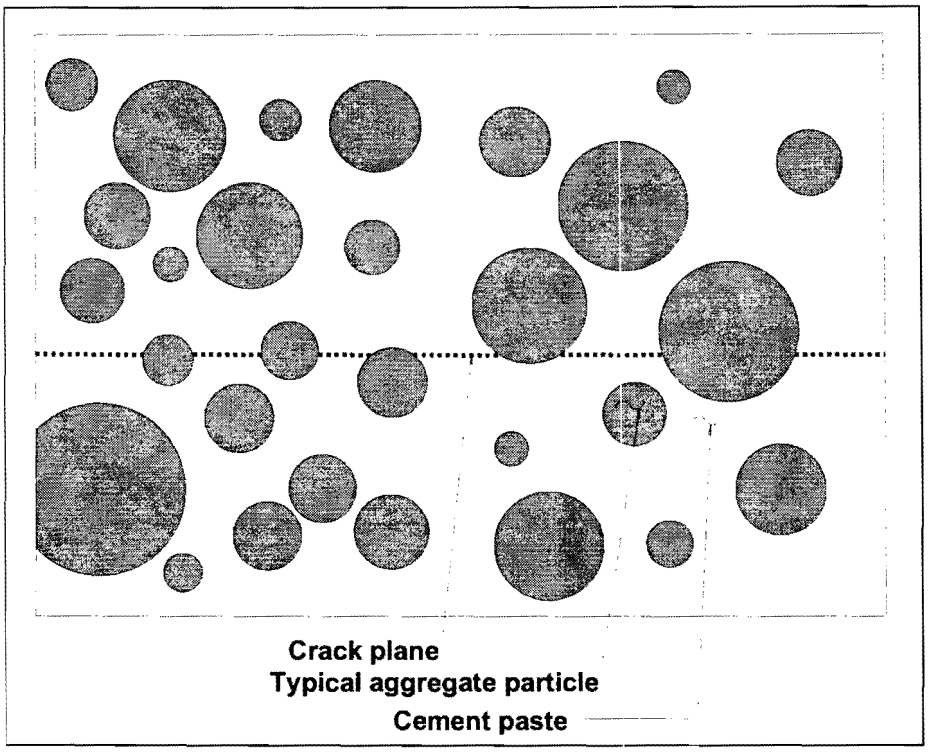

Figure 2.16: Crack plane and distribution of aggregate particles (Davids et al., 1998a)

As a result of these assumptions, it is possible to consider a cracked concrete body as an assemblage of a large number of slices each of finite width, thus reducing the crack to a two-dimensional problem of finite width. The stresses at the contact area are resolved into a stress, σ_{pu}, normal to the contact area and a stress, τ_{pu}, tangential to this area (see Figure 2.17). These stresses are interrelated by the condition that the contact areas are about to slide and therefore:

$$\tau_{pu} = \mu.\sigma_{pu} \tag{2.22}$$

Where μ is the coefficient of friction between the paste and the aggregate, and σ_{pu} is the ultimate strength of the paste, which can be calculated as follows:

$$\sigma_{pu} = 6{,}39 f_{cu}^{\,0{,}56} \tag{2.23}$$

Where:

f_{cu} = Concrete cube crushing strength (MPa)

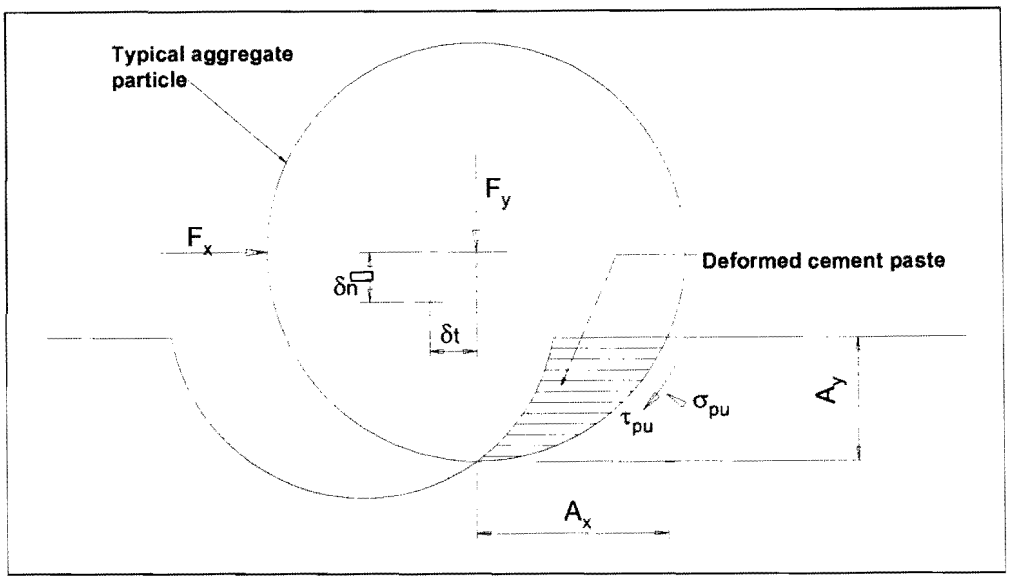

Figure 2.17: Deformed cracked plane (Davids et al., 1998a)

The equilibrium of the crack plane requires that the net forces be balanced as follows:

$$F_x = \sigma_{pu}\left(\Sigma A_y + \mu \Sigma A_x\right) \tag{2.24}$$

$$F_y = \sigma_{pu}\left(\Sigma A_x - \mu \Sigma A_y\right) \tag{2.25}$$

Where:

ΣA_x = X-projection of the sum of the most probable contact areas; and

ΣA_y = Y-projection of the sum of the most probable contact areas.

The determination of the x- and y-projections is based on the statistical distribution of the aggregate in the concrete matrix, and the geometry of the spherical aggregate particles intersecting the crack plane at a given tangential and normal displacement.

In an attempt to verify the theory, a series of tests were run in which the crack width was maintained at a constant value, and the shear stress, normal stress, and shear displacement were measured. The values of σ_{pu}, and μ were determined to provide the best fit to the experimental data for a crack opening of 1,0 mm. These values were then used to calculate the stress-displacement curves for other crack opening values. The theory was generally in good agreement with the experimental data for all values of crack openings. In addition, parametric studies were conducted which allowed the role of friction between aggregate and matrix, the contribution of various aggregate fractions to transmissions of stresses in the crack, the influence of aggregate size, and of the grading curve to be studied.

Building forth on the same physical and mechanical concepts developed in his initial study (Walraven, 1981), Walraven (1994) presented a model that makes it possible to explain and predict the behaviour of cracks under cyclic loading.

Walraven (1994) recognised the fact that the behaviour of cracks under cyclic shear loading is characterised by a considerable irreversible damage of the crack faces. The response of cracks to reversed and alternate actions can only be well described if load-history effects are taken into account. The load-history of rough cracks subjected to earthquake loading, can be determined from the severity of the earthquake, which in turn can be related to the cyclic loading of traffic across a joint in a concrete pavement, relying on aggregate interlock load transfer.

Tests on cracks subjected to earthquake loading showed that there is a considerable difference between the first and the subsequent loading cycles. Irreversible damage to the cement matrix takes place when the hard aggregate particles are pushed into this softer cement matrix. Any new cycle of loading leads to further damage of the crack faces, resulting into steadily increasing values of the shear displacement and the crack width at peak loading.

The statistical basis for the aggregate particle distribution is identical to that developed for the previous study by Walraven (1981). To simplify calculations, both the distribution of particle diameters and all possible embedment depths were added one by one into a finite number, with the embedment depth assumed to be uniformly distributed between a minimum of zero and the maximum of the radius of a given particle. This allows the representation of an aggregate particle D_{ij} with diameter $D_i = (0,1i - 0,05)D_{max}$ and embedment depth $d_j = 0,1j[(1/2)D_i]$ as shown in Figure 2.18. For each embedment/diameter combination, D_{ij}, the cement paste is subdivided into a finite number of layers, allowing computation of the projected contact area by summing the contact areas of the individual paste layers. Figure 2.18 gives a graphical representation of this discretisation.

For a given normal and tangential displacement of the crack plane, the likely contact area for any particle diameter is determined by summing the contact areas for all embedments and multiplying by n_i, the likely number of occurrences of D_i. The total contact area is then determined by summing over all particle diameters, and the shear and normal stresses may be computed by using Equations (2.24) and (2.25).

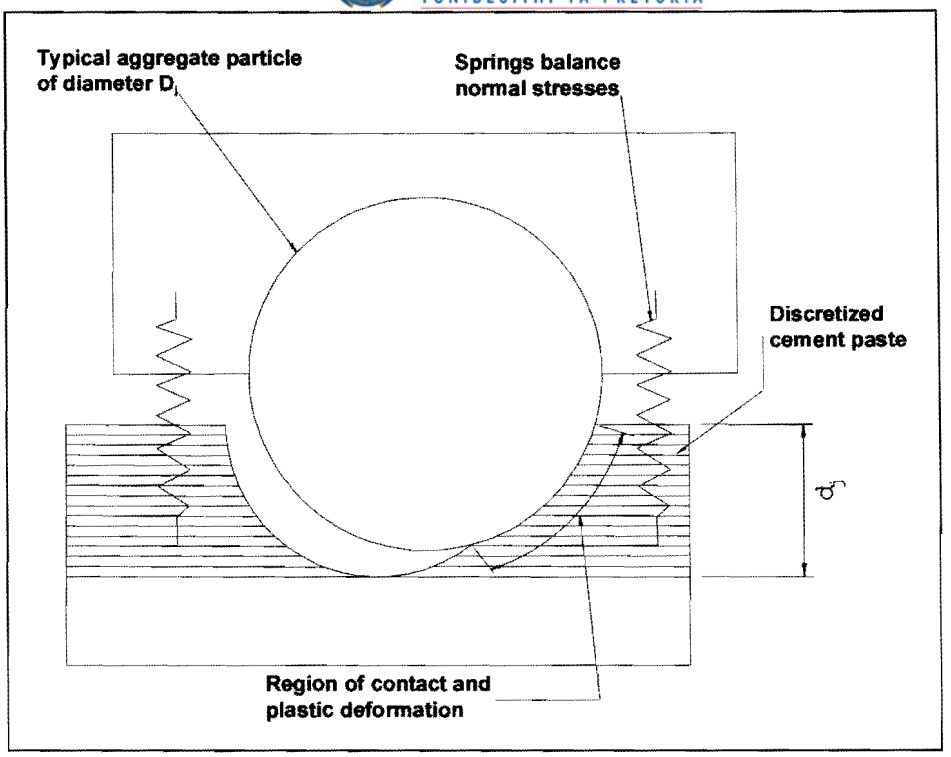

Figure 2.18: Subdividing aggregate particles and cement paste into discrete particles (Davids et al., 1998a)

The normal stresses generated across the crack are balanced by the springs assumed to cross the crack plane as shown in Figure 2.18. These springs may represent some external restraint mechanism, or reinforcing bars intersecting the crack plane. The discretisation of the cement paste also allows the damage to the cement paste to be updated throughout the loading history by tracking the geometry of the paste layers for each particle diameter/embedment depth combination. A simple programme may be written to perform simulations of both static and cyclic loading for different parameters such as initial crack opening, restraining spring stiffness, etc.

Up to now, it has been assumed that the aggregate is so strong, that no aggregate particle will fracture during cracking of the concrete, so that all the particles in the crack contribute to the aggregate interlock mechanism. To take this effect into account the fracture index, C_f was introduced. This is used to proportionally reduce both the shear and normal stress transferred across the crack, and account for the fracturing of the aggregate particles. The value of C_f is characteristic of the specific concrete mixture, and must be determined from static load testing of a specimen and curve-fitting the resulting data.

Some of the relevant conclusions to these studies were:

a) The experimental results were adequately described by the adopted physical model.

b) The mechanism of aggregate interlock can only be adequately described if normal stress, shear stress, crack width, and shear displacement are all involved.

c) All particle fractions contribute qualitatively in the same way to the transfer of stresses across the crack; only fractions containing particles with a diameter smaller than two times the crack width may be considered to be inactive.

d) A friction coefficient of, $\mu = 0{,}4$, between the aggregate particles and the matrix, independent of the concrete quality and the level of the stresses, results in the best fit between experimental data and the model. The yielding strength of the cement paste, which has to be used to obtain the best results, is a function of the concrete strength. Both parameters are in good agreement with experimental data described in the literature.

e) The resistance to shear deformations is governed by the concrete strength, with the diameter of the aggregate playing a secondary role.

f) The grading curve of the aggregate has some influence on the shear stiffness at larger crack widths. The development of the normal stresses is hardly influenced.

g) The behaviour of cracks, subjected to cyclic loading can be well explained and described by the theoretical model.

h) The load-history effect is caused by crushing of the matrix, irreversibly damaging the matrix during load cycles, which in turn influences the behaviour during the next cycles of loading.

i) The influence of the damage on the geometrical shape of the crack faces can be followed cycle by cycle.

2.4.2.2 Empirical and semi-empirical models

Reinhardt and Walraven (1982)

Following on the development of the micro-mechanics-based theoretical model and to increase the database on aggregate interlock, Reinhardt and Walraven (1982) conducted a series of experimental investigations. Push-off type tests were conducted on specimens with embedded bars (reinforcing bars intersecting the crack plane), as well as on specimens with external restraint bars. The advantage of these tests was that the normal stresses acting on the crack plane could be measured directly on the restraint bars. Typical measurements in these tests were the shear stress, the normal stress, the crack opening, and the shear displacement.

Millard and Johnson (1984)

In an attempt to study the internal mechanisms of shear transfer and dowel action across a single crack to enable more accurate modelling of shear stiffness, Millard and Johnson (1984) *devised tests of a new type* to examine independently the aggregate interlock and dowel action (see paragraph 2.5) effects in reinforced concrete. The primary goal of the aggregate interlock tests was comparison with previously developed theoretical models, including that developed by Walraven (1981).

The aggregate interlock test results showed that the two-phase model by Walraven (1981), involving a combination of crushing and sliding of the crack faces, is the most realistic one. In this model, shear

forces were resisted by a combination of crushing and sliding of the rigid spheres into and over the softer cement matrix: contact and interaction between spheres projecting from opposite crack faces was not considered. Closely similar results were obtained from nominally identical specimens. It was deduced from this repeatability that the aggregate interlock mechanism is not dependent upon the random path of propagation of a tensile crack. There was crack widening associated with shear slip, regardless of the size of the initial crack width. Increasing axial stiffness increased the shear stiffness and ultimate shear stress. For tests where the crack width was allowed to increase under increasing shear stress, the concrete strength had only a small effect on the ultimate shear stress. The test with a constant crack opening exhibited significantly higher ultimate shear stress and stiffness than similar tests, which permitted progressive crack opening. The conclusion that bearing/crushing predominates for small crack widths (≤ 0,25 mm) and sliding predominates for larger crack widths was not supported by these test results.

Soroushian, Obaseki and Choi (1988)

Soroushian et al. (1988) investigated the combined effect of aggregate interlock and dowel action in reinforced concrete against sliding shear at a crack.

Algorithms were developed for predicting the aggregate interlock constitutive behaviour using some empirical formulations. The analytical results obtained from these algorithms compared well with tests performed with either constant or variable crack widths. A numerical study with the developed algorithms indicated that sliding shear stiffness and strength provided by aggregate interlock increased significantly with decreasing crack width, and increasing concrete compressive strength, and also increased to some extent with increasing maximum aggregate size and restraining stiffness.

At typical crack widths (of the order of 0,5 mm), as the sliding shear deformations increased, the aggregate interlock tended to become more dominant over dowel bars in contributing to the sliding-shear resistance of cracks in typical reinforced concrete beams. The dominance of aggregate interlock was expected to diminish at very large crack widths or when cyclic loadings reduced the roughness of the crack faces.

Ioannides and Korovesis (1990)

During a mechanistic analysis of aggregate interlock load transfer mechanisms Ioannides and Korovesis (1990) developed the dimensionless joint stiffness parameter, *AGG/kl*. Aggregate interlock (or any pure-shear device, in general) was modelled in ILLI-SLAB as a set of linear springs, acting at each node along the discontinuity.

Seasonal variations in the efficiency of load transfer at the cracks were also noted. These were the result of expansion of the slabs in the summer, and their corresponding contraction in the winter. Joint opening was clearly established as a major determinant of aggregate interlock and efficiency of load transfer. Results of non-destructive testing (NDT) using the Falling Weight Deflectometer (FWD)

suggested that an increase in ambient temperature improve the efficiency of joints/cracks that are free to open or close.

At the commencement of the FE investigation the problem was described as fairly complex, even after the simplifying assumptions of linear elasticity, plate theory, and dense liquid (Winkler) foundation have been adopted. The purpose of the assumptions was to reduce the number of variables involved and thus improve the engineer's ability to understand, if not solve, the problem. The effect of the size of the loaded area was analysed, as well as the effect of slab length and width. The results of previous studies were also re-interpreted.

The major relationship established in this study is depicted in the form of an S-shaped curve, which is a non-dimensional plot of LTE_{Δ} versus AGG/kl (see Figure 2.19). This S-curve (Equation (B.44), Appendix B) offers the designer the possibility of investigating the factors influencing the spring constant AGG, which characterises the aggregate interlock shear stiffness per unit length of crack (AGG is also commonly referred to as the aggregate interlock factor (AIF)). This parameter expresses the relative stiffness of the joint itself to the stiffness of the pavement system in which it is installed. A large AGG for a crack indicates that the crack is relatively stiff, and has a good potential for aggregate interlock load transfer. Computation of this parameter involves determining LTE_{Δ}, obtaining k and l, and then using the graphical relation between LTE_{Δ} and AGG/kl, developed through a theoretically based (mechanistic) design approach to determine AGG.

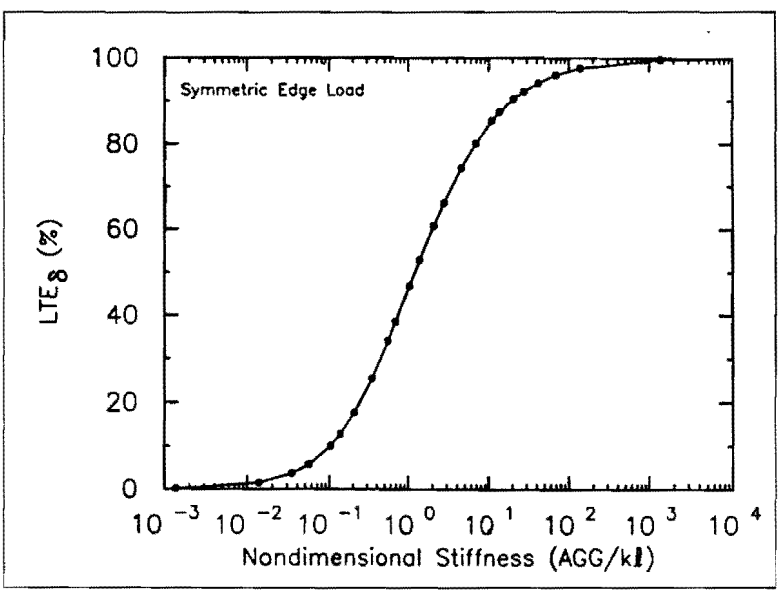

Figure 2.19: LTE_{Δ} as a function of dimensionless joint stiffness (AGG/kl) (Ioannides and Korovesis, 1990)

When determining the effect of the size of the loaded area, it was found that the load size ratio (a/l) (where a is the radius of the applied load) influences LTE_σ significantly. At any value of LTE_Δ, much higher LTE_σ values are obtained as a/l increases, i.e. as the load becomes less concentrated. The effect of slab length and slab width was also specifically investigated by determining the effect of the slab size ratios (L/l and W/l), (where L and W are the length and width of the slab, respectively) on LTE_Δ and LTE_σ. Both the slab length and slab width investigations suggested that slab size effects on TLE, LTE_Δ, and LTE_σ are not significant.

One of the primary concerns in designing load transfer mechanisms for a pavement system is the possibility of a detrimental effect when external loads and a temperature differential are considered simultaneously. Daytime conditions are often considered to be critical when combined with an externally applied load. Three loading conditions were analysed: external load only, curling only, and curling and external loading combined. Under curling-only conditions, joint stiffness caused by a pure-shear mechanism does not affect the response of either a short or a long slab. In contrast, a mechanism that involves bending as well may be expected to increase the curling-only stresses, particularly in shorter slabs. Thus, a pure-shear load transfer system would reduce edge stresses caused by the load, without increasing the curling-only stresses. This response would be especially desirable during the early life of the pavement system when the slab strength has not yet developed fully.

The methodology described in this mechanistic design approach by Ioannides and Korovesis (1990) offer the possibility to back calculate in situ joint stiffness using NDT data and to re-interpret available laboratory and field test results. They also concluded that the long-held false perception pertaining to the uniqueness of the relationship between deflection load transfer efficiency and stress load transfer efficiency should be abandoned.

Ioannides, Alexander, Hammons and Davis (1996)

Ioannides et al. (1996) applied the principles of dimensional analysis and Artificial Neural Network Training (ANN) to concrete pavement joint evaluation. Using these principles they developed a method for assessing the deflection and stress load transfer efficiencies of concrete pavement joints and for back-calculating joint parameters.

The computer programme BACKPROP 3.0 was used to train the algorithm using data developed by numerical integration of Westergaard-type integrals. The predictions of the programme were verified by comparisons with closed-form and finite element solutions pertaining to data collected at three major civilian airports in the United States. They further demonstrated that significant savings could be achieved through reduction of the dimensionality of the problem, which could be reinvested by broadening the range of the applicability of the neural network.

Dong and Guo (1999)

The Runway Instrumentation Project at Denver International Airport, as a part of the Federal Aviation Administration (FAA) airport pavement research program, started in 1992. Dong and Guo (1999) used a Heavy Falling Weight Deflectometer (HFWD) in conjunction with deflectometers and strain gauges installed in the pavement to collect data to investigate the behaviour of the joints and interfaces in the pavement.

Load transfer efficiency at the joints was measured in terms of deflection transfer efficiency (DTE) and stress transfer efficiency (STE). All transverse joints were un-doweled, relying on aggregate interlock load transfer, and all longitudinal joints were either hinged or doweled. The hinged joints experienced the highest DTE, followed by the doweled joints, with the transverse joints the lowest. The FAA design specification assumes STEs of 25%. For hinged joints the STE was higher than 25% and for the doweled joints slightly less than 25%. For the transverse joints the STE was almost totally lost after only three years.

During this study, it appeared as if environmental effects played a more important role than the traffic load on the reduction of load transfer capability of the transverse joints. Although no serious structural distresses were observed during the investigation, it was verified that cold weather might significantly reduce the load and deflection transfer capability of transverse joints.

Wattar, Hawkins and Barenberg (1999)

Wattar et al. (1999) confirmed through laboratory studies that the two-phase model, initially developed for a crack width of 1 mm could adequately describe the static loading behaviour of aggregate interlock joints with large crack widths. In this instance a crack width of 2 mm was used. The authors further stated that additional experimental testing was needed to finalise an analytical model for joint shear behaviour, and suggested that the primary tests should involve subjecting the specimens to cyclic loading at constant amplitude stresses until failure occurs.

2.4.3 Laboratory studies

Various researchers have attempted to measure load transfer at joints in concrete pavements through laboratory studies. These models varied from full-depth pavement structures constructed in a test box (Colley and Humphrey, 1967; Jensen, 2001), to part-slab test specimens on a simulated subgrade (Buch, 1998; Wattar et al., 1999; Vandenbossche, 1999).

Table 2.3 presents a summary of some of the laboratory studies conducted by various researchers. The variables considered significant to the performance of aggregate interlock joints are singled out.

Table 2.3: Summary of laboratory studies by various researchers

Reference	Concrete strength and model size	Aggregate size and type	Crack width	Load	Foundation support	Crack inducer
Colley and Humphrey, 1967	38,5 MPa. 1168,4 mm wide, 5,5 m long, and 177,8 mm / 228,6 mm thick	38 mm – natural siliceous gravel and dolomitic crushed stone.	0,1 mm to 2,54 mm.	40 kN load applied to both sides of crack with two actuators at a simulated speed of 48,3 km/h on circular loading plates.	Silty clay soil subgrade, with two types of subbase – sand-gravel and cement-treated material	Removable metal strip + groove in top of concrete directly above metal strip.
Millard and Johnson, 1984	29 – 52 MPa. 300 mm high x 125 mm wide x 100 mm thick - short test specimen 2/300 mm high x 225 mm wide x 100 mm thick for long test specimen	10 mm rounded gravel.	0,063 mm to 0,75 mm.	Shear loading through direct forces acting through knife-edge bearing adjacent to crack up to 4 MPa.	-	Applying a direct tensile force to the end plates.
Buch, 1998	38 MPa. 254 mm thick x 915 mm long x 1220 mm wide.	19,0 mm and 25 mm -crushed limestone and river gravel.	0 mm to 1,4 mm.	40 kN load applied to both sides of crack with two actuators at a simulated speed of 48,3 km/h on circular loading plates.	FABCEL-25 neoprene pads with a k-value of 27 MPa/m.	Metal strip inserted in fresh concrete.
Wattar et al., 1999	39 MPa. 305 x 305x 610 mm.	25 mm – river gravel	2 mm.	Horizontal shear force applied statically, and at constant amplitude.	-	Tensile force a few hours after casting
Jensen, 2001	30,6 – 34,8 MPa 250 mm thick, 3 m long, 1,8 m wide	25 mm limestone and 25 mm and 50 mm glacial gravel	0,1 mm to 2,5 mm.	Cyclic wheel load of 40 kN at one side of crack at 3 Hz.	Michigan Highway foundation: 102 mm open-graded drainage course on a 400 mm thick subbase.	Slab subjected to horizontal displacement at surface slot, 7 to 10 days after casting

There was no correlation between the sizes of the models used, nor the concrete strengths achieved, although the average was approximately 37 MPa. The maximum aggregate sizes used, varied from 10 mm to 50 mm. The researchers basically used the types of aggregate available in their immediate vicinity, and therefore there was also no real relationship as far as aggregate type is concerned. Consensus was however reached that the more angular the aggregate, the greater the load transfer potential.

Both Colley and Humphrey (1967) and Jensen (2001) tested up to a maximum crack width of 2,5 mm. Repetitive testing showed that the deflections tended to reach an upper asymptote from a crack width of 2,5 mm and larger. This region was therefore considered to represent the contribution from the elastic deformation of the foundation, where aggregate interlock did not play the primary role in the results obtained anymore.

The maximum load applied to large-scale models (Colley and Humphrey, 1967; Buch, 1998; Jensen, 2001) were 40 kN. This represented the load on one side of a standard 80 kN single axle heavy vehicle with two wheels on each side of the axle.

Foundation support models also differed greatly, varying from neoprene pads with an equivalent k-value of 27 MPa/m (Buch, 1998) to a typical Michigan Highway foundation (Jensen, 2001). To further contribute to dissimilarities in the laboratory studies, the methods used to induce a crack/joint in the test specimens, also differed. Two of the studies induced cracks by inserting metal joint formers in the fresh concrete (Colley and Humphrey, 1967; Buch, 1998), two studies used direct tensile forces (Millard and Johnson, 1984; Wattar et al., 1999), and a third method used was the application of a horizontal displacement with the aid of a surface slot by Jensen (2001).

Invariably, laboratory studies went hand-in-hand with either finite element analyses or theoretical modelling. Test results were mostly calibrated with field investigations. Colley and Humphrey (1967) collected data from in service pavement joints instrumented in a manner similar to the laboratory slabs. Millard and Johnson (1984) used Walraven's model to calibrate the aggregate interlock test results. Buch (1998) used the finite element programme ILLI-SLAB to conduct theoretical modelling, as well as dimensional analysis procedures to develop a non-linear regression equation to predict load transfer efficiency. Wattar et al. (1999) also used Walraven's two-phase model for theoretical analysis, as well as the test data obtained by Colley and Humphrey (1967). Jensen (2001) focussed mainly on the data obtained from the laboratory study, but also made use of Colley and Humphrey's (1967) data.

Apart from the definition of deflection load transfer efficiency already given in paragraph 2.2 (equation (2.4)), load transfer/joint effectiveness was also rated by the following equation (Colley and Humphrey, 1967; Ioannides and Korovesis, 1990):

$$JE(\%) = \frac{2\Delta_U}{\Delta_L + \Delta_U}(100) \tag{2.26}$$

Where:

JE = Joint effectiveness;

Δ_L = Deflection of loaded slab; and

Δ_U = Deflection of unloaded slab.

As illustrated in Figure 2.3, if load transfer at a joint was perfect, the deflections of the loaded and unloaded slabs would be equal, and the effectiveness would be 100%. Depending on the specific data set, this latter equation (2.26) tends to give values 1% to 2% higher than the former (2.4).

Further to determining the load transfer efficiency at joints, researchers also attempted to develop methods to determine equivalence of performance, for example:

Colley and Humphrey (1967) developed a summary statistic of joint performance, called the endurance index (EI), through regression analysis. This index is expressed in percent and is obtained by dividing the area under the curve of effectiveness versus cycles by the area that would be developed if the joint retained an effectiveness of 100 percent throughout one million load applications. This equation included only data obtained from the rounded natural gravel. The equation is as follows:

$$EI = 230\frac{h_e}{Pw}\sqrt{k} \tag{2.27}$$

Where:

h_e = Effective thickness (inch);

k = Modulus of subgrade reaction (pci);

P = Wheel load (lb); and

w = Joint opening (inch)

The nomograph developed from Equation (2.27) is presented in Figure 2.20.

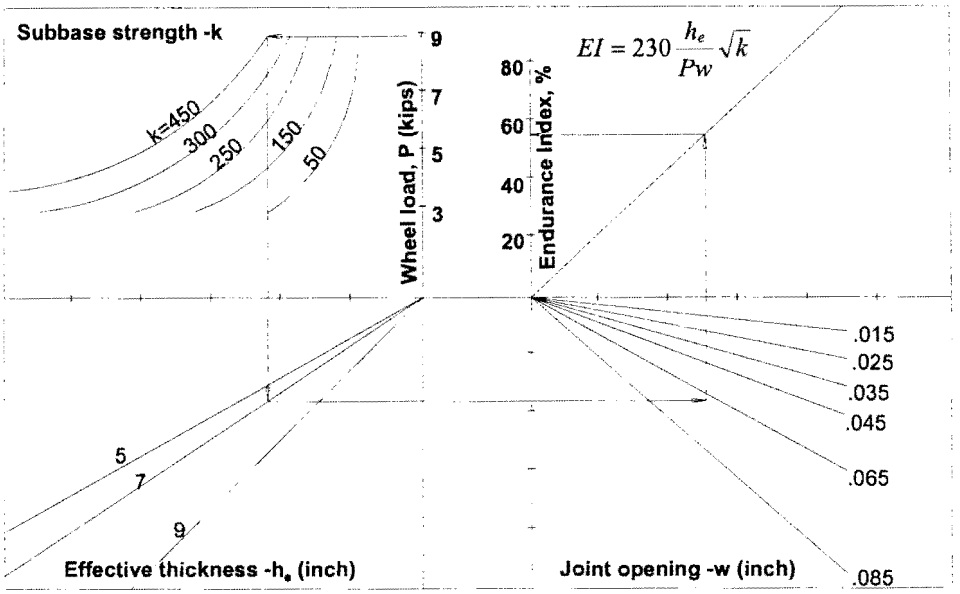

Figure 2.20: Endurance of joints (Colley and Humphrey, 1967)

Frabizzio and Buch (1999) found that fatigue cracking, caused by repeated cycles of temperature curling and moisture warping, combined with repeated loading applications of traffic load at mid-slab location, is a major source of transverse cracking in jointed concrete pavements (JCP's). Data obtained from forty-nine test sites, comprising of in-service JCP's throughout southern Michigan was used in the field investigation. Sites were chosen to represent each of four concrete coarse aggregate types: carbonate, natural gravel, recycled concrete, and slag. Each site was 25 to 65 m long and consisted of two to eight slabs. Jointed plain and jointed reinforced concrete pavements were not distinguished from one another, as it has often been found in practice that the reinforcing steel has fallen to the bottom of the slab or has been sheared off during crack formation. The effect of temperature reinforcement was therefore not considered.

The primary objective was to use field data to identify significant design parameters that affect the occurrence and performance of these transverse cracks. Another objective was to demonstrate how crack performance could be characterised using performance parameters. A void analysis procedure was also performed to characterise void potential near selected cracks and joints.

Of the parameters used to characterise crack performance were:

a) Transferred load efficiency (*TLE*), a derived parameter, which quantifies load transfer efficiency in terms of load itself (rather than deflection); the ratio of the amount of load transferred across a crack to the total applied load. The ideal condition is where the load is equally shared between both sides of a crack, in other words where *TLE* = 50%.

b) P_T; the total shear load transferred from the loaded to the unloaded side of a crack along its length, is directly derived form *TLE* using (Ioannides and Korovesis, 1990):

$$P_T = \frac{TLE}{100\%} \times P \tag{2.28}$$

Where:

P_T = Total shear load transferred (kN);
TLE = Total load efficiency (%); and
P = Total load (kN).

P_T and *TLE* provide the same information regarding characterisation of crack performance, but in different forms. It was suggested that P_T be used rather than *TLE*, as it has a more physical meaning than its counterpart (Ioannides and Korovesis, 1990).

c) The aggregate interlock shear stiffness per unit length of crack, *AGG*, parameter was computed by determining LTE_Δ, obtaining k and l, and then using the graphical relation between LTE_Δ and *AGG/kl*, developed through a theoretically based (mechanistic) design approach by Ioannides and Korovesis (1990) (see Figure 2.19).

Performance parameter thresholds were developed for LTE_Δ, P_T and *TLE* with limits that allow for evaluation of cracks in a pavement network. Ideally, rehabilitation activities would be performed before the parametric values reach threshold limits, allowing the integrity of cracked JCPs to be restored, prior to the development of crack-related distresses. A threshold value of 70% for LTE_Δ is commonly accepted. Similar values were not established for P_T and *TLE* prior to this study. In developing these thresholds, it was necessary to establish an indicator of the ability of the transverse crack to transfer load, other than the crack performance parameters. Faulting was selected as this indicator, as inadequate load transfer is a mechanism for faulting. The appropriate threshold value for P_T was determined as 16,5 kN, and for *AGG* as 200 MPa.

2.4.4 Joint deterioration mechanisms

As important as it is to define the load transfer mechanisms, it is equally important to define the joint deterioration mechanisms. The main mechanisms that cause joint deterioration are: aggregate wear out, loss of dowel support, and development of erosion as it pertains to faulting in jointed concrete pavements or punch-out development in continuously reinforced concrete pavements (Jeong and Zollinger, 2001). Of these three mechanisms, aggregate wear out will be discussed here, whereas dowel looseness is described in the following paragraph. As it has been envisaged to construct the experimental slabs on a rubber foundation, the mechanism of subbase erosion is cancelled out of the present study, although it is still considered for follow-up studies.

Two studies were singled out to describe the results of research work that has already been conducted on the subject of aggregate wear out or abrasion within the crack face, namely: the development of the volumetric surface texture (VST) test by Vandenbossche (1999), and the function developed by Jeong and Zollinger (2001).

Vandenbossche (1999) was part of the team at the University of Minnesota that developed the VST test. Although this test was developed to provide an estimate of the load transfer potential available through aggregate interlock across a concrete fracture plane, it was also stated that the test could provide an estimate of the abrasion that has taken place since fracture.

The test apparatus consisted of a spring-loaded probe with a digital readout, mounted on a frame over a computer-controlled microscope of the type typically used to obtain linear traverse and other measurements of concrete air void systems. The distance from an arbitrarily established datum to the fractured surface at any chosen point was measured in a predetermined grid pattern to map the three-dimensional fractured surface. A 3,2 mm grid was established by determining how far apart readings could be measured while still maintaining a precision of $\pm$ 0,0001 cm^3/cm^2 over a specified area, regardless of the positioning of the grid. The average area measured was about 161 cm^2 per specimen. After completion of this testing the surface texture was quantified in terms of a VST ratio (VSTR), defined as the ratio of the volume of texture per unit surface area (in cm^3/cm^2). A high VSTR indicated a rough surface texture, while a low value indicated a smooth texture.

To validate the VST test, tests were performed on both laboratory and field specimens. The laboratory study included tests performed on flexural beam specimens broken after 18 h, 7 days, and 28 days of curing. The beams were companion specimens cast in conjunction with full-scale concrete pavement test slabs, which were cracked 18 h after casting and were then subjected to simulated vehicle loads after 28 days of curing. Deflection, load and crack width data were collected for each slab. VST testing was also performed on cores retrieved from cracks and un-doweled joints of several concrete pavements across the USA. Joint and crack load transfer measurements were obtained for each pavement section by using a falling weight deflectometer at the time that the cores were retrieved.

Both the laboratory and the field data indicated a significant increase in VSTR with an increase in maximum aggregate size (an increase in maximum aggregate size from 38 to 63 mm, increased the VSTR by 66%), especially for angular aggregates. Durable (limestone) aggregates also had higher VSTRs than weaker aggregates (slag). The same applied to concrete prepared with virgin aggregates compared to recycled rounded aggregate concrete. A further observation was that cracks tended to propagate through weaker aggregates and around stronger aggregate particles, and that weaker aggregates tended to abrade more easily under repeated joint and crack movements.

Vandenbossche (1999) stated that this study had demonstrated that the VST test provides a means of accurately measuring surface texture so that the selection of concrete aggregates can be performed with

consideration of potential aggregate interlock at cracks and un-doweled joints. It also provides the engineer with an early indication of the extent of aggregate wear out that could be expected from a particular aggregate size, type, gradation, or blend.

Jeong and Zollinger (2001) investigated all three joint deterioration mechanisms as part of the prediction of faulting or punch-out distress at a joint or crack (The combined effect of aggregate interlock and dowel modelling is discussed in paragraph 2.5.4). They built forth on the work conducted by Ioannides and Korovesis during 1990 and 1992 (Ioannides and Korovesis, 1990; Ioannides and Korovesis, 1992) as the basis for this prediction.

It is generally accepted that joint or crack opening affects the degree of load transfer as far as it is sustained through aggregate interlock. Based on research the following relation has been established (Jeong and Zollinger, 2001):

$$\log(J_{cki}) = a.\exp\left[-\exp\left(-\frac{J_s-b}{c}\right)\right] + d.\exp\left[-\exp\left(-\frac{s_0-e}{f}\right)\right] + g.\exp\left[-\exp\left(-\frac{J_s-b}{c}\right)\right] x \exp\left[-\exp\left(-\frac{s_0-e}{f}\right)\right] \quad (2.29)$$

Where:

a	=	-4,00;
b	=	-11,26;
c	=	7,56;
d	=	-28.85;
e	=	0,35;
f	=	0,38;
g	=	56,25;
J_s	=	Load transfer on the shoulder of longitudinal joint;
s_0	=	Shear capacity $ae^{-0.039\omega}$, with a = 0,55 to 1,3 as a function of slab thickness = $0,0312h^{1,4578}$;
τ	=	Shear stress on the crack face = s_0P/h^2;
P	=	Wheel load; and
h	=	Slab thickness.

The shear capacity term (s_0) in Equation (2.29) is a significant parameter in the transfer of load relative to the aggregate interlock mechanism that can be used to represent the deterioration or wear out of aggregate interlock due to load repetition. The function for aggregate interlock wear out is important to account for the development of punch-out or faulting distress (Jeong and Zollinger, 2001):

$$\Delta s_{ij} = \sum_i \sum_j (0{,}069 - 1{,}5317 e^{-w_i/h}) \left(\frac{n_{ij}}{10^6}\right) \left(\frac{\tau_{stress}}{\tau_{ref}}\right) \quad (2.30)$$

Where:

n_{ij} = Number of axle load applications for current sub increment i and load group j;

τ_{stress} = Shear stress on the transverse crack;

τ_{ref} = Reference shear stress derived from Portland Cement Association test results; and

w_i = Crack width in sub-increment i.

Shear stresses (τ_{stress} and τ_{ref}) are computed as follows:

$$\tau_{stress} = sP_i / h^2 \quad (2.31)$$

$$\tau_{ref} = 111{,}1 . s_{pca} = 111{,}1 . [a + b \ln(J)^2 + c \ln(J) + de^{-1}] \quad (2.32)$$

Where:

s = Dimensionless shear;

J = Joint stiffness computed on the transverse crack;

a = 0,0848;

b = -0,000364;

c = 0,0188; and

d = -0,006357.

Equation (2.30) constitutes the wear-out function that allows for consideration of the deterioration of the aggregate interlock. Setting this equation to zero shear loss yields a threshold value of the dimensionless term ω/h = 3,1 below which no loss in shear capacity occurs. Examination of crack width data obtained from field measurements of continuously reinforced concrete pavements indicated that an LTE of about 91% is associated with a ω/h of 3,1. The data trends suggested that with an LTE above the 90 to 92% range, minimal loss of shear capacity is expected to occur. The crack widths were back calculated from Equations (B.44) (Equation (2.48)) and (2.29) for the given slab thickness and measured LTE. Equation (2.30) provides an estimate of the loss of shear capacity as a function of key slab characteristics and load repetition. The deteriorated level of shear capacity can be determined with the equation:

$$s_{new} = s_{old} - \Delta s \quad (2.33)$$

Where Δs is based on Equation (2.30) and s_{old} is the shear capacity before the loading increment and s_{new} is the resultant capacity due to the loading increment. The Δs may also be due to a change in the joint or crack opening. The new stiffness value can be determined with Equation (2.29) and s_{new}.

2.4.5 Summary of aggregate interlock modelling

This paragraph gives an overview of the studies conducted by various researchers on the subject of aggregate interlock shear load transfer at a joint in a concrete pavement. Although some of the studies used/tested the same micro-mechanics-based analysis model developed by Walraven, there were just as many different methods and models as research projects. Probably the only aspect these research projects really had in common was the fact that they all attempted to somehow understand the mechanics of aggregate interlock, and test/develop a method of quantifying it.

It has been agreed that the effectiveness of aggregate interlock load transfer at a joint in a concrete pavement depends on load magnitude, number of load repetitions, slab thickness, joint opening, subbase characteristics, subgrade bearing value, and aggregate angularity.

Aggregate interlock in cracks is not only a relation between shear stresses and shear displacements, but it is an interaction between normal and shear displacements on the one hand and normal and shear stresses on the other hand. The shear resistance depends on contributions from all particles with diameters larger than the crack width (Reinhardt and Walraven, 1982).

Studies conducted by Dong and Guo (1999), as well as by Vuong et al. (2001), indicated that environmental effects played a more important role than the traffic load on the reduction of load transfer capability of transverse joints relying on aggregate interlock load transfer. Although no serious structural distresses were observed during these investigations, it was verified that cold weather might significantly reduce the load and deflection load transfer efficiency of transverse joints. Hot weather on the other hand can cause such high compressive stresses in the pavement that blow-ups can occur.

The width of the joint/crack opening controlled the performance of the joint (Jensen, 2001). Opening the joint by 0,8 mm resulted in a loss of load transfer of 50% (Buch, 1998). In other words, aggregate interlock was considered effective in stress control when the joints were closed or under compression, but that it was not dependable when the joints opened 0,9 mm or more, irrespective of the maximum size of the aggregate in the concrete.

The surface texture of the crack directly influences the aggregate interlock and load transfer capacity of the joint. The texture of the crack face is a function of the coarse aggregate type, size, and gradation. It is also dependent on the maturity of the concrete. It is therefore logical that rough surfaced coarse aggregate will have better interlock characteristics than rounded smooth aggregate (Buch, 1998).

Davids et al. (1998) considered the micro-mechanics-based modelling technique of Walraven (1981) as the best choice for modelling aggregate interlock shear transfer. Davids et al. (1998) incorporated Walraven's model in the finite element models of the EverFE software programme. EverFE was

therefore considered the best tool available to conduct theoretical analyses, prior to laboratory studies, for the research project described in this thesis (see Appendix D).

In essence the VST (Vandenbossche, 1999) provides a practical tool for determining the aggregate interlock potential of a crack face, whereas the two-phase model by Walraven (1981) provides the theoretical tool, and the S-curve developed by Ioannides and Korovesis (1990) a mechanistic method.

The VST can also be used to provide an estimate of the abrasion or aggregate wear out that has taken place since fracture (Vandenbossche, 1999), together with the aggregate interlock wear-out function developed by Jeong and Zollinger (2001).

2.5 DOWEL MODELLING

2.5.1 Introduction

As was stated in paragraph 2.4, load transfer at joints is accomplished by two primary load transfer mechanisms, namely aggregate interlock and dowel bars. Aggregate interlock load transfer has been dealt with in detail in the previous paragraph and although the main objective was to investigate aggregate interlock load transfer through laboratory modelling, dowel modelling is just as important and warranted an in depth discussion.

Dowel bars have been used as load transfer devices in jointed concrete pavements at least since 1917 (Teller and Cashell, 1958). The use of dowel bars was justified by the fact that it prevents faulting, reduce pumping, and reduce corner breaks. The design of dowel bar diameter, length, and spacing, is based mostly on experience. For normal concrete pavements in South Africa the slab length, aggregate size, dowel diameter and spacing, are usually specified as 4,5 m, 37,5 mm maximum, 22 mm bars spaced at 600 mm, respectively (Manual M10, 1995).

Across the 50 states of America, however, disparities existed among the practices adopted by agencies, as well as among those reported from other countries (Ioannides et al., 1990). The main reasons were:

a) The theoretical treatment of the pertinent problems was still fairly elementary and strictly applicable to only highly idealised conditions.
b) Climatic and geotechnical conditions varied widely from state to state and from country to country.
c) The number, frequency, magnitude and geometry of traffic loadings were considerably different in each locality, and the concepts used to reduce mixed traffic to a design traffic number were sometimes flawed.

d) A large degree of empiricism derived from local experience entered the design and construction approaches of each agency.

This paragraph presents an overview of previous investigations by which various researchers attempted to develop fundamental design theory based on mechanistic design principles for the modelling of doweled slab-on-grade pavement systems. The logic behind the development of the dowel bar model used in the three-dimensional finite element (3DFE) computer programme, EverFE (Davids et al., 1998a; 1998b), is also summarised. Further literature reviews on the subject of modelling of dowel-shear load transfer across cracks in concrete pavements that have merit are summarised in Appendix C.

2.5.2 Analytical dowel modelling

The first procedure for the design of doweled joints in concrete pavements was presented by Westergaard (1926). However, the main theoretical definition of dowel behaviour to date has been presented by Friberg (1940). Experimental evidence presented by Teller and Cashell (1958) that suggested a direct exponential relation between dowel diameter and efficiency of load transfer lent credibility to the Friberg methodology. Furthermore, Teller and Cashell (1958) provided data suggesting that an increase in the modulus of subgrade reaction, k will cause a decrease in the amount of load transferred. This indicated that a dowel would show its highest effectiveness on a flexible subgrade where it is needed, and its lowest effectiveness on a stiff subgrade where it is not needed.

The length of dowel embedment necessary to develop maximum load transfer is not a constant function of dowel diameter as has sometimes been assumed. With a 19,0 mm (¾ inch) dowel diameter, maximum load transfer requires an embedded length of about eight dowel diameters. With larger dowels, such as the 25,4 mm (1 inch) and 31,8 mm ($1^1/_4$ inch) diameters, full load transfer is obtained with a length of embedment of about six diameters, both initially and after hundreds of thousands of repetitive loading (Teller and Cashell, 1958).

An experimental study by Snyder (1989) verified that a larger diameter dowel would ensure smaller dowel deflections, leading to reduced concrete bearing stresses and simultaneous decreased dowel looseness. The condition of dowel looseness has an important effect on the structural performance of the dowel; since it can function at full efficiency only after this looseness is taken up by load deflection. This is true for both initial looseness and that which develops during repetitive loading. *Tests that do not include repetitive loading and complete stress reversal provide no information on this important condition and no measure of its effects* (Teller and Cashell, 1958).

During the laboratory study conducted by Teller and Cashell (1958) the increase in looseness around the dowel, developed during the first 40 000 load application cycles, equalled that developed by the subsequent 1,96 million (up to 2 million) cycles (see Figure 2.21).

Another subject of debate was the number of dowels effective in distributing the load. Based upon Westergaard's theory, Friberg (1940) noted that for loadings a considerable distance from the edge, the maximum positive moment occurs beneath the load, and the maximum negative moment occurs a distance 1,8*l* from the point of loading. Beyond 1,8*l*, sometimes referred as the effective length (*e*), the moment changes very little. Finite element (FE) studies led to the conclusion that the assumption by Friberg was appropriate but that the effective length was 1,0*l*. These conclusions are appropriate for a single wheel loading only; multiple gear configurations will lead to different values of the effective length. Two important conclusions that have been a prominent point of debate in the decades that followed, even to the present day, are (Ioannides et al., 1990):

a) Only the two, or at most four, dowels nearest to the load need to be considered as active, since the contribution of more remote bars is negligible.
b) Dowels are affective in reducing bending stress developed in the loaded slab only if they are spaced closely enough (at less than 600 mm (2 ft) apart).

It is thought that bearing stresses under the dowel are responsible for spalling and looseness of the dowels. Analytical methods for quantifying the bearing stresses in dowel bars have been in existence since the late 1930's. Several investigators have presented formulae for calculating the concrete bearing stress. All of these formulations for bearing stress (σ_b) may be represented by the following relationship (Ioannides at el, 1990):

$$\sigma_b = A(structural) * B(load) \tag{2.34}$$

The first term *A*, is determined from the structural characteristics of the pavement system, while the second term, *B*, quantifies the transferred load.

Friberg (1940) based his analysis upon considering the dowel as a semi-infinite beam on a Winkler foundation (see Figure 2.22). His basic relationship for dowel stresses was:

$$\sigma_b = K\Delta_0 \tag{2.35}$$

Where:

K = Modulus of dowel support (FL^{-3}); and
Δ_0 = Deflection of the dowel with respect to the concrete at the face of the joint (L).

Friberg's (1940) analysis of dowel bar support is given in Figure 2.23, and his relationship for the maximum deformation of concrete under a dowel bar with a shear force P is given in Equation (2.36).

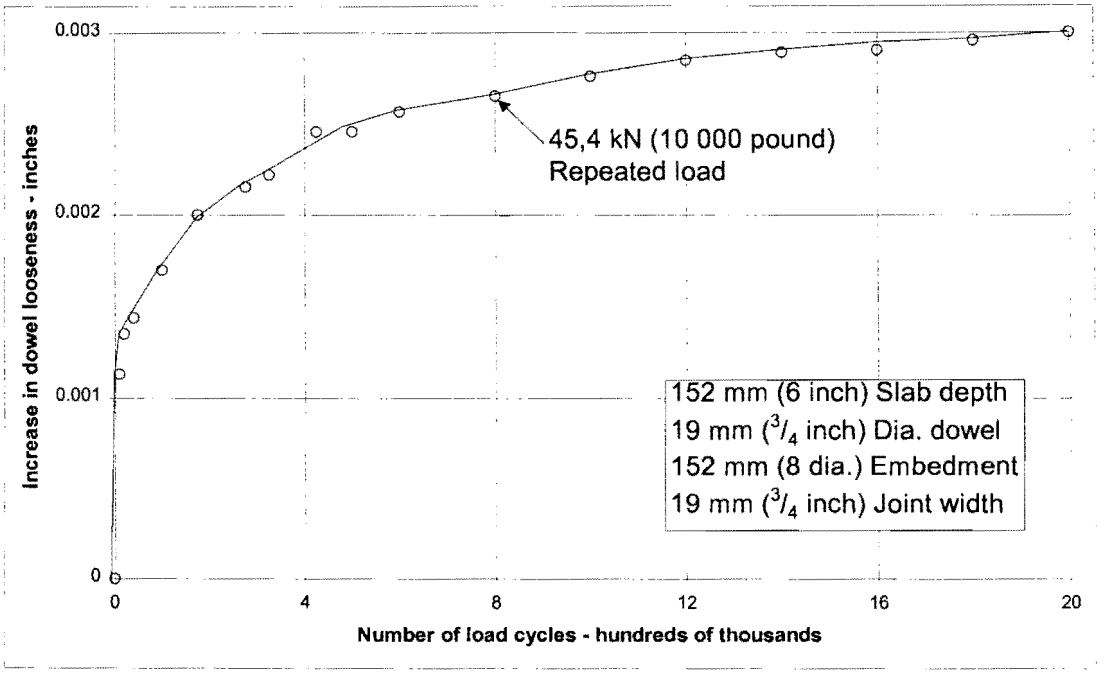

Figure 2.21: Effect of repetitive loading on the development of dowel looseness (Teller and Cashell, 1958)

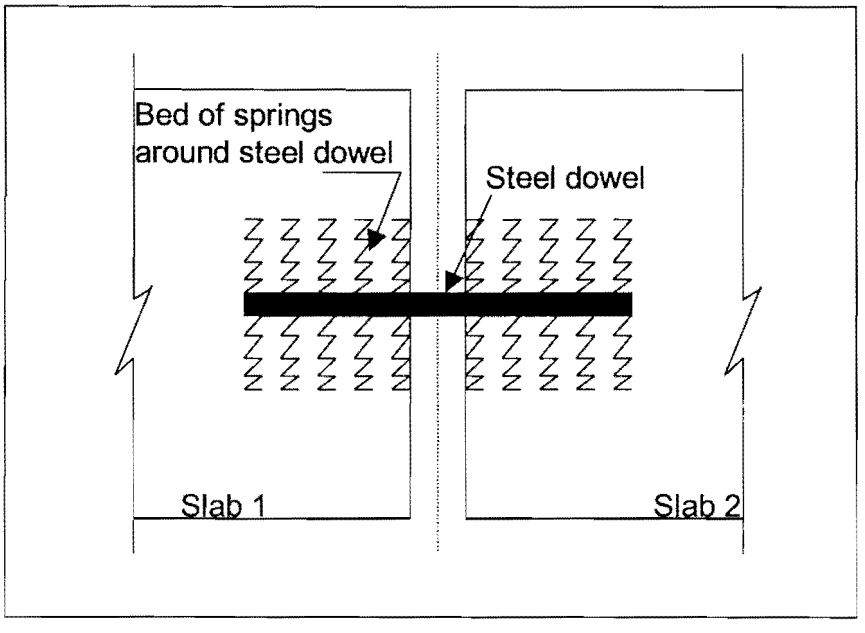

Figure 2.22: Winkler foundation between dowel and slab (Friberg, 1940)

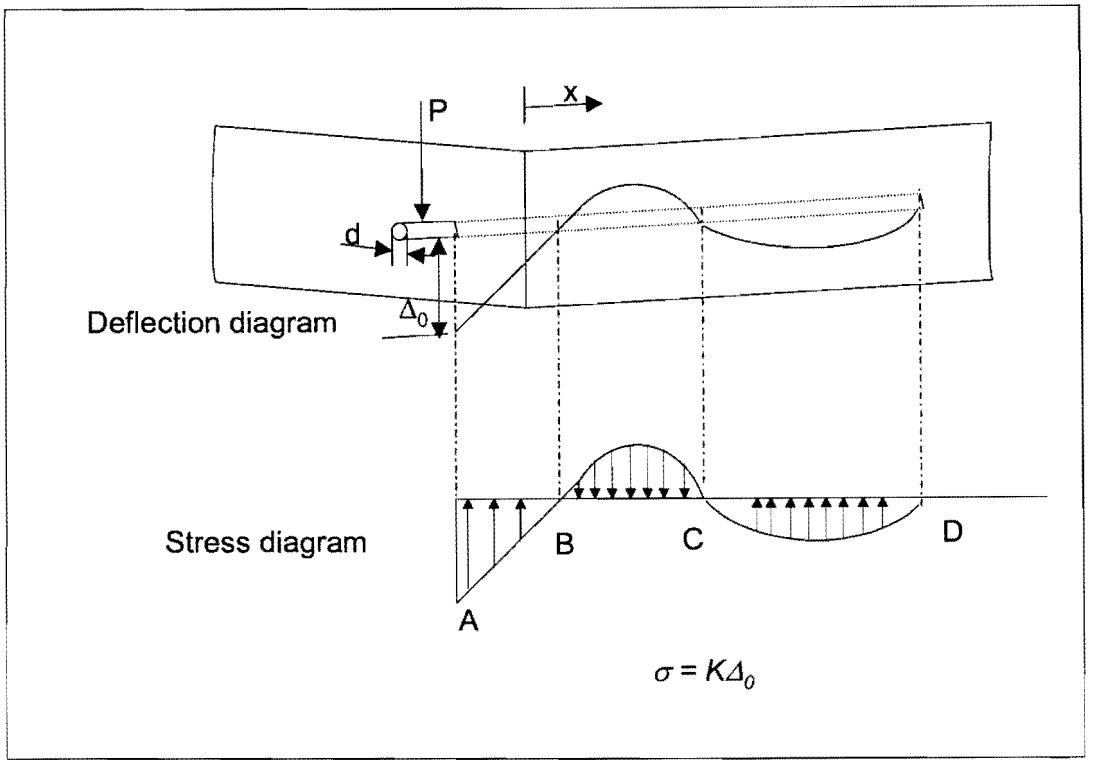

Figure 2.23: Analysis of dowel bar support (Friberg, 1940)

$$\Delta_0 = \frac{P_i}{4\beta^3 E_d I_d}(2 + \beta\omega) \tag{2.36}$$

Where:

Δ_0 = Deflection of the dowel relative to the concrete at the joint face (L);

P_i = Shear force acting on any particular dowel, transferred across the joint (F);

ω = Width of joint opening (L);

E_d = Modulus of elasticity of the dowel (FL^{-2}); and

I_d = Moment of inertia of the dowel (L^4).

Note that the primary dimensions are abbreviated as L for length and F for force.

For solid round bars,

$$I_d = \frac{\pi dia^4}{64} \tag{2.37}$$

Where dia is the dowel bar diameter (L) and β is the relative stiffness of the dowel/concrete system, as defined by Equation (2.38).

$$\beta = \sqrt[4]{\frac{Kdia}{4E_dI_d}} \tag{2.38}$$

The bearing stress on the concrete then becomes:

$$\sigma_b = \frac{KP}{4\beta^3 E_d I_d}(2 + \beta\omega) \tag{2.39}$$

Through dimensional analysis Ioannides et al., (1996) used the Friberg (1940) formula as basis and incorporated a dimensionless term quantifying the portion of the load carried by the critical dowel (f_{dc}), as shown in Equation (2.40):

$$\sigma_b = \frac{K(2 + \beta\omega)}{4\beta^3 E_d I_d} * P * TLE * f_{dc} \tag{2.40}$$

The critical dowel is the dowel carrying the largest shear force. Approximations for f_{dc} is given by S/e for edge load, and by $(2S/(e+S))$ for corner load, where:

e	=	Effective length;
S	=	Dowel spacing, and
TLE	=	$P_T/P * 100$, where:
P_T	=	Total load transferred across the entire length of joint.

In a study similar to the mechanistic analysis of aggregate interlock load transfer mechanisms (Ioannides and Korovesis, 1990) in which the dimensionless joint stiffness parameter AGG/kl, has been developed, Ioannides and Korovesis (1992) also developed the concept of a dimensionless joint stiffness for the doweled joint, D/skl. The major load transfer mechanism in doweled joints is also shear, since bending of the bar over the very small span afforded by the joint opening has a relatively minor effect.

Comparison of the stiffness matrices used to describe the aggregate interlock and doweled joint load transfer mechanisms in the ILLI-SLAB FE programme, suggested a correspondence between AGG and D/s where D is the composite shear stiffness of the supported dowel (FL^{-1}), and s is the dowel spacing (L). The dimensionless ratio D/skl is therefore the governing independent variable.

The ILLI-SLAB model considers the dowel bar as a thick beam element whose shear stiffness (i.e. resistance to deformation in the vertical direction) is $12C$ (FL^{-1}). This term expresses the shear force in the dowel per unit vertical deformation of the dowel. The support provided by the concrete matrix is modelled as a single spring that acts at the joint face and whose stiffness is dowel-concrete interaction

parameter (DCI) parameter (FL^{-1}). This is the shear force transferred by the dowel per unit deflection of the dowel with respect to the concrete matrix. For the supported dowel, therefore, the composite springs-in-series shear stiffness, D, is defined as (Ioannides and Korovesis, 1992):

$$D = \frac{1}{\frac{1}{DCI} + \frac{1}{12C}} \tag{2.41}$$

In which:

$$C = \frac{E_d I_d}{\omega^3(1+\phi)} \tag{2.42}$$

$$\phi = \frac{12E_d I_d}{G_d A_z \omega^2} \tag{2.43}$$

Where:

G_d = Shear modulus of dowel bar (FL^{-2}),

$$G_d = \frac{E_d}{2(1+\mu_d)} \tag{2.44}$$

Where:

E_d = Modulus of elasticity of dowel (FL^{-2}), as before;

μ_d = Poisson's ratio of dowel;

A_z = Cross-sectional area of dowel effective in shear (L^2);

$A_z = 0{,}9A_d$ for solid round bars, (2.45)

A_d = the cross-sectional area of the dowel (L^2), with

$$A_d = \frac{\pi dia^2}{4} \tag{2.46}$$

The DCI assuming the dowel to be a beam on a spring foundation (Friberg, 1940) is given by the following relationship:

$$DCI = \frac{P_i}{\Delta_{di}} = \frac{4\beta^3 E_d I_d}{(2+\beta\omega)} \tag{2.47}$$

Where:

Δ_{di} = Deflection of any given dowel relative to the concrete (L).

The proposed dimensionless independent variable (D/skl) lumps together all the necessary input parameters pertaining to the dowel bars (d, s, E_d, μ_d, K, ω), as well as those used in characterising the materials of a slab-on-grade pavement (k, E, H, μ). The only parameter missing is the embedment length, which, is not incorporated in the ILLI-SLAB model, either (Ioannides and Korovesis, 1992).

Guo, Sherwood and Snyder (1995) addressed this "missing" parameter by using ILLI-SLAB FE analyses in comparisons with experimental results to determine that the longer the dowel bar embedment length, the higher the load transfer capability of the dowel bar system. This led to an increase of maximum displacement and stress in the unloaded slab, a decrease of maximum displacement in the loaded slab, and more total shear force transmitted from the loaded to the unloaded slab. Also, when the half-embedded length is greater than five times the bar diameter, the difference of results between finitely and infinitely long dowel bar models can be neglected. Based on this, Guo et al. (1995) came to the conclusion that current dowel bars can be approximately modelled by assuming the embedded length to be infinitely long.

The dimensionless joint stiffness (*D/skl*) addressed earlier concerns that the behaviour of dowels is not merely a function of their own flexibility properties, but is influenced considerably by the stiffness characteristics (including slab thickness) of the entire pavement system in which they are incorporated.

Through a number of executions of the ILLI-SLAB FE code, the shear-only data plot exactly on the previously determined *AGG/kl* curve (See Figure 2.19). These results therefore confirmed the direct correspondence between *AGG/kl* and *D/skl*.

To complete the overview on analytical-empirical modelling by various researchers, the results of a few studies are presented below:

Buch and Zollinger (1996)

This paper presented the results of an in-depth study of factors that affect dowel looseness in jointed concrete pavements. The laboratory investigation revealed the influence of aggregate type (in relation to oxide content), aggregate texture and shape, bearing stress (dowel diameter and crack width), load magnitude, and number of load cycles on the magnitude of dowel looseness and the subsequent loss in load transfer efficiency (LTE) across saw-cut joints. They developed an empirical-mechanistic dowel looseness prediction model based on the experimental results.

The causes for initial dowel looseness were summarised as follows:

a) Coating applied to dowels to prevent bond or to protect the dowel bar against corrosion.
b) Water or air voids in the concrete around the dowels due to improper construction procedures.
c) Shrinkage of concrete during hardening.

A two-phase modelling approach was adopted: an experimental phase and an analytical phase. The variables considered for the model development were aggregate type and texture, dowel diameter, and magnitude of load. An experimental program was developed to study the effect of load cycles (N), and load (P) on the magnitude of dowel looseness.

Apart from conclusions that have already been drawn from the above-mentioned investigations, this specific study has shown the following:

a) The analysis of dowel looseness revealed that the magnitude of dowel looseness increased with increasing number of load cycles, and also that the magnitude of dowel looseness for a given load level was greater in specimens made with river gravel when compared with concrete samples made with limestone.
b) Further research must be conducted to develop a correlation between dowel looseness, aggregate angularity, and aggregate abrasive characteristics.
c) The prediction model (Friberg, 1940) can be further improved by investigating the influence of a non-dimensional parameter $\sigma_b h^2/P$ on dowel looseness. This will lead to the elimination of the variable P.

Hossain and Wojakowski (1996)

Hossain and Wojakowski (1996) reported the results of a survey, conducted over a period of 9 years, where six jointed reinforced concrete pavement (JRCP) and one jointed plain concrete (JPCP) pavement test sections were surveyed annually for faulting. The main focus of the investigation was to determine the effect of *concrete mix consolidation* with time on joint faulting and LTE.

Twenty-three test sections with lengths from 32 m to 1 584 m were constructed with various adjustments to vibrator settings (frequency and amplitude), concrete admixtures, and other special features of JRCP. Seven of these test sections were monitored for long-term performance for this joint faulting and LTE study.

Joint fault depth measurements were made with a fault meter built from the plans provided by the University of Illinois. Falling weight deflectometer (FWD) tests were done using a Dynatest-8000 FWD to assess the load transfer efficiencies of the joints.

The results of this study showed that:

a) As the original concrete density increased because of improved consolidation, the rate of increase of joint fault depth decreased at doweled joints.
b) The occurrence of joint faulting was much more severe when load transfer devices were not present.
c) Improved concrete mix consolidation appeared to improve load transfer, resulting in a lower rate of faulting.

2.5.3 Finite element dowel modelling

Certain key attributes of the more common FE programmes as reported in the literature have been summarised in Tables 2.1 (2D studies) and 2.2 (3D studies) of paragraph 2.3. During development of the 3DFE computer programme, EverFE, Davids et al. (1998a, 1998b) also conducted a review of current dowel modelling techniques. They confirmed that several different approaches have been used to model load transfer in jointed concrete pavements via dowel action, and that the interaction of the dowel and the slab is complex, but that it consists mainly of two portions, namely:

a) Looseness (gaps) between the dowel and the slab.
b) Compression of the slab around the dowel.

Several investigators had shown that dowel looseness has a significant effect on joint performance (Buch and Zollinger, 1996; Snyder, 1989). Zaman and Alvappillai (1995) did a two-dimensional (2D) FE study that explicitly considered dowel looseness. The study by Parsons, Eom, and Hjelmstad (1997) examined this problem with contact modelling using a 2D plane strain model.

Most attempts to model dowel-slab interaction approximately accounted for compression of the slab around the dowel by assuming a Winkler foundation between the dowel and the surrounding slab. This approach was even used before the development of the FE analysis. Investigators have typically modelled dowel bars with discrete beam elements between adjacent slabs having springs between the dowels and the slabs to account for the effect of dowel-slab interaction, as in ILLI-SLAB (Tabatabaie and Barenberg, 1980) and JSLAB. The spring stiffnesses were derived by considering the embedded portion of the dowel as an infinitely long beam on a Winkler foundation.

No 3DFE models have considered the effect of dowel looseness on joint performance. Davids et al. (1998a, 1998b) proposed and developed a new technique for modelling dowel load transfer, which relies on an embedded formulation of the dowel, and allows the explicit and rigorous consideration of gaps between the dowel and the slab through nodal contact modelling. The details for the necessary inclusion of a bond-slip law were also presented.

The dowel was modelled as an embedded quadratic beam element within a solid, quadratic, iso-parametric element. Three types of embedment were considered:

a) A bonded (axially constraining the dowel to the embedding element), constrained (constraint of transverse dowel displacements to the embedding element) embedded dowel.
b) A de-bonded, constrained dowel.
c) A de-bonded dowel with a gap.

Specific advantages of the embedding formulation are as follows:

a) Slab mesh divisions are not restricted to coincide with dowel lines.

b) The element may be de-bonded at selected nodes.

c) The non-linear effect of gaps between the dowel and surrounding slab concrete can be explicitly modelled.

d) The element stiffness is easily computed using a matrix transformation, and does not require special integration techniques. Both the effects of de-bonding and gaps are incorporated in this transformation.

e) The dowel element permits the incorporation of a general bond-slip law, making it appropriate for modelling reinforcement in conventional reinforced concrete structures.

2.5.4 Combined aggregate interlock and dowel modelling

Soroushian et al. (1988) investigated the combined effect of aggregate interlock and dowel action in reinforced concrete beam elements against sliding shear at a crack. Algorithms were developed for predicting the aggregate interlock constitutive behaviour using some empirical formulations. They concluded that at very small sliding-shear deformations (below 0,2 mm) the dowel action tended to dominate the shear resistance. At larger deformations, however, the aggregate interlock became more dominant. At sliding-shear deformations greater than 0,7 mm, about 65% of the total shear resistance in the case studied was provided by aggregate interlock. One of the results of their tests is given in Figure 2.24.

A theoretical analysis to determine the combined effect of aggregate interlock and dowel action was also conducted with EverFE (see Appendix D). The same model as the one used in aggregate interlock modelling with a cement stabilised subbase was used. To determine the effect of dowels in the model, 16 mm diameter dowels at 300 mm spacing were placed across the joint. During theoretical modelling the crack width was varied, while the gap around the dowel was initially kept constant.

The deflection LTE obtained for 9 mm and 63 mm aggregate sizes are presented in Figure 2.25. From this figure, it is obvious that the combined efficiency of aggregate interlock and dowels is far greater than for aggregate interlock only.

The maximum aggregate interlock shear stress measured in the wheel path was less for the combined aggregate interlock and dowel action models than for the models relying on aggregate interlock only (see Figure 2.26). This could be ascribed to the dowels relieving some of the stress in the aggregate.

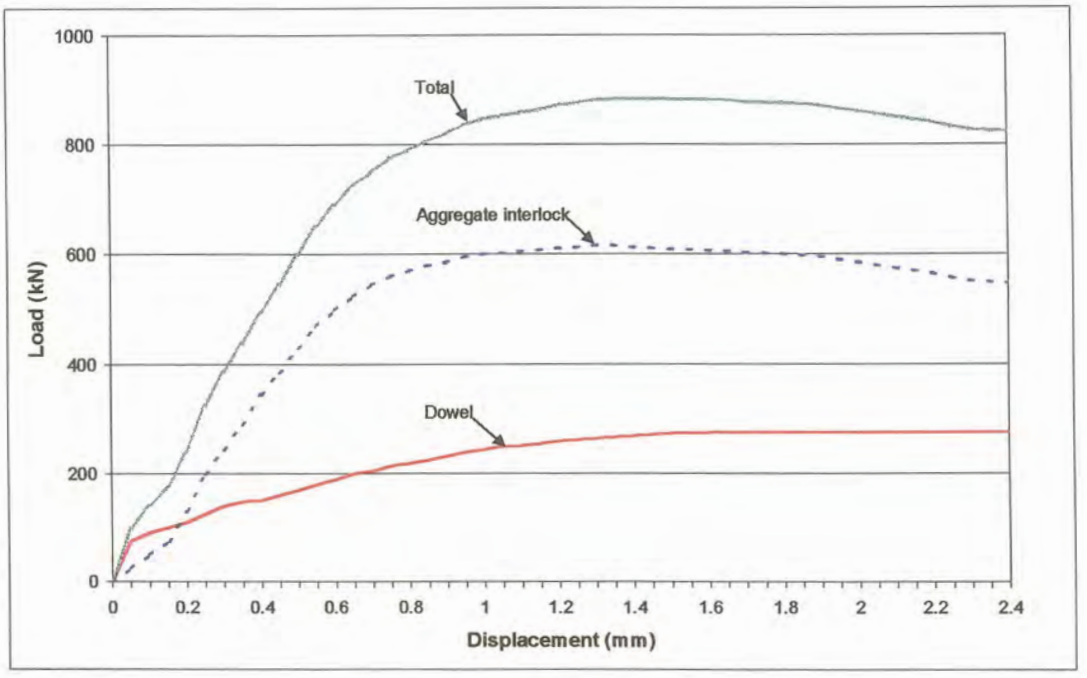

Figure 2.24: Sliding shear behaviour at a constant crack width of 0,5 mm (Soroushian et al., 1988)

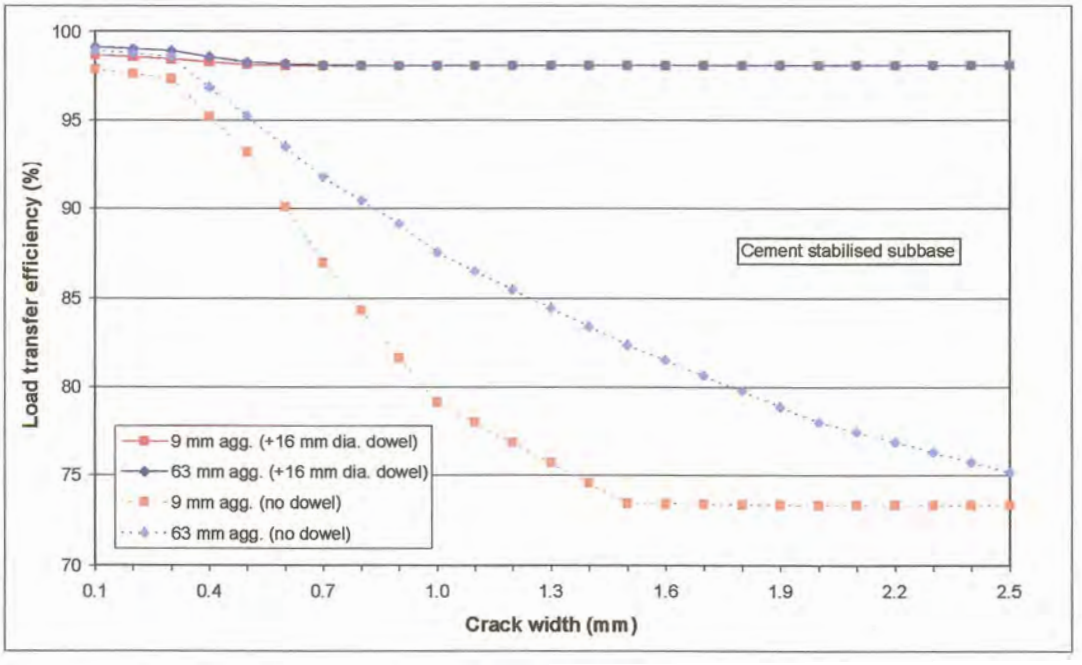

Figure 2.25: Deflection LTE in the wheel path – aggregate interlock versus combined effect of aggregate interlock and dowel action (no gap around dowel)

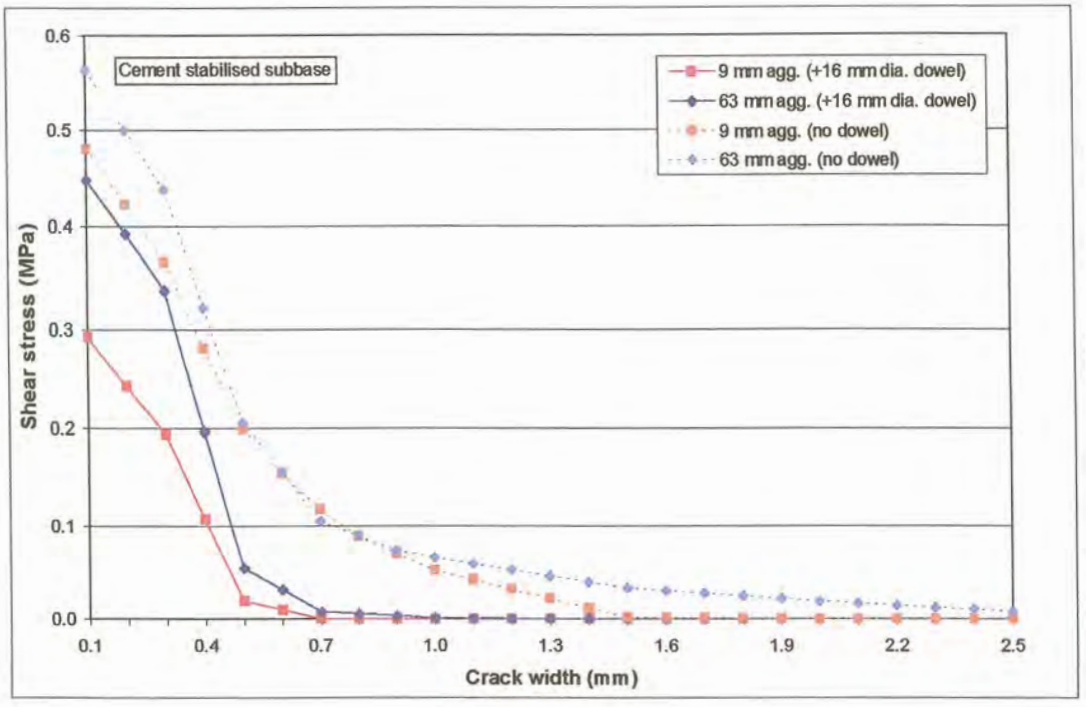

Figure 2.26: Maximum shear stress at joint in wheel path – aggregate interlock versus combined effect of aggregate interlock and dowel action (no gap around dowel)

Just as for the shear stress, the total aggregate interlock shear force transferred across the joint was also less for the combined model than for the aggregate interlock model, as can be seen from Figure 2.27.

The LTE of various dowel configurations was obtained during analyses with EverFE, for situations where the gap around the dowel was considered to be zero (see Appendix D). These analyses were repeated, but in the latter case the gap around the dowel was varied from 0,00 mm to 0,10 mm. The bigger the gap around the dowel, the lower the LTE. For comparison purposes, the values obtained for a joint relying on aggregate interlock only (no dowel), was also determined. At a gap of 0,10 mm the LTE approximated the "no dowel" case, which indicated that the dowel did not fulfil its purpose any more (see Figures 2.28 and 2.29). This emphasised the importance of considering a gap around the dowel as well, but also that high load transfer conditions are obtained through aggregate interlock (Jeong and Zollinger, 2001). The further analyses conducted with EverFE is described in detail in Appendix D.

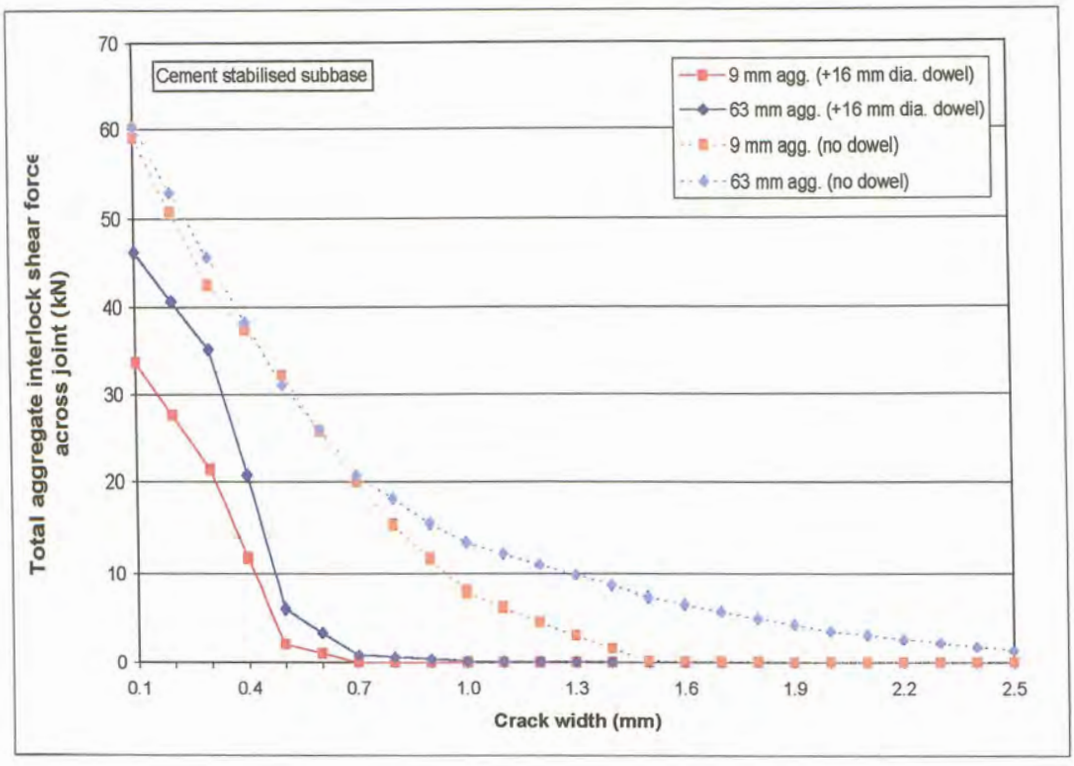

Figure 2.27: Total shear force transferred across joint – aggregate interlock versus combined effect of aggregate interlock and dowel action (no gap around dowel)

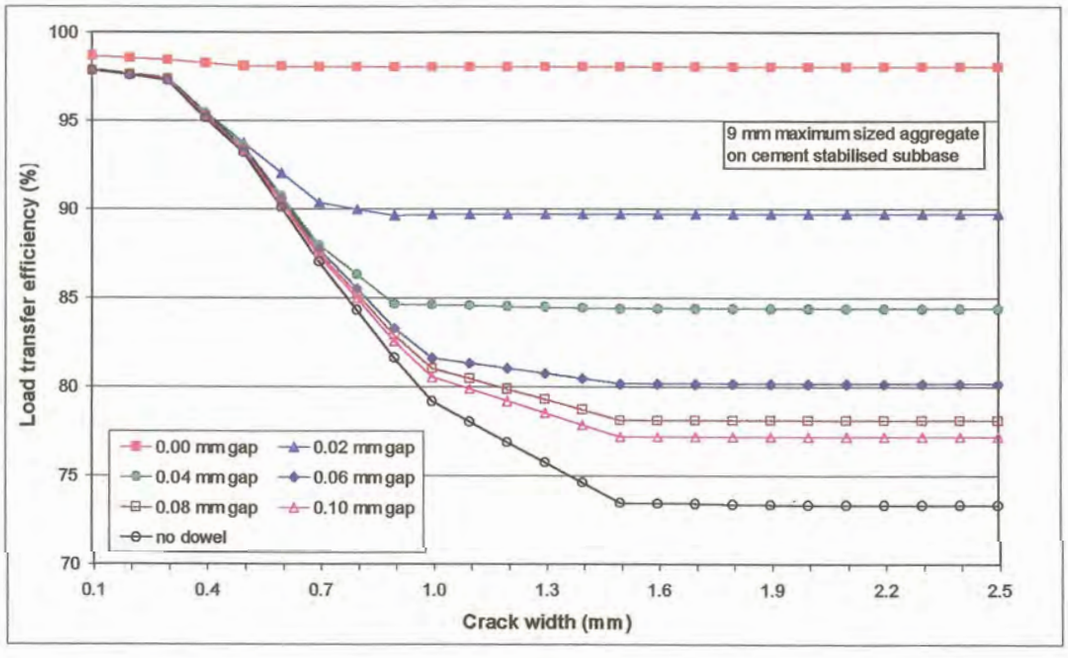

Figure 2.28: Deflection LTE in the wheel path – 9 mm maximum sized aggregate – combined affect of aggregate interlock and dowels (gap around dowel)

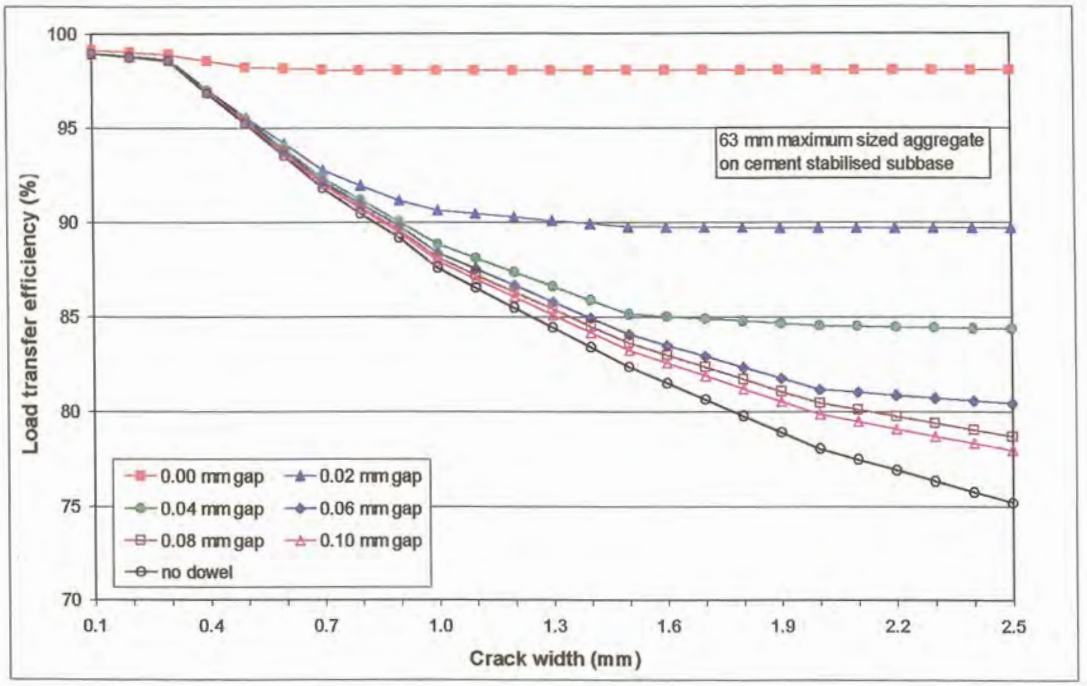

Figure 2.29: Deflection LTE in the wheel path – 63 mm maximum sized aggregate – combined affect of aggregate interlock and dowels (gap around dowel)

Jeong and Zollinger (2001) also conducted a study where the combined effect of aggregate interlock and dowel action was characterised in terms of a mechanistic process to address faulting and punch-out development. They used the work conducted by Ioannides and Korovesis during 1990 and 1992 (Ioannides and Korovesis, 1990; Ioannides and Korovesis, 1992) as the basis for this characterisation.

It was stated that shear capacity (s_0) is a parameter that represents the maximum shear stress that a slab joint or crack is capable of carrying for a given crack or joint opening. In combination the dimensionless joint stiffness ratios for aggregate interlock ($Agg/kl = J_{AI}$) and for dowel action ($D/skl = J_D$) represent a total stiffness ratio, $J = J_{AI} + J_D$ which in effect can be related to load transfer (in percent) as follows (Ioannides and Hammons, 1996):

$$LTE = \frac{100}{1+\log^{-1}\left[\frac{0{,}214 - 0{,}183\left(\frac{a}{l}\right) - \log(J)}{1{,}18}\right]} \qquad (2.48)$$

Where:

LTE = Load transfer efficiency;

a = Radius of applied load;

l = Radius of relative stiffness of the slab-foundation; and

J = Total stiffness ratio.

The aggregate interlock joint stiffness ($f = Agg/kl$) in Equation (B.44) is replaced by the total stiffness ratio (J) in Equation (2.48).

By combining Equation (2.48) with Equation (2.29) the effect of stiffness due to dowels or aggregate interlock can be taken into account. This study confirmed that the degree to which dowels can transfer load is limited. A greater load transfer capability can be achieved only through aggregate interlock and small crack opening. In other words, as stated above, high load transfer can be achieved through aggregate interlock. Even though dowels make a significant contribution to the transfer of load from one slab to another, crack width is critical to achieving and maintaining a high load transfer condition.

2.5.5 Summary of dowel modelling

Probably the most important aspect when modelling load transfer in concrete pavements due to dowel action, is the effect of dowel looseness. Dowel looseness has an important effect on the structural performance of the dowel; since it can function at full efficiency only after this looseness is taken up by load deflection. This is true for both initial looseness and that which develops during repetitive loading. Teller and Cashell (1958) made the statement that *tests that do not include repetitive loading and complete stress reversal, provide no information on dowel looseness and no measure of its effects.* An exponential relation was found to exist between dowel diameter and load transfer capacity, other conditions being constant (Teller and Cashell, 1958).

Most attempts to predict the initial shear stiffness of the dowels across a crack in reinforced concrete modelled the dowel as a beam on elastic foundation (Friberg, 1940; Millard and Johnson, 1984). In their follow-up study Millard and Johnson (1985) investigated the combined effect of aggregate interlock and dowel action. They found that large initial crack width; low concrete strength or the use of large-diameter bars all had an adverse effect upon the anchorage stiffness of the reinforcement and consequently upon the aggregate interlock shear stiffness and strength. Guo et al. (1995) used the same model as Millard and Johnson (1984), calling it the component dowel bar model. They verified through a comparison between experimental and analytical (ILLI-SLAB) results that this model could be used to reasonably predict responses of a dowel bar load transfer system.

Buch and Zollinger (1996) presented an in-depth study of factors affecting dowel looseness in an attempt to develop a dowel looseness prediction model. They found that dowel looseness and deflection were reduced considerably when the dowel diameter was increased. As far as the dowel looseness is concerned, this is contrary to the findings by Millard and Johnson (1985) where the larger-diameter dowels had lower anchorage stiffness than smaller-diameter dowel bars.

Hammons and Ioannides (1996) demonstrated the usefulness of using the concept of dimensionless joint stiffness for developing a mechanistic-based design approach for doweled joints, in that the experimental data they used, confirmed the usefulness of the dimensionless joint stiffness as a means of modelling the response of the doweled joint.

Most important though of the research done by Ioannides et al. (1990) and by Ioannides and Korovesis (1992) was to emphasise the fact that accurate theoretical equations for dowel modelling have been in place since the 1930's. It was pointed out that the so-called Friberg (1940) equations, based on the original Westergaard (1926) theory, are still applicable. Using the principles of dimensional analysis, combined with a number of executions of the ILLI-SLAB FE code Ioannides and Korovesis (1992) demonstrated the direct correspondence between aggregate interlock shear transfer (*AGG/kl*) and dowel shear transfer (*D/skl*) across a crack in a concrete pavement. The *D/skl* shear-only data plotted exactly on the previously determined *AGG/kl* curve.

The results of studies on the combined effect of aggregate interlock and dowel modelling have also been investigated. These studies emphasised that high load transfer is achieved through aggregate interlock and small crack widths.

The computer software programme, EverFE (Davids et al., 1998a, 1998b) was used for FE modelling of load transfer between concrete pavement slabs via dowel action (see Appendix D).

2.6 GUIDANCE FOR LABORATORY MODELLING

Bearing all these facts in mind, the essence of the literature review presented in this chapter had to be extracted to lend a meaningful input in order to compile the experimental programme for the current thesis.

The effectiveness of aggregate interlock load transfer at a joint in a concrete pavement depends on load magnitude, number of load repetitions, slab thickness, joint opening, subbase characteristics, subgrade bearing value, and aggregate angularity.

As the texture of the crack face is a function of the coarse aggregate type, size, and gradation, with the surface texture of the crack directly influencing the aggregate interlock and load transfer capacity of the joint (Buch, 1998) it was decided to perform a 2-level, 2-parameter experimental design. For this purpose two types of aggregates and two coarse aggregate sizes were chosen. The aggregate types chosen were Granite with an E-modulus of 27 GPa, and Dolomite with an E-modulus of 40 GPa, representing the range in modulus of crushed aggregates used in the construction industry in South Africa. The coarse aggregate sizes chosen were 19 mm and 37.5 mm.

In order to minimise the number of variables tested, it was recognised that some parameters had to be kept constant during the experiments. These were:

a) Concrete design strength – 35 MPa (standard strength used in the construction of concrete pavements in South Africa).
b) Concrete slab thickness – 230 mm (average slab thickness of jointed concrete pavements in South Africa).
c) Sand grading - had to be kept constant to ensure that the volume of coarse aggregate would be the same for different aggregate types.
d) Subbase support – construct the concrete slabs on a re-usable rubber (approximating a Winkler) subbase (The three primary response parameters in the analysis of a slab-on-grade pavement system are deflection (Δ), bending stress (σ), and subgrade stress (q). When the dense liquid foundation model is adopted, the latter may be eliminated because $q = k\Delta$ (Ioannides and Korovesis, 1990)).
e) Constant temperature during testing – by testing inside a laboratory facility temperature variation could be controlled eliminating curling of the concrete.
f) Angle of the fracture face – by inducing the crack in the slab within 24 hours after casting the concrete it was ensured that the angle of the fracture face would be as vertical as possible.
g) Dynamic loading frequency – apply the dynamic loading at a constant frequency of 3 Hz, with the interval between the maximum loading of the dynamic loading actuators, simulating a vehicle crossing the joint at 80 km/h (Colley and Humphrey, 1967).

Factors that were controlled during the testing, were:

a) Crack width, in order to determine the crack width up to which LTE is affected through aggregate interlock caused by specific sized aggregates.
b) The foundation support, which were either a continuous (top rubber layer intact) or a discontinuous (top rubber layer cut through) foundation.

The literature review indicated that there could be a difference between the performance of the laboratory models, and the results of field investigations, due to the following reasons:

a) Larger deflections could be measured in the laboratory due to a smaller resisting cross-section.
b) The effective height of the roughened interface would be less than in the field due to the crack inducer that has to be placed in the bottom of the slab.
c) To be able to test at a constant crack width, the crack width will have to be kept constant, whereas in the field temperature cycles cause opening and closing of the crack.

It was also decided to measure the VST of the experimental beams and compare the results with those published by Vandenbossche (1999).

Little research has been done on the subject of aggregate interlock shear load transfer at joints in concrete pavements in South Africa, and therefore the literature published on the subject is scarce. The main concern is that the accepted analysis models have been developed in the Northern hemisphere with environmental conditions quite different to the conditions encountered in Southern Africa. Modelling of aggregate interlock joints, using South African aggregates, and investigation into the efficiency of aggregate interlock joints in in-service pavements was therefore required.

CHAPTER 3: LABORATORY AND FIELD PROGRAMMES

TABLE OF CONTENTS

LIST OF TABLES

LIST OF FIGURES

LIST OF SYMBOLS / ABBREVIATIONS

ACV	Aggregate crushing value
Agg	Dimensionless joint stiffness per unit length of joint/crack;
ARAN	Automatic road analyser
C	Continuous
DC	Discontinuous
$E_{c,28}$	Theoretical 28-day elastic modulus of concrete
FWD	Falling weight deflectometer
$f_{cu,28}$	28-day characteristic cube strength
h	Slab thickness
LTE	Load transfer efficiency
RM	Relative vertical movement at joint
τ	Shear stress at crack face

3 LABORATORY AND FIELD PROGRAMMES

3.1 LABORATORY PROGRAMME

3.1.1 Introduction

The primary objectives of this research project were stated in Chapter 1. Existing methods for modelling aggregate interlock shear transfer to develop a model applicable to South African conditions that reflects variations in joint load transfer with joint opening, load magnitude, subbase support, aggregate size and concrete properties, were investigated through a literature review presented in paragraph 2.4. EverFE (Davids et al., 1998a) was used for three-dimensional finite element modelling as summarised in Appendix D. The difference in jointed concrete pavement response in terms of deflections, to static and moving impulse or dynamic loads (equivalent to traffic loads), has also been pointed out in paragraph 2.3.

Apart from the design guidelines found in Manual M10 (1995) very little was found in the literature that focussed on the aggregate interlock load transfer characteristics of South African crushed aggregates, and under South African environmental conditions.

With the advancement in technology and an ever changing environment, it was logical that more sophisticated methods would be developed for designing pavements. With 3D FE methods it is possible to adequately capture the structural response of pavement systems as they are encountered in the field.

In line with this advancement in technology, a mechanistically based design method for concrete pavements has been developed in South Africa, to facilitate interaction with the mechanistic flexible pavement design methods currently in use, and to promote the use of concrete to rehabilitate flexible pavements.

Suitable models have been developed from finite element and multi-layer evaluations and a user-friendly computer program has been compiled. The design procedure takes into account a large number of input variables, the fact that pavement characteristics change with time, and that the different parameters show statistical variation. All of the above, together with actual field performance, was taken into account in generating an output, which is expressed in terms of risk of failure. The design method has been calibrated against actual performance on various sections and pavement types, such as roads, streets and hard standings.

The insight gained in the mechanics of aggregate interlock at joints/cracks in concrete pavements through the literature review, provided the guidance for the experimental programme followed in the present study as set out in Chapter 2.

As mentioned in Chapter 2, the experimental programme was set up according to a 2-level, 2-parameter design. The aggregate types chosen were Granite with an E-modulus of 27 GPa (Aggregate crushing value (ACV) = 27%), and Dolomite with an E-modulus of 40 GPa (ACV = 15%), representing the range in modulus of crushed aggregates used in the construction industry in South Africa. To cover the spectrum of aggregate sizes used in the construction of concrete, 19 mm as well as 37,5 mm coarse aggregates were used. For this purpose four concrete slabs were cast, as follows:

a) Experiment 1 – 19 mm granite aggregate.
b) Experiment 2 – 37,5 mm granite aggregate.
c) Experiment 3 – 19 mm dolomite aggregate.
d) Experiment 4 – 37,5 mm dolomite aggregate.

Apart form the above mentioned four slabs, a fifth concrete slab with a pre-deformed plastic joint former was also cast to investigate the performance of a different type of joint under both dynamic and static loading. Although this experiment was not part of the original design, it will be pointed out in Chapter 5 how the results from this experiment were used to complete the picture of relative movement (RM) versus load transfer efficiency (LTE) results analysed. This slab was also used to quantify the difference between a continuous (C) and a discontinuous (DC) subbase. Wherever reference is made in the text, hereafter to a plastic joint, it implies the joint with a pre-deformed plastic sheet as joint former.

The following paragraphs cover inter alia the test set-up used for the experiments, materials testing conducted, and practical aspects that needed sorting out to obtain relevant data.

3.1.2 Test set-up

Four slabs (1 800 mm long, 600 mm wide, and 230 mm thick) were cast in the laboratory to investigate aggregate interlock LTE at a joint/crack. The thickness of the slab was specifically chosen to represent the average thickness of jointed concrete pavements in South Africa. The slab thickness also has a direct effect on the radius of relative stiffness (l) of the concrete.

The slabs were cast on approximately 55 mm thick rubber (made up out of three layers of rubber on top of each other). The slabs cast for Experiments 1 and 2 were cast with all three layers of rubber intact, whereas before casting the slabs for Experiments 3 and 4, the top layer of rubber was cut through at mid-length directly beneath the position where the crack was formed. This was in order to simulate a crack propagating into the subbase.

When tested in a California Bearing Ratio (CBR) press to determine the equivalent bearing capacity of the rubber, it was measured as 24% CBR. This is equivalent to a selected gravel layer with a resilient modulus of approximately 150 MPa (Theyse et al., 1996), and a k-modulus of 80 MPa/m. This same subgrade k-value was used in theoretical analyses with EverFE (see Appendix D).

The rubber and shuttering were placed on a timber pack (2 800 mm long, 700 mm wide, and 140 mm thick). The timber pack had to render a sound base for transporting the slab from the position where it was cast to where it was tested. A crack inducer in the form of an angle iron was placed across the floor of the slab at mid-length on the rubber foundation, before casting (see Photos G.1 and G.2). For Experiment 1 a 40 mm deep incision was cut into the concrete surface with a grinder (vertically above the angle iron), where after the desired crack was formed. For Experiments 2, 3 and 4 the incision was formed by casting a flat bar into the top of the concrete slab vertically above the angle iron.

The joint/crack had to be formed within 24 hours after casting the concrete (see Photo G.4). By then the concrete had already set, and was strong enough that the surface would not be damaged, but on the other hand still weak enough that a vertical crack could be induced without applying too much force. With the strength of the cement matrix being weaker than the aggregate at the time of forming the crack, the crack typically formed around the aggregate, with little or no cracked aggregates. This method of cracking the slab also ensured that a coarse aggregate interlock surface was created with little loose particles inside the crack. This was verified after completion of each test by taking the two sections of the slab apart, and attempting to collect the fines that formed through abrasion. Very little loose material could be collected, even after completion of Experiments 1 and 2 where the slabs were subjected to 2 million dynamic load cycles, and it was therefore not considered practical. A schematic layout of the test set-up is given in Figure 3.1.

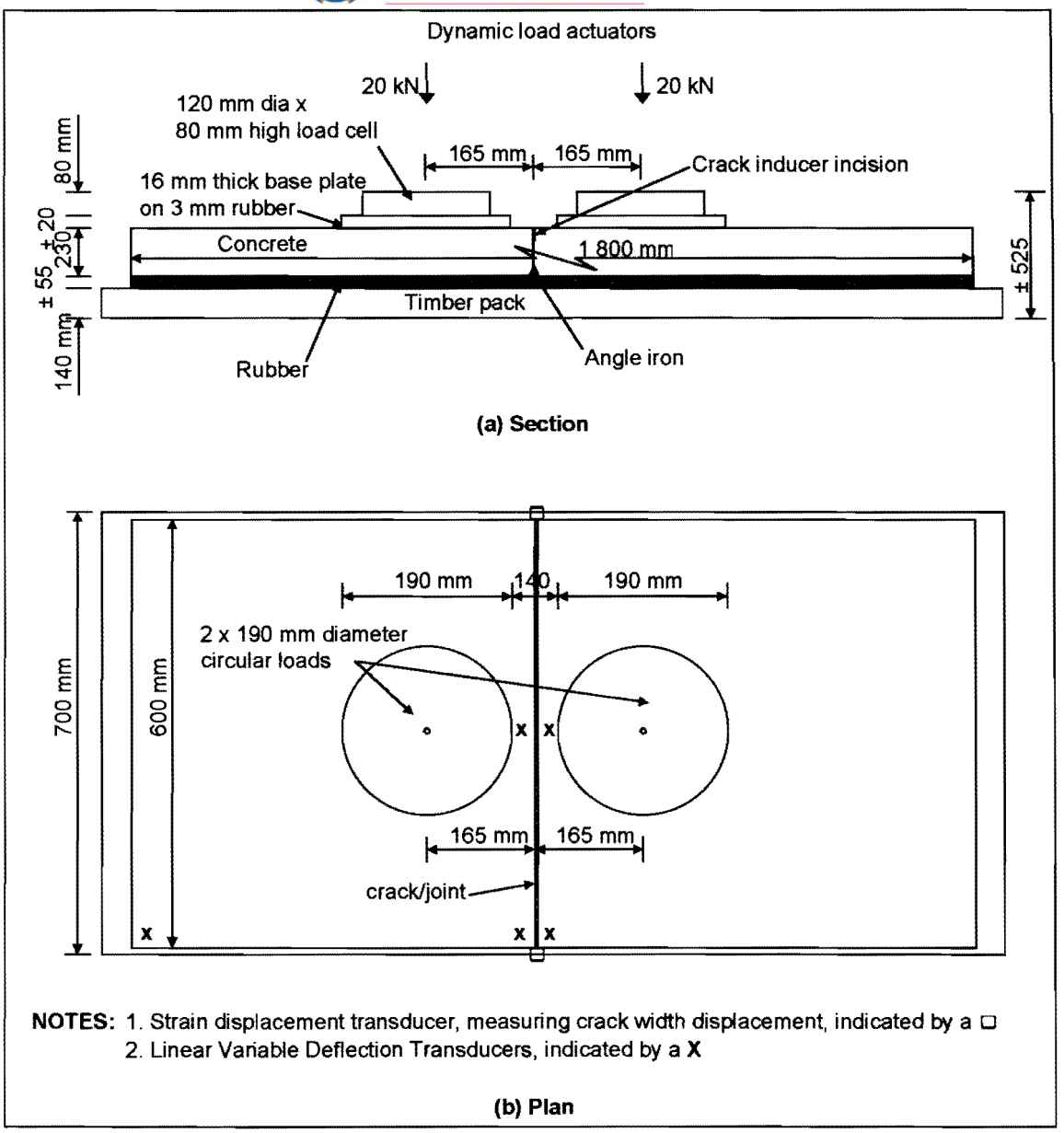

Figure 3.1: Schematic layout of test set-up

3.1.3 Material tests

The slabs were cast, using the materials as summarized in Appendix F. To ensure that a 28-day compressive strength of 35 MPa would be obtained with the materials used, test cubes were made up beforehand, using water/cement ratios of 0,59 and 0,63. The test cubes were crushed after 7 days, and the 28-day strengths were calculated from the assumption that the 7-day compressive strength is approximately two-thirds that of the 28-day compressive strength (Fulton, 1994). The average 7-day compressive strength values obtained for water/cement ratios of 0,59 and 0,63 were 21,5 MPa and 20,5 MPa, respectively, which indicated that the corresponding 28-day compressive strength would be

32,5 MPa and 30,5 MPa. From these results it was determined that a water/cement ratio of 0,56 should be used to obtain a 28-day compressive strength of 35 MPa. The actual strengths obtained are summarised in Table F.13. Only one set of cubes had an average strength of less than 35 MPa at 28 days. These were the 19 mm granite air-cured cubes, which averaged 30 MPa. The water-cured cubes therefore met the required specification. Apart from the slab, a number of cubes, beams and cylinders were also cast for testing purposes, as summarised in Table 3.1 (see Photos, G.3, and G.5 to G.10).

Table 3.1: Basic information on cubes, beams and cylinders cast for testing purposes

Test specimen	Dimensions (mm)	Number	Time of test
Compressive strength cubes (SABS 863: 1994 / ASTM C39/C39M-01, 2001*)	150 x 150 x 150	18	At 7 and 28 days after casting slab, and at end of 2 million load cycles.
Modulus of rupture beams (SABS 864: 1994 / ASTM C133-97, 1997)	750 x 150 x 150	6	At 28 days after casting slab, and at end of 2 million load cycles.
Shrinkage beams (SABS 1085: 1994 / ASTM C426-99, 1999)	300 x 100 x 100	4	Measure gauge length L_0 before casting specimen, and L_1 after 7 days in curing bath. Place in drying oven with temperature 50°C, and relative humidity 25%, and measure L_2 at 48 hour intervals thereafter, until difference in length less than 2μm/100 mm.
Modulus of elasticity cylinders (BS1881: Part 121: 1993 / ASTM C469-94, 1994)	300 x 150 diameter	3	At 28 days after casting.

*NOTE: ASTM test methods give equivalent test results, although the test methods are not necessarily the same.

The volume of 19 mm and 37,5 mm coarse aggregate in both the granite and the dolomite concrete mixes had to be the same, in order to obtain the same aggregate interlock contact areas. In other words, the coarseness of the joint area formed by the 19 mm granite aggregate had to be the same as for the 19 mm dolomite aggregate. The same applied to the 37,5 mm coarse aggregate concrete mixes. To achieve this, the grading of the granite sand and the dolomite sand had to be approximately the same.

Figure F.1 (Appendix F) shows the grading of the sands used in the concrete mixes, within the grading envelope, and Table F.11 (Appendix F) gives a summary of the mix designs used. The volumetric surface texture (VST) of the crack faces of the experimental slabs, as well as crack faces formed during modulus of rupture testing of concrete beams, was used to verify that the crack faces were similar. The methodology followed to obtain the VST of the samples is described in Appendix F.

As mentioned above, granite and dolomite aggregates were chosen as they represented the lowest and highest stiffness moduli, respectively, of the crushed aggregates used in the construction of concrete in South Africa. The results of the cubes, beams and cylinders tested are summarised in Table F.13

(Appendix F). The strength of the aggregate, as well as the size of the aggregate had an effect on the modulus of elasticity results obtained for the four concrete mixes (see Table 3.2). For both the granite and dolomite concrete mixes, the larger sizes coarse aggregate had higher elastic moduli.

The theoretical 28-day elastic modulus, $E_{c,28}$, was calculated using the actual 28-day concrete cube strength obtained in the laboratory, instead of the 28-day characteristic cube strength ($f_{cu,28}$) of 35 MPa (according to the mix design) (Fulton, 2001). This was in order to facilitate a more realistic comparison with what was physically measured in the laboratory. Both 19 mm coarse aggregate concrete mixes had lower elastic moduli than the theoretically calculated moduli. On the other hand, both 37,5 mm coarse aggregate concrete mixes rendered elastic moduli higher than the theoretical values. This in turn indicated that not only the aggregate type, but also the aggregate size, has an influence on the elastic modulus of the concrete.

Table 3.2: Elastic modulus of the concrete – comparison between laboratory results and theoretical results

Aggregate type	Laboratory E (GPa)	$E_{c,28} = K_0 + \alpha f_{cu,28}$ (Fulton, 2001)		
		K_0 (GPa)	α (GPa/MPa)	Calculated E (GPa)
Granite – 19 mm	21,0	17 – 18	0,25	26,5 – 27,5
Granite – 37,5 mm	29,0	17 – 18	0,25	28,0 – 29,0
Dolomite – 19 mm	41,0	24 – 25	0,45	42,5 – 43,5
Dolomite – 37,5 mm	48,0	24 – 25	0,45	43,5 – 44,5

3.1.4 Dynamic loading

The Falling Weight Deflectometer (FWD) measuring instrument is commonly used to determine deflection LTE at a joint in a concrete pavement. With the FWD, dropping a load onto the pavement on the one side of a joint/crack, and measuring the deflection at both sides apply a static impulse load. The deflection LTE is then calculated using Equation (2.4). In practice, however, the loads applied to a pavement are not "one-sided", but dynamic loads are transferred from one slab to the next under moving vehicle traffic. The response of the slabs therefore had to be captured under dynamic loading as well as under static loading to be able to capture real-life conditions and to compare the results.

When subjecting the slab to a simulated dynamic load, it was logical that there would not only be vertical downward forces acting across the crack, but also horizontal forces due to the effects of moment and inertia induced across the crack (see paragraph 2.3). The effect of horizontal forces acting across the crack were controlled by controlling the crack width.

An impulse force that simulates the impact of one wheel (20 kN) of a standard 80 kN dual wheel truck axle load, crossing a joint/crack at 80 km/h, was developed. This was achieved by using two actuators. The first actuator had to simulate a wheel approaching the crack by increasing the applied load from zero to 20 kN within 0,11 seconds. The load on the leave slab was then released to zero in 0,01 seconds. In this same 0,01 second interval that the first actuator reverted back to zero, the second actuator had to move from zero load to 20 kN load on the approach slab, where after it was released back to zero in 0,11 seconds to simulate a wheel moving away from the crack. This action was followed by an interval of approximately 0,11 seconds when there was no load on either actuator, and the slabs returned to a no-load position. The two waveforms thus created had a total duration of 0,12 seconds each, with a rest period of 0,11 seconds (corresponding to approximately 3 Hz), as shown in Figure 3.2. These waveforms were similar to the ones used by Colley and Humphrey (1967), but at approximately twice the speed.

It was initially planned to conduct testing in a standard MTS, using one actuator with a load arm on a hinge. This meant that the actuator had to apply a 20 kN compressive force, move through zero force, and apply a 20 kN tensile force within 0,01 seconds. This however was not possible, as the actuator load cell became unstable when it went through zero, and the tensile force values could not be controlled. Two actuators were therefore used to apply the load waveforms.

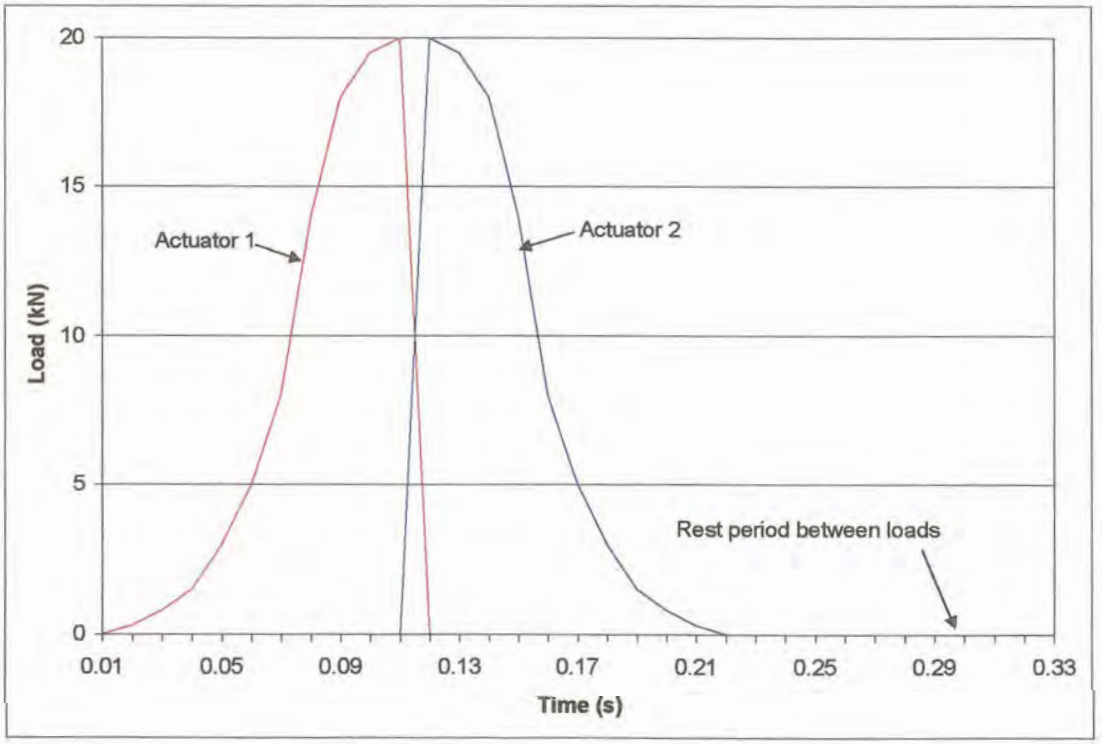

Figure 3.2: Typical load waveforms for dynamic loading

3.1.5 Test procedure

During Experiment 1 a total of 15 data channels were recorded continuously on a computer using HBM KWS and HBM Spider-8 amplifiers (see Photo G.11), namely:

- 2 Load cells
- 2 Actuators
- 1 Actuator deflection
- 5 Linear Variable Displacement Transducers (LVDT's)
- 2 Strain Displacement Transducers
- 3 Thermocouples

Measuring the loads applied, as well as the deflections induced during dynamic loading necessitated accurate measuring equipment. The deflection measuring devices, especially, had to be accurate to at least 0,1 μm, as the magnitude of the expected deflections (obtained from the theoretical modelling in Appendix D) was expected to be between 0,0 mm and 1,0 mm.

As indicated in Figure 3.1, the two load cells were placed at positions, determined by the load waveforms induced by the two actuators to simulate a wheel crossing the crack at 80 km/h. The deflection of the actuator on the leave slab was also measured. Two LVDT's were positioned on opposite sides of the crack in the centre of the slab between the load cells to measure deflections in the wheelpath. Another two LVDT's were placed on opposite sides of the crack on the edge of the slab to determine the deflections at the edge, and one LVDT was placed in an outside corner of the slab to measure the movement that took place away from the crack. The fifth LVDT in the outside corner of the slab was also used as a control to ensure that the ends of the slab did not lift up. For Experiment 1 only two strain displacement transducers were fixed on both sides of the slab at the top of the crack, but for further experiments this number was increased to four in order to be able to measure horizontal opening and closing movements at the top as well as at the bottom of the crack. The total number of data channels logged was therefore increased to 17.

The thermocouples were read every 30 minutes. All other data channels were logged continuously during the dynamic loading process. This created a large data file. In order to save file space only data from 2 load cycles at 1-minute intervals were sampled and saved to a smaller file for analysis purposes.

3.1.6 Experimental programme

As mentioned above, there were practical aspects of the experimental procedures that needed sorting out during the first experiment. Initially the intention was to subject all four concrete slabs to at least 2 million dynamic load cycles. It was reasoned that it would be possible to measure deterioration of the

crack face through a decrease in deflection measurements. The slab cast for Experiment 1 was therefore subjected to 2 million dynamic load applications. After every 0,5 million load applications, static loading tests were carried out, and the data analysed to determine general trends. The equipment was also calibrated at the time of static load testing.

Figure 3.3 presents typical deflection data obtained for the 1,5 to 2 million load cycles that the first slab was subjected to at the initial crack width of 0,1 mm. There was no significant deterioration of the crack up to 2 million dynamic load cycles, which indicated that both the cement paste and aggregate particles were so tightly knit together that little vertical sliding could occur (Benkelman, 1933). On the other hand, while applying the dynamic loads, the crack width was also monitored continuously. The relative horizontal opening movement at the crack did increase during application of the 2 million dynamic load applications, yet when the load was removed the actual crack width stayed at 0,1 mm.

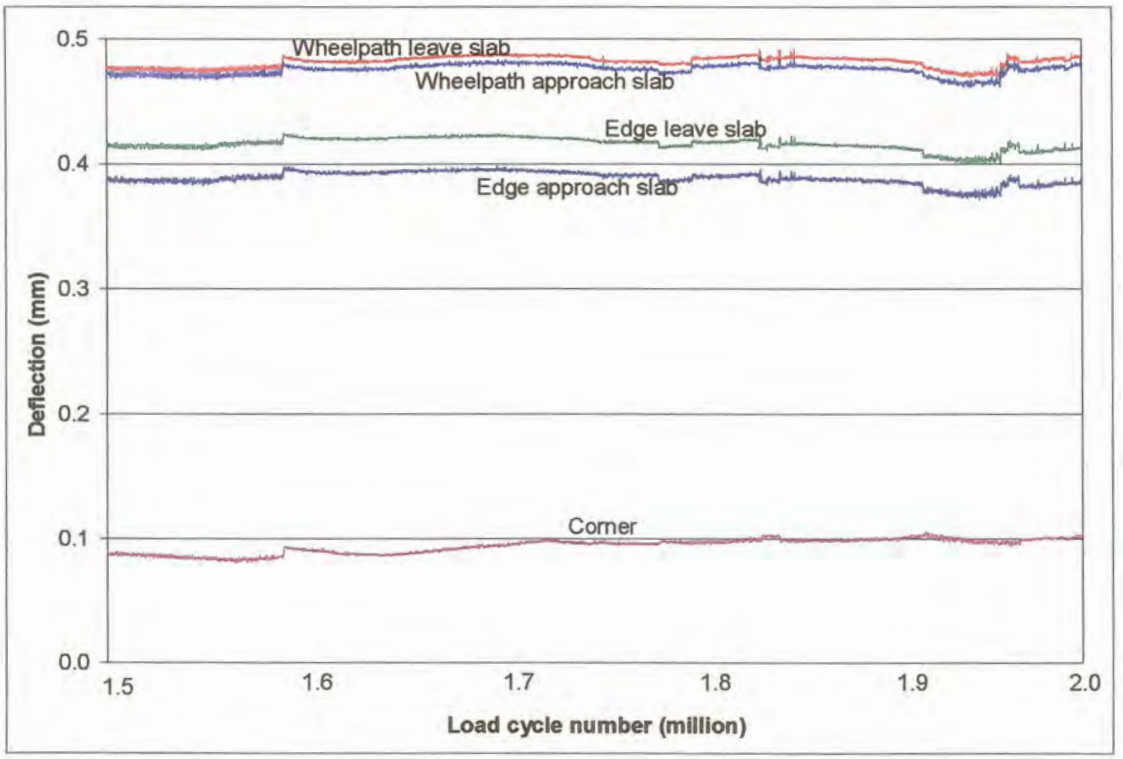

Figure 3.3: Deflection measurements – 1,5 to 2 million dynamic load cycles at 0,1 mm crack width

This indicated that little abrasion of the aggregates at the joint face took place at the initial crack width, as the narrow crack restricted vertical shear movement. Therefore no loose particles were dislodged, or got trapped in a different position when the crack opened and closed. This could also be attributed to the high quality of crushed stone used in South Africa (see Appendix F), and to the time that the crack was formed, as the cement matrix was still soft enough not to splinter off.

To test the above statements, the slab cast for Experiment 2, using 37,5 mm granite aggregate in the concrete was also subjected to 2 million dynamic load cycles, with static load tests and calibration of equipment after every 0,5 million load cycles. Once again there was no significant deterioration of the concrete at the crack face, and the crack width also did not increase. The further implication was that it was not necessary to allow so much time (18 days for Experiment 1) for dynamic load testing at the initial crack width, but that testing at different crack widths could commence as soon as the test set-up was complete. Other factors that had to be borne in mind, were that testing was conducted inside a laboratory building, and that the slab was not subjected to normal day-night temperature variations, nor exposed to rain, and other environmental effects detrimental to a joint in a concrete pavement.

Another explanation could be that the shear stress on the crack face at the initial crack width was too low due to lack of support from the rubber subbase. The shear stress at the crack face was therefore calculated using the following equation:

$$\tau = \frac{Agg(RM)}{h} \tag{3.1}$$

Where:

τ	=	Shear stress (MPa);
Agg	=	Dimensionless joint stiffness per unit length of joint/crack;
RM	=	Relative vertical movement at joint (mm); and
h	=	Slab thickness (mm)

The shear stress at the crack face during the initial 2 million dynamic load cycles was calculated as 0,32 MPa for Experiment 1 and as 0,21 MPa for Experiment 2. These results were low in comparison with both the 28-day compressive strength results, as well as with the elastic modulus results. As mentioned previously the equivalent k-value of the rubber subbase was 80 MPa/m. It was therefore not that the support was not stiff enough, but due to the fact that high LTE's with low RM's were measured during the dynamic loading.

After completion of the dynamic loading cycles the two sections of the slab were pulled apart horizontally in a controlled fashion, to measure responses under static and dynamic loading at different crack widths. However, before pulling the two sections of the slab apart at the crack, the ends of the slab were pressed down by inserting jacks beneath the steel frame holding the actuators. This was done in order to ensure that the aggregate interlock bond that still existed across the crack was broken, in order to be able to pull the two sections apart (see Photos G.12 to G.15).

Following on the conclusion already reached from the first two Experiments, that little or no deterioration of the crack face occurred at the initial crack width during loading, the slabs cast for Experiments 3 and 4 were not subjected to the 2 million dynamic load cycles applied to the first two slabs. The focus was therefore shifted from determining the effect of abrasion under repeated dynamic

loading to determining the response of the concrete at different crack widths. The slabs for Experiments 3 and 4 were therefore subjected to only three cycles of 10 minutes of dynamic loading, followed by static loading at the initial crack width. Thereafter, as for the previous two experiments the two sections of the slab were pulled apart and subjected to dynamic and static loading at different crack widths. The slabs were pulled open and tested at different crack widths up to a maximum crack width of 2,5 mm to be on par with similar studies researched during the literature survey (Davids et al., 1998). The slabs were then pushed together again to as close as possible to the initial crack width, and pulled open again, at least three times to verify the repeatability of the tests.

These opening and closing cycles to a maximum crack width of 2,5 mm were conducted for all the experiments (see Photos G.17 and G.18), except for Experiment 3 that was pulled open to a maximum crack width of 4,0 mm. This was in order to test the assumptions of previous researchers that at crack widths greater than 2,5 mm the deflection measurements reached an upper asymptote. 2,5 mm was also considered the crack width at which the subbase started to play an important role in the LTE of the concrete pavement system (Colley and Humphrey, 1967; Davids et al., 1998b; Jensen, 2001). Figure 3.4 illustrates this upper plateau reached in the deflection measurements, and confirmed that testing up to a crack width of 2,5 mm was sufficient to measure the effects of aggregate interlock. At least for 19 mm coarse aggregate concrete.

As mentioned above, a major difference between Experiments 1 and 2, and Experiments 3 and 4 was that the top layer of rubber beneath the concrete was cut through at mid-length directly beneath the joint for the latter, but that all three layers of rubber were left intact for the former.

3.2 AGGREGATE INTERLOCK EXPERIMENTS

The following paragraphs present a chronological description of the testing done in order to collect the data necessary for analysis purposes. Each experiment is described separately with specific reference to deflection measurements, horizontal crack displacement, LTE, and RM. Where appropriate comparisons are also made with a combination of results from more than one experiment. Some observations on the general behaviour of the slabs during testing, as well as the effect of temperature cycles are also presented.

EverFE is also plotted on the graphs. As mentioned above, the larger RMs calculated with EverFE, resulting in lower LTEs did not compare well with the experimental results. The relative vertical movement at the joint for both coarse aggregate sizes considered was calculated using Equation (2.12). The values of the line plotted for 37,5 mm coarse aggregate was initially lower than the laboratory values, but the line increased exponentially with increasing crack width, to values higher than what was measured. The main concern, however, was the large difference between the experimental results and the line plotted for 19 mm coarse aggregate using values calculated with Equation (2.12) (Figure 3.15) The magnitude of the difference in results is more obvious when comparing the scale of the vertical axes of Figures 3.15 and 3.16. The former has a maximum value of 3,5 mm, versus the 0,35 mm of the latter.

From Figure 3.15 it is obvious that Equation (2.12) that was still incorporated as one of the design parameters in Manual M10 (1995) was inaccurate and needed revision.

3.2.3 Experiment 3

The slab cast for Experiment 3, using 19 mm dolomite aggregate (see Photo G.21), was subjected to three cycles of 10 minutes of dynamic loading followed by static loading at the initial crack width. Thereafter, as for the previous two experiments the two sections of the slab were pulled apart and subjected to dynamic and static loading at different crack widths. The slab was pulled open and tested at different crack widths up to a maximum crack width of 4,0 mm, closed back to the initial crack width and pulled open again. This procedure was done at least three times to verify the repeatability of the tests.

One major difference between Experiment 3 and Experiments 1 and 2 was that the top layer of rubber beneath the concrete was cut through directly beneath the joint. This was to simulate a crack projecting into the subbase, and test the assumption made previously that the high LTE obtained for Experiments 1 and 2 was partly due to the continuous support provided by the rubber subbase. The fact that the top layer of rubber was cut through necessitated that the mechanisms by which the opening and closing of the slab were performed be more closely controlled, as the possibility existed that the top layer of rubber could slide off during opening of the crack.

The increase in deflection with increasing crack width for both dynamic and static loading is shown in Figure 3.17. When comparing this figure with Figure 3.5, it is obvious that in Experiment 3, the deflections measured were far less than what was measured for Experiment 1. On the other hand, the results were less than the theoretical predictions from EverFE, but within a factor of 10 of the results reported by Jensen (2001). The dynamic loading results were on average 124% that of the static loading results. This was similar to results reported by Bergan and Papagiannakis (1984).

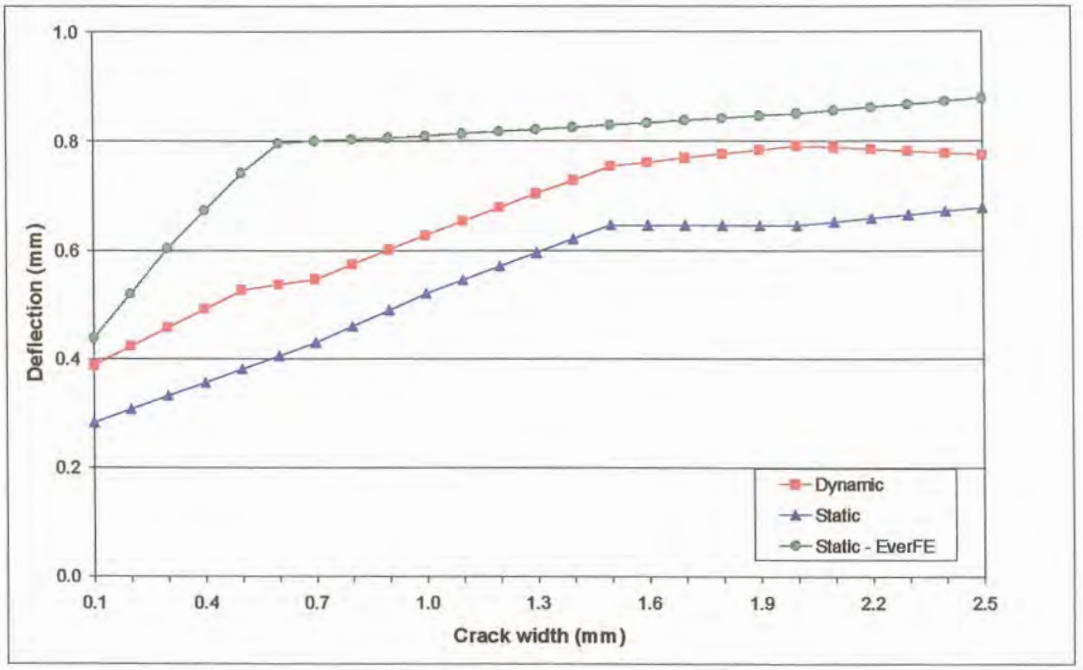

Figure 3.17: Deflection (of leave slab) versus crack width (19 mm dolomite aggregate)

The development of horizontal crack displacement at different crack widths is plotted on Figures 3.18 and 3.19 for dynamic and static loading, respectively. For comparison purposes the scale of the vertical axes have been kept constant (see also Figures 3.6, 3.11 and 3.12). Once again, it was noticeable that larger horizontal movements occurred as the crack started to open up at a crack width of 0,5 mm.

Both Experiments 1 and 3 contained 19 mm coarse aggregate, although from different sources, namely granite and dolomite aggregate, respectively. The deflection LTE graphs obtained for these two Experiments are plotted on Figure 3.20. The theoretical line determined with EverFE is also plotted on the graph for comparison purposes.

The deflection LTE obtained for the 19 mm dolomite (Experiment 3) was less than what was previously calculated for the 19 mm granite (Experiment 1). As it has already been established through VST testing (see Appendix F) that the crack faces of these two slabs were similar, this difference in results could be attributed to the fact that in the case of Experiment 3, the top layer of the rubber supporting the concrete was cut through directly beneath the joint/crack position. This simulated crack into the subbase therefore inhibited the transfer of shear stresses, thereby reducing the efficiency of the system. As previously, the theoretical LTE determined with EverFE was initially close to a 100%, but at a crack width greater than 0,5 mm, it decreased to values considerably lower than what was calculated from the laboratory results. The apparent explanation for this difference has been dealt with in paragraphs 3.2.1 and 3.2.2, above.

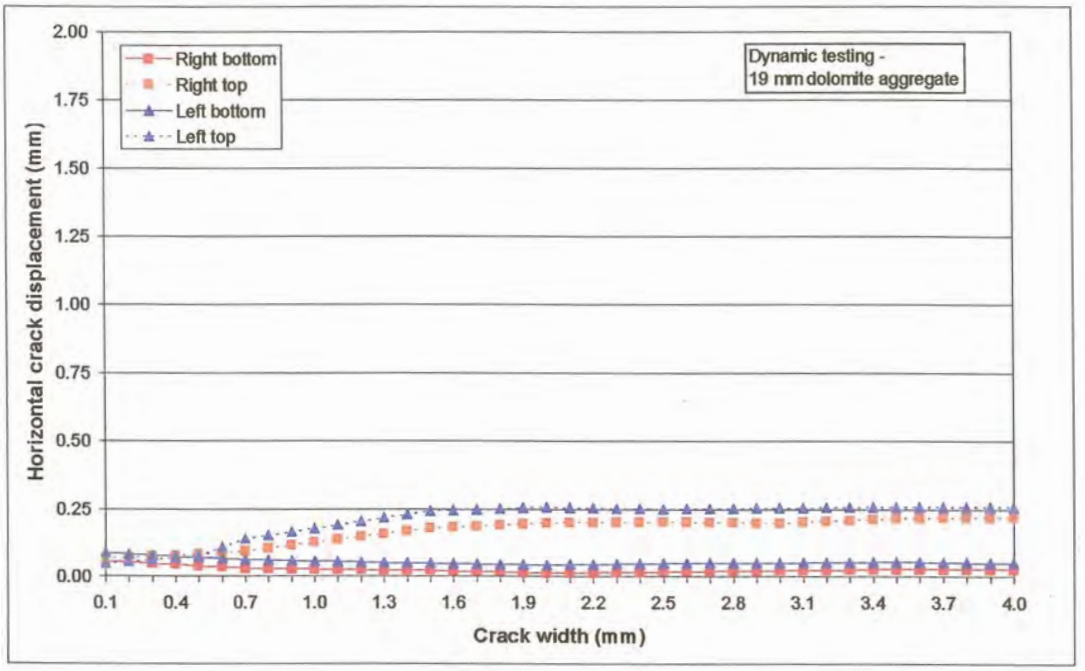

Figure 3.18: Horizontal crack displacement versus crack width under dynamic loading (19 mm dolomite aggregate)

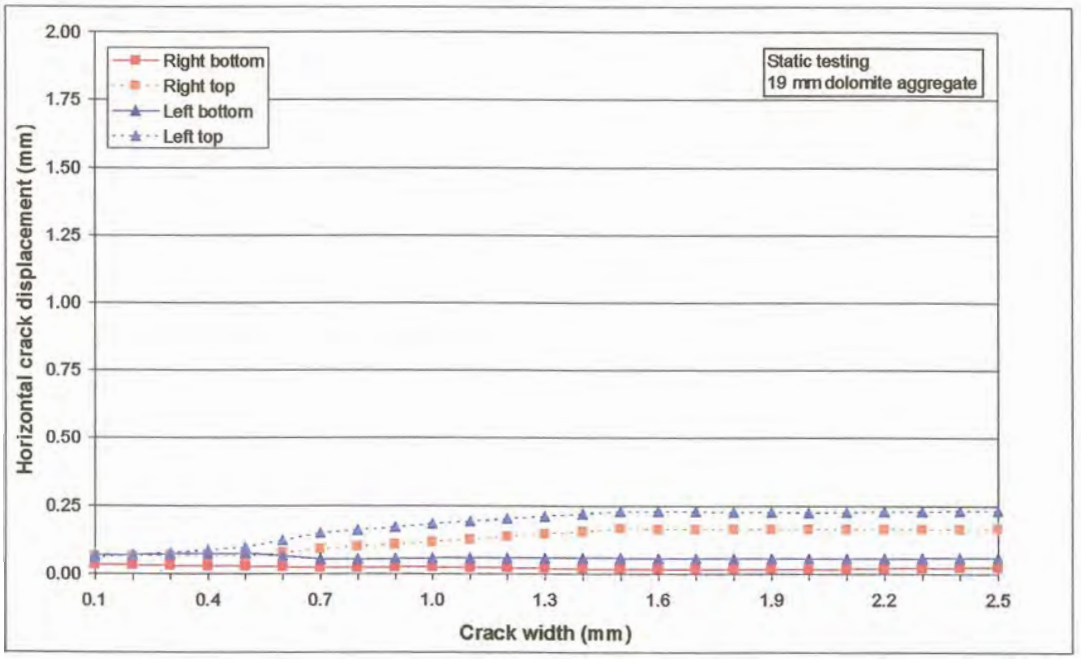

Figure 3.19: Horizontal crack displacement versus crack width under static loading (19 mm dolomite aggregate)

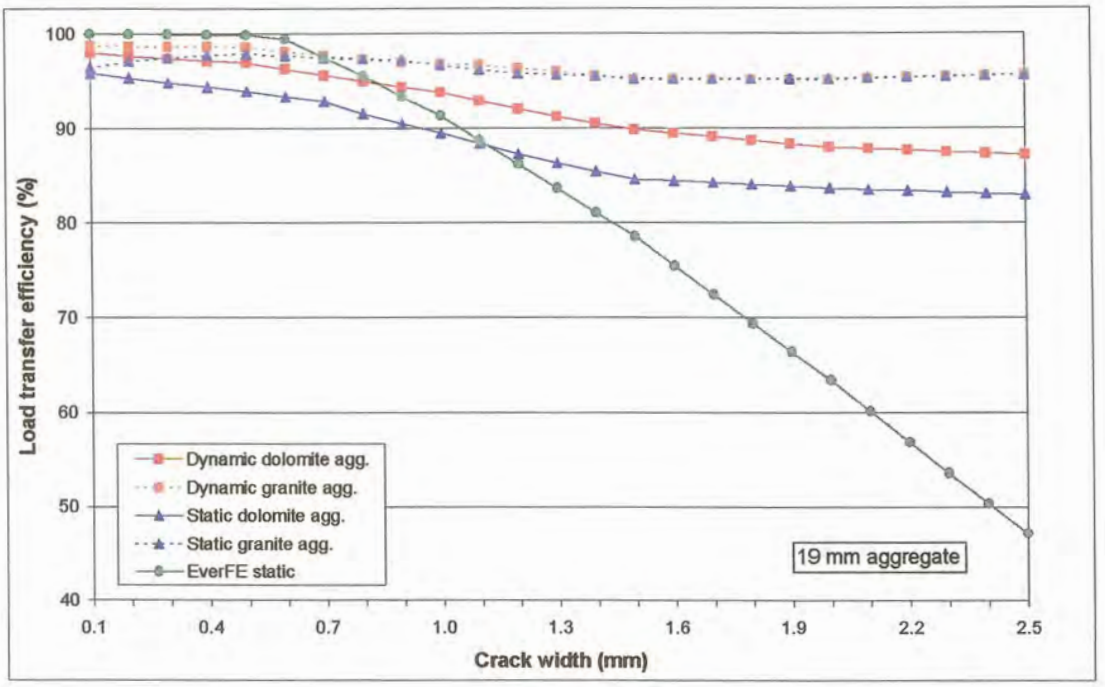

Figure 3.20: Deflection LTE versus crack width – 19 mm aggregate

When the results obtained on the granite and dolomite were compared in terms of RM, the results were almost the same. The average of the RM results of the 19 mm granite aggregate and the 19 mm dolomite aggregate was therefore calculated. The logistic model was used to fit the data as the dependent variables showed dichotomous (two-value or high-low) behaviour. The software package Mathcad 2000 (Version 8) was used to fit the data in terms of RM (y) and crack width (x), as follows:

Dynamic loading:

$$y(x) = \frac{0{,}103}{1 + 22{,}375 \cdot e^{-2{,}639x}}; \qquad R^2 = 96{,}9\% \tag{3.2}$$

Static loading:

$$y(x) = \frac{0{,}114}{1 + 18{,}644 \cdot e^{-2{,}609x}}; \qquad R^2 = 96{,}5\% \tag{3.3}$$

For both curves, the R-squared value, also known as the coefficient of determination, was used as an indicator of how closely the estimated values for the logit functions corresponded to the actual data. A fitted function is most reliable when its R-squared value is at or near 1. Figure 3.21 show the curves fitted for the logistic equations (logit) of both dynamic and static loading, together with the experimental data.

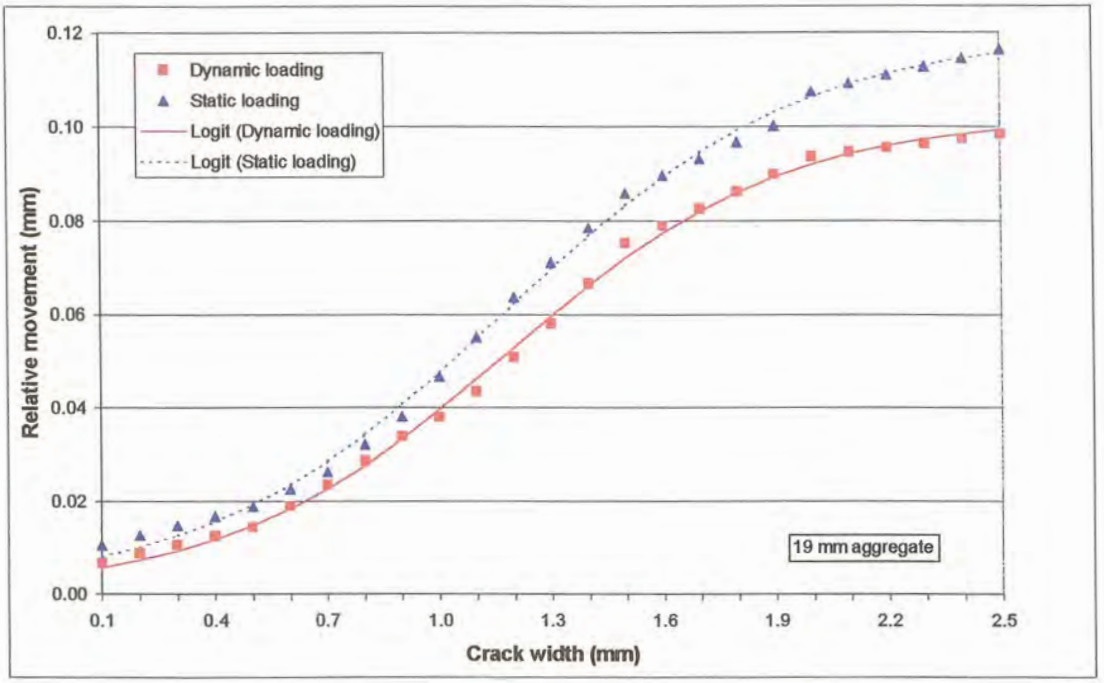

Figure 3.21: Average of RM versus crack width results for dynamic and static loading on 19 mm granite and dolomite aggregate

Evaluating the aggregate interlock efficiency of the joint in terms of RM is contrary to the generally accepted method of determining the efficiency of a joint in terms of deflection LTE, but similar to the method used by Strauss (1992), as well as by Strauss et al. (2001). Strauss (2001) considered that evaluating the efficiency of a joint in terms of deflection LTE is not necessarily the correct method, as it gives results based on the efficiency of the whole system. In other words, it not only takes into account the deflection of the concrete slab, but also indirectly the deflection of the subbase and subgrade. On the other hand, when analysing the RM measured on top of the concrete, the deflection of the concrete is isolated.

However, this approach is not logical as there are three components involved during load transfer at a joint/crack, namely: the portion carried by the slab, the portion carried by the subbase/subgrade, and the portion carried by the load transfer mechanism. These components have to be in equilibrium, and during the measurement of LTE, if one carries more of the imposed load, the others will carry less.

On completion of the initial set of dynamic and static tests at different crack widths, the steel frame holding the actuators was turned 90 degrees. This was in order to apply a 40 kN (the 2 actuators adjacent to each other) static load on the one side of the joint/crack. The results were then compared to those previously obtained under 20 kN static loading.

Due to the repeated cycle of opening and closing the two parts of the slab during initial testing, some particles were loosened on the crack face, which prevented closing the crack to less than 1,0 mm. Results under 40 kN load application were therefore only obtained for crack widths between 1,0 mm and 2,5 mm. Figure 3.22 shows the deflection versus crack width measured on the leave slab for both 20 kN and 40 kN static loading, with the deflection under the heavier load 40 kN load on average 19% higher than under the lighter 20 kN load.

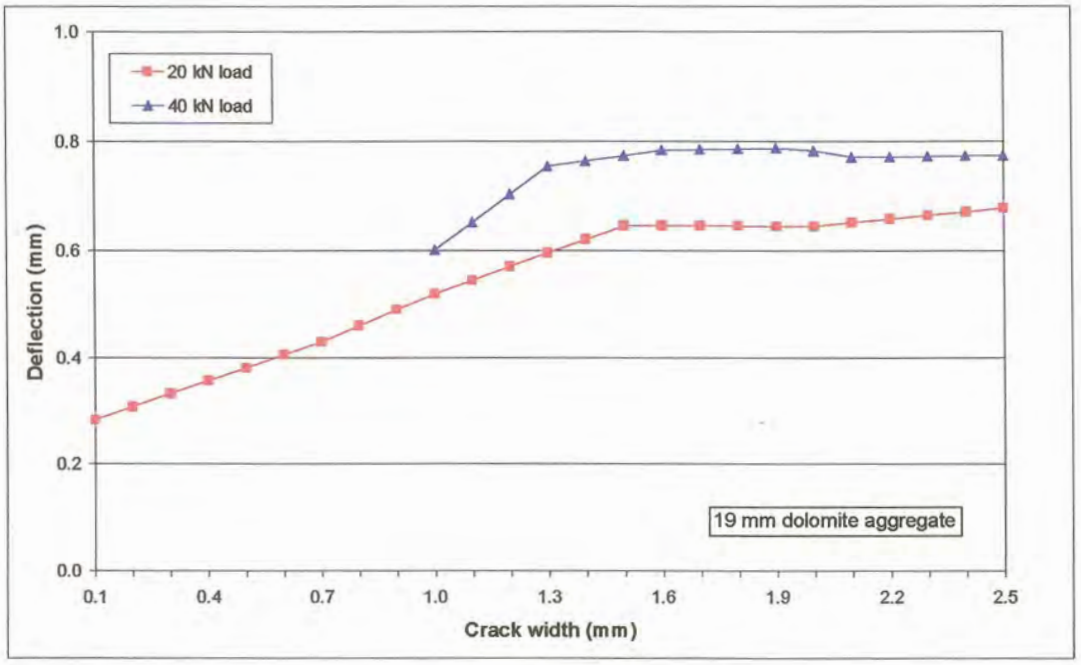

Figure 3.22: Deflection (of leave slab) versus crack width for 20 kN and 40 kN static loading (19 mm dolomite aggregate)

The deflection LTE in the wheelpath obtained for the 19 mm dolomite aggregate, subjected to both 20 kN and 40 kN static loads, is plotted on Figure 3.23. The deflection LTE lines plotted for the 20 kN and 40 kN loads were approximately parallel to each other, with the 40 kN loading results on average 2% higher than the values for the 20 kN load. Considering the magnitude of the deflections, this difference in results is negligible.

Similarly, the RM measured beneath 20 kN static loading, was compared with the RM measured beneath 40 kN static loading, and is plotted on Figure 3.24. The RMs calculated from the 40 kN loading results were 5% lower than those calculated for 20 kN loading. Despite the fact that the 40 kN load caused higher deflections at the crack than the 20 kN load, the relative deflection/movement between the leave slab and the approach slab was smaller. This was primarily due to the 40 kN load transferring larger forces across the crack than the 20 kN, and therefore the smaller RM. Once again the magnitude of the difference is remarkably small.

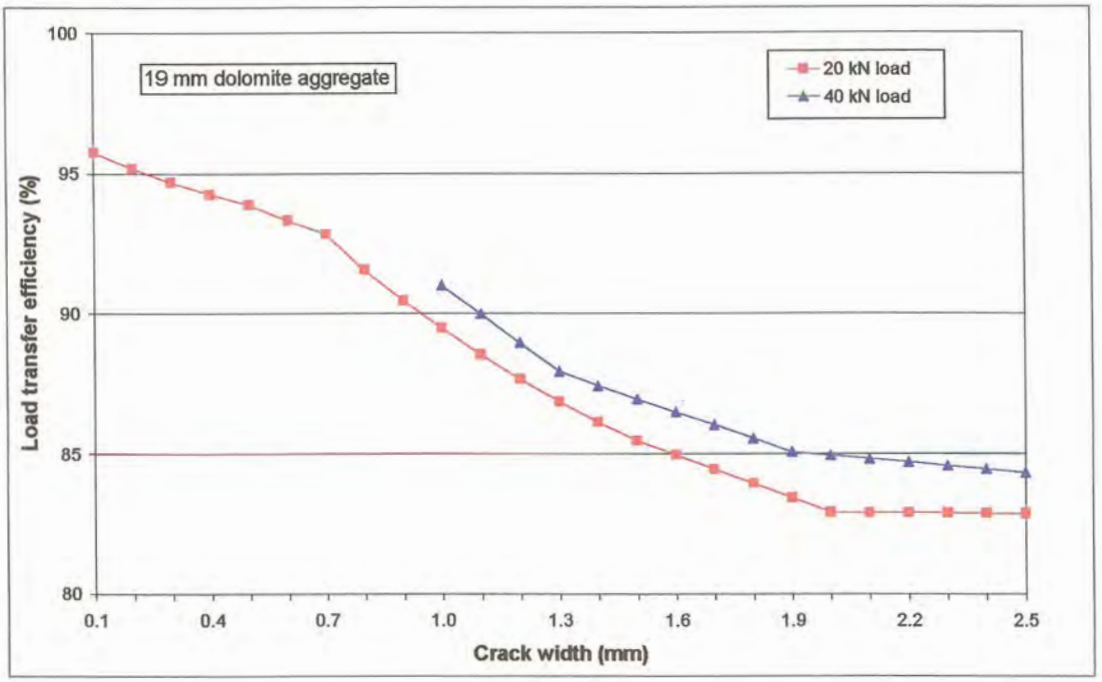

Figure 3.23: Deflection LTE – 20 kN versus 40 kN static loading (19 mm dolomite aggregate)

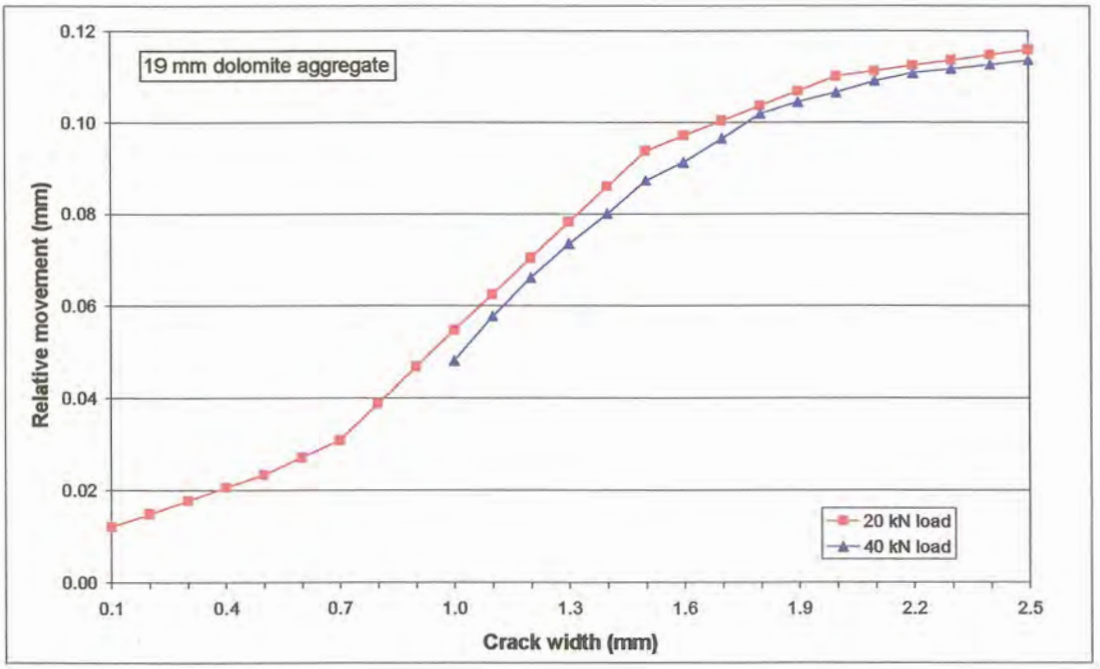

Figure 3.24: RM at joint – 20 kN versus 40 kN static loading (19 mm dolomite aggregate)

3.2.4 Experiment 4

The slab cast for Experiment 4 contained 37,5 mm dolomite aggregate (see Photo G.22). Similar to Experiment 3, this slab was also subjected to three cycles of 10 minutes of dynamic loading followed by static loading at the initial crack width. Thereafter, the two sections of the slab were pulled apart and subjected to dynamic and static loading at different crack widths. The slab was pulled open and tested at different crack widths up to a maximum of 2,5 mm, closed back to the initial crack width, and pulled open again, at least three times to verify the repeatability of the tests.

As for Experiment 3, the top layer of rubber beneath the concrete was cut through directly beneath the joint to simulate a crack projecting into the subbase. The results of Experiment 4 with 37,5 mm dolomite aggregate were compared with that of Experiment 2, where 37,5 mm granite aggregate was used. This was also in order to test the assumption made previously that the high LTE obtained for Experiments 1 and 2 was partly due to the continuous support provided by the rubber subbase

The increase in deflection with increasing crack width for both dynamic and static loading is shown in Figure 3.25. When comparing this figure with Figure 3.13, it is obvious that in the latter case, the deflections measured were less than what was measured for Experiments 1 and 2. Once again the results were also less than the theoretical predictions from EverFE, but similar to the results reported by Jensen (2001). The dynamic loading results were on average 140% that of the static loading results. This was similar to results reported by Bergan and Papagiannakis (1984).

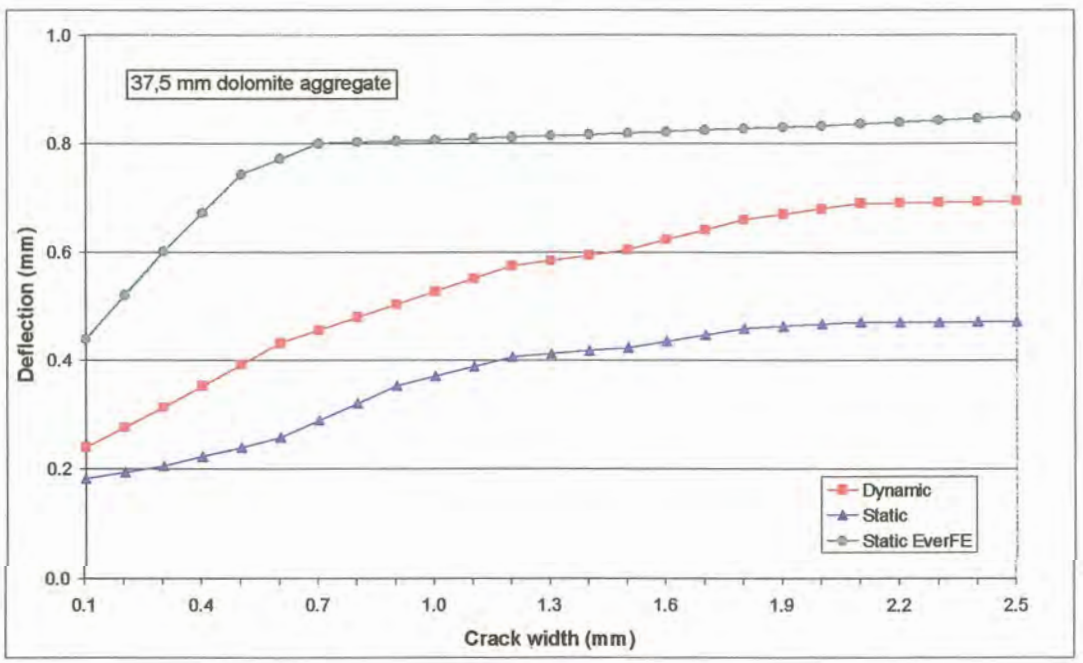

Figure 3.25: Deflection (of leave slab) versus crack width (37,5 mm dolomite aggregate)

The development of horizontal crack displacement at different crack widths is plotted on Figures 3.26 and 3.27 for dynamic and static loading, respectively. For comparison purposes the scale of the vertical axes have been kept constant (see also Figures 3.6, 3.11, 3.12, 3.18 and 3.19). The horizontal displacement at the top of the crack was larger under dynamic loading than under static loading, and also larger than the results plotted for Experiment 3 (Figures 3.18 and 3.19) with the 19 mm dolomite aggregate. In this particular instance the crack tended to open up at the top from smaller crack widths than measured during Experiment 3.

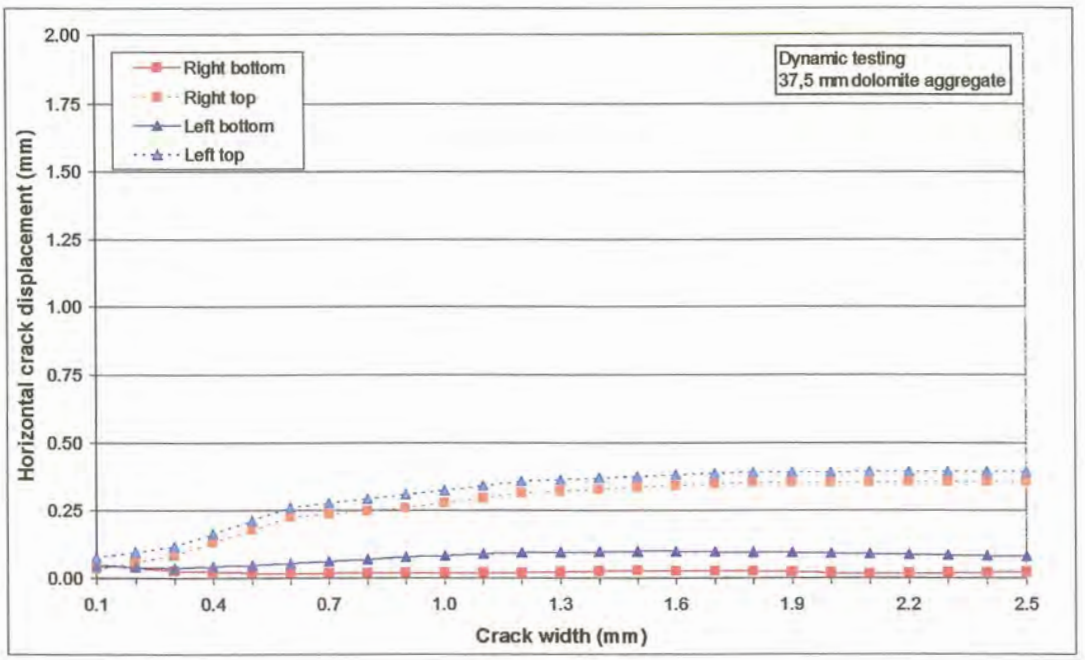

Figure 3.26: Horizontal crack displacement versus crack width under dynamic loading (37,5 mm dolomite aggregate)

Both Experiments 2 and 4 contained 37,5 mm aggregate, although from different sources. Experiment 2 contained, granite and Experiment 4, dolomite aggregate. The deflection LTE graphs obtained for these two Experiments are plotted on Figure 3.28. As for the 19 mm aggregate, it has also been established through VST testing (see Appendix F) that the crack faces of these two slabs were similar. The difference in results could once again be attributed to the fact that in the case of Experiment 4, the top layer of the rubber supporting the concrete was cut through directly beneath the joint/crack position. This simulated crack into the subbase therefore inhibited the transfer of shear stresses, thereby reducing the efficiency of the system. As previously, the theoretical LTE determined with EverFE was initially close to a 100%, but at a crack width greater than 0,5 mm, it decreased to values considerably lower than what was calculated from the laboratory results. The apparent explanation for this difference has been dealt with in paragraphs 3.2.1 and 3.2.2, above.

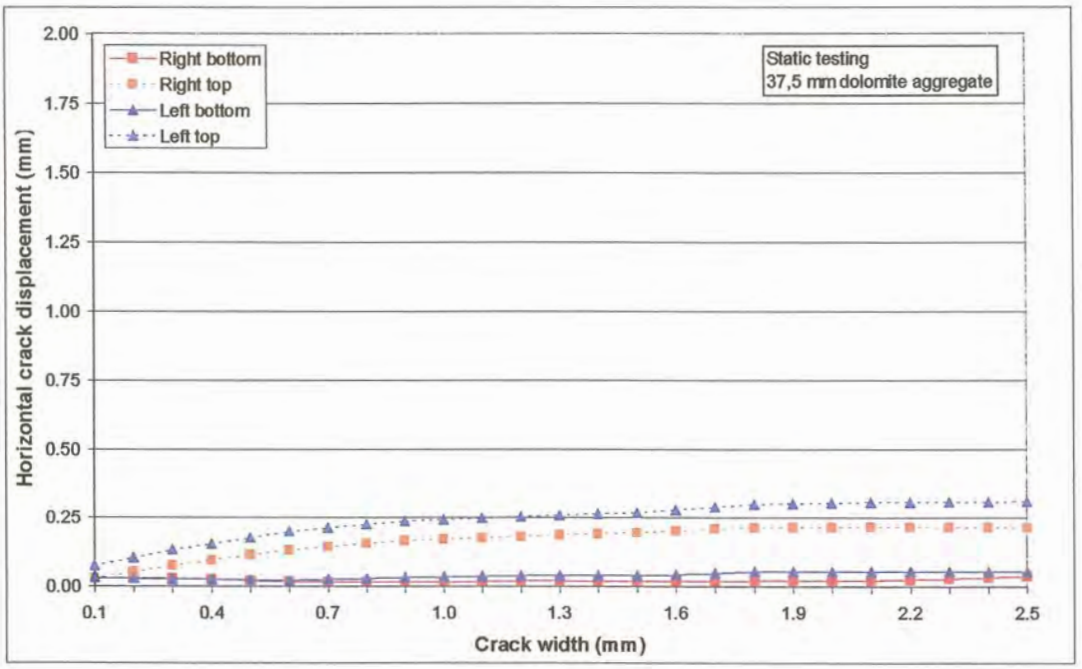

Figure 3.27: Horizontal crack displacement versus crack width under static loading (37,5 mm dolomite aggregate)

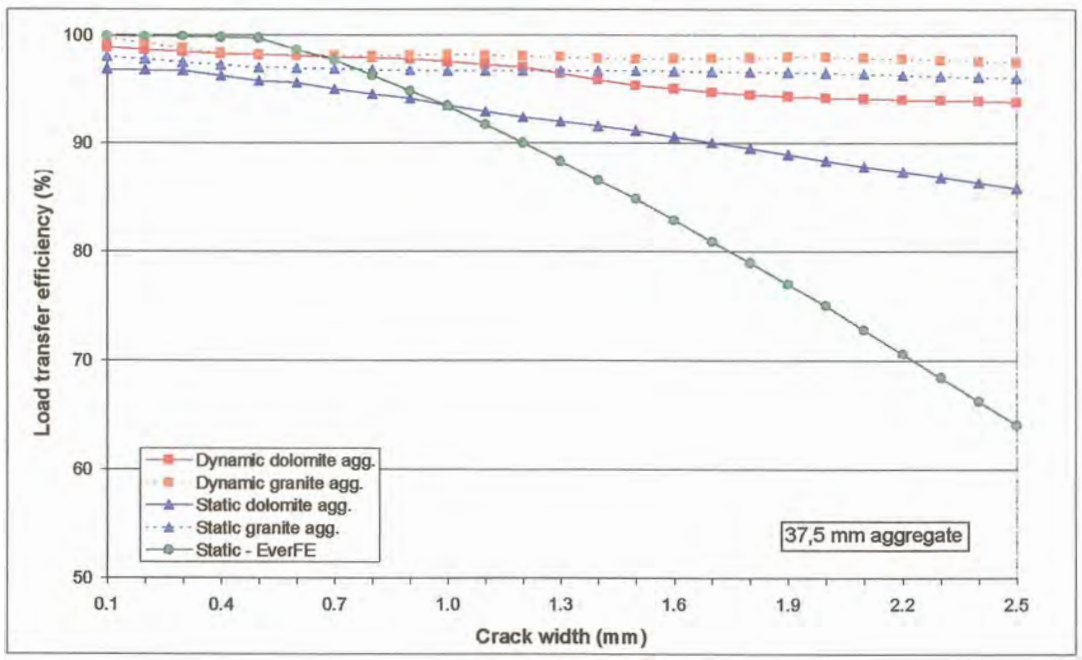

Figure 3.28: Deflection LTE versus crack width – 37,5 mm aggregate

The forces applied to the slab across the crack still rendered higher load transfer efficiencies for dynamic loading than for static loading due to the effect of momentum.

On comparison of the RM results obtained on Experiments 2 and 4, the results were also approximately the same. The software package Mathcad 2000 (Version 8) was used to do a logistic regression on the averages of the dynamic and static loading data in terms of RM (y) and crack width (x), as follows:

Dynamic loading:

$$y(x) = \frac{0{,}060}{1 + 27{,}857 \cdot e^{-2{,}213x}}; \qquad R^2 = 98{,}6\% \tag{3.4}$$

Static loading:

$$y(x) = \frac{0{,}110}{1 + 14{,}522 \cdot e^{-1{,}567x}}; \qquad R^2 = 98{,}8\% \tag{3.5}$$

As for the curves fitted for the 19 mm maximum sized aggregate data, the R-squared values for Equations (3.4) and (3.5) were also near 1, indicating a reliable fit to the data. Figure 3.29 show the curves fitted for the logistic equations (logit) of the dynamic and static loading data.

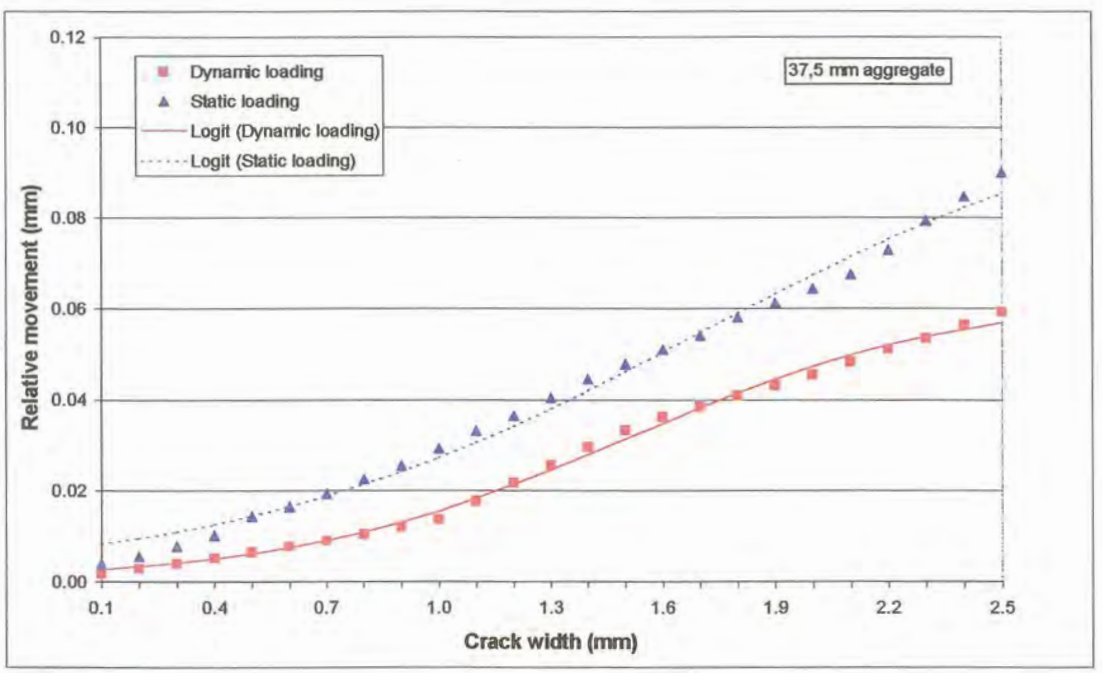

Figure 3.29: Average of RM versus crack width results for dynamic and static loading on 37,5 mm granite and dolomite aggregate

Due to the fact that the RM results for the 37,5 mm aggregate did not reach an upper asymptote at a crack width of 2,5 mm, it was decided to extend the graph to a crack width of 5,0 mm (see Figure 3.30). This was in order to establish the crack width at which the 37,5 mm aggregate tends to reach an

asymptote. From Figure 3.30 it is clear that for both dynamic and static loading of the 19 mm aggregate slabs, an almost complete S-curve was obtained with the aggregate size being small enough for the curve to reach an asymptote at approximately 2,5 mm. The crack width at which an asymptote is reached for the 37,5 mm aggregate slab seemed to be at 3,5 mm and 4,0 mm for dynamic and static loading, respectively.

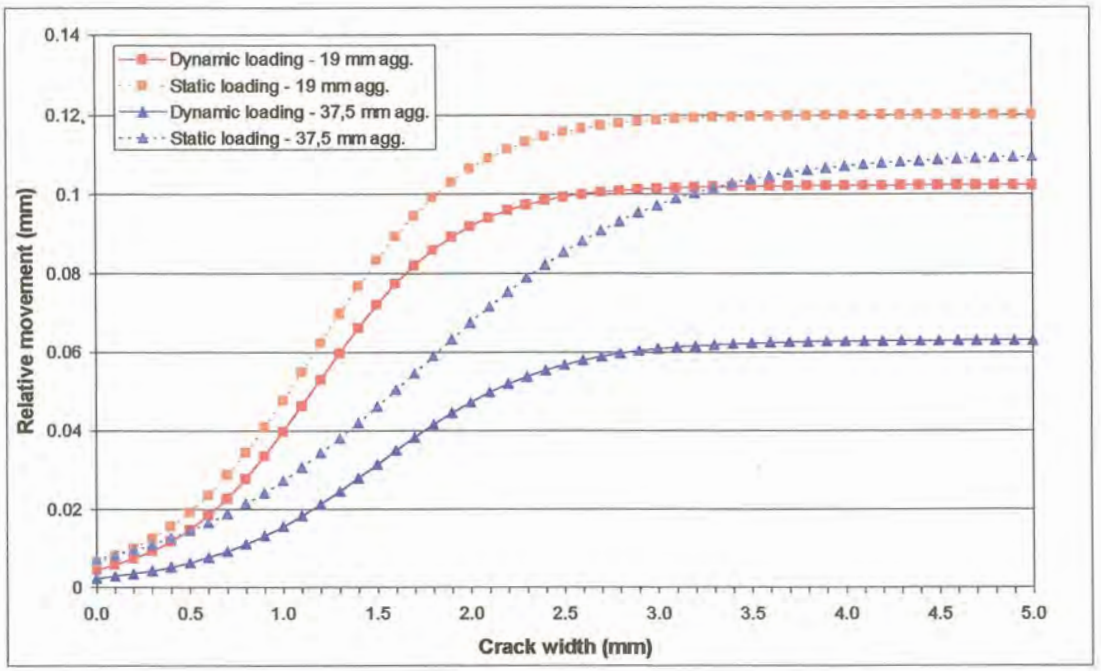

Figure 3.30: Logit function plot

It has already been mentioned that previous research projects (Colley and Humphrey, 1967; Davids et al., 1998b; Jensen, 2001) pointed out that at crack widths greater than 2,5 mm the deflection measurements tended to reach an upper asymptote and that 2,5 mm was considered as the crack width at which the subbase started to play an important role in the LTE of the concrete pavement system. The range of crack widths from 0,5 mm to 2,5 mm is considered to be the region in which aggregate interlock plays the major role in the shear load transferred across the crack. However, the results of these experiments suggest that it may be the case for the 19 mm aggregate, but not for the 37,5 mm aggregate. The fact that the asymptote for the 37,5 mm aggregate is reached at a larger crack width indicates that the region, over which aggregate interlock is still active, is also larger. This statement warrants further research, but was outside the scope of the current investigation.

The deflection and LTE results were compared with the results of a similar study conducted in the USA (Jensen, 2001). It showed that although the deflections measured were similar, the LTE obtained with the more angular crushed granite and dolomite aggregates used in South Africa, was significantly higher than the results obtained with the limestone and glacial gravel used in the USA. The 19 mm

dolomite aggregate rendered a greater LTE than a 50 mm glacial gravel blend, at a crack width of 2,5 mm.

Just as for Experiment 3, the steel frame holding the actuators was turned 90 degrees. This was in order to apply a 40 kN (the 2 actuators together) static load on the one side of the joint/crack, and compare it with the results previously obtained under 20 kN static loading.

Due to the repeated cycle of opening and closing of the two parts of the slab during initial testing, some particles were once again loosened on the crack face, which prevented closing the crack to less than 1,0 mm. Results under 40 kN load application were therefore only obtained for crack widths between 1,0 mm and 2,5 mm. Figure 3.31 show the deflection versus crack width measured on the leave slab for both 20 kN and 40 kN static loading. Although slightly higher, the deflection under 40 kN load did not differ much from the deflection under 20 kN load.

The deflection LTE in the wheelpath obtained for the 37,5 mm dolomite aggregate, subjected to both 20 kN and 40 kN static loads, is plotted on Figure 3.32. The deflection LTE lines plotted for the 20 kN and 40 kN loads were almost parallel to each other, with the 20 kN loading results slightly less than the values for the 40 kN load.

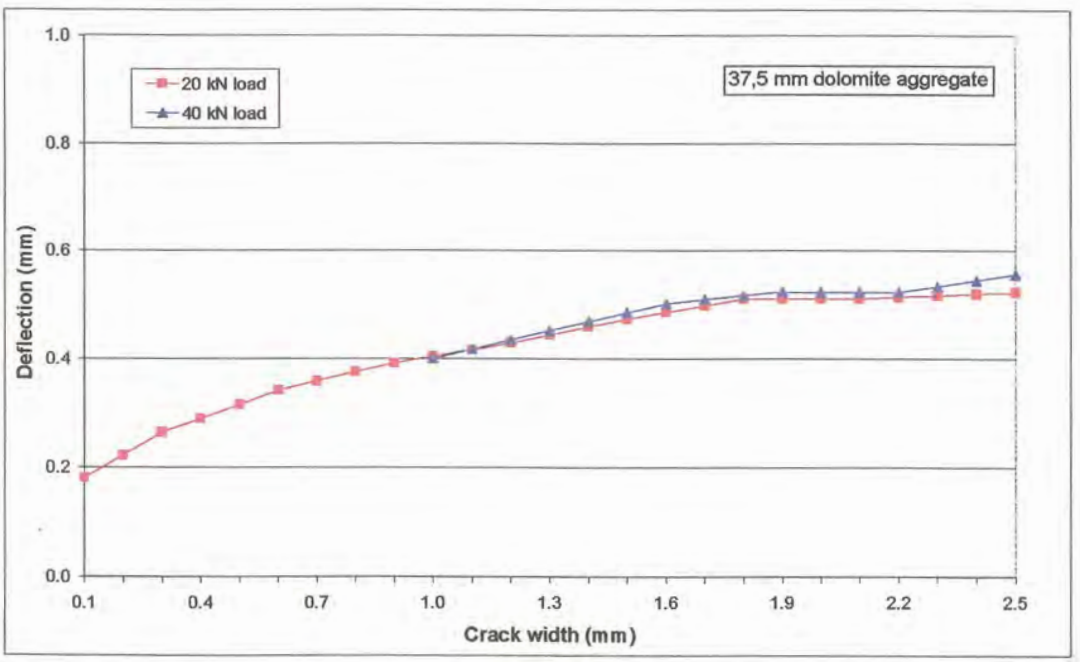

Figure 3.31: Deflection (of leave slab) versus crack width for 20 kN and 40 kN static loading (37,5 mm dolomite aggregate)

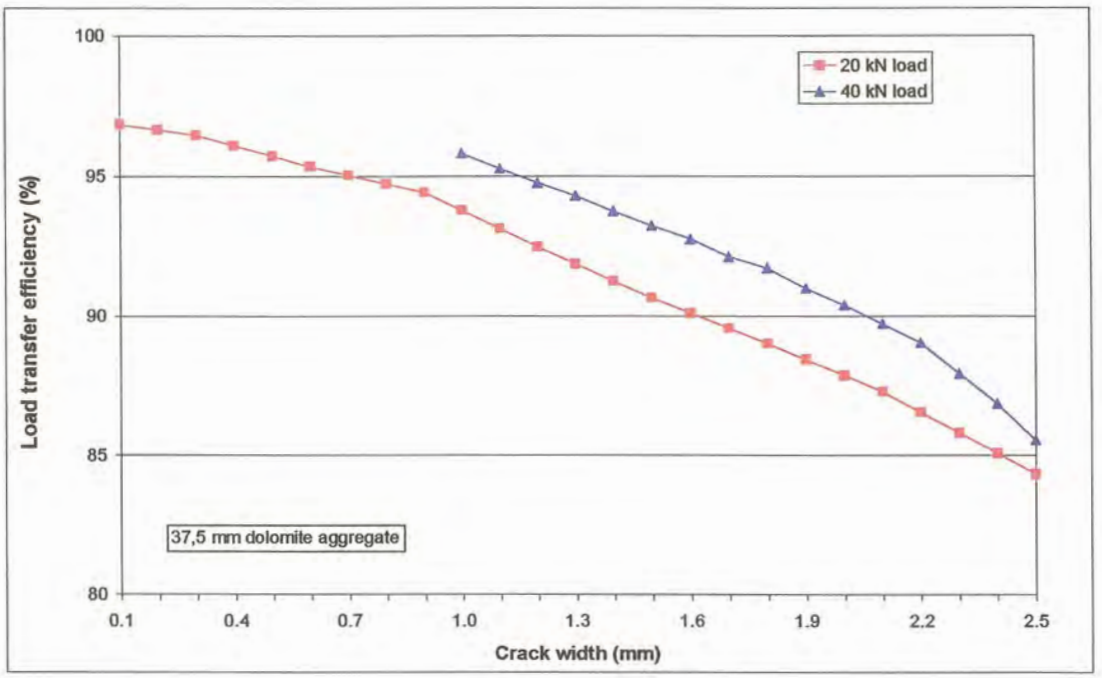

Figure 3.32: Deflection LTE – 20 kN versus 40 kN static loading (37,5 mm dolomite aggregate)

The RM measured beneath 20 kN static loading, was also compared with the RM measured beneath 40 kN static loading, and is plotted on Figure 3.33.

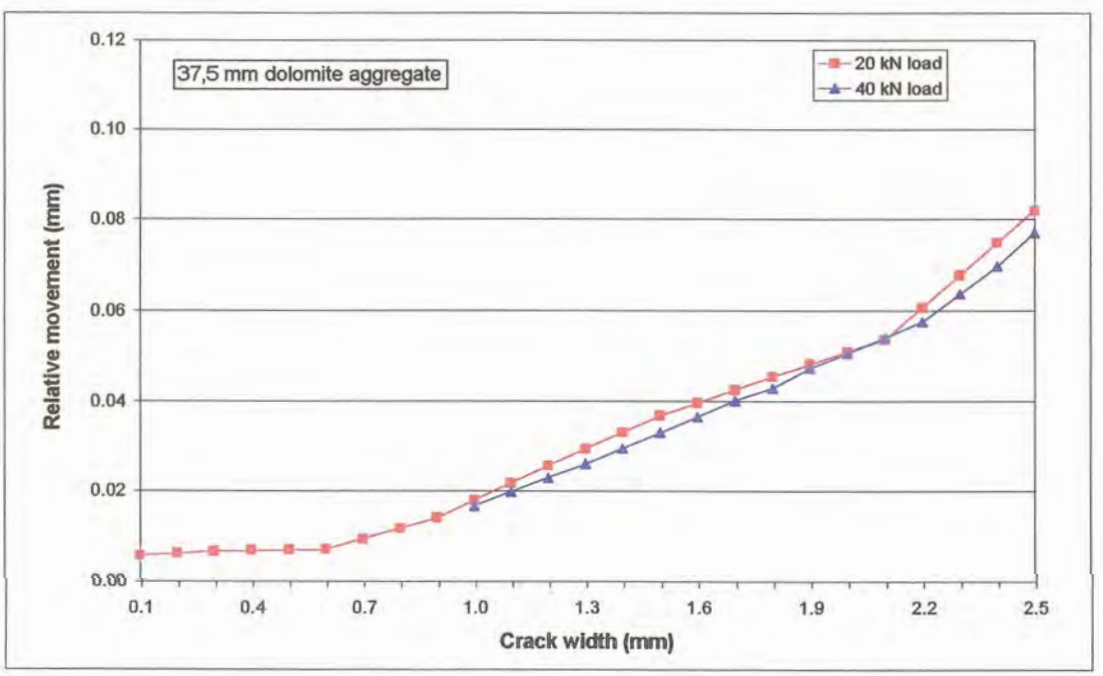

Figure 3.33: RM at joint – 20 kN versus 40 kN static loading (37,5 mm dolomite aggregate)

The RM calculated from the 20 kN loading results were higher than those calculated for the 40 kN loading. With the deflection LTE of the 40 kN load once again higher than the 20 kN load, smaller RMs for the heavier load should be expected. The scale of the vertical axis has been kept the same as that of Figure 3.24 to facilitate easier comparison between the results obtained with the 19 mm aggregate and the 37,5 mm aggregate, the RMs measured with the 37,5 mm aggregate being lower than the 19 mm aggregate.

3.3 PRE-DEFORMED PLASTIC JOINT

A fifth slab was cast using the same concrete mix design as for Experiment 1, but with a 100 micron plastic sheet at the crack position. To ensure that the concrete met the design strength requirements of 35 MPa, the 7-day cube compressive strength was determined, and a forecast made of what the 28-day results would be. This was merely for control purposes as the properties of the concrete for this specific mix design has already been determined through the tests listed in Table 3.1, and the results summarised in Appendix F.

A standard glass light bulb was used to form bubbles in the plastic, and to create an interlock effect. Figure 3.34 shows schematically what the sheet and bubbles looked like. The sheet was 600 mm wide, and 240 mm high to fit exactly into the shuttering for the slab, but with a small edge sticking out at the top (See Photo G.23).

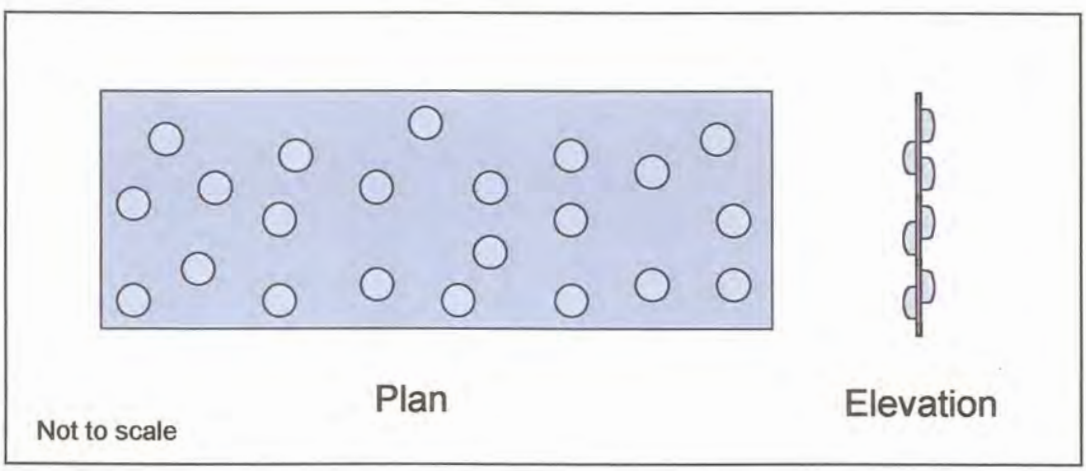

Figure 3.34: Schematic presentation of plastic joint/crack former

3.3.1 20 kN dynamic and static loading on discontinuous rubber subbase

The slab was cast on a rubber subbase with the top layer of rubber cut through. The same testing procedures as for Experiments 3 and 4 were followed for testing the characteristics of the plastic joint. The slab was subjected to three cycles of 10 minutes of dynamic loading followed by static loading at the initial crack width, where after the two sections of the slab were pulled apart and subjected to dynamic and static loading at different crack widths. The slab was pulled open up to a maximum crack width of 2,5 mm.

The data obtained was analysed in a similar fashion as the previous experimental results. The deflection versus crack width for both dynamic and static loading is shown on Figure 3.35. The deflection of the leave slab measured under dynamic loading was initially slightly higher than under static loading, due to the effect of momentum keeping the slab in a deflected position. However, as soon as the two sections of the slab were pulled apart, the smooth texture (see Photo G.24) of the surface created by the plastic sheet permitted higher deflections under static loading than under dynamic loading. The leave slab deflections increased to a maximum at a crack width of 1,2 mm under both static and dynamic loading, and then decreased again up to a crack width of 1,5 mm, where after it remained constant. For comparison purposes, the deflections measured on the approach slab were also plotted on Figure 3.35.

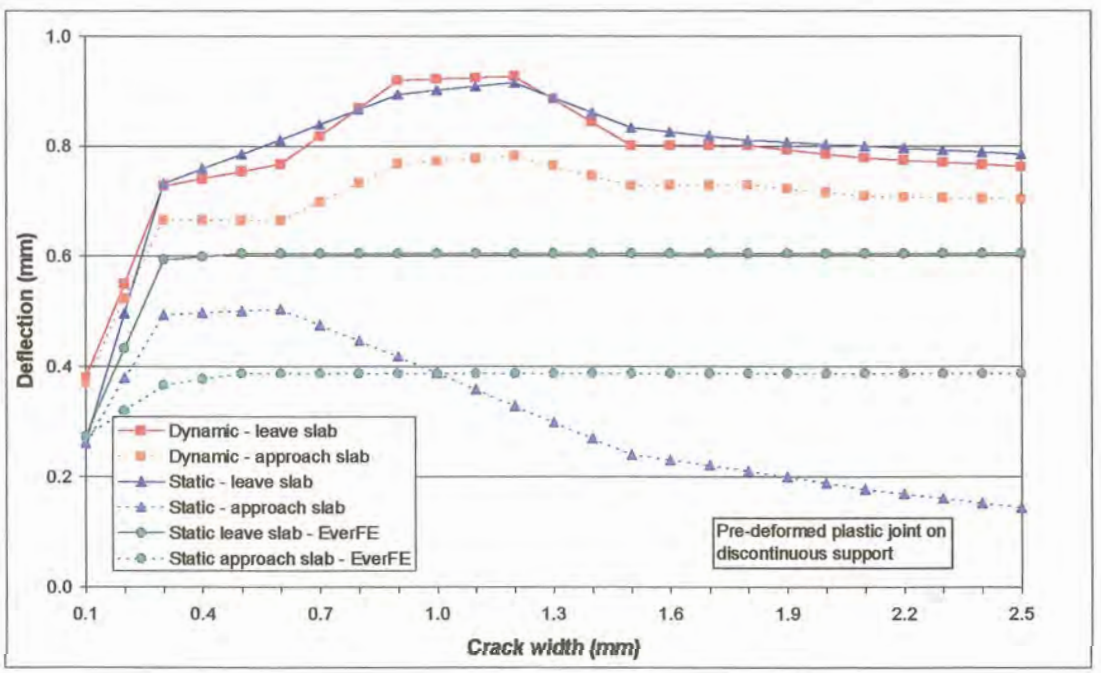

Figure 3.35: Deflection versus crack width (plastic joint on DC rubber subbase)

The deflections measured on the approach slab during both dynamic and static loading also reached a maximum, where after it decreased gradually. The increase in the difference between the deflection results with increasing crack width of the leave and approach slabs under static loading was far greater than the comparative results measured under dynamic loading.

The plastic joint was also theoretically analysed with EverFE, and the results plotted on Figure 3.35. The initial deflection calculated with EverFE for 20 kN static loading was slightly higher than the measured results. The EverFE deflection results also increased as soon as the joint/crack opened, but already levelled out after a crack width of 0,5 mm which was far sooner than the laboratory results. On the leave slab the maximum deflection calculated with EverFE was 0,60 mm, while the maximum measured varied between 0,85 mm and 0,95 mm for static and dynamic loading, respectively.

The horizontal crack displacement under both dynamic and static loading versus the crack width is given in Figures 3.36 and 3.37. For comparison purposes, the vertical axes of these two figures were once again kept the same as the previously reported horizontal crack displacement results (see also Figures 3.6, 3.11, 3.12, 3.18, 3.19, 3.26, and 3.27). The horizontal crack displacement at the top of the crack tended to be larger under dynamic loading than under static loading. At the bottom of the crack the difference in results was not so marked.

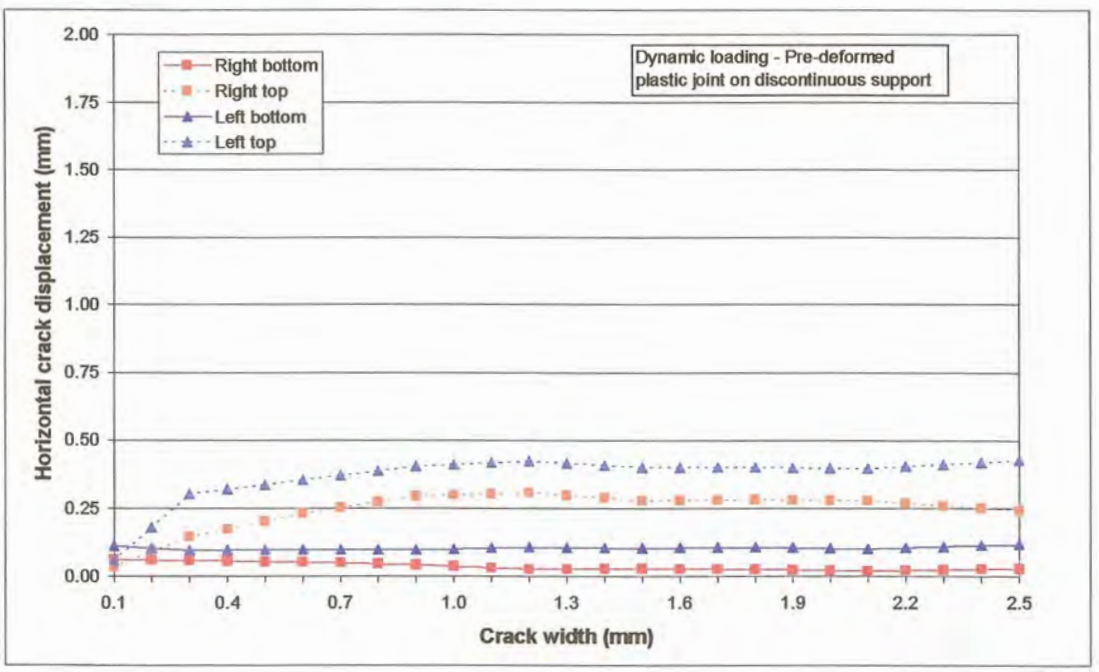

Figure 3.36: Horizontal crack displacement versus crack width under dynamic loading (plastic joint on DC rubber subbase)

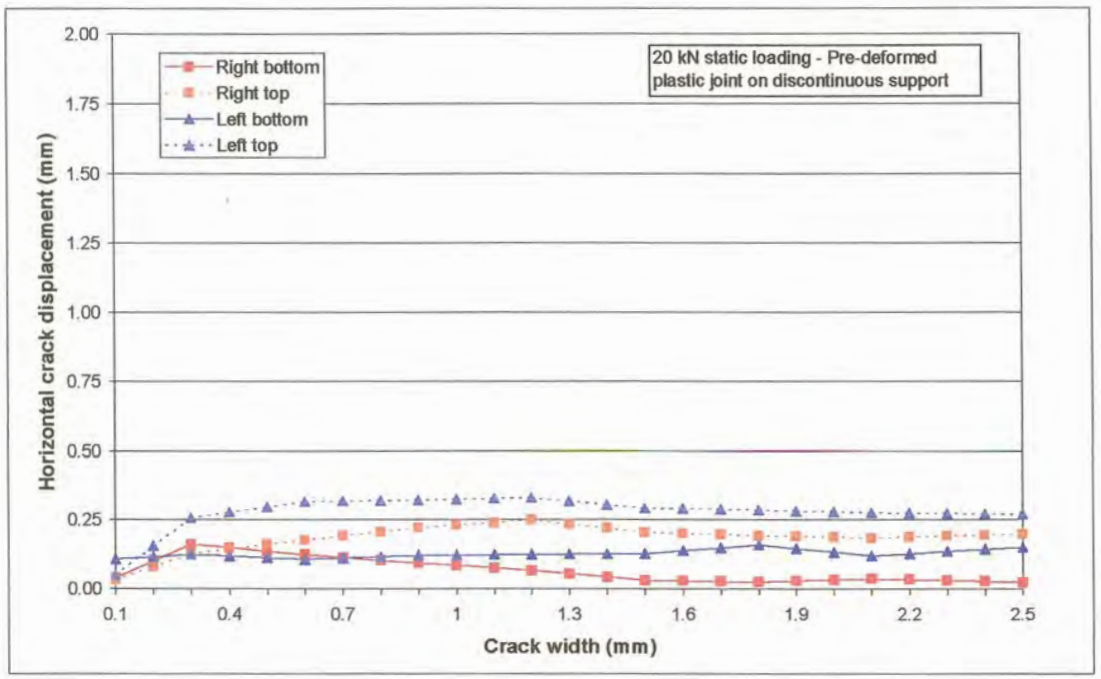

Figure 3.37: Horizontal crack displacement versus crack width under static loading (plastic joint on DC rubber subbase)

The deflection LTE for both dynamic and static loading at the initial crack width, shown on Figure 3.38, was close to 100%. The parameter controlling the performance of the slab at 0,1 mm joint/crack width was therefore the crack width itself. In this initial locked up position the two sections of the slab reacted together, with little differential horizontal or vertical movement. However, as soon as the two sections of the slab were pulled apart, the two sections slipped and slided over each other and the LTE dropped dramatically. The effect of moment and inertia in the system causing continual horizontal forces to be transferred across the joint during dynamic loading with the LTE levelling out to a value of 92% at a crack width of 2,5 mm, was remarkable during this test. A further phenomenon, is the fact that specifically under dynamic loading the LTE decreased, reached a turning point, and then increased again, where after it levelled out (the reverse of the deflection measurements).

Under static loading, on the other hand, there was a constant decrease in deflection LTE, with increasing crack width. This showed that the horizontal forces transferred across the joint were far less under static loading than what was transferred through momentum forces under dynamic loading. The EverFE results, reached a minimum turning point at a crack width of 0,3 mm, but then it also turned, increased, and levelled out similar to the dynamic loading results. Although, once again, the EverFE results levelled out at a crack width of 0,5 mm, compared to the 1,5 mm crack width where the dynamic loading results levelled out.

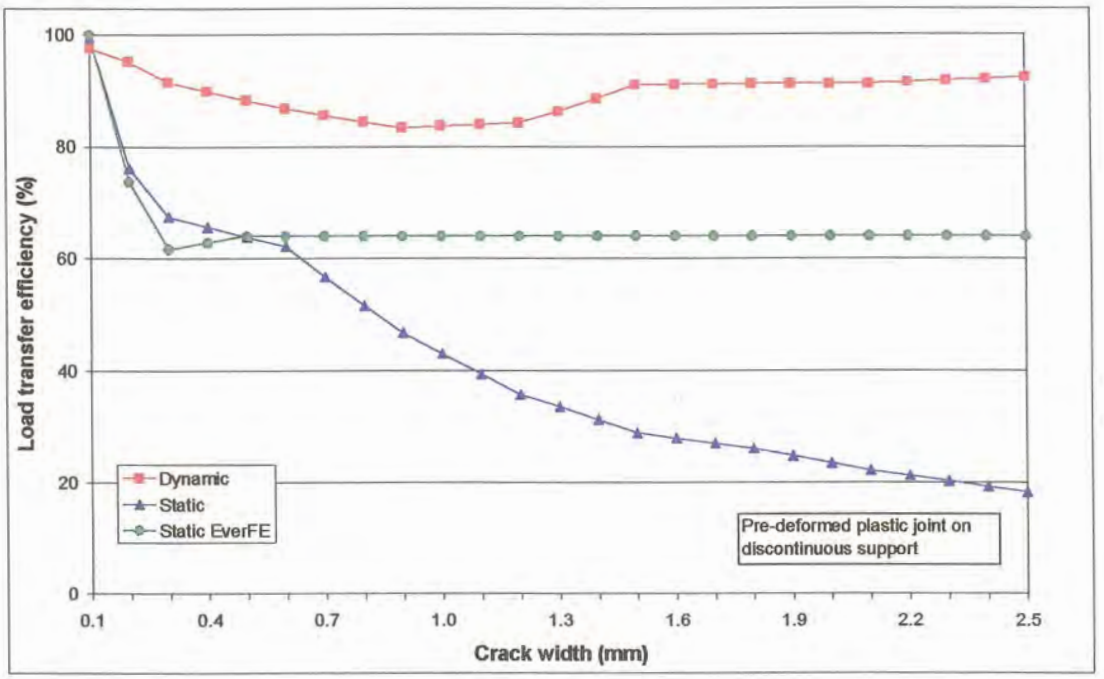

Figure 3.38: Deflection LTE versus crack width (plastic joint on DC rubber subbase)

It is the opinion of the author that the response of the plastic joint was that measured up to a crack width of 1,5 mm, and that specifically the results under dynamic loading thereafter were influenced by the subbase stiffness. This would imply that the smoother the texture of the crack face, the sooner the system will rely on the support of the subbase to transfer stresses and strains from one slab to another. This study has already indicated three such transition zones, namely: 1,5 mm for the smooth joint, 2,5 mm for the 19 mm aggregate interlock joint, and between 3,5 mm and 4,0 mm for the 37,5 mm aggregate interlock joint.

Furthermore, although it is on a micro scale, the turning point in the dynamic loading data of the plastic joint, indicate a re-orientation of the leave slab relative to the approach slab. While the two sections of the slab moved both vertically and horizontally relative to each other, the leave slab also rotated slightly. This explains why during the first slipping and sliding phase there was initially a decrease in LTE. The leave slab then rotated slightly, and found a new equilibrium point, where the graph levelled out. After this the rotation movement caused the leave slab to "lock" into a more stable position, from there the increase in LTE, where after the two sections of the slab were supported by the subbase. The smooth texture of the plastic surface inside the joint made it possible for the two sections of the slab to repeat a specific action during crack-opening testing, and thereby ensured continuity in the data.

The RMs measured at the joint/crack under dynamic and static loading, as well as the theoretical RMs determined with EverFE is shown on Figure 3.39. The RM results under dynamic loading started at zero, reached a maximum turning point, decreased again, and tended to converge to a constant value.

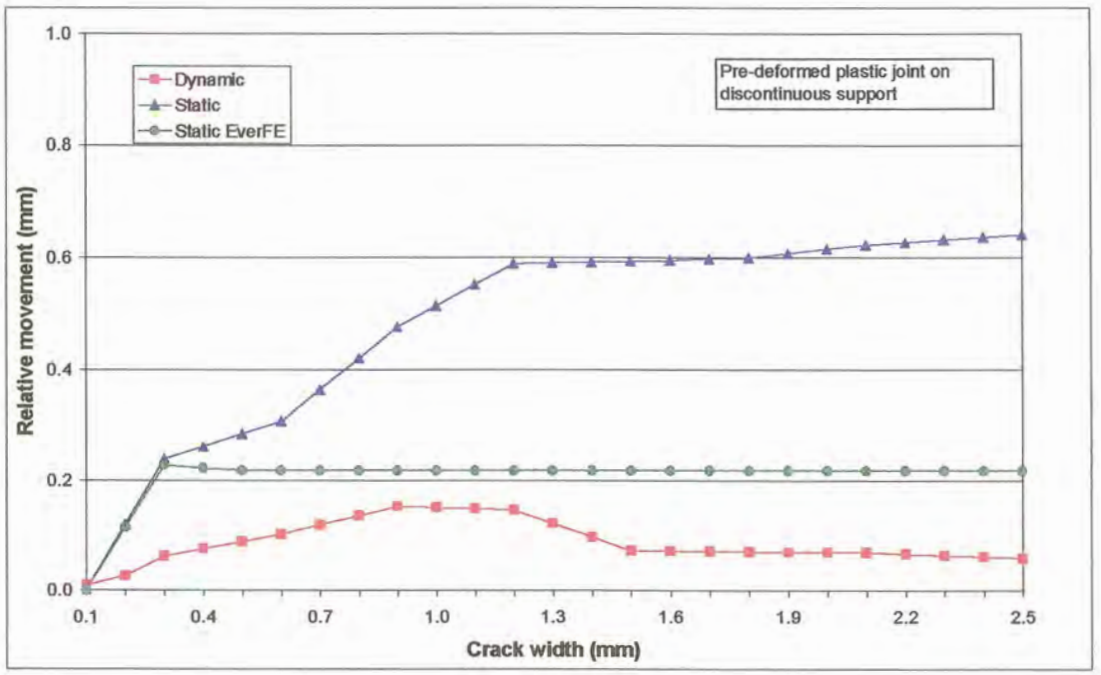

Figure 3.39: RM versus crack width (plastic joint on DC rubber subbase)

The RM results under static loading increased with increasing crack width. The theoretical EverFE results were initially approximately the same as the static loading laboratory results, but it already stabilised after a crack width of 0,3 mm.

Contrary to the RM S-curve formulas that could be derived from the aggregate interlock experiments no formula was derived from the curves drawn from the plastic joint laboratory results. After re-orientation of the leave slab relative to the approach slab, under dynamic loading, the plastic joint had a RM at a crack width of 2,5 mm about the same as the 37,5 mm maximum aggregate size results (see Figure 3.29). These results show that the actual re-orientation movement in terms of vertical slipping and horizontal sliding took place from a crack width just larger than 0,1 mm to 1,5 mm for this particular plastic joint. At crack widths larger than 1,5 mm the RM of the subbase was measured.

The RM for the plastic joint under static loading, however, gradually increased up to a value where it was 6 times higher at a crack width of 2,5 mm than the RM under static loading for the aggregate interlock joints.

3.3.2 40 kN static loading on discontinuous rubber subbase

Similar to the procedure followed during Experiments 3 and 4, the steel frame holding the actuators was turned 90 degrees, and a 40 kN static load was applied on the one side of the joint. The results

were then compared with the 20 kN static loading results already obtained. The smooth surface finish of the plastic joint face made it possible to close the crack to its original 0,1 mm width, prior to commencement of the 40 kN loading test. The deflections measured for the 20 kN and 40 kN static loading results are shown on Figure 3.40.

On the leave slab the deflection measurements under the heavier 40 kN load gradually increased with increasing crack width. The transfer of normal stresses to the approach slab could be maintained reasonably well up to a crack width of 0,6 mm, where after the deflections on the approach slab decreased with increasing crack width. This indicates a decrease in LTE with increasing crack width as can be seen from Figure 3.41. Although the heavier load initially had a lower LTE than the lighter load, it was eventually twice as effective in transferring the load across this particular type of joint.

As a final comparison for this specific test set-up, the RMs measured across the joint for 20 kN and 40 kN static loading, as well as the theoretical results determined with EverFE are plotted on Figure 3.42. The RMs under both 20 kN and 40 kN static loading seem to be still on the increase at a crack width of 2,5 mm, whereas the EverFE results already levelled out after a crack width of 0,3 mm.

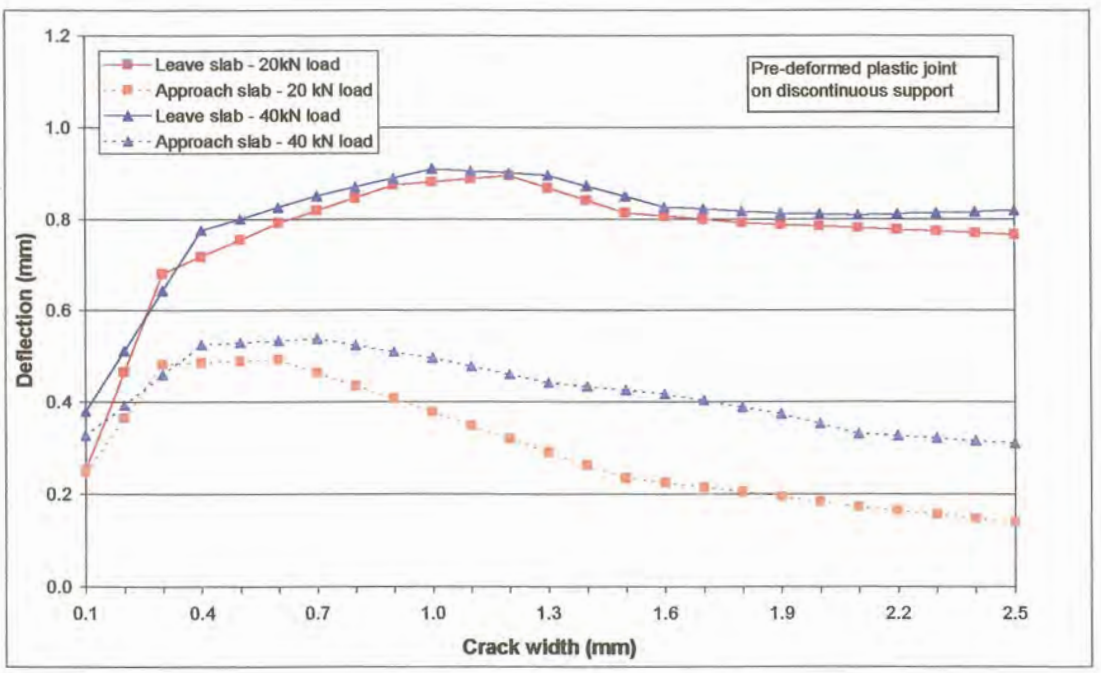

Figure 3.40: Deflection versus crack width for 20 kN and 40 kN static loading (plastic joint on DC rubber subbase)

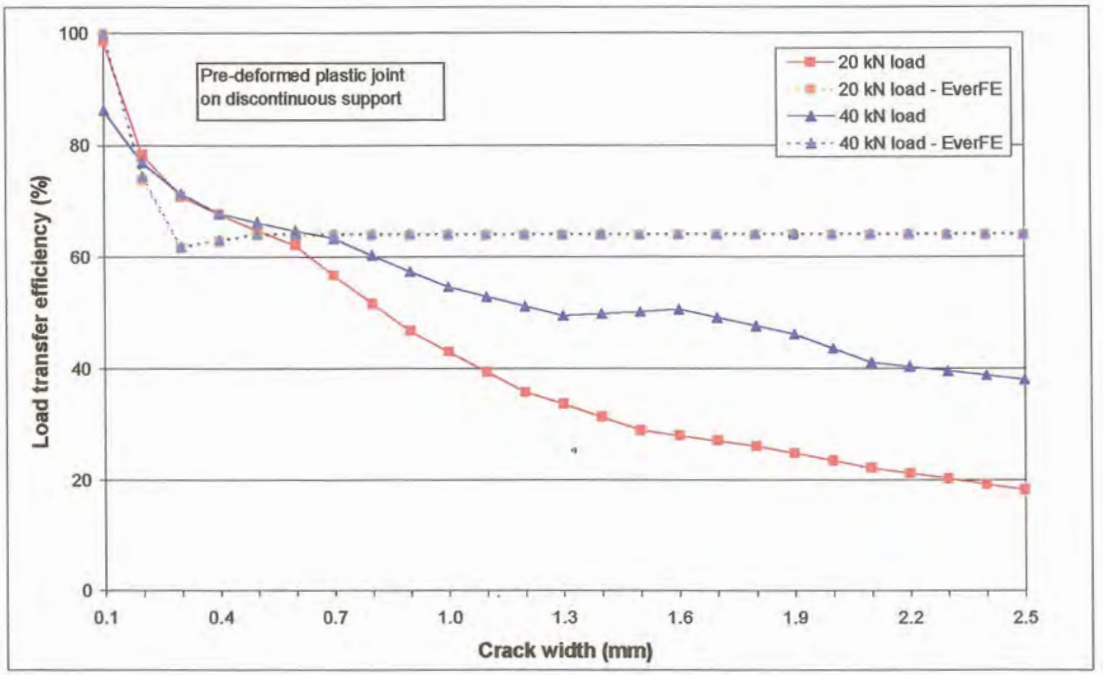

Figure 3.41: Deflection LTE versus crack width for 20 kN and 40 kN static loading (plastic joint on DC rubber subbase)

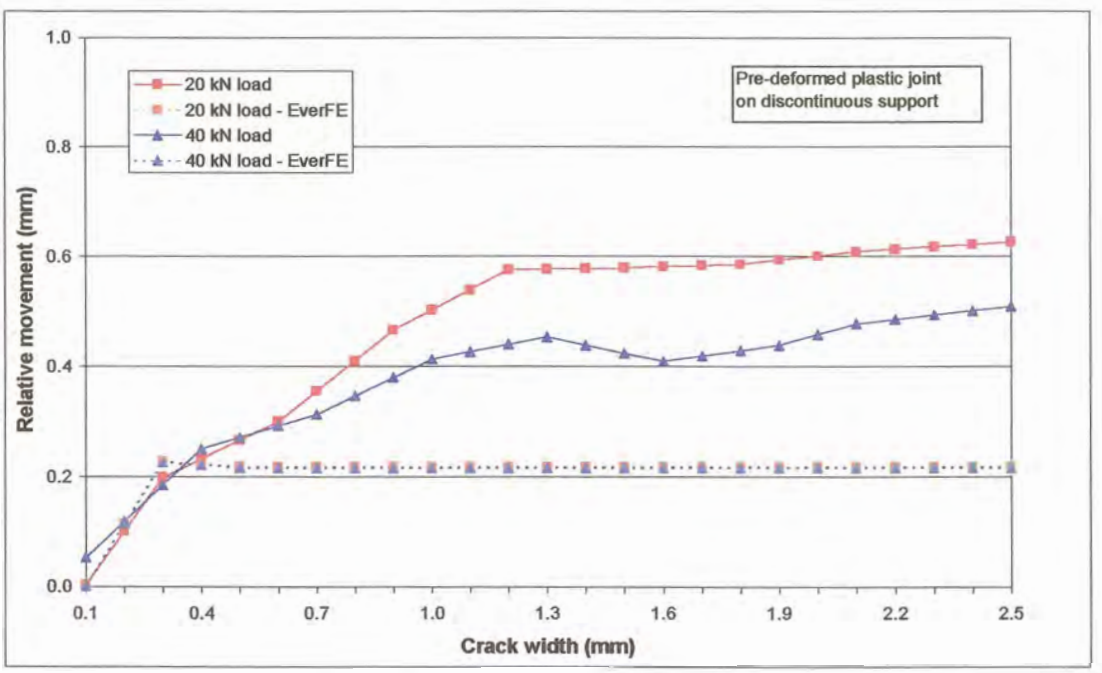

Figure 3.42: RM versus crack width for 20 kN and 40 kN static loading (plastic joint on DC rubber subbase)

3.3.3 20 kN dynamic and static loading on continuous rubber subbase

Due to the fact that the crack face formed by the plastic was relatively smooth, it was possible to lift the two sections of the slab off the top layer of rubber that was cut through, and replace it with a continuous piece of rubber, without damaging the crack face. This was in order to compare the behaviour of the concrete at the joint on a continuous (C) as well as on a discontinuous (DC) rubber subbase, and also to quantify assumptions already made in the analyses. The testing procedure with the DC rubber subbase, described in paragraphs 3.3.1 and 3.3.2, was repeated with the C rubber subbase.

The deflection versus crack width for both dynamic and static loading is shown on Figure 3.43. The deflection of the leave slab measured under dynamic loading was higher than under static loading, due to the "speed" of loading, thus due to the effect of momentum keeping the slab in a deflected position. The leave slab deflections were constantly higher than the approach slab deflections under both static and dynamic loading.

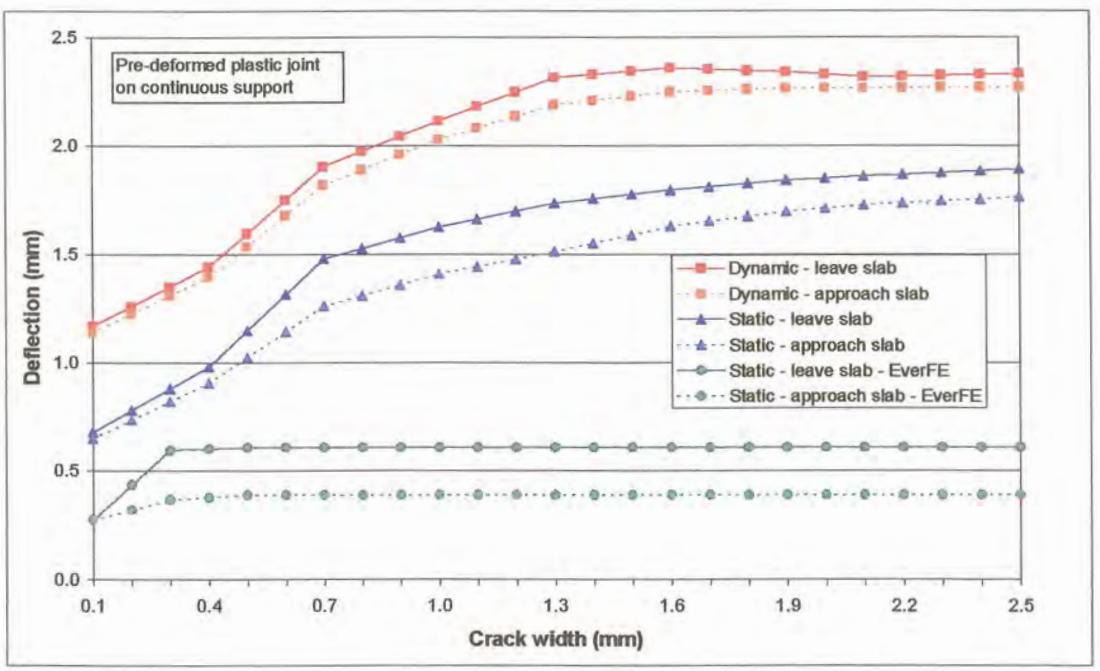

Figure 3.43: Deflection versus crack width (plastic joint on C rubber subbase)

Contrary to the marked difference between the dynamic and static loading deflection results measured on the DC rubber subbase (see Figure 3.35), the lines plotted from the deflections measured on the leave slab for both dynamic and static loading were close to parallel to the lines plotted from the deflections measured on the approach slab of the C rubber subbase. This was directly due to the greater load transfer capacity of the C rubber subbase.

The plastic joint was also theoretically analysed with EverFE, and the results plotted on Figure 3.43. The initial deflection calculated with EverFE for 20 kN static loading was only 40% of the static loading results, and only 23% of the dynamic loading results. The EverFE deflection results were consistently lower than the laboratory results.

The horizontal crack displacement under both dynamic and static loading versus the crack width is given in Figures 3.44 and 3.45. As before, the vertical axes of these two figures were kept the same as the previously reported horizontal crack displacement results. The bending through of the slab at narrow crack widths, with a reversal (between 0,7 mm and 1,3 mm crack widths), and the opening up of the top of the crack at larger crack widths was more pronounced in this instance than what was previously measured during for example Experiment 3. This could be attributed to the smooth surface of the joint/crack face. The movement at the top of the crack under dynamic loading was approximately twice the movement under static loading, which could be attributed to the effects of momentum.

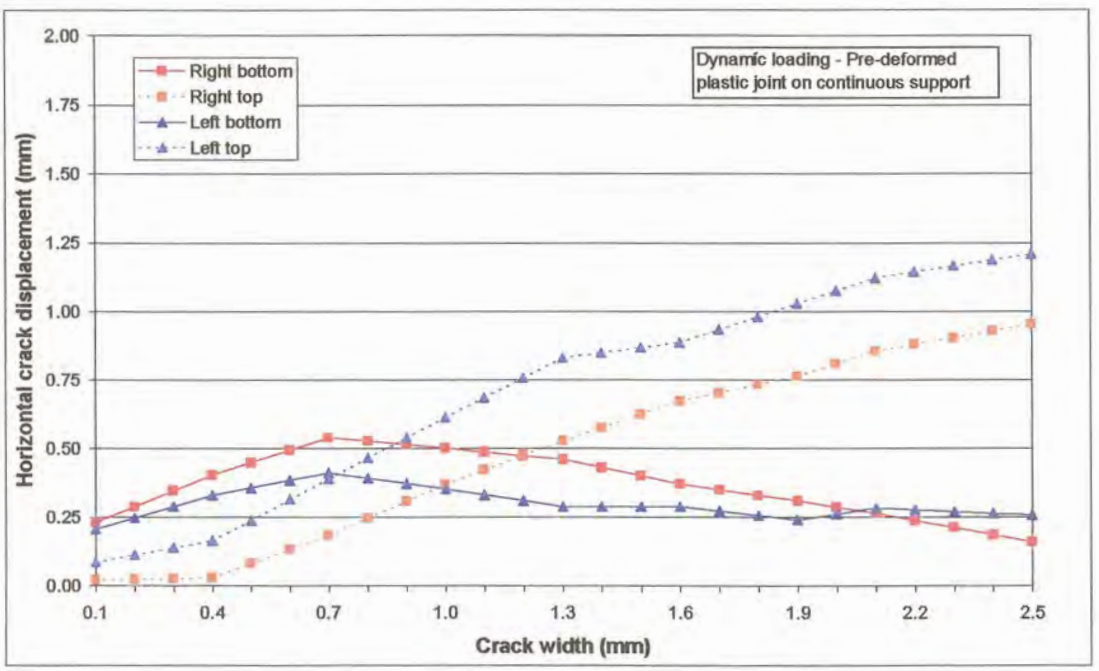

Figure 3.44: Horizontal crack displacement versus crack width under dynamic loading (plastic joint on C rubber subbase)

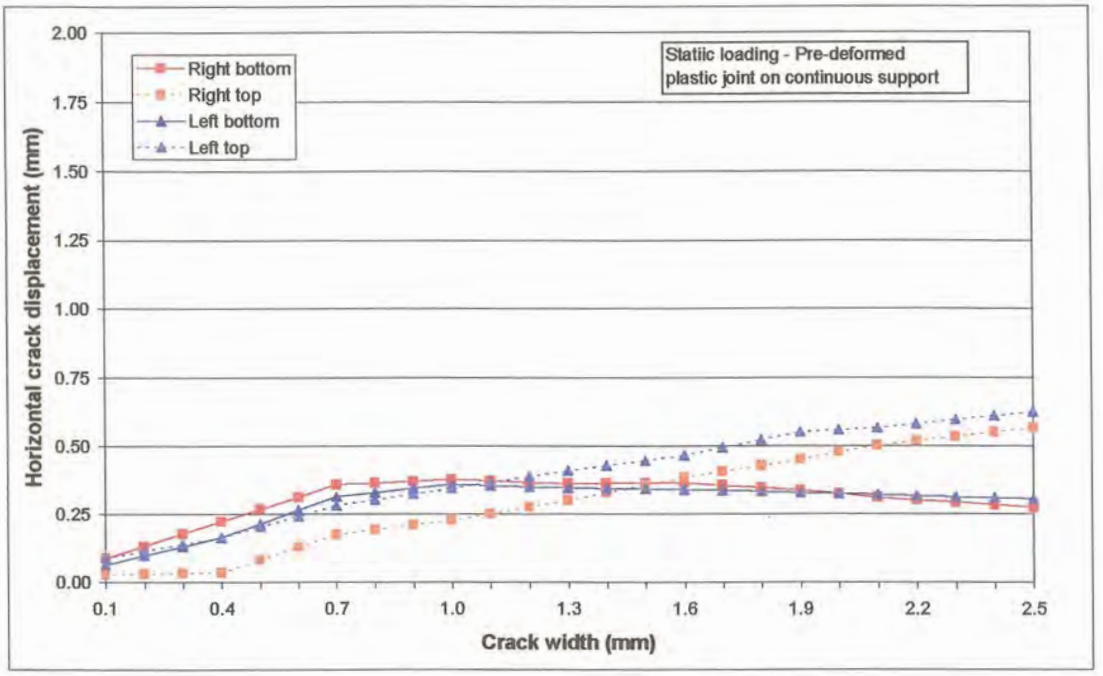

Figure 3.45: Horizontal crack displacement versus crack width under static loading (plastic joint on C rubber subbase)

The deflection LTE under dynamic loading at the initial crack width, shown on Figure 3.46, was close to 100%, with an average LTE of 96% at larger crack widths up to 2,5 mm. This was primarily due to the effect of momentum, but also due to the C rubber subbase. The LTE at a crack width of 0,1 mm under static loading was 96%. As before, applying a static load at the one side of the crack allowed sliding of the leave slab relative to the approach slab. The LTE under static loading therefore decreased, levelled out, and increased again, with the continuous subbase support ensuring greater LTE than the DC rubber subbase under similar loading conditions. From Figure 3.46 it is also obvious that the theoretical EverFE analysis results did not approximate the laboratory results.

The RMs measured between the leave slab and the approach slab under dynamic and static loading, as well as the EverFE results are shown on Figure 3.47. Both the dynamic and static loading results increased levelled out, and then decreased again, indicating a re-orientation of the leave slab relative to the approach slab. Between 0,7 mm and 1,3 mm crack widths the static loading and EverFE results were basically the same.

The most probable reason for this similarity between the laboratory and the EverFE results may lie in Walraven's (1981) aggregate interlock model incorporated in EverFE. The rounded shape of the "bubbles" in the plastic sheet can be considered as a close representation of Walraven's (1981) model where the aggregate is modelled as spherical in shape.

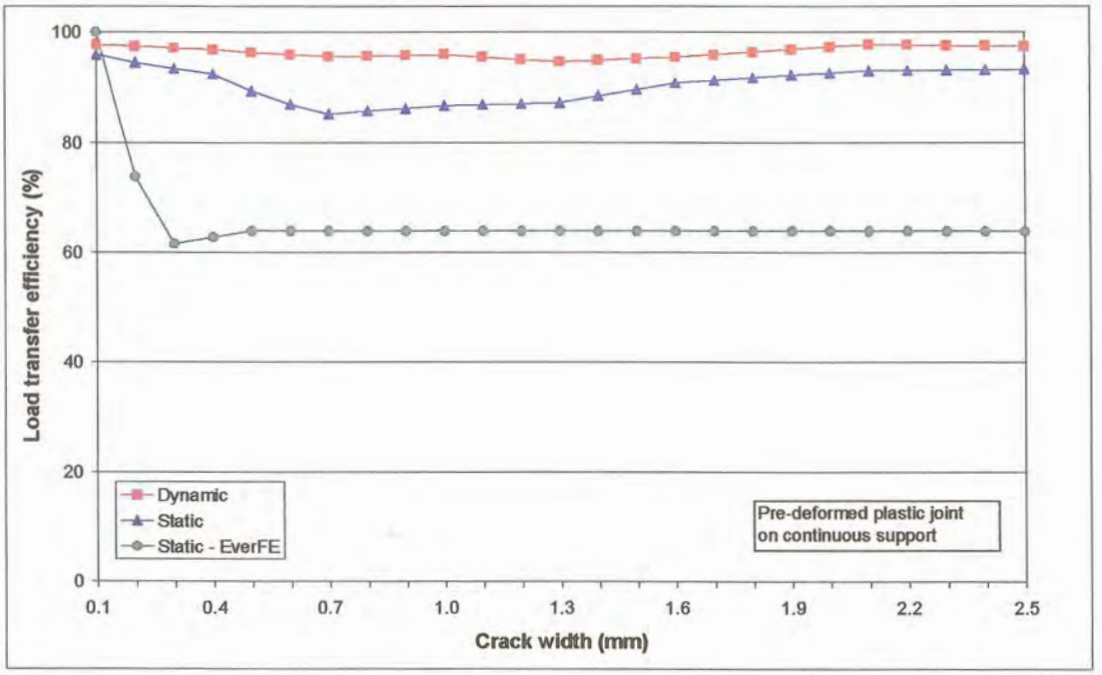

Figure 3.46: Deflection LTE versus crack width (plastic joint on C rubber subbase)

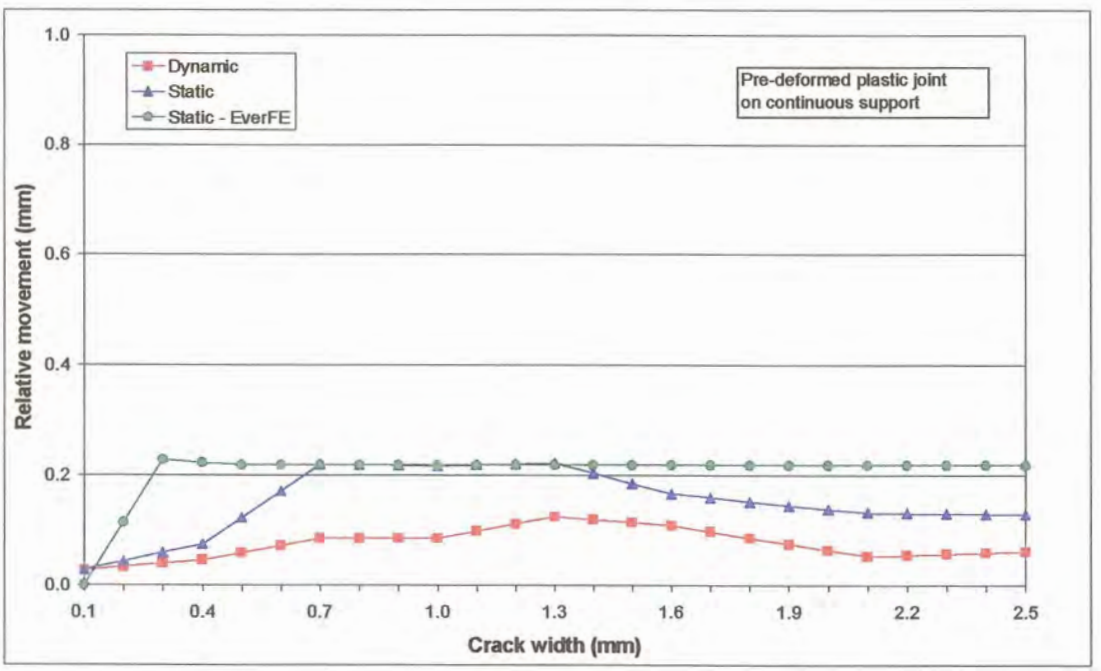

Figure 3.47: RM versus crack width (plastic joint on C rubber subbase)

3.3.4 40 kN static loading on continuous rubber subbase

As before, the steel frame holding the actuators was turned 90 degrees, and a 40 kN static load was applied on the one side of the joint. The results were then compared with the 20 kN static loading results already obtained. The deflections measured for the 20 kN and 40 kN static loading results are shown on Figure 3.48.

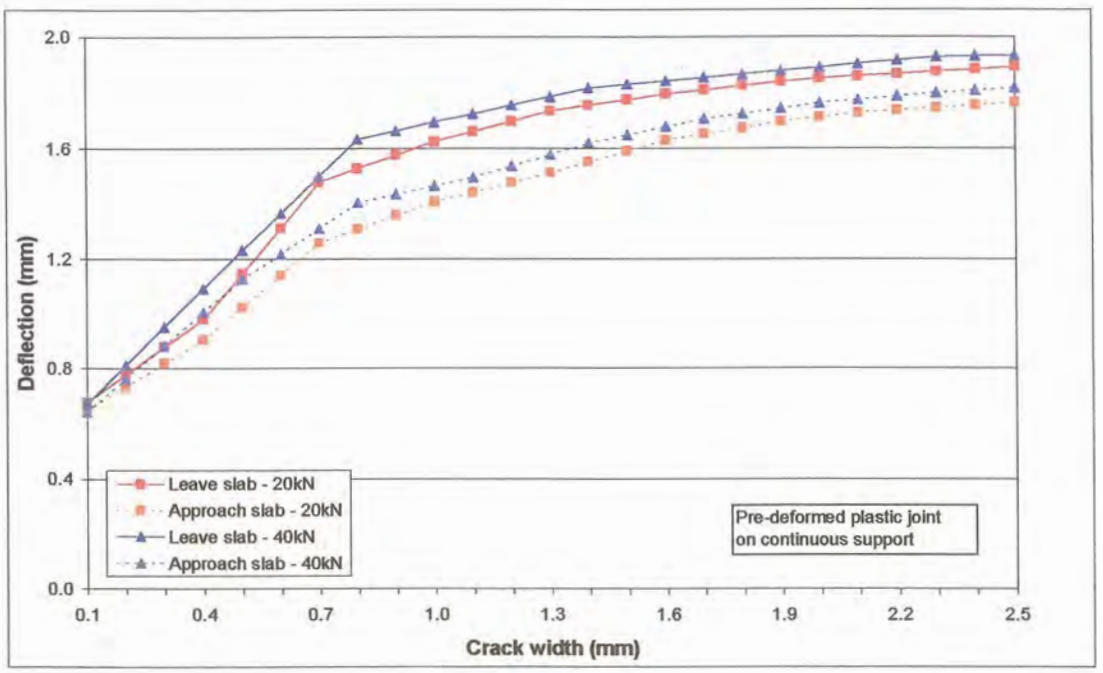

Figure 3.48: Deflection versus crack width for 20 kN and 40 kN static loading (plastic joint on C rubber subbase)

The deflection measurements under both the 20 kN and 40 kN loads gradually increased with increasing crack width. The deflections under the heavier 40 kN load were consistently higher than the deflections under the 20 kN load, with the two data sets running parallel to each other.

The deflection LTE for both the 20 kN and 40 kN static loading results are shown on Figure 3.49. The results were approximately the same, with the LTE under the heavier 40 kN load marginally higher than under the lighter 20 kN load. The theoretical results calculated with EverFE levelled out after a crack width of 0,5 mm, and eventually predicted an efficiency of only 70% of what was measured in the laboratory.

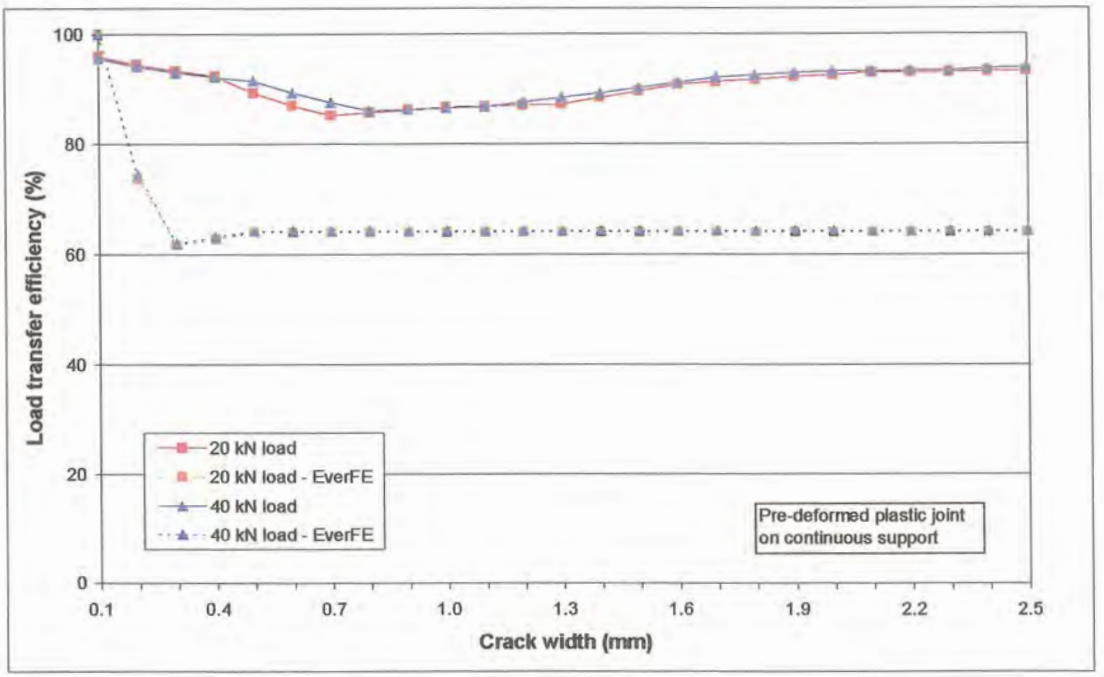

Figure 3.49: Deflection LTE versus crack width for 20 kN and 40 kN static loading (plastic joint on C rubber subbase)

The RM calculated across the joint/crack under the 40 kN load closely resembled the RM calculated under the 20 kN load (see Figure 3.50). In other words, the leave slab re-orientated itself relative to the approach slab, to the same extent under the 40 kN load as under the 20 kN load. As before, the theoretical RMs determined with EverFE are also shown on Figure 3.50. At crack widths from 0,7 mm to 1,4 mm the experimental results and the theoretical results were approximately the same.

3.3.5 20 kN dynamic and static loading - comparison between discontinuous and continuous rubber subbase

By subjecting the same concrete slab to the same set of tests, but with different subbase types, it was possible to quantify the effect of the subbase support on deflection, LTE, and RM at the joint/crack.

Figure 3.51 illustrates the fact that the continuous, rubber subbase accommodated greater deflections at the same crack width than the DC rubber subbase. This was already noticed during analysis of the data obtained from the first four experiments. The deflection results of Experiments 1 and 2 (see Figures 3.5 and 3.13) on the C rubber subbase were approximately 3 times higher than the comparative results of Experiments 3 and 4 (see Figures 3.17 and 3.25).

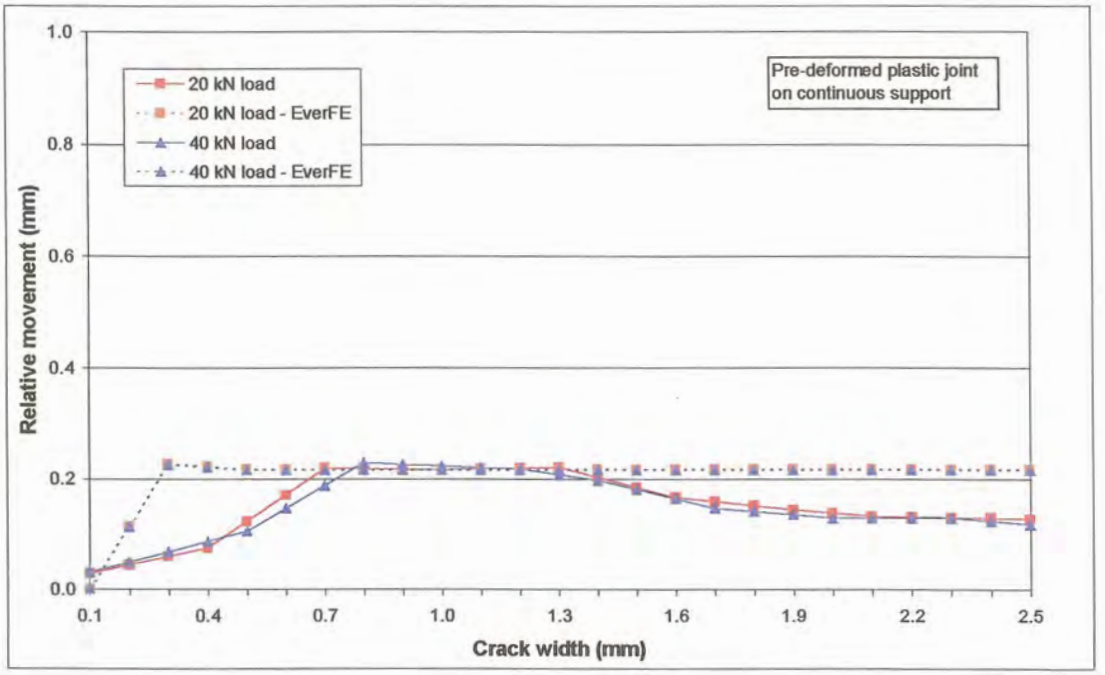

Figure 3.50: RM versus crack width for 20 kN and 40 kN static loading (plastic joint on C rubber subbase)

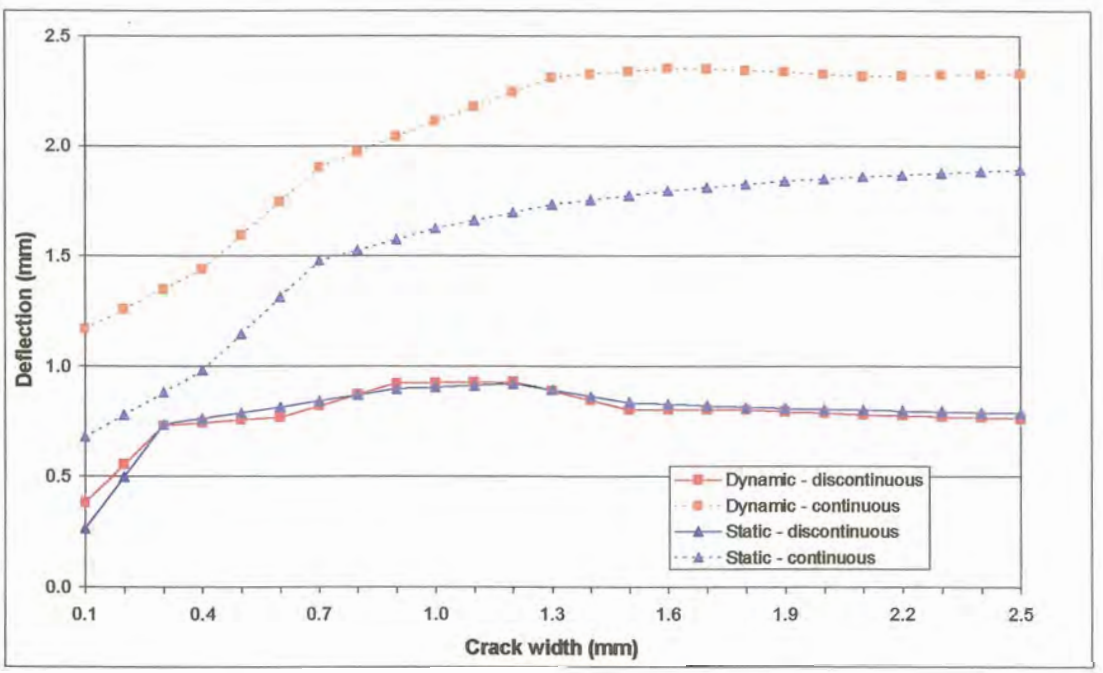

Figure 3.51: Deflection versus crack width – comparison between DC and C rubber subbase (plastic joint)

Despite the higher deflections measured with the C rubber subbase, than with the DC rubber subbase, the LTE was also higher on the C rubber subbase than on the DC rubber subbase. This is illustrated in Figure 3.52.

The C rubber subbase therefore assisted the concrete to have a greater capacity to transfer both horizontal and vertical stresses and strains across the joint/crack. Under dynamic loading the effects of momentum further increased this capacity with the LTE under dynamic loading higher than under static loading in all instances.

The LTE calculated on the DC rubber subbase under dynamic loading was similar to the static loading results from the C rubber subbase. The DC rubber subbase therefore inhibited the transfer of stresses and strains across the joint/crack. This was obvious from the constant decrease in LTE with increasing crack width under static loading. But, on the other hand, the effect of momentum aided the transfer of load across the joint, and therefore the similarity between the above mentioned results.

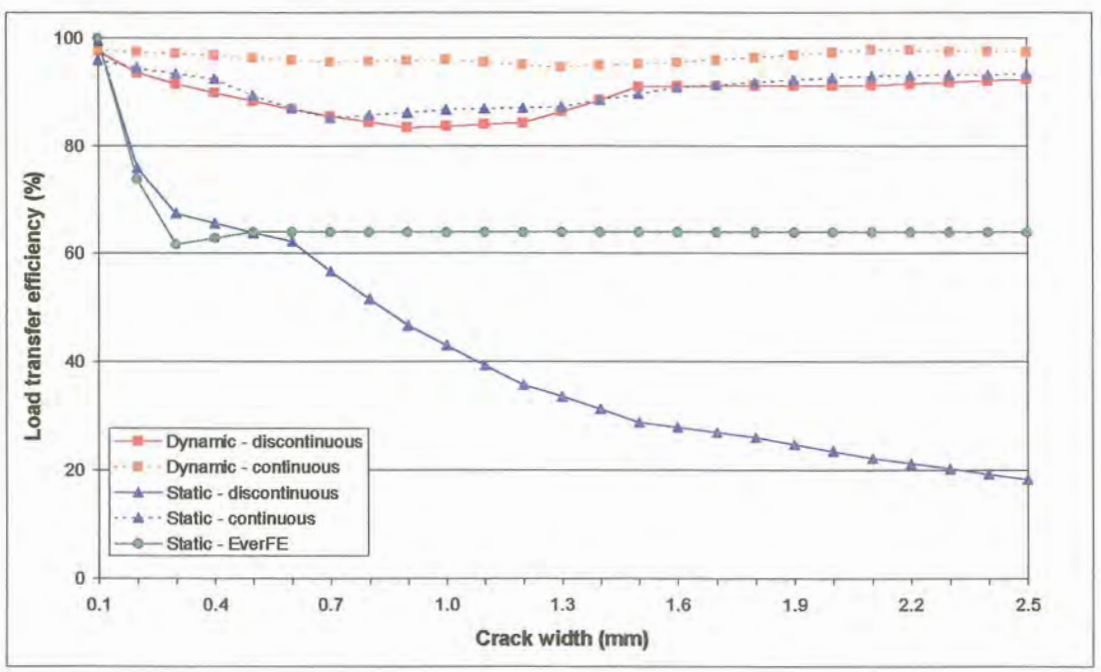

Figure 3.52: Deflection LTE versus crack width – comparison between DC and C rubber subbase (plastic joint)

When comparing the RMs calculated from the deflection results, the dynamic loading results for both subbases tested were remarkably close, as shown on Figure 3.53.

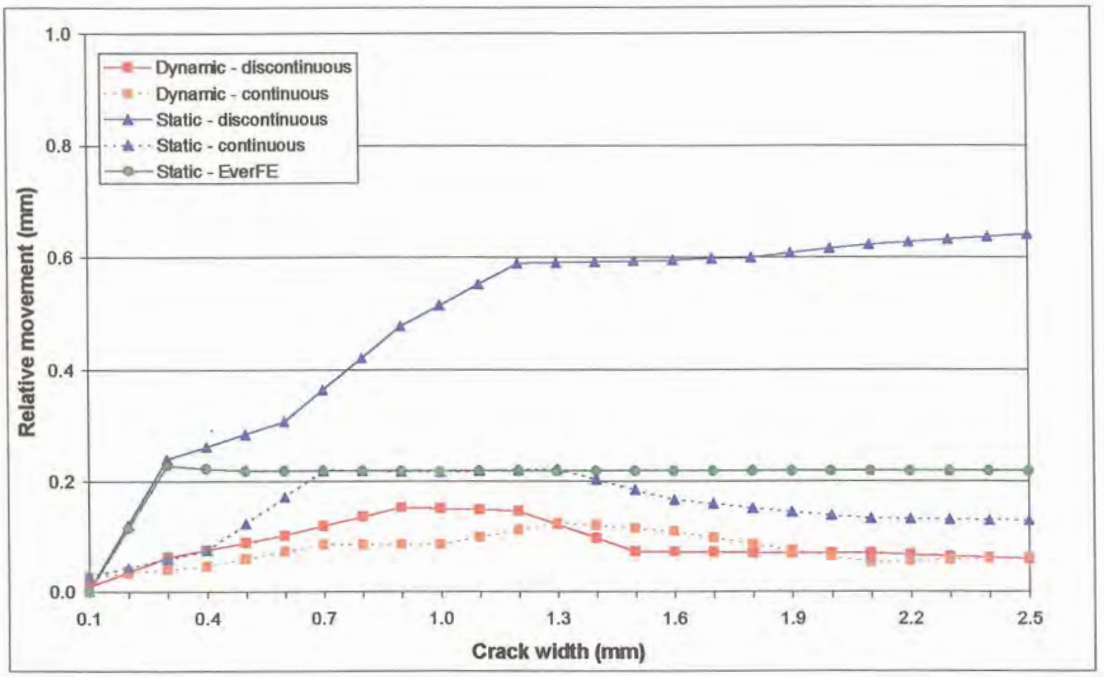

Figure 3.53: RM versus crack width – comparison between DC and C rubber subbase (plastic joint)

Bearing in mind that the smooth plastic joint surface had little interlock capacity, it could be expected that the RMs under static loading would not be similar. Just as the continuous subbase had a greater LTE under static loading than the discontinuous subbase, it therefore had the ability to reduce RM between the two sections of the slab, thereby yielding smaller RMs for the continuous subbase than for the discontinuous subbase.

An important point that needs to be stressed here, is that due to the smooth surface texture of the plastic joint, the static loading results were different, but during analysis of the results obtained for Experiments 1 to 4, the static loading results for the same maximum aggregate size concrete mixes were similar, and could therefore be combined. This could be attributed to the coarseness of the aggregate interlock crack faces. This factor was quantified by conducting volumetric surface texture tests on all relevant samples, as described in Appendix F.

3.3.6 20 kN and 40 kN static loading - comparison between discontinuous and continuous rubber subbase

The application of a 40 kN static load on the one side of the crack has been discussed in paragraphs 3.3.2 and 3.3.4. To facilitate an easier comparison, the data from these experiments has also been combined into single graphs. Figure 3.54 present the deflections measured for the leave slab on both the DC and the C rubber subbases, for 20 kN and 40 kN static loading.

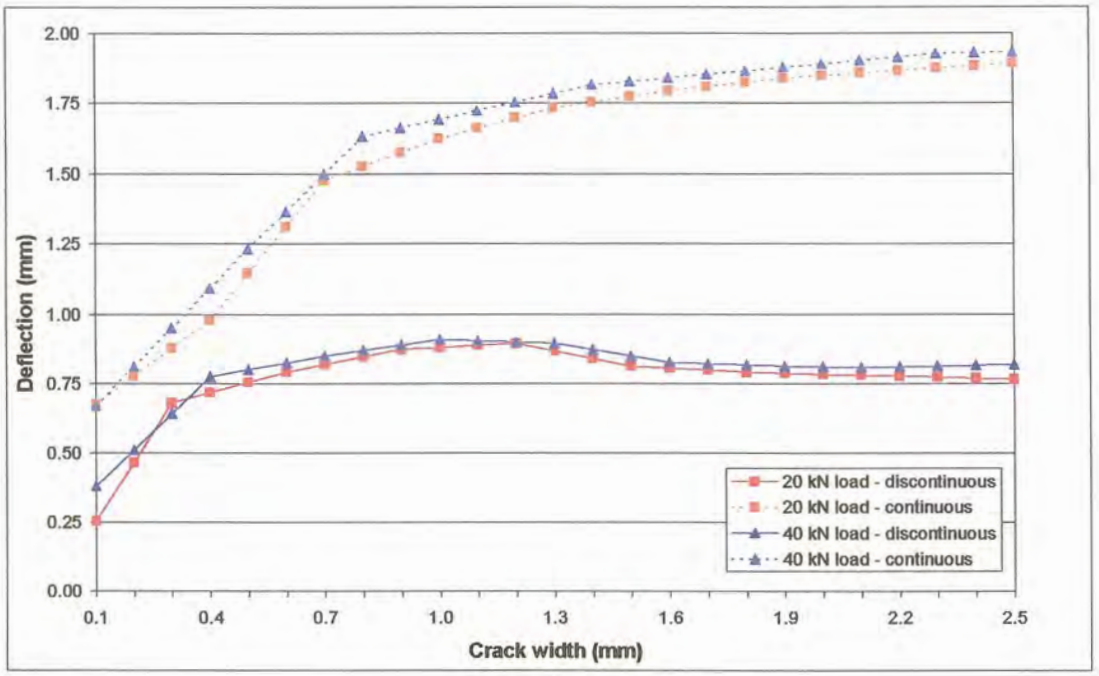

Figure 3.54: Deflection versus crack width – comparison between 20 kN and 40 kN static loading on DC and C rubber subbases (plastic joint)

Although the 20 kN and 40 kN loading results on the distinguishable subbases were similar, the deflections on the C subbase were approximately 2,5 times that of the DC subbase. As before, the C rubber subbase assisted the concrete to have a greater capacity to transfer both horizontal and vertical stresses and strains across the crack.

The combined LTE data is presented in Figure 3.55. As indicated before, the C rubber subbase, although it allowed higher deflections, had a LTE of 5 times that of the DC rubber subbase with the 20 kN static loading and 2,5 times that of the DC rubber subbase for 40 kN loading. As mentioned before, although the heavier load on the DC rubber subbase initially had a lower LTE than the lighter load, it was eventually twice as effective in transferring the load across this particular type of crack and the only case where doubling the load, doubled the LTE at a crack width of 2,5 mm. On the other hand, the LTE on the C rubber subbase for both 20 kN and 40 kN loading was very similar. The implication of this is that the smoother the crack face, combined with a crack reflecting into the subbase, the greater the effect or influence of the magnitude of the load. The opposite has however also been shown here and that is that although the crack face was smooth, the C (sound) rubber subbase supported the two parts of the slab to such an extent that the magnitude of the load did not have a large influence. The LTE calculated with EverFE did not resemble either of the two subbase conditions tested.

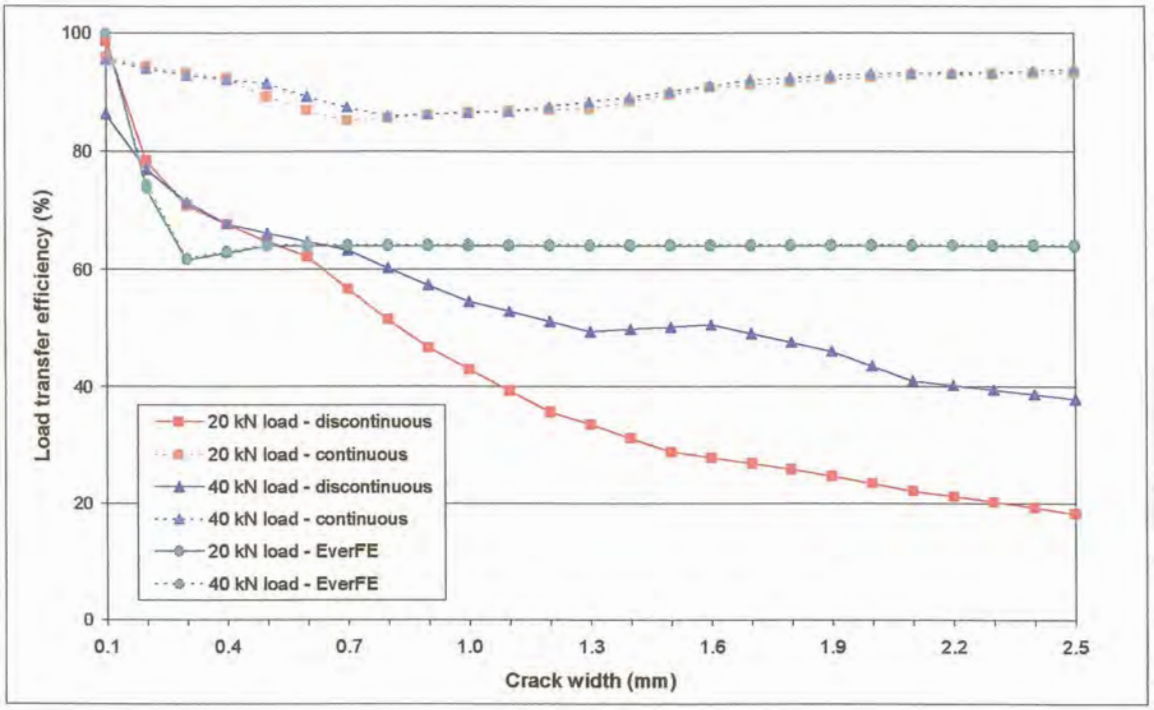

Figure 3.55: Deflection LTE versus crack width - comparison between 20 kN and 40 kN static loading on DC and C rubber subbases (plastic joint)

The RM data is presented in Figure 3.56. On the DC rubber subbase, the RMs under both 20 kN and 40 kN static loading seem to be still on the increase at a crack width of 2,5 mm, whereas the EverFE results already levelled out after a crack width of 0,3 mm. The RM calculated across the joint/crack on the C rubber subbase under the 40 kN load closely resembled the RM calculated under the 20 kN load (see Figure 3.56). In other words, the leave slab re-orientated itself relative to the approach slab, to the same extent under the 40 kN load as under the 20 kN load. The theoretical RMs determined with EverFE are also shown on Figure 3.56. At crack widths from 0,7 mm to 1,4 mm the experimental results and the theoretical results were approximately the same. The rounded shape of the "bubbles" in the plastic sheet can be considered as a closer representation of Walraven's (1981) model where the aggregate is modelled as spherical in shape and therefore the similarity between the laboratory and EverFE results over this range of crack widths.

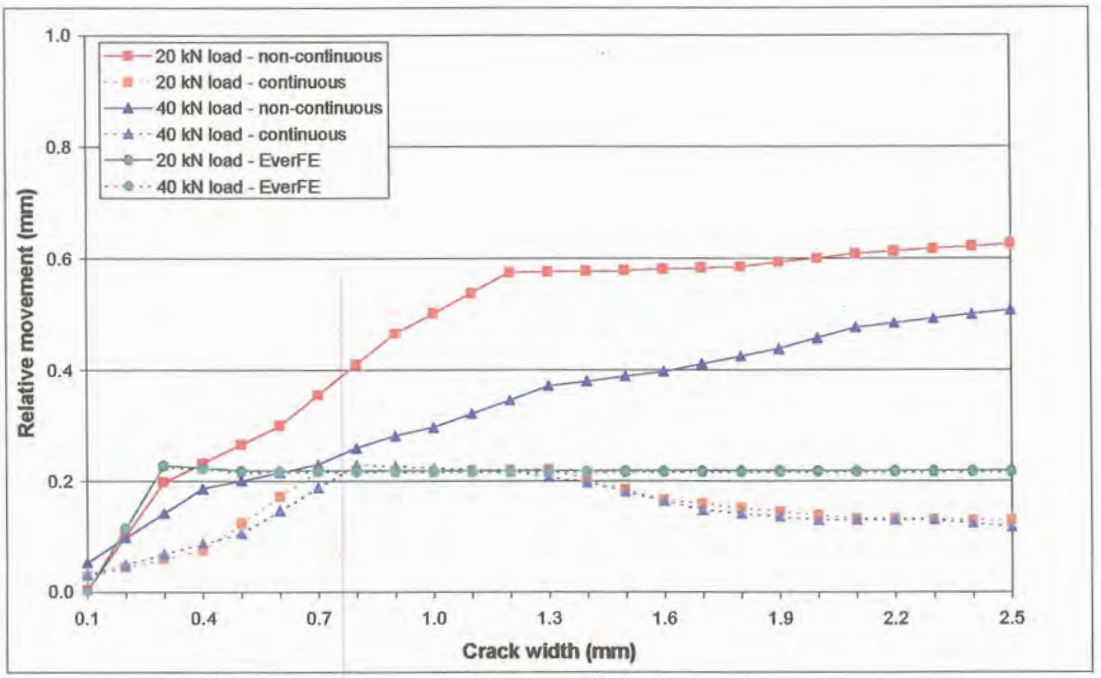

Figure 3.56: RM versus crack width - comparison between 20 kN and 40 kN static loading on DC and C rubber subbases (plastic joint)

3.4 FIELD INVESTIGATIONS

3.4.1 Introduction

Four existing southern African jointed concrete pavements (JCPs) were chosen at random for comparison of field investigation results. These pavements varied in condition from a pavement in a terminally failed condition, in service for more than 30 years, to a pavement in a good condition of which the concrete overlay has been in service for approximately 14 years. Three of the pavements had concrete shoulders, and one had asphalt shoulders. Each of the concrete pavement sections is described in terms of existing pavement design, field investigations conducted, and a structural evaluation with remaining life (RM) predictions. The data presented here has been published in design reports and were analysed by different individuals through various methods and techniques to calculate the RM for each.

The four concrete pavement sections will be discussed under the following headings:

a) Road Section 1 - concrete pavement with concrete shoulders, situated in a moderate climatic region, in a terminal condition

b) Road Section 2 - concrete overlay (on asphalt) with concrete shoulders, situated in a wet climatic region, in a good condition

c) Road Section 3 - concrete pavement with asphalt shoulders, situated in a wet to moderate climatic region, in a fair condition

d) Road Section 4 - concrete pavement with concrete shoulders, situated in a moderate climatic region, in a good condition

In the context of this study, a pavement in a terminal condition will be expected to show extensive slab cracking, both transverse and longitudinal cracks, with edge breaks, and large relative movements (RMs) with low load transfer efficiency (LTE) at joints. The effect of this will be that the pavement will have a poor riding quality. On the other hand, a pavement in a good condition typically has a sound appearance with little slab cracking and edge breaks, and low deflections with high LTE at joints. The latter pavement will also have a good riding quality.

The following paragraphs present a summary of the data from four in-service pavements. In the following chapter (Chapter 4), the data is compared by analysing the RMs measured, calculating the joint shear stiffness from the LTE results, and conducting CncRisk analyses.

3.4.2 Road Section 1

3.4.2.1 Existing pavement design

Road Section 1 is situated in a moderate climatic region (5 > N > 2; Weinert, 1964) in the South African province of Mpumalanga. Mechanical weathering could therefore be expected as the main mode of deterioration of the in situ and pavement materials under the prevailing environmental conditions. The design of the pavement, originally constructed in 1972, is given in Table 3.3.

Table 3.3: Existing pavement of Road Section 1

Layer	Thickness (mm)	Description	CBR values	
			Range	Average
Surfacing	200	Jointed Portland cement concrete	-	-
Subbase	150	Cement stabilised natural gravel	19 – 265	95
Selected	150	Natural gravel	10 – 160	30
Subgrade or fill	Varying	In situ or natural gravel	2 – 400	85

Since construction the pavement has undergone two cycles of heavy rehabilitation involving extensive crack and joint sealing and repair work to the concrete surfacing. The first cycle was during 1985, and the second during 1999. In total approximately 10% of the concrete blocks were replaced during these rehabilitation actions.

3.4.2.2 Field investigations

Field investigations consisted of visual surveys to determine typical distress types. Falling Weight Deflectometer (FWD) testing was conducted to obtain maximum deflection, deflection bowl characteristics, and RM at joints. Elastic modulus values for the layers beneath the concrete were derived from Dynamic Cone Penetrometer (DCP) testing, and cores drilled in the concrete pavement provided slab thickness, the depth of the void between the slab and subbase, and the condition of the surfacing of the subbase. Cores were also tested in the laboratory to obtain the compressive strength of the concrete.

Measured in terms of 5 block units (= 22,5 m road length) of distress, the extent of structural cracks were 32%, pumping 1,2%, and faulting (> 4 mm) 8,4%. The extent of small, medium and large repairs were 32,3%, 12,6%, and 3,5%, respectively.

The average mid-slab deflection under 40 kN load was 0,114 mm and values ranged from 0,071 to 0,247 mm for the eastbound lane. For the westbound lane the average value was 0,116 mm with a range from 0,074 to 0,189 mm. The average RMs at joints on the eastbound lane were 0,10 mm, compared to 0,07 mm for the westbound lane. The eastbound lane also had a higher average joint deflection of 0,27 mm, versus 0,22 mm for the westbound lane.

Compressive strengths obtained from the cores drilled at positions between joints where the concrete was considered to be undamaged ranged from 32,5 MPa to 40,5 MPa with an average of 37,0 MPa. Slab thicknesses determined from cores drilled at joints ranged from 185 mm to 215 mm with an average of 198,3 mm.

Measurements of voids between the concrete slab and the subbase ranged from 0 mm to 20 mm. No voids were found where cores were drilled in the middle of slabs between joints, but voids occurred at joints where the voids were generally bigger on the approach side of the joint as compared to the leave side. The actual crack widths could not be determined on site due to the failed condition of the concrete at the joints, and the fact that sound cores could not be retrieved.

Observations made during field investigations included the following:

a) Signs of pumping were only observed where the subbase appeared to be in a sound, un-cracked condition, due to abrasion of the subbase material
b) Deflections were significantly higher where voids could be detected beneath the slab. This is logical, as the bigger the void, the larger the space that can be taken up during deflection testing.
c) Muddy material could be detected on top of the subbase under the leave slab, whereas the surface of the subbase under the approach slab was clean where faulting was found. This can

be attributed to the mechanism of pumping, and the formation of voids beneath the approach slabs in the concrete overlay. When a vehicle approaches a transverse joint in the concrete pavement moisture and loose particles inside and beneath the joint position get pushed forward, and accumulate beneath the approach slab. As soon as the vehicle then moves across the joint, the loose particles and moisture are ejected back in the direction opposite to the direction of vehicle movement, as well as up through the joint. This results in a gap beneath the approach slab, and the build-up of muddy material beneath the leave slab, thereby the faulting (Barksdale, 1991).

d) Faulting occurred more frequently where traffic moved at lower speeds against steep uphill gradients. The mechanism that creates faulting is similar to that of pumping, but in this instance the material projected back from the approach slab during dynamic loading, gets compacted beneath the leave slab, causing the leave slab to lift up relative to the approach slab.

e) Faulting also occurred where no gaps existed between subbase and slab. In these cases, a crack also occurred in the subbase directly below the joint as the layer below the subbase deformed due to a low elastic modulus (measured with the DCP).

f) The crack/joint faces were in a deteriorated condition with abrasion of both the concrete and the aggregate due to repeated RMs at the joint face. Stress cracking through the aggregate as well as rounding of the aggregate through this abrasion also occurred. The fact that stress cracking occurred through the aggregate indicates that although individual aggregates may have had weak planes, the crack formed in mature, hardened concrete where the cement paste has already hardened around the aggregate. In the present study, the crack was forced to form within 24 hours after casting the slabs, to make certain that cracking took place around aggregate particles and thereby ensuring the coarsest possible crack face. The rounding of the aggregates through abrasion could be attributed to the fact that Road Section 1 has already been exposed to environmental influences and traffic loading for more than 30 years and that it has taken far more than the 2 million load cycles initially applied in the laboratory.

3.4.2.3 Structural evaluation and remaining life

Mechanistic models of the pavement were developed from field data and testing conducted at selected positions, representing the conditions encountered along the entire road section. Table 3.4 shows models from these typical positions where the pavement was investigated in detail.

Table 3.4: Detailed modelling of the pavement structure

Position		Westbound (km)			Eastbound (km)		
		1,59	**38,6**	**33,8**	**35,1**	**38,4**	**5,2**
Slab thickness (mm)*		215/213	200/202	200/197	187/200	190/190	185/195
Back-calculated Elastic modulus (MPa)	Slab	35 000	37 000	37 000	30 000	37 000	31 000
	Subbase	1700/750	500/450	350/120	200/70	700/700	100/400
	Selected	160	75	125	80	60	90
	Subgrade	300	75	250	95	80	30
40 kN Deflection (mm)*		0,12/0,29	0,18/0,28	0,19/0,33	0,27/0,38	0,21/0,26	0,27/0,34
RM (mm)*		-/0,26	-/0,07	-/0,18	-/0,17	-/0,11	-/0,08
LTE (%)		10	75	45	55	58	76
Void length (m)*		-/3,0	-/2,0	-/3,0	-/1,5	1,5/2,5	2,0/2,0
Load transfer constant*		0,2/0,6	0,2/0,4	0,2/0,6	0,2/0,4	0,2/0,3	0,2/0,3
Condition		Pumping	5 mm fault	Fault/crack	5 mm fault	10 mm fault	Crack
*Note: Values given are for mid-slab (internal) and at the joint itself							

Although the average deflections at joints were 0,26 mm to 0,38 mm, localised high deflection values of 0,83 mm and 0,96 mm were also recorded during the deflection survey. Deflections were measured every 200 m along the length of the road section.

It is interesting to note that the subbase stiffness at joints was generally lower than at mid-slab positions. Assuming an initial subbase stiffness modulus of 1 500 MPa (Theyse et al., 1996), the values in Table 3.4 indicate a loss of some 44% in subbase stiffness with time. This was probably due to the ingress of water at the joints.

Using the data from typical sections along Road Section 1 as summarised in Table 3.4, the average deflection (0,25 mm) and movement at joints (0,10 mm) were simulated in the original software (containing Equation (2.12)) developed for the new mechanistic concrete pavement design method (Strauss et al., 2001). It was found that the average RM was between 1,0 and 1,5 million standard 80 kN (E80) axles. This implied that after a further 1,5 million E80's, the risk of failure was 50%. The load transfer constant for the average condition was 0,49 and the length of the void between slab and subbase 1,5 m. A load transfer constant of 0,18 is used for internal loading, 0,6 for a free moving joint (edge loading), and normally a value of 0,35 is applicable for an un-dowelled joint which has been exposed to the environment and traffic for some 15 years.

The reasons for the pavement having been in such a poor condition could be summarised as follows:

a) The pavement was designed for an expected 6 million E80's. At the time of investigation the axle loading was 858 E80's/day westbound and 677 E80's/day eastbound. Projected over a period of 4 years, assuming a traffic growth rate of 3%, this meant 1,3 million E80's westbound and 1,1 million E80's eastbound. An average RM of 1,5 million E80's therefore indicated that the pavement was close to the end of its structural service life.

b) Higher than normal deflections occurred at the joints due to heavy loading and a relatively thin concrete slab.

c) Water that entered through the joints that were not watertight caused erosion of the subbase, resulting in voids between the slab and the subbase.

3.4.3 Road Section 2

3.4.3.1 Existing pavement design

Road Section 2 is situated in a wet climatic region (N < 2; Weinert, 1964) in the South African province of Kwazulu-Natal. Chemical weathering of the in situ and pavement materials could therefore be expected as the main mode of deterioration caused by the environment. The asphalt pavement, originally constructed in 1970, was rehabilitated in 1987 by a jointed concrete overlay. No rehabilitation actions, apart from minor resealing of joints have been recorded since 1987. The pavement structure is summarised in Table 3.5 (N3 HS1 PD, 1999).

Test pit investigations confirmed the thickness and quality of the asphalt layer and the crushed stone base. However, no sign of stabilisation of the original subbase could be found, probably due to carbonation action. From a depth of 750 mm and deeper, the pavement is underlain by a mixture of silty and sandy clay of poor quality, less than a G10 Class material (Draft TRH14, 1985).

Table 3.5: Existing pavement of Road Section 2

Layer	Thickness (mm)	Description (year constructed)	CBR values	
			Range	Average
Surfacing	230 80	Jointed Portland cement concrete (1987) Gap-graded asphalt (1970)	-	-
Base	200	Crushed stone (1970)		
Subbase	150	Cement stabilised natural gravel (1970)	-	-
Selected	250	Natural gravel (1970)	14 – 44	32

3.4.3.2 Field investigations

Field investigations included an extensive visual survey, coring the concrete at selected positions, and determining the deflection at joints and mid-slab, as well as RMs at joints with a FWD, as summarised in Table 3.6. The statistics given in Table 3.6 indicate the average, minimum and maximum of the deflection, RM, and the calculated LTE results. The maximum RM, for example, therefore does not necessarily correlate with the maximum LTE. The functional condition of the pavement was determined with an Automatic Road Analyser (ARAN) vehicle.

Table 3.6: Summary of FWD test results on Road Section 2

Direction	Statistics	40 kN Deflection (mm)		RM at joint (mm)	LTE (%)
		Mid-slab	Joint		
Northbound	**Average**	0,083	0,109	0,018	74
	Minimum	0,044	0,052	0,000	13
	Maximum	0,400	0,332	0,187	100
Southbound	**Average**	0,098	0,093	0,028	78
	Minimum	0,036	0,064	0,002	20
	Maximum	0,805	0,207	0,121	100

From the visual survey, it could be concluded that the pavement structure was generally in a good condition with isolated areas showing distress such as cracking, pumping and spalling. There was only one construction related problem that was identified in the visual survey, namely, double saw-cutting of longitudinal joints at places. The conditions of the crack and joint seals varied from fair to poor which, if not maintained properly will be to the detriment of the joint behaviour.

A core drilled at a position where faulting of approximately 15 mm occurred showed signs of dirt and mud washed into the crack. On the other hand, the majority of cores taken at sawn joints showed little signs of distress with good aggregate interlock load transfer. It was difficult to determine the in situ joint width, as this required specialised drilling techniques.

3.4.3.3 Structural evaluation and remaining life

The FWD test results were analysed with Evercalc to determine the elastic moduli of the existing pavement layers. The RM of the pavement was determined with Kenslabs (Huang, 1993). The results of the modelling are summarised in Table 3.7.

Table 3.7: Modelling of the concrete pavement structure

Direction	Back-calculated elastic modulus (MPa)			RM -Kenslabs (years)
	Slab	Subbase	Subgrade	
Northbound	36 700	1 600	180	14
Southbound	37 800	1 650	175	15

The future rehabilitation strategy proposed for this pavement at the time of investigation was to maintain the pavement by replacing joint seals and conducting minor repairs for approximately 14 years. Thereafter minor concrete repairs, and a stress absorbing membrane interlayer (SAMI) combined with a 40 mm asphalt overlay was proposed.

3.4.4 Road Section 3

3.4.4.1 Existing pavement design

The pavement of Road Section 3 was constructed in 1978 as a jointed concrete pavement with asphalt shoulders. This road section is situated in a wet to moderate climatic region (5 > N > 2, Weinert, 1964) in the South African province of Kwazulu-Natal. A combination of both chemical and mechanical weathering of the in situ and pavement materials could therefore be expected as the mode of deterioration caused by the environment. Minor rehabilitation works were carried out during 1991 when the joint sealant was replaced, cracks sealed and distressed areas on the asphalt shoulder repaired by patching with new asphalt. Minor repair works were also carried out on the concrete during 1998 as part of routine maintenance. The existing pavement structure is summarised in Table 3.8 (N3 HS4 PD. 1999).

Test pit investigations in the asphalt shoulders showed that the asphalt layer was approximately 50 mm thick. The pavement as-built data indicated cement stabilised crushed stone subbase layers, but during the test pit investigations it was found that the concrete lies on top of two stabilised decomposed dolerite layers, each approximately 200 mm thick. Below the two stabilised layers the material is a mixture of decomposed dolerite and shale.

Table 3.8: Existing pavement of Road Section 3

Layer	Thickness (mm)	Description	CBR values	
			Range	Average
Surfacing	210	Jointed Portland cement concrete	-	-
Upper subbase	100	Cement stabilised crushed stone	79 – 93	87
Lower subbase	100	Cement stabilised natural gravel	42 – 53	49
Selected	190	Natural gravel	21 – 41	28

3.4.4.2 Field investigations

Visual surveys indicated that the main defects of the pavement were cracked slabs and the poor condition of the flexible shoulders. The predominant forms of distress in the concrete pavement were as follows:

a) Mid-slab longitudinal cracking, due to the settlement of high fills, as well as the relieving of "kick-out" stresses around horizontal curves in the road.
b) Patches co-existing with longitudinal cracks near transverse joints. The patches were a result of maintenance actions to repair spalling and punch-outs at joints.
c) Transverse cracking occurred to a lesser extent than longitudinal cracks, and was more prevalent at the beginning and end of the section due to the formation of "restraint" stresses.
d) Corner cracking was the least pronounced form of cracking suggesting pumping distress with subsequent creation of voids and corner cracks.

The visual appearance of the shoulders varied greatly. Detail recorded included local structural failures, potholes, crocodile cracks, pumping, transverse cracks, block cracks and deformation. During construction of the pavement a no-fines concrete drain (100 mm wide and 210 mm deep) with a drainage pipe at the bottom was constructed between the outer asphalt shoulder and the concrete on both carriageways. This proved an inefficient measure as the drainage pipe itself initially blocked up, the plastic pipe disintegrated, and the area surrounding the pipe and inside the no-fines concrete got saturated with moisture. It could also be reasoned that failure of the drain occurred due to heavy vehicles travelling partly on the shoulder, but this rarely happened, as investigations showed that the automatic delineation of the white concrete travelling lane against the black asphalt shoulder, kept the vehicles on the concrete itself. The end result was a 350 mm wide failed section in the asphalt shoulder adjacent to the concrete, which necessitated the removal of the no-fines drain and failed asphalt section along the entire length of road, and filling up the trench with dense-graded asphalt.

Instrument measurements carried out during field investigations included determining deflections and RM at joints with a FWD, skid resistance with a SCRIM, and riding quality with an Inertial Profilometer. The functional condition of the pavement was determined with an ARAN. FWD testing was also conducted on the asphalt shoulders. The FWD test results for the concrete pavement are summarised in Table 3.9.

Table 3.9: Summary of FWD test results on Road Section 3

Direction	Statistics	40 kN Deflection (mm)		RM at joint (mm)	LTE at joint (%)
		Mid-slab	Joint		
Northbound	Average	0,095	0,216	0,119	52
	Minimum	0,044	0,065	0,001	11
	Maximum	0,453	0,622	0,554	100
Southbound	Average	0,101	0,225	0,126	85
	Minimum	0,024	0,065	0,002	8
	Maximum	0,598	0,680	0,586	100

3.4.4.3 Structural evaluation and remaining life

The concrete pavement and asphalt shoulder FWD test results were analysed separately to determine the elastic moduli of the existing pavement layers, as well as the RM of each. The results of the modelling are summarised in Tables 3.10 and 3.12.

Table 3.10: Detailed modelling of the concrete pavement structure

Location (km – km)	Maximum deflection 90 percentile (mm)	Back-calculated elastic modulus (MPa)		Modulus of subgrade reaction (MPa/m)
		Slab	Subbase	
Northbound carriageway				
12,3 – 17,8	0,065	16 000	2 500	200
18,0 – 21,8	0,087	18 200	1 800	100
22,0 – 27,6	0,072	16 800	830	140
27,8 – 38,0	0,115	15 350	2 000	50
Southbound carriageway				
12,3 – 17,4	0,080	17 500	1 050	110
17,6 – 24,4	0,074	23 750	2 150	155
24,6 – 33,2	0,104	15 900	1 600	115
33,4 – 38,0	0,101	12 550	1 400	155

Table 3.11: Detailed modelling of the asphalt shoulder pavement structure

Pavement Layer	Average 40 kN deflection (mm)	Average thickness (mm)	Back-calculated elastic modulus (MPa) Average (Range)
Northbound carriageway			
Asphalt surfacing	0,194	50	4 450 (1 000 – 6 500)
Stabilised base		170	1 800 (300 – 4 500)
Stabilised subbase		250	860 (200 – 3 000)
Selected		300	190 (70 – 400)
Subgrade			100 (60 – 160)
Southbound carriageway			
Asphalt surfacing	0,276	50	4 740 (1 500 – 6 150)
Stabilised base		170	1 780 (310 – 4 500)
Stabilised subbase		250	710 (210 – 2 250)
Selected		300	230 (90 – 400)
Subgrade			100 (60 – 160)

The RM of the concrete pavement was determined with Kenslabs (Huang, 1993), a finite element software program that can be used to determine the pavement response under load. The concrete pavement structural capacity was calculated as 7,7 million E80's. The pavement had adequate structural capacity for the estimated traffic loading to last another 6 years, provided that timely maintenance in the form of crack sealing, patching, and replacement of some cracked slabs and poor patches was carried out.

The RM of the shoulders was calculated as 12,5 million E80's in the northbound direction, and 11,9 million E80's in the southbound direction. It was important that the shoulders should also have an adequate RM, as it is part of the maintenance strategy of this specific pavement that, firstly, the entire pavement width be provided with a bitumen rubber single seal, after repairing the no-fines concrete drain, and sealing and repairing the shoulders where necessary. This single seal will then act as a SAMI for the asphalt overlay to be constructed after 6 year's time.

3.4.5 Road Section 4

3.4.5.1 Existing pavement design

Road Section 4 is situated in a moderate climatic region (N > 5; Weinert, 1964), in the South African province of Kwazulu-Natal. Mechanical weathering of the in situ and pavement materials could therefore be expected as the main mode of deterioration caused by the environment. The pavement was constructed in 1988 as a jointed concrete pavement with concrete shoulders. Due to sideways

slipping/settlement of the subgrade across high fills stitching repairs had to be done on longitudinal cracks and longitudinal joints in 1988/1989 already. Apart from that, no major rehabilitation works have been carried out on this pavement since construction. Minor repair works were carried out during 1998 during maintenance activities. The structure of the existing pavement is summarised in Table 3.12 (N3 HS5 PD, 1999).

Table 3.12: Existing pavement structure of Road Section 4

Layer	Thickness (mm)	Description	CBR values	
			Range	Average
Surfacing	210	Jointed Portland cement concrete	-	-
Subbase	100	Cement stabilised crushed stone	-	-
Selected	300	Natural gravel. Top 150 mm lime modified	15 – 18	17

3.4.5.2 Field investigations

From the visual survey, it was concluded that the pavement was generally in a good condition with isolated instances of cracking, pumping and spalling. The condition of the crack and joint sealants varied from fair to poor. Settlement of the subgrade occurred in a few areas (N3 HS5 PrD, 2001).

Construction-related distresses were encountered on the pavement, which necessitated the stitching repair done on the longitudinal cracks and joints during 1988/1989. This was necessary because in some places the tie-bars were not placed beneath the position where the longitudinal joint had to be cut, but next to it. The tie-bars could therefore not perform the function it was meant to. These stitching repairs kept longitudinal cracks from propagating at certain places, but were less successful in other places, especially over high fills. It was found that due to a scarcity of good construction material during construction, materials of poor quality were used in the middle of the fill. Although a shield of better quality material protected these materials some settlement did take place.

The visual distresses on this road could be grouped into six categories, as follows:

a) Widening of longitudinal joints.
b) Corner breaks next to stitches where the stitch over-stressed the concrete, or where the stitch was too close to a transverse joint.
c) Localised settlement of the subgrade over short sections of road at a few locations.
d) Problems related to poor subsoil drainage in some cuts.
e) Transverse and longitudinal cracks occurred randomly, and were considered to be traffic related.

f) Fine shrinkage-related cracks at two bridge (underpass) sites. This was not considered a matter of great concern.

Instrument measurements carried out during field investigations included determining skid resistance using the SCRIM apparatus, determining the functional condition of the pavement using the ARAN, and determining deflections and RMs at joints with FWD testing.

Poor deflection and riding quality results were obtained. Low LTE across joints was attributed to a loss of aggregate interlock. The deflection and RM results at mid-slabs and at joints are summarised in Table 3.13.

Table 3.13: Summary of FWD test results for Road Section 4

Section	Direction	Statistics	40 kN Deflection parameters			
			Deflection (mm)		RM at joint (mm)	LTE at joint (%)
			Mid-slab	Joint		
N3/5 km 38-54	Northbound	Average	0,039	0,071	0,030	84
		Minimum	0,018	0,024	0,000	2
		Maximum	0,068	0,386	0,454	100
	Southbound	Average	0,047	0,068	0,018	83
		Minimum	0,021	0,026	0,002	24
		Maximum	0,163	0,183	0,146	100
N3/6 km 0-29	Northbound	Average	0,044	0,181	0,181	19
		Minimum	0,019	0,050	0,010	1
		Maximum	0,091	0,486	0,537	85
	Southbound	Average	0,044	0,117	0,107	27
		Minimum	0,021	0,043	0,008	2
		Maximum	0,163	0,331	0,341	96
N3/6 km 29-36	Northbound	Average	0,067	0,177	0,159	28
		Minimum	0,028	0,057	0,002	5
		Maximum	0,169	0,451	0,490	100
	Southbound	Average	0,115	0,329	0,256	43
		Minimum	0,025	0,042	0,000	1
		Maximum	0,358	0,975	1,052	100

3.4.5.3 Structural evaluation and remaining life

The FWD test results were analysed using Evercalc back-calculation software to estimate the elastic stiffness values of the various layers of the existing pavement. The RM was also determined with Kenslabs (Huang, 1993), as for the previous section. The stiffness moduli determined for the concrete pavement ranged from 27 700 MPa to 53 000 MPa, and for the subgrade from 185 MPa to 320 MPa.

The concrete pavement structural capacity was calculated as 36 million E80's. The pavement had adequate structural capacity for the estimated traffic loading to last another 20 years, provided that timely maintenance in the form of crack sealing, patching, and replacement of some cracked slabs and poor patches was carried out.

3.5 CONCLUSIONS

The conclusions reached so far from the laboratory studies are as follows:

a) There was no significant deterioration or abrasion of the crack up to 2 million dynamic load cycles at the initial crack width, which indicated that the two sections of the slab were still so tightly knit together that little vertical sliding could take place. As there was little movement of the two parts of the slab relative to each other, fatigue or abrasion of the aggregates at the joint face did not play a role. On the other hand, the horizontal displacement movement did increase during dynamic loading. The fact that the deflections (vertical movement) did not increase can therefore be attributed to the high quality of the crushed stone used in South Africa.

b) An increase in crack width caused an increase in deflection.

c) The larger 37,5 mm aggregate had lower deflections than the smaller 19 mm aggregate at the same crack widths during dynamic and static loading.

d) Moment and inertia in the slab contributed to the greater LTE under dynamic loading, than under static loading.

e) Beyond a crack width of 2,5 mm the data for the 19 mm coarse aggregate tended to remain constant, and it was therefore not considered necessary to test at crack widths greater than 2,5 mm. It was also specifically stated in previous research studies (Davids et al., 1998b; Jensen, 2001) that at crack widths greater than 2,5 mm the stiffness of the subbase starts to play a role in levelling out the measured response of the slabs. However, this study has shown that the smoother the texture of the crack face, the sooner the system would rely on the support of the subbase to transfer stresses and strains from one slab to another. This study has indicated three such transition zones, namely: 1,5 mm for the smooth joint, 2,5 mm for the 19 mm aggregate interlock joint, and between 3,5 mm and 4,0 mm for the 37,5 mm aggregate interlock joint.

f) At small crack widths (< 0,5 mm) the bottom crack displacement measurements tended to be higher than the top crack displacement measurements. The slab tended to bend through with the top of the crack closing, and the bottom of the crack opening during loading. This was more evident during dynamic loading than during static loading, due to the effects of momentum.

g) At crack widths greater than 0,5 mm the top crack displacement became larger than the bottom crack displacement, indicating that the two parts of the slab were being pushed apart during loading. This demonstrated why large crack widths are so detrimental to pavement

performance, as the opening up of the crack at the top during loading, makes it so much easier for debris and loose particles to be driven into the cracks, which in turn cause spalling of the concrete at the crack face. Once again the effect was greater during dynamic than static loading.

h) The deflection LTE was greater during dynamic than static loading in all instances. Larger maximum sized aggregates had greater deflection load transfer efficiencies than smaller maximum sized aggregates.

i) For the same coarse aggregate size concrete mixes, the LTE was larger where there was a continuous rubber support (rubber not cut through) than where there was a crack simulated into the subbase (top rubber layer cut through).

j) Due to the effects of momentum forces acting across the crack, the LTE under 40 kN static loading was higher than under 20 kN static loading.

k) Also due to the effects of momentum acting across the joint, the LTE under dynamic loading of a plastic joint remained remarkably high (92% at a crack width of 2,5 mm), compared to the gradual decrease in LTE with increasing crack width under static loading (18% at a crack width of 2,5 mm).

l) Although the deflections were similar, the load transfer efficiencies achieved using South African crushed stone were significantly higher when compared to published results. The 19 mm dolomite aggregate rendered greater load transfer efficiencies than a 50 mm glacial gravel blend commonly used in the USA.

m) The joint shear stiffness (*AGG*) under dynamic loading was approximately 1,5 times that of the *AGG* under static loading on the continuous rubber subbase, and approximately 3 times higher on the discontinuous rubber subbase.

n) The range of shear stiffness per unit length of crack face that could typically be expected from South African aggregates under static loading has been established.

o) Logistic regression equations were fitted to the data in terms of relative movement (y) versus crack width (x) for both 19 mm and 37,5 mm, maximum sized aggregate. These functions apply to the relative movement induced at a joint/crack by each wheel of an 80 kN dual wheel truck axle crossing the joint/crack.

The laboratory and the field data are analysed in more detail in the next chapter (Chapter 4).

CHAPTER 4: ANALYSIS AND MODELLING

TABLE OF CONTENTS

LIST OF TABLES

LIST OF FIGURES

LIST OF SYMBOLS / ABBREVIATIONS

C	Continuous
DC	Discontinuous
LTE	Load transfer efficiency
RM	Relative movement
VST	Volumetric surface texture
VSTR	Volumetric surface texture ratio

4 ANALYSIS AND MODELLING

4.1 INTRODUCTION

Following on Chapter 3 in which the laboratory and the field data were discussed in detail, this chapter further summarises the results and points the way to specific applications of the results from this research project. The application of the aggregate interlock equation developed as the primary objective of this thesis is described in Chapter 5.

4.2 DISCUSSION OF LABORATORY RESULTS

4.2.1 Deflection

An increase in crack width caused an increase in deflection. For Experiments 1 and 2, the repeated dynamic loads caused the slab to stay in a deflected state with deflections higher than under static loading at small crack widths. The dynamic loading line crossed the static loading line at a crack width of between 1,0 and 1,1 mm. At this crack width the two slabs started to react independent of each other, resulting in higher deflections under static loading than dynamic loading (see also Figures 3.5 and 3.13). The larger 37,5 mm aggregate had lower deflections than the smaller 19 mm aggregate at the same crack widths during dynamic and static loading at crack widths larger than 1,1 mm. This confirmed the greater resistance to deflection movement of the larger aggregate.

The deflections measured during Experiments 3 and 4 were lower than for Experiments 1 and 2. Furthermore, contrary to the situation where the dynamic and static loading lines crossed at a crack width of between 1,0 and 1,1 mm during Experiments 1 and 2, the dynamic loading line was constantly higher than the static loading line during Experiments 3 and 4.

The deflection results of Experiments 1 and 2 (see Figures 3.5 and 3.13) on the C rubber subbase were approximately 3 times higher than the comparative results of Experiments 3 and 4 (see Figures 3.17 and 3.25). This difference in deflection results was primarily due to the C rubber subbase that allowed larger shear forces to be transferred from the leave slab to the approach slab than the DC rubber subbase.

The results from Experiments 3 and 4 corresponded better with published results (Jensen, 2001). Jensen (2001) compared the response of 25 mm limestone, 25 mm glacial gravel, and a 50 mm glacial gravel blend under 40 kN static loading. The deflections obtained by Jensen (2001), especially for 25 mm limestone, corresponded well with the 40 kN results obtained for 19 mm dolomite in Experiment 3 (see Figure 3.22).

It is the opinion of the author that the response of the plastic joint was that measured up to a crack width of 1,5 mm, and that specifically the results under dynamic loading thereafter were influenced by the subbase stiffness. This would imply that the smoother the texture of the crack face, the sooner the system would rely on the support of the subbase to transfer stresses and strains from one slab to another. This study has already indicated three such transition zones, namely: 1,5 mm for the smooth joint, 2,5 mm for the 19 mm aggregate interlock joint, and between 3,5 mm and 4,0 mm for the 37,5 mm aggregate interlock joint.

EverFE (Davids et al., 1998a) was used to perform theoretical analyses. Up to a crack width of 0,5 mm EverFE predicted initial deflection values similar to what was measured in the laboratory. However, at crack widths larger than 0,5 mm there was a smaller increase in deflection with increasing crack width. The results seemed to reach an asymptote and were eventually far less than those measured during execution of Experiments 1 and 2, but slightly higher than the results of Experiments 3 and 4. The main reason for the difference in results could be attributed to the foundation model used in the EverFE software, as described in paragraph 3.2.1 in Chapter 3.

4.2.2 Horizontal crack displacement

The main function of the clip gauges at the top and bottom of both sides of the crack was to control the crack width during opening and closing of the two parts of the slab for deflection testing at different crack widths. Analysis of the data rendered interesting information regarding the opening-closing movements across the crack.

The magnitude of the horizontal crack displacement measurements were both influenced by the methods applied to open and close the slab, as well as by the type of subbase beneath the slab. The C rubber subbase allowed far greater movement than the DC rubber subbase.

At small crack widths (< 0,5 mm) the bottom crack displacement measurements tended to be higher than the top crack displacement measurements (Figures 3.18, 3.19, 3.44 and 3.45). In other words, the slab tended to bend through with the top of the crack closing, and the bottom of the crack opening during loading at narrow crack widths.

At crack widths greater than 0,5 mm this was reversed with the top crack displacement becoming larger than the bottom crack displacement, indicating that the crack was being pushed open during loading. The movement at the top of the crack under dynamic loading was approximately twice as much as the movement under static loading, which could be attributed to the effects of momentum. This demonstrated why large crack widths are so detrimental to pavement performance, as the opening up of the crack at the top during loading, makes it easier for debris and loose particles to be driven into the cracks, which in turn cause spalling of the concrete at the crack face.

4.2.3 Load transfer efficiency

The deflection LTE obtained for both dynamic and static loading for the first four experiments at different crack widths was presented graphically on Figures 3.7, 3.14, 3.20, and 3.28.

Firstly, the deflection LTE was greater during dynamic than static loading in all instances. Larger maximum sized aggregates had greater deflection load transfer efficiencies than smaller maximum sized aggregates. For the same maximum aggregate size concrete mixes, the LTE was larger where there was a C subbase support (rubber not cut through) than where there was a crack simulated into the subbase (top rubber layer cut through). The LTE on the C subbase was on average 105% that of the DC subbase, for both dynamic and static loading.

Due to the effect of greater momentum forces acting across the crack, the LTE under 40 kN static loading was slightly higher than under 20 kN static loading.

Demonstration of the contribution of the high quality crushed stone used in manufacturing concrete pavements in Southern Africa is of great importance. The formulae used in the software package, EverFE, are mostly based on experimental results obtained from tests conducted on concrete pavements constructed with the lesser quality aggregates found in the USA. To quantify this statement, the relevant properties of the granite and dolomite used for this research study were compared with those of the limestone and glacial gravel used by Jensen (2001) (see Table 4.1).

The physical properties of the South African aggregates were obtained from the suppliers of the materials, and the properties of the USA aggregates not reported by Jensen (2001) were obtained from the Nordberg Process Machinery Reference Manual (1983).

Table 4.1: Comparison between South African and USA aggregate properties

Aggregate type	Description of test				
	Aggregate crushing value (%)	Relative density (kg/m^3)	Water absorption (%)	Los Angeles abrasion value (%)	Stiffness modulus (GPa)
South Africa					
Granite (19 mm)	25	2,65	0,33	33	27,0
Granite (37,5 mm)	27	2,65	0,33	33	29,0
Dolomite (19 mm)	15	2,86	0,2	21	42,0
Dolomite (37,5 mm)	15	2,86	0,2	21	48,0
USA					
Limestone (25 mm)	18	2,61	0,61	34	22,0
Glacial gravel (50 mm)	30	2,58	-	22	24,0

The crushing value of the limestone was similar to that of the dolomite, and that of the glacial gravel slightly higher than the granite aggregate. The relative densities of the USA aggregates were slightly less than the South African granite, with the water absorption of the limestone twice as high as that of the granite aggregate. The Los Angeles abrasion value of the South African granite aggregate compared well with that of the USA limestone, and the South African dolomite and USA glacial gravel had similar results. The important difference in physical properties lay in the lower stiffness moduli of the USA aggregates, where both the limestone and glacial gravel had lower stiffnesses than the South African granite. As mentioned before, the granite was chosen as representative of the weaker of the concrete construction aggregates crushed in South Africa, and that the stiffness of the aggregate largely contributes to the stiffness of the concrete. This would imply that the concrete constructed with low stiffness aggregates would be less resistant to cracking and abrasion than the concrete constructed with stronger aggregates.

When comparing the results published by Jensen (2001) during a similar study using typical aggregates found in the USA with the results obtained in this study, it was obvious that even though the deflections were similar, the LTE achieved using South African crushed stone were significantly higher. The 50 mm glacial gravel blend, the largest aggregate size used by Jensen (2001), rendered load transfer efficiencies of less than 80% at a crack width of 2,5 mm. On the other hand for the comparatively small 19 mm dolomite aggregate used in this study a LTE of 84% was calculated for the same crack width.

The fact that little abrasion occurred at the crack face during testing inside the laboratory was confirmed by Will Hansen (2003) through follow-up testing conducted on the experimental slabs used in the study of which preliminary results were published during 2001 (Jensen, 2001). This was despite the fact that they used softer aggregates with lower relative densities and stiffness moduli, and also had lower concrete strengths than what was achieved in this study (see Table 4.1).

Another tool that was used to quantify that the South African crushed aggregates are more angular and have a greater aggregate interlock potential than the USA aggregates, was through VST testing (Vandenbossche, 1999) as described in Appendix F. The VSTR results obtained for the 19 mm and 37,5 mm coarse aggregate concrete were 37% and 44%, respectively, higher then the USA results (see Photo G.25). VST has however not been included in the modelling effort, as no South African field data was available to calibrate the laboratory results. Obtaining such field data from the road sections investigated was also not considered viable, as it would have been a too costly exercise.

4.2.4 Relative movement

Some researchers are of the opinion that the generally accepted method of determining the efficiency of a joint in terms of deflection LTE is not necessarily the correct method, as it gives results based on the efficiency of the whole system. In other words, measuring efficiency in terms of LTE not only takes

into account the deflection of the concrete slab, but also the deflection of the subbase and subgrade. On the other hand, it was stated that when analysing the RM measured on top of the concrete, the deflection of the concrete is isolated (Strauss, 2001).

This further led to the assumption that the RM data of similar coarse aggregate concrete mixes should have the same RM results, irrespective of the type of subbase support. The RM measured for both aggregate types at different crack widths for dynamic and static loading, respectively, were approximately the same. Logistic regression equations were therefore fitted to the data in terms of relative movement (y) versus crack width (x) for both 19 mm and 37,5 mm maximum sized aggregate (Equations (3.2) to (3.5)).

These logistic equations were developed from data where a single 20 kN truck wheel load crossed the joint/crack, and it was therefore still necessary to determine the effect of a 40 kN dual wheel load crossing the joint/crack. Equations (3.3) and (3.5) were plotted against the relative movement data obtained during application of the 40 kN static loads at one side of the crack during Experiments 3 and 4 (see Figure 4.1). From this figure it is clear that the curves fitted to the data are basically the same. The 40 kN data for the 19 mm maximum sized aggregate being slightly higher than the plot of Equation (3.3), and the 40 kN data for the 37,5 mm maximum sized aggregate slightly lower than the plot of Equation (3.5). It can therefore be assumed that the relative movement induced at a joint/crack by an 80 kN dual wheel truck axle crossing the joint will be that caused by each 20 kN wheel crossing the joint/crack.

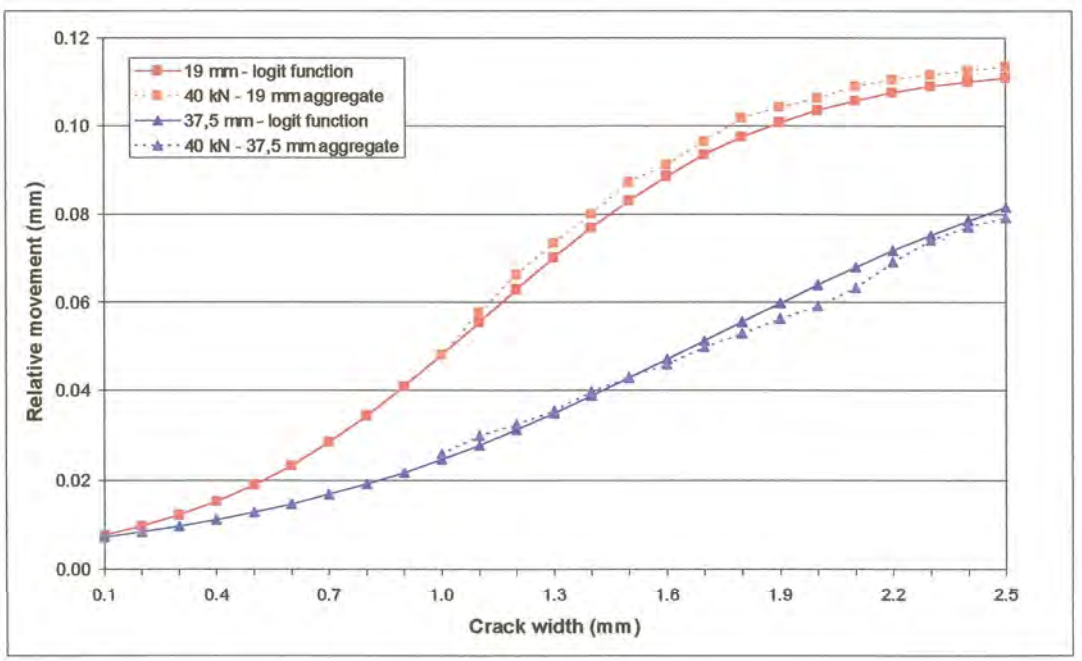

Figure 4.1: Relative movement at joint – 20 kN versus 40 kN static loading for 19 mm and 37,5 mm coarse aggregates

Although the RM results for the same coarse aggregate size mixes were similar, and it was possible to calculate the average RM from different experiments, this approach is not logical. There are three components involved during load transfer at a joint/crack, namely: the portion carried by the slab, the portion carried by the subbase/subgrade, and the portion carried by the load transfer mechanism. These components have to be in equilibrium, and during the measurement of LTE, if one carries more of the imposed load, the others will carry less.

The real contribution from the RM data was the development of a single equation that has already been incorporated in the source code of the CncRisk software, as discussed below.

4.2.5 Aggregate interlock joint/crack shear stiffness

The relationship between deflection LTE and the dimensionless joint stiffness (*AGG/kl*) developed by Ioannides and Korovesis (1990) was used to calculate the shear stiffness per unit length (*AGG*) of the crack faces of the experimental slabs. The LTE calculated from the laboratory deflections, together with Equation B.44 (Appendix B) was used. The values used in the calculation of the shear stiffness are summarised in Table 4.2.

Table 4.2: Input values for calculating shear stiffness (*AGG*) of crack faces

Description	Granite		Dolomite		Plastic joint
	19 mm	37,5 mm	19 mm	37,5 mm	
Poisson's ratio of concrete (μ)	0,15				
Subgrade modulus (k) (MPa/mm)	0,08				
Elastic modulus of concrete (E) (MPa)	21 000	29 000	41 000	48 000	24 000
Concrete slab thickness (h) (mm)	230				
Radius of relative stiffness (l) (mm)	722,4	783,1	853,9	888,2	746,9
Load radius (a) (mm)	95				
Load size ratio (a/l)	0,132	0,121	0,111	0,107	0,127

Figure 4.2 presents the joint shear stiffness calculated by using Equation B.44, the data presented in Table 4.2 and the LTE calculated from the laboratory deflections. For this particular figure only the static loading data has been plotted.

The unusual appearance of the plot for the 19 mm granite aggregate on a C rubber subbase under 20 kN load, shows the sensitivity of the parameter *AGG* to a change in LTE. The LTE for this particular test, presented on Figure 3.7, did not appear to vary that much. The LTE at 0,1 mm crack width was 96,4%,

from there it increased gradually to a maximum of 97,8% at a crack width of 0,5 mm. Although the difference in LTE was only 1,4%, the difference in *AGG* was more than 3 700 MPa.

The *AGG* values calculated for crack widths of 0,1 mm to 0,4 mm for the 37,5 mm granite aggregate are not shown on the graph, as the *AGG* increases rapidly the closer the LTE gets to a 100%. This is the region where the LTE approximates the upper asymptote, as shown on Figure 2.19. For a LTE of 99,2 % the *AGG* was calculated as 30 284 MPa.

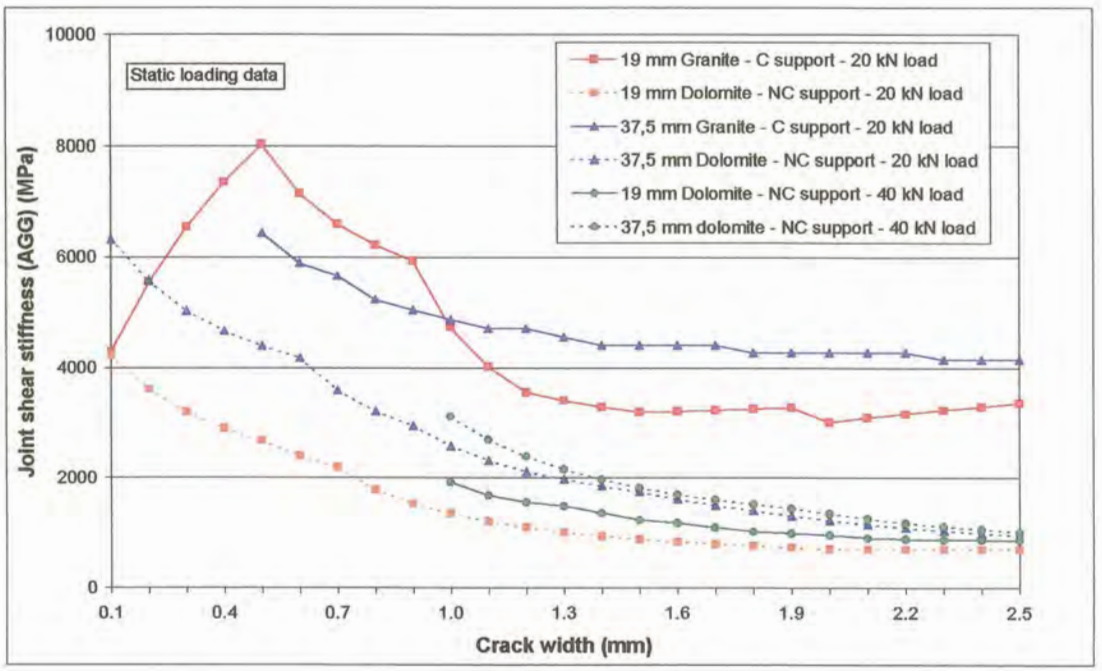

Figure 4.2: Joint shear stiffness versus crack width for static loading LTE results of aggregate interlock experiments

Generally the trends in the data were logical, with the 37,5 mm coarse aggregate having higher joint shear stiffnesses than the 19 mm coarse aggregate for the same subbase support and loading conditions. The 40 kN loading results were also higher than the 20 kN loading results, indicating that the heavier "action" required a greater "reaction" to resist it.

Figure 4.3 presents the joint shear stiffness values calculated for the static loading LTE of the plastic joint under both 20 kN and 40 kN loading.

Figure 4.3 further illustrates the influence of the subbase support on the behaviour of the joint. The C rubber subbase supported the slab to such an extent that initial shear stiffness results similar to that of the 19 mm coarse aggregate were calculated. Due to the smoothness of the plastic joint face the *AGG*, however, decreased quickly to a crack width of 0,7 mm where after it gradually increased again. As has been mentioned before, the response of the plastic joint, itself, were the results measured up to a

crack width of 1,5 mm, where after the response of the subbase was measured. It is also suspected that during this particular experiment the C rubber was pulled tight during crack opening, which explains the increase in LTE noticed earlier, as well as the increase in shear stiffness, at crack widths larger than 1,5 mm.

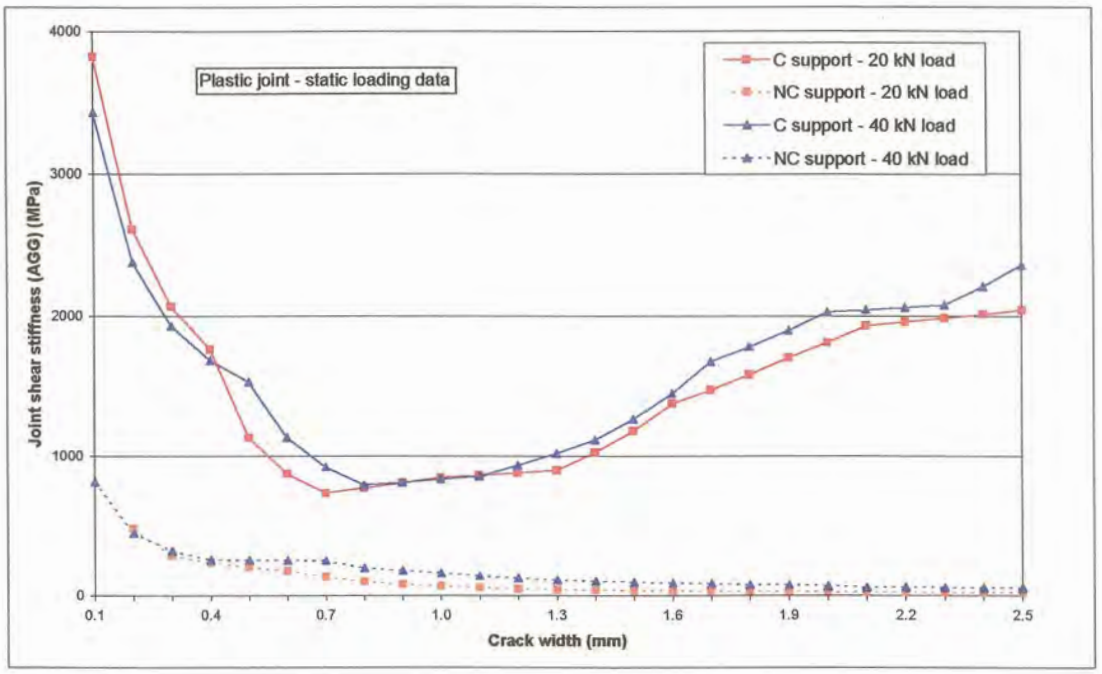

Figure 4.3: Joint shear stiffness versus crack width for static loading LTE results of the plastic joint

On the DC rubber support, on the other hand, the shear stiffness values were particularly low as could be expected from a smooth joint face. Of particular interest, is the fact that the shear stiffness calculated from the 40 kN load LTE values was approximately twice that of the 20 kN load LTE values. Once again showing that the larger "action" required a larger "reaction" in return. This was contrary to the results of for example the Endurance Index (EI), developed using rounded natural gravel, where doubling the load halved the EI (Colley and Humphrey, 1967).

An attempt has also been made to use the calculated joint shear stiffness to quantify the effect of dynamic loading versus static loading, as the difference in *AGG* results was more pronounced than the difference in LTE results. There was however no definite relationship that could be established in this instance. The only fact that can be stressed is that the *AGG*, just as the LTE, was higher under dynamic loading than under static loading. The average percentage increase in the *AGG* under dynamic loading over static loading, due to the effects of momentum, for the four aggregate interlock experiments is summarised in Table 4.3.

Table 4.3: Average increase in *AGG* due to dynamic loading

Experiment number	Aggregate size and type	Subbase	Increase in *AGG* due to dynamic loading (%)
1	19 mm granite	C rubber	128
2	37,5 mm granite	C rubber	183
3	19 mm dolomite	DC rubber	270
4	37,5 mm dolomite	DC rubber	282

The results in Table 4.3 indicated that the *AGG* under dynamic loading was approximately 1,5 times that of the *AGG* under static loading on the C rubber subbase, and approximately 3 times higher on the DC rubber subbase. The effect of different types of loads on the sound (C rubber) subbase is therefore not as big as the effect on the "weaker" (DC rubber) subbase. The further practical implication of this is that the forces induced in the pavement due to fast moving dynamic loads are able to "bridge" the discontinuities in the "weaker" (DC rubber) subbase with little detriment (small RM) to the pavement structure. But, the opposite is also true and that is that especially the vertical shear forces induced in the pavement due to slow moving heavy vehicles have a large detrimental effect (large RM) on the pavement with the "weaker" subbase.

4.3 ANALYSIS OF FIELD DATA

In practice concrete pavements are designed for a structural service life of up to 30 years (TRH4, 1985). The thickness of a specific pavement is mainly determined by future traffic projections, the quality of road construction materials and subgrade conditions. Therefore, when comparing the four road sections, discussed above, there are certain aspects that need to be highlighted. To facilitate the comparison the joint and mid-slab deflections, the RM and the LTE at joints, as well as the calculated remaining lives of each road section have been summarised in Table 4.4.

Table 4.4: Summary of FWD test results for all road sections

Road Section	40 kN Deflection (mm)				RM at joint (mm)	LTE at joint (%)	RM (years)
	Joint		Mid-slab				
	Average	Standard deviation	Average	Standard deviation			
1	0,250	0,047	0,116	0,043	0,07–0,26	44	4
2	0,101	0,058	0,083	0,038	0,00–0,19	76	14
3	0,225	0,097	0,091	0,057	0,06-0,12	67	6
4	0,157	0,088	0,059	0,026	0,03-0,20	84	20

At the time of investigation, the ages of the four pavements were 32, 14, 23, and 13 years, respectively. The fact that Road Section 1 had a RM of only 4 years maximum could be expected, as it was older than 30 years. Road Section 1 also had the highest average mid-slab and joint deflection values, with the lowest LTE at the joints.

When comparing Road Sections 2 and 4, which were constructed at approximately the same time, and carried the same amount of traffic, it could have been expected that their remaining lives would be the same. The concrete pavement on Road Section 2 was an overlay on an existing asphalt pavement. The subbase beneath the concrete of Road Section 2 was therefore more elastic than the cement stabilised subbase beneath the concrete pavement of Road Section 4. The result of this was lower deflections and RMs for the former than for the latter at the joints, but higher mid-slab deflections. Other factors that contributed to the lower RM of Road Section 2 were poorer subgrade conditions, and a wetter climate subjecting the pavement to chemical weathering processes.

In terms of design age and RM, it could be expected that Road Section 3 would still have a structural capacity of 8 to 10 years. However, the no-fines subsoil drain between the concrete pavement and the asphalt shoulder, as well as the asphalt shoulder, itself, did contribute to a reduction in the RM, and to the fact that the pavement already received a SAMI.

4.3.1 Relative movement analysis

The pavement models derived through back-calculation of the field investigation data of the four road sections were analysed using the software package, EverFE. The main purpose in this theoretical analysis was to demonstrate the difference between the RMs measured, using the FWD and the actual RMs across the joint itself. The reason for this is that the FWD measures the deflection at a point in the centre of the load, next to a joint, with the first geophone with which the RM is determined situated 200 mm away on the other side of the joint. During the laboratory experiments, on the other hand, the LVDT's measuring RM across the crack were situated as close as possible to the edge of the crack, and on opposite sides of the crack.

For comparison purposes the RMs were therefore determined theoretically beneath the load, on both sides of the joint, and 200 mm away from the centre of the load, on the opposite side of the joint. The results are plotted on Figures 4.4 to 4.7. The vertical axes of the graphs on these figures have been kept the same to facilitate an easier comparison of the deflection behaviour of the four different road sections.

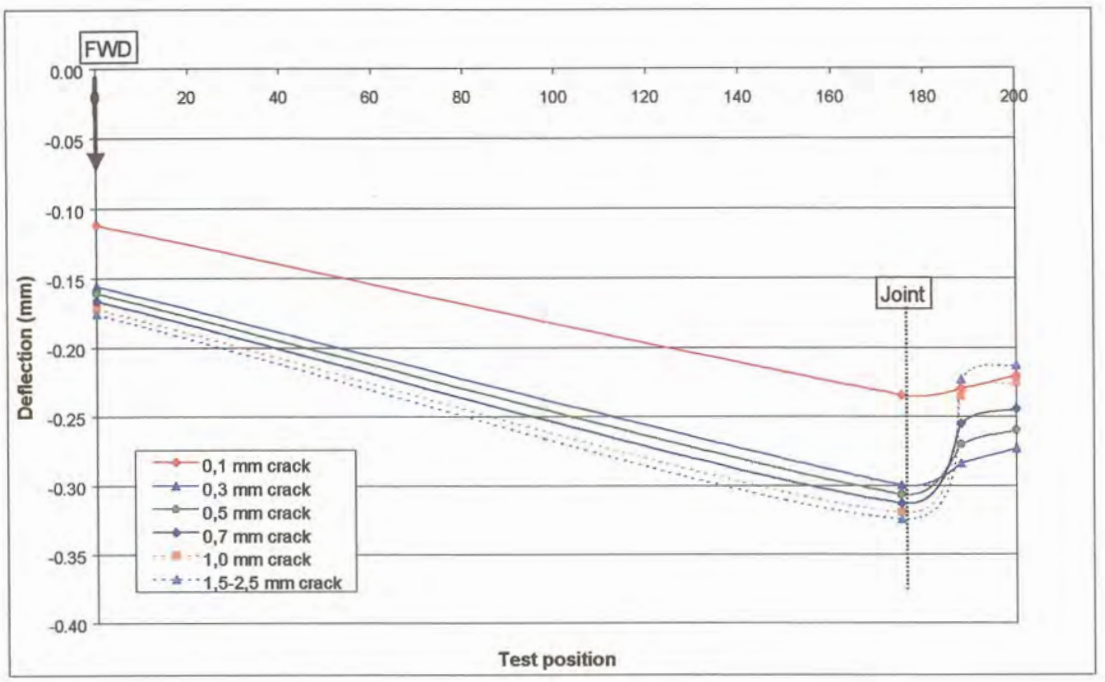

Figure 4.4: Simulated deflection across joint – Road Section 1

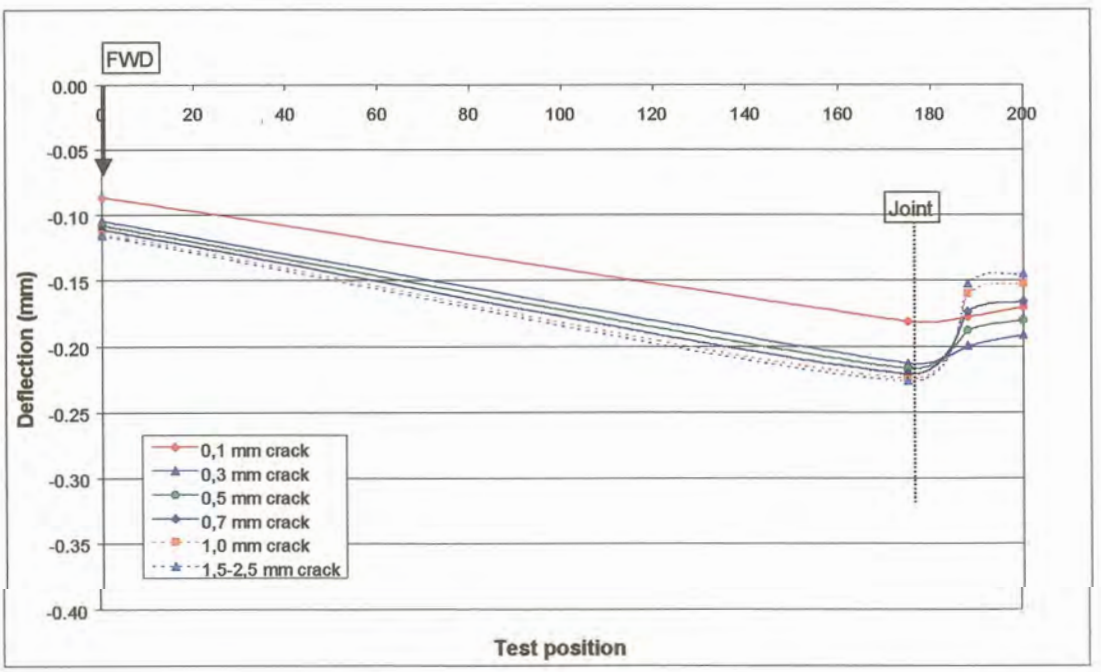

Figure 4.5: Simulated deflection across joint – Road Section 2

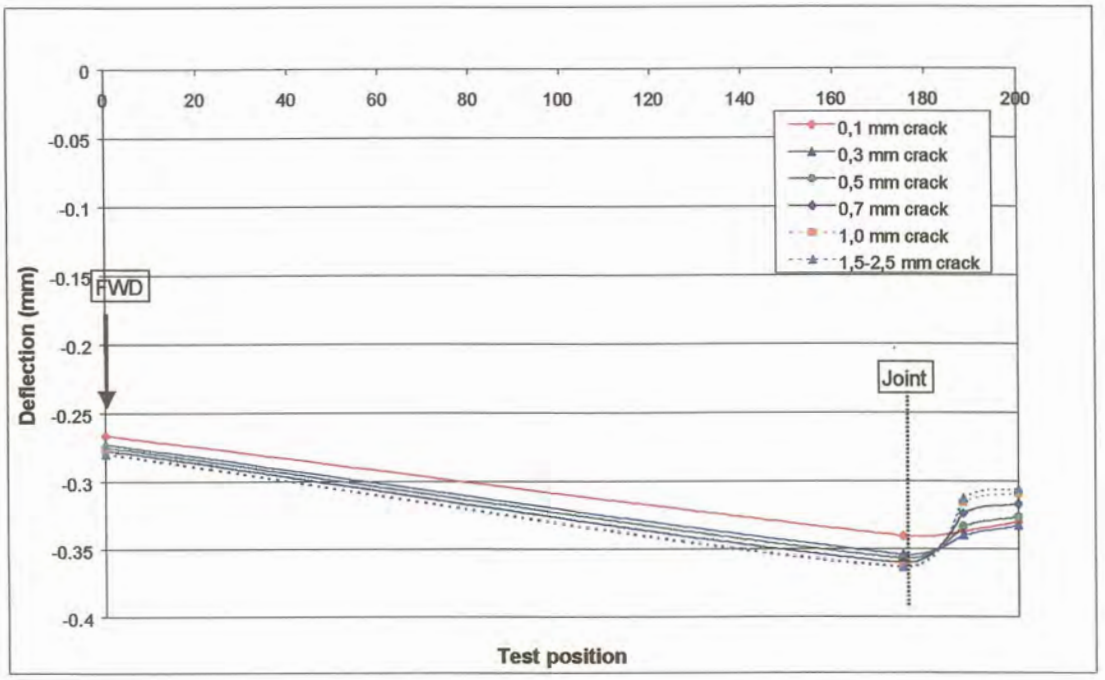

Figure 4.6: Simulated deflection across joint – Road Section 3

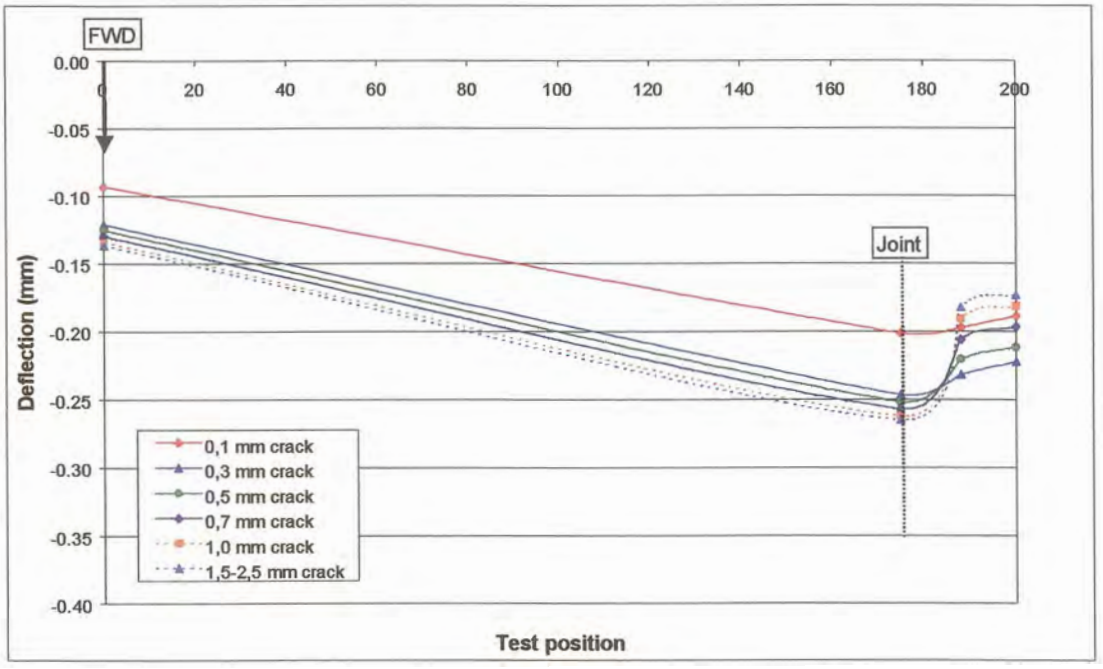

Figure 4.7: Simulated deflection across joint – Road Section 4

At narrow crack widths, the RM between the load position and the first geophone, 200 mm away, was larger than the RM across the joint. However, at crack widths between 0,7 mm and 1,0 mm, with the crack opening up and the LTE decreasing, the leave slab was pressed down further relative to the approach slab, the RM was reversed with the RM directly across the joint larger than the RM at 200 mm from the load position.

According to the theoretical analysis, Road Section 3 has the highest deflections, followed by Road Section 1, and Road Section 4, with Road Section 2 having the lowest deflections. The shape of the deflection curve was also influenced by the assumption that FWD testing would normally be conducted during the daytime, while the temperature of the concrete surface is typically 10°C greater than at the bottom. From there the upward curled shape of the slab from the joint position to the FWD load position. The distance between the deflection measurement at the joint, and the next point across the joint, is to allow for the reamed width at the top of the joint.

4.3.2 Aggregate interlock joint/crack shear stiffness

Similar to the analysis done for the laboratory data, the aggregate interlock joint shear stiffness was also determined. The relationship between deflection LTE and the dimensionless joint stiffness (*AGG/kl*) developed by Ioannides and Korovesis (1990) was used to calculate the shear stiffness per unit length (*AGG*) of the crack faces of the experimental slabs. The LTE calculated from the field data, together with Equation B.44 (Appendix B) was used. The values used in the calculation of the shear stiffness are summarised in Table 4.5.

Table 4.5: Input values for calculating shear stiffness (*AGG*) of crack faces

Description	Road Section			
	1	2	3	4
Poisson's ratio of concrete (μ)	0,15			
Subgrade modulus (k) (MPa/mm)	0,10	0,085	0,10	0,12
Elastic modulus of concrete (E) (MPa)	35 000	37 000	24 000	35 000
Concrete slab thickness (h) (mm)	200	230	210	210
Radius of relative stiffness (l) (mm)	699,0	819,7	659,8	692,7
Load radius (a) (mm)	135			
Load size ratio (a/l)	0,193	0,165	0,205	0,195

For Road Section 1 the LTE data in Table 3.4 was used, but for Road Sections 2, 3 and 4, the LTE from the original database was used. The graph presented in Figure 4.4 (Ioannides and Korovesis, 1990) was

used as the basis for the comparison, but in order to distinguish between the Road Sections, only the *AGG* values were plotted on a logarithmic scale on the X-axis and not *AGG/kl* (see Figure 4.8).

With the LTE data varying from nearly 0% to 100%, it was logical that the AGG values would also vary greatly. As can be seen from Figure 4.8 the AGG varied from approximately 4 MPa to 22 400 MPa. However, it was still possible to distinguish that the joint stiffness, calculated from the structural characteristics of the individual road sections, indicated that the road section with the highest RM (Road Section 4), also had the highest joint stiffness for a specific LTE. Simultaneously Road Section 3 had the lowest *AGG*, with Road Section 2 plotting in between. The values plotted for Road Section 1 were too little to draw a conclusion. This trend in the data was similar to the RM results presented in Table 4.4, above.

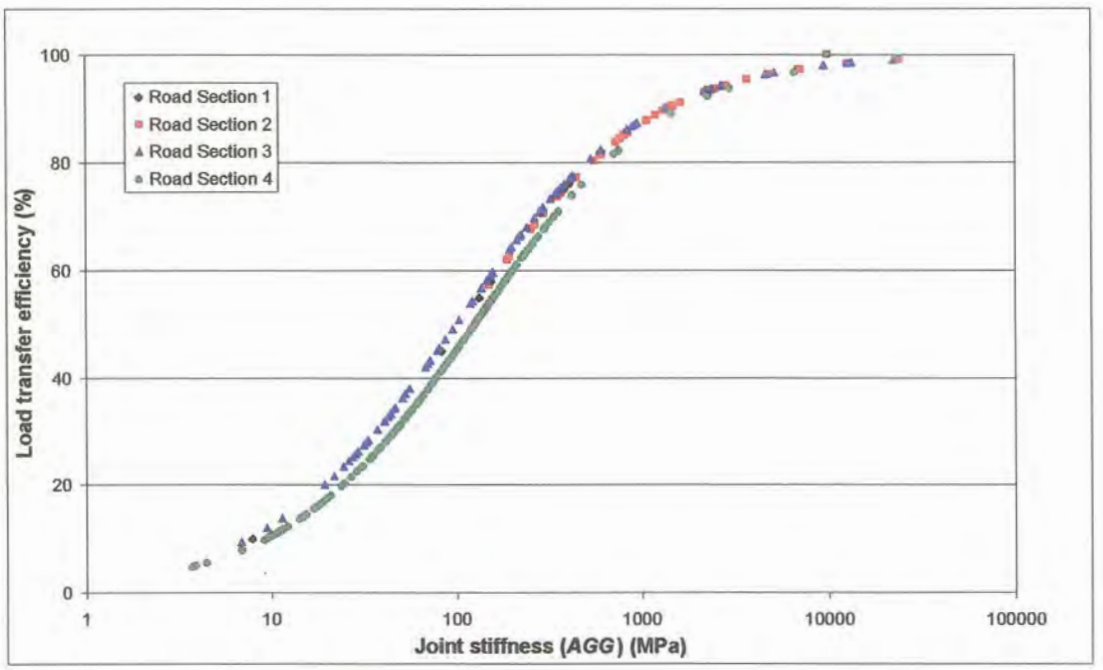

Figure 4.8: LTE versus joint stiffness calculated for field data

4.3.3 South African mechanistic concrete pavement design software

4.4 CONCLUSIONS

During the laboratory studies conducted for this research project, an attempt was made to reach a better understanding of the intricacies involved in defining the mechanism of aggregate interlock. This mechanism can only be understood adequately if it is borne in mind that normal stress, shear stress,

crack width, and shear displacement are all involved. On the other hand, concrete strength, aggregate size, and subbase support also influenced the results.

Tests on cracks subjected to earthquake loading Walraven (1981) showed that there is a considerable difference between the first and the subsequent loading cycles. Irreversible damage to the cement matrix takes place when the hard aggregate particles are pushed into this softer cement matrix. Any new cycle of loading leads to further damage of the crack faces, resulting into steadily increasing values of the shear displacement and the crack width at peak loading. In effect this was also proven during this study. The load applied to induce the crack in the less than 24-hour old concrete can be described as the first loading cycle, during which irreversible damage took place, in other words, during which the crack was formed. Subsequent loading and opening and closing of the crack caused further damage and the dislodging of fine particles in some instances that prevented the closing of the crack back to 0,1 mm once it has been pulled open.

Yet, despite this "damage" to the crack faces, the results obtained using the high quality crushed stone found in South Africa were superior to results obtained using USA aggregates. The common practice in South Africa of constructing jointed concrete pavements without dowels at the joints relying on aggregate interlock load transfer only has therefore been vindicated by this study.

The main contribution to the current state of knowledge was the development of a mechanistic equation quantifying the effect of aggregate interlock at a joint/crack in a concrete pavement. This equation has already been included and tested in the CncRisk software package, developed as part of the upgrading of the new mechanistic concrete pavement design manual for Southern Africa.

The structural performance of four different road sections was analysed in this chapter. The pavements were analysed by comparing the existing pavement designs, results of field investigations, and the structural RM of each.

At the time of investigation, the ages of Road Sections 1 to 4 were 32, 14, 23, and 13 years, respectively. Road Section 1 had a RM of only 4 years maximum, which could be expected, as it was older than 30 years. Road Section 1 also had the highest average mid-slab and joint deflection values, with the lowest LTE at the joints.

Road Sections 2 and 4 were constructed at approximately the same time, and carried the same amount of traffic, and it could have been expected that their remaining lives would be the same. But, the concrete pavement on Road Section 2 was an overlay on an existing asphalt pavement. The subbase beneath the concrete of Road Section 2 was therefore more elastic than the cement stabilised subbase beneath the concrete pavement of Road Section 4. The result of this was lower deflections and RMs for the former than for the latter at the joints, but higher mid-slab deflections. Other factors that

contributed to the lower RM of Road Section 2 were poorer subgrade conditions, and a wetter climate subjecting the pavement to chemical weathering processes.

The aggregate interlock joint shear stiffness was determined for each road section through the process developed by Ioannides and Korovesis (1990). The joint stiffness, calculated from the structural characteristics of the individual road sections, indicated that the road section with the highest RM (Road Section 4), also had the highest joint stiffness for a specific LTE. Simultaneously Road Section 3 had the lowest *AGG*, with Road Section 2 plotting in between. This was similar to the RM results presented in Table 4.4, above.

CHAPTER 5: APPLICATION OF LABORATORY AND FIELD MODELLING

TABLE OF CONTENTS

LIST OF TABLES

LIST OF FIGURES

LIST OF SYMBOLS / ABBREVIATIONS

agg	Nominal size of 20% biggest particles in concrete mix
C	Continuous
DC	Discontinuous
$E_{subbase}$	Subbase stiffness modulus
F	Shift factor
k	Subgrade modulus
l	Radius of relative stiffness

LTE	Load transfer efficiency
RM	Relative movement
v	Vehicle speed
x	Crack width
y(x)	Relative vertical movement

5 APPLICATION OF LABORATORY AND FIELD MODELLING

5.1 INTRODUCTION

The primary objectives of this thesis have been achieved. This has been done through a detailed literature survey in order to lend guidance to the research and laboratory modelling conducted for this thesis and a thorough analysis of laboratory and field data. But not only that, insight has also been gained in the relationship between relative movement and load transfer efficiency of laboratory and field data through the development of a shift factor to fit the laboratory data to specific field data sets. The details are discussed below.

5.2 AGGREGATE INTERLOCK FORMULA FOR SOUTH AFRICAN MECHANISTIC CONCRETE PAVEMENT DESIGN MANUAL

5.2.1 Laboratory data

Reference has been made to the fact that the research done for this thesis formed part of the overall process of producing a new mechanistically based concrete pavement design manual for South Africa. The software package CncRisk has been developed as part of the new design manual. However, the original software still contained Equation (2.12) for the calculation of the aggregate interlock factor, Ca, referred to by Strauss et al. (2001). The RM data calculated from the deflections was used to develop a single equation to replace Equation (2.12) in the source code of the software package. A Weibull probability density function was generated, as follows:

$$y(x) = 0{,}118(1 - e^{-((v + \frac{11{,}413}{agg})x)^{1{,}881}}) \qquad (5.1)$$

Where:

$y(x)$	=	Relative vertical movement at joint/crack (mm);
v	=	0,136 for static loading (speed = 0 km/h);
	=	0,035 for dynamic loading (speed = 80 km/h);
x	=	Crack/joint width (mm); and
agg	=	Nominal size of 20% biggest particles in concrete mix (mm).

So-called "before" analyses were conducted with the original version of the software, containing Equation (2.12). For the input on the Main Control Panel of the software, typical jointed concrete pavement parameters were used (see Figure 5.1). The variation in the theoretical expected life of the pavement with 19 mm and 37,5 mm aggregate sizes, at specific crack widths was determined. Actual relative movements measured at specific crack widths during the laboratory studies were used.

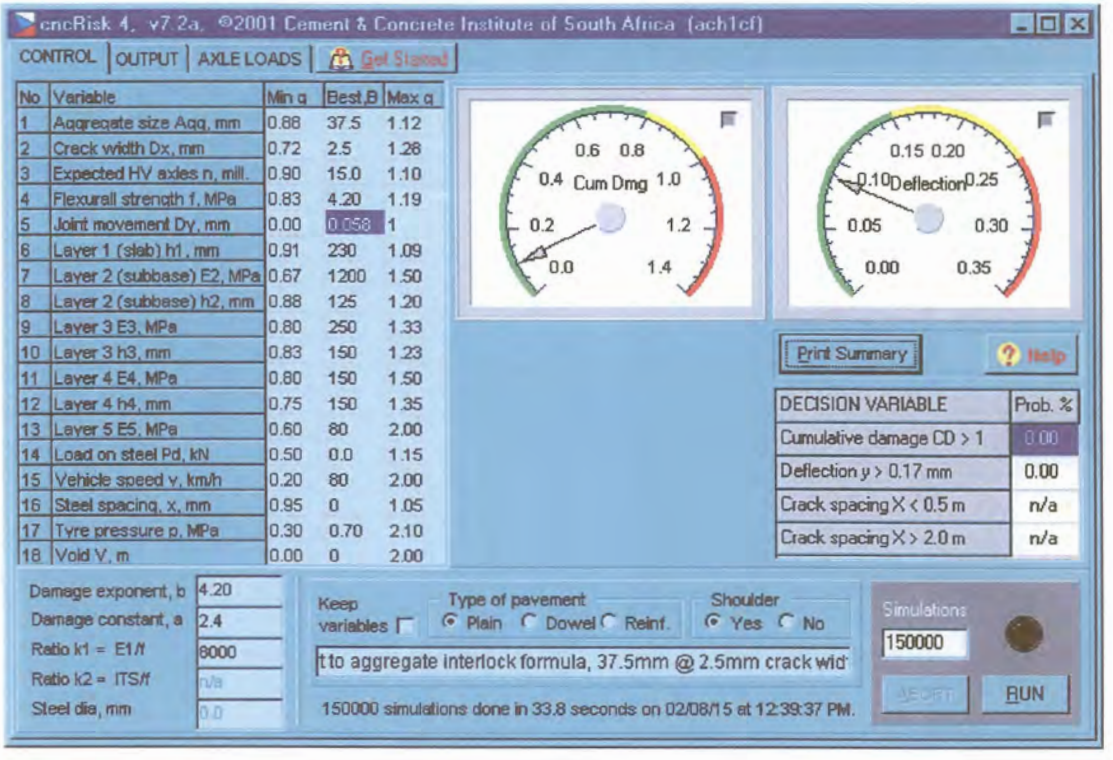

Figure 5.1: Input detail for Main Control Panel

Equation (5.1) was then included in the source code, and the same sets of input data re-used to conduct "after" analyses with the revised version of the software. The results of these "before" and "after" analyses are summarized in Table 5.1.

The discrepancy in Equation (2.12) for the smaller 19 mm sized aggregate, illustrated in Figure 3.15, was confirmed, by the fact that the expected life calculated through the software increased with increasing crack width, and relative movement during the "before" analyses. This is contrary to what physically happens in a concrete pavement where the life decreases with an increase in crack width and relative movement. The results for the larger 37,5 mm sized aggregate were more realistic, decreasing with an increase in crack width and relative movement. The pavement life calculated after the inclusion of Equation (5.1) decreased with increasing crack width and relative movement, for both aggregate sizes. The pavement life was also higher for the 37,5 mm aggregate concrete than for the 19 mm aggregate concrete. The results obtained were for illustration purposes, and should not be taken as absolute values

However, a more practical method to illustrate the contribution of the newly developed Equation (5.1) is to graphically illustrate the adjustment in the line plotted with the previous Equation (2.12) versus this new equation. This is shown on Figure 5.2.

Table 5.1: Comparison between "before" and "after" CncRisk analyses

Aggregate size (mm)	Crack width (mm)	Relative movement (mm)	Pavement Life (N x 10^6)	
			Before	After
19	1,0	0,040	46,6	52,6
	2,0	0,092	50,7	48,7
	2,5	0,100	55,1	48,0
37,5	1,0	0,015	54,0	58,2
	2,0	0,042	47,8	52,8
	2,5	0,058	46,8	51,3

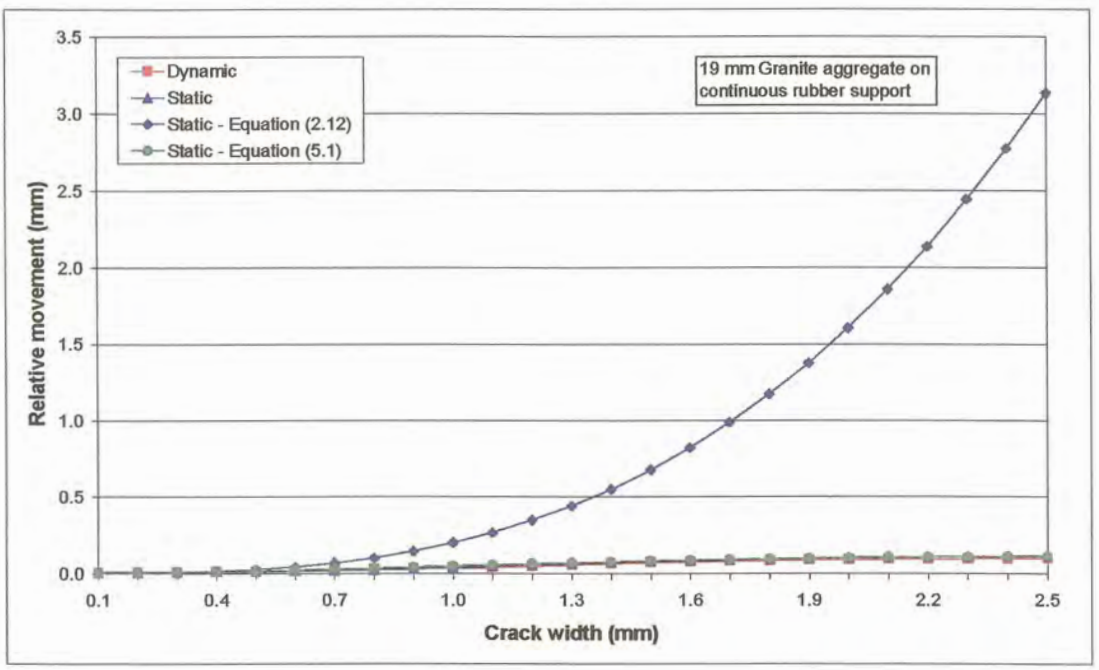

Figure 5.2: Graphic illustration of improvement to aggregate interlock equation

From Figure 5.2 it is obvious that there is little difference between the results measured in the laboratory and the results calculated with Equation (5.1).

5.2.2 *Field data*

In paragraph 3.4.2, it was mentioned that the original version of the CncRisk software was used to calculate the RM of Road Section 1. After inclusion of Equation (4.1) in CncRisk, all four road sections were analysed again. The laboratory data indicated that at a relative movement of approximately 0,12 mm, the crack width was 2,5 mm. Bearing this in mind and to be a bit more

optimistic, it was decided to set the crack width at 2,0 mm with a RM of 0,12 mm. The void length was set at 1,0 m. The pavement layer thicknesses and back-calculated stiffness moduli presented in the previous paragraphs were used. The vehicle speed was set at 0 km/h to be on par with the FWD test results. The projected heavy vehicles (E80's) over the remaining lives predicted from previous analyses (see Table 4.4) was 1,5 million for Road Section 1, 80 million for Road Section 2, 22 million for Road Section 3 and 68 million for Road Section 4.

The results were as follows:

a) Road Section 1 already showed cumulative damage of 27,5% with a RM of 0,8 million E80's at a crack width of only 0,5 mm and void length of 0 m. This confirmed that the pavement was already in a terminal condition and brought the RM down to only two years, which is half of what was calculated with the earlier version of CncRisk.

b) CncRisk confirmed that after 14 years the pavement of Road Section 2 will show cumulative damage of 10,5%, which is the maximum percentage damage allowed, before rehabilitation is required (Manual M10, 1995). The projected RM is 103 million E80's, which indicates that the pavement will still be in a reasonable condition, but will need attention.

c) The cumulative damage calculated for Road Section 3 was 54% with a RM of 11 million E80's (4 years) at a crack width of 2 mm, RM of 0,12 mm and void length of 1 m. This, according to CncRisk, is a clear indication that the pavement was already in a distressed state and needed attention. The repair work that has already been done on this road section was therefore necessary.

d) Given the projected traffic and back-calculated layer stiffness moduli, the cumulative damage calculated for Road Section 4 was 54% with a RM of only 33 million E80's (12 years) at a crack width of 2 mm, RM of 0,12 mm and void length of 1 m. This was far less than what has been predicted above. On the one hand the stiffness moduli may have been under-estimated, but with average deflections higher than that of Road Section 2, it may not be far off. This road section will have to be monitored closely.

These analyses have shown that the software package CncRisk is a handy tool to determine the RM of an existing pavement. Further investigation is required to determine the reason for the large difference in the result of Road Section 4.

5.3 RELATIVE MOVEMENT VERSUS LOAD TRANSFER EFFICIENCY

The original database for Road Sections 2, 3 and 4 was used to evaluate the RM versus the LTE calculated from the field data (the original data for Road Section 1 was not available). The data together with an exponential curve fitted through the points for each individual Road Section, is shown on Figure 5.3. These curves were all of the format $y(x) = 100e^{-Fx}$. With RM = 0 at LTE = 100%, the

intercept of all three curves was 100. The factor, F, was assumed to be a function of the subbase support, the radius of relative stiffness, as well as the subgrade k-modulus, which still had to be determined.

Contrary to the maximum RM of approximately 0,12 mm measured in the laboratory for the aggregate interlock experiments, values of up to 0,5 mm were measured in the field. In this instance, if LTE is considered to be indicative of the RM of a pavement, the RM versus LTE did not seem to correlate with the remaining lives already calculated. Of the three sections, Road Section 4 supposedly has the largest RM, but according to the exponential curve fitted to the data, it approximates a lower LTE at a RM of 0,5 mm than Road Section 3.

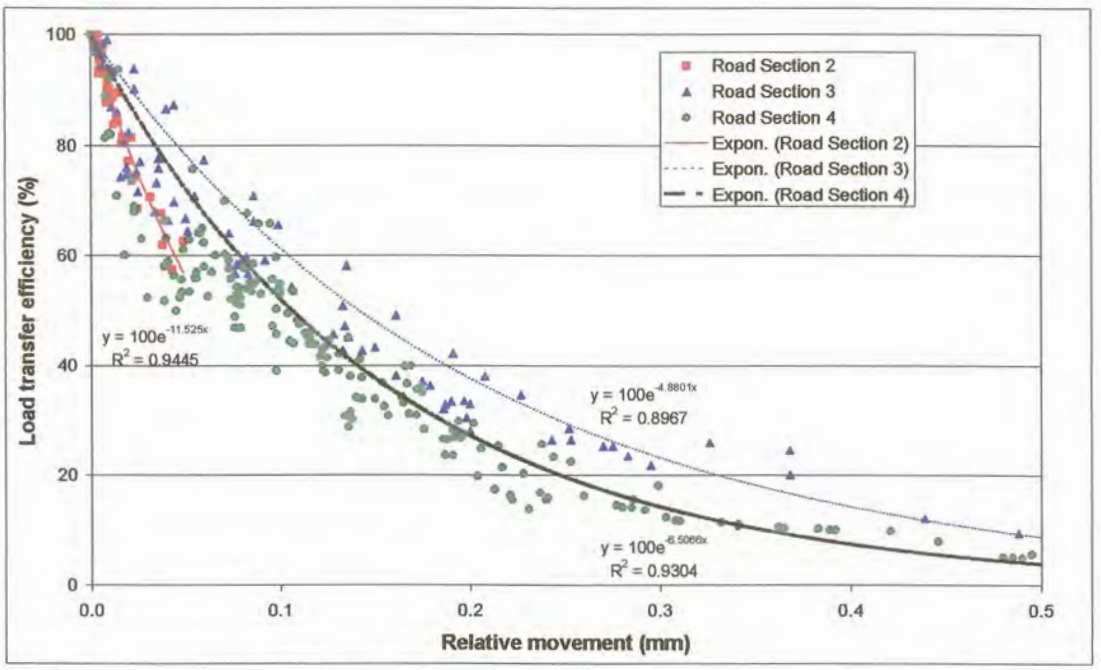

Figure 5.3: RM versus LTE for Road Sections 2, 3 and 4

Road section 3 with the lowest RM of the three sections considered showed the largest LTE. The amount of data available for Road Section 2 was little in comparison with Road Sections 3 and 4. Most of the LTE results for Road Section 2 were between 60% and 100%, with the maximum RM only 0,05 mm. A summary of the statistical parameters of the LTE and RM data for the three road sections is given in Table 5.2.

Table 5.2: Summary statistics of LTE and RM data for Road Sections 2, 3 and 4

Statistical parameter	Road Section 2		Road Section 3		Road Section 4	
	RM	LTE	RM	LTE	RM	LTE
Average	0,013	87,3	0,126	57,4	0,146	42,2
Standard deviation	0,012	11,5	0,120	25,5	0,109	20,6
Minimum	0,000	57.4	0,002	9,4	0,000	4,9
Maximum	0,049	100,0	0,586	99,0	0,495	100,0

Further to the above comparison, the field data was also used to calibrate the laboratory data (from Chapter 3). For this purpose, the 40 kN static loading data for the 19 mm and 37,5 mm coarse aggregates as well as for the plastic joint on the discontinuous subbase was used, as the combined results covered the same range of RM measurements as the field data (see Figure 5.4).

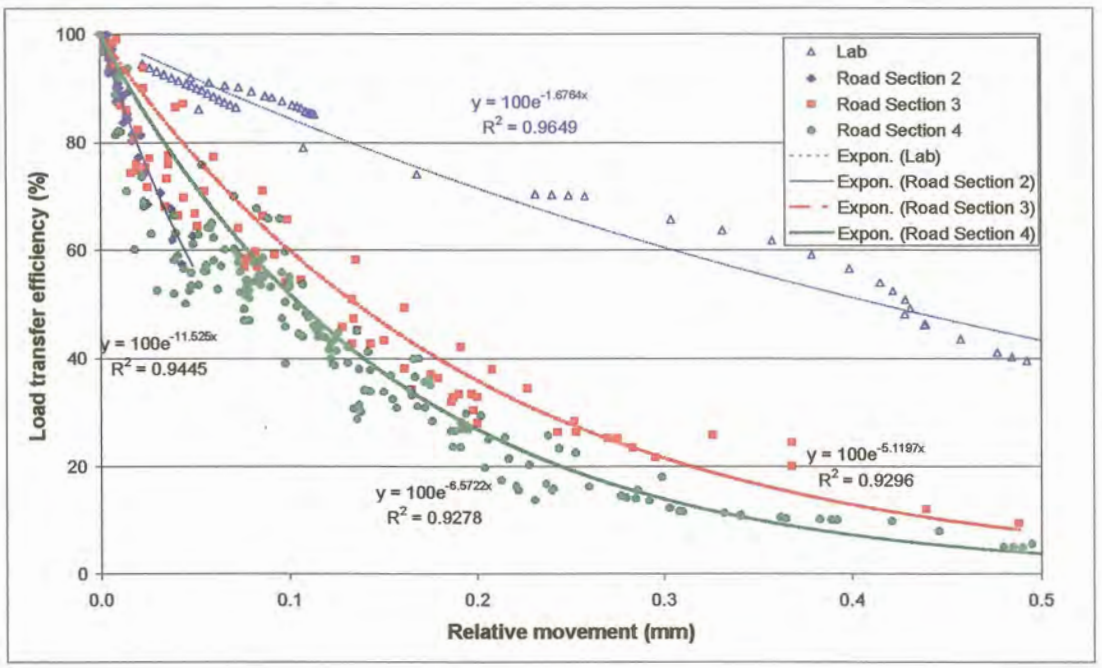

Figure 5.4: RM versus LTE – comparison between laboratory and field data

When analysing the results plotted on Figure 5.4, the sensitivity of the model developed in this thesis can be summarised as follows:

a) The larger the crack width, the greater the RM.

b) The greater the vehicle speed, the smaller the RM.

c) The larger the aggregate size, the smaller the RM.

d) The higher the elastic modulus of the concrete the smaller the RM for the same LTE.

e) The higher the elastic modulus of the subbase, the smaller the RM, also for the same LTE.

In order to calculate a "shift" factor between the laboratory and field data, an exponential curve was fitted through the laboratory data as well. The values calculated with the exponential fit for the laboratory data was then divided by the comparative values for the field data of each road section. The relationships between each of the field data sets and the laboratory data set were also exponential curves (with $R^2 = 1$), which increased with increasing crack with. For example, LTE (Lab/Road Section 4) = $100e^{-1.6764RM}/100e^{-6.5722RM} = e^{4.8958RM}$. This is illustrated in Figure 5.5, where the laboratory and Road Section 4 data were compared. The relationship Lab/Road Section 4 with the exponential curve fitted through it, is also plotted on Figure 5.5. The curve F4 was obtained by dividing the curve fitted through the laboratory data by the curve fitted through the relational curve, in other words $100e^{-1.6764RM}/e^{4.8958RM}$. This implied that in order to "shift" the laboratory data to either of the field data sets, the RM-coefficient (F) of the relational curve had to be established for each data set.

Various combinations of the subgrade modulus (k), radius of relative stiffness (l) and the subbase stiffness ($E_{subbase}$) were used. For the equation $LTE = e^{F*RM}$, the combination that gave the closest results for the shift factor (F) was:

$$F = l/(k*E_{subbase}) \quad (5.2)$$

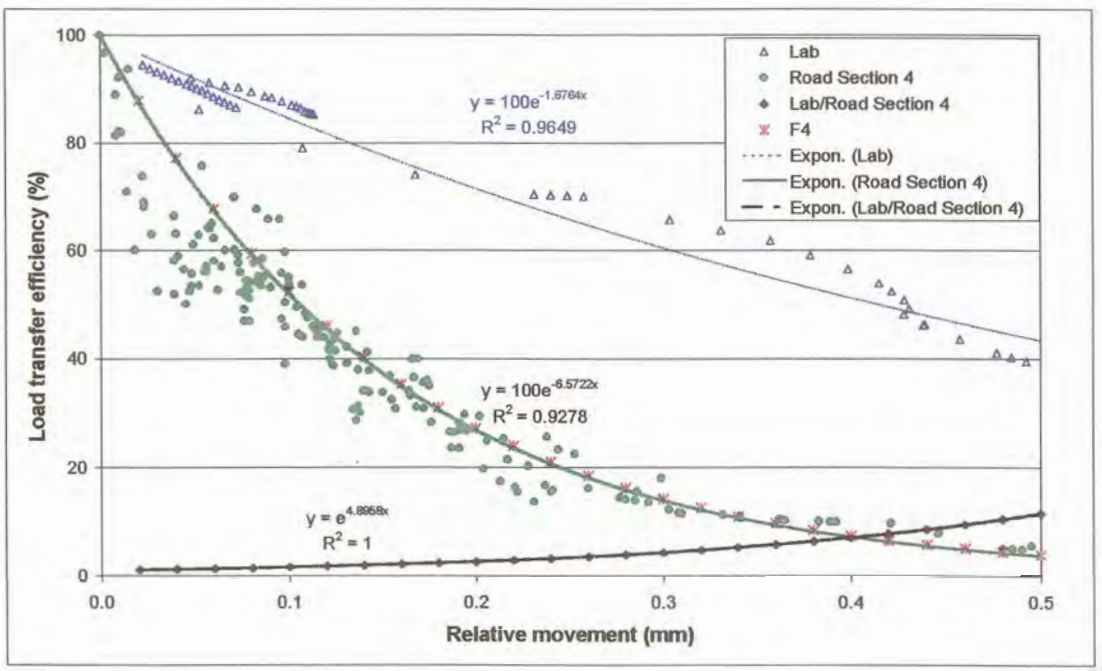

Figure 5.5: RM versus LTE – relationship between laboratory data and Road Section 4

The F of the exponential curve fitted to the laboratory data in effect already incorporated these three parameters as an inherent characteristic. It was therefore logical that these three parameters would also contribute to the shift in data. The shift factor by itself has the units mm^2/MPa^2, which is a surface area over a surface stress. When, however the exponential curve fitted to the laboratory data is divided by the shift factor, the units are cancelled out, making it dimensionless.

Another important aspect that has to be emphasised here and which the range achieved in the laboratory RM shows, is that the RM over which aggregate interlock plays the primary role in load transfer, varies from approximately 0 mm to 0,12 mm. At larger RMs the subbase influenced the results to a great extent, which is clearly shown by the RM of the smooth plastic joint. This was also one of the main reasons for including the stiffness modulus of the subbase during determination of the F-factor.

To test whether this shift factor would apply to any data set, the results of the three road sections were combined into one set of data and an exponential curve fitted through it. The average k, l and $E_{subbase}$ of the three road sections was calculated and used as the x-coefficient to plot curve F in Figure 5.6. It was remarkably close to the exponential curve fitted to the field data.

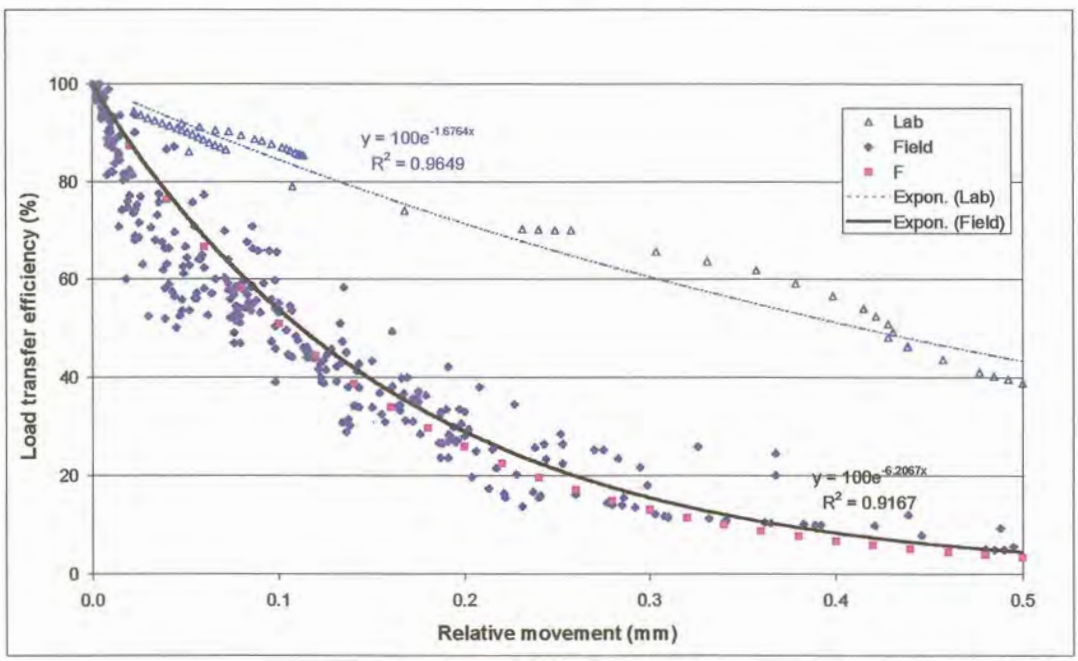

Figure 5.6: RM versus LTE – relationship between laboratory data and average of field data

Where the RM in the field is larger than 0,12 mm, two main assumptions can be made from this comparison between the laboratory and the field data, namely:

a) The aggregate interlock capacity of the crack face, itself is still intact, but the crack width is larger than 2,5 mm, or

b) The crack face has been eroded due to traffic loading to such an extent, that the crack face has become smooth, and has little aggregate interlock capacity.

Bearing in mind the high quality of the crushed stone in South Africa, the first of the two assumptions seems to be the more likely option.

5.4 SUMMARY

The main contribution to the current state of knowledge was the development of a mechanistic equation quantifying the effect of aggregate interlock at a joint/crack in a concrete pavement. This equation has already been included and tested in the CncRisk software package, developed as part of the upgrading of the new mechanistic concrete pavement design manual for Southern Africa. Furthermore, application of the revised version of the CncRisk software that included Equation (5.1) mostly confirmed the remaining lives of the road sections as predicted by different individuals in the reports used to compile the field investigation data.

The RM and LTE data from three of the four road sections was used to calibrate the laboratory data. The calibration factor was a function of the subgrade modulus (k), radius of relative stiffness (l) and the subbase stiffness ($E_{subbase}$). In effect this calibration of the data has also shown that one of the main objectives of the particular test set-up used for the aggregate interlock experiments has been achieved in that the RM range over which load transfer is enabled due to aggregate interlock of the 19 mm coarse aggregate could be established. Indications are however; that for larger 37,5 mm coarse aggregates this range extends past the values tested. The main contribution of the plastic joint results in combination with the aggregate interlock results, was that the same range of RM measurements as the field measurements was obtained. This therefore clearly indicated where the LTE measured in the field, relies mainly on the subbase stiffness, due to either crack widths larger than 2,5 mm, or an aggregate crack face that has been abraded under traffic movement to such an extent that it gives the same relative movement results as a smooth joint.

The sensitivity of the model developed in this thesis can be summarised as follows:

a) *The larger the crack width, the greater the RM.*

b) The greater the vehicle speed, the smaller the RM.

c) The larger the aggregate size, the smaller the RM.

d) The higher the elastic modulus of the concrete the smaller the RM for the same LTE.

e) The higher the elastic modulus of the subbase, the smaller the RM, also for the same LTE.

CHAPTER 6: SUMMARY, CONCLUSIONS AND RECOMMENDATIONS

TABLE OF CONTENTS

LIST OF SYMBOLS / ABBREVIATIONS

agg	Nominal size of 20% biggest particles in concrete mix
$E_{subbase}$	Subbase stiffness modulus
F	Shift factor
k	Subgrade modulus
l	Radius of relative stiffness
LTE	Load transfer efficiency
RM	Relative movement
v	Vehicle speed
x	Crack width
y(x)	Relative vertical movement

6 SUMMARY, CONCLUSIONS AND RECOMMENDATIONS

6.1 SUMMARY

6.1.1 Aggregate interlock

The primary objective of this study was to investigate existing methods for modelling aggregate interlock shear transfer across a joint in a concrete pavement, and to develop a model that reflects variations in joint load transfer with joint opening, load magnitude and concrete properties. It was envisaged that this model / equation could replace an existing equation as part of the upgrading of the south African concrete pavement design manual to a manual based on mechanistic design principles. During a process of investigating the background of concrete pavements constructed in South Africa, defining the rigid pavement system, investigating historical developments in concrete pavement design, and a thorough literature review, this objective has been explored.

The software package EverFE (Davids et al, 1999) was used to do theoretical modelling, and to determine the accuracy of equipment required for experimental modelling. Part-slab studies were conducted inside a laboratory to reduce the effect of temperature variations on the test set-up, as well as eliminate exposure of the slab to environmental influences such as direct sunlight, and/or rain. Instrumentation included thermocouples to collect slow responses due to environmental influences. Linear variable displacement transducers (LVDT's) and strain displacement transducers collected fast responses induced by dynamic and static loads. The testing also included determining the relevant engineering properties for South African concrete aggregates.

The experimental programme was set up according to a 2-level, 2-parameter design. The aggregate types chosen were Granite with an E-modulus of 27 GPa (Aggregate crushing value (ACV) = 27%), and Dolomite with an E-modulus of 40 GPa (ACV = 15%), representing the range in modulus of crushed aggregates used in the construction industry in South Africa. To cover the spectrum of aggregate sizes used in the construction of concrete, 19 mm as well as 37,5 mm coarse aggregates were used. Four concrete slabs were cast to determine the effects of aggregate interlock, as follows:

a) Experiment 1 – 19 mm granite aggregate.
b) Experiment 2 – 37,5 mm granite aggregate.
c) Experiment 3 – 19 mm dolomite aggregate.
d) Experiment 4 – 37,5 mm dolomite aggregate.

A fifth concrete slab with a pre-deformed plastic joint former was cast to investigate the performance of a different type of joint under both dynamic and static loading. This slab was used to quantify the difference between a continuous and a discontinuous Winkler subbase and also to complete the data in the relative movement (RM) and LTE analysis..

The response of the experimental slabs was captured under moving impulse or dynamic loading (equivalent to traffic loading) as well as under static loading to be able to capture real-life conditions and to compare the results. An impulse force that simulates the impact of one wheel (20 kN) of a standard 80 kN dual wheel axle load, crossing a joint/crack at 80 km/h was developed. The impulse force was applied across the crack formed in the slab (within 24 hours after casting) by means of two actuators at a frequency of 3 Hz for 2 million load cycles each on the slabs cast for Experiments 1 and 2. During Experiment 1 it became apparent that even the weaker of the two aggregate types, namely granite, experienced no significant deterioration inside the crack face at the initial crack width up to 2 million dynamic load cycles. This could be attributed to the fact that both the cement paste and aggregate particles were so tightly knit together at the initial crack width that little vertical sliding could occur. This indicated that little abrasion of the aggregates at the joint face took place at the initial crack width, as the narrow crack restricted vertical shear movement, and that the shear stress developed within the crack face was too low for fatigue to take place. Therefore no loose particles were dislodged, or got trapped in a different position when the crack opened and closed. This could also be attributed to the high quality of crushed stone used in South Africa. This was confirmed by subjecting Experiment 2 to 2 million dynamic load cycles as well, and confirming that the deflections measured, as well as the LTE calculated stayed constant during the full loading cycle.

Experiments 1 and 2 were constructed on continuous rubber support layers, whereas for Experiments 3 and 4, the top rubber layer was cut through right beneath the crack, to simulate a crack propagating into the subbase. Both of these subbases represented a liquid (Winkler) foundation, for the first two experiments it was continuous, and for the latter two, discontinuous.

The RM data calculated from the deflections was used to obtain an equation to replace a previous, inaccurate equation in the source code of the software package CncRisk (written as part of the development of a new South African mechanistic concrete pavement design method). A Weibull probability density function was generated, as follows:

$$y(x) = 0{,}118(1 - e^{-((v + \frac{11{,}413}{agg})x)^{1{,}881}}) \tag{6.1}$$

Where:

$y(x)$	=	Relative vertical movement at joint/crack (mm);
v	=	0,136 for static loading (speed = 0 km/h);
	=	0,035 for dynamic loading (speed = 80 km/h);
x	=	Crack/joint width (mm); and
agg	=	Nominal size of 20% biggest particles in concrete mix (mm).

The sensitivity of the model developed in this thesis can be summarised as follows:

a) The larger the crack width, the greater the RM.

b) The greater the vehicle speed, the smaller the RM.

c) The larger the aggregate size, the smaller the RM.

d) The higher the elastic modulus of the concrete the smaller the RM for the same LTE.

e) The higher the elastic modulus of the subbase, the smaller the RM, also for the same LTE.

6.1.2 Dowel modelling

A thorough literature review was conducted to investigate existing methods for modelling steel dowel/concrete interaction at joints in jointed concrete. It was concluded that the main function of dowels is to prevent faulting, reduce pumping, and reduce corner breaks. From the literature review, as well as the theoretical dowel modelling, it is obvious that even relatively small gaps around the dowels has a significant effect on joint displacements, and the ability of the dowel to transfer shear load from the loaded to the unloaded slab (Davids et al, 1998a, 1998b). These gaps are already in existence at the time of construction over at least half the length of the dowel, because of de-bonding agents, or sleeves around the dowels. It is therefore just a matter of time before the other half of the dowel also develops a gap around it, and that the shear force transferred through the dowel reduces to such an extent that it approximates the shear force transferred across the joint through aggregate interlock only. This was plainly presented in Appendix D where the combined affect of aggregate interlock and dowel modelling with both an increase in crack width and an increase in the gap width around the dowel was investigated theoretically. In effect these facts imply that eventually the main function of dowels revert back to that which has been stated at the beginning of this paragraph, that of preventing faulting, reducing pumping, and reducing corner breaks. Dowel bars can therefore be expected to act as load transfer devices, but it should not be expected of a dowel bar to transfer shear forces across the joint, once dowel looseness has developed.

Research done by Hammons and Ioannides (1996) emphasised the fact that accurate theoretical equations for dowel modelling have been in place since the 1930's. It was pointed out that the so-called Friberg (1940) equations, based on the original Westergaard (1926) theory, are still applicable. The Friberg (1940) equations also form the basis of the dowel load transfer coefficient determined for the new mechanistic M10 design method (Strauss et al, 2001). It was therefore not deemed necessary to concentrate on dowel modelling experiments at this stage, but focus on the aspects involved with aggregate interlock modelling.

6.1.3 Field investigation

When addressing the first secondary objective stated in Chapter 1, field measurements of crack widths, LTE, and the RM at joints of four existing jointed concrete pavements in South Africa were obtained.

At the time of investigation, the ages of the four pavements were 32, 14, 23, and 13 years, respectively.

According to the reports from which the data was taken, the predicted remaining lives of each road section was 4, 14, 6, and 20 years, respectively. CncRisk analyses gave more pessimistic remaining life results, especially for Road Section 4. Road Section 4 had comparatively high RM measurements at the joints, which were not only due to the test load on the pavement, but also due to temperature effects, as well as the probability of voids beneath the concrete. This emphasised the importance of proper maintenance of concrete pavement joints. Properly sealed and maintained joints prevent the ingress of water and debris into the pavement structure, which in turn cause poor LTE or high RMs at joints relying on aggregate interlock.

The field data was also used to calibrate the laboratory results. The shift factor to adjust the laboratory RM versus LTE data to the field data was a function of the subgrade modulus (k), radius of relative stiffness (l) and the subbase stiffness ($E_{subbase}$). For the equation $LTE = e^{F*RM}$, the combination that gave the closest results for the shift factor (F) was:

$$F = l/(k*E_{subbase}) \tag{6.2}$$

In effect this calibration of the data has also shown that one of the main objectives of the particular test set-up used for the aggregate interlock experiments has been achieved. Through the specific test set-up, an attempt has been made to test the effects of aggregate interlock, and although the load transfer efficiencies were optimistic when compared to the field data, the range of RMs over which load transfer takes place through aggregate interlock has been established. This range varies from approximately 0 mm to 0,12 mm, especially for the smaller 19 mm coarse aggregate. Indications are however, that for larger 37,5 mm coarse aggregates this range extends past the values tested. At larger RMs the subbase influenced the results to a great extent, which is clearly shown by the RM of the smooth plastic joint. The main contribution of the plastic joint results in combination with the aggregate interlock results therefore, was that the same range of RM measurements as the field measurements was obtained. This therefore clearly indicated where the LTE measured in the field, relies mainly on the subbase stiffness, due to either crack widths larger than 2,5 mm, or an aggregate crack face that has been abraded under traffic movement to such an extent that it gives the same RM results as a smooth joint.

6.2 CONCLUSIONS

The main conclusions reached after interpretation of experimental results were as follows:

a) An increase in crack width caused an increase in deflection, a decrease in deflection LTE, and an increase in RM.

b) The larger 37,5 mm aggregate had lower deflections than the smaller 19 mm aggregate at the same crack widths during dynamic and static loading.

c) Beyond a crack width of 2,5 mm the data for the 19 mm coarse aggregate tended to remain constant, and it was therefore not considered necessary to test at crack widths greater than 2,5 mm. It was specifically stated in previous research studies (Davids et al, 1998b; Jensen, 2001) that at crack widths greater than 2,5 mm the stiffness of the subbase starts to play a role in levelling out the measured response of the slabs. However, this study has shown that the smoother the texture of the crack face, the sooner the system would rely on the support of the subbase to transfer stresses and strains from one slab to another. This study has indicated three such transition zones, namely: 1,5 mm for the smooth joint, 2,5 mm for the 19 mm aggregate interlock joint, and between 3,5 mm and 4,0 mm for the 37,5 mm aggregate interlock joint.

d) At small crack widths (< 0,5 mm) the bottom crack displacement measurements tended to be higher than the top crack displacement measurements. The slab tended to bend through with the top of the crack closing, and the bottom of the crack opening during loading. This was more evident during dynamic loading than during static loading, due to the effects of momentum.

e) At crack widths greater than 0,5 mm the top crack displacement became larger than the bottom crack displacement, indicating that the crack was being pushed open during loading. This demonstrated why large crack widths are so detrimental to pavement performance, as the opening up of the crack at the top during loading, makes it easier for debris and loose particles to be driven into the cracks, which in turn cause spalling of the concrete at the crack face. Once again the effect was greater during dynamic than static loading.

f) The deflection LTE was greater during dynamic than static loading in all instances. Larger sized coarse aggregates had greater deflection load transfer efficiencies than smaller sized coarse aggregates.

g) For the same coarse aggregate size concrete mixes, the LTE was larger where there was a continuous subbase support (rubber not cut through) than where there was a crack simulated into the subbase (top rubber layer cut through).

h) Due to the effects of momentum forces acting across the crack, the LTE under 40 kN static loading was higher than under 20 kN static loading.

i) Due to the effects of momentum acting across the joint, the LTE under dynamic loading of a bubble plastic joint on the non-continuous subbase remained remarkably high (92% at a crack width of 2,5 mm), compared to the gradual decrease in LTE with increasing crack width under static loading (18% at a crack width of 2,5 mm).

j) Although the deflections were in the same order of magnitude, the load transfer efficiencies achieved using South African crushed stone were significantly higher when compared to published results. The 19 mm dolomite aggregate rendered greater load transfer efficiencies than a 50 mm glacial gravel blend commonly used in the USA.

k) The joint shear stiffness (*AGG*) under dynamic loading was approximately 1,5 times that of the *AGG* under static loading on the continuous rubber subbase, and approximately 3 times higher on the discontinuous rubber subbase.

l) The range of shear stiffness per unit length of crack face that could typically be expected from South African aggregates (for crack widths of 0,1 mm to 2,5 mm) under static loading has been established.

During the experiments conducted for this research project, an attempt has been made to reach a better understanding of the intricacies involved in defining the mechanism of aggregate interlock. This mechanism can only be understood adequately if it is borne in mind that normal stress, shear stress, crack width, and shear displacement are all involved. On the other hand, concrete strength, aggregate size, and subbase support also influenced the results.

Tests on cracks subjected to earthquake loading Walraven (1981) showed that there is a considerable difference between the first and the subsequent loading cycles. Irreversible damage to the cement matrix takes place when the hard aggregate particles are pushed into this softer cement matrix. Any new cycle of loading leads to further damage of the crack faces, resulting into steadily increasing values of the shear displacement and the crack width at peak loading. In effect this was also proven during this study. The load applied to induce the crack in the less than 24-hour old concrete can be described as the first loading cycle, during which irreversible damage took place, in other words, during which the crack was formed. Subsequent loading and opening and closing of the crack caused further damage and the dislodging of fine particles that prevented the closing of the crack back to 0,1 mm once it has been pulled open.

Yet, despite this "damage" to the crack faces, the results obtained using the high quality crushed stone found in South Africa were superior to results obtained using USA aggregates. The common practice in South Africa of constructing jointed concrete pavements without dowels at the joints relying on aggregate interlock load transfer only has therefore been vindicated by this study.

The main contribution to the current state of knowledge was the development of a mechanistic equation quantifying the effect of aggregate interlock at a joint/crack in a concrete pavement. This equation has already been included and tested in the CncRisk software package, developed as part of the upgrading of the new mechanistic concrete pavement design manual for Southern Africa.

6.3 RECOMMENDATIONS

Further research is required to confirm up till which crack width aggregate interlock is still active for the larger 37,5 mm coarse aggregate, as the deflection results did not reach an asymptote at a crack width of 2,5 mm.

An aspect that has not been specifically addressed during the present study, was the effect of abrasion or aggregate wear out within the aggregate interlock joint, as little abrasion took place during

application of the 2 million dynamic load cycles at the initial crack width. As mentioned, this was partly due to the little relative vertical movement that could take place in the still "locked-up" state of the crack. Abrasion within the aggregate interlock joint should be established by applying up to 2 million dynamic loads across the crack at different crack widths, and measuring the deterioration in LTE.

The equation developed for the aggregate interlock factor, using data from this research study has already been included and tested in the CncRisk software package, as part of the upgrading of the new mechanistic concrete pavement design manual for Southern Africa, and can be used with confidence. The literature review on dowel modelling has also shown that the theory applied in the software does not need revision. Equation (6.1) does not include slab thickness as a variable, due to the fact that all the experimental slabs were 230 mm thick. It is logical that the shear stress developed at the crack face of a thin concrete slab will be less than the shear stress developed at the crack face of a thick concrete slab. Exactly how slab thickness forms part of the equation will have to be determined through follow-up testing. Another aspect that has been identified is that the erosion model used in the software needs revision. This can also be determined through further research projects.

6.3.1 Follow-up testing

The success of this study has laid the foundation for further testing involving dowel bars, as well as different subbase types to study the effect of erosion.

It is proposed that a test method similar to that used by Snyder (1989) be developed for testing dowel looseness in concrete. Instead of inserting the dowel bars into the concrete afterwards (as was done in the concrete repair study by Snyder (1989)), it should however be cast into the concrete from the start. The dowel should be instrumented with strain gauges on at least three positions inside the embedment length, as well as close to the edge of the concrete, in order to measure the bending moment on the dowel bar. The dowel should be subjected to cyclic loading with complete stress reversal at a frequency of 3 Hz. A method should be devised for measuring the movement in the dowel, and determine after how many load cycles dowel looseness started to develop, as well as the size of the gap created during loading. The method used by Snyder (1989) with a linear variable displacement transducer (LVDT) mounted on an aluminium bracket attached to the face of each specimen and connected to the load collar using a small threaded nylon rod, seems to have been quite successful. This device was used to measure electronically the movement of the load collar and dowel relative to the concrete. In this manner different dowel diameters, as well as specimens with different aggregate types, can be tested.

Erosion of the subbase can be determined by constructing various types of subbases inside a timber box. It is proposed that the same dimensions, namely 230 mm thick, 600 mm wide, and 1 800 mm long concrete beams be cast. The mould for the concrete can be fastened onto the timber, and the concrete

beam with crack inducer and flat bar can be cast on top of it as has been done in the study described in this document. The crack should be induced within 24 hours after casting the concrete. During testing, deflections should be measured with LVDT's on top of the concrete, and at the top and bottom of the subbase. The timber box containing the subbase should be constructed in such a manner that the section beneath the joint/crack in the concrete is visible/accessible from both sides with for example, removable panels. The concrete slab can then be subjected to dynamic loading, as was done during the initial stages of this study. The development of erosion as well as a reflection crack, if any, can then be monitored.

In a test set-up similar to the one used in the research done for this thesis, an eroded subbase can also be simulated by cutting away specific lengths of rubber beneath the leave slab. The effect of "erosion" on aggregate interlock LTE under static and dynamic loading can then be determined.

LIST OF REFERENCES

LIST OF REFERENCES

AASHTO. 1993. *Guide for Design of Pavement Structures*. American Association of State Highway and Transportation Officials. Washington D.C.

American Standard Test Method (ASTM) C39/C39M-01. 2001. *Standard Test Method for Compressive Strength of Cylindrical Concrete Specimens*. West Conshohocken, PA.

American Standard Test Method (ASTM) C133-97. 1997. *Standard Test Methods for Cold Crushing Strength and Modulus of Rupture of Refractories*. West Conshohocken, PA.

American Standard Test Method (ASTM) C426-99. 1999. *Standard Test Method for Linear Drying Shrinkage of Concrete Masonry Units*. West Conshohocken, PA.

American Standard Test Method (ASTM) C469-94e1. 1994. *Standard Test Method for Static Modulus of Elasticity and Poisson's Ratio of Concrete in Compression*. West Conshohocken, PA.

American Standard Test Method (ASTM) D1196-93. 1997. *Standard Test Method for Non-repetitive Static Plate Load Tests of Soils and Flexible Components, for Use in Evaluation and Design of Airport and Highway Pavements*. West Conshohocken, PA.

Barksdale, R.D. 1991. *The Aggregate Handbook.* National Stone Association. Washington D.C.

Benkelman, A.C. 1933. Tests of Aggregate Interlock at Joints and Cracks. *Engineering News Record*, Vol 111, No 8, August, pp 227-232.

Bergan, A.T. and Papagiannakis, A.T. 1984. Axle and Suspension Systems of Heavy Trucks for Minimizing Pavement Distress. *Fourth Conference on Asphalt Pavements for Southern Africa*, Vol. 1, March, pp 177-200.

Bhatti, M.A., Molinas –Vega, I. and Stoner, J.W. 1998. Nonlinear Analysis of Jointed Concrete Pavements. . *Transportation Research Record,* No 1629, TRB National Research Council. National Academy Press, Washington D.C., pp 50-57.

Brill, D.R. and Lee, X. 1999. Three Dimensional Finite Element Modeling of Portland Cement Concrete Airport Pavements Part I: Model Development. *Proceeding of Federal Aviation Administration Worldwide Airport Technology Transfer Conference*. Paper No p281678.

Brill, D.R. and Lee, X. 1999. Three Dimensional Finite Element Modeling of Portland Cement Concrete Airport Pavements Part II: Finite Element Prediction vs Field-Measured Data. *Proceeding of Federal Aviation Administration Worldwide Airport Technology Transfer Conference*. Paper No p291711.

British Standard (BS) 1881: Part 121. 1993. *Method for Determination of Static Modulus of Elasticity in Compression.* British Standard Specification. London. Her Majesty's Stationery Office.

Buch, N. 1998. Factors Affecting Load Transfer Across Transverse Joints in Jointed Concrete Pavements. *Recent Developments in the Design and Specification of Concrete Pavement Systems.* Report No 99/06847, pp 43-64.

Buch, N. and Zollinger, D.G. 1996. Development of Dowel Looseness Prediction Model. *Transportation Research Record,* No 1525, TRB National Research Council. National Academy Press, Washington D.C., pp 21-27.

Channakeshawa, C., Barzegar, F. and Voyiadjis, G. 1993. Non-linear FE Analysis of Plain Concrete Pavement With Doweled Joints. *Journal of Transportation Engineering,* ASCE, Vol 119, No 5, pp763-781.

Chatti, K., Lysmer, J. and Monismith, C.L. 1994. Dynamic Finite-Element Analysis of Jointed Concrete Pavements. *Transportation Research Record,* No 1449, TRB National Research Council. National Academy Press, Washington D.C., pp 79-90.

Coetzee, C.H. 1989. *Evaluation of Different Concrete Pavement Designs with Finite Element Analysis and HVS Testing.* Annual Transportation Convention. Concrete Pavements, Vol 2A, Paper 4.

Colley, B.E. and Humphrey, H.M. 1967. Aggregate Interlock at Joints in Concrete Pavements. *Bulletin 189.* HRB. National Research Council. Washington D.C. pp 1-18.

Darter, M.I. 1977. *Design of Zero-Maintenance Plain Jointed Concrete Pavement.* Vol 1: Development of Design Procedures, Federal Highway Administration.

Das, B.M. 1990. *Principles of Geotechnical Engineering.* 2nd Edition, PWS-Kent. Boston, Ma.

Davids, W.G. 2000. Personal communication and correspondence.

Davids, W.G. and Mahoney, J.P. 1998. *Experimental Verification of Rigid Pavement Joint Loading Transfer Modeling with EverFE.* Department of Civil and Environmental Engineering. Report No 990105. University of Maine. Orono, ME.

Davids, W.G., Turkiyyah, G.M. and Mahoney, J.P. 1998a. *Modeling of Rigid Pavements: Joint Shear Transfer Mechanisms and Finite Element Solution Strategies.* Washington State Department of Transportation. Washington State Transportation Commission Planning and Programming Service Center in Cooperation with the US Department of Transportation Federal Highway Administration. WA-RD 455.1.

Davids, W.G., Turkiyyah, G.M. and Mahoney, J.P. 1998b. EverFE Rigid Pavement Three-Dimensional Finite Element Analysis Tool. *Transportation Research Record,* No 1629, TRB National Research Council, National Academy Press, Washington D.C., pp 41-49.

Dominichini, L. and la Torre, F. 1998. Design of Concrete Pavements on a Non-Uniform Support, *4th International Workshop and Design Theories of Concrete Slabs for Pavements*, Bucaco, Portugal.

Dong, M. and Guo, E. 1999. Pavement Joint and Interface Behavior at the FAA Test Site at Denver Airport. *Proceedings of Federal Aviation Administration Worldwide Airport Technology Transfer Conference.* Paper No p103638.

Du Plessis, H.W. and Freeme, C.R. 1989. *The future of Cement Concrete Pavements for the Year 2000.* Annual Transportation Convention. Concrete Pavements, Vol 2A, Paper 2.

Frabizzio, M.A. and Buch, N.J. 1999. Performance of Transverse Cracking in Jointed Concrete Pavements. *Journal of Performance of Constructed Facilities,* Vol 13, No 4, November, pp 172-180.

Friberg, B.F. 1940. *Design of Dowels in Transverse Joints of Concrete Pavements.* Transactions of the American Society of Civil Engineers, Vol. 105, pp 1076-1095.

Fulton, F.S. 2000. *Fulton's Concrete Technology.* 8th ed. Cement & Concrete Institute, Midrand, South Africa.

Guo, H., Sherwood, J.A. and Snyder, M.B. 1995. Component Dowel-Bar Model for Load-Transfer Systems in PCC Pavements. *Journal of Transportation Engineering*, Vol 121, No 3, pp 289-298.

Hammons, M.I, 1998. Validation of Three-Dimensional Finite Element Modeling Technique for Joints in Concrete Airport Pavements. *Transportation Research Record,* No 1629, TRB National Research Council, National Academy Press, Washington D.C., pp 67-75.

Hammons, M.I. and Ioannides, A.M. 1996. *Developments in Rigid Pavement Response Modelling.* US Army Corps of Engineers. Waterways Experiment Station. Technical Report GL-96-15. Washington D.C.

Hansen, W. 2003. Personal communication.

Haque, E.H., Zaman, M. and Soltaine, A.A. 1998. Cracking Characteristics of Model Continuously Reinforced Concrete Pavements. *Transportation Research Record,* No 1629, TRB National Research Council, National Academy Press, Washington D.C., pp 90-98.

Hilsdorf, H.K. and Kesler, C.E. 1966. *Fatigue Strength of Concrete Under Varying Flexural Stresses.* ACI Journal, Vol 63, No 10.

Hogg, A.H.A. 1938. *Equilibrium of a Thin Plate Symmetrically Loaded Resting on an Elastic Subgrade of Infinite Depth*, Phil. Magazine. 7, Vol 25.

Hossain, M. and Wojakowski, J.B. 1996. Effect of Concrete Mix Consolidation on Joint Faulting and Load Transfer Efficiency. *Transportation Research Record,* No 1544, TRB National Research Council, National Academy Press, Washington D.C., pp 3-8.

Huang, Y.H. 1993. *Pavement Analysis and Design.* Prentice-Hall, Inc. Englewood Cliffs, New Jersey.

Ioannides, A.M. 1990. Dimensional Analysis in NDT Rigid Pavement Evaluation. *Journal of Transportation engineering,* ASCE, Vol 116, No 1, Jan/Feb. pp 23-36.

Ioannides, A.M., Alexander, D.R., Hammons, M.I. and Davis, C.M. 1996. Application of Artificial Neural Networks to Concrete Pavement Joint Evaluation. *Transportation Research Record,* No 1540, TRB National Research Council, National Academy Press, Washington D.C., pp 56-64.

Ioannides, A.M., Davis, C.M. and Weber, C.M. 1999. Westergaard Curling Solution Reconsidered. *Transportation Research Record,* No 1684, TRB National Research Council, National Academy Press, Washington D.C., pp 61-70.

Ioannides, A.M. and Donelly, J.P. 1988. Three-Dimensional Analysis of Slab on Stress-Dependent Foundation.. *Transportation Research Record,* No 1196, TRB National Research Council, National Academy Press, Washington D.C., pp 72-84.

Ioannides, A.M. and Hammons, M.I. 1996. Westergaard-Type Solutions for Edge Load Transfer Problem. *Transportation Research Record,* No 1525, TRB National Research Council, National Academy Press, Washington D.C., pp 28-34.

Ioannides, A.M and Khazanovich, L. 1995. Analytical and Numerical Methods for Multi-Layered Concrete Pavements. *Proceedings Third Interim Workshop on Concrete Pavements*, Krumbach, Austria.

Ioannides, A.M. and Korovesis, G.T. 1990. Aggregate Interlock: A Pure-Shear Load Transfer Mechanism. *Transportation Research Record,* No 1286, TRB National Research Council, National Academy Press, Washington D.C., pp 14-24.

Ioannides, A.M. and Korovesis, G.T. 1992. Analysis and Design of Doweled Slab-on-Grade Pavement Systems. *Journal of Transportation Engineering*. ASCE, Vol 118, No 6, pp745-768.

Ioannides, A.M. Lee, Y.-H. and Darter, M.I. 1990. Control of Faulting Through Joint Load Transfer Design. *Transportation Research Record,* No 1286, TRB National Research Council, National Academy Press, Washington D.C., pp 49-56.

Ioannides, A.M., Thompson, M.R. and Barenberg, E.J. 1985a. Westergaard Solutions Reconsidered. *Transportation Research Record,* No 1043, TRB National Research Council, National Academy Press, Washington D.C., pp 13-23.

Ioannides, A.M., Thompson, M.R. and Barenberg, E.J. 1985b. Finite Element Analysis of Slabs-On-Grade Using a Variety of Support Models. *Proceedings Third International Conference on Concrete Pavement Design and Rehabilitation.* Purdue University, West Lafayette, IN, pp 309-324.

Jensen, E.A. 2001. Mechanism of Load Transfer-Crack Width Relation in JPCP: Influence of Coarse Aggregate Properties. *Proceedings of 7th International Conference on Concrete Pavements*, Session 10. Orlando, Florida.

Jeong, J. and Zollinger, D. 2001. Characterization of Stiffness Parameters in Design of Continuously Reinforced and Jointed Pavements. *Transportation Research Record,* No 1778, TRB National Research Council, National Academy Press, Washington D.C., pp 54-63.

Khazanovich, L. and Ioannides, A.M. 1993. Finite Element Analysis of Slabs-On-Grade Using Improved Subgrade Soil Models. In Airport Pavement Innovations – Theory to Practice, *Proceedings of a Specialty Conference sponsored by the Airfield Pavement Committee.* Air Transport Division, ASCE, Jim W. Hall, Jr., Ed., New York, NY(1993), pp 16-30.

Kuo, C.-M., Hall, K.T. and Darter, M.I. 1996. Three-dimensional Finite Element Model for Analysis of Concrete Pavement Support. *Transportation Research Record.* No 1505, TRB National Research Council, National Academy Press, Washington D.C., pp 119-127.

Lourens, J.P. and Strauss, P.J. 1988. *Meganistiese Ontwerp van Aaneengewapende Betonplaveisels: Fase 1 (Mechanistic Design of Continuously Reinforced Pavements: Phase 1).* Annual Transportation Convention. Concrete Pavements, Vol 4E, Paper 4.

Lourens, J.P. and Strauss, P.J. 2000. *National Route 3 Section 3 Deflections and Strains in Experimental Pavements*, Report to South African National Roads Agency and Cement and Concrete Institute, South Africa.

Majidzadeh, K, and Ilves, E.J. 1983. *Evaluation of Rigid Pavement Overlay Design Procedure, Development of the OAR Procedure.* Final Report DTFH II-9489.

Malan, G.W., Strauss, P.J. and Jordaan, G.J. 1988. *Betonplaveisels: 'n Oorsig van 'n Navorsingsprojek Gemik op die Hersiening van Ontwerp- en Konstruksiemetodes (Concrete Pavements: Review of a Research Project Aimed at the Revision of Design and Construction Methods).* Annual Transportation Convention. Concrete Pavements, Vol 4E, Paper 5.

Manual M10. 1995*: Concrete Pavement Design and Construction.* Department of Transport. Pretoria.

Masad, E., Taha, R. and Muhunthan, B. 1997. Finite-Element Analysis of Temperature Effects on Plain-Jointed Concrete Pavements. *Journal of Transportation Engineering*, Vol 122, No 5, pp 388-398.

Millard, S.G. and Johnson, R.P. 1984. Shear Transfer Across Cracks in Reinforced Concrete Pavement Due to Aggregate Interlock and to Dowel Action. *Magazine of Concrete Research,* Vol 36, No 126, March, pp 9-21.

Millard, S.G. and Johnson, R.P. 1985. Shear Transfer in Cracked Reinforced Concrete. *Magazine of Concrete Research,* Vol 37, No 130, March, pp 3-15.

Mitchell, M.F. 1988. *Concrete Pavements – an Overview.* Annual Transportation Convention. Concrete Pavements, Vol 4E, Paper 1.

Mitchell, M.F., Marais, L. and Freeme, C.R. 1988. *Experience With Concrete Pavements in the Republic of South Africa.* Paper presented to Transportation Research Board Annual Meeting, Washington, January.

N3 Consultants Consortium (N3 HS1 PD). 1999. N3 Toll Road Concession Project, Preliminary Design, Highway Section 1, Cedara to Umgeni River. Vol 1, May.

N3 Consultants Consortium (N3 HS4 PD). 1999. N3 Toll Road Concession Project, Preliminary Design, Highway Section 4, Estcourt to Frere. Vol 1, May.

N3 Consultants Consortium (N3 HS5 PD). 1999. N3 Toll Road Concession Project, Preliminary Design, Highway Section 5, Frere to Keeversfontein. Vol 1, February.

N3 Consultants Consortium (N3 HS4 MI&U). 1999. N3 Toll Road Concession Project, Materials Investigation and Utilisation Report, Highway Section 4, Estcourt to Frere. Vol 6, December.

N3 Consultants Consortium (N3 HS5 PrD). 2001. N3 Toll Road Concession Project, Project Document, Highway Section 5, Frere to Keeversfontein. Vol 6, May.

Nishizawa, T., Koyanagawa, M., Takeuchi, Y. and Kimura, M. 2001. Study on Mechanical Behavior of Dowel Bar in Transverse Joint of Concrete Pavement. *Proceedings of 7th International Conference on Concrete Pavements*. Session 10. Orlando, Florida.

Nordberg Process Machinery Reference Manual. 1983. 2nd Edition. Rexnord Incorporated. Wisconsin, USA.

Oehlers, D.J. 1985. Discussion on: "Millard, S.G. and Johnson, R.P. 1984. Shear Transfer Across Cracks in Reinforced Concrete Pavement Due to Aggregate Interlock and to Dowel Action. *Magazine of Concrete Research,* Vol 36, No 126, March, pp 9-21" . *Magazine of Concrete Research,* Vol 37, No 130, March pp 49-51.

Older, C. 1924. Highway Research in Illinois. *Transactions*, ASCE, Vol 87, Paper 1546, pp 1180-1224.

Papagiannakis, T., Haas, R.C.G., Woodroffe, J.H.F. and Leblanc, P.A. 1988. Effects of Dynamic Loads on Flexible Pavements. *Transportation Research Record.* No 1207, TRB National Research Council, National Academy Press, Washington D.C., pp 187-196.

Parsons, I.D., Eom, I-S. and Hjelmstad, K.D. 1997. Numerical Simulations of Load Transfer Between Doweled Pavement Slabs. *Aircraft Pavement Technology: In the Midst of Change.* ASCE. pp 166-177.

Pittman, D.W. 1996. Factors Affecting Joint Efficiency of Roller-Compacted Concrete Pavement Joints and Cracks. *Transportation Research Record,* No 1525, TRB National Research Council, National Academy Press. Washington D.C. pp 10-20.

Pittman, D.W. 1996. Load Transfer Characteristics of Roller-Compacted Concrete Pavement Joints and Cracks. *Transportation Research Record,* No 1525, TRB National Research Council, National Academy Press. Washington D.C. pp 10-20.

Reinhardt, H.W. and Walraven, J.C. 1982. Cracks in Concrete Subject to Shear. *Journal of the Structural Division,* ASCE, Vol 108, No ST1, pp 207-224.

Sale, J.P. 1977. Rigid Pavement Design for Airfields. *Proceedings First International Conference on Concrete Pavement Design.* Purdue University. West Lafayette, IN.

Sale, J.P. and Hutchinson, R.L. 1959. Development of Rigid Pavement Design Criteria for Military Airfields. *Journal of the Air Transportation Division*, 85(AT3), pp 129-151.

Sargand, S. 1999. Measurement of Dowel Bar Response in Rigid Pavement. *Ohio Research Institute for Transportation and the Environment.* ORITE-1 (FHWA). Ohio.

Skarlatos, M.S. and Ioannides, A.M. 1998. The Theory of Concrete Pavement Joints, *4th International Workshop on Design Theories of Concrete Slabs for Pavements*, Bucaco, Portugal.

Snyder, M.B. 1989. Cyclic Shear Load Testing of Dowels in PCC Pavement Repairs. *Transportation Research Record,* No 1215. TRB National Research Council, National Academy Press, Washington D.C., pp 246-257.

Soroushian, P., Obaseki, K. and Choi, K.-B. 1988. Analysis of Aggregate Interlock Behaviour at Cracks in Reinforced Concrete. . *Magazine of Concrete Research,* Vol 40, No 142, March, pp 9-21.

Sousa, J.B., Lysmer, J., Chen, S. and Monismith, C.L. 1988. Effects of Dynamic Loads on Performance of Asphalt Concrete Pavements. *Transportation Research Record.* No 1207, TRB National Research Council, National Academy Press, Washington D.C., pp 145-168.

South African Bureau of Standards (SABS) 863. 1994. *Compressive Strength of Hardened Concrete.* South African Bureau of Standards. Pretoria.

South African Bureau of Standards (SABS) 864. 1994. *Flexural Strength of Hardened Concrete.* South African Bureau of Standards. Pretoria.

South African Bureau of Standards (SABS) 1085. 1994. *Initial Drying Shrinkage and Wetting Expansion of Concrete.* South African Bureau of Standards. Pretoria.

Stet, M., Van den Bol-de Jong, M.E. and Verbeek, J.-P. 1999. Dutch Standard for Evaluation of Concrete Airfield Pavements. *Proceedings of Federal Aviation Administration Worldwide Airport Technology Transfer Conference.* Paper No p473638.

Steyn, W.J. vd M. and Visser, A.T. 2001. Guidelines for Incorporation of Vehicle-Pavement Interaction Effects in Pavement Design. *Journal of the South African Institution of Civil Engineering*, Vol. 43(1). Paper 495. pp 34-39.

Strauss, P.J. 2001. Personal communication and correspondence.

Strauss, P.J. 1992. *The Evaluation of Performance of Rigid Pavements in South Africa.* by BKS Incorporated for South African Roads Board, Research and Development Advisory Committee. Project Report PR88/215. Pretoria.

Strauss, P.J. and Lourens, J.P. 1998. The Importance of Continuous Slab Support and Load Transfer at Joints in the Performance of Thin Concrete Overlays. *8th International Symposium and Concrete Roads*, Lisbon.

Strauss, P.J., Slavik, M. and Perrie, B.D. 2001. A Mechanistically and Risk Based Design Method For Concrete Pavements in Southern Africa. *Proceedings of 7th International Conference on Concrete Pavements*, Session 3. Orlando, Florida.

Tabatabaie, A.M. and Barenberg, E.J. 1980. Structural Analysis of Concrete Pavement Systems. *Transportation Engineering Journal*, ASCE, Vol 106, No TE5, pp 493-506.

Technical Recommendations for Highways: Draft TRH14 (TRH14). 1985. *Guidelines for Road Construction Materials*. Pretoria.

Technical Recommendations for Highways: TRH4 (TRH4). 1985. *Structural Design of Interurban and Rural Road Pavements*. Pretoria.

Technical Recommendations for Highways: Draft TRH4 (TRH4). 1996. *Structural Design of Flexible Pavements for Interurban and Rural Roads*. Pretoria.

Teller, L.W. and Cashell, H.D. 1958. Performance of Doweled Joints under Repetitive Loading. *Public Roads,* Vol 30, No 1, April, pp 1-24.

Theyse, H.L., De Beer, M. and Rust, F.C. 1996. *Overview of the South African Mechanistic Pavement Design Analysis Method.* CSIR, Divisional Publication DP-96/005, March.

PCA. 1984. *Thickness Design for concrete Highway and Street Pavements*. Portland Cement Association, Skokie, Illinois.

Treybig, H.J. McCullough, B.F. Smith, P. and Von Quintus, H. 1977. *Overlay Design and Reflection Cracking Analysis for Rigid Pavements.* Vol 1, FHWA Report No FHWA-RD-77-76.

Uddin, W., Hackett, R.M., Joseph, A., Pan, Z. and Crowley, A.B. 1996. Three-Dimensional Finite-Element Analysis of Jointed Concrete Pavement Having Discontinuities. *Transportation Research Record.* No 1482, TRB National Research Council, National Academy Press, Washington D.C., pp 26-32.

Vandenbossche, J.M. 1999. Estimating Potential Aggregate Interlock Load Transfer Based on Measurements of Volumetric Surface Texture of Fracture Plane. *Transportation Research Record.* No 1673, TRB National Research Council, National Academy Press, Washington D.C., pp 59-63.

Visser, A., Nothnagel, J.P. and Cilliers, M.J. 1989. *Joint design and installation of liquid sealants in concrete pavements*. Annual Transportation Convention, Concrete Pavements, Vol 2A, Paper 5.

Vuong, B.T., Dash, D.M. and Jameson, G.W. 2001. *Performance of Plain Concrete Pavements Under Accelerated Loading*. APRG Document 01/99 (DA),

Walraven, J.C. 1981. Fundamental Analysis of Aggregate Interlock. *Journal of the Structural Division*, ASCE, Vol 107, No ST11, pp 2245-2270.

Walraven, J.C. 1994. Rough Cracks Subjected to Earthquake Loading. *Journal of Structural Engineering,* Vol 120, No 5, pp 1510-1524.

Wattar, S.W., Hawkins, N. and Barenberg, E. 1999. Aggregate Interlock Behavior of Large Crack Width Concrete Joints. *Proceeding of Federal Aviation Administration Worldwide Airport Technology Transfer Conference.* Paper No p181578.

Westergaard, H.M. 1923. Om Beregning Af Plader Paa Elastisk Underlag Med Sæligt Henblik Pass Ppørgsmaalet Om Spændinger I Betonveje (In Danish). *Ingeniøren*, pp 513-524.

Westergaard, H.M. 1926. Stresses in Concrete Pavements Computed by Theoretical Analysis. *Public Roads*, Vol 7, No 2, pp 25-35.

Westergaard, H.M. 1941. Stresses in Concrete Runways of Airports. *Portland Cement Association*, Chicago. Illinois., pp 1-13.

Westergaard, H.M. 1947. New Formulas for Stresses in Concrete Pavements of Airfields. *American Society of Civil Engineers,* Pavements of Airfields. May, pp 687-701.

Westergaard, H.M. 1948. Professor Westergaard's Formulae for Stresses in Concrete Roads and Runways. *Construction & Engineering,* November, pp 358-360.

Wu, C., Tia, M. and Larsen, T.J. 1993. Analysis of Structural Response of Concrete Pavements Under Critical Thermal Loading Conditions. *Proceedings, Fifth International Conference on Concrete Pavement Design and Rehabilitation.* Purdue University, West Lafayette, IN.

Wu, C.-P. and Shen, P.-A. 1996. Dynamic Analysis of Concrete Pavements Subjected to Moving Loads. *Journal of Transportation Engineering,* Vol 122, No 5, September/October, pp 367-373.

Yoder, E.J. and Witczak, M.W. 1975. *Principles of Pavement Design*. John Wiley. New York.

Zaghloul, Z.M., White, T.D. and Kuzcek, T. 1994. Evaluation of Heavy Load Damage Effect on Concrete Pavements Using Three-Dimensional, Nonlinear Dynamic Analysis. *Transportation Research Record.* No 1449, TRB National Research Council, National Academy Press, Washington D.C., pp 123-133.

Zaman, M. and Alvappillai, A. 1995 Contact-Element Model for Dynamic Analysis of Jointed Concrete Pavements. *Journal of Transportation Engineering*, Vol 121, No 5, pp 425-433.

APPENDIX A: WESTERGAARD SOLUTIONS

APPENDIX A: WESTERGAARD SOLUTIONS

A.1 ACKNOWLEDGEMENT

Ioannides et al (1985a) published the results of a study, during which a thorough re-examination of the Westergaard solutions was conducted, using the tool of finite element analysis (Tabatabaie and Barenberg, 1980). They discussed the form, theoretical background, limitations and applicability of Westergaard's equations, and presented what are considered to be the most accurate versions of his formulae.

In view of the fact that these equations are also largely applicable to this thesis, they are reproduced here for clarity with recognition of the work of Ioannides et al (1985a).

A.2 INTRODUCTION

The pioneering analytical work of Harald Malcolm Westergaard (1888 -- 1950) has been at the heart of slab-on-grade pavement design since the 1920's. Every code of practice since then makes reference to the "Westergaard solutions". These solutions are only available for three particular loading conditions (interior, edge and corner) and assume a slab of infinite or semi-infinite dimensions (Ioannides et al, 1985a).

Westergaard equations have often been misquoted or misapplied. To remedy this situation a re-examination of these solutions using the finite element method has been conducted. The Winkler type subgrade assumed by Westergaard is modelled as a uniform, distributed subgrade through an equivalent mass formation.

A.3 INTERIOR LOADING

This is the case of a wheel load at a "considerable distance from the edges", with pressure "assumed to be uniformly distributed over the area of a small circle with radius a".

Maximum bending stress, σ_i

Ordinary theory $$BSIOT = \{[3P(1+\mu)]/2\pi h^2\}[\ln(2l/a) + 0{,}5 - \gamma] + BSI2OT \quad (1a)$$

Special theory $$BSIST = \{[3P(1+\mu)]/2\pi h^2\}[\ln(2l/b) + 0{,}5 - \gamma] + BSI2ST \quad (1b)$$

For square $$BSISQ = \{[3P(1+\mu)]/2\pi h^2\}[\ln(2l/c') + 0{,}5 - \gamma] + BSI2SQ \quad (1c)$$

Supplementary, σ_2 (ordinary theory) $$BSI2OT = \{[3P(1+\mu)]/64h^2\}[(a/l)^2] \quad (1d)$$

Supplementary, σ_2 (special theory) $$BSI2ST = \{[3P(1+\mu)]/64h^2\}[(b/l)^2] \quad (1e)$$

Supplementary, σ_2 (for square) $$BSI2SQ = \{[3P(1+\mu)]/64h^2\}[(c'/l)^2] \quad (1f)$$

Maximum deflection, δ_i

Circle $$DEFIC = (P/8kl^2)\{1 + (1/2\pi)[\ln(a/2l) + \gamma - 5/4](a/l)^2\} \quad (1g)$$

Where:

P	=	total applied load;
E	=	slab Young's modulus;
μ	=	slab Poisson's ratio;
h	=	slab thickness;
k	=	modulus of subgrade reaction;
a	=	radius of circular load;
c	=	side length of square load;

$l^4 = \{Eh^3/[12(1-\mu^2)k]\}$ which is radius of relative stiffness;

$b = [(1{,}6a^2 + h^2)^{1/2}] - 0{,}675h$ if a < 1,724h

= a if a > 1,724h;

$c' = (e^{\pi/4 - 1}/2^{1/2})c$; and

γ = Euler's constant (= 0,577 215 664 90).

Equation 1b employs Westergaard's "special theory" in which radius b replaces the true radius, a, of the loaded area. This was introduced to account for the effect of shear stresses in the vicinity of the load, which was neglected in the "ordinary theory" of medium-thick plates.

To obtain the interior stress in the case of a square loaded area, radius a is replaced in equation 1c by a constant c', related to the length of the side of the square, c, as follows:

$$c' = \left(e^{\pi/4-1}/2^{1/2}\right)c = 0{,}573804c$$

Westergaard stress values (Equation 1a) agree with finite element results for a loaded area whose side length, c (if square), is about 0,2 times the radius of the relative stiffness, *l*; if the load is circular, its radius, a, must be about 0,1*l*. As (c/*l*) or (a/*l*) increase, finite element stresses become progressively higher than Westergaard's.

A.4 EDGE LOADING

Edge loading is the case in which "the wheel load is at the edge, but at a considerable distance from any corner". The pressure is assumed to be distributed uniformly over the area of a small semi-circle with the centre at the edge".

Maximum bending stress, σ_e

Ordinary theory (semicircle)
$$BSEWOT = 0{,}529(1+0{,}54\mu)(P/h^2)[\log_{10}(Eh^3/ka_2^4) - 0{,}71] \quad (2a)$$

Special theory (semicircle)
$$BSEWST = 0{,}529(1+0{,}54\mu)(P/h^2)[\log_{10}(Eh^3/kb_2^4) - 0{,}71] \quad (2b)$$

"New" formula (circle)
$$BSEIC = [3(1+\mu)P/\pi(3+\mu)h^2]x \{\ln(Eh^3/100ka^4) + 1{,}84 - 4\mu/3 + [(1-\mu)/2] + 1{,}18(1+2\mu)(a/l)\} \quad (2c)$$

"New" formula (semi-circle)
$$BSEIS = [3(1+\mu)P/\pi(3+\mu)h^2]x \{\ln(Eh^3/100ka_2^4) + 3{,}84 - 4\mu/3 + 0{,}5(1+2\mu)(a_2/l)\} \quad (2d)$$

Simplified "new" formula (semi-circle)
$$BSELS = (-6P/h^2)(1+0{,}5\mu)[0{,}489\log_{10}(a_2/l) - 0{,}091 - 0.027(a_2/l)] \quad (2e)$$

Simplified "new" formula (circle)
$$BSELC = (-6P/h^2)(1+0{,}5\mu)[0{,}489\log_{10}(a/l) - 0{,}012 - 0.063(a/l)] \quad (2f)$$

Maximum deflection, δ_e

Original formula $DEFEW = (1/6^{1/2})(1+0,4\mu)(P/kl^2)$ (2g)

"New" formula $DEFEIC = (\{P[(2+1,2\mu)^{1/2}]\}/[(Eh^3k)^{1/2}])[1-(0,76+0,4\mu)(a/l)]$ (2h)
(circle)

"New" formula $DEFEIS = (\{P[(2+1,2\mu)^{1/2}]\}/[(Eh^3k)^{1/2}])[1-(0,323+0,17\mu)(a_2/l)]$ (2i)
(semi-circle)

Simplified "new" $DEFELS = (1/6^{1/2})(1+0,4\mu)(P/kl^2)[1-0,323(1+0,5\mu)(a_2/l)]$ (2j)
formula (semi-circle)

Simplified "new" $DEFELC = (1/6^{1/2})(1+0,4\mu)(P/kl^2)[1-0,76(1+0,5\mu)(a/l)]$ (2k)
formula (circle)

Where:

a_2 = radius of semi-circle

b_2 = $[(1,6a_2+h^2)^{1/2}]-0,675h$ if $a_2 < 1,724h$

= a_2 if $a_2 > 1,724h$ and other symbols are as defined for Equations 1.

Edge stresses calculated from the "new" formula are considerably different from those computed using the original formula. The "new" formulas typically lead to stresses 55% higher and deflections 8% lower than the values obtained using the original formulas. The semi-circular load is more severe than the circular load, because the centre of gravity of the circle is further toward the interior of the slab than is that of the semi-circle.

A.5 CORNER LOADING

Of the three fundamental cases of loading investigated by Westergaard, corner loading is undoubtedly the most obscure and debatable.

Deflection

$\delta_c = (P/kl^2)[1,1-0,88(a_1/l)]$ *Westergaard, 1926* (3a)

Stress

$$\delta_c = (3P/h^2) \qquad \textit{Goldbeck, Older} \qquad (3b)$$

$$\delta_c = (3P/h^2)[1-(a_1/l)^{0,6}] \qquad \textit{Westergaard} \qquad (3c)$$

$$\delta_c = (3P/h^2)[1-(a/l)^{0,6}] \qquad \textit{Bradbury} \qquad (3d)$$

$$\delta_c = (3P/h^2)[1-(a_1/l)^{1,2}] \qquad \textit{Kelly, Teller and Sutherland} \qquad (3e)$$

$$\delta_c = (3{,}2P/h^2)[1-(a_1/l)] \qquad \textit{Spangler} \qquad (3f)$$

$$\delta c = (4{,}2P/h2)(1-\{[(a/l)^{1/2}]/[0{,}925+0{,}22(a/l)]\}) \qquad \textit{Pickett} \qquad (3g)$$

Distance to point of maximum stress along corner bisector

$$X_1 = 2[(a_1/l)^{1/2}] \qquad \textit{Westergaard, 1926} \qquad (3h)$$

Where:

a = radius of circular load tangent to both edges at corner and

a_l = distance to point of action resultant along corner angle bisector

= $(2^{1/2})$a. (See Equations 1 for other symbols)

A.5.1 EQUATIONS FOR THE CORNER LOADING CONDITION BASED ON THE FINITE ELEMENT METHOD

A straight line may be used to describe *corner deflections,* δ_c. This line has the following equation:

$$\delta_c = (P/kl^2)[1{,}205 - 0{,}69(c/l)] \qquad (4)$$

Where c is the side length of square loaded area. The finite element results obtained are typically 10% higher than those predicted by Westergaard.

The ILLI-SLAB maximum *corner stresses,* σ_C, curve fitting suggested the following equation:

$$\sigma_C = (3P/h^2)[1{,}0-(c/l)^{0,72}] \qquad (5)$$

A.5.2 LOCATION OF MAXIMUM STRESS

The curve fitting equation obtained by extrapolation of the results from a selected number of ILLI-SLAB runs for the location of the *maximum stress,* X_l, is as follows:

$$X_1 = 1{,}80c^{0{,}32}l^{0{,}59} \qquad (6)$$

This equation indicates that the influence of the radius of relative stiffness, l, is much greater than that of the size of the loaded area.

A.5.3 SLAB SIZE REQUIREMENTS FOR CORNER LOADING WESTERGAARD RESPONSES

Ioannides, Thompson and Barenberg (1985) determined the slab size requirements for Westergaard responses based on the finite element method, as summarised in Table A.1.

Table A.1: Slab size requirements for Westergaard responses based on the finite element method

Load Placement	(*L*/*l*) Values for	
	Maximum Deflection	Maximum Bending Stress
Interior	8,0	3,5
Edge	8,0	5,0
Corner	5,0	4,0

Note: L = least slab dimension and *l* = radius of relative stiffness

APPENDIX B: WESTERGAARD-TYPE SOLUTION FOR EDGE LOAD TRANSFER PROBLEM

APPENDIX B: WESTERGAARD-TYPE SOLUTION FOR EDGE LOAD TRANSFER PROBLEM

B.1 ACKNOWLEDGEMENT

During an examination of the archives of the U.S. Army Engineer Waterways Experiment Station, Ioannides and Hammons (1996) discovered a report that Westergaard submitted to the Corps of Engineers in 1949. This report contained a detailed examination of the edge load transfer problem, prepared by Westergaard's associate, M.S. Skarlatos. The result of an investigation that sought to extend and refine the edge load transfer solution by Skarlatos, using modern computational tools were presented by Ioannides and Hammons in 1996. They followed the same approach as Skarlatos and Westergaard, by deriving closed-form equations for the maximum deflection and bending stress occurring on the unloaded side of an edge capable of load transfer.

The general solution for edge load transfer formulas is reproduced here for clarity with recognition to Ioannides and Hammons (1996). To quote the authors: "the formulas derived in this study constitute a complete solution of the edge load transfer problem, recognised over the years as a critical consideration in the PCC pavement design."

B.2 GENERAL SOLUTION FOR EDGE LOAD TRANSFER

B.2.1 SKARLATOS FORMULAS

The deflection at the origin of the coordinates (0,0) on the unloaded side of a joint due to a point load, P, applied at (x, y) is given by:

$$\Delta_U^* = \frac{\Delta_U k l^2}{P} = \frac{4}{\pi}\int_0^\infty \frac{\gamma^2}{F(4\gamma + F/f)} \times \cos\frac{\alpha x}{l}\left(\cos\frac{\beta y}{l} + \kappa \sin\frac{\beta y}{l}\right) e^{-\gamma y/l} d\alpha \tag{B.1}$$

Where:

$$\kappa = (1-\mu)\alpha^2 \tag{B.2}$$

$$F = 1 + 4\kappa\gamma^2 - \kappa^2 \tag{B.3}$$

$$\beta = \sqrt{\frac{1}{2}\left(\sqrt{1+\alpha^4} - \alpha^2\right)} = \frac{1}{2\gamma} \tag{B.4}$$

$$\gamma = \sqrt{\frac{1}{2}\left(\sqrt{1+\alpha^4} + \alpha^2\right)} = \sqrt{\alpha^2 + \beta^2} \tag{B.5}$$

$$f = \frac{q_0}{kl} = \frac{AGG}{kl} \tag{B.6}$$

Equation B.6 defines a dimensionless joint stiffness, f, in terms of the slab-subgrade radius of relative stiffness, l; the subgrade modulus, k; and parameter q_0, referred to as spring constant AGG. Parameter q_0 has dimensions of FL^{-2} and represents the force transferred across a unit length of joint per unit differential deflection across the joint. The slab Poisson's ratio is denoted by μ. The x-axis runs along the joint, while the y-axis is perpendicular to the joint and is positive in the direction of the loaded slab. Accordingly, determination of the dimensionless deflection, Δ_U*, for a loaded area of finite size involves a triple integral in dx, dy and $d\alpha$, the latter being a dummy integration variable (see Figure B.1).

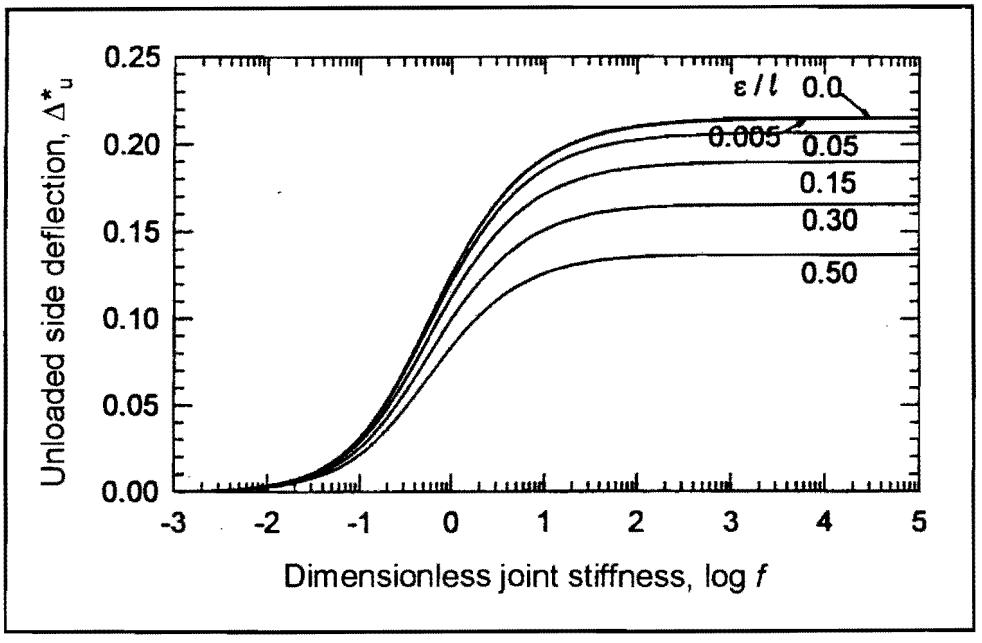

Figure B.1: Variation of maximum dimensionless deflection for unloaded side with dimensionless joint stiffness and dimensionless load size ratio

Similarly, according to Skarlatos, the bending stress at the origin of the coordinates (0,0) on the unloaded side of a joint due to a point load, P, applied at x, y is given by:

$$\sigma_{tl}^{*} = \frac{\sigma_{tl} h^2}{P} = \frac{24(1-\mu^2)}{\pi} \int_0^{\infty} \frac{\alpha^2 \gamma^2}{F(4\gamma + F/f)} \cos\frac{\alpha x}{l} \left(\cos\frac{\beta y}{l} + \kappa \sin\frac{\beta y}{l} \right) e^{-\gamma y/l} d\alpha \tag{B.7}$$

Here, h denotes the thickness of the slab. Proceeding as outlined above for the unloaded deflection, and setting the slab Poisson's ratio, μ, to 0,15, the curves in Figure B.2 were obtained.

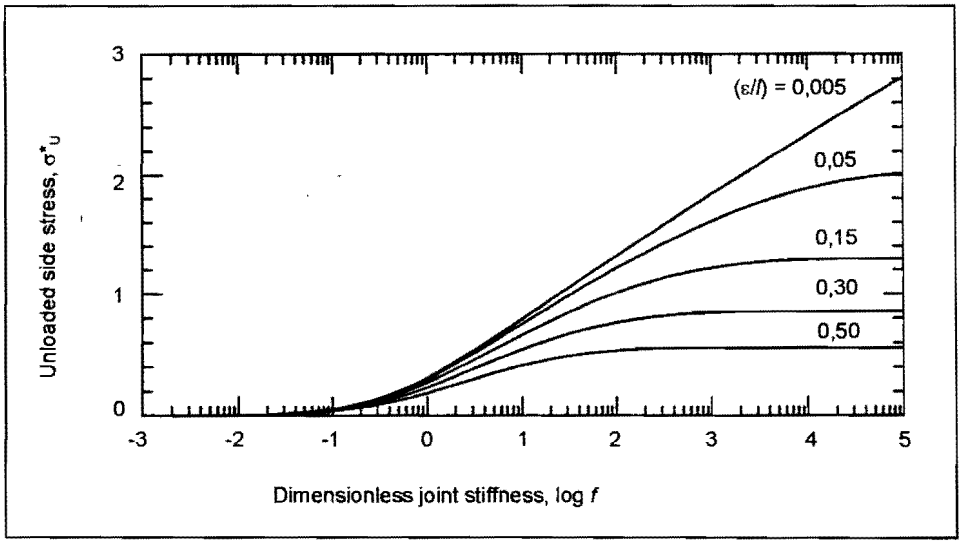

Figure B.2: Variation of maximum dimensionless bending stress for unloaded side with dimensionless joint stiffness and dimensionless load size ratio

For a slab resting on a dense liquid foundation and equipped with a pure-shear load transfer mechanism, the corresponding responses on the loaded side can be obtained as follows:

$$\Delta_L = \Delta_f - \Delta_U \tag{B.8}$$

and

$$\sigma_L = \sigma_f - \sigma_U \tag{B.9}$$

Where Δ_f and σ_f are the maximum responses of a free edge. Equations for the latter integral form were given by Westergaard (1947), as follows:

$$\Delta_f^* = \frac{\Delta_f k l^2}{P} = \frac{2}{\pi}\int_0^\infty \frac{\gamma}{F}\cos\frac{\alpha x}{l}\left(\cos\frac{\beta y}{l} + \kappa \sin\frac{\beta y}{l}\right)e^{-\gamma y/l}d\alpha \tag{B.10}$$

and

$$\sigma_f^* = \frac{\sigma_f h^2}{P} = \frac{12(1-\mu^2)}{\pi}\int_0^\infty \frac{\alpha^2\gamma}{F}\cos\frac{\alpha x}{l}\left(\cos\frac{\beta y}{l} + \kappa\sin\frac{\beta y}{l}\right)e^{-\gamma y/l}d\alpha \qquad \text{(B.11)}$$

In this case, the y-axis is perpendicular to the joint and is positive in the direction of the loaded slab. The results are shown in Figures B.3 and B.4, where they are compared to Westergaard's (1948) for a circular load, radius *a*. Such direct application of Westergaard's circular load formulas can lead to errors of up to 8 percent for the loaded area sizes considered.

B.2.2 INTERPOLATION FORMULAS

B.2.2.1 Free edge deflection

The Westergaard formula for the deflection at the origin of coordinates due to a distributed load placed tangentially to a free edge with its centroid located at a distance $\bar{y}$ from the free edge:

$$\Delta_f^* = \frac{\Delta_f k l^2}{P} = \left[B_3 - B_4\left(\frac{\bar{y}}{l}\right)\right] \qquad \text{(B.12)}$$

In this expression B_3 and B_4 are dimensionless constants dependent only on the value of the slab Poisson's ratio, μ. For a circular load, radius *a* simply replaces centroidal distance $\bar{y}$ (and by ε for a square load). Equation B.12 represents the Taylor series for the complete solution, with only the linear term retained. By considering the deflection and slope at the origin due to a point load at the same location, and setting μ = 0,15, Westergaard evaluated B_3 and B_4 as 0,4314 and 0,3510, respectively. For other values of μ, he provided the following interpolation formulas for the two constants:

$$B_3 = \frac{\sqrt{2+1{,}2\mu}}{\sqrt{12(1-\mu^2)}} \qquad \text{(B.13)}$$

$$\frac{B_4}{B_3} = 0{,}76 + 0{,}4\mu \qquad \text{(B.14)}$$

A better approximation to the complete solution for a square load may be obtained by adding a quadratic term to Equation B.12:

$$\Delta_f^* = \frac{\Delta_f k l^2}{P} = \left[B_3 - B_4\left(\frac{\varepsilon}{l}\right) + \frac{1}{2}B_6\left(\frac{\varepsilon}{l}\right)^2\right] \qquad \text{(B.15)}$$

With μ = 0,15, B_6 should be set to 0,1305.

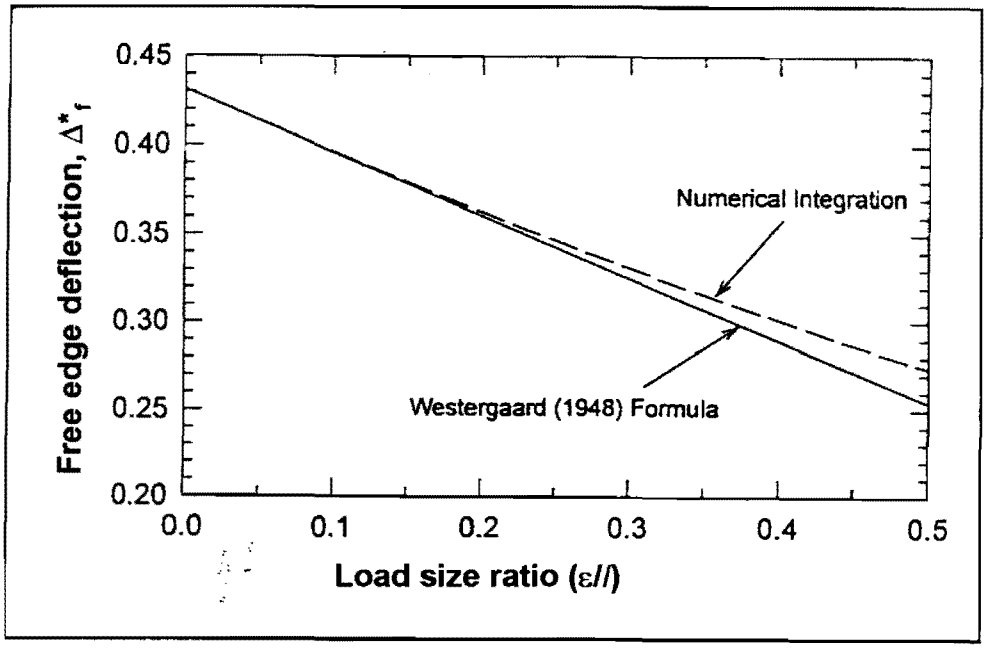

Figure B.3: Variation of maximum dimensionless deflection for free edge with dimensionless load size ratio

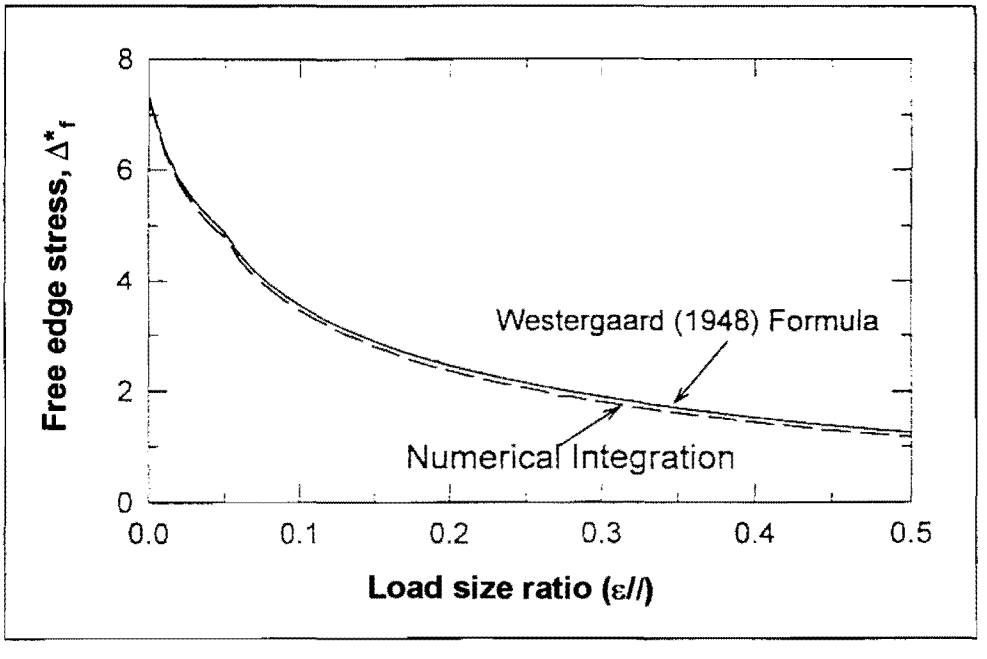

Figure B.4: Variation of maximum dimensionless bending stress for free edge with dimensionless load size ratio

B.2.2.2 Free edge bending stress

Because of a singularity in Equation B.11, Westergaard split into two parts the bending stress arising at the origin of coordinates under the action of a tangential distributed load area:

$$\sigma_f = \overline{\sigma} + \sigma_c \tag{B.16}$$

Westergaard wrote the first term in Equation B.16 as:

$$\overline{\sigma}^* = \frac{\overline{\sigma} h^2}{P} = \frac{12(1+\mu)}{\pi(3+\mu)}\left[0{,}1159 + K + \frac{1-\mu}{4}S\right] \tag{B.17}$$

For a circular load, radius a:

$$K = -\log_e\left(\frac{a}{l}\right) \tag{B.18}$$

and

$$S = \frac{1}{2} \tag{B.19}$$

As for the second term in equation B.16, Westergaard again expressed it in terms of a Taylor series, retaining only the linear term:

$$\sigma_c^* = \frac{\sigma_c h^2}{P} = \frac{12((1+\mu)}{\pi(3+\mu)}\left[\frac{3-\mu}{4} - B_1 + B_2\left(\frac{a}{l}\right)\right] \tag{B.20}$$

For $\mu = 0{,}15$, Westergaard obtained $B_1 = 0{,}9544$ and $B2 = 0{,}3822$. In adapting this solution for a square load, Westergaard's first term was retained (Equations B.17, B.18, and B.19, with a replaced by ε), but quadratic and cubic terms were added to Equation B.20.

$$\sigma_c^* = \frac{\sigma_c h^2}{P} = \frac{12((1+\mu)}{\pi(3+\mu)}\left[\frac{3-\mu}{4} - B_1 + B_2\left(\frac{a}{l}\right) + \frac{1}{2}B_9\left(\frac{\varepsilon}{l}\right)^2 + \frac{1}{6}B_{10}\left(\frac{\varepsilon}{l}\right)^3\right] \tag{B.21}$$

For $\mu = 0{,}15$, $B_9 = -4{,}225$ and $B_{10} = 24{,}12$.

B.2.2.3 Unloaded side deflection

The deflection of the unloaded side is as follows:

$$\Delta_U^* = \frac{\Delta_U k l^2}{P} = \left[B_3' - B_4' \left(\frac{\varepsilon}{l} \right) \right] \tag{B.22}$$

Where

$$B_3' = \frac{4}{\pi} \int_0^\infty \frac{\gamma^2}{F(4\gamma + F/f)} d\alpha \tag{B.23}$$

and

$$B_4' = \frac{2}{\pi} \int_0^\infty \frac{\gamma^2 (2\gamma^2 - \kappa))}{F(4\gamma + F/f)} d\alpha \tag{B.24}$$

The following regression equations were derived for the B coefficients, retaining the functional forms first suggested by Skarlatos:

$$B_3' = \frac{f - 0{,}6367 \log(1+f)}{4{,}6516 f + 1{,}8210} \tag{B.25}$$

and

$$\frac{B_4'}{B_3'} = 0{,}6984 + 0{,}0441 \log(1+f) - 0{,}0065 f^{0{,}24} \tag{B.26}$$

Substituting Equations B.25 and B.26 into Equation B.22 and rounding off the regression coefficient leads to:

$$\Delta_U^* = \frac{\Delta_U k l^2}{P} = 0{,}215 \left[\frac{f - 0{,}6 \log(1+f)}{f + 0{,}4} \right] * \left\{ 1 - 0{,}7 \left(\frac{\varepsilon}{l} \right) \left[1 + 0{,}06 \log(1+f) - 0{,}01 f^{0{,}2} \right] \right\} \tag{B.27}$$

The predictive ability of Equation B.27 deteriorates slightly as ε/l and f increase. For $\varepsilon/l = 0{,}5$, the ratio of the (predictive/exact) values of Δ_U ranges between 0,91 and 0,99 for log f values between –3 and 5. Equation B.27 affords approximately the same precision as direct application of the free edge deflection equation given by Westergaard. By analogy to Equation B.15, a quadratic term is added to Equation B.22 as follows:

$$\Delta_U^* = \frac{\Delta_U k l^2}{P} = \left[B_3' - B_4' \left(\frac{\varepsilon}{l} \right) + \frac{1}{2} B_6' \left(\frac{\varepsilon}{l} \right)^2 \right] \tag{B.28}$$

Where:

$$B_6' = \frac{1}{\pi} \int_0^\infty \frac{-1 + 4\gamma^4 - 4\gamma^2 \kappa}{F(4\gamma + F/f)} d\alpha \tag{B.29}$$

The integral in Equation B.29 was evaluated for $\mu = 0{,}15$ and for $\log f$ ranging between –3 and 5. Results were fitted with a regression algorithm. The choice of algorithm was guided by the desire to keep the number of regression coefficients to a minimum. The resulting relationship was:

$$\begin{aligned} B_6' = {} & (0{,}01945 + 0{,}009348 \log f - 0{,}002093 \log^2 f - 0{,}001086 \log^3 f) \\ & \div (1 - 0{,}1474 \log f + 0{,}2666 \log^2 f - 0{,}02004 \log^3 f) \end{aligned} \tag{B.30}$$

The functional form in Equation B.30 was then added to Equation B.27 as suggested by Equation B.28. In this manner the following simplified expression was obtained:

$$\Delta_U^* = \frac{1}{2} [0{,}015 + 0{,}005 \log f] \left(\frac{\varepsilon}{l} \right)^2 \tag{B.31}$$

B.2.2.4 Unloaded side bending stress

Retaining only the linear term in the Taylor series expansion for the unloaded side bending stress results in:

$$\sigma_U^* = \frac{\sigma_U h^2}{P} = \frac{24(1-\mu^2)}{\pi} \left[B_1' - B_2' \left(\frac{\varepsilon}{l} \right) \right] \tag{B.32}$$

Where:

$$B_1' = \int_0^\infty \frac{\alpha^2 \gamma^2}{F\left(4\gamma + \frac{F}{f}\right)} d\alpha \tag{B.33}$$

and

$$B_2' = \frac{1}{2} \int_0^\infty \frac{\alpha^2 \gamma (2\gamma^2 - \kappa)}{F\left(4\gamma + \frac{F}{f}\right)} d\alpha \tag{B.34}$$

The integrals in Equations B.33 and B.34 were evaluated for $\mu = 0,15$ and for values of $\log f$ ranging between –3 and 5. The following regression equations for the B coefficients in Equation B.32 were derived, retaining the functional forms first suggested by Skarlatos:

$$B_1' = 0,03316 + 0,07205\log(1+f) + \frac{0,00773\sqrt{f} - 0,03360}{f+1} \tag{B.35}$$

and

$$\frac{B_2'}{B_1'} = \left[0,08281f + 0,4790 - \frac{0,000149}{f}\right]^{\frac{1}{4,209}} \tag{B.36}$$

Substituting Equations B.35 and B.36 into Equation B.32 leads (upon rounding off the regression coefficients) to:

$$\sigma_U^* = \frac{\sigma_U h^2}{P} = 0,54\left[0,42 + \log(1+f) + 0,1\frac{\sqrt{f} - 4,2}{f+1}\right] * \left[1 - 0,54\left(\frac{\varepsilon}{l}\right)^{\sqrt[4,1]{f+5,0}}\right] \tag{B.37}$$

The predictive ability of Equation B.37 deteriorates rapidly as f increases to over 10, especially for $(\varepsilon/l) > 0,3$. To address this limitation, a second-order term in the Taylor expansion for σ_U^* was derived in the study, expanding Equation B.32 to:

$$\sigma_U^* = \frac{\sigma_U h^2}{P} = \frac{24(1-\mu^2)}{\pi}\left[B_1' - B_2'\left(\frac{\varepsilon}{l}\right) - \frac{1}{2}B_9'\left(\frac{\varepsilon}{l}\right)^2\right] \tag{B.38}$$

Where:

$$B_9' = \int_0^{\infty} \frac{\alpha^2\gamma^2(\gamma^2 - \beta^2 - \kappa)}{F\left(4\gamma + \frac{F}{f}\right)} d\alpha \tag{B.39}$$

The integral in Equation B.39 was evaluated for the case $\mu = 0,15$ and for values of $\log f$ ranging from –3 to 5. The following regression equation was derived for coefficient B_9':

$$B_9' = \log^{-1}[0,6671\log f - 1,6570] \tag{B.40}$$

Proceeding as outlined above for the unloaded side deflection, the following simplified equation is derived for the quadratic bending stress increment $\sigma_U^{*'}$ to be added to Equation B.37:

$$\sigma_U^{*'} = 7,5\log^{-1}[0,74\log f - 1,94] * \frac{1}{2}\left(\frac{\varepsilon}{l}\right)^2 \tag{B.41}$$

It is recommended that the increment in Equation B.41 be used for $f > 10$, subject to the constraint that the resulting unloaded side stress not exceed half the corresponding free edge stress for the case considered.

B.2.3 LOAD TRANSFER EFFICIENCY

Figures B.5 and B.6 illustrate the load transfer efficiencies with respect to deflection, LTE_{Δ}, and with respect to stress, LTE_{σ}, with the dimensionless joint stiffness, f or (AGG/kl), and the dimensionless loaded area size, ε/l The load transfer definitions for deflection and stress, respectively, are:

$$LTE_{\Delta} = \frac{\Delta_U}{\Delta_L} \tag{B.42}$$

and

$$LTE_{\sigma} = \frac{\sigma_U}{\sigma_L} \tag{B.43}$$

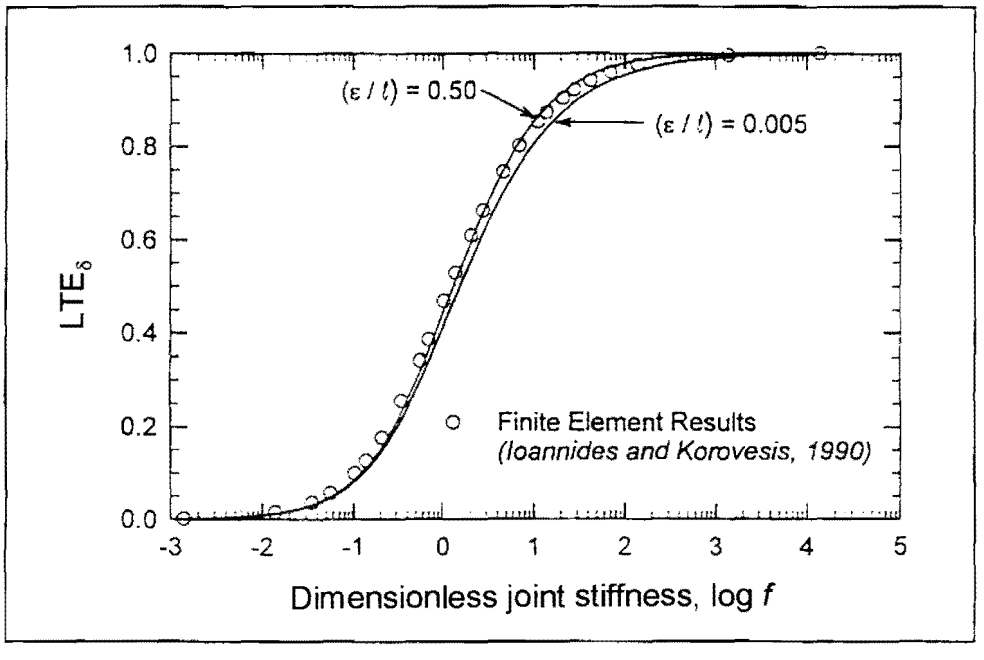

Figure B.5: Variation of load transfer efficiency with respect to deflection with dimensionless joint stiffness and dimensionless load size ratio

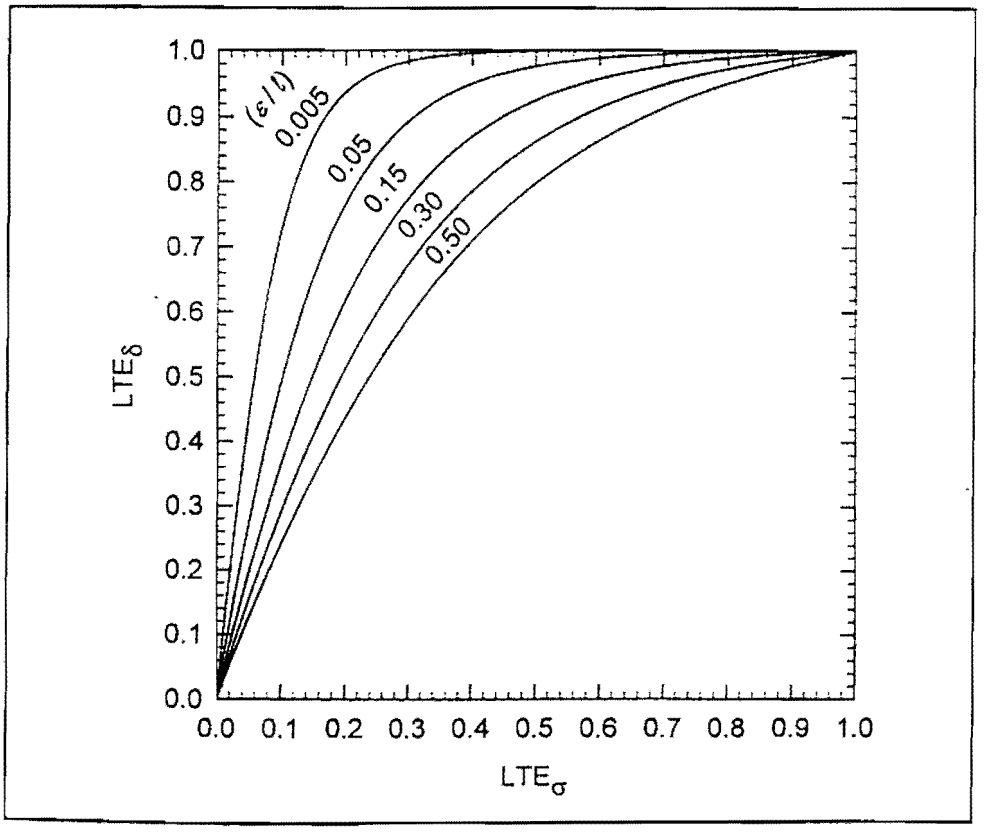

Figure B.6: Relationship between load transfer efficiencies with respect to deflection and stress for various dimensionless load size ratios

Figures B.5 and B.6 confirm the observations that LTE_Δ is rather insensitive to ε/l, where as the sensitivity of the relationship between these two efficiencies to ε/l is quite pronounced. The improvement achieved using the solution by Skarlatos and modern computational tools is clearly discernible in Figure B.7, in which the newly derived LTE_Δ versus LTE_σ relationships for two extreme load size ratios are compared with earlier finite element results.

Non-linear regression was used to develop an expression for LTE_Δ as a function of the dimensionless joint stiffness, f, and of the dimensionless load size ratio, ε/l. Assuming a linear variation with ε/l, the resulting relationship was as follows:

$$LTE_\Delta = \frac{1}{1+\log^{-1}\left[\dfrac{0{,}214-0{,}183\left(\dfrac{\varepsilon}{l}\right)-\log f}{1{,}180}\right]} \qquad \text{(B.44)}$$

(R^2 = 1,0)

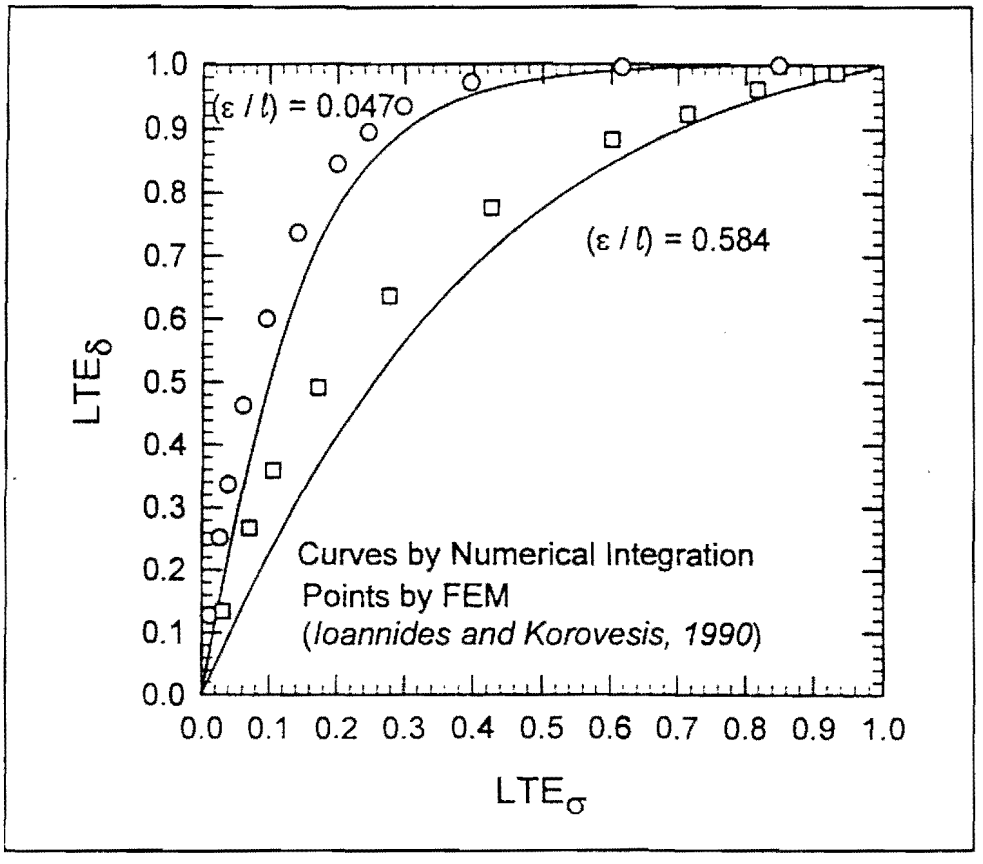

Figure B.7: Comparison of newly derived solution with earlier finite element results

Likewise, non-linear regression was used to develop an expression for LTE_Δ as a function of LTE_σ and of ε/l. The regression formula obtained in this fashion was:

$$LTE_\Delta = \frac{\left[1206\left(\frac{\varepsilon}{l}\right)+377\right]LTE_\sigma^2 - 393\left(\frac{\varepsilon}{l}\right)LTE_\sigma^3}{1+689\left(\frac{\varepsilon}{l}\right)LTE_\sigma + \left[370-154\left(\frac{\varepsilon}{l}\right)\right]LTE_\sigma^2} \qquad \text{(B.45)}$$

($R^2 = 0{,}999$)

APPENDIX C: DOWEL MODELLING

TABLE OF CONTENTS

LIST OF FIGURES

LIST OF SYMBOLS

a, b, c	Constants for a particular value of f_r ($0{,}05 < f_r < 0{,}065$)
β	Relative stiffness of dowel/concrete system
c	Dowel bar radius
d	Diameter of dowel bar
Δ_S	Shear displacement across crack
Δ_X	Local bond slip
η_{shear}	Shear load transfer efficiency (range 0 – 1)
E_d	Modulus of elasticity of dowel
E_s	Modulus of elasticity of steel
$\varepsilon_b, \varepsilon_t$	Strain at bottom and top of dowel
F_d	Dowel force
F_{du}	Ultimate dowel shear force
f_{cu}	Ultimate compressive strength of concrete cube
f_y	Yield stress of reinforcing steel
G_f	Specific gravity of foundation

I_d	Moment of inertia of the dowel
k	Modulus of subgrade reaction
K	Modulus of dowel support
K_i	Initial shear stiffness of dowel bar
M_P	Plastic moment capacity of dowel bar
M_z	Bending moment
P	Total load applied
σ_b	Bearing stress of concrete
σ_d	Maximum stress in dowel bar
τ_x	Local bond stress
V_{dowel}	Shear force transferred across the gap through the dowel bar
V_{slab}	Shear force transferred through a continuous slab

APPENDIX C: DOWEL MODELLING

C.1 DOWEL MODELLING

C.1.1 INTRODUCTION

The essence of the literature review on dowel modelling has been presented in Chapter 2. However, in order not to cloud the issue, some of the analytical and finite element (FE) studies that have merit are summarised here.

C.1.2 ANALYTICAL DOWEL MODELLLING

C.1.2.1 Millard and Johnson (1984)

In an attempt to study the internal mechanisms of shear transfer and dowel action across a single crack to enable more accurate modelling of shear stiffness, Millard and Johnson (1984) *devised tests of a new type* to examine independently the aggregate interlock (see paragraph 2.5) and dowel action effects in reinforced concrete.

Aggregate interlock action was eliminated from the *dowel action* specimens (2 / 300 mm high x 225 mm wide x 100 mm thick rectangular concrete prisms) by the construction of a smooth, low-friction crack passing through the centre of the specimen. This was achieved by casting each specimen in two stages. The first half was cast against a flat steel plate positioned across the centre of the mould. After 24 hours this plate was removed and the exposed face covered with two layers of thin polythene sheeting. The remainder of the specimen was then cast against this sheeting. Each reinforcing bar cast into the dowel action specimens was fitted with two strain gauges at the location of the crack to measure the axial and flexural strains.

In theoretical dowel action models, it has been suggested that there are three mechanisms of shear transfer through dowel action, namely: direct shear, kinking, and flexure of the dowel bars. If the concrete supporting each bar were considered to be rigid, the first two mechanisms would predominate, however, significant deformation of the concrete does occur, so that flexure of the dowel bar within the concrete is the principal action. This has been modelled by considering the dowel bar as a beam on an elastic foundation. The dowel force, F_d is given by:

$$F_d = 0{,}166\Delta_s G_f^{0{,}75} d^{1{,}75} E_s^{0{,}25} \qquad \text{(C.1)}$$

Where the constant term is dimensionless, and:

Δ_s = Shear displacement across the crack (mm);

G_f = Specific gravity of foundation;

d = Diameter of the bar (mm); and

E_s = Elastic modulus of steel (MPa).

However, the high stress concentration in the concrete supporting the bar results in a non-linear behaviour, so that only the initial dowel stiffness can be predicted using Equation (C.1).

The softening of the concrete supporting the dowel bar results in a redistribution of the reactions, so that the maximum bending moment in the bar moves away from the crack location. Failure occurs either by tensile splitting of the concrete or when the bar reaches its ultimate bending moment. In the latter case the plastic moment is given by:

$$M_p = \frac{1}{6} f_y d^3 \tag{C.2}$$

Where:

f_y = Yield stress of reinforcing steel (MPa).

A study of the internal equilibrium required to produce this moment gave the ultimate dowel force, as:

$$F_{du} = 1{,}30 d^2 f_y^{0,5} f_{cu}^{0,5} \tag{C.3}$$

Where:

f_{cu} = Compressive cube strength for concrete (MPa).

The presence of an axial tensile force in a dowel bar has been shown to reduce the shear stiffness. It is presumed that this is due to localised damage to the concrete adjacent to the bar. However, a tensile force will also cause a reduction in M_p, so that the ultimate dowel force would also be expected to diminish.

Equation (C.3) can predict the ultimate shear force in a dowel bar quite accurately, for specimens without axial tension. For a dowel bar with an axial force of αf_y, Equation (C.2) is modified to:

$$M_p = \frac{1}{6} d^3 f_y (1 - \alpha^2) \tag{C.4}$$

Consequently, Equation (C.3) becomes:

$$F_{du} = 1{,}30 d^2 f_{cu}^{0,5} \{ f_y (1 - \alpha^2) \}^{0,5} \tag{C.5}$$

Which predicts the ultimate dowel force quite closely.

An exponential function was selected to describe the over-all dowel action behaviour. Millard and Johnson (1984) experienced that the actual deterioration of the concrete beneath the reinforcement and the resulting redistribution of internal forces was too complex to permit realistic analytical modelling, and therefore assumed that the dowel force was given by:

$$F_d = F_{du}\left(1 - \exp\left\{-K_i\Delta_s / F_{du}\right\}\right) \tag{C.6}$$

Where:

F_{du} = Ultimate dowel force given by Equation (C.5); and

K_i = Initial dowel stiffness given by Equation (C.1).

The dowel action test results showed that increasing the diameter of the reinforcement resulted in higher shear stiffness and ultimate stress. There was also an increasing tendency for the smooth crack to widen, although this was much less than observed in the aggregate interlock tests. The specimens were cut open after testing to expose the faces of the cracks. This revealed a splitting failure crack in those specimens with 12 mm or 16 mm diameter bars, but also that there was more spalling associated with the larger dowel bars.

C.1.2.2 Millard and Johnson (1985)

In their previous study Millard and Johnson (1984) investigated the shear transfer across cracks in reinforced concrete due to aggregate interlock and to dowel action. Separate specimens were prepared for aggregate interlock testing (see Chapter 2) and for dowel action testing. In this follow-up study (Millard and Johnson, 1985) the combined effect of aggregate interlock and dowel action was studied.

Specimens similar to those prepared for the 1984 study were prepared. The specimens were cracked in direct tension. The tensile force was then maintained while in-plane shear forces were applied across the crack. Measurements of the shear stiffness and subsequent crack widening, together with the tensile forces in the reinforcement were taken, using strain gauges embedded within the bars. A technique of resin injection was used to study the variation in the width of the crack beneath the surface of the concrete. No significant variation was observed.

Initially, two bars of each diameter used in the study (8, 12, and 16 mm) were tested in axial tension up to failure to obtain a calibration curve for each. A study of the anchorage properties of reinforcing bars embedded in concrete showed that the axial stiffness is dependent upon the relative rib area, f_r. An empirical expression was used to relate the local bond stress, τ_x, on the surface of a short length of embedded bar to the local bond slip, Δ_x:

$$\frac{\tau_x}{f_{cu}} = a + b\Delta_x^{17c}$$

(C.7)

Where:

f_{cu} = Ultimate compressive strength of the concrete (MPa)

a, b, c = Constants for a particular value of f_r ($0{,}05 < f_r < 0{,}065$)

The initial axial stiffness at the face of the crack, normal to the plane of cracking, which restrain crack widening, was found to be up to five times higher than when similar reinforcement was used in aggregate interlock tests, because of the effect of local bond. A reduction in the width of the initial crack from 0,5 mm to 0,125 mm resulted in an increase in the shear stiffness and the ultimate shear stress of up to five times. Increasing the diameter of the reinforcement resulted in an increase in the shear stiffness and ultimate shear stress, but it had less influence upon the ratio of crack widening to shear slip than might be expected. The normal stiffness did not increase proportionately to the reinforcement ratio. This was attributed to the poorer anchorage properties of the larger-diameter bars.

When cutting open some of the specimens, the results indicated that some slip occurred between the reinforcement and the concrete. It has been found that if the angle of the slope of the reinforcing bar spiral rib and the axis of the bar is less than 40°, slip is likely to occur. In this study the mean slope of the ribs were found to be 28°, thus slip was likely to occur, resulting in very little variation in the width of the crack beneath the surface. From this it was deduced that the shear stiffness due to aggregate interlock in those reinforced concrete specimens could be assumed to be the same as that obtained from an aggregate interlock specimen, when the normal stiffnesses are the same. Changes in initial crack width had a greater effect upon the shear stiffness of reinforced concrete specimens than upon aggregate interlock specimens.

In conclusion Millard and Johnson (1985) remarked that a comparison of the reinforced concrete test results with the previous aggregate interlock and dowel action tests had shown that no fundamentally different mechanics occur. There was, however, an interaction between the two modes of behaviour. Aggregate interlock caused additional tensile forces in the reinforcement due to overriding of the crack faces. This caused a reduction in the dowel action shear stiffness and strength. Likewise, local bond between the reinforcement and the concrete, absent from the aggregate interlock tests, produced a higher tensile stiffness normal to the plane of cracking, resulting in an increase in the aggregate interlock shear stiffness and strength, but this was sensitive to deterioration of the local bond. *Large initial crack widths, low concrete strengths or the use of large-diameter bars all had an adverse effect upon the anchorage stiffness of the reinforcement and consequently upon the aggregate interlock shear stiffness and strength.*

Therefore, when the tensile stiffness of the reinforcement normal to the plane of cracking is known, the two-phase aggregate interlock model and the elasto-plastic dowel-action model can be used to predict

the behaviour of reinforced concrete specimens cracked in tension and then subjected to in-plane shear across the cracks.

C.1.2.3 Snyder (1989)

The construction of full-depth repairs of Portland cement concrete (PCC) pavements has become a major part of pavement rehabilitation programs throughout the United States. Many of these repairs failed due to failure of the repaired load transfer system. During 1985 the University of Illinois Department of Civil Engineering contracted with the Federal Highway Administration (FHWA) to conduct extensive field, laboratory, and analytical studies concerning the evaluation and rehabilitation of concrete pavements. This study included repeated shear load testing of dowels installed in concrete and surveys of more than 2 000 in-service, full-depth repairs with various load transfer system designs.

This study involved the application of repeated shear loads to dowels anchored in holes drilled in concrete specimens. Data collection and analysis focused on the relationship between applied load and dowel deflection. The purpose of the laboratory study was to estimate the effects of several design and construction variables on the performance of dowels that are anchored into existing PCC slabs during the placement of full-depth repairs.

Five design and construction variables were included in the main test matrix:

a) Dowel diameter.
b) The width of the void to be filled with anchor material when the dowel is placed in the exact centre of the drilled hole.
c) Anchor material.
d) Embedment length.
e) Drill type (varying drill impact energy).

PCC slabs were obtained from Interstate 70 near Effingham, Illinois, for the fabrication of test specimens. Four undamaged slabs (1,2 m by 3,6 m) were lifted out of the pavement and transported to the University of Illinois, where they were cut into 310 mm by 460 mm test specimens. The specimen bases were capped with cement mortar to provide a stable base for testing. A steel drilling frame was assembled to hold the specimens and drill rigs, ensuring that the holes were drilled perpendicular to and centred within one of the 310 mm faces of each test specimen.

Anchor materials were prepared just prior to installation of the non-coated steel dowels. A two-cylinder caulking-gun arrangement provided by the manufacturer dispensed the epoxy mortar. The cement grout was mixed in accordance with the manufacturer's recommendations for achieving a "flow able" mix. A vinyl bag was filled with the grout and squeezed to force the grout through an attached

nozzle into the drilled hole. A tight-fitting nylon disk was fixed on each dowel at a distance equal to the embedment length to prevent the anchor material from flowing out of the holes and creating voids around the dowels.

Two specimens were prepared using 25 mm diameter dowels cast in fresh (20,7 MPa) concrete with 229 mm of embedment. These specimens were cured for 24 hours, subjected to 5 000 load cycles (to simulate early opening of the repair), cured for an additional 27 days, and subjected to an additional 595 000 load cycles. This was to set a standard of deflection performance against which to compare the anchored dowels, and to simulate the conditions imposed on the end of the dowel embedded in the repair.

Two specimens were also prepared to test the performance of the dowels installed in close-fitting holes. Dowels were turned on a metal lathe to achieve dowel diameters of 27 and 28 mm. The dowels were inserted in holes drilled with 27 mm nominal diameter steel drills. The smaller of the two bars was loose enough to be moved slightly in any direction. Some epoxy mortar was placed around this dowel at the concrete face. The larger bar could not be inserted to full depth by hand and was forcibly hammered into the hole without epoxy mortar.

Specimens fabricated using cement grout were allowed to cure in the lab for 7 to 14 days prior to testing. Specimens prepared using epoxy mortar were cured for 24 hours to 7 days.

Repeated bi-directional vertical shear loads were applied to the dowel installed in the test specimens Several load waveforms (simulating the passage of 160 kN tandem axles) were tried during preliminary tests. Specimen response was found to be relatively insensitive to the waveforms being considered. Thus a sinusoidal form with a peak magnitude of 13,4 kN (3 000 lb) and a frequency of 6 Hz was ultimately selected. This resulted in the application of nearly 520 000 load cycles per day, or about a year's worth of heavy traffic loads daily.

Loads were generated hydraulically using an MTS Model 661 ram with a 50 kN capacity. The load was applied to the dowel through a specially fabricated, high-strength steel-loading collar that allowed vertical deflection and associated angular dowel movement about a lateral axis.

A linear variable displacement transducer (LVDT) was mounted on an aluminium bracket attached to the face of each specimen and connected to the load collar using a small threaded nylon rod. This device was used to measure electronically the movement of the load collar and dowel relative to the PCC specimen.

The following conclusions and observations were drawn from this study:

a) The use of grout disks was essential to achieve the potential performance of any anchored dowel installation. These disks should be specified for all doweled, full-depth repair construction projects to ensure good bearing support around the dowel.

b) The epoxy mortar anchoring material was easier to use and produced more consistent results than the cement grout.

c) The use of larger dowel diameters significantly reduced concrete bearing stresses, dowel deflections, and dowel looseness when all factors were held constant.

d) Increasing the size of the *drilled hole radius minus dowel radius* from 0,8 mm to 3,2 mm improved the performance of dowels anchored in cement grout, because better distribution of stiff grout could be achieved. Very fluid grouts performed poorly, regardless of the gap.

e) Small gaps improved the performance of dowels anchored in epoxy mortar, because thinner supporting layers of epoxy mortar, which was softer than the concrete specimens, deformed less than thick layers.

f) Reducing dowel embedment resulted in very small increases in dowel deflection and looseness when epoxy mortar was used. Even smaller increase resulted when good cement grout specimens were tested.

g) Close-fitting holes offered promise when used with good anchor materials, quality control, and grout retention disks.

h) The hollow stainless steel dowel performed adequately, although it did not bond with the epoxy mortar that was used. Concurrent testing by FHWA demonstrated the need to fill hollow dowels with concrete or some other stiff material to reduce deformation of the dowel at the joint face.

i) It appeared that the following design and construction parameters could provide excellent field performance:

   i) 38 mm diameter (nominal), corrosion-resistant solid steel dowels.

   ii) 39,7 mm diameter (nominal), guided drills for epoxy mortar anchor materials.

   iii) 44,5 mm diameter (nominal), guided drills for cement grout anchor materials.

   iv) 178 mm or greater dowel embedment.

   v) Use of rapid-curing, consistent, easy-to-use anchor material (reduction of the emphasis to use cheaper materials when they are difficult to install adequately).

   vi) Use of grout retention disks during curing of the anchor materials.

C.1.2.4 Hossain and Wojakowski (1996)

Hossain and Wojakowski (1996) reported the results of a survey, conducted over a period of 9 years, where six jointed reinforced concrete pavement (JRCP) and one jointed plain concrete (JPCP) pavement test sections were surveyed annually for faulting. The main focus of the investigation was to determine the effect of *concrete mix consolidation* with time on joint faulting and load transfer efficiency.

The fundamentals on which the study was based, reached prior to the investigation, are that four major types of distress affect the performance of concrete pavements:

a) Loss of foundation support, caused by erosion and pumping of subbase materials from beneath the slab.
b) Joint or crack faulting, arising from heavy loads moving across the joint.
c) Slab cracking, caused by fatigue damage resulting from repeated heavy loads, bending stresses due to loss of support, tensile stresses due to thermal and moisture gradients, and uneven foundation settlement.
d) Joint deterioration, caused by poor joint design, non-working or frozen load transfer devices and D-cracking caused by frost-susceptible, non-durable aggregates.

Twenty-three test sections with lengths from 32 to 1 584 m were constructed with various adjustments to vibrator settings (frequency and amplitude), concrete admixtures, and other special features of JRCP. Seven of these test sections were monitored for long-term performance for this joint faulting and load transfer efficiency study.

Joint fault depth measurements were made with a fault meter built from the plans provided by the University of Illinois. Falling weight deflectometer (FWD) tests were done using a Dynatest-8000 FWD to assess the load transfer efficiencies of the joints.

The results of this study showed that:

a) As the original concrete density increased because of improved consolidation, the rate of increase of joint fault depth decreased at doweled joints.
b) The occurrence of joint faulting was much more severe when load transfer devices were not present.
c) Improved concrete mix consolidation appeared to improve load transfer, resulting in a lower rate of faulting.

C.1.2.5 Parsons, Eom, and Hjelmstad (1997)

A two-dimensional finite element model of a doweled joint in a rigid pavement system was described by Parsons et al (1997). They introduced and tested a definition of joint efficiency based on load transferred through dowel action, as follows:

$$\eta_{shear} = \frac{V_{dowel}}{V_{slab}} \qquad (C.8)$$

Where:

η_{shear} = Shear load transfer efficiency (range 0 – 1)

V_{dowel} = Shear force transferred across the gap through the dowel bar (kN);

V_{slab} = Shear force transferred through a continuous slab (kN); and

This shear load transfer efficiency was found to be a more useful measure of joint performance, as it captured the reduction in efficiency that accompanies an increase in the misfit of a joint.

C.1.2.6 Sargand (1999)

The Ohio Research Institute for Transportation and the Environment, together with the Ohio University installed 12 dowel bars in an in-service pavement to monitor their response under environmental cycling and dynamic loading.

Suitable sites were located approximately 5 miles east of Athens, Ohio where U.S.50 was being upgraded from a 2-lane facility to a 4-lane divided highway to instrument and install 12 dowel bars and monitor their response under environmental cycling and dynamic loading. The concrete slab was constructed 254 mm (10 inch) thick.

Six dowel bars were instrumented to monitor dynamic and environmental response. A small area was machined flat on the top and bottom of each bar at its midpoint for Micro-Measurements uniaxial strain gauges and on one side for a 45° rosette. The gauges were either welded to the bars or cemented with AE-10 epoxy. Micro-Measurements M-Coat F components were then used to prevent the intrusion of moisture and protect the gauge and sensor leads. Shallow grooves were cut from the midpoint to the end of the bars to house the lead wires. A small cavity was cut in the end of the bars where the lead wires could be epoxied and protected from the concrete. Three instrumented bars were inserted into each of two dowel bar baskets at positions corresponding to 0,152, 0,762, and 1,981 m from the outside edge of the pavement. The two baskets were set at consecutive joints.

Thermocouples were installed 0, 76, 152, and 229 mm from the bottom of the slab at four locations near the dowel bars to monitor pavement temperature. The three sensors closest to the bottom of the slab were fabricated into a single unit and attached to the dowel baskets. The top thermocouple was installed during placement of the concrete by making a 25 mm deep groove in the green concrete, placing the sensor in the groove, and covering it before finishing was initiated. Contraction joints were sawed in the pavement directly above the strain gauges to control shrinkage cracking.

Six additional bars were machined in a similar manner and used in two joints placed at a different time. Some of these dowel bars were instrumented with fibre optic gauges and installed at identical positions

in the pavement to provide redundant strain measurements. Slightly smaller areas were required on the bars for mounting the fibre optic gauges than was required for the wire gauges.

The uniaxial and rosette strain gauges were both capable of collecting slow responses due to changes in the environmental conditions and fast responses induced by dynamic loads. For environmental responses, data collection was initiated one hour before placement of the concrete and continued at 30-minute intervals for 37 days. Each data point was the average of five readings taken at 60-second increments.

Bending moments in the steel dowel bars were calculated using the following formula:

$$M_z = \frac{E_d I_d (\varepsilon_b - \varepsilon_t)}{2c} \tag{C.9}$$

Where:

M_z	=	Bending moment (Nm);
E_d	=	Modulus of elasticity (MPa);
I_d	=	Moment of inertia of the dowel;
ε_b, ε_t	=	Strain at bottom and top; and
c	=	Dowel bar radius (mm).

A strong correlation between differential temperature in the pavement slab and bending moment in the dowel bars was observed. The magnitude of these bending moments and the corresponding stresses in the dowel bars was much higher than expected. Bearing stresses are of particular concern early in the life of the pavement because the concrete has not attained its full compressive strength.

The magnitude of these bending moments will depend upon the amount of curvature being induced in the slab by curling and warping as well as the extent to which curvature is being resisted by dowel bar stiffness and the bearing resistance of the concrete surrounding the bars.

The relationship between bending moment and maximum stress in the dowel bars were calculated with the formula:

$$\sigma_d = \frac{M_z c}{I_d} \tag{C.10}$$

Where:

σ_d	=	Stress (MPa);
M_z	=	Bending moment (Nm); and
c	=	Dowel bar radius (mm).

The calculation of concrete bearing stress around the dowel bars involved certain assumptions, as shown in the following equation:

$$\sigma_b = K\left[\frac{P - \beta M}{2\beta^3 E_d I_d}\right] \qquad \text{(C.11)}$$

Where:

σ_b = Bearing stress (MPa);

K = Modulus of dowel support;

P = Shear Force on a dowel bar (kN);

β = $\sqrt[4]{\frac{Kd}{4E_d I_d}}$; and

d = Dowel bar diameter (mm).

The allowable bearing stress of fully cured concrete is 23 MPa (3300 psi) as calculated with the empirical formula:

$$\sigma_b = \frac{(4 - d)}{3} f_{cu} \qquad \text{(C.12)}$$

Where:

σ_b = Allowable bearing stress (MPa);

f_{cu} = Ultimate compressive strength of concrete (MPa).

During curing, the allowable bearing stress of PCC increases as its ultimate compressive strength increases. Therefore, the rate at which concrete attains its bearing strength must exceed the rate at which bearing stress is developed around the dowel bars. If the applied bearing stress is greater than the concrete is able to withstand, some type of distress will ensue. Increasing the number and diameter of the bars to reduce concrete bearing stress may not be effective since the overall rigidity of the joint and the induced moment will be increased.

The data collected strongly suggest the need to include environmental parameters in dowel bar design procedures.

In conclusion Sargand (1999) noted that in this study, the magnitude of bending moments generated in the instrumented steel dowel bars as they resist slab curvature during curing and temperature cycling exceeded those generated by FWD loading over the joints. These environmental moments will be even greater in situations where larger temperature gradients are present. As repeated applications of high bearing stress are incurred throughout the life of the pavement, concrete at the dowel bar interface will

wear away, gradually resulting in looseness around the bars. This will reduce the effectiveness with which dowel bars transfer load and limit environmental slab deformations.

Sargand (1999) further concluded that the design of dowel bars for rigid pavement joints involves a delicate balance between resisting slab curvature induced by concrete curing and temperature gradients, transferring dynamic load to adjacent slabs, and maintaining an acceptable bearing stress in concrete around the bars. As load transfer systems become more rigid, slab curvatures are reduced and dynamic loads are distributed better across the slabs, but this rigidity result in greater bending moments being transferred to the concrete. If load transfer systems are made less rigid, slabs will experience greater environmental curvature and more non-uniform support for carrying traffic loads, leading to higher tensile stress in the slab and higher compressive stress in the supporting layers.

He recommended that additional research is needed to clearly identify the manner in which dowel bars can be designed most effectively to carry traffic loads without exceeding the strength limitations of the materials involved.

C.1.3 FINITE ELEMENT DOWEL MODELLING

C.1.3.1 Nishizawa, Koyanagawa, Takeuchi and Kimura (2001)

The objective of this study was to develop a mechanical design method for a doweled joint. In order to investigate the mechanical behaviour of a dowel bar, a mechanical model of a dowel bar in a transverse joint in a concrete pavement was developed based on the three dimensional finite element (3D FE) method PAVE3D.

In the model, a dowel bar is divided into two segments embedded in concrete and a segment between them (see Figure C.1). The segment between slabs is represented with a beam element, connected to two solid elements (P and Q) at both nodes as well as at the inner nodes p and q, because there is no support of concrete surrounding the segment (see Figure C.2). These segments were modelled as a beam on elastic foundation and a 3D-beam element, respectively. The model was verified by comparing the predicted strains in the concrete slab and dowel bar with the experimental data obtained from loading tests conducted on a model pavement and an actual pavement. The effects of the transverse joint structure and subbase stiffness on the stresses in the dowel bar and concrete slab were investigated using numerical simulations with PAVE3D.

In accordance with the design manual used in Japan, the geometry and spacing of the dowel bars are determined empirically. A survey of the condition of concrete pavements in Japan showed that many concrete pavements in heavy-duty roads have suffered from longitudinal cracks that initiated at

transverse joints in wheel paths. It was also found that some dowel bars were broken inside the joint opening of transverse joints.

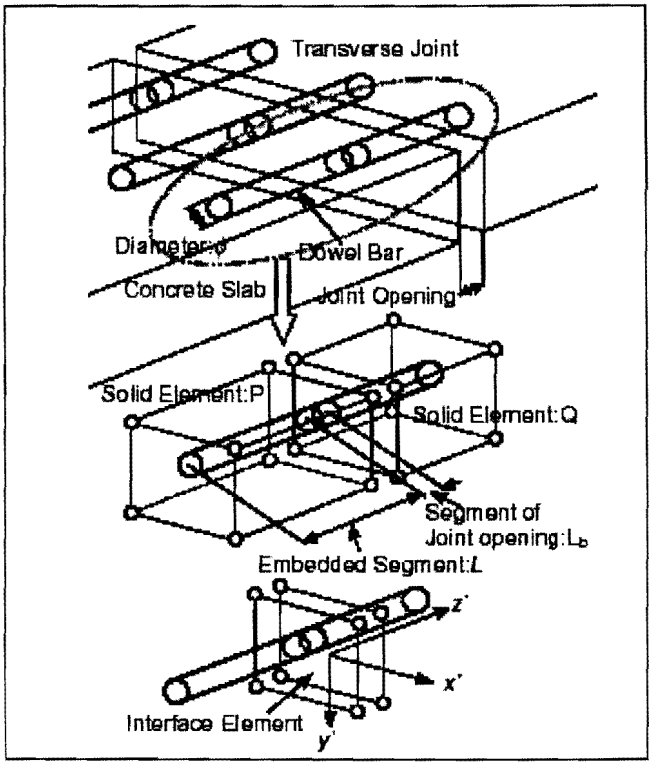

Figure C.1: Dowel bar element (Nishizawa et al, 2001)

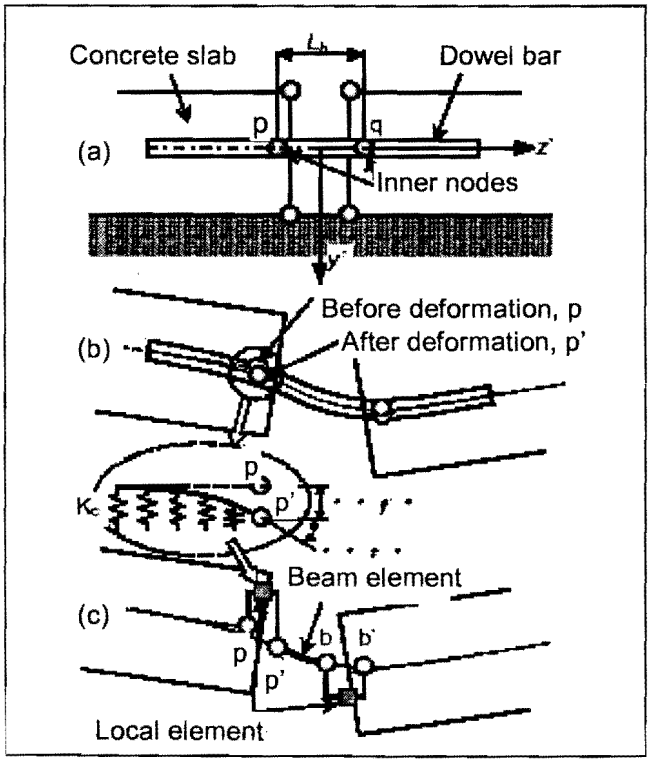

Figure C.2: Displacement of dowel bar element (Nishizawa et al, 2001)

These facts suggested that the current design methods used to determine the diameter, length, and spacing of dowel bars at transverse joints were inappropriate. A rational design method based on mechanical analyses was therefore required.

In order to experimentally investigate the mechanical behaviour of dowel bars, a model pavement with a 100 mm thick concrete slab on a granular subbase was constructed in a laboratory. Two types of transverse joints with 23 mm diameter and 11 mm diameter dowel bars were installed. Strains in the dowel bars produced by a vertical load applied at the transverse joint edge were measured with gauges attached on the surface of the dowel bars. The experiment was analysed by PAVE3D, which allowed the computation of displacements and stresses in the dowel bars as well as in the concrete slab, subbase and subgrade, taking into account the geometry and spacing of dowel bar. The model was verified by comparing the predicted strains in the concrete slab and dowel bars with experimental data obtained from loading tests conducted on a model pavement and an actual pavement. The comparison showed a fairly good agreement and confirmed the validity of PAVE3D. The results showed that the geometry and spacing of dowel bars had a great effect on the stress in the dowel bar but the effect of the stresses on the concrete slab was relatively small. It was also found that increasing the subbase stiffness decreased the stresses in both the dowel bars and in the concrete slab. Therefore, it was concluded from this study that strengthening the subbase might be a good measure to enhance the structural capacity of a concrete pavement system.

APPENDIX D: THEORETICAL CONCRETE PAVEMENT MODELLING WITH 3DFE PROGRAMME EVERFE

TABLE OF CONTENTS

LIST OF TABLES

LIST OF FIGURES

LIST OF SYMBOLS

α	Coefficient of thermal expansion
E	Modulus of elasticity
μ	Poisson's ratio
ρ	Density

APPENDIX D: THEORETICAL CONCRETE PAVEMENT MODELLING WITH 3DFE PROGRAMME EVERFE

D.1 INTRODUCTION

The decisions reached so far as to the modelling techniques that would be used in this study determined the input variables used to first conduct a theoretical analysis of the envisaged concrete pavement models. This was in order to determine the ranges for the different input variables that could be expected during modelling in the laboratory.

D.2 PAVEMENT SYSTEM AND LOADING

The concrete pavement was modelled as two slabs with dimensions 3 700 mm (wide) x 2 250 mm (long) x 230 mm (thick), with 35 MPa compressive strength. These dimensions were chosen as the standard lane width in South Africa is 3,7 m, the standard joint interval for jointed concrete pavements is 4,5 m, and the average concrete thickness is 230 mm. For simplicity the joint was not skewed. Three different types of subbases were evaluated, namely: crushed stone (G1), cement stabilised gravel (C2), and continuously graded asphalt (AC). The natural soil was modelled as an elastic solid foundation using rubber mats to simulate a uniform subgrade and provide continuous support. The rubber used in the modelling was tested beforehand and had a k-modulus of 80 MPa/m. The properties of the materials used in the analyses are summarised in Table D.1.

Table D.1: Input variables for material properties

Portion of system	E (MPa)	μ	α ($^{\circ}C^{-1}$)	ρ (kg/m^3)
Concrete slab (230 mm)	30 000	0,15	$1,1 \times 10^{-5}$	2 400
Crushed stone subbase (125 mm)	450	0,35		2 200
Cement stabilised subbase (125 mm)	3 000	0,35		2 400
Asphalt subbase (40 mm)	2 500	0,44		2 400
Steel	200 000	0,25		

The loading used for each study was a single 80 kN axle, applied at the edge of the first slab. The axle had dual wheels, and each wheel was idealised as a rectangular patch with uniform pressure, acting over a 180 mm wide by 200 mm long contact area. The tyre contact area gave a uniform pressure of approximately 555 kPa (80 psi). The load was placed symmetrically across the centreline of the slab, as shown in Figure D.1. Aggregate interlock load transfer efficiency on each subbase was determined using 9, 19, 37,5, and 63 mm aggregate, by varying the width of the crack or joint between the slabs.

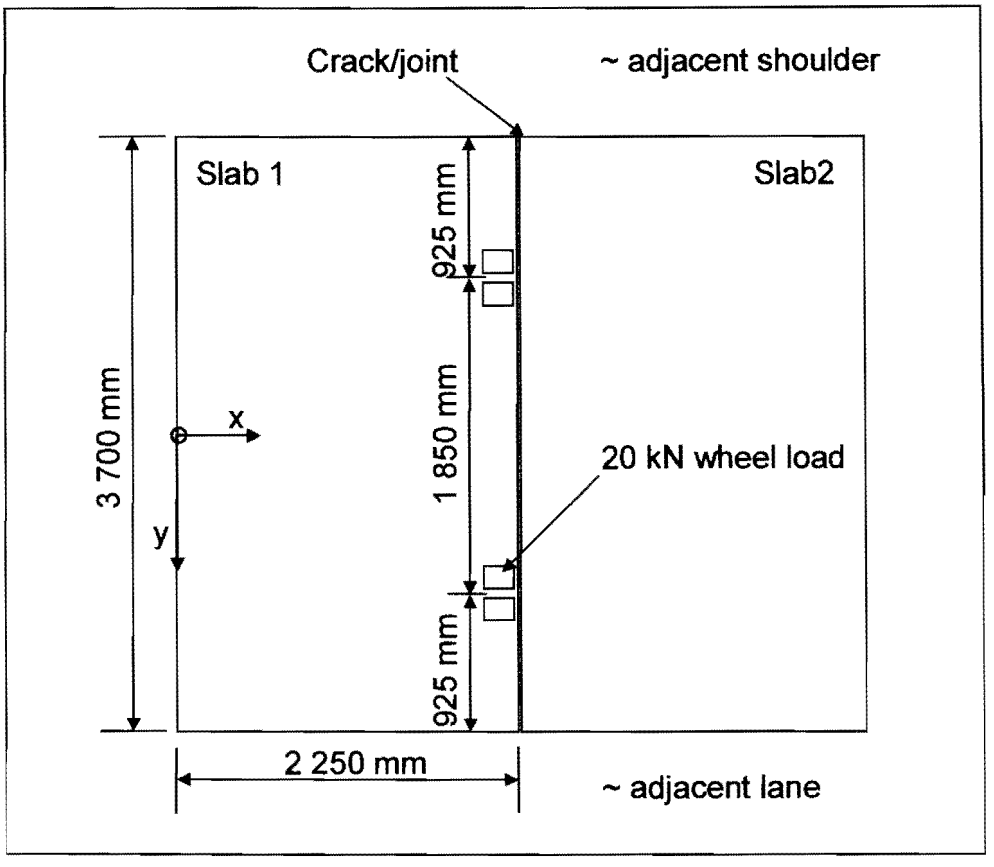

Figure D.1: Plan view of slabs showing wheel loads

The effect of temperature variations through the slab was taken into account by choosing a uniform baseline temperature of 20°C. Assuming that the temperature at the bottom of the slab was 10°C, and at the top of the slab 30°C, implied that the temperature difference was -10°C for the bottom of the slab and +10°C for the top of the slab in relation to the baseline temperature.

All these parameters were set in the three dimensional finite element (3D FE) computer software programme EverFE. The deflection load transfer efficiency of each model was determined at the joint between the slabs, at the centre of the wheel load at (x, y, z) = (2250, 925, -230) and (2263, 925, -230). With the load being placed symmetrically across the centreline of the slab, it was only necessary to evaluate the results at one dual wheel load position. For comparison purposes the deflection load transfer efficiency was also determined at the centre of the slab at (x, y, z) = (2250, 0, -230) and (2263, 0, -230). This was in order to compare the difference between the reaction of the slab at a loaded position versus an unloaded position.

The initial version of EverFE used in the analyses was not able to calculate the aggregate interlock shear force transferred across the joint accurately, nor the shear force transferred through to the dowels.

After personal communication with the developer of EverFE (Davids, 2000) a specific executable file was upgraded so that the theoretical shear load transferred could be determined.

D.3 THEORETICAL AGGREGATE INTERLOCK MODELLING

The deflection load transfer efficiency in the wheel path for each combination of aggregate sizes on the different subbases is presented in Figures D.2 to D.4. The vertical scale was kept constant for all three these figures to facilitate visual comparison. The larger the aggregate size the greater the deflection load transfer efficiency at a specific crack width. This held true for crack widths between 0,1 mm and 2,5 mm. However, the results started to converge to a constant value at a crack width of about 2,5 mm. This was especially noticeable for the smaller aggregate sizes. This "convergence" in the theoretical load transfer efficiency predicted by EverFE confirmed the statement made by Jensen (2001) that the load transfer efficiency of the concrete pavement at crack widths larger than 2,5 mm is a function of the subbase strength. Theoretical analyses with EverFE were carried out at crack widths of 10 mm. The Deflection load transfer efficiency at 10 mm for all aggregate sizes was exactly the same as the minimum deflection value already reached at 2,5 mm in the analysis for the 9 mm maximum sized aggregate. What was also important was the fact that the thin, flexible asphalt subbase had the largest theoretical load transfer efficiency. This could be attributed to easier "embedment" of the concrete in the subbase, compared to "lift-off" that may be experienced on a cement stabilised subbase. To facilitate an easier comparison the deflection load transfer efficiency obtained for the 19 mm maximum sized aggregate on all three subbases evaluated was plotted on one graph (see Figure D.5).

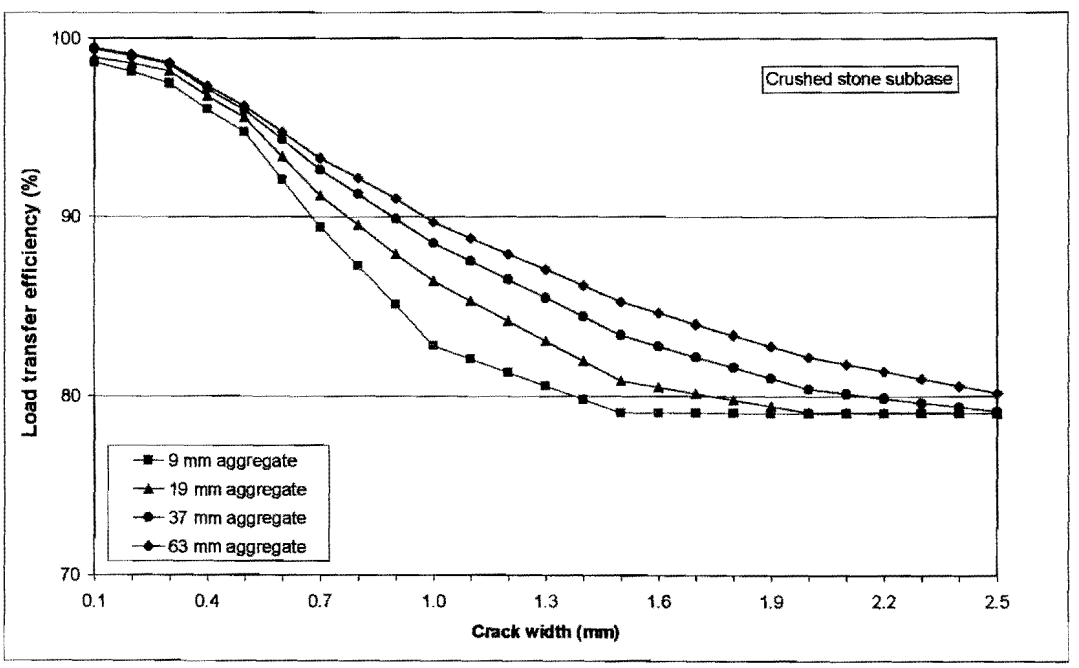

Figure D.2: Deflection load transfer efficiency in the wheel path (crushed stone subbase)

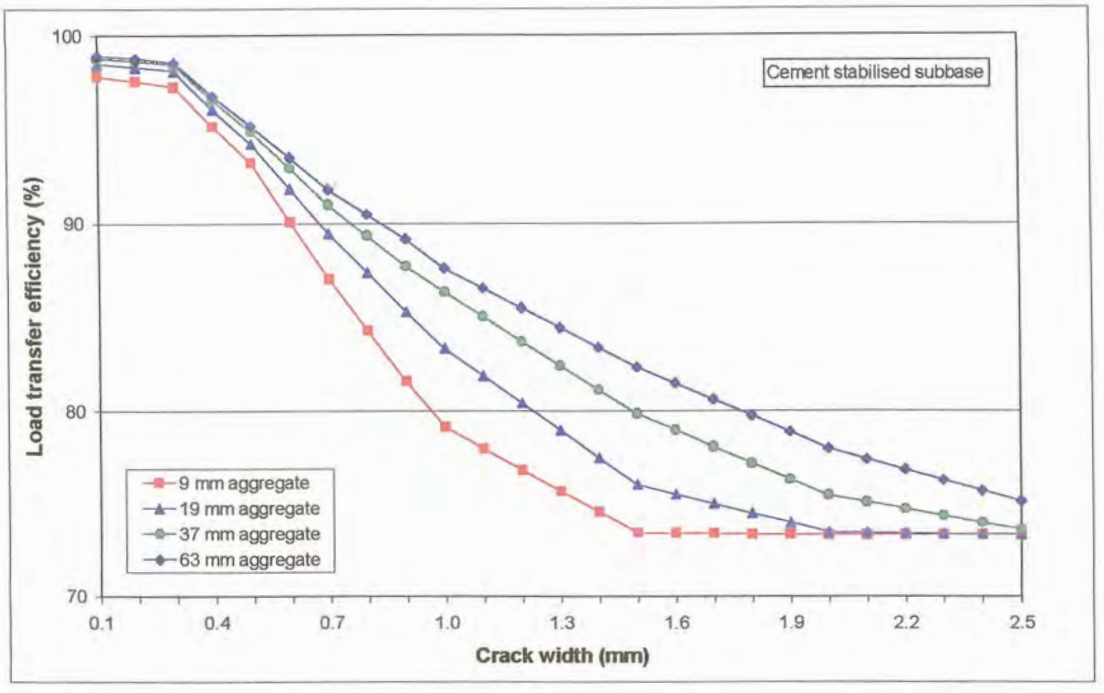

Figure D.3: Deflection load transfer efficiency in the wheel path (cement stabilised subbase)

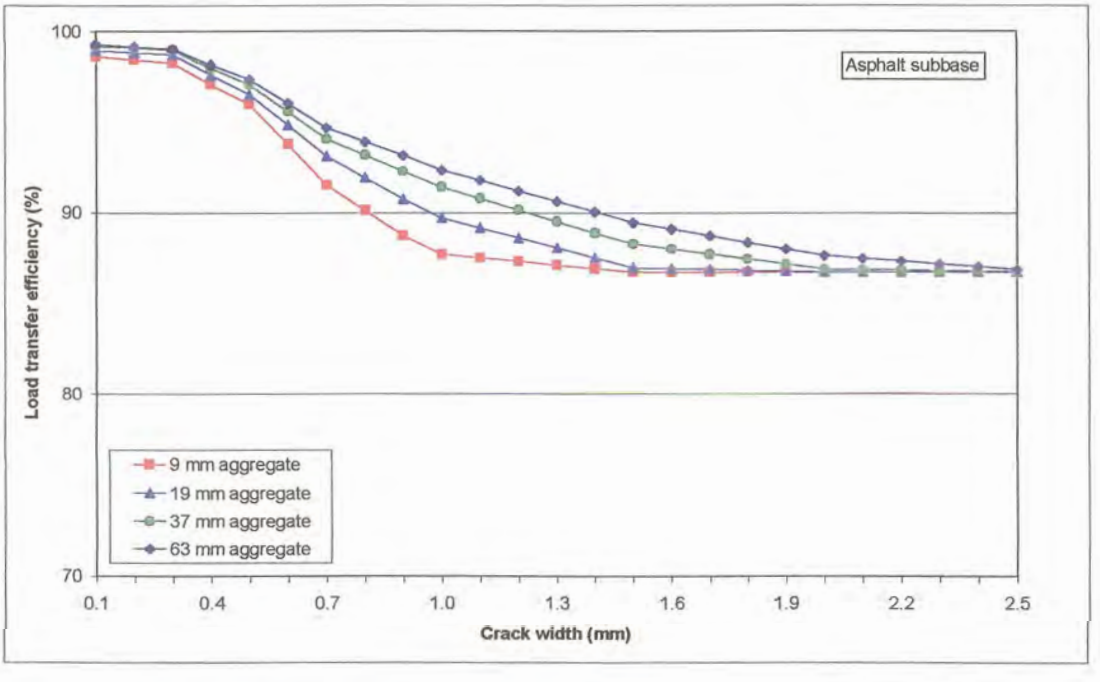

Figure D.4: Deflection load transfer efficiency in the wheel path (asphalt subbase)

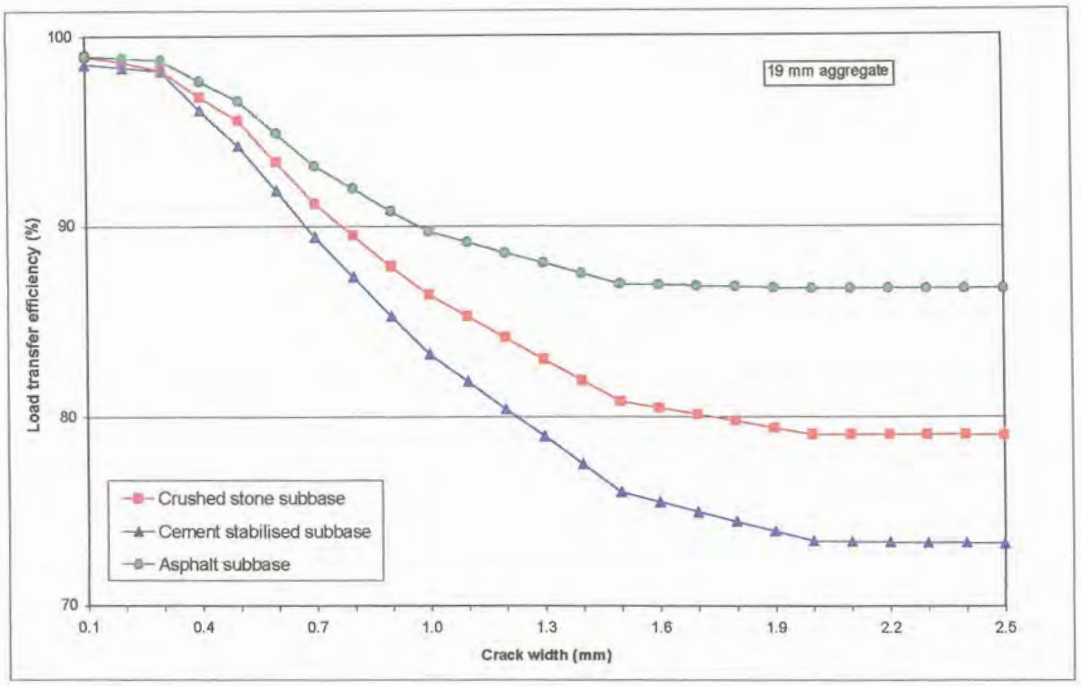

Figure D.5: Deflection load transfer efficiency in the wheel path for all three subbases (19 mm aggregate)

The deflection load transfer efficiency at the centreline of the slab was also determined. Figures D.6 to D.8 present these comparisons for 9 mm and 63 mm aggregate sizes on the different subbases. At small crack widths (< 0,4 mm) the deflection load transfer efficiency at the centreline of the slab was close to 100% in all three figures, and higher than in the wheel path. However, as the crack width increased beyond 0,4 mm, the load transfer efficiency at the centreline became less than in the wheel path. This typically occurred at crack widths of approximately 0,8 mm for the 9 mm maximum aggregate size concrete, and at crack widths of approximately 1,5 mm for 63 mm maximum aggregate sized concrete. This implied that during traffic loading little or no movement takes place at the centreline of the traffic lane, between the wheel loads at small crack widths, but as the crack width increases, the crack tends to open up at the centreline, while it tends to close up in the wheel path. Another practical explanation of this tendency is that the concrete pavement experiences less of the effects of moment and inertia at the centreline than in the wheel path. The larger aggregate size yielded higher load transfer efficiencies than the smaller aggregate size at the centreline between the wheel loads. The load transfer efficiency values at the centreline also tended to converge to a constant value at a crack width of about 2,5 mm, but the eventual load transfer efficiencies were less than in the wheel path

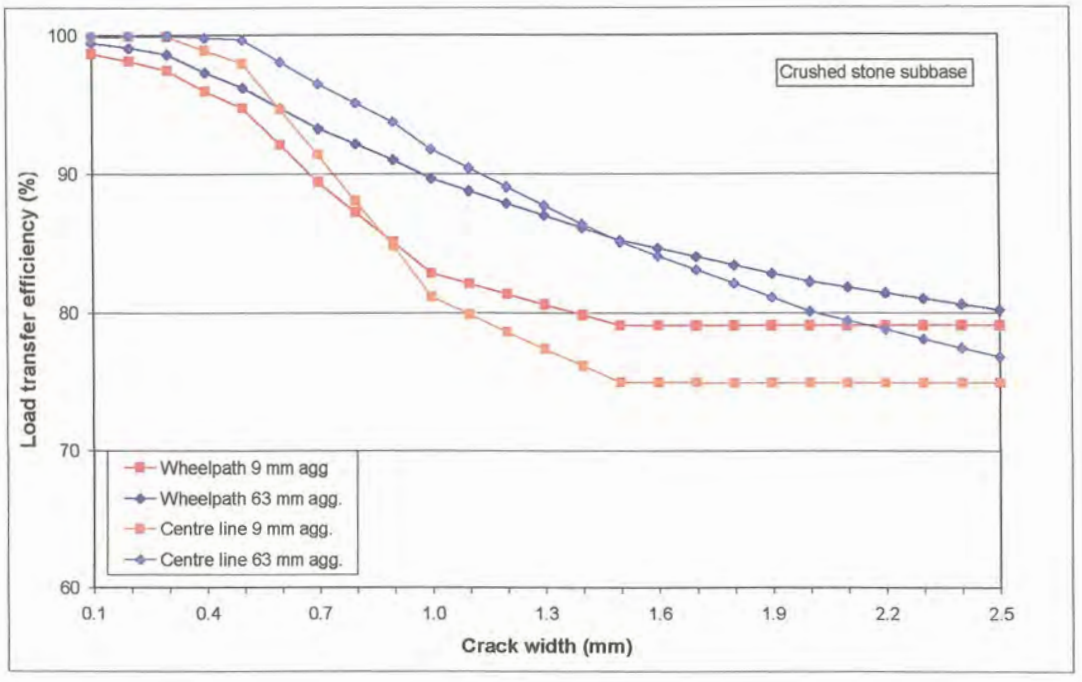

Figure D.6: Deflection load transfer efficiency – wheel path versus centreline (crushed stone subbase)

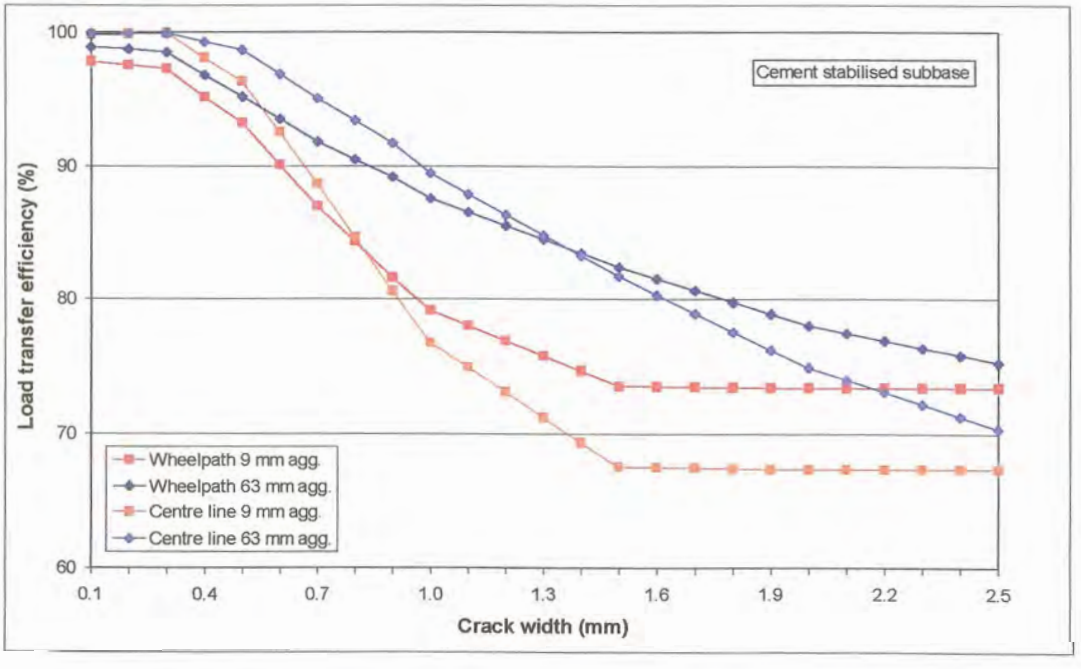

Figure D.7: Deflection load transfer efficiency – wheel path versus centreline (cement stabilised subbase)

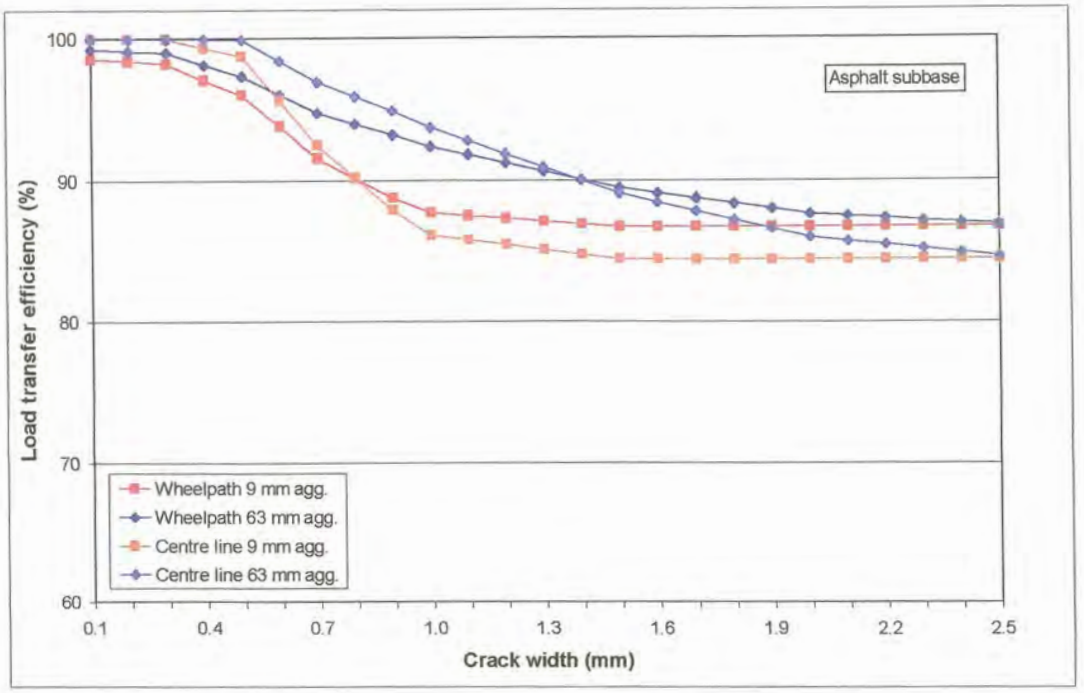

Figure D.8: Deflection load transfer efficiency – wheel path versus centreline (asphalt subbase)

The point of maximum shear stress was in the wheel path at (x, y, z) = (2250, 925, -230). Figures D.9 to D.11 show the maximum shear stress measured in the wheel path for the three subbases considered. The initial lower stress value obtained for the 9 mm aggregate on a crushed stone subbase, can be ascribed to an initial slip that takes place on the weaker subbase, before the maximum stress is reached at a crack width of 0,3 mm.

The numerically integrated sum of the shear force transferred across the joint, reached a maximum at 0,3 mm crack width (due to an initial slip that takes place on the weaker subbase), where after it decreased to approximately 0 kPa at 2,5 mm crack width for the model with a crushed stone subbase. Both the cement stabilised model, as well as the asphalt subbase model had maximum values at 0,1 mm crack width, decreasing to approximately 0 kPa at 2,5 mm crack width (see Figures D.12 to D.14).

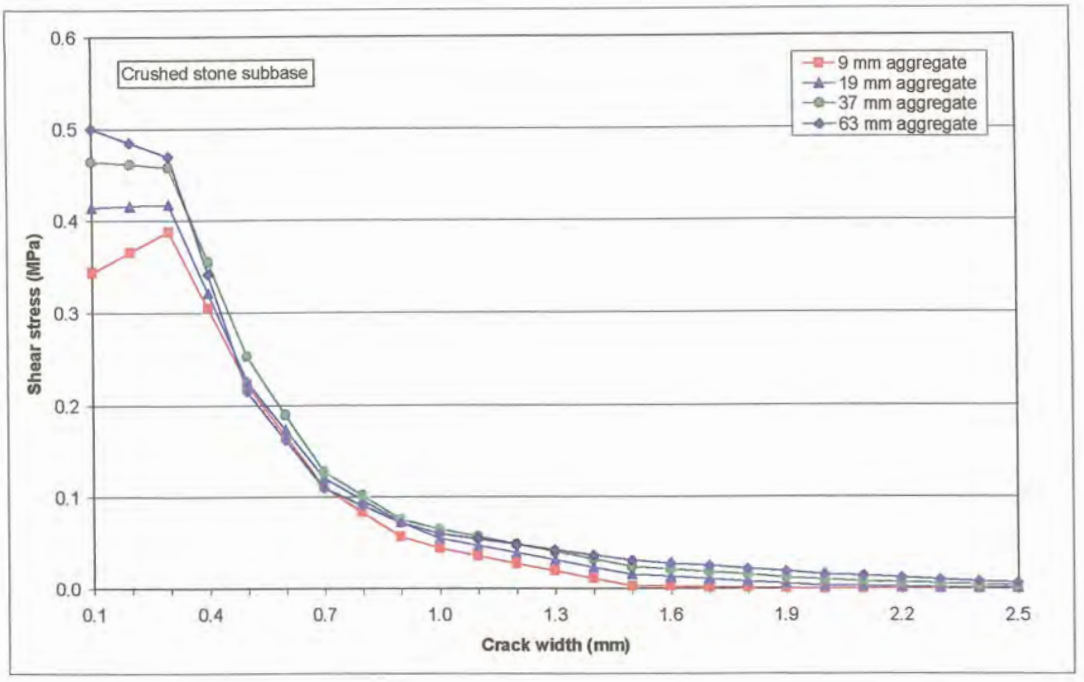

Figure D.9: Maximum shear stress at joint in wheel path (crushed stone subbase)

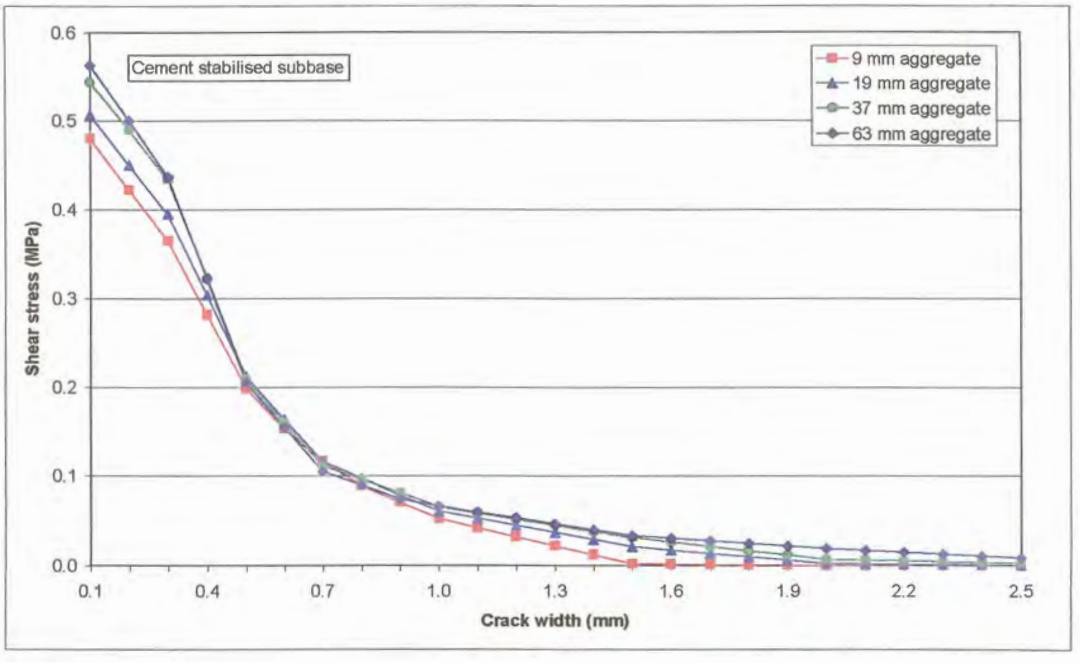

Figure D.10: Maximum shear stress at joint in wheel path (cement stabilised subbase)

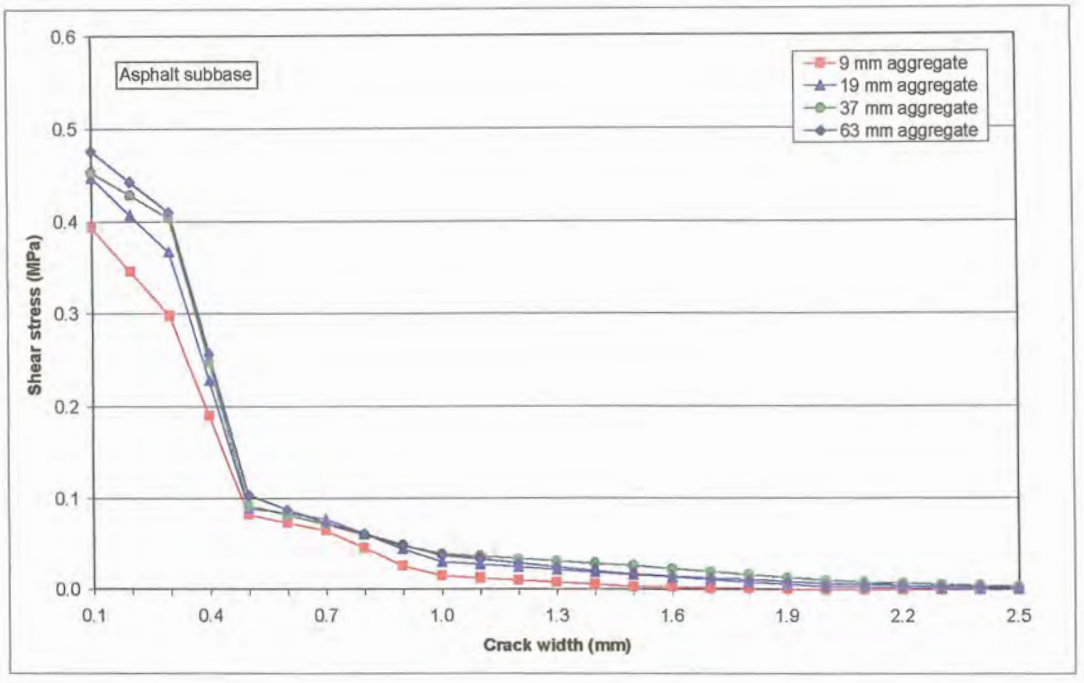

Figure D.11: Maximum shear stress at joint in wheel path (asphalt subbase)

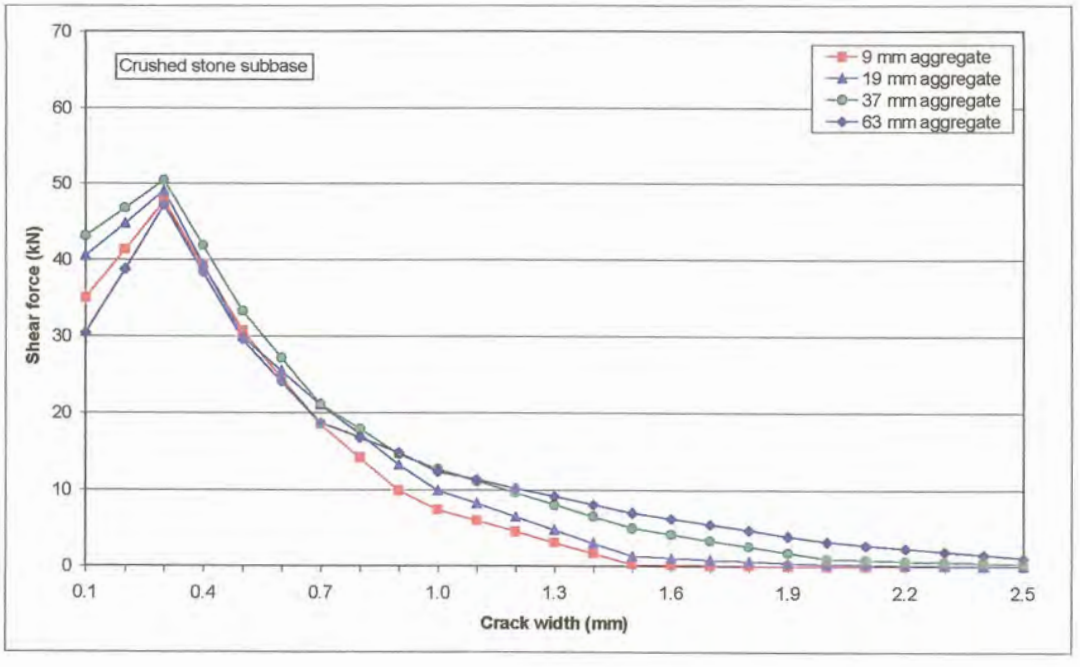

Figure D.12: Total shear force at joint (crushed stone subbase)

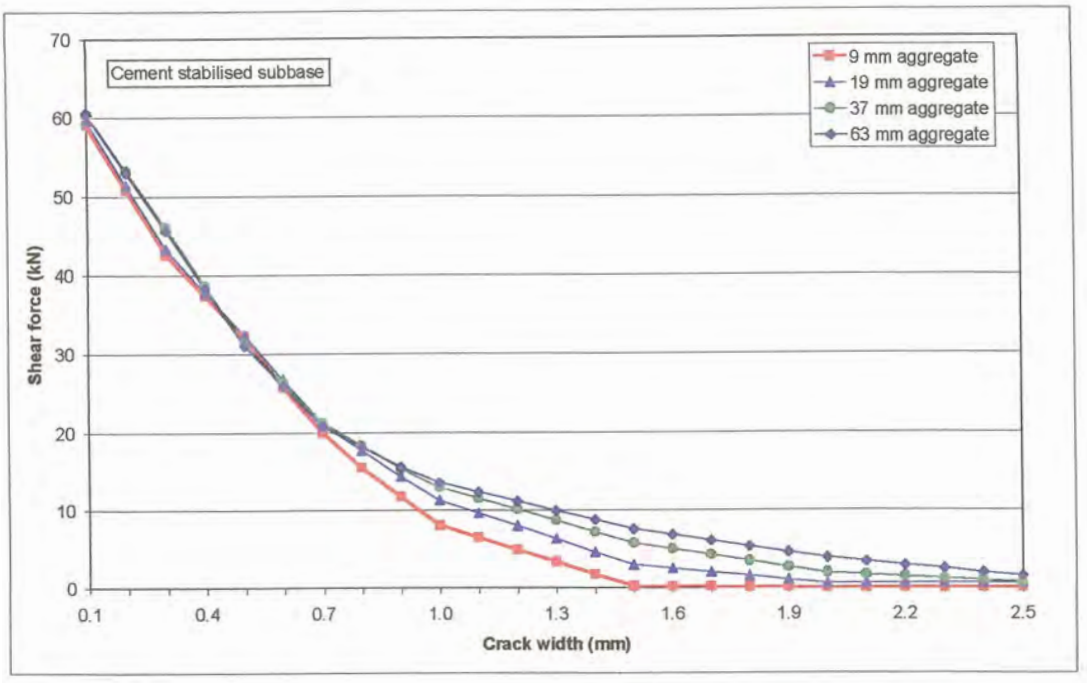

Figure D.13: Total shear force at joint (cement stabilised subbase)

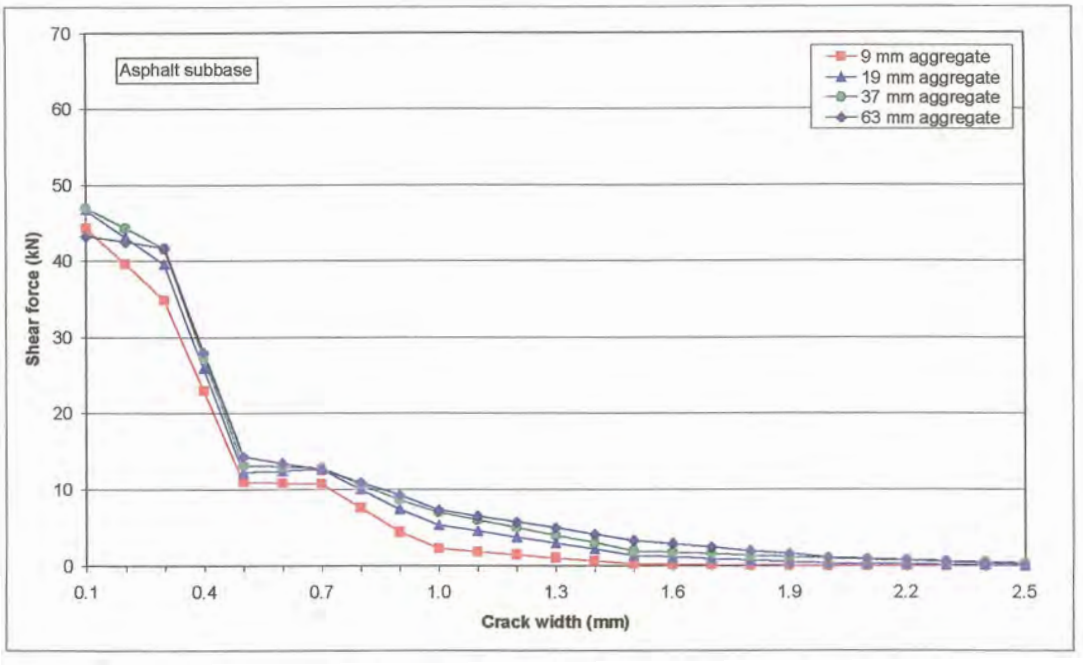

Figure D.14: Total shear force at joint (asphalt subbase)

To quantify the effect of a temperature gradient through the concrete the cement stabilised subbase modelling was repeated with a zero temperature gradient in the concrete, and the results were compared with those previously obtained. The load transfer efficiency in the wheel path showed a marked

difference, with the results converging at approximately 57%, compared to the previous 75% (see Figure D.15). The maximum shear stress and shear force results obtained with the zero temperature gradient models are given in Figures D.16 and D.17. In both instances the graphs showed the same trend, parallel to the previously obtained graphs, but at much lower initial stresses and forces. Depending on the temperature gradient chosen, the results could also have been the opposite. This emphasised the importance of measuring temperature differentials through the pavement when attempting to model the performance.

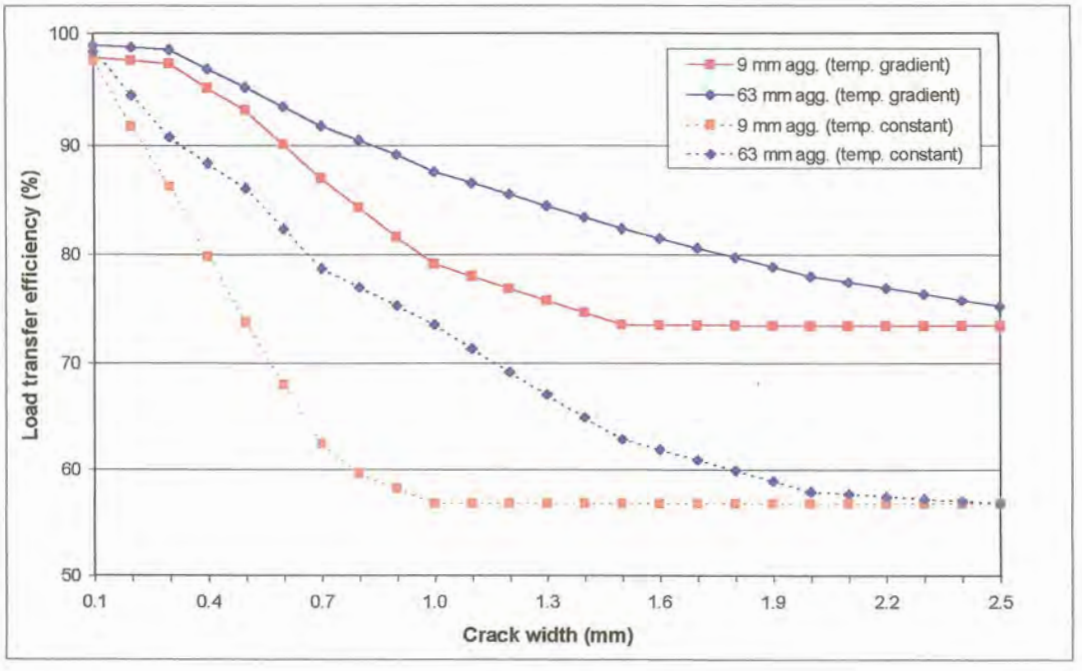

Figure D.15: Deflection load transfer efficiency in wheel path – cement stabilised subbase with and without temperature gradient through concrete slab

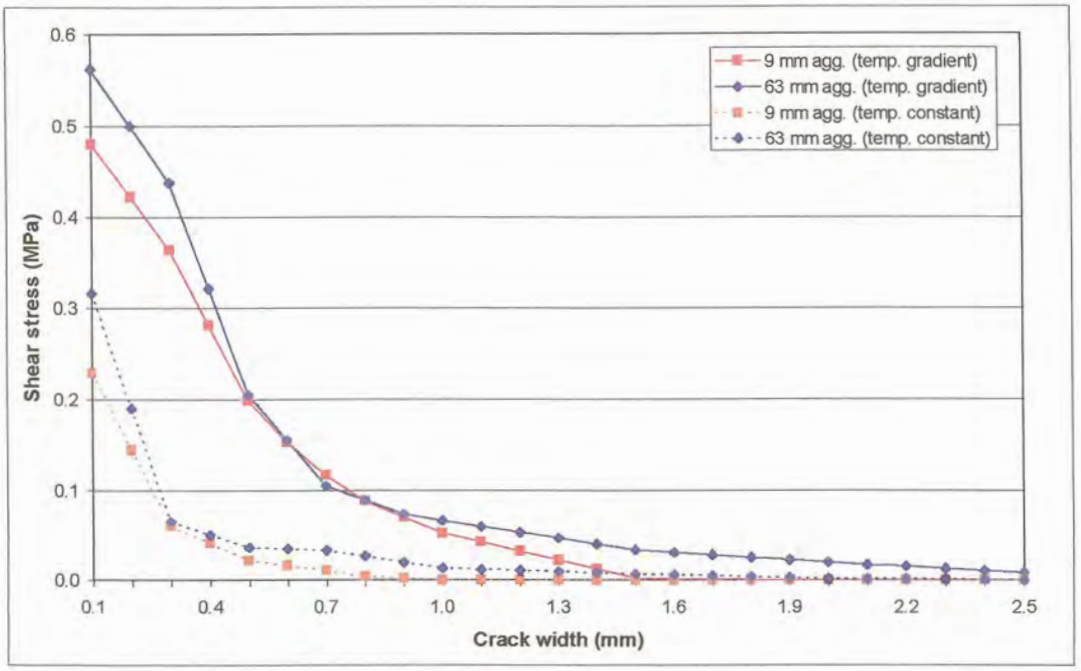

Figure D.16: Maximum shear stress at joint in wheel path – cement stabilised subbase with and without temperature gradient through the concrete slab

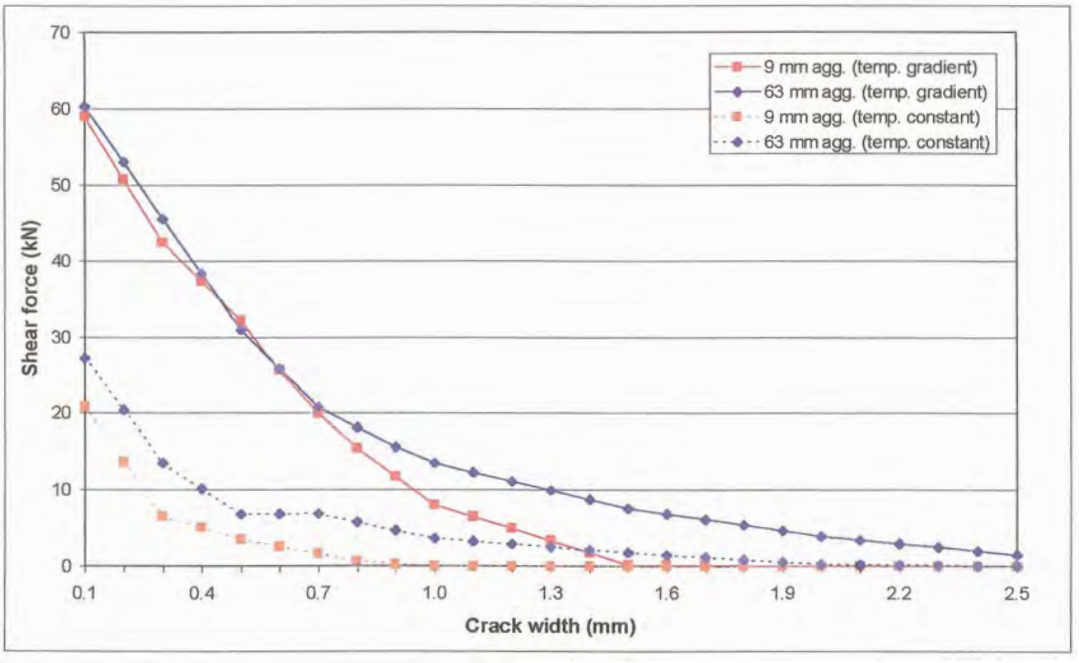

Figure D.17: Total shear force at joint – cement stabilised subbase with and without temperature gradient through the concrete slab

D.4 THEORETICAL DOWEL MODELLING

The effect of dowel looseness was determined using 16, 25, and 32 mm diameter bars (460 mm long) at 300, 450, and 600 mm spacing, respectively, on each subbase, by varying the size of the gap around the dowel. The joint width was set at 12,5 mm to eliminate the effect of aggregate interlock in this case. Figure D.18 (similar to Figure D.1) shows a plan view of the placement of the wheel loads, as well as the dowel bars.

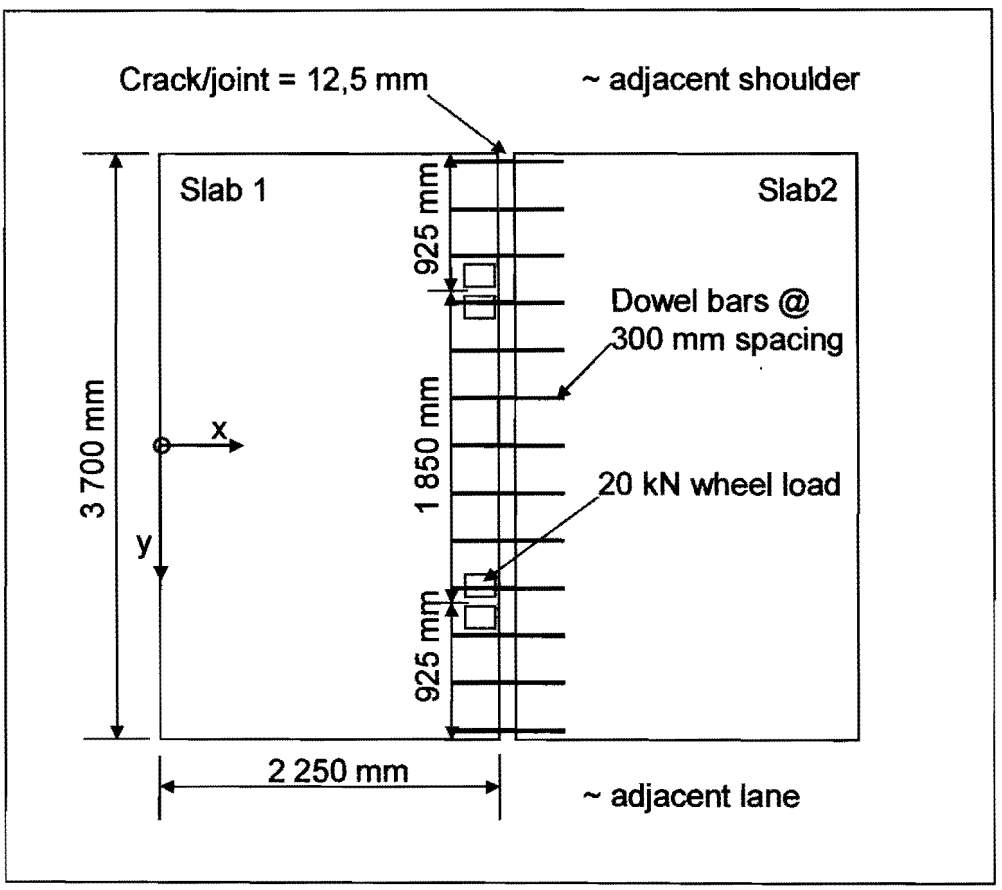

Figure D.18: Plan view of slabs showing wheel loads and dowel bars

The model used to study the effect that dowel looseness has on the response of the pavement is shown in Figure D.19. After setting up the different models, all the parameters were kept constant (as defined in Table D.1), while only the value of the gap between the dowel bar and the surrounding concrete at the joint face was varied from 0,00 mm to 0,10 mm.

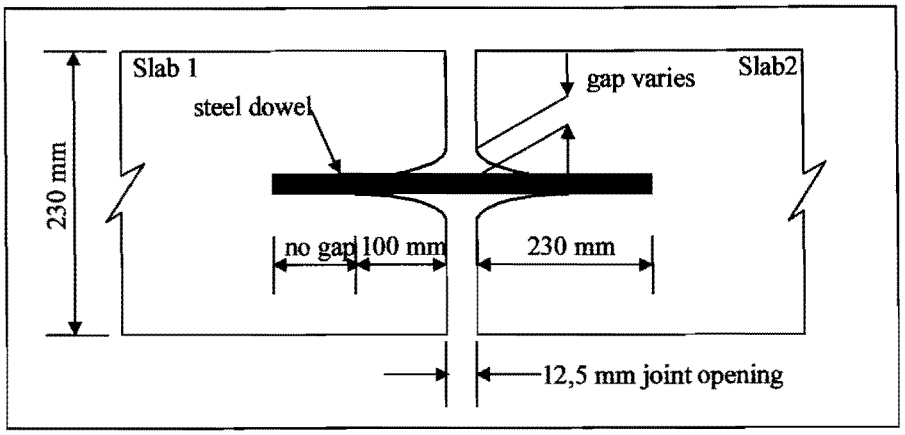

Figure D.19: Cross-section of gap around dowel at joint

D.4.1 CONSTANT DOWEL BAR SPACING AT INCREASED DOWEL BAR DIAMETER

D.4.1.1 Dowel bar spacing – 300 mm

Figures D.20 to D.22 present the deflection load transfer efficiency for 16, 25, and 32 mm diameter dowel bars at 300 mm spacing with increasing gap width around the dowels, on the three subbases considered. The deflection load transfer efficiency increased with increasing dowel diameter.

Once again, the load transfer efficiency at the centre of the slab was compared with that in the wheel path to represent the performance of the pavement at an unloaded position, as well as at the position of loading. The deflection load transfer efficiency in the wheel path for the models with the crushed stone subbase decreased from between 97,4% and 98,7% at 0,0 mm gap width to between 88% and 90% at 0,06 mm gap width, where after it remained constant. Similarly, the values obtained for the models with the cement stabilised subbase also decreased from between 96,7% and 98,5% efficiency at 0,0 mm gap width, to a constant 83,6% for the 16 mm diameter dowel bar, and 87,3% for the 32 mm diameter dowel bar at 0,06 mm gap width. The asphalt subbase models showed a decrease from between 96,9% and 98,4% at 0,0 mm gap width to between 80,8% for the 16 mm diameter dowel bar, and 84,8% for the 32 mm diameter dowel bar at 0,08 mm gap width. Where after it also remained constant. From Figures D.20 to D.22 it is obvious that the load transfer efficiency was higher at the centreline (unloaded position) than in the wheel path (loaded position) for all three subbases considered.

Figure D.23 present a comparison between the deflection load transfer efficiencies determined in the wheel path for 16 mm diameter dowel bars at 300 mm spacing on each of the three subbases simulated in the theoretical analyses. In this theoretical analysis, the crushed stone subbase had the highest and the asphalt the lowest load transfer efficiencies.

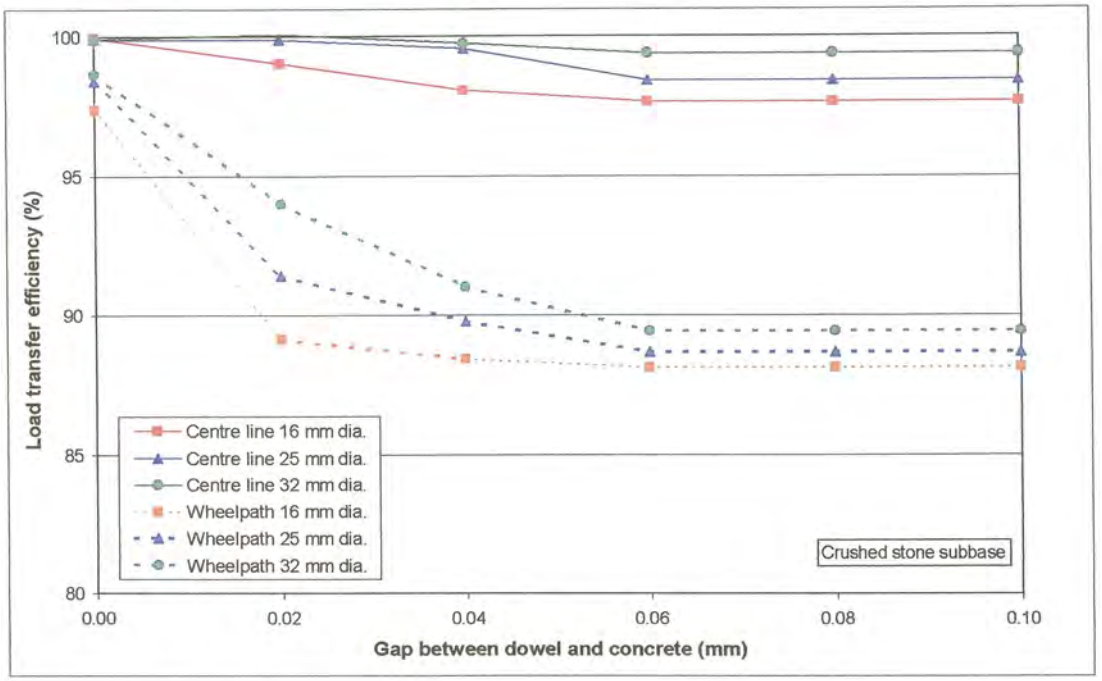

Figure D.20: Deflection load transfer efficiency with dowel bar spacing at 300 mm (crushed stone subbase)

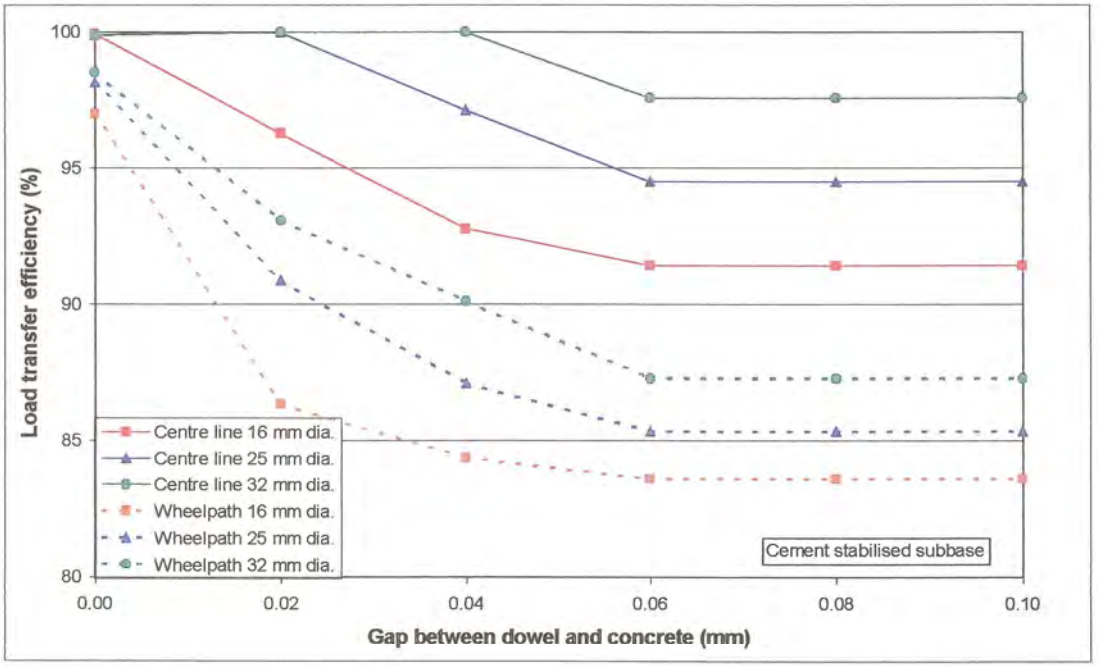

Figure D.21: Deflection load transfer efficiency with dowel bar spacing at 300 mm (cement stabilised subbase)

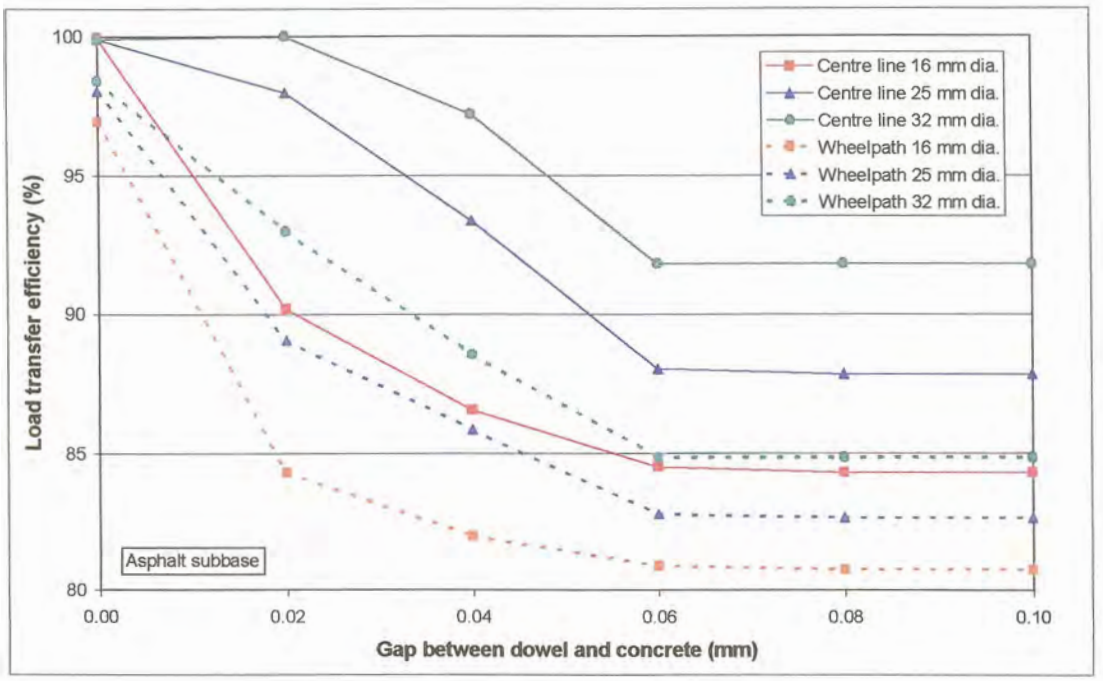

Figure D.22: Deflection load transfer efficiency with dowel bar spacing at 300 mm (asphalt subbase)

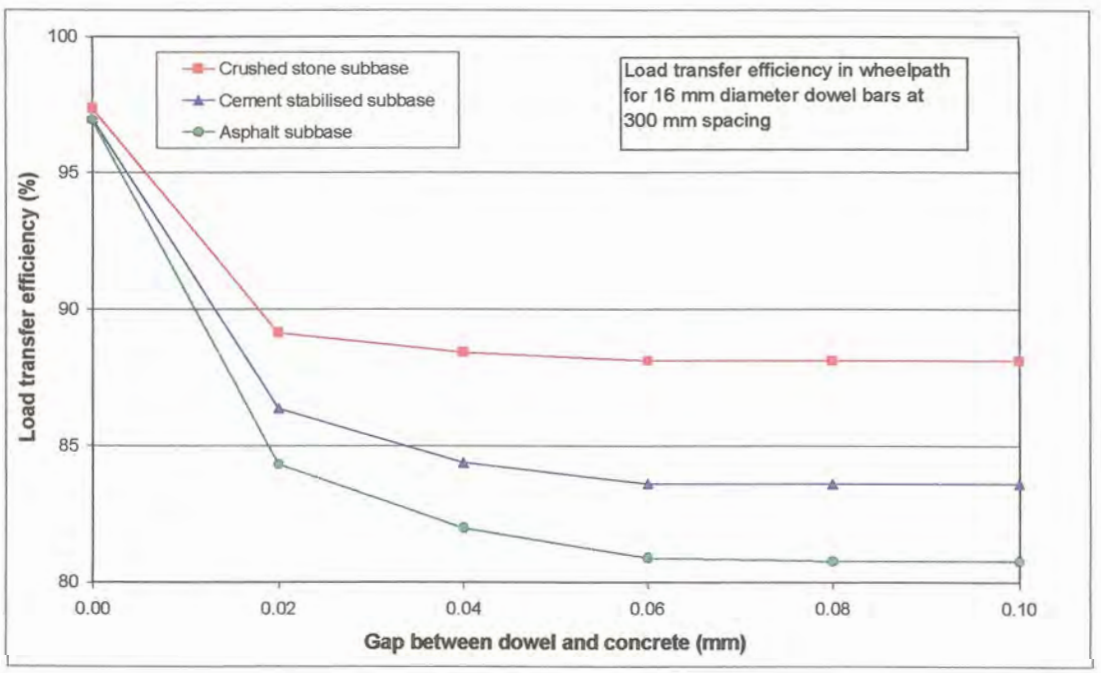

Figure D.23: Deflection load transfer efficiency for 16 mm diameter dowel bars at 300 mm spacing on all three subbases

The total shear force transferred across the joint due to the dowels at increasing gap widths is presented in Figures D.24 to D.26. According to these theoretical modelling results, an increase in dowel diameter results in an increase in shear force transferred across the joint.

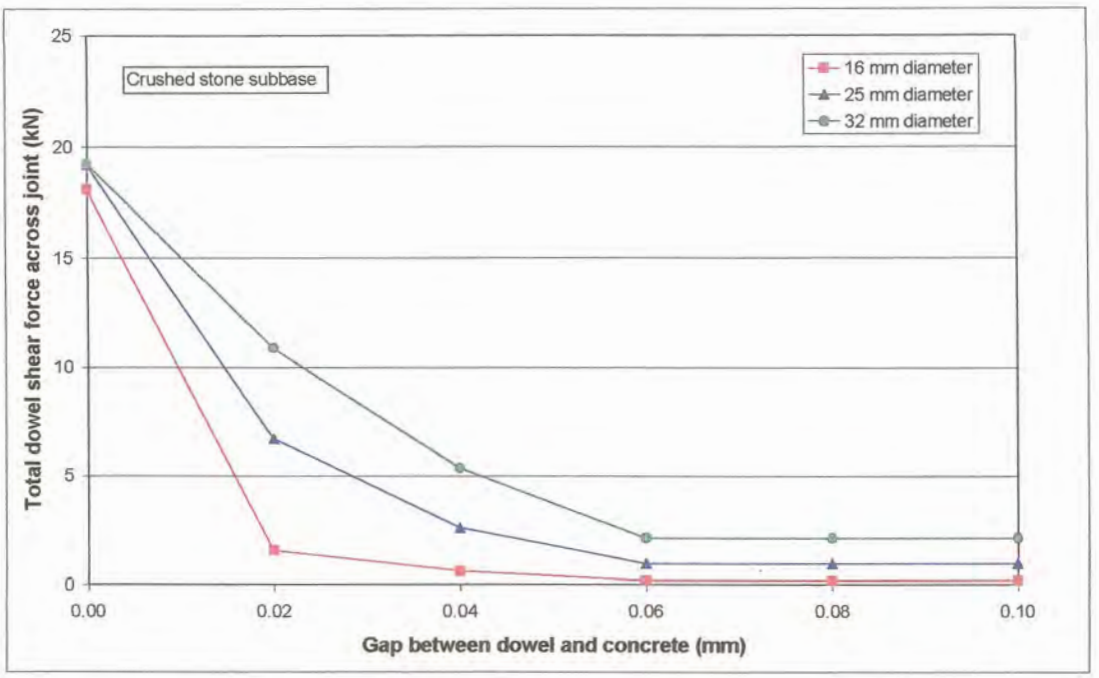

Figure D.24: Total shear force transferred across joint due to dowels (crushed stone subbase)

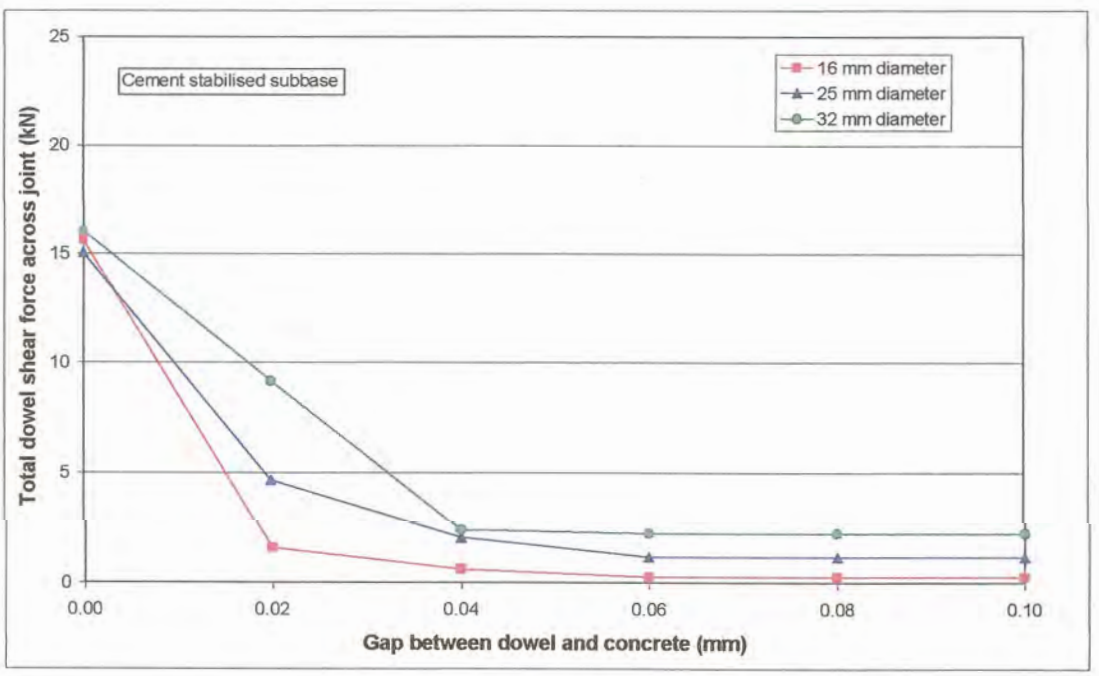

Figure D.25: Total shear force transferred across joint due to dowels (cement stabilised subbase)

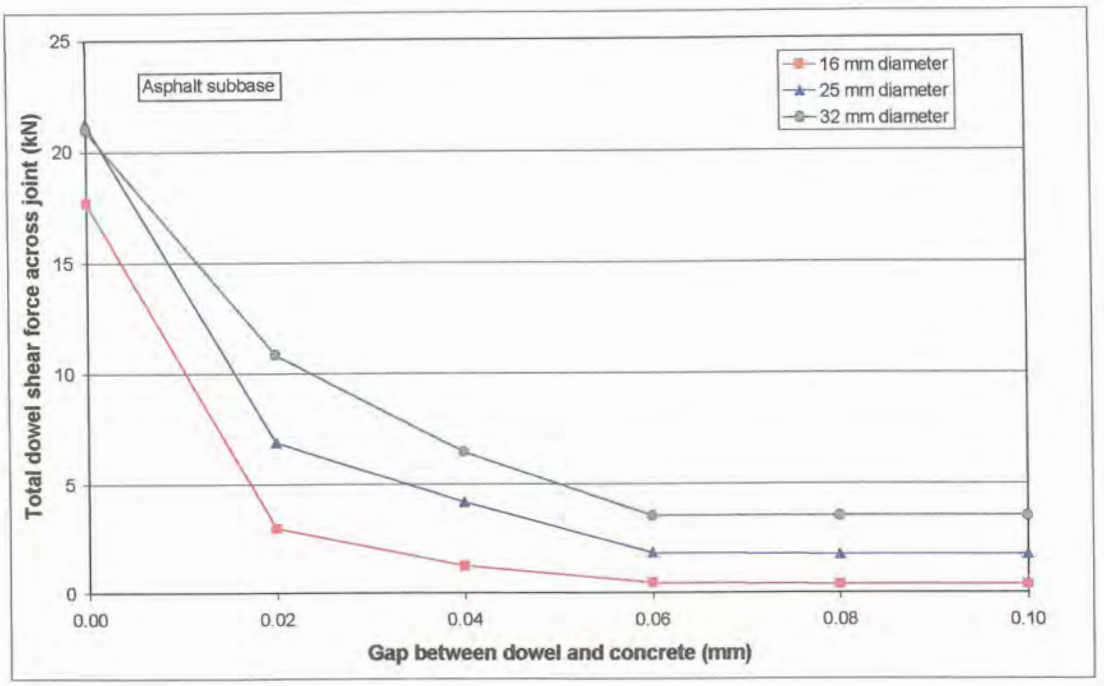

Figure D.26: Total shear force transferred across joint due to dowels (asphalt subbase)

To determine the effect of dowel spacing on the load transfer efficiency of the doweled slabs and on the shear force the dowels have to transfer across the joint, the above three sets of theoretical analyses were repeated with dowel bar spacing of 450, and 600 mm. The results of these analyses are presented below. It followed intuition that the load transfer efficiency would decrease with increasing dowel bar spacing for a constant dowel diameter. Similarly, the total shear load transferred across the joint through the dowels decreased for increasing dowel bar spacing for a specific dowel diameter, especially for the 16 mm diameter dowel bars. On the other hand, the total shear load transferred across the joint through the 25, and 32 mm diameter dowel bars at 600 mm spacing increased at 0 mm gap width in each case considered. This indicated that a too large dowel bar spacing can over-stress the dowel bars and cause it to fail.

D.4.1.2 Dowel bar spacing – 450 mm

Figures D.27 to D.29 present the deflection load transfer efficiency for 16, 25, and 32 mm diameter dowel bars at 450 mm spacing with increasing gap width around the dowels.

The total shear force transferred across the joint due to the dowels at increasing gap widths is presented in Figures D.30 to D.32.

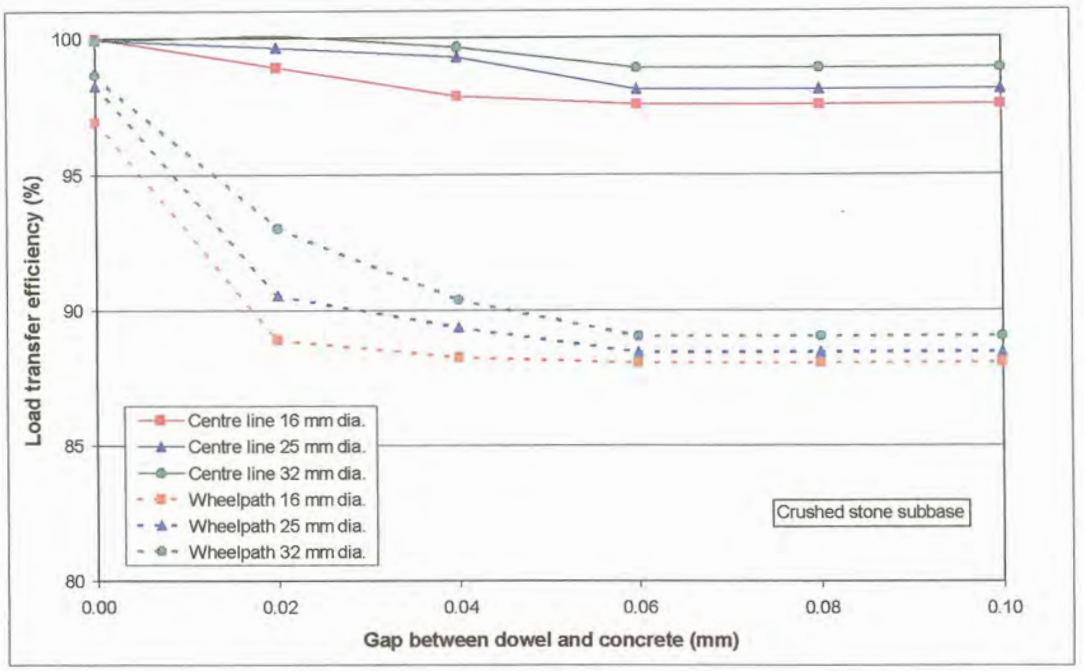

Figure D.27: Deflection load transfer efficiency with dowel bar spacing at 450 mm (crushed stone subbase)

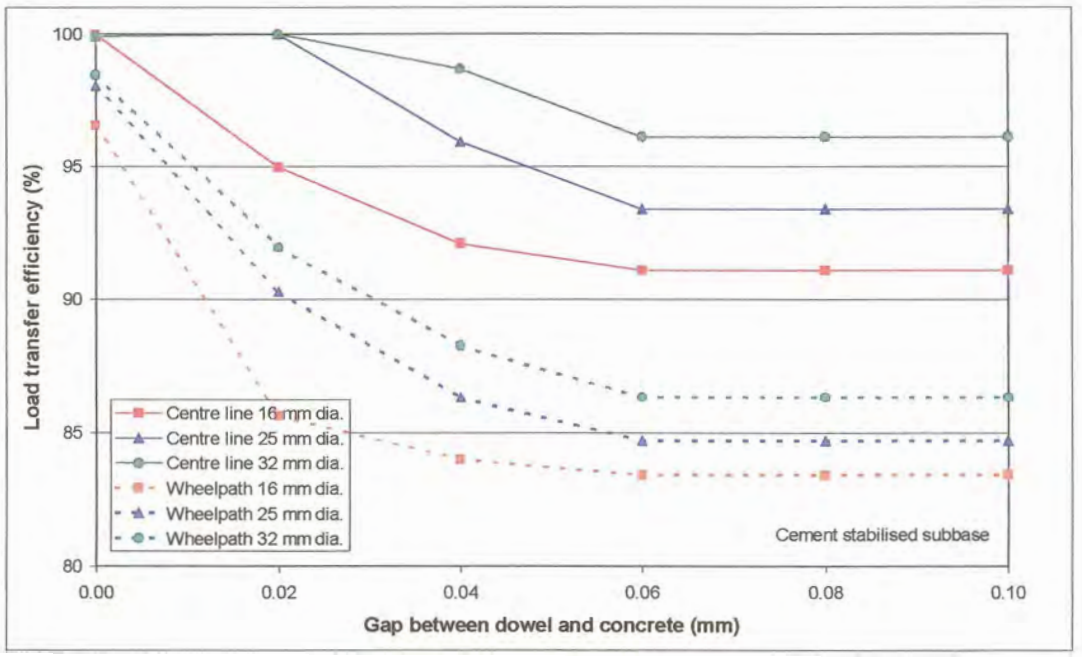

Figure D.28: Deflection load transfer efficiency with dowel bar spacing at 450 mm (cement stabilised subbase)

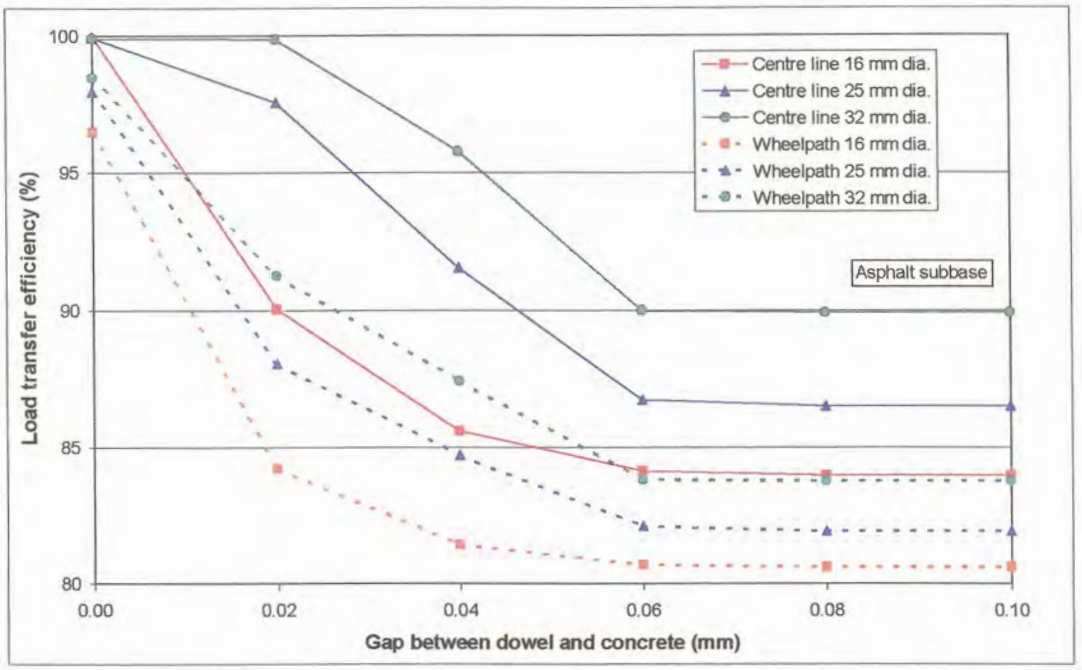

Figure D.29: Deflection load transfer efficiency with dowel bar spacing at 450 mm (asphalt subbase)

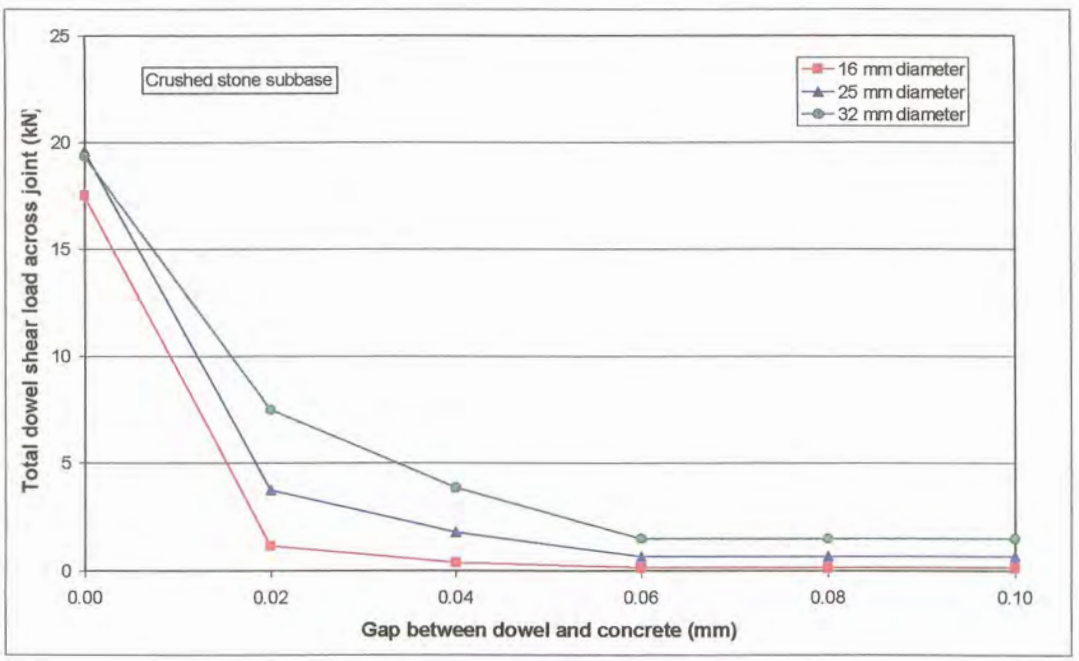

Figure D.30: Total shear load transferred across joint due to dowels with dowel bar spacing at 450 mm (crushed stone subbase)

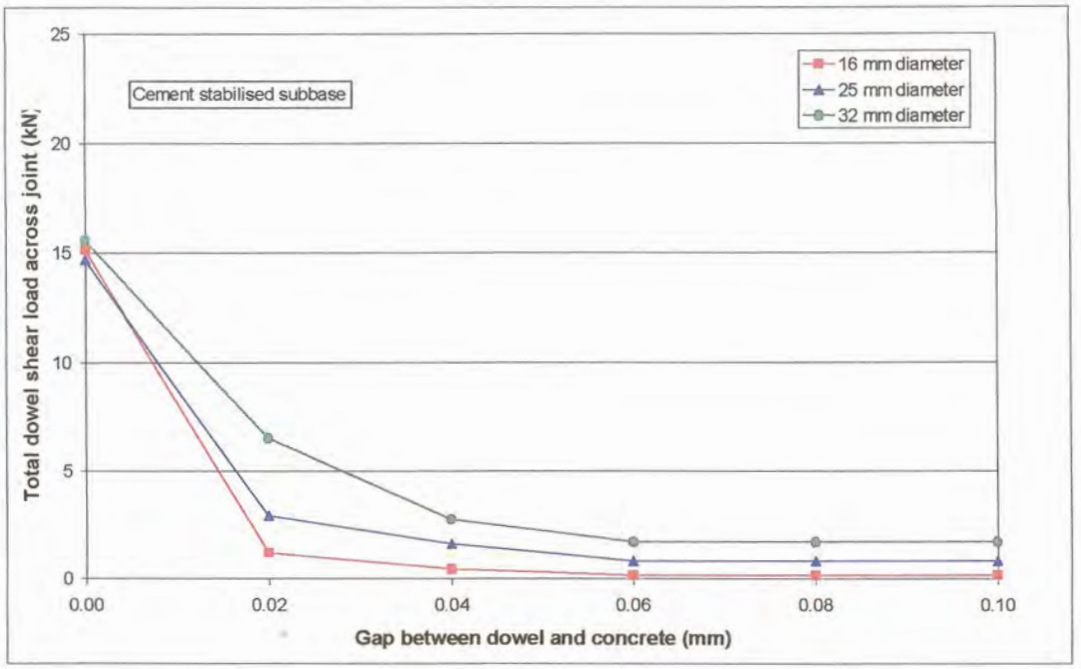

Figure D.31: Total shear load transferred across joint due to dowels with dowel bar spacing at 450 mm (cement stabilised subbase)

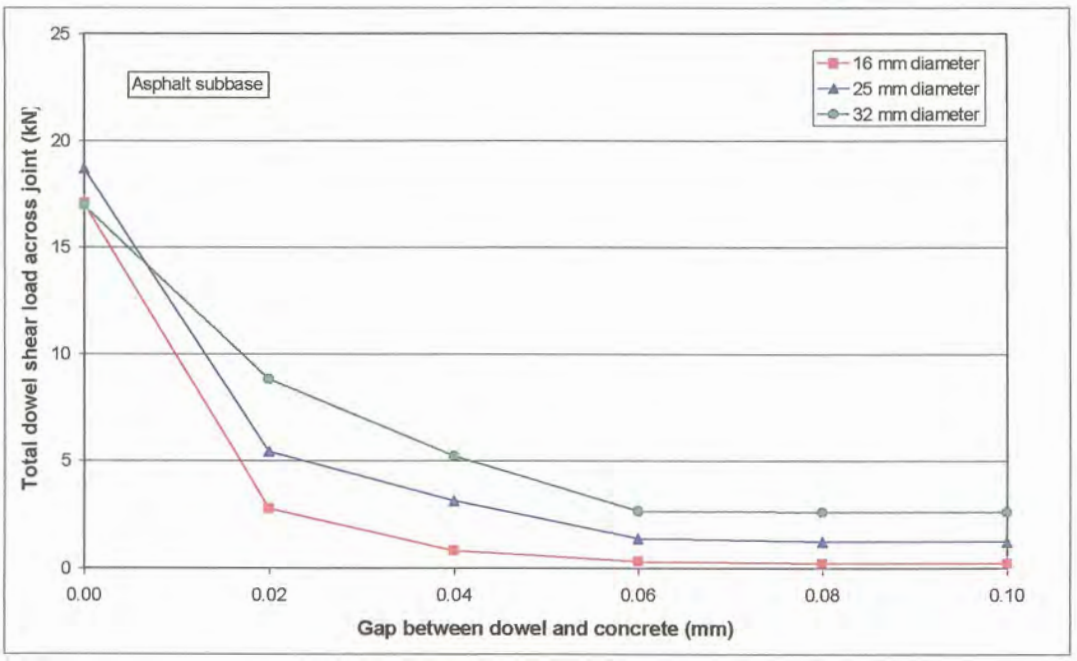

Figure D.32: Total shear load transferred across joint due to dowels with dowel bar spacing at 450 mm (asphalt subbase)

D.4.1.3 Dowel bar spacing – 600 mm

Figures D.33 to D.35 present the deflection load transfer efficiency for 16, 25, and 32 mm diameter dowel bars at 600 mm spacing with increasing gap width around the dowels.

The total shear force transferred across the joint due to the dowels at increasing gap widths is presented in Figures D.36 to D.38.

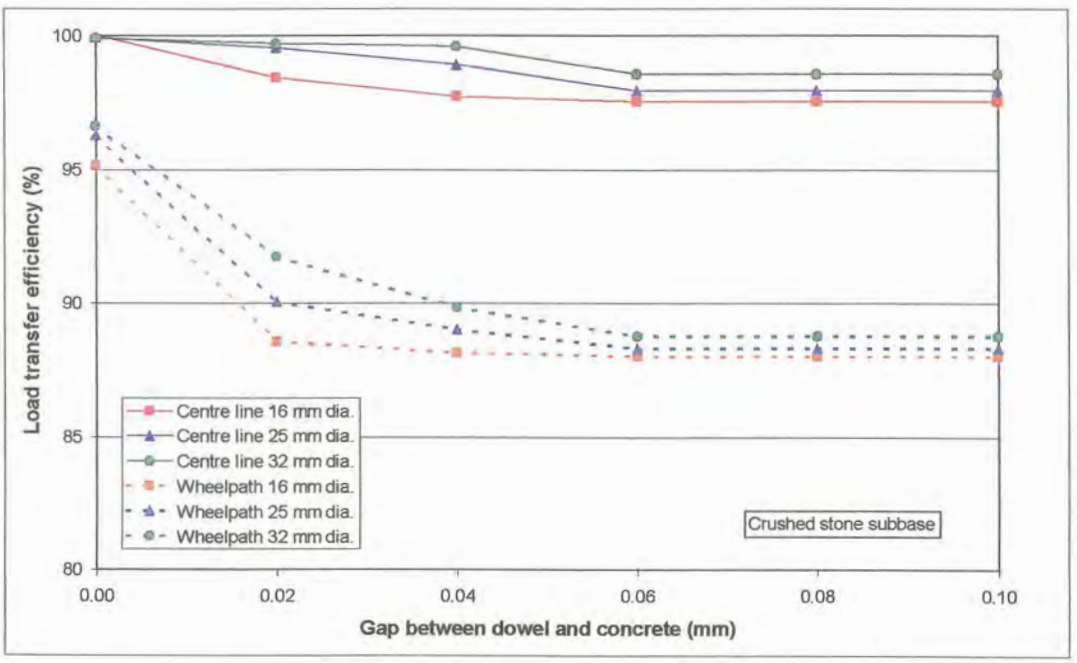

Figure D.33: Deflection load transfer efficiency with dowel bar spacing at 600 mm (crushed stone subbase)

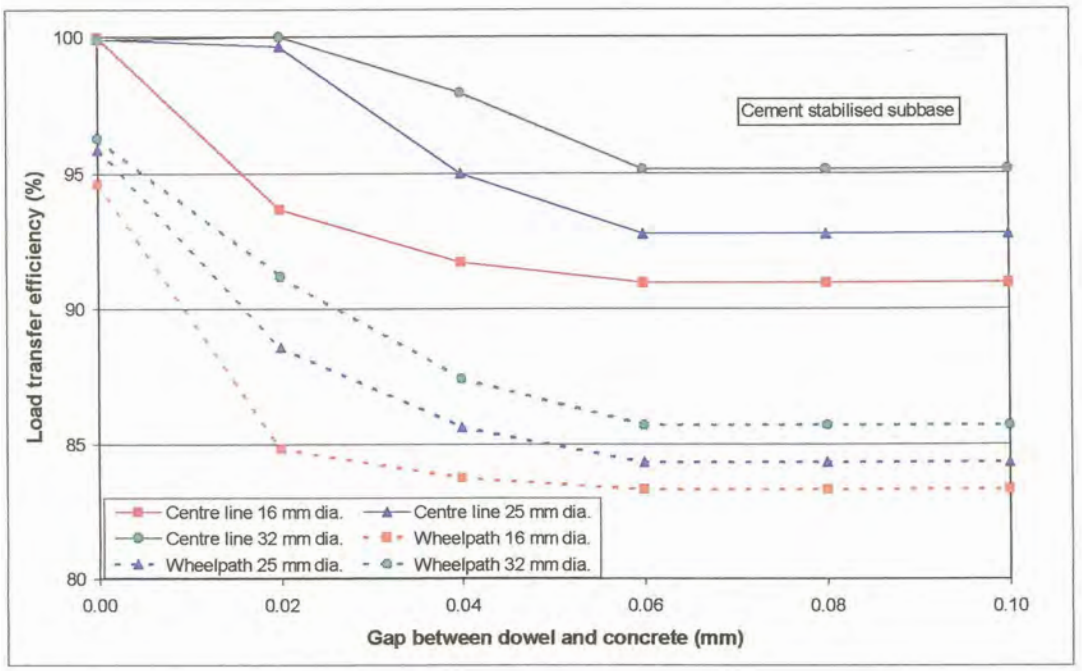

Figure D.34: Deflection load transfer efficiency with dowel bar spacing at 600 mm (cement stabilised subbase)

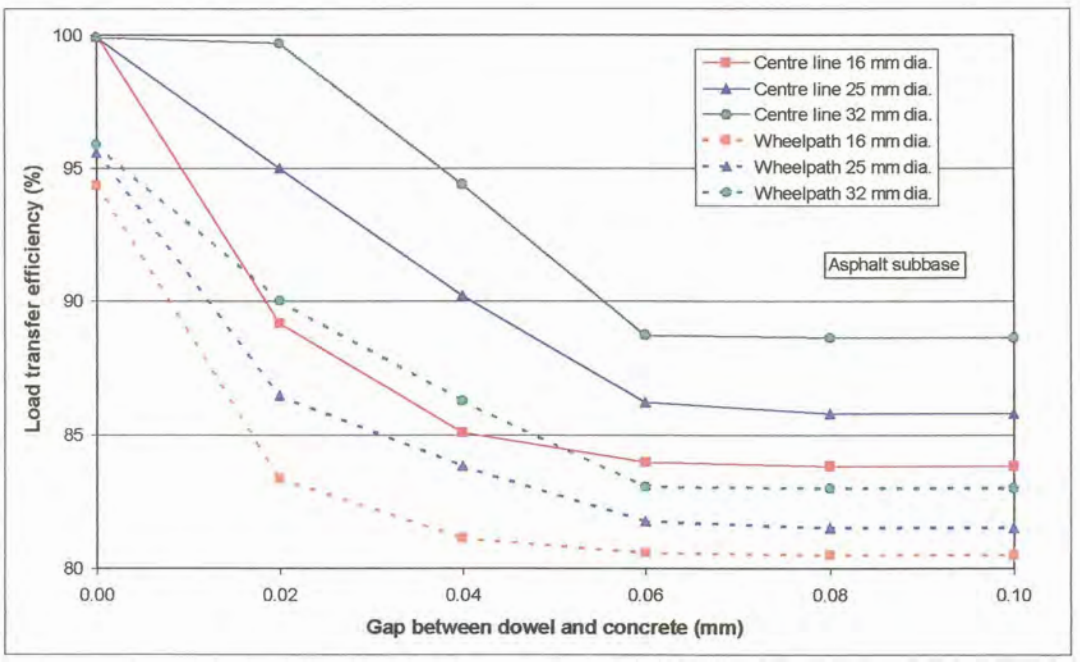

Figure D.35: Deflection load transfer efficiency with dowel bar spacing at 600 mm (asphalt subbase)

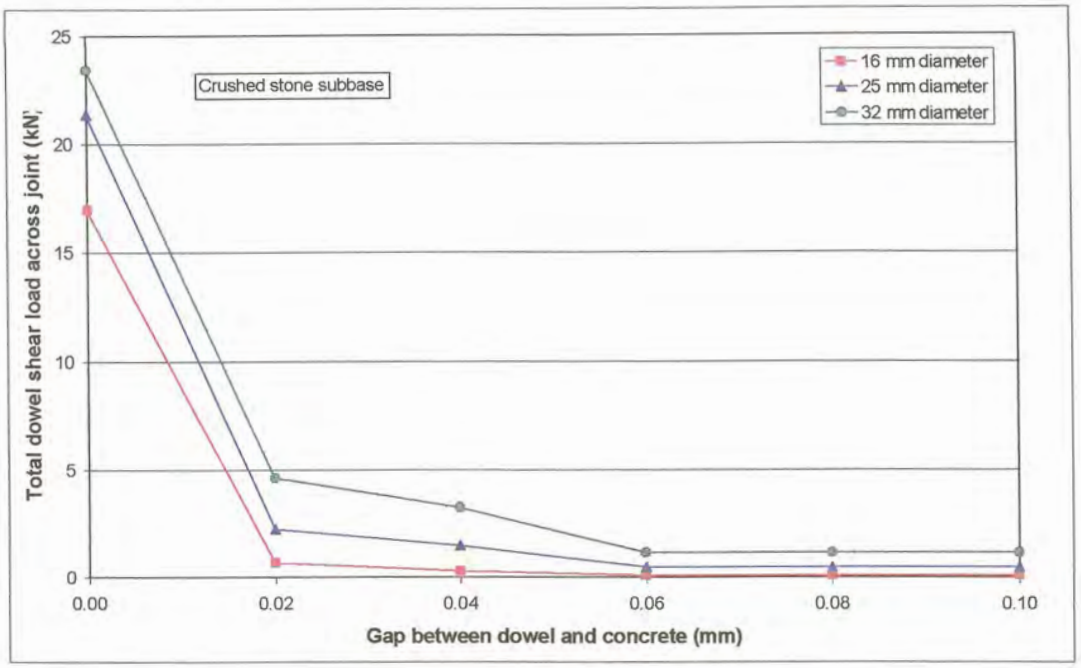

Figure D.36: Total shear load transferred across joint due to dowels with dowel bar spacing at 600 mm (crushed stone subbase)

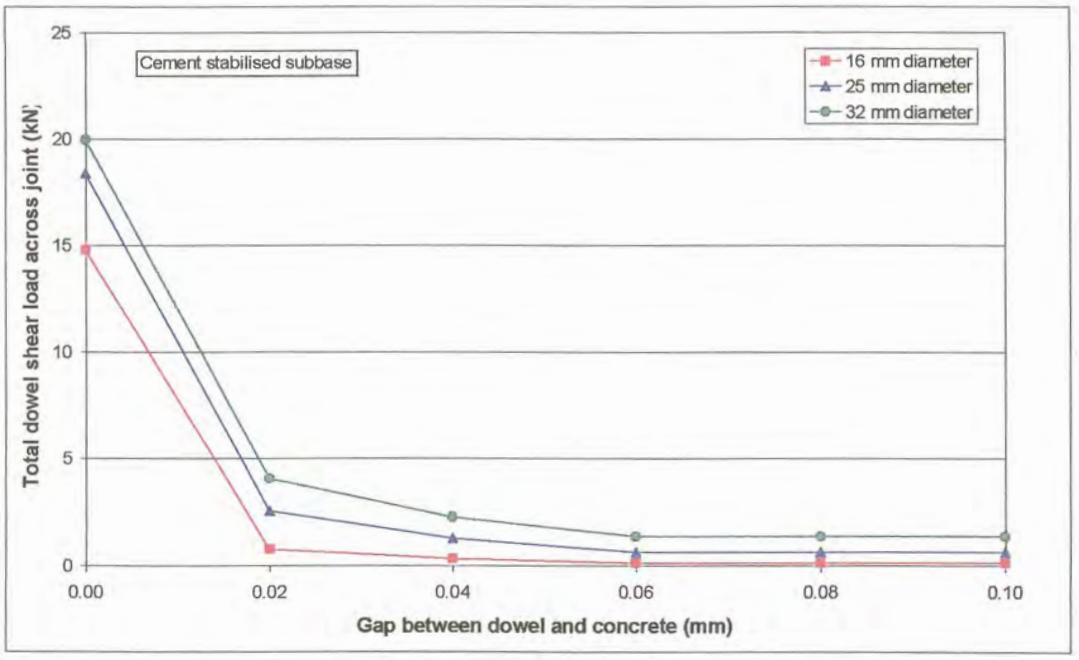

Figure D.37: Total shear load transferred across joint due to dowels with dowel bar spacing at 600 mm (cement stabilised subbase)

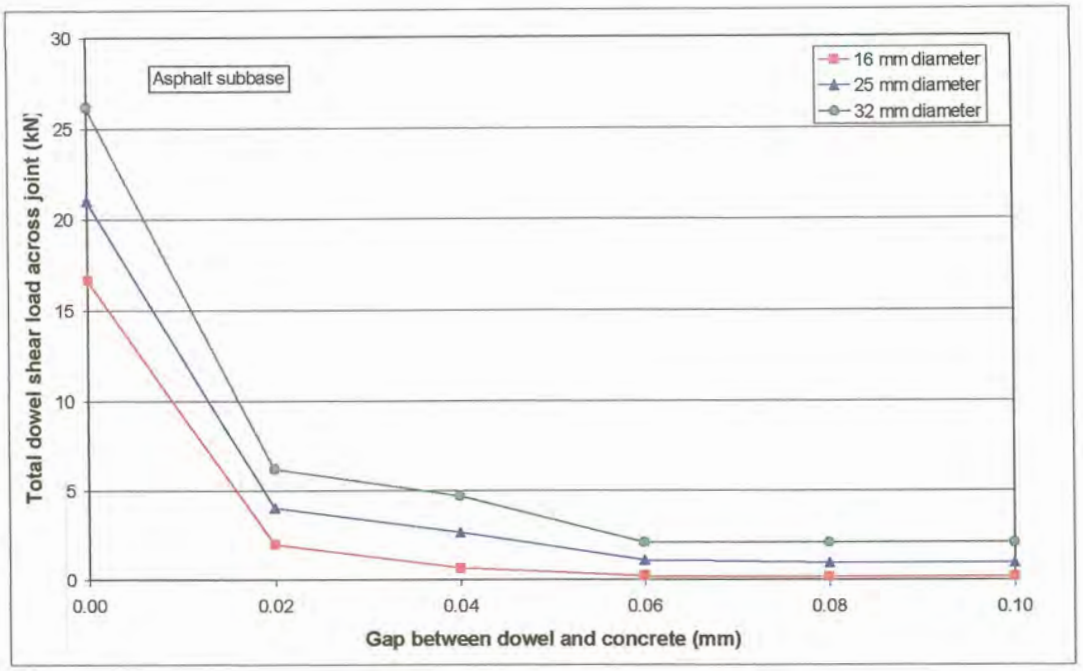

Figure D.38: Total shear load transferred across joint due to dowels with dowel bar spacing at 600 mm (asphalt subbase)

D.4.2 CONSTANT DOWEL BAR DIAMETER AT INCREASED DOWEL BAR SPACING

The effect of increasing the dowel bar spacing for a specific dowel bar diameter was also investigated. The results already obtained were regrouped for this purpose.

D.4.2.1 16 mm Diameter dowels

The deflection load transfer efficiency for 16 mm diameter dowel bars with increasing gap width between the dowel and the concrete at dowel bar spacings of 300, 450, and 600 mm, for each of the subbases considered, are presented in Figures D.39 to D.41. The deflection load transfer efficiency of an unloaded position, centre line (CL) was compared with that of a loaded position, wheelpath (WP).

Similarly the total shear load transferred across the joint through the dowels for 16 mm diameter dowels are presented in Figures D.42 to D.44.

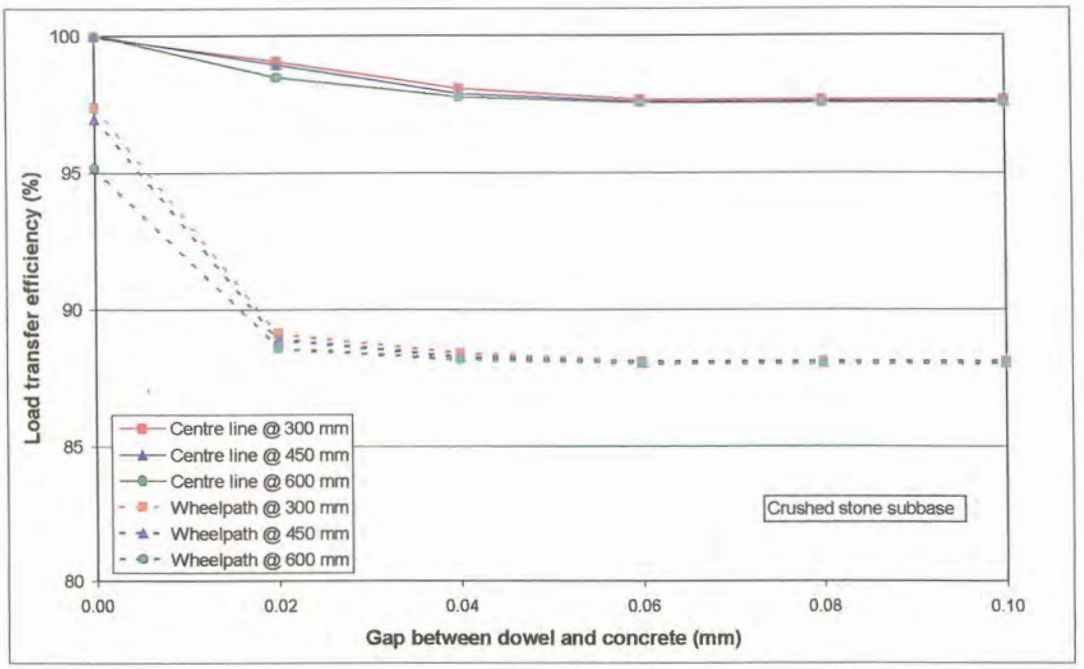

Figure D.39: Deflection load transfer efficiency for 16 mm diameter dowel bars at increased dowel bar spacing (crushed stone subbase)

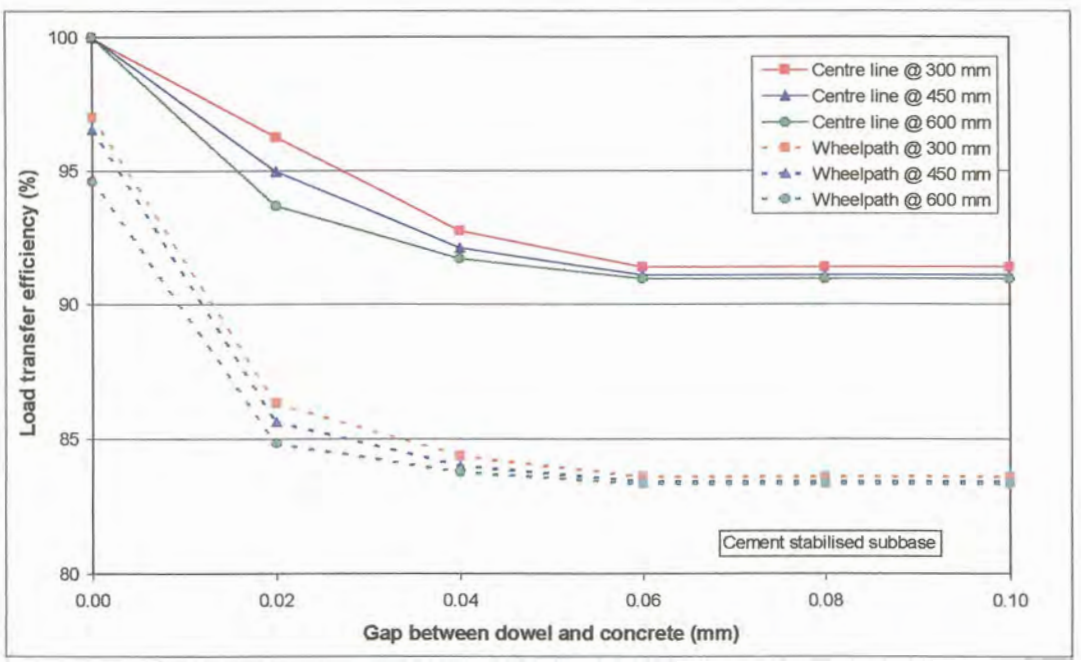

Figure D.40: Deflection load transfer efficiency for 16 mm diameter dowel bars at increased dowel bar spacing (cement stabilised subbase)

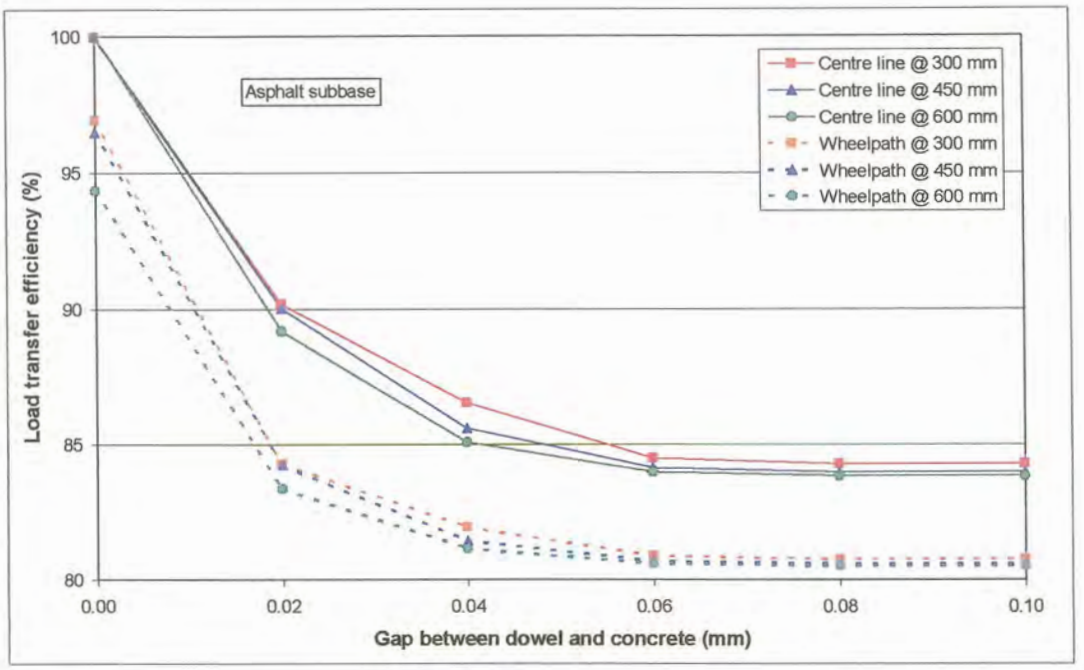

Figure D.41: Deflection load transfer efficiency for 16 mm diameter dowel bars at increased dowel bar spacing (asphalt subbase)

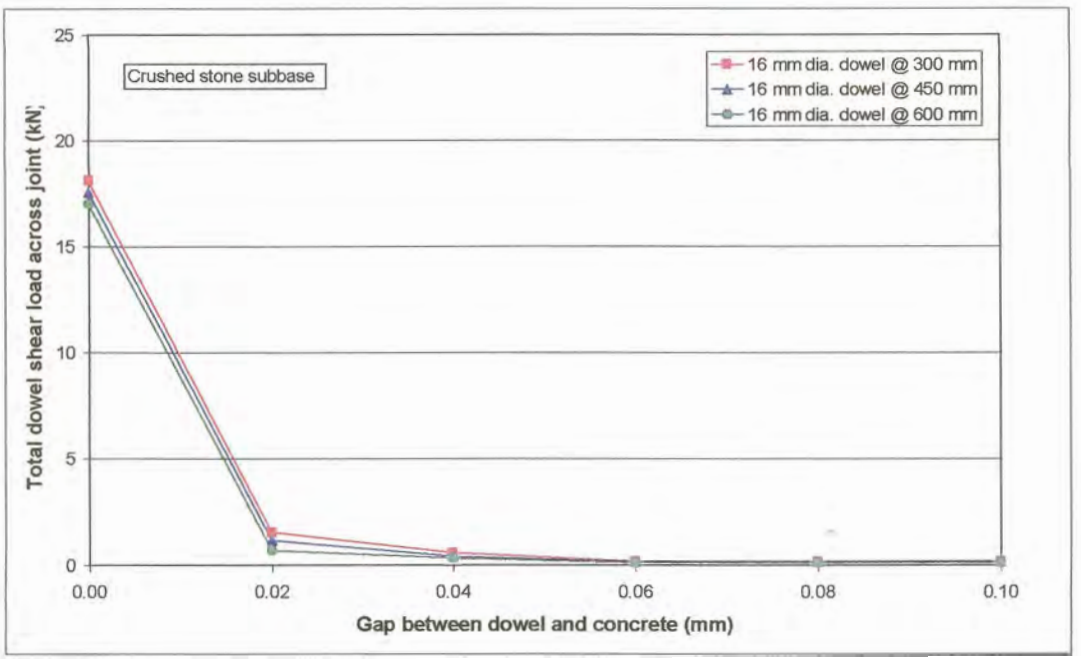

Figure D.42: Total shear load transferred across joint due to 16 mm diameter dowels with increased dowel bar spacing (crushed stone subbase)

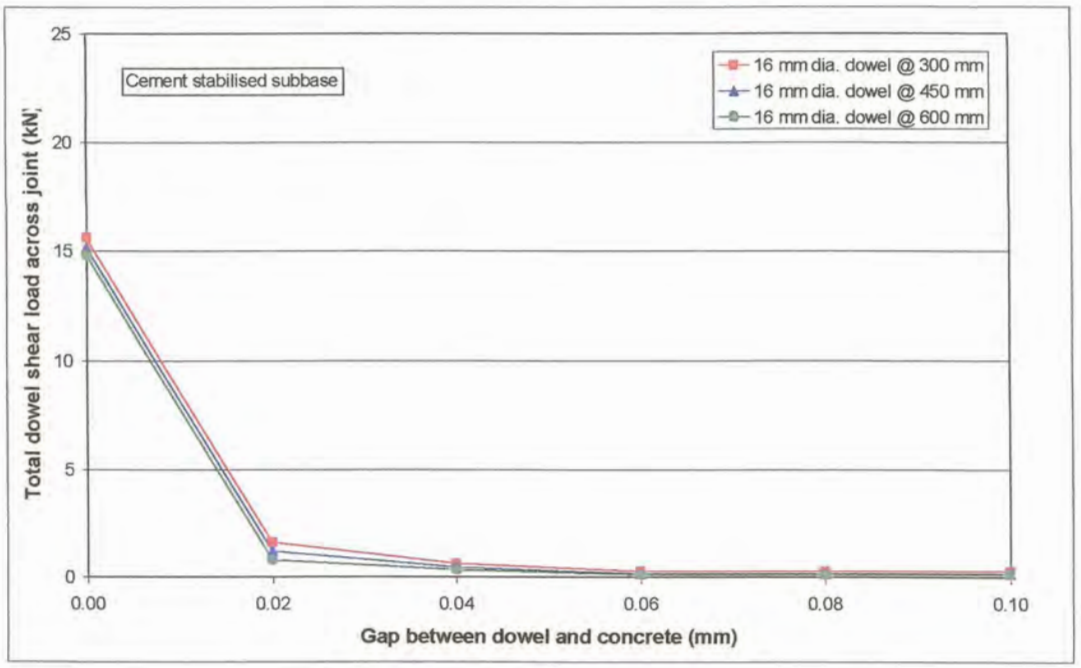

Figure D.43: Total shear load transferred across joint due to 16 mm diameter dowels with increased dowel bar spacing (cement stabilised subbase)

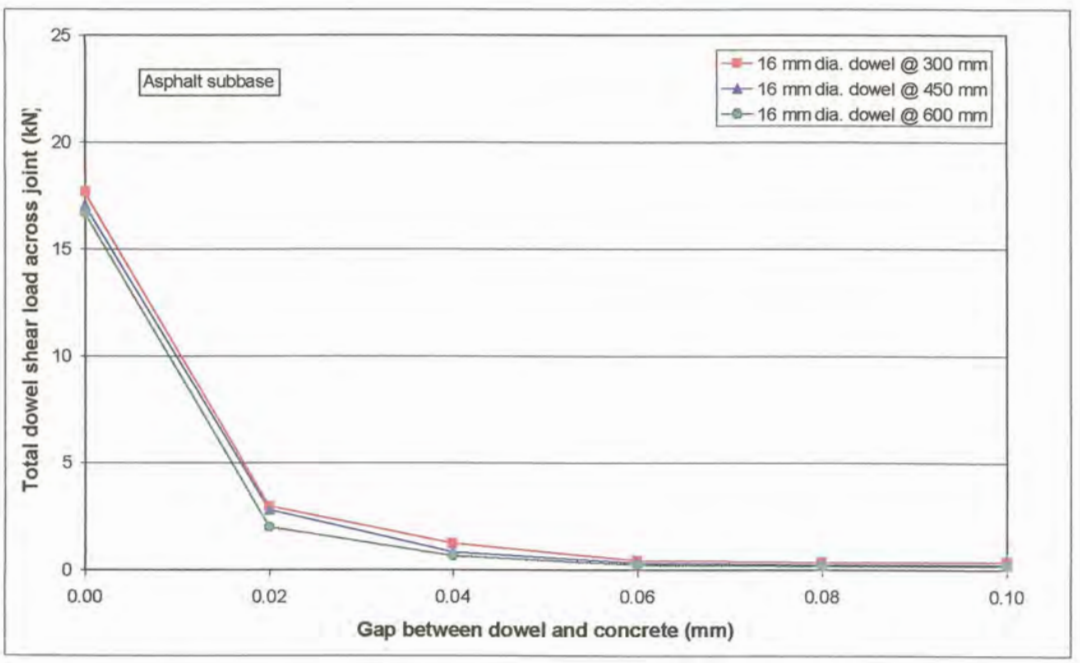

Figure D.44: Total shear load transferred across joint due to 16 mm diameter dowels with increased dowel bar spacing (asphalt subbase)

D.4.2.2 25 mm Diameter dowels

The deflection load transfer efficiency for 25 mm diameter dowel bars with increasing gap width between the dowel and the concrete at dowel bar spacings of 300, 450, and 600 mm, for each of the subbases considered, are presented in Figures D.45 to D.47. The deflection load transfer efficiency of an unloaded position, centre line (CL) was compared with that of a loaded position, wheel-path (WP).

Similarly the total shear load transferred across the joint through the dowels for 25 mm diameter dowels are presented in Figures D.48 to D.50.

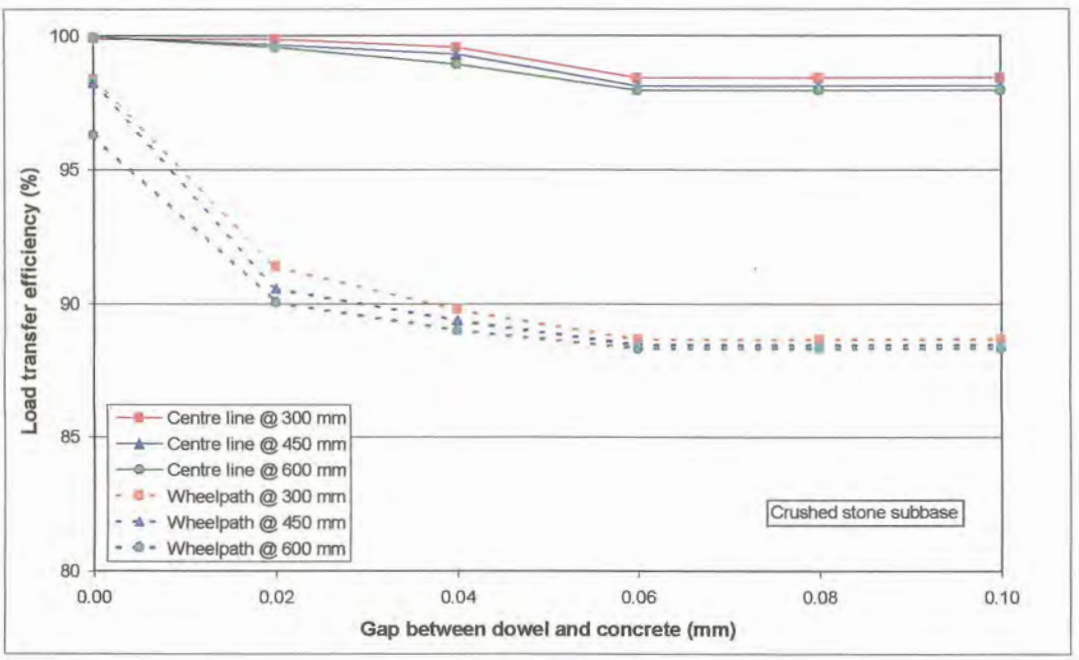

Figure D.45: Deflection load transfer efficiency for 25 mm diameter dowel bars at increased dowel bar spacing (crushed stone subbase)

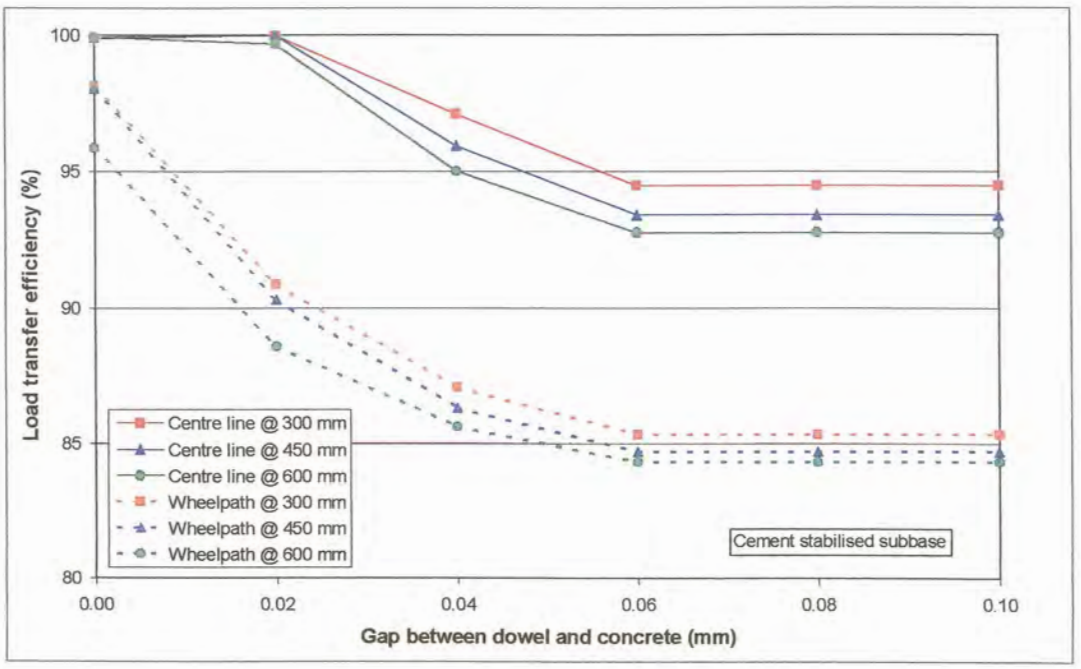

Figure D.46: Deflection load transfer efficiency for 25 mm diameter dowel bars at increased dowel bar spacing (cement stabilised subbase)

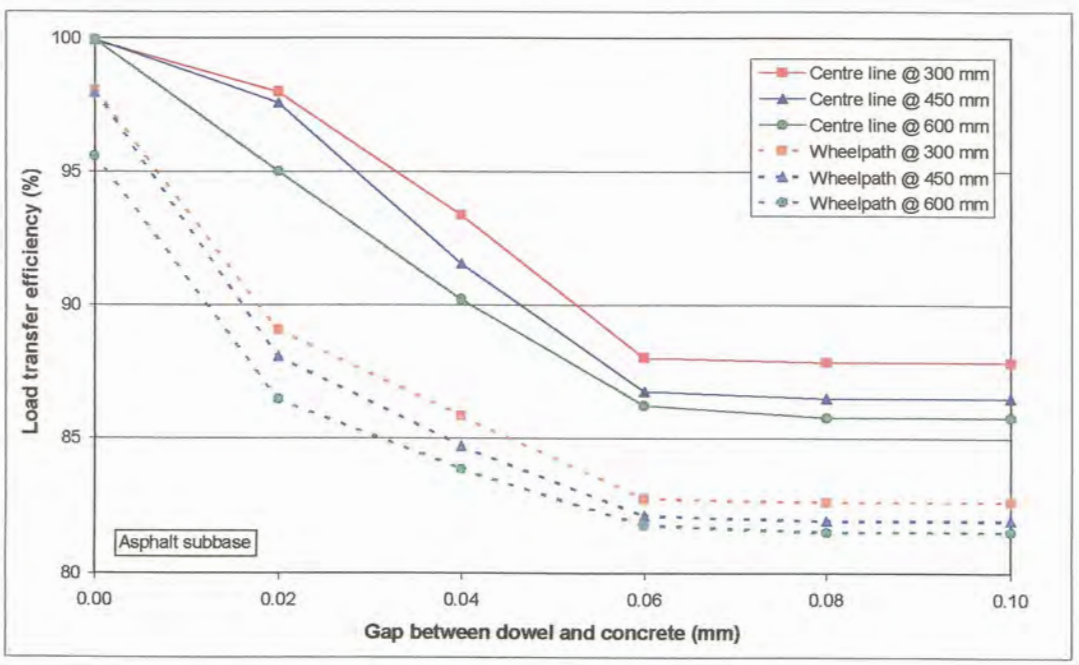

Figure D.47: Deflection load transfer efficiency for 25 mm diameter dowel bars at increased dowel bar spacing (asphalt subbase)

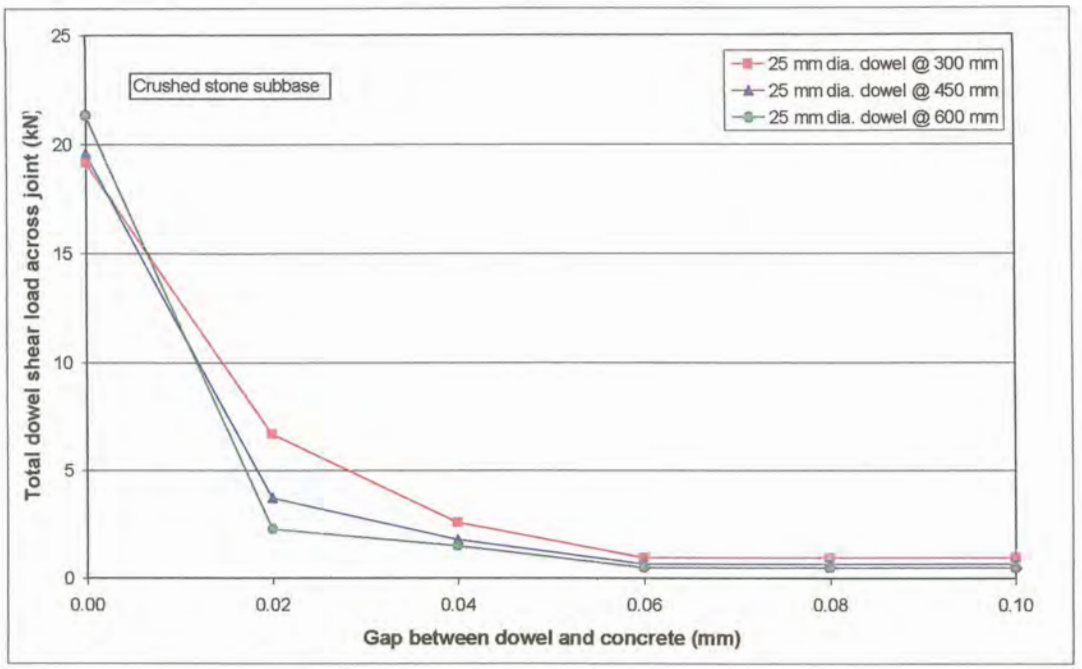

Figure D.48: Total shear load transferred across joint due to 25 mm diameter dowels with increased dowel bar spacing (crushed stone subbase)

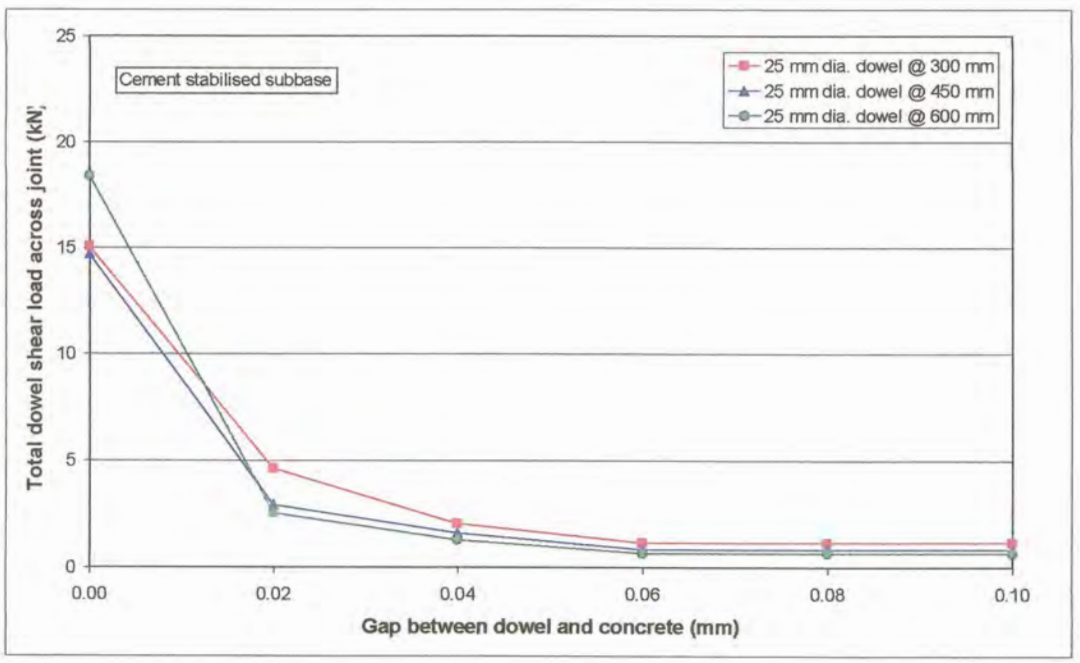

Figure D.49: Total shear load transferred across joint due to 25 mm diameter dowels with increased dowel bar spacing (cement stabilised subbase)

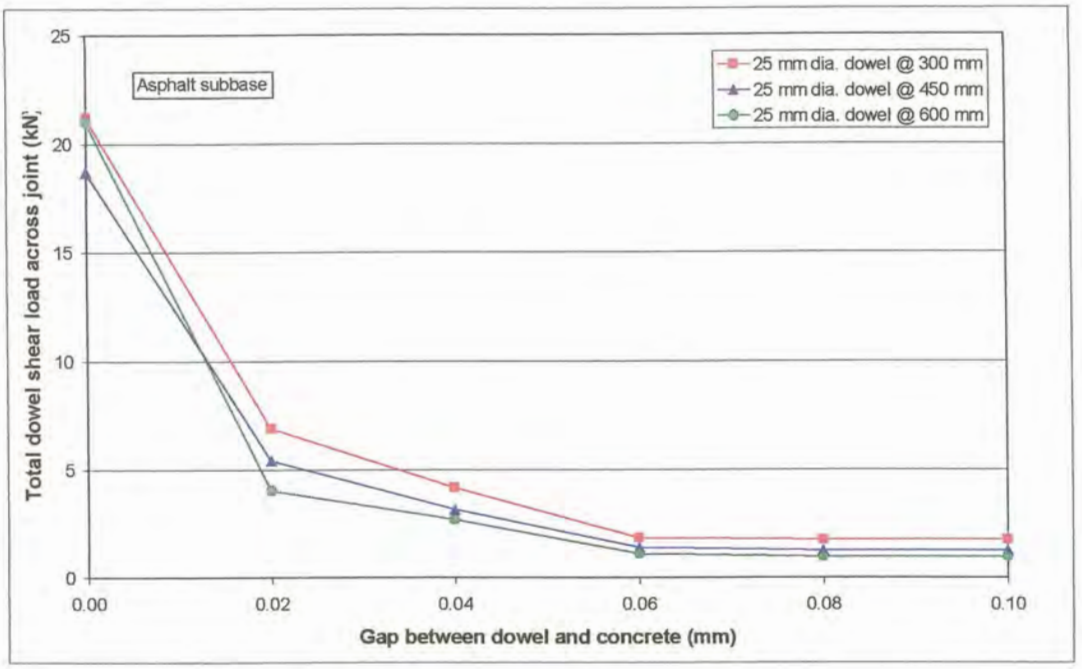

Figure D.50: Total shear load transferred across joint due to 25 mm diameter dowels with increased dowel bar spacing (asphalt subbase)

D.4.2.3 32 mm Diameter dowels

The deflection load transfer efficiency for 32 mm diameter dowel bars with increasing gap width between the dowel and the concrete at dowel bar spacings of 300, 450, and 600 mm, for each of the subbases considered, are presented in Figures D.51 to D.53. The deflection load transfer efficiency of an unloaded position, centre line (CL) was compared with that of a loaded position, wheel-path (WP).

Similarly the total shear load transferred across the joint through the dowels for 32 mm diameter dowels are presented in Figures D.54 to D.56.

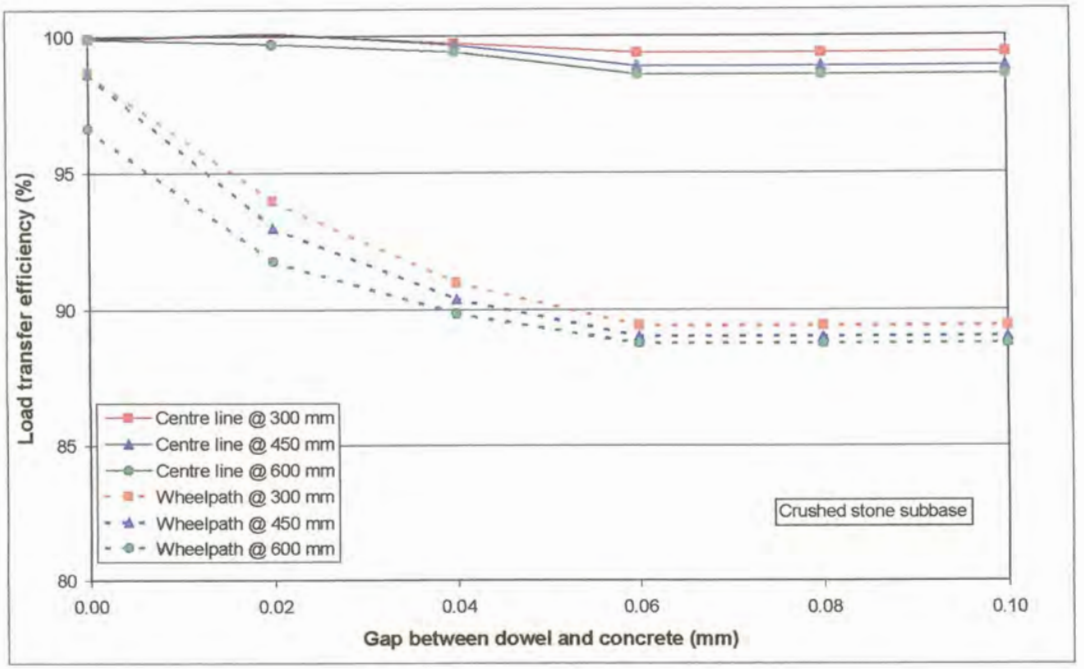

Figure D.51: Deflection load transfer efficiency for 32 mm diameter dowel bars at increased dowel bar spacing (crushed stone subbase)

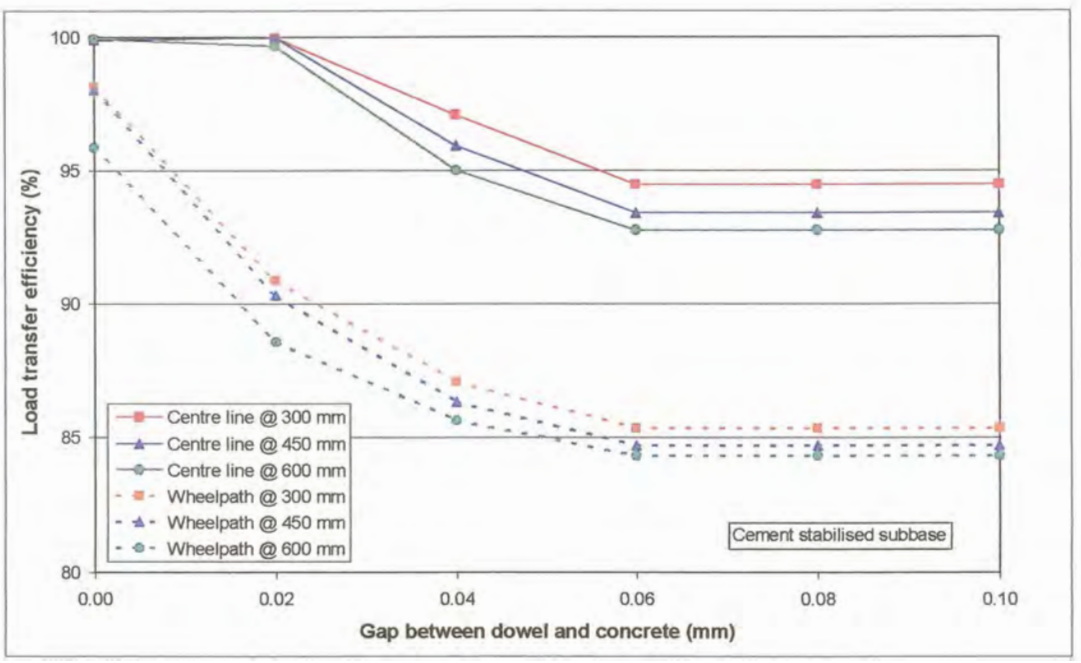

Figure D.52: Deflection load transfer efficiency for 32 mm diameter dowel bars at increased dowel bar spacing (cement stabilised subbase)

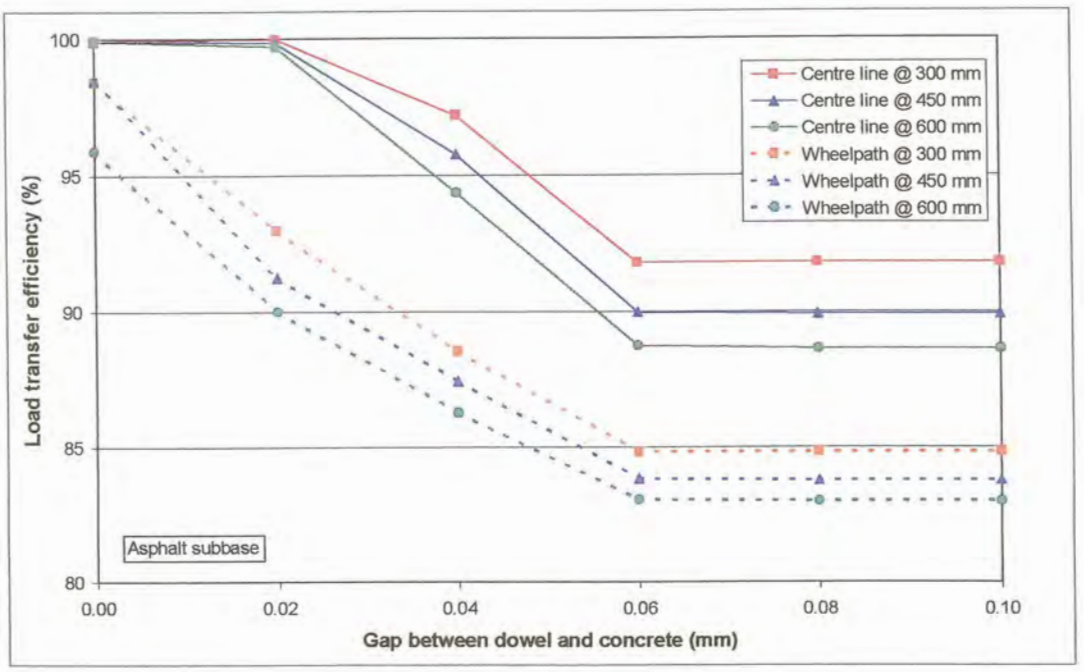

Figure D.53: Deflection load transfer efficiency for 32 mm diameter dowel bars at increased dowel bar spacing (asphalt subbase)

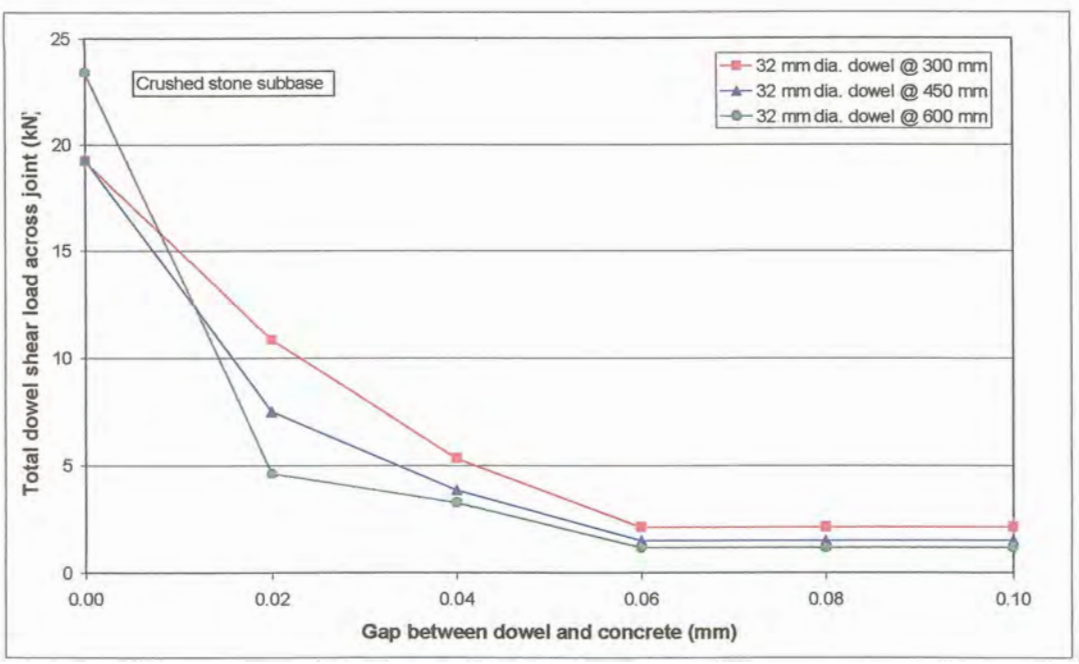

Figure D.54: Total shear load transferred across joint due to 32 mm diameter dowels with increased dowel bar spacing (crushed stone subbase)

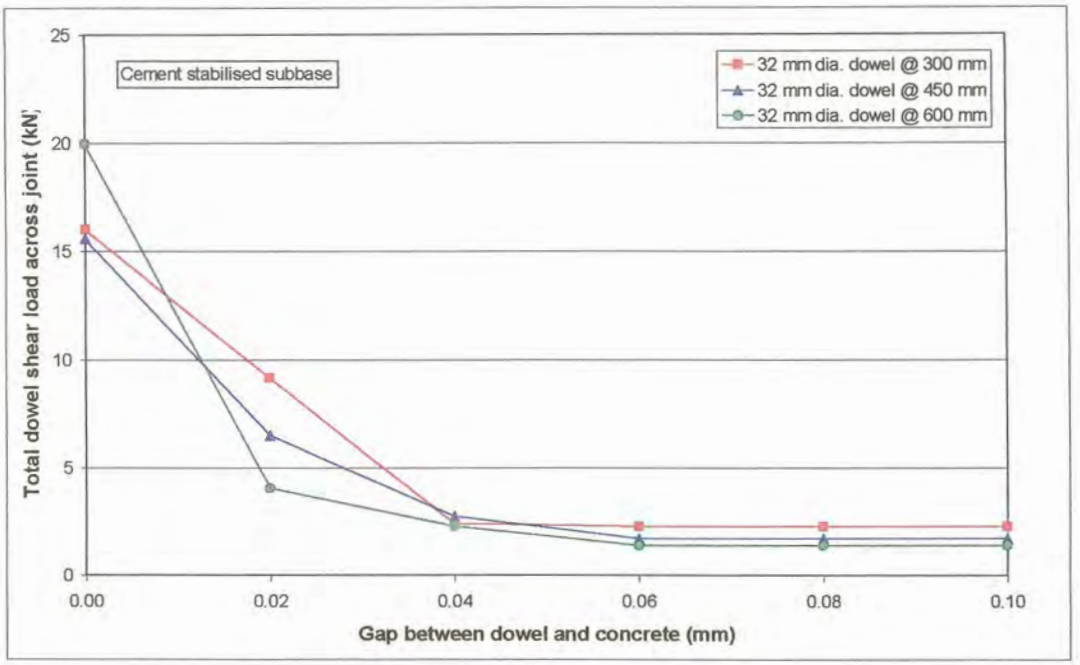

Figure D.55: Total shear load transferred across joint due to 32 mm diameter dowels with increased dowel bar spacing (cement stabilised subbase)

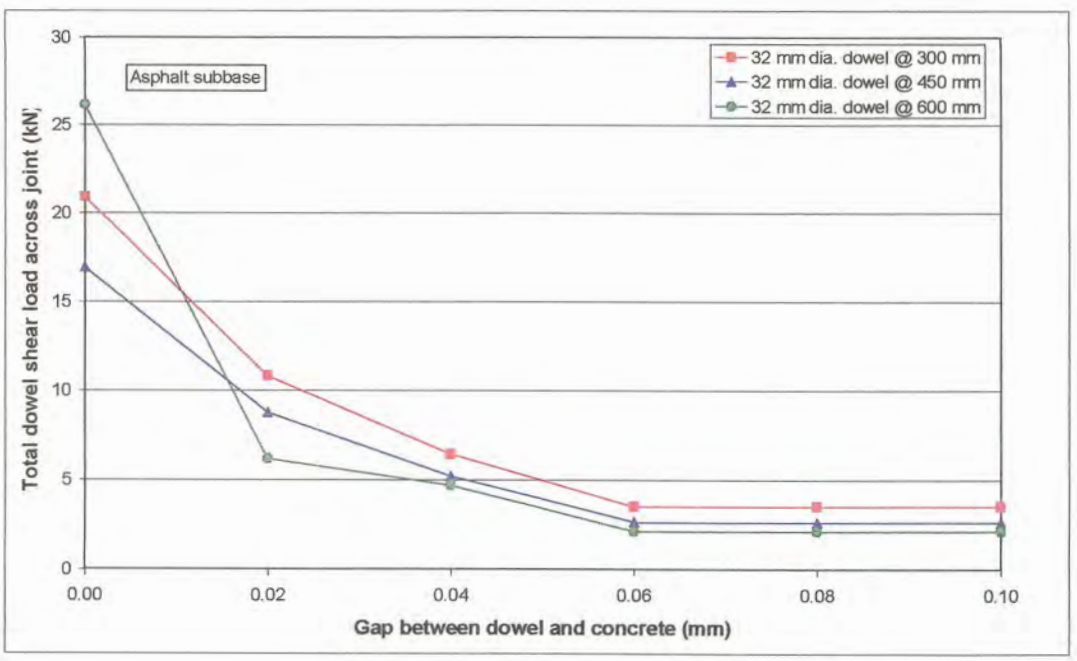

Figure D.56: Total shear load transferred across joint due to 32 mm diameter dowels with increased dowel bar spacing (asphalt subbase)

D.5 COMBINED AGGREGATE INTERLOCK AND DOWEL MODELLING

Soroushian et al (1988) investigated the combined effect of aggregate interlock and dowel action in reinforced concrete beam elements against sliding shear at a crack. Algorithms were developed for predicting the aggregate interlock constitutive behaviour using some empirical formulations. They concluded that at very small sliding-shear deformations (below 0,2 mm) the dowel action tended to dominate the shear resistance. At larger deformations, however, the aggregate interlock became more dominant. At sliding-shear deformations greater than 0,7 mm, about 65% of the total shear resistance in the case studied was provided by aggregate interlock. One of the results of their tests is given in Figure D.57.

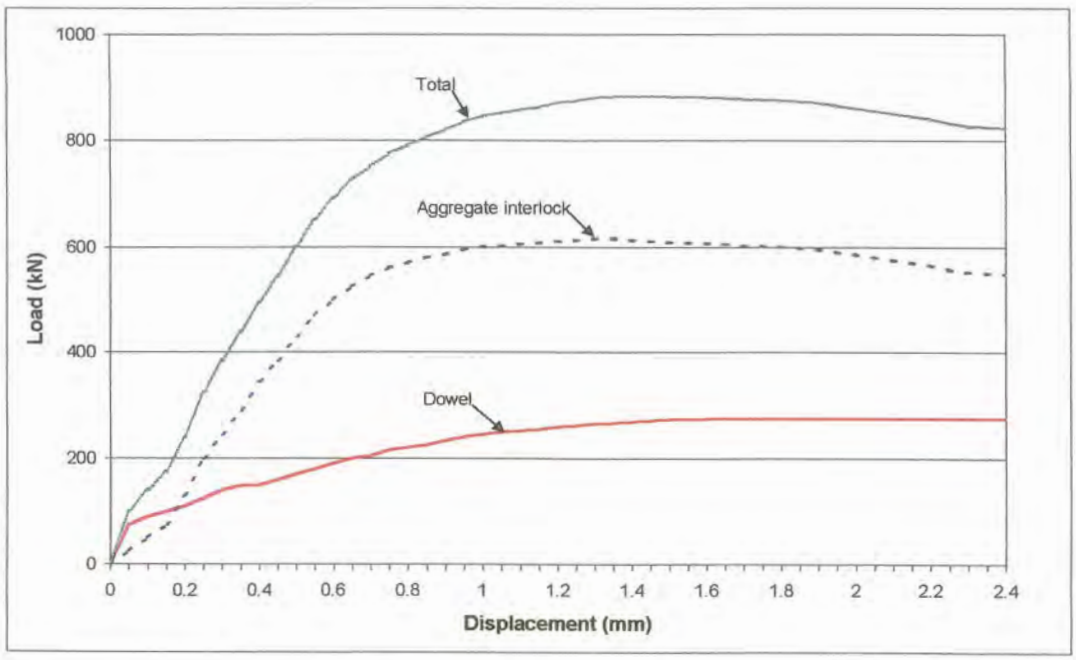

Figure D.57: Sliding shear behaviour at a constant crack width of 0,5 mm (Soroushian et al, 1988)

The combined effect of aggregate interlock and dowel action was also determined with EverFE. The same model as the one used in aggregate interlock modelling (par. D.3) with a cement stabilised subbase was used. To determine the effect of dowels in the model, 16 mm diameter dowels at 300 mm spacing were placed across the joint. During theoretical modelling the crack width was varied, while the gap around the dowel was kept constant.

The deflection load transfer efficiency obtained for 9 mm and 63 mm aggregate sizes are presented in Figure D.58. From this figure, it is obvious that the combined efficiency of aggregate interlock and dowels is far greater than for aggregate interlock only.

The maximum aggregate interlock shear stress measured in the wheel path was less for the combined aggregate interlock and dowel action models than for the models relying on aggregate interlock only (see Figure D.59). This could be ascribed to the dowels relieving some of the stress in the aggregate.

Just as for the shear stress, the total aggregate interlock shear force transferred across the joint was also less for the combined model than for the aggregate interlock model, as can be seen from Figure D.60.

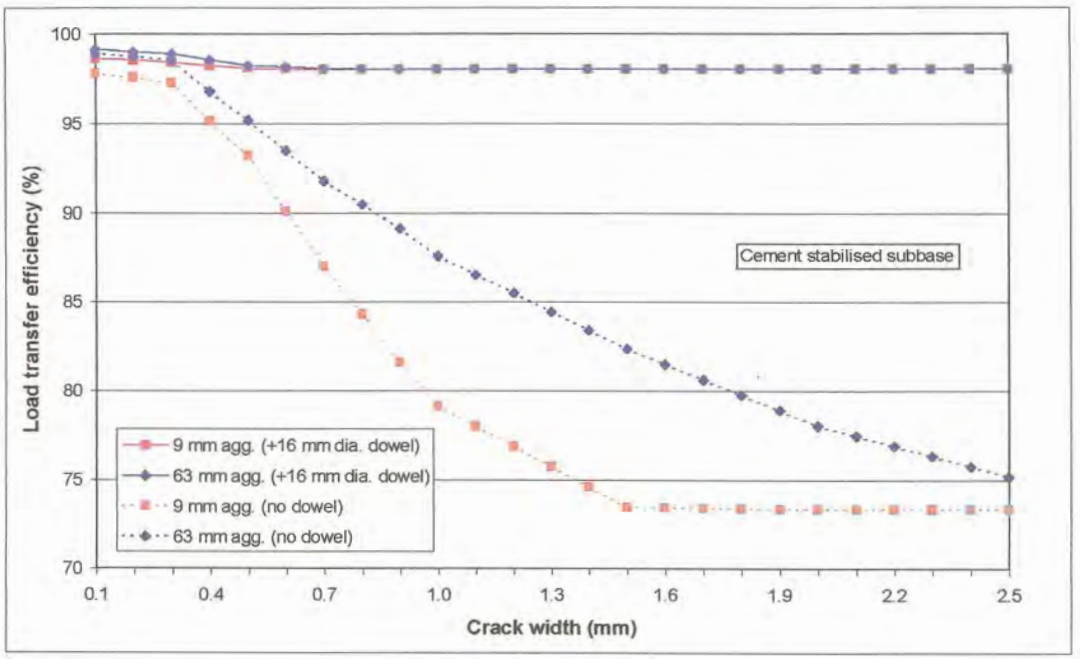

Figure D.58: Deflection load transfer efficiency in the wheel path – aggregate interlock versus combined effect of aggregate interlock and dowel action (no gap around dowel)

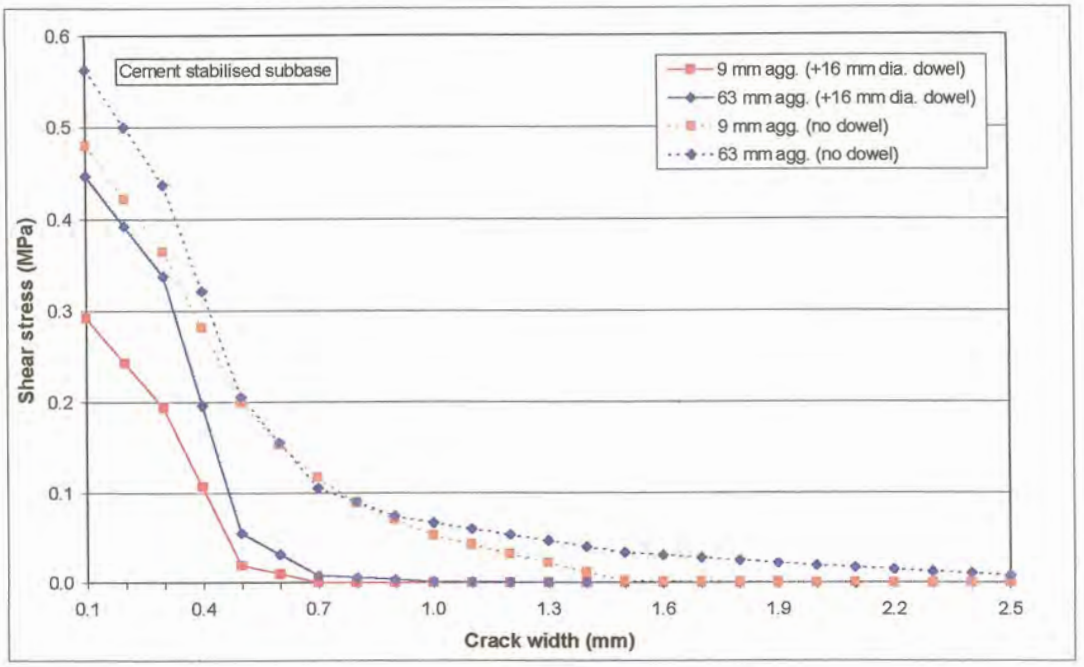

Figure D.59: Maximum shear stress at joint in wheel path – aggregate interlock versus combined effect of aggregate interlock and dowel action (no gap around dowel)

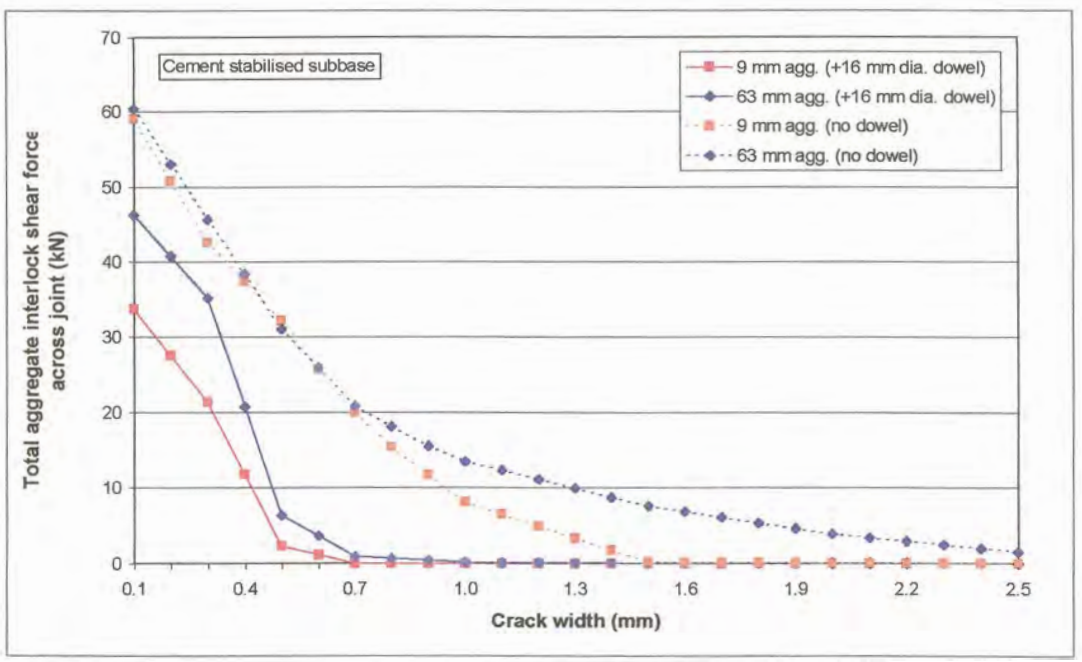

Figure D.60: Total shear force transferred across joint – aggregate interlock versus combined effect of aggregate interlock and dowel action (no gap around dowel)

The total shear force transferred across the crack due to dowel action was plotted on Figure D.61 together with the shear force transferred due to aggregate interlock for 9 mm and 63 mm maximum aggregate sizes. From this figure it could be concluded that aggregate interlock was initially the main factor contributing to the transfer of shear forces across a joint. However, the forces transferred due to aggregate interlock decreased rapidly, and was already close to zero at 0,7 mm crack width. On the other hand, the shear force transferred across the joint due to dowel action was initially (at 0,1 mm crack width) approximately 45% and 17% of the aggregate interlock shear force transferred for 9 mm and 63 mm aggregate sizes, respectively. Where after it decreased slightly and then increased to become the main contributing factor to the transfer of shear forces across the joint at 0,7 mm crack width. The forces transferred through the dowels at small crack widths for the 63 mm aggregate was less than for the 9 mm aggregate, due to the greater efficiency of the larger aggregate size.

Figures D.62 and D.63 present the total shear force transferred across the joint obtained by summing the forces due to aggregate interlock and dowel action for 9 mm and 63 mm maximum size aggregate, respectively.

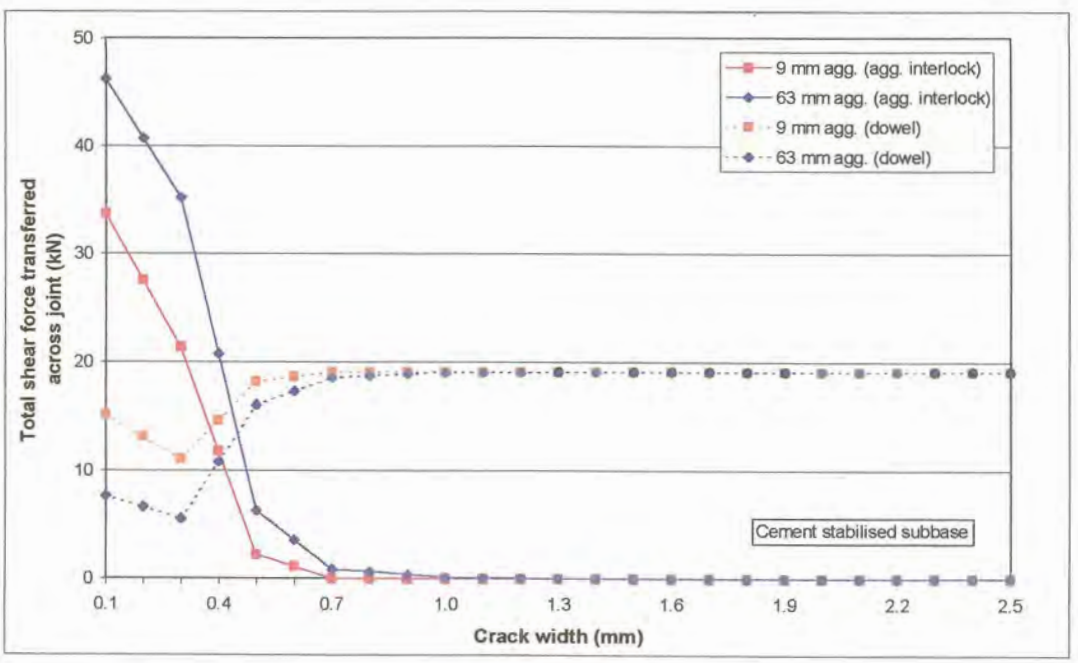

Figure D.61: Total shear force transferred across joint – combined effect of aggregate interlock and dowel action (no gap around dowel)

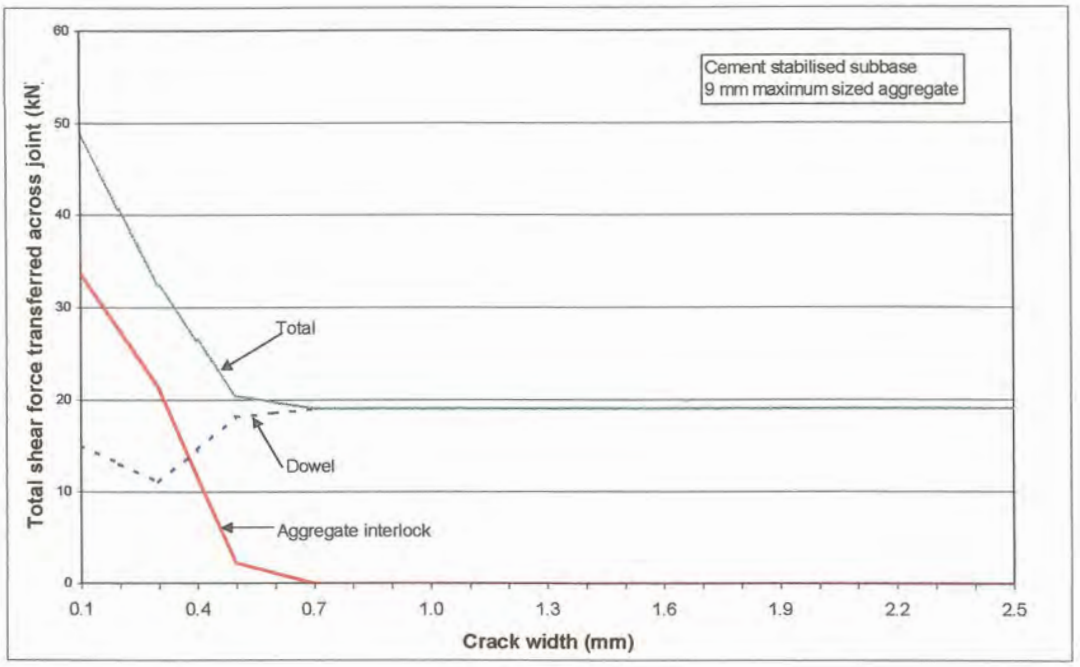

Figure D.62: Total shear force transferred across joint – 9 mm maximum sized aggregate – combined effect of aggregate interlock and dowel action (no gap around dowel)

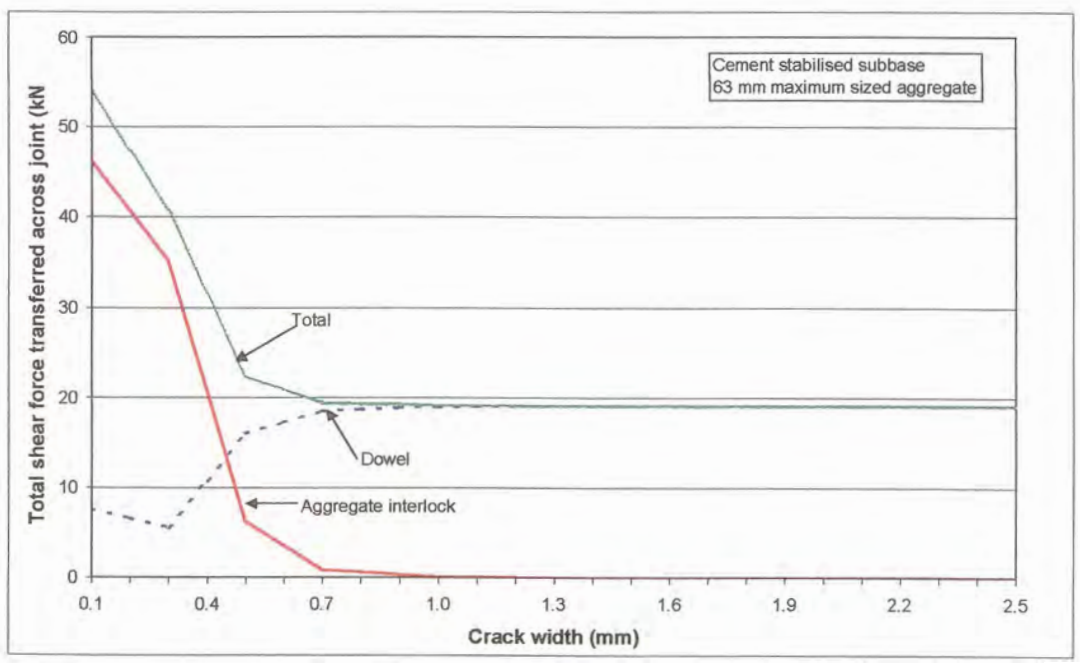

Figure D.63: Total shear force transferred across joint – 63 mm maximum sized aggregate – combined effect of aggregate interlock and dowel action (no gap around dowel)

The above theoretical analysis where the combined effect of aggregate interlock and dowel action was determined with EverFE, while varying the crack width, but keeping the gap around the dowel at zero, was repeated but in this instance, the gap around the dowel was also varied from 0,00 mm to 0,10 mm as described in paragraph D.3. The same model as the one used in aggregate interlock modelling (par. D.2) with a cement stabilised subbase was used. To determine the effect of dowels in the model, 16 mm diameter dowels at 300 mm spacing were placed across the joint.

The deflection load transfer efficiency obtained for 9 mm and 63 mm aggregate sizes and increasing gap sizes around the dowel bars are presented in Figures D.64 and D.65, respectively. From these figures, it is obvious that the bigger the gap around the dowel, the lower the load transfer efficiency. For comparison purposes, the values obtained for a joint relying on aggregate interlock only (no dowel), was also plotted on the graph. At a gap of 0,10 mm the load transfer efficiency approximated that of the "no dowel" case, which indicated that the dowel did not fulfil its purpose any more. This emphasised the importance of considering a gap around the dowel as well.

The development of maximum aggregate interlock shear stress relationships with increasing gap width around the dowel, measured in the wheel path for both 9 mm and 63 mm maximum aggregate sizes, are presented in detail in Figures D.66 to D.77. Once again, it is significant to note that the relationships obtained approximated the "no dowel" case.

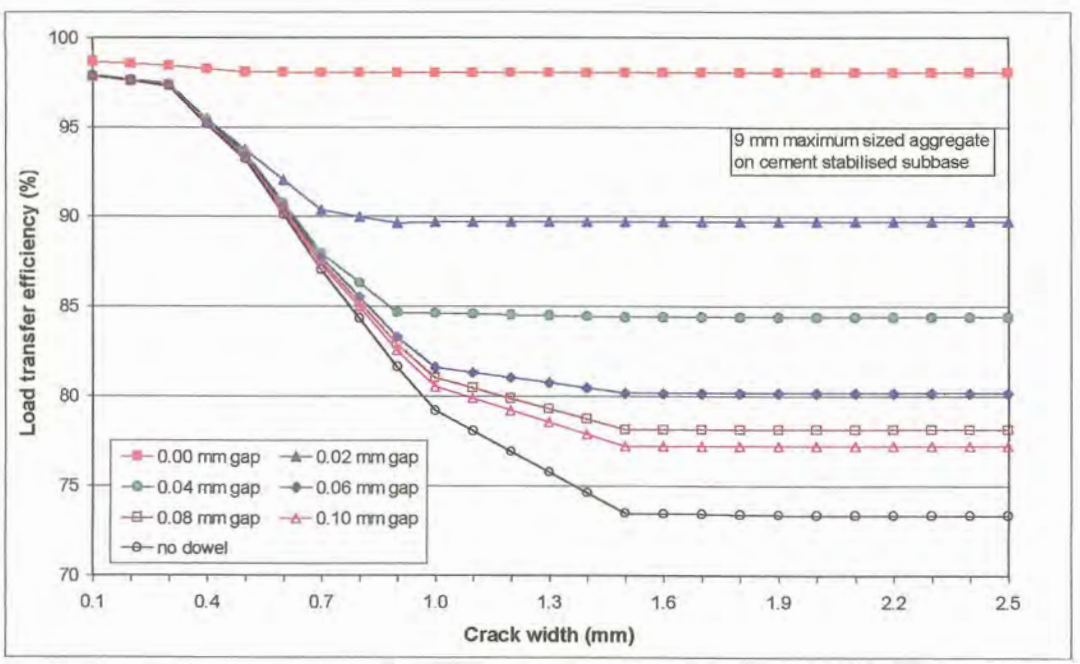

Figure D.64: Deflection load transfer efficiency in the wheel path – 9 mm maximum sized aggregate – combined affect of aggregate interlock and dowels (gap around dowel)

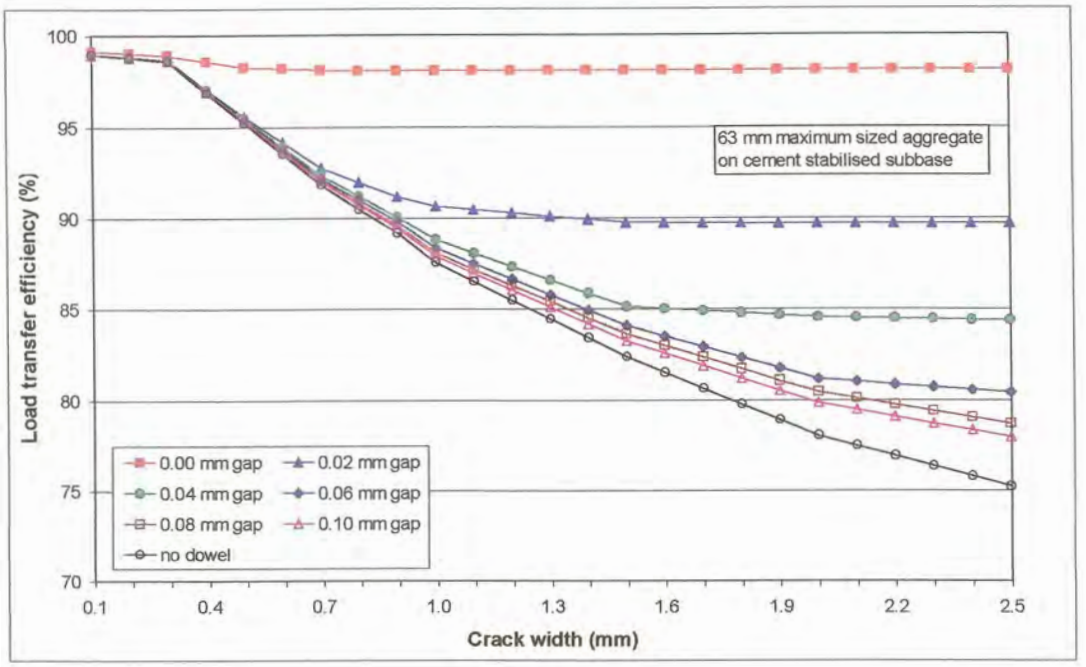

Figure D.65: Deflection load transfer efficiency in the wheel path – 63 mm maximum sized aggregate – combined affect of aggregate interlock and dowels (gap around dowel)

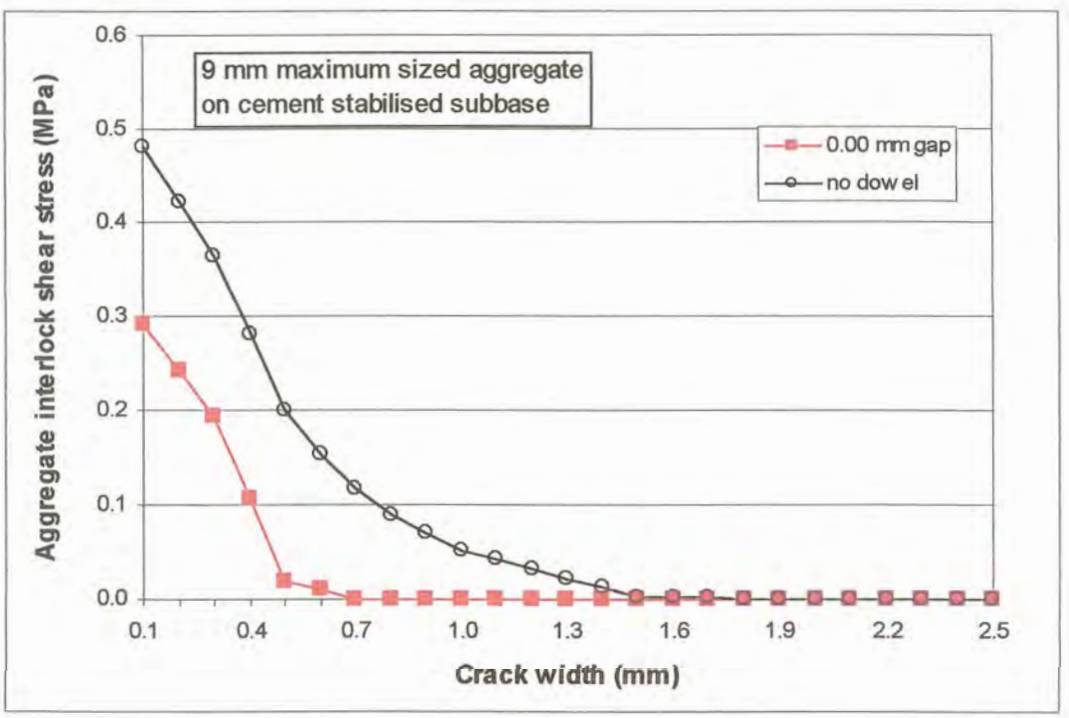

Figure D.66: Maximum aggregate interlock shear stress in the wheelpath – 9 mm maximum sized aggregate – combined affect of aggregate interlock and dowels (gap around dowel)

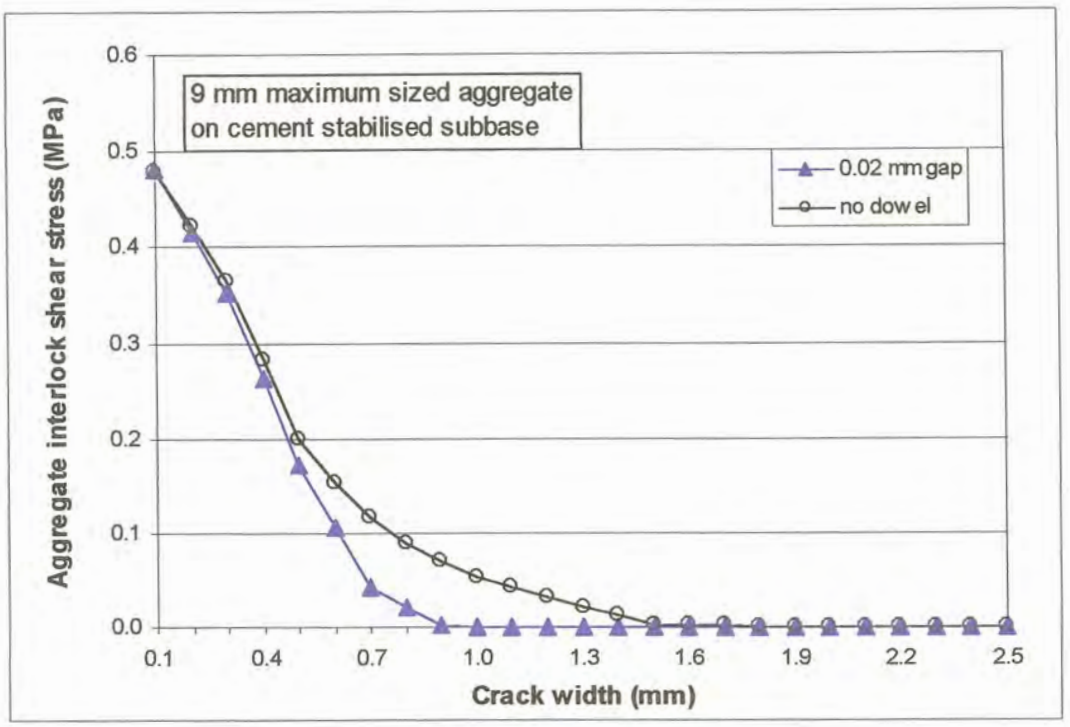

Figure D.67: Maximum aggregate interlock shear stress in the wheelpath – 9 mm maximum sized aggregate – combined affect of aggregate interlock and dowels (gap around dowel)

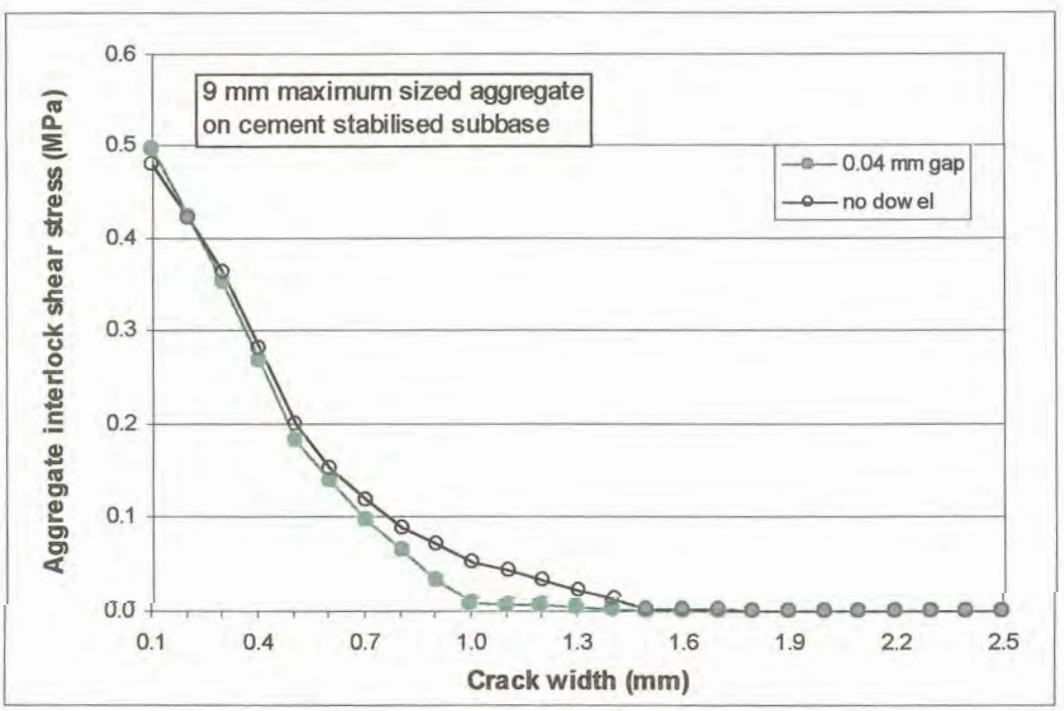

Figure D.68: Maximum aggregate interlock shear stress in the wheelpath – 9 mm maximum sized aggregate – combined affect of aggregate interlock and dowels (gap around dowel)

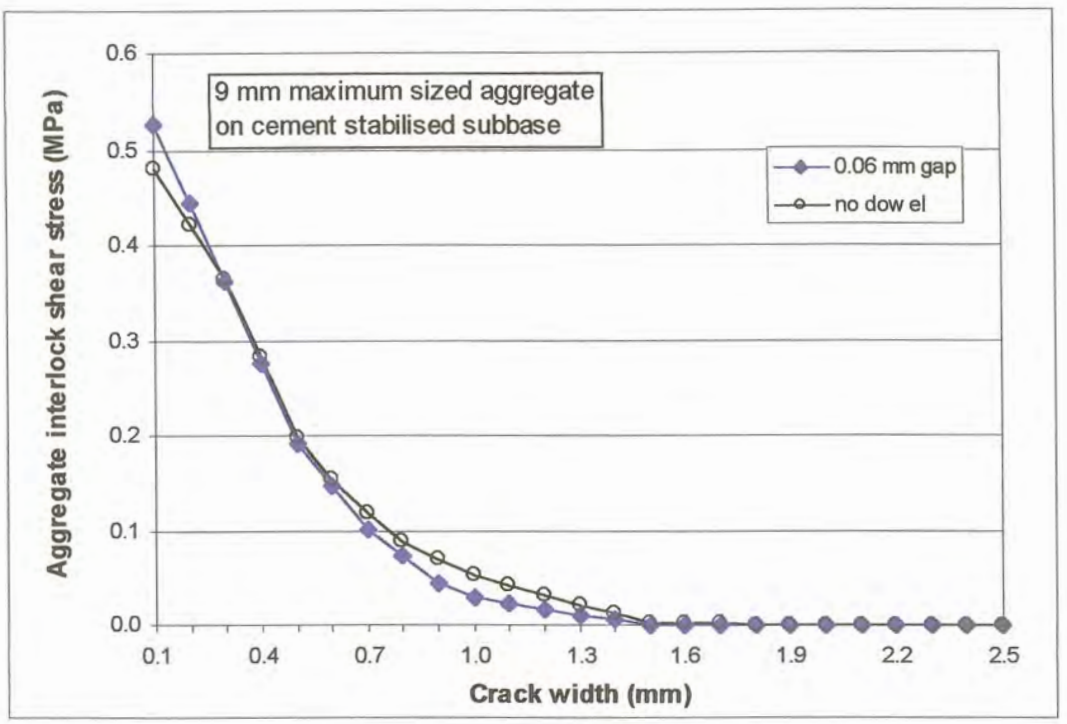

Figure D.69: Maximum aggregate interlock shear stress in the wheelpath – 9 mm maximum sized aggregate – combined affect of aggregate interlock and dowels (gap around dowel)

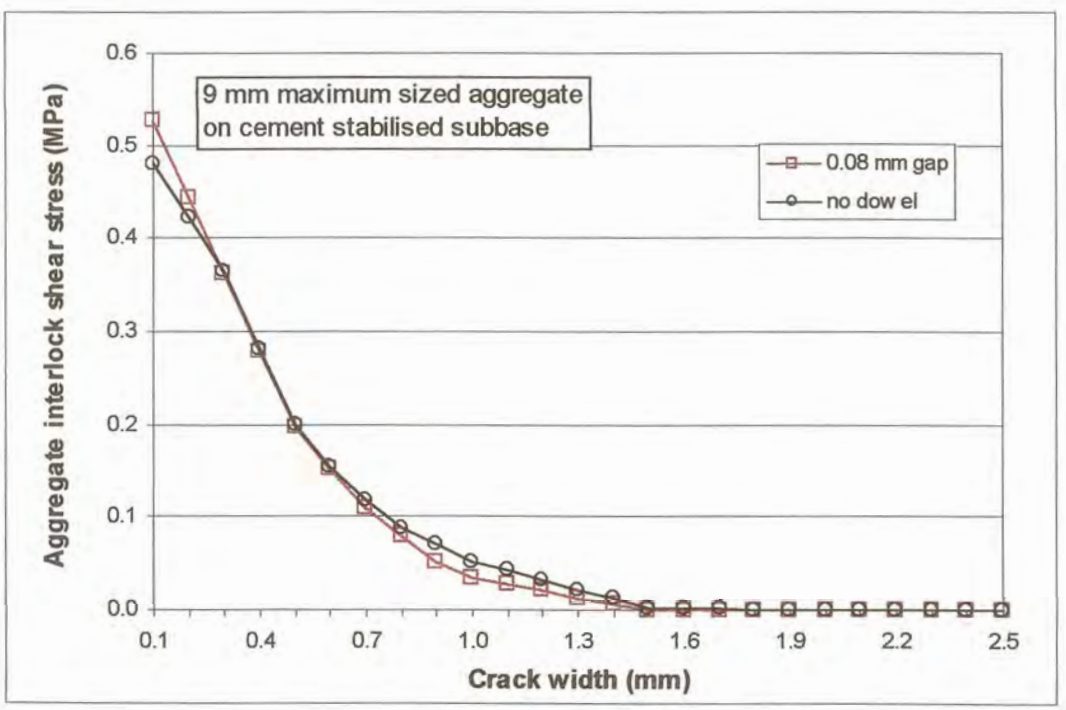

Figure D.70: Maximum aggregate interlock shear stress in the wheelpath – 9 mm maximum sized aggregate – combined affect of aggregate interlock and dowels (gap around dowel)

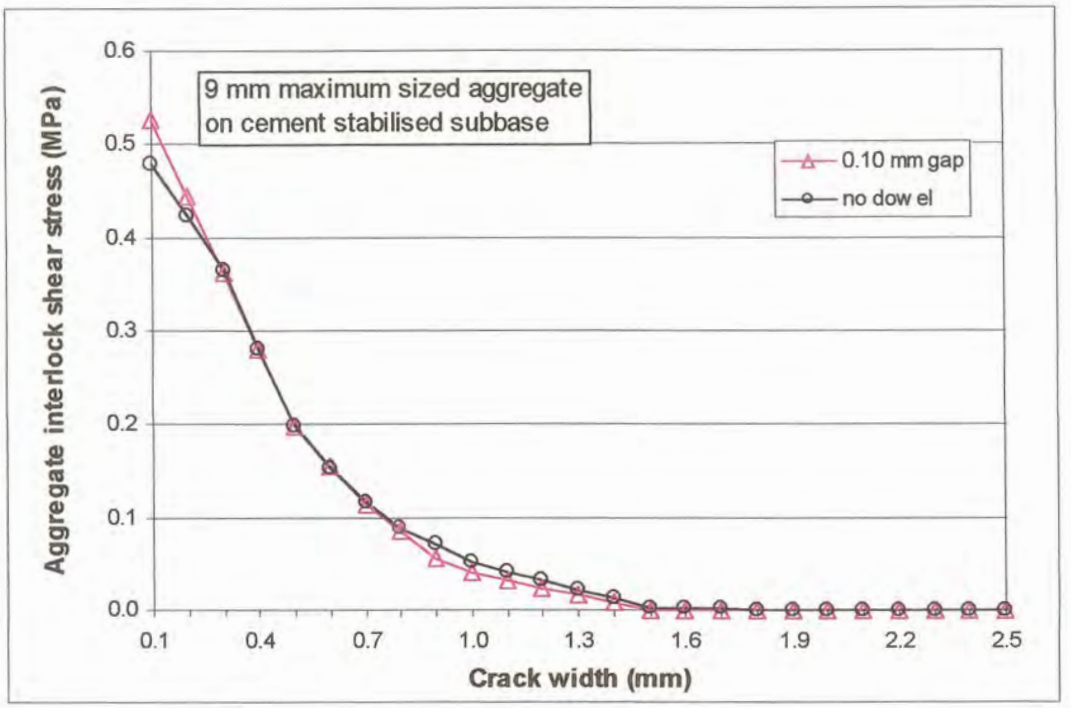

Figure D.71: Maximum aggregate interlock shear stress in the wheelpath – 9 mm maximum sized aggregate – combined affect of aggregate interlock and dowels (gap around dowel)

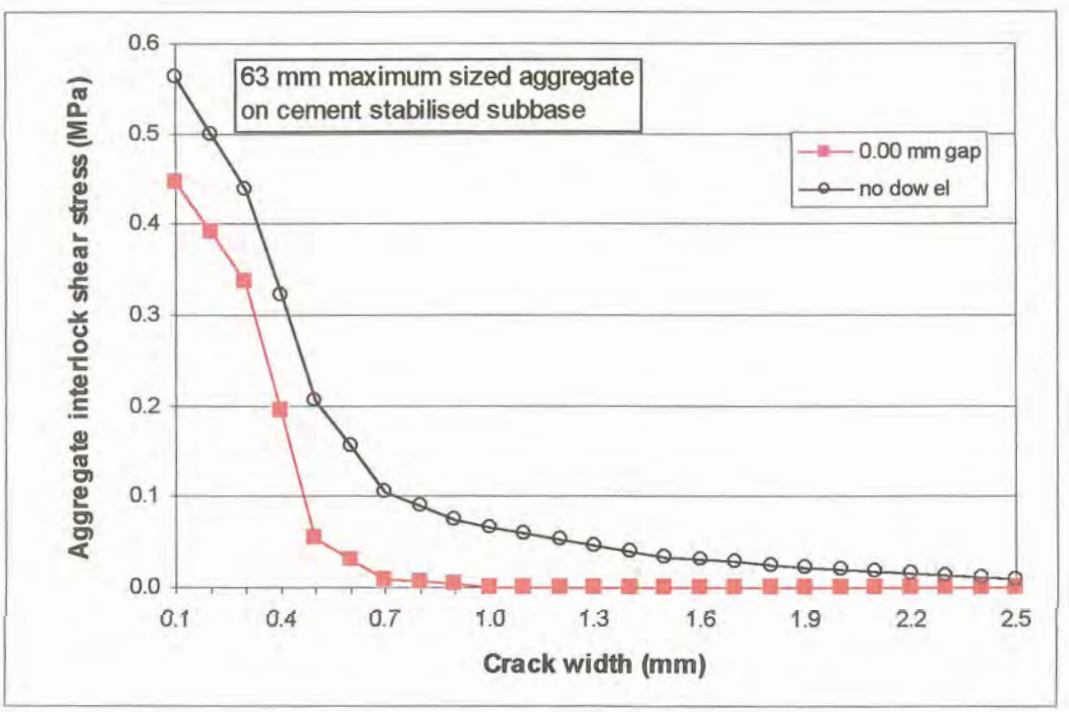

Figure D.72: Maximum aggregate interlock shear stress in the wheelpath – 63 mm maximum sized aggregate – combined affect of aggregate interlock and dowels (gap around dowel)

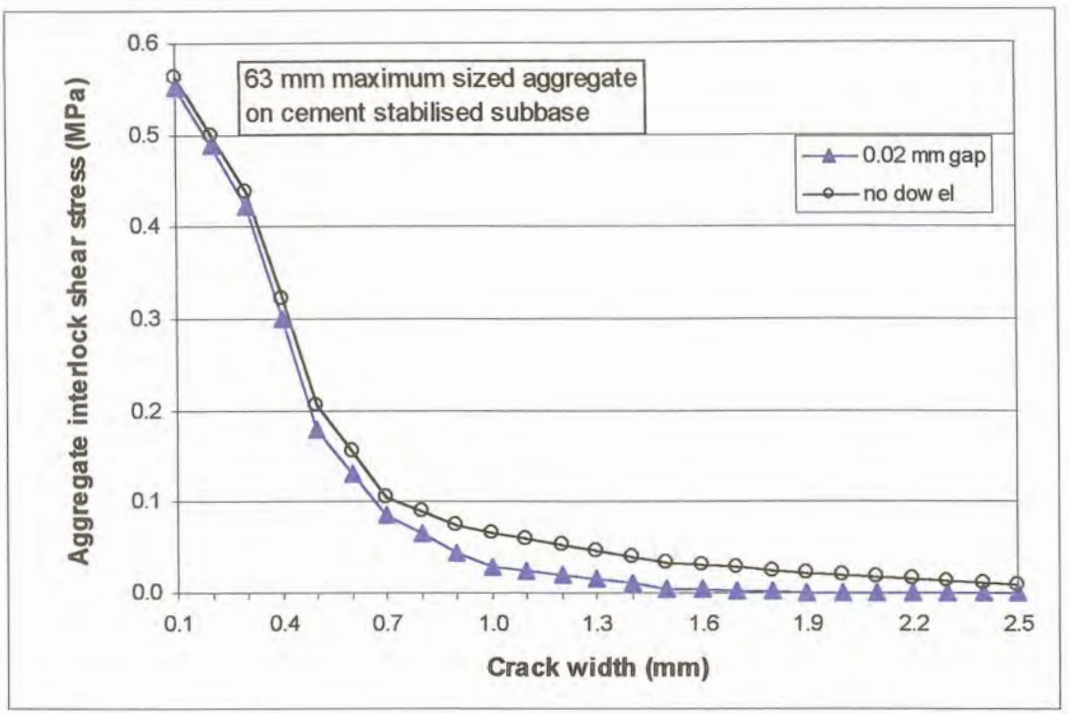

Figure D.73: Maximum aggregate interlock shear stress in the wheelpath – 63 mm maximum sized aggregate – combined affect of aggregate interlock and dowels (gap around dowel)

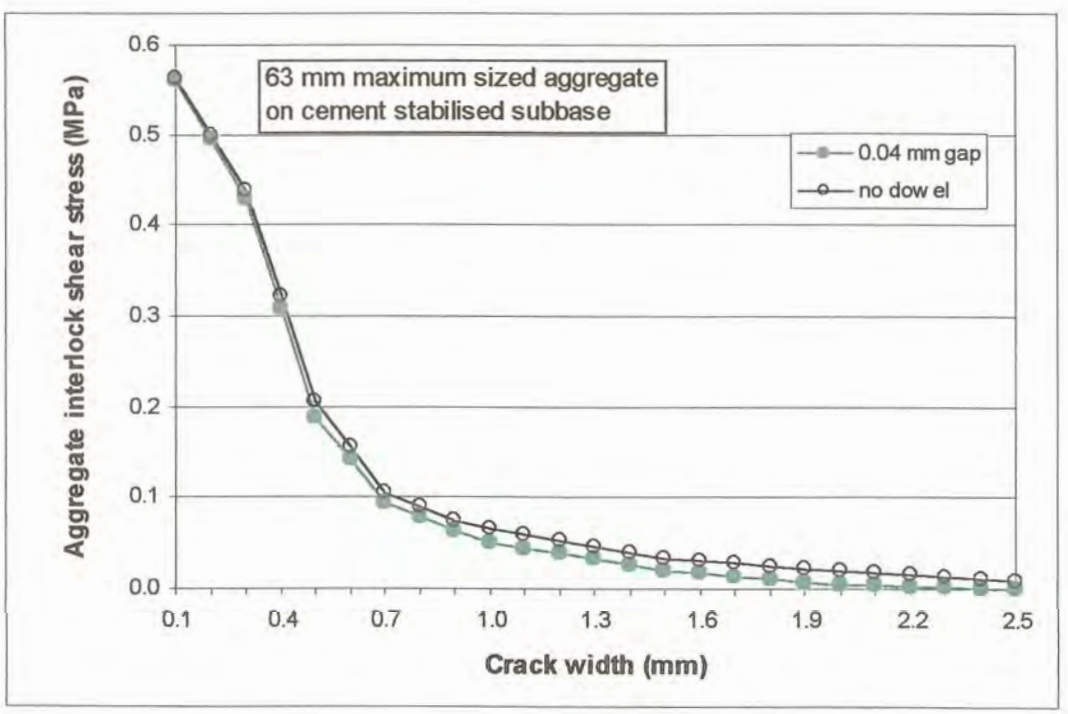

Figure D.74: Maximum aggregate interlock shear stress in the wheelpath – 63 mm maximum sized aggregate – combined affect of aggregate interlock and dowels (gap around dowel)

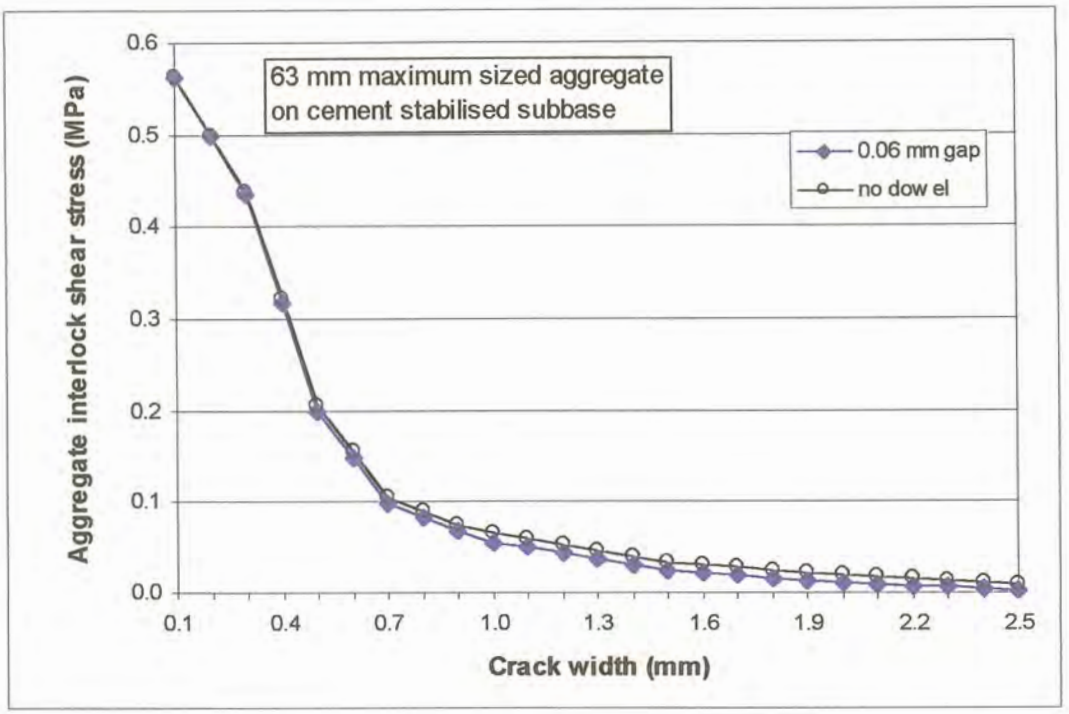

Figure D.75: Maximum aggregate interlock shear stress in the wheelpath – 63 mm maximum sized aggregate – combined affect of aggregate interlock and dowels (gap around dowel)

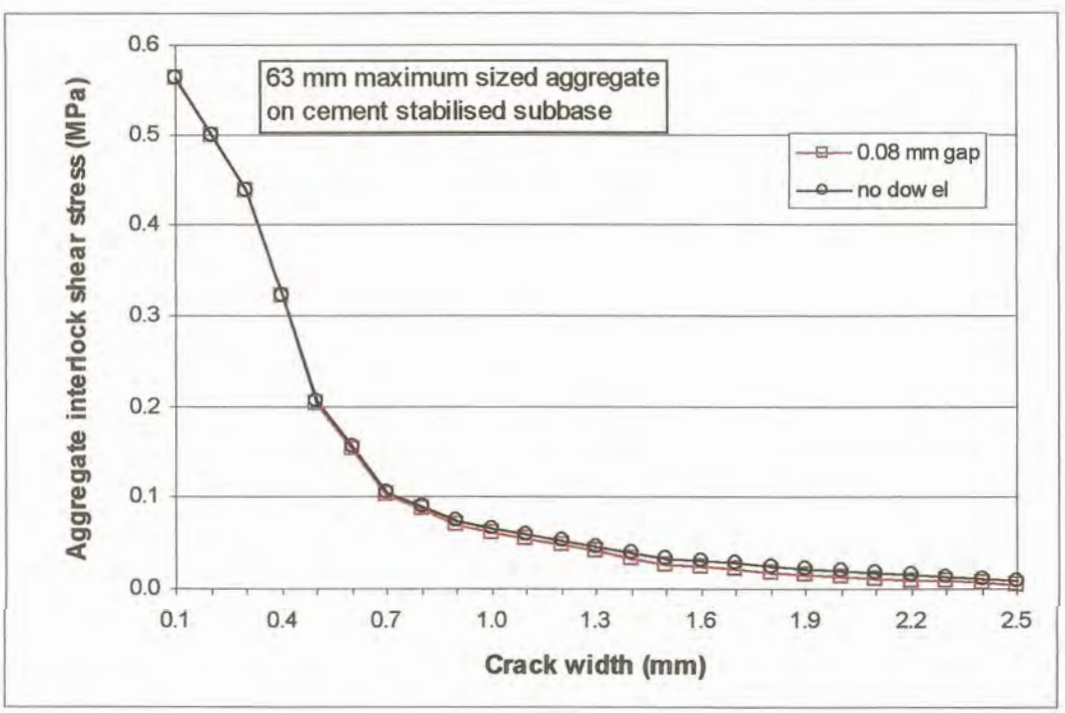

Figure D.76: Maximum aggregate interlock shear stress in the wheelpath – 63 mm maximum sized aggregate – combined affect of aggregate interlock and dowels (gap around dowel)

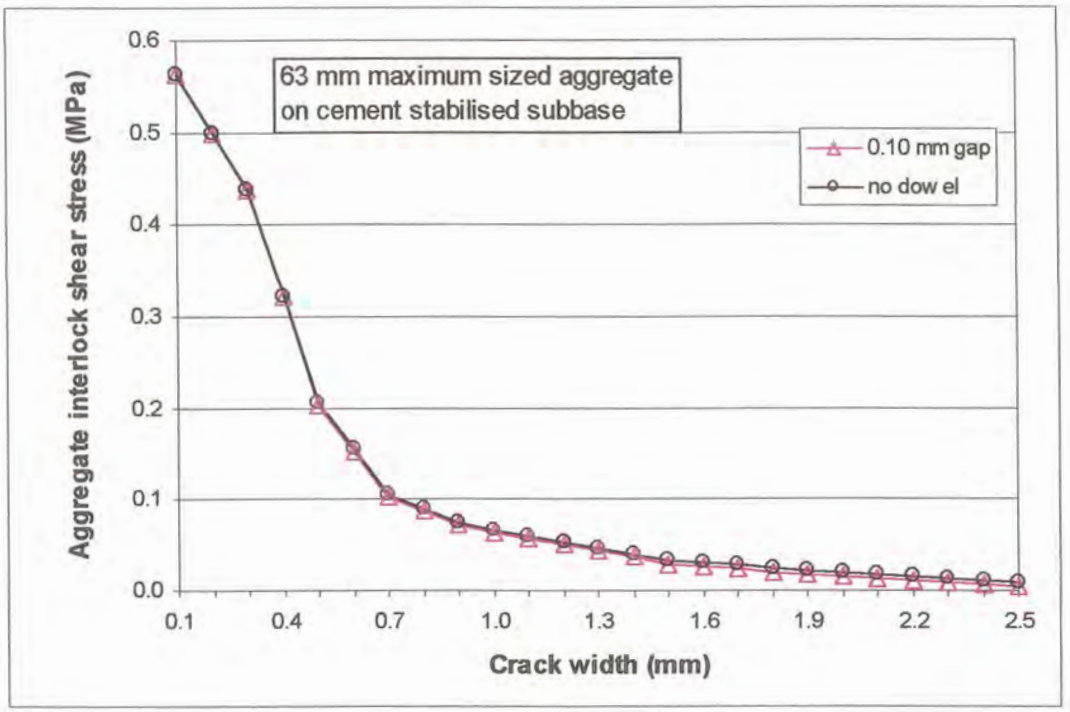

Figure D.77: Maximum aggregate interlock shear stress in the wheelpath – 63 mm maximum sized aggregate – combined affect of aggregate interlock and dowels (gap around dowel)

The development of the total shear force transferred across the joint through both aggregate interlock and dowel action, at increased gap width around the dowel, is presented in Figures D.78 to D.89. As for the deflection load transfer efficiency, as well as the maximum shear stress transferred across the joint in the wheel path, the relationships obtained approximated the "no dowel" case.

Where the total shear force transferred across the joint/crack by both aggregate interlock, and dowel action was calculated, aggregate interlock contributed the major component of the forces transferred at narrow crack widths. The aggregate interlock component then decreased to zero, with the influence of the 9 mm aggregate concrete reaching zero sooner, and at a smaller gap width than the 63 mm aggregate concrete. On the other hand, the dowels initially contributed between 44% and 17% of the force transferred for 9 mm and 63 mm aggregate, respectively at narrow crack and gap widths. The forces transferred through the dowels increased while the forces transferred through aggregate interlock decreased with increasing crack widths, at narrow gap widths. The dowels contributed the major portion of the total shear force transferred at narrow gap widths, but at large crack widths. However, as before, the larger the gap around the dowels, the less the contributions of the dowels in transferring shear forces across the joint/crack. According to these theoretical analyses conducted with EverFE, it seems as if even a relatively small gap width of 0,10 mm around the dowels, renders the dowels ineffective in transferring shear stresses across the joint/crack.

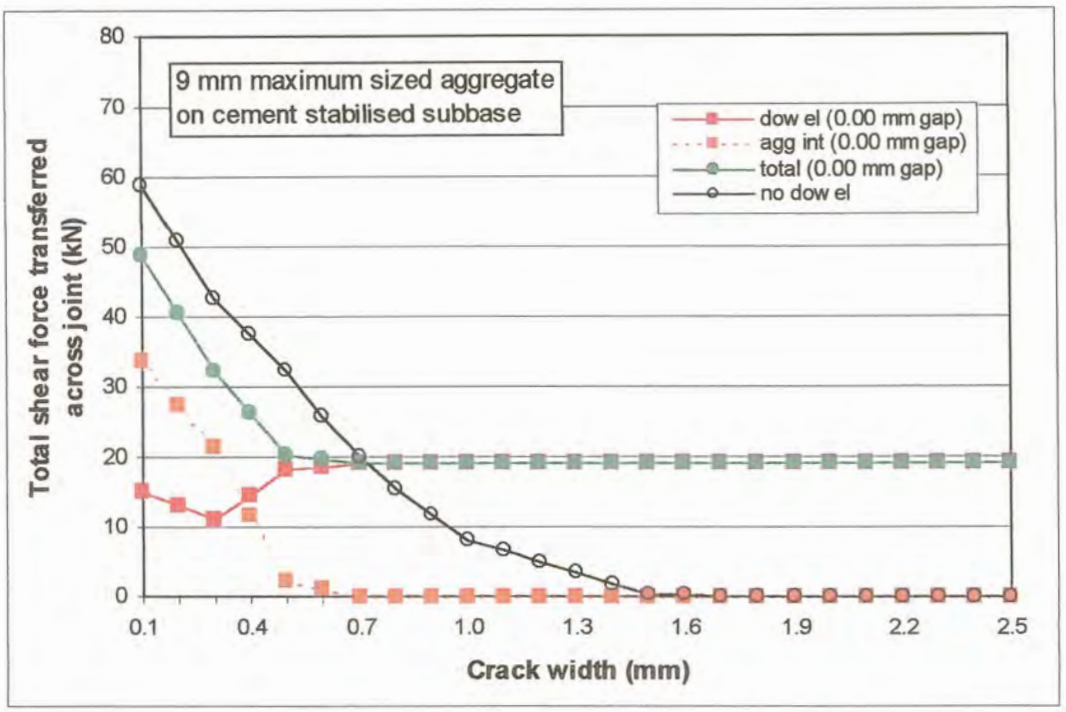

Figure D.78: Total shear force transferred across joint – 9 mm maximum sized aggregate – combined effect of aggregate interlock and dowel action (gap around dowel)

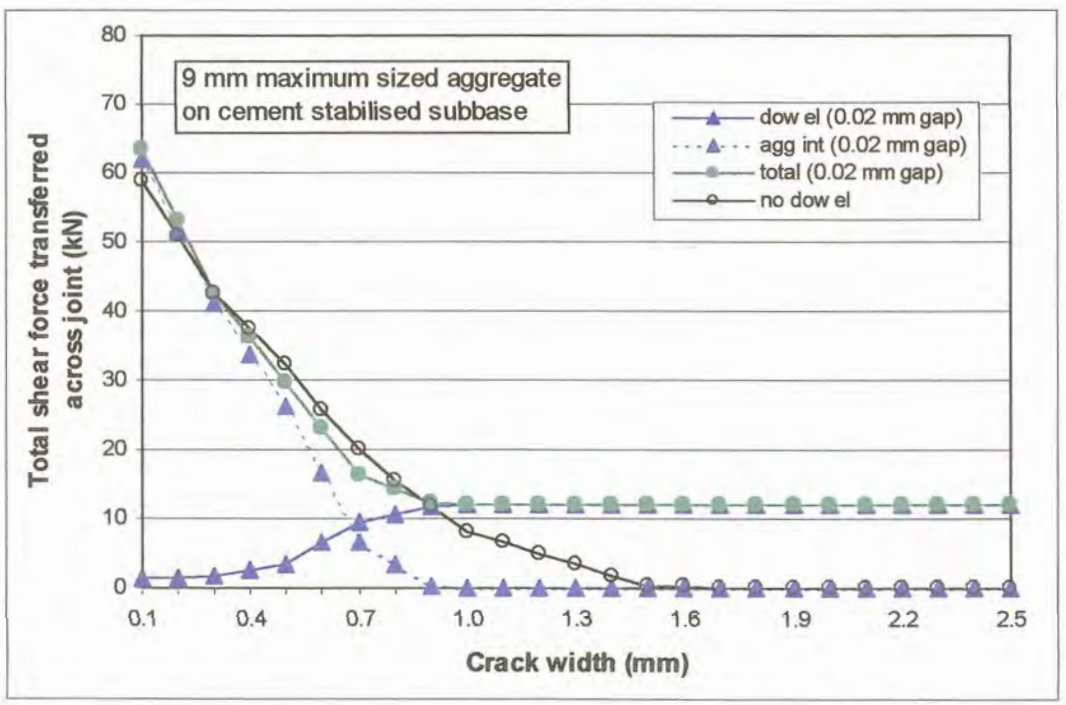

Figure D.79: Total shear force transferred across joint – 9 mm maximum sized aggregate – combined effect of aggregate interlock and dowel action (gap around dowel)

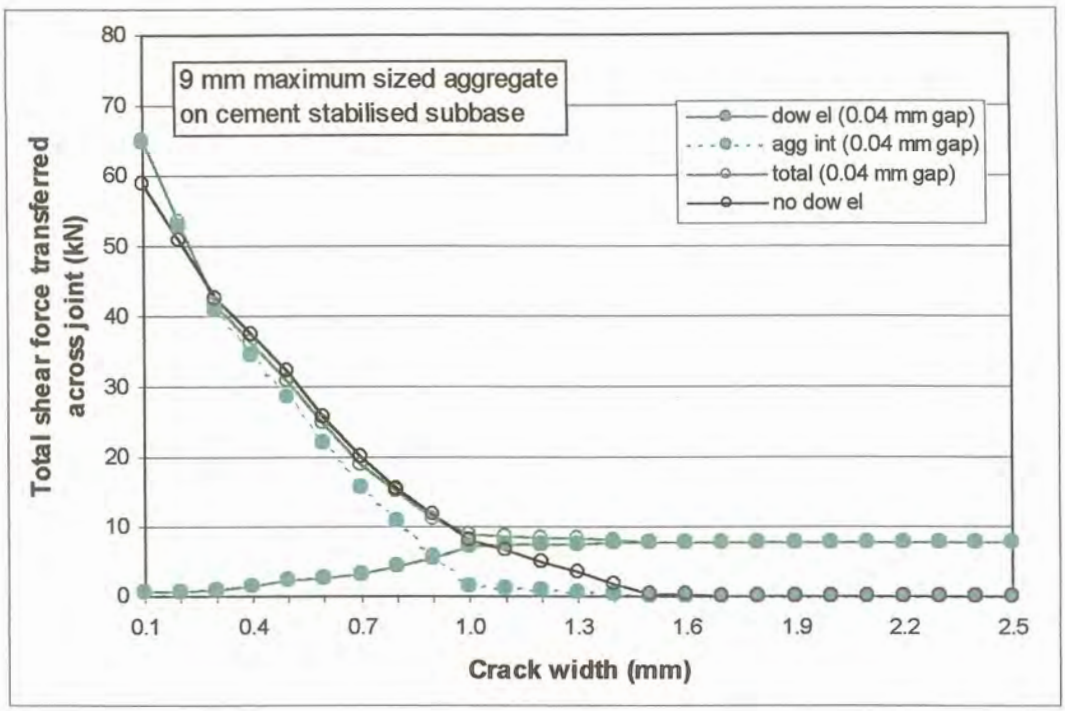

Figure D.80: Total shear force transferred across joint – 9 mm maximum sized aggregate – combined effect of aggregate interlock and dowel action (gap around dowel)

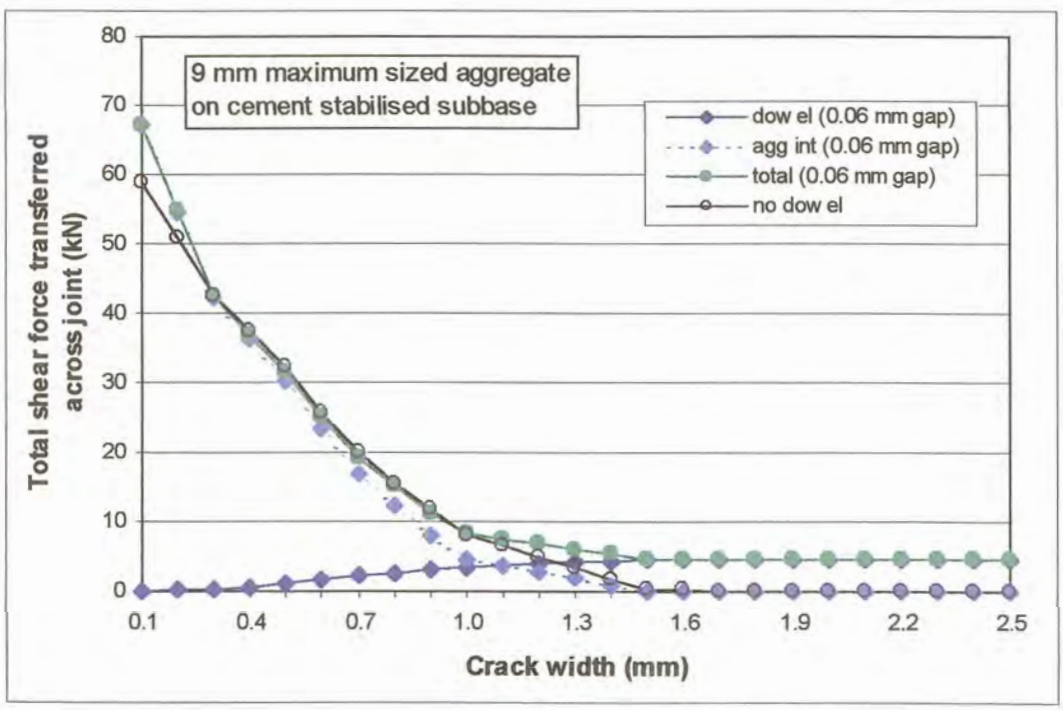

Figure D.81: Total shear force transferred across joint – 9 mm maximum sized aggregate – combined effect of aggregate interlock and dowel action (gap around dowel)

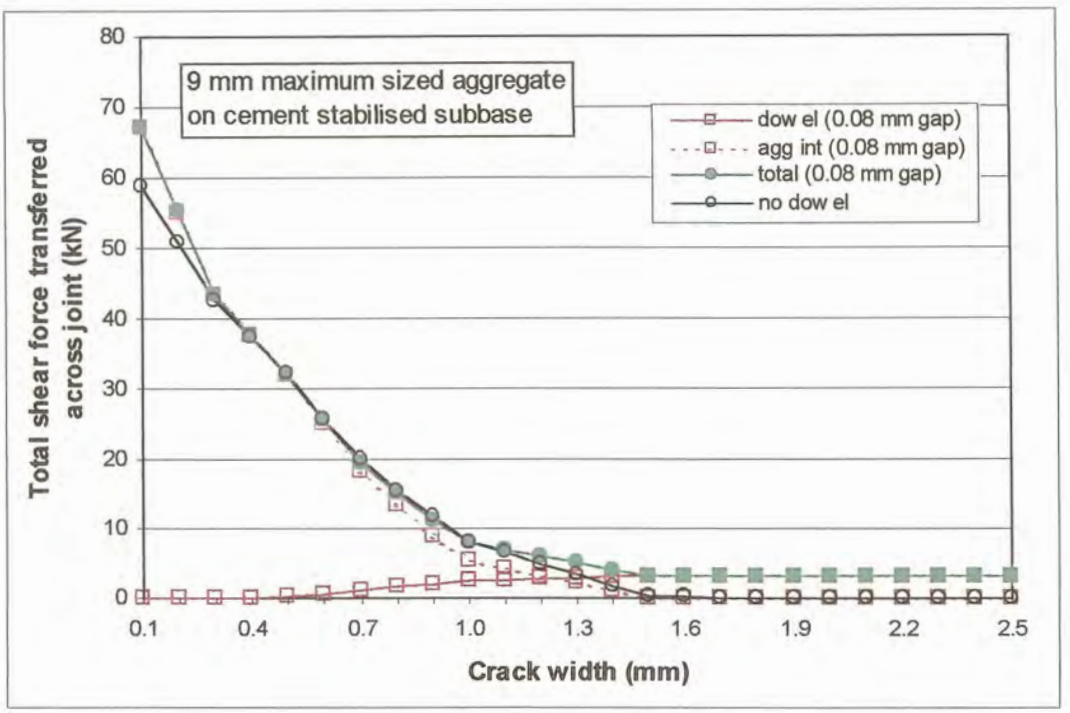

Figure D.82: Total shear force transferred across joint – 9 mm maximum sized aggregate – combined effect of aggregate interlock and dowel action (gap around dowel)

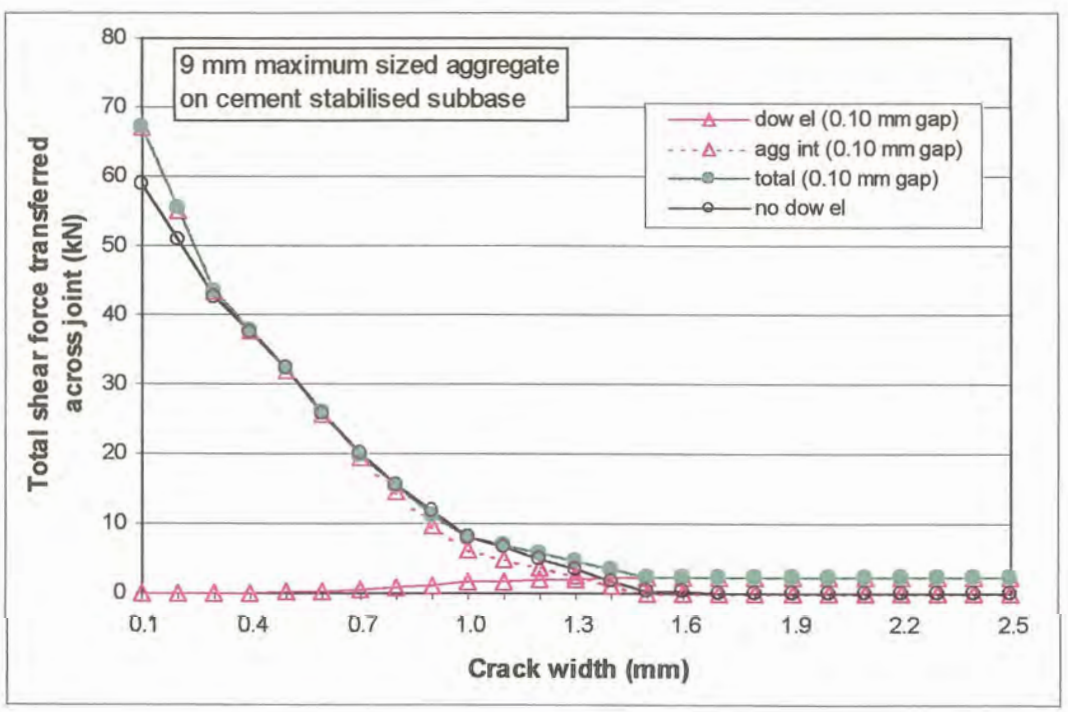

Figure D.83: Total shear force transferred across joint – 9 mm maximum sized aggregate – combined effect of aggregate interlock and dowel action (gap around dowel)

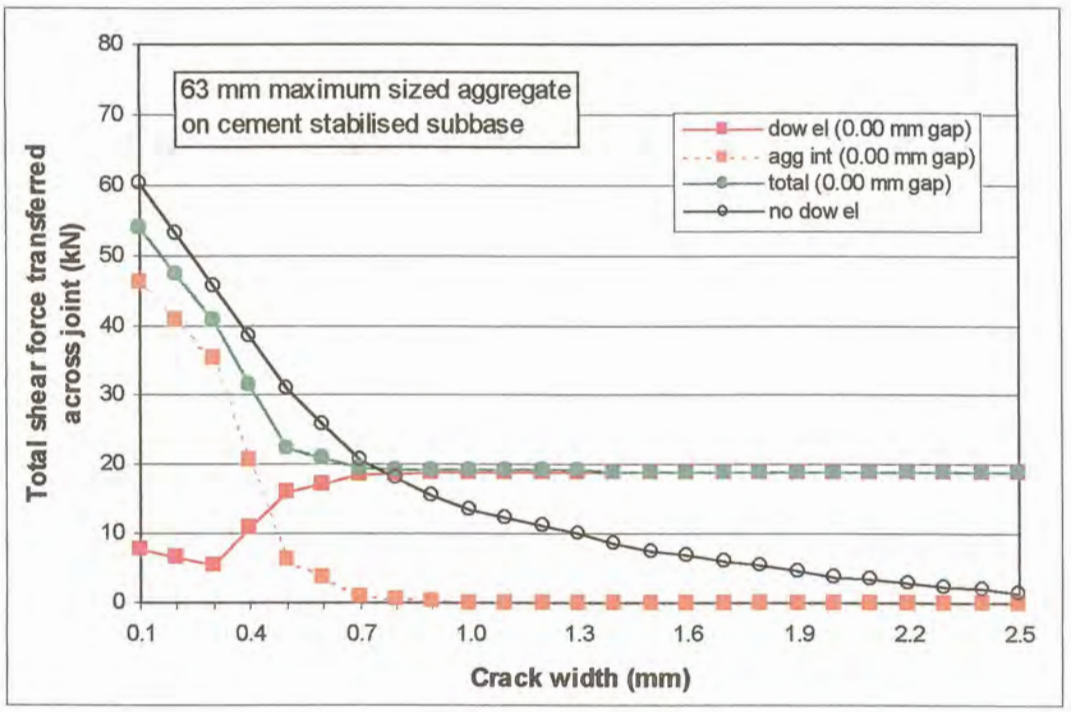

Figure D.84: Total shear force transferred across joint – 63 mm maximum sized aggregate – combined effect of aggregate interlock and dowel action (gap around dowel)

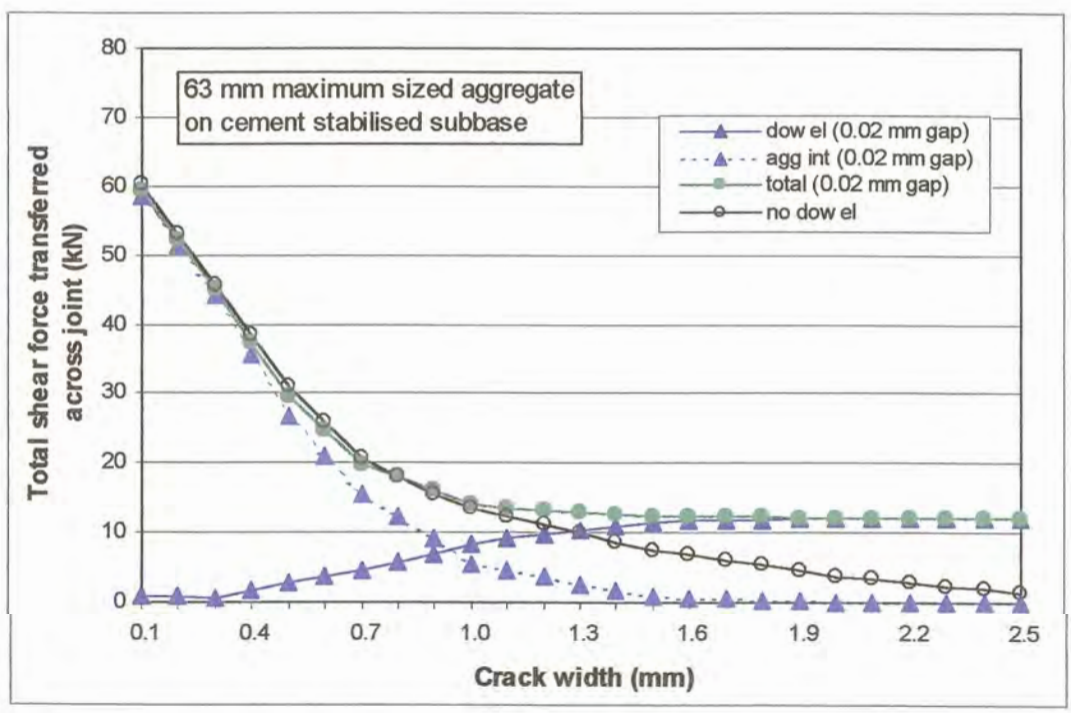

Figure D.85: Total shear force transferred across joint – 63 mm maximum sized aggregate – combined effect of aggregate interlock and dowel action (gap around dowel)

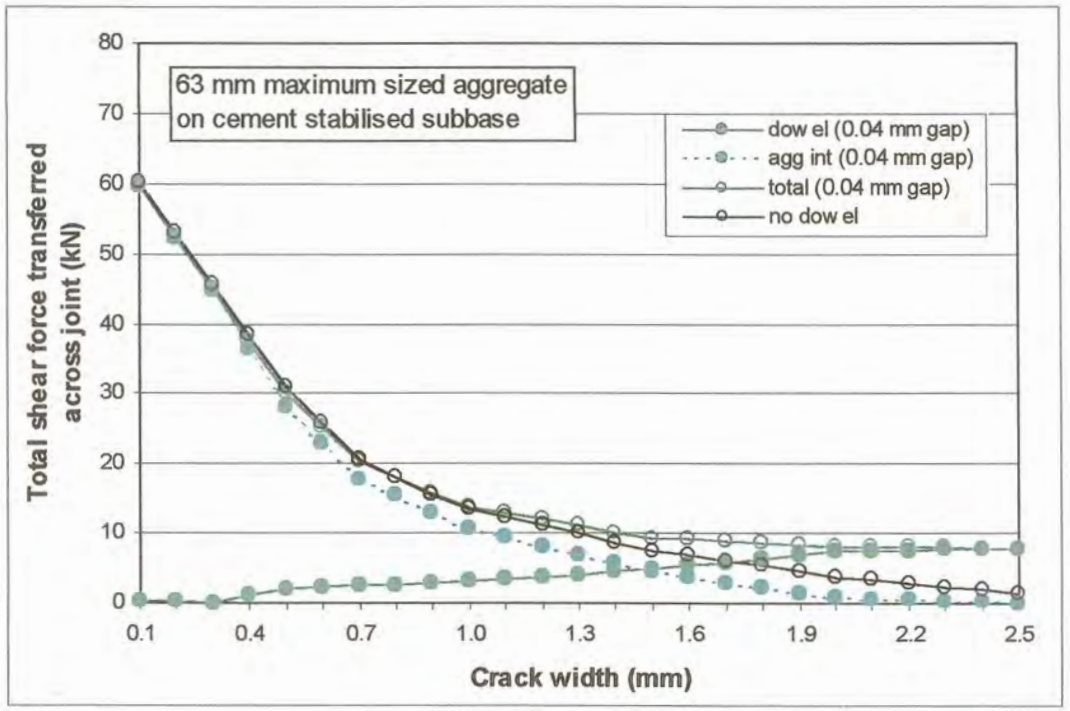

Figure D.86: Total shear force transferred across joint – 63 mm maximum sized aggregate – combined effect of aggregate interlock and dowel action (gap around dowel)

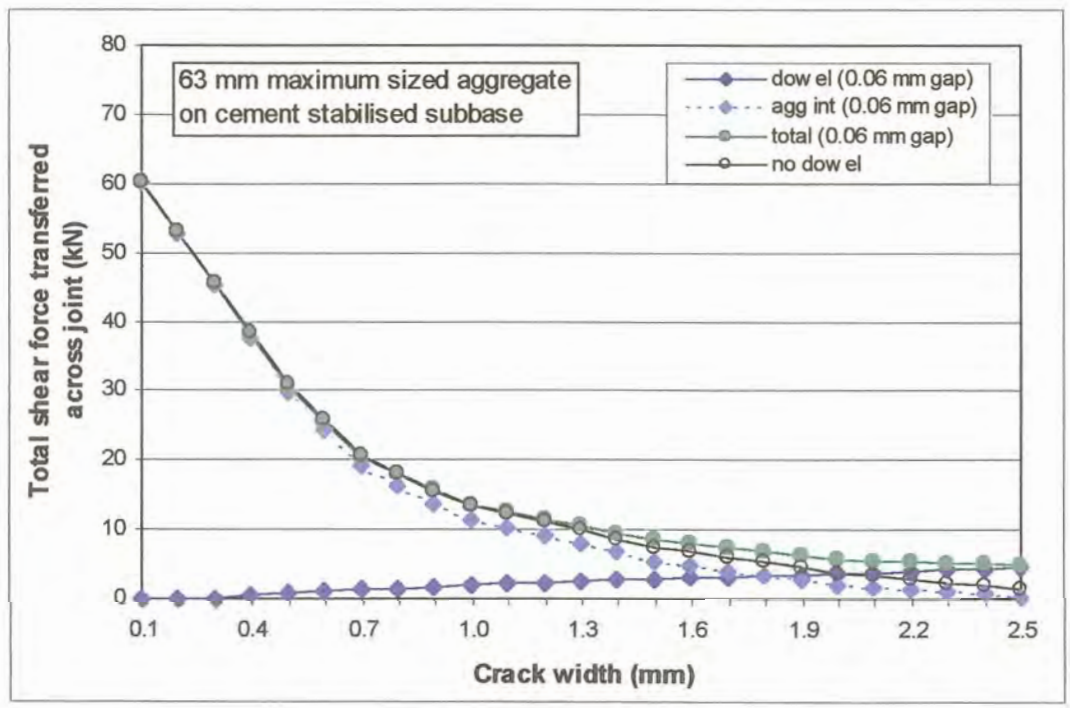

Figure D.87: Total shear force transferred across joint – 63 mm maximum sized aggregate – combined effect of aggregate interlock and dowel action (gap around dowel)

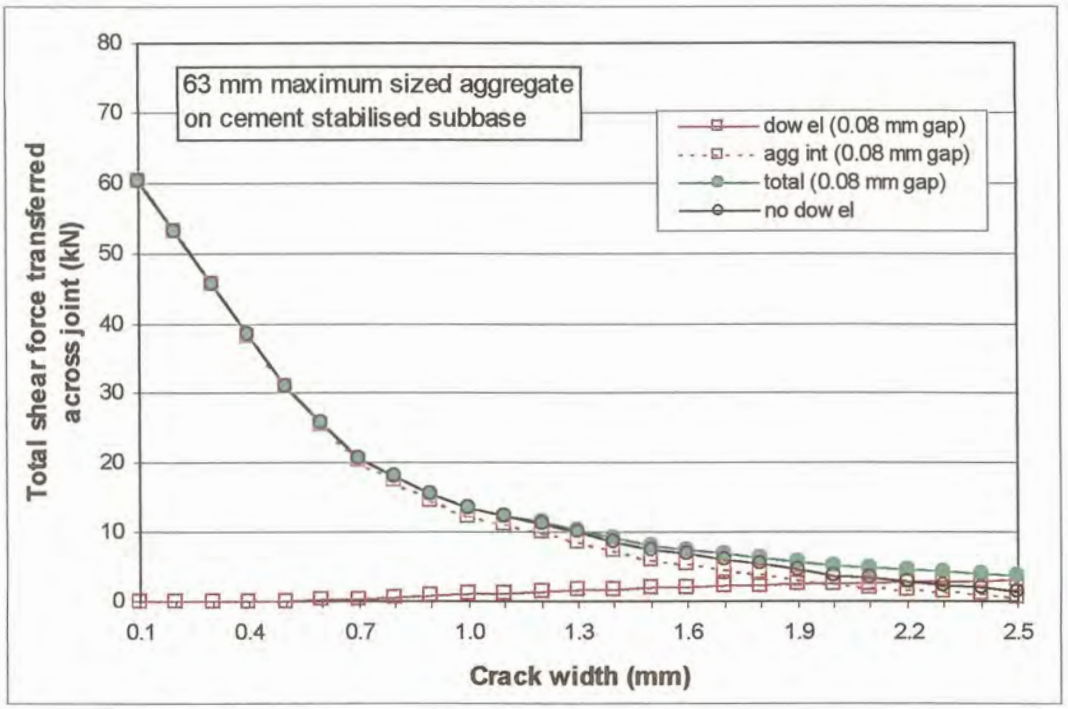

Figure D.88: Total shear force transferred across joint – 63 mm maximum sized aggregate – combined effect of aggregate interlock and dowel action (gap around dowel)

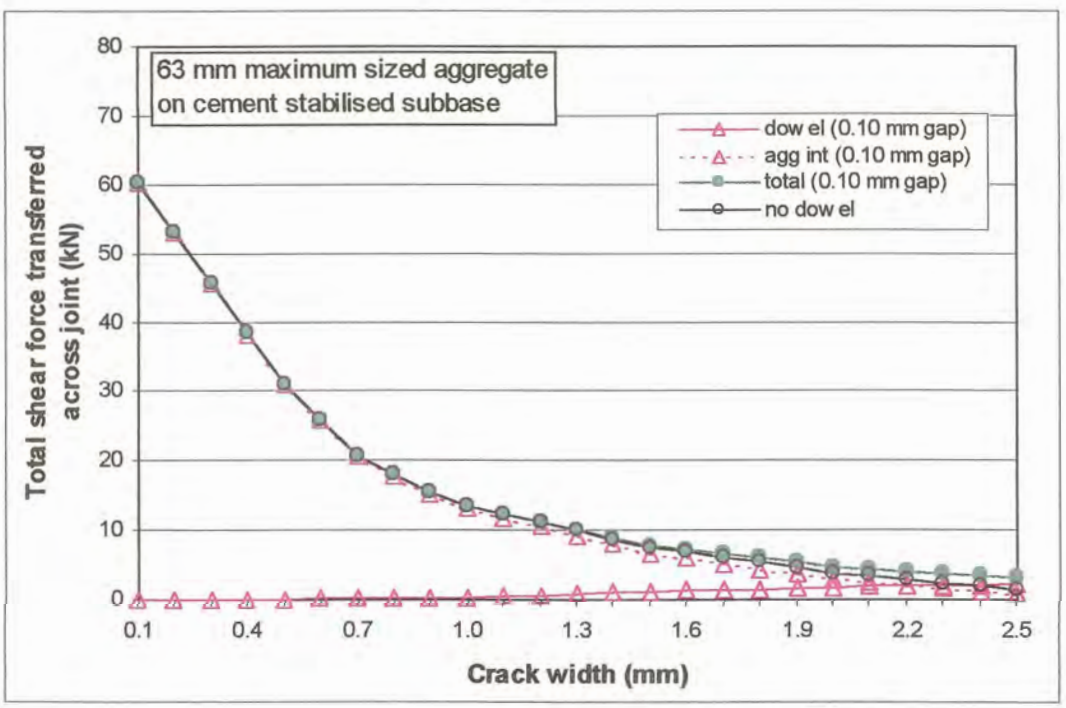

Figure D.89: Total shear force transferred across joint – 63 mm maximum sized aggregate – combined effect of aggregate interlock and dowel action (gap around dowel)

D.6 SUMMARY AND CONCLUSIONS

In order to determine the ranges for the different input variables that could be expected during modelling in the laboratory, theoretical analyses of the envisaged concrete pavement models were first conducted. The 3D FE computer software programme EverFE, specifically developed for the investigation of concrete pavement performance at a joint/crack in the pavement, was used to conduct the theoretical analyses.

The effect of aggregate interlock load transfer efficiency was determined using concrete containing 9 mm, 19 mm, 37,5 mm, and 63 mm maximum aggregate sizes. The effect of dowel looseness was further determined using 16 mm, 25 mm and 32 mm diameter bars (460 mm long) at 300 mm, 450 mm, and 600 mm spacing. Both the aggregate interlock and dowel looseness models were analysed using three different subbases beneath the concrete, namely crushed stone (G1), cement stabilised gravel (C2), and continuously graded asphalt (AC). The natural soil was modelled as an elastic solid foundation using rubber mats with a modulus of 80 MPa/m to simulate a uniform subgrade and provide continuous support.

Generally, the larger the aggregate, the greater the deflection load transfer efficiency calculated, and the stiffer the subbase, the greater the initial shear stresses and shear forces that were transferred across the joint/crack. In most of the aggregate interlock models the values converged at a crack width of about 2,5 mm which was then taken as the maximum crack width for analysis purposes.

During dowel looseness modelling, it was found that the larger the dowel bar diameter, the greater the deflection load transfer efficiency for the same dowel bar spacing. The initial shear force carried in the dowels at a zero gap width around the dowel was the least for the model supported on a cement stabilised subbase. This indicated that the stronger subbase support reduced the shear forces experienced in the dowel bars. The values converged at a gap width around the dowels of about 0,10 mm, which was then taken as the maximum for analysis purposes.

The combined effect of aggregate interlock and dowels was also investigated theoretically. The same model as the one used in aggregate interlock modelling (par. 7.2.1) with a cement stabilised subbase was used. To determine the effect of dowels in the model, 16 mm diameter dowels at 300 mm spacing were placed across the joint. For the first set of combined models, the crack width was varied, while the gap around the dowel was kept constant, and for the second set of combined models, both the crack width and the gap around the dowels were varied.

The combined deflection load transfer efficiency of aggregate interlock and dowels with no gap around the dowels was far greater than for aggregate interlock only. This efficiency, however, decreased gradually with increasing gap width around the dowel, and closely approximated the aggregate

interlock (no dowel) efficiency at a gap width of 0,10 mm. The maximum shear stress measured in the wheel path, as well as the total shear force transferred across the joint/crack, was initially less than the "no dowel" situation, but also approximated the values obtained for the "no dowel" case at a gap width of 0,10 mm.

According to the theoretical analyses conducted with EverFE, it seems as if even a relatively small gap width of 0,10 mm around the dowels, rendered the dowels ineffective in transferring shear stresses across the joint. The shear stress transferred across a joint through the dowels in a doweled joint, but with a gap around the dowels was therefore found to be equivalent to the stress transferred due to aggregate interlock only in an un-doweled joint.

The results of the analyses conducted, implied that the ultimate function of dowels are to prevent joint faulting, because as soon as a gap has developed around the dowel, the shear stress transfer efficiency through the dowels became negligible. This confirmed the conclusions already reached by inter alia Buch and Zollinger (1996) and Sargand (1999) who recognised the reduced effectiveness of dowel bars with an increase in dowel looseness, due to repeated applications of high bearing stresses during the life of the pavement.

APPENDIX E: TEST METHODS USED

APPENDIX E: TEST METHODS USED

E.1 INTRODUCTION

The basic test methods used to determine specific characteristics of the concrete used in the experiments are as follows:

a) SABS test method 863: 1994 - Compressive strength of hardened concrete.
b) SABS test method 864: 1994 – Flexural strength of hardened concrete.
c) SABS test method 1085: 1994 – Initial drying shrinkage and wetting expansion of concrete.
d) BS1881: Part 121: 1993 – Method for determination of static modulus of elasticity in compression.

The scopes of each of these test methods, as well as the prescribed procedure of expressing results are summarised below.

E.1.1 SABS 863: 1994 – COMPRESSIVE STRENGTH OF HARDENED CONCRETE

This test describes a method for determining compressive strength of test specimens of hardened concrete.

The test specimens consist of 150 mm x 150 mm x 150 mm concrete cubes, cured under water for 3, 7, 28 days, etc. depending on the specifications.

Each specimen has to be tested while still saturated. Prior to testing the mass of each specimen is determined to an accuracy of 1%.

During testing, a compression load is applied to each specimen without shock at 0,3 MPa/s + 0,1 MPa/s to failure. The maximum load applied, is recorded, and the compressive strength calculated as follows:

$$f_{cc} = \frac{F}{A_c} \qquad \text{(E.1)}$$

Where:

f_{cc} = Compressive strength (MPa);
F = Maximum load at failure (N); and
Ac = Cross-sectional area of specimen on which compressive force acts (mm^2).

The average compressive strength is recorded to the nearest 0,5 MPa. Test results are considered accurate if a result does not exceed 15% of the average.

To report the apparent saturated density of each specimen, calculate it by dividing the mass by its volume.

E.1.2 SABS 864: 1994 – FLEXURAL STRENGTH OF HARDENED CONCRETE

This test method describes a:

a) Two-point loading method that produces a constant bending moment along the central part of a test specimen – standard method.
b) Centre-point loading method – alternative method.

The dimensions of the moulds depend on the maximum nominal size of the aggregate in the concrete. A 100 mm x 100 mm x 500 mm mould could be used for 19,0 mm aggregate, but the 150 mm x 150 mm x 750 mm mould, used for 37,5 mm aggregate, is the preferred size.

The compression-testing machine consists of two pairs of steel rollers of nominal diameter 38 to 40 mm, and length at least 10 mm more than the width of the specimen. One pair of rollers is used to support the specimen, and the other two to apply the load.

Each specimen has to be tested while still saturated. Determine dimensions to 1 mm accuracy, and mass to 1%.

Increase the load continuously at a constant rate of between 0,03 MPa/s + 0,01 MPa/s to failure. Measure the distance between the line of fracture and the position of the nearer supporting roller, along the centre-line of the bottom surface.

The flexural strength for two-point loading is calculated as follows:

$$f_{cf} = \frac{Fl}{bd^2} \qquad \text{(E.2)}$$

Where:

Fcf	=	Flexural strength (MPa);
F	=	Maximum load at failure (N);
l	=	Distance between axes of supporting rollers (mm);
b	=	Width of specimen (mm); and
d	=	Depth of specimen (mm).

The flexural strength for centre-point loading is calculated as follows:

$$f_{cf} = \frac{3Fl}{2bd^2} \qquad \text{(E.3)}$$

Where the parameters are as defined for Equation D.2.

Calculate the average of the results to the nearest 0,05 MPa. The difference between the highest and the lowest result should not exceed 15% of the average. The apparent saturated density of each specimen is the mass divided by the volume.

E.1.3 SABS 1085: 1994 – INITIAL DRYING SHRINKAGE AND WETTING EXPANSION OF CONCRETE

This test describes a method of determining initial drying shrinkage and wetting expansion of freshly cast concrete. It is not applicable to matured or hardened concrete or to concrete containing expansion inducing agents or to pre-cast concrete products.

The mould dimensions for nominal aggregate sizes of 37,5 mm and less, are 100 mm cross-section x 300 mm length.

Cure the test specimens for 20 to 24h in the moulds, covered with impervious sheeting at 22 to 25°C at a relative humidity of 90%. De-mould the specimens, and calculate the gauge length L_0 to the nearest mm. Cover with an impervious sheet and store for a further 24h ± 0,5h. Submerge specimens for 5 days in clean, potable water at 22 to 25°C.

Remove specimens from water, 7d ± 2h after moulding. Measure L_1 to nearest 2µm (always measure in the same direction). Store in a drying facility for 7d. Remove and allow to cool to between 22 to 25°C. Measure L_2. Repeat drying for periods of 48h and measuring, until two successive readings do not exceed 2µm/100 mm of specimen length. Take lowest reading as final dry measurement.

The percentage drying shrinkage is calculated by:

$$\frac{L_1 - L_2}{L_0} x100 \qquad \text{(E.5)}$$

Where:

L_1 = Measurement after initial wet curing (mm);

L_2 = Measurement after drying (mm); and

L_0 = Distance between innermost faces of anvils (mm).

The wetting expansion of the specimen is determined after storing the specimen in a drying facility for 7d, by immersing it in water for periods of 48h, and measuring L3, until the difference between successive measurements is leas than 2μm/100 mm of specimen length. Take the highest reading as the final wet measurement.

The percentage wetting expansion is calculated by:

$$\frac{L_3 - L_2}{L_0} x100 \tag{E.6}$$

Where:

L_3 = Final wet measurement (mm);

L_2 = Measurement after drying (mm); and

L_0 = Distance between innermost faces of anvils (mm).

Record the drying shrinkage and wetting expansion to the nearest 0,001% for individual values, as well as the mean value.

E.1.4 BS1881: PART 121: 1993 – METHOD FOR DETERMINATION OF STATIC MODULUS OF ELASTICITY IN COMPRESSION

This test describes a method for determination of the static modulus of elasticity in compression of hardened concrete.

The static modulus of elasticity in compression is the secant modulus = $\Delta\sigma/\Delta\varepsilon$, where $\Delta\sigma$ and $\Delta\varepsilon$ are the differences in stress and strain, respectively, between a basic loading level of 0,5 MPa and an upper loading level of 1/3 the compressive strength of the concrete.

The test specimens consist of 150 mm diameter x 300 mm long concrete cylinders. The specimens are subjected to 3 loading and unloading cycles, during which the strain ε_a is recorded for stress σ_a (= $f_{cc}/3$), and strain ε_b is recorded for stress σ_b (= 0,5 MPa).

Calculate mean stress ε_a and ε_b, respectively.

The static modulus of elasticity in compression, is given by:

$$E_c = \frac{\Delta_\sigma}{\Delta_\varepsilon} = \frac{\sigma_a - \sigma_b}{\varepsilon_a - \varepsilon_b} \tag{E.7}$$

Where:

E_c = Static modulus of elasticity (MPa);

σ_a = Upper loading stress (MPa);

σ_b = Basic stress (0,5 MPa);

ε_a = Mean strain under upper loading stress; and

ε_b = Mean strain under basic loading stress.

Express results to nearest 500 MPa for values over 10 000 MPa, and to nearest 100 MPa for values below 10 000 MPa.

APPENDIX F: MATERIAL TEST RESULTS

APPENDIX F: MATERIAL TEST RESULTS

F.1 INTRODUCTION

The materials used to manufacture the concrete for the experiments were supplied by Alpha Stone, Lyttleton (Pty) Ltd, and Lafarge Readymix, as summarised in Table F.1.

Table F.1: Summary of concrete material sources

Material	Supplier	Source
Cement – Duratech CEM I 42,5	Lafarge Readymix	Lafarge Readymix
Granite sand	Lafarge Readymix	Rossway Quarry
19 mm granite aggregate	Lafarge Readymix	Rossway Quarry
37,5 mm granite aggregate	Alpha Stone	Jukskei Quarry
Dolomite sand	Lyttleton (Pty) Ltd	Lyttleton Quarry
19 mm dolomite aggregate	Lafarge Readymix	Mooiplaas Quarry
37,5 mm dolomite aggregate	Lafarge Readymix	Mooiplaas Quarry

The properties of the various materials as tested in the laboratory at the University, as well as by the laboratories of Alpha Stone, Lyttleton (Pty) Ltd, and Lafarge Readymix and are given below.

F.2 MATERIAL PROPERTIES

F.2.1 CEMENT

The cement properties (summarised in Table F.2) were determined by Lafarge Readymix in accordance with SABS ENV 197-1:1992, in their laboratory on a split sample of the cement supplied by them.

Table F.2: Properties of Duratech CEM I 42,5 cement

Description of test	Result number TSD 00/493/2
Consistency (%)	25,3
Initial setting time (min)	213
EN prism 2 day (N/mm^2)	14,9
EN prism 28 day (N/mm^2)	49,1

F.2.2 GRANITE SAND

Granite washed crusher sand from Rossway Quarry was supplied by Lafarge Readymix. The grading of the sand was determined in the laboratory at the University, prior to using it in the concrete mix, as summarised in Table F.3. Further properties of the granite sand as reported by Lafarge Readymix are summarised in Table F.4.

Table F.3: Granite washed crusher sand grading analysis

Sieve sizes (μ)	Weight retained (g)	% Weight retained		Total % actual	Specification	
		Individual	Cumulative		Lower	Upper
9 500				100,0	100	100
6 700	1,8	0,2	0,2	99,8	90	100
4 750	48,0	4,1	4,2	95,8	75	100
2 360	231,7	19,7	23,9	76,1	55	85
1 180	242,8	20,7	44,6	55,4	35	65
600	200,7	17,1	61,7	38,3	20	45
300	171,6	14,6	76,3	23,7	10	30
150	116,0	9,9	86,1	13,9	5	20
75	65,3	5,6	91,7	8,3	0	10
Pan	97,7	8,3	100,0	0,0		
Total	1175,6					
Fineness modulus		2,97				

Table F.4: Properties of granite washed crusher sand

Test method	Description of test	Result
SABS 835	Water demand (liter)	198
SABS 844	Relative density	2,63
SABS 843	Water absorption (%)	1,1
SABS 845	Uncompacted bulk density (kg/m^3)	1590
SABS 845	Compacted bulk density (kg/m^3)	1740
SABS 1243	Methylene blue value	0,2

F.2.3 DOLOMITE SAND

The grading of the dolomite crusher sand, obtained from Lyttleton Quarry, is summarised in Table F.5. Further properties of the dolomite sand as reported by Lyttleton Dolomite (Pty.) Ltd. are summarised in Table F.6.

Table F.5: Dolomite crusher sand grading analysis

Sieve sizes (μ)	Weight retained (g)	% Weight retained		Total % actual	Specification	
		Individual	Cumulative		Lower	Upper
9 500				100,0	100	100
6 700	0,0	0,0	0,0	100,0	90	100
4 750	14,0	0,0	0,0	100,0	75	100
2 360	175,0	17,5	17,5	82,5	55	85
1 180	315,0	31,5	49,0	51,0	35	65
600	227,0	22,7	71,7	28,3	20	45
300	130,0	13,0	84,7	15,3	10	30
150	77,0	7,7	92,4	7,6	5	20
75	48,0	4,8	97,2	3,6	0	10
Pan	28,0	2,8	100,0	0,0		
Total	1000,0					
Fineness modulus		3,15				

Table F.6: Properties of dolomite crusher sand

Test method	Description of test	Result
SABS 835	Water demand (liter)	185
SABS 844	Relative density	2,82
SABS 843	Water absorption (%)	1,2
SABS 845	Uncompacted bulk density (kg/m^3)	1671
SABS 845	Compacted bulk density (kg/m^3)	1845
SABS 1243	Methylene blue value	0,05

The volume of 19 mm and 37,5 mm aggregate in both the granite and the dolomite concrete mixes had to be the same, in order to obtain more or less the same aggregate interlock contact areas. In other words, the coarseness of the joint area formed by the 19 mm granite aggregate had to be the same as for the 19 mm dolomite aggregate. The same applied to the 37,5 mm aggregate concrete mixes. To

achieve this, the grading of the granite sand and the dolomite sand had to be more or less the same. Figure F.1 shows the grading of the sands used in the concrete mixes, within the grading envelope.

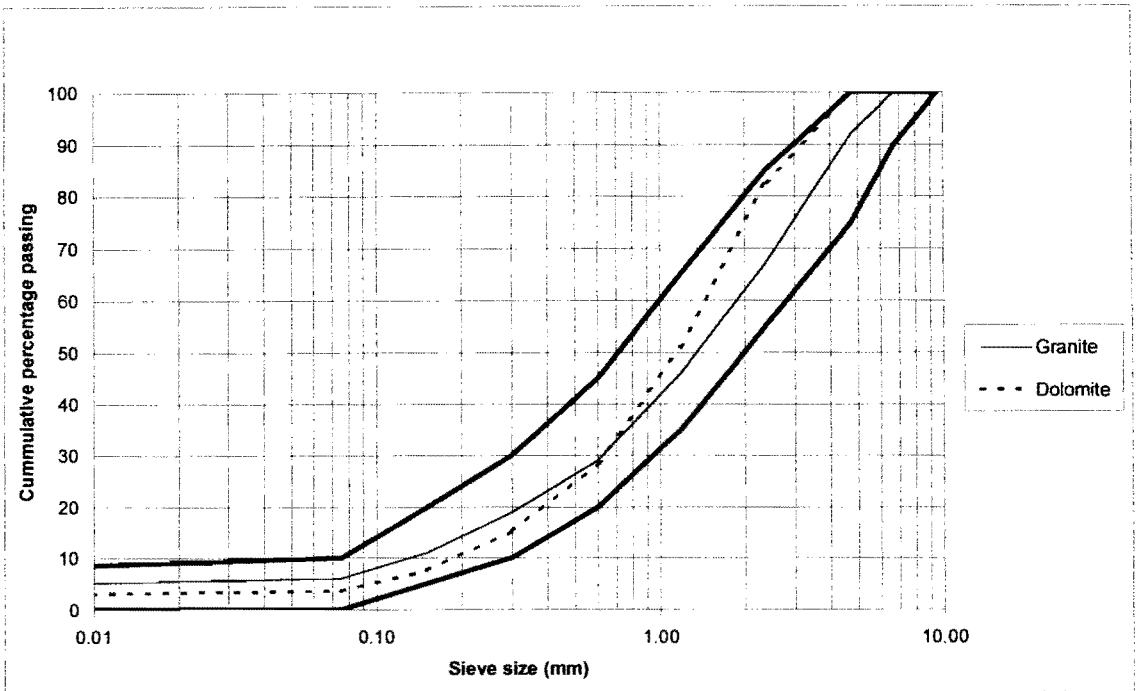

Figure F.1: Sand grading

F.2.4 19 mm GRANITE AGGREGATE

19 mm granite aggregate from Rossway Quarry was supplied by Lafarge Readymix. The properties of the aggregate are summarised in Table F.7.

Table F.7: Properties of 19 mm granite aggregate

Test method	Description of test	Result
SABS 841	Aggregate crushing value (%)	25
SABS 842	10% Fines aggregate crushing value (FACT) (kN)	130 (wet) 150 (dry)
SABS 844	Relative density (kg/m^3)	2,65
SABS 843	Water absorption (%)	0,33
SABS 846	Los Angeles abrasion value (%)	33

F.2.5 37,5 mm GRANITE AGGREGATE

Normally quarries do not produce 37,5 mm concrete aggregate. It was therefore necessary to approach another supplier to obtain the 37,5 mm granite aggregate used in the research. Fortunately a stockpile was located at the Jukskei Quarry operated by Alpha Stone, where production of this stone size was also discontinued. The typical aggregate properties for the 37,5 mm granite aggregate are summarised in Table F.8.

Table F.8: Properties of 37,5 mm granite aggregate

Test method	Description of test	Result
SABS 841	Aggregate crushing value (%)	27
SABS 842	10% Fines aggregate crushing value (FACT) (kN)	122
SABS 844	Relative density (kg/m^3)	2,65
SABS 843	Water absorption (%)	0,33
SABS 848	Polished stone value	47
SABS 846	Los Angeles abrasion value (%)	33

F.2.6 19 mm and 37,5 mm DOLOMITE AGGREGATE

Dolomite aggregates were obtained from Mooiplaas Quarry. The 19 mm aggregate was from their standard concrete aggregate production line, and the 37,5 mm was from their so-called "Metallurgical leg" where they produce a –40 - +20 aggregate. The properties of the dolomite aggregate are summarised in Table F.9.

Table F.9: Properties of dolomite aggregate

Test method	Description of test	Result
SABS 841	Aggregate crushing value (%)	15
SABS 842	10% Fines aggregate crushing value (FACT) (kN)	275
SABS 844	Relative density	2,86
SABS 843	Water absorption (%)	0,2
SABS 846	Los Angeles abrasion value (%)	21

F.3 MATERIAL TEST RESULTS

A total of four concrete beams were cast, using the materials as summarised in Table F.10. In all instances the design strength of the concrete was a minimum 28-day compressive strength of 35 MPa for water-cured cubes. For control purposes a fifth beam was cast using a bubble plastic sheet (supplied by Hyson Cells) to act as joint former. Ordinary Portland Cement - Duratech CEM I 42,5 cement was used for all five beams.

Table F.10: Composition of experimental beams

Experiment number	Materials	Crack inducer
1	Granite sand & 19 mm granite aggregate	Angle iron
2	Granite sand & 37,5 mm granite aggregate	Angle iron
3	Dolomite sand & 19 mm dolomite aggregate	Angle iron
4	Dolomite sand & 37,5 mm dolomite aggregate	Angle iron
5 (control)	Granite sand & 19 mm granite aggregate	Bubble plastic sheet

To ensure that a 28-day compressive strength of 35 MPa would be obtained with the granite sand and 19 mm granite aggregate, used in Experiment 1, test cubes were made up beforehand, using water/cement ratios of 0,59 and 0,63. The test cubes were crushed after 7 days, and the 28-day strengths were calculated from the assumption that the 7-day compressive strength is approximately two-thirds that of the 28-day compressive strength (Fulton, 1994). The average 7-day compressive strength values obtained for water/cement ratios of 0,59 and 0,63 were 21,5 MPa and 20,5 MPa, respectively, which indicated that the corresponding 28-day compressive strength would be 32,5 MPa and 30,5 MPa. From these results it was determined that a water/cement ratio of 0,56 should be used to obtain a 28-day compressive strength of 35 MPa. The actual strengths obtained were 38,7 MPa and 30,0 MPa for the water-cured cubes and the air-cured cubes, respectively.

The concrete mix designs used are as summarised in Table F.11.

Table F.11: Concrete mix designs

Experiment number	Materials ($/m^3$)			
	Water (l)	Cement (kg)	Sand (kg)	Stone (kg)
1 & 5	201	360	775	1025
2	185	335	800	1075
3	201	360	830	1115
4	185	335	854	1160

Apart from the beams, a number of cubes, beams and cylinders were also cast for testing purposes, as summarised in Table F.12. The test methods used are described in Appendix E.

Table F.12: Basic information on cubes, beams and cylinders cast for testing purposes

Test specimen	Dimensions (mm)	Number	Time of test
Compressive strength cubes (SABS 863: 1994 / ASTM C39/C39M-01, 2001*)	150 x 150 x 150	18	At 7 and 28 days after casting slab, and at end of 2 million load cycles.
Modulus of rupture beams (SABS 864: 1994 / ASTM C133-97, 1997)	750 x 150 x 150	6	At 28 days after casting slab, and at end of 2 million load cycles.
Shrinkage beams (SABS 1085: 1994 / ASTM C426-99, 1999)	300 x 100 x 100	4	Measure gauge length L_0 before casting specimen, and L_1 after 7 days in curing bath. Place in drying oven with temperature 50°C, and relative humidity 25%, and measure L_2 at 48 hour intervals thereafter, until difference in length less than 2μm/100 mm.
Modulus of elasticity cylinders (BS1881: Part 121: 1993 / ASTM C469-94, 1994)	300 x 150 diameter	3	At 28 days after casting.

*NOTE: ASTM test methods give equivalent test results, although the test methods are not necessarily the same.

The results obtained for the tests conducted on the cubes, beams and cylinders mentioned above are summarised in Table F.13.

The complete set of tests to determine the properties of the concrete, described above, were not conducted for the fifth experiment with the bubble plastic joint, as these results for this specific mix design were already obtained during Experiment 1. However, six cubes were cast for control purposes to calculate the 28-day characteristic strength of the concrete. The average 7-day strengths obtained for the air-cured cubes and the water-cured cubes were 29,0 MPa and 32,0 MPa, respectively. The calculated 28-day strengths for the air-cured cubes and the water-cured cubes were therefore 43,5 MPa and 48,0 MPa, respectively.

Table F.13: Material test results

Experiment number	Curing method	Compressive strength (MPa) at:			Modulus of Rupture (MPa) at:		Shrinkage (%)	Modulus of elasticity (GPa)
		7 days	28 days	Time of test*	28 days	Time of test*		
1	water	24,5	38,7	50,0	4,75	4,90	0,019	21,0
	air	20,0	30,0	36,7				
2	water	27,2	45,0	57,5	4,40	5,00	0,018	29,0
	air	29,0	41,7	50,0				
3	water	27,7	41,5	55,0	5,00	5,10	0,016	41,0
	air	27,7	38,5	48,2				
4	water	29,8	43,5	49,3	4,80	5,03	0,035	48,0
	air	27,5	39,3	45,0				

*NOTES:

1. The **Time of test** for experiments number 1 and 2 was after the application of 2 million dynamic load cycles, at 66 days and 138 days after casting, respectively. For Experiments 3, and 4 it was at the commencement of the testing at different crack widths, at 133 days, and 120 days after casting, respectively.
2. The slab for Experiment 5 was cast using the same concrete mix design as for Experiment 1. Only the 7-day cube compressive strength was determined, and a forecast made of the 28-day results. This was only for control purposes as the properties of the concrete for this specific mix design has already been determined through the results listed above.

F.4 VOLUMETRIC SURFACE TEXTURE

In an attempt to establish a method of quantifying the decrease in load transfer efficiency with an increase in crack width, and to provide an estimate of the abrasion that has taken place since fracture, Vandenbossche (1999) developed a volumetric surface texture (VST) test at the University of Minnesota. The test apparatus consisted of a spring-loaded probe with a digital readout, mounted on a frame over a computer-controlled microscope of the type typically used to obtain linear traverse and other measurements of concrete air void systems.

As mentioned before, dolomite and granite sand with approximately the same grading was used for both the 19 mm and 37,5 mm maximum sized aggregate concrete mixes. This was in order to obtain equivalent crack surfaces for both 19 mm and 37,5 mm beams, respectively. A milling machine was modified to measure the VST of representative samples of each of the first four experiments. The milling machine had an automatic longitudinal feed, with a manual transverse feed. A laser-measuring unit was mounted at the required standoff distance of 200 mm from the sample. A 24 Volt DC power supply needed by the laser unit was built for the measurements (See Photo G.25).

The volumetric surface texture ratio (VSTR) of the crack faces of the experimental beams, as well as crack faces formed during modulus of rupture testing of concrete beams, was determined to:

a) Quantify whether the 19 mm granite and dolomite crack face volumes similar, and also the 37,5 mm granite and dolomite crack face volumes.
b) Quantify whether the crack faces formed by breaking beams during modulus of rupture testing could be taken as representative of the crack surface in the experimental beams itself. In other words, whether it may only be necessary to cast a beam, break it and measure the VST, to determine the VSTR of a crack inside a pavement.
c) Compare the VST results from this study, obtained using the high quality South African crushed aggregates, with the results obtained from crack faces of concrete constructed with typical USA aggregates, published by Vandenbossche (1999).

Prior to measuring the VST of the crack faces with the laser, a total of 20 longitudinal scans were done in one location on a sample chosen at random to determine the accuracy and/or repeatability of the laser scans, as shown on Figure F.2. All 20 lines were superimposed, with an average standard deviation of 0,02 mm.

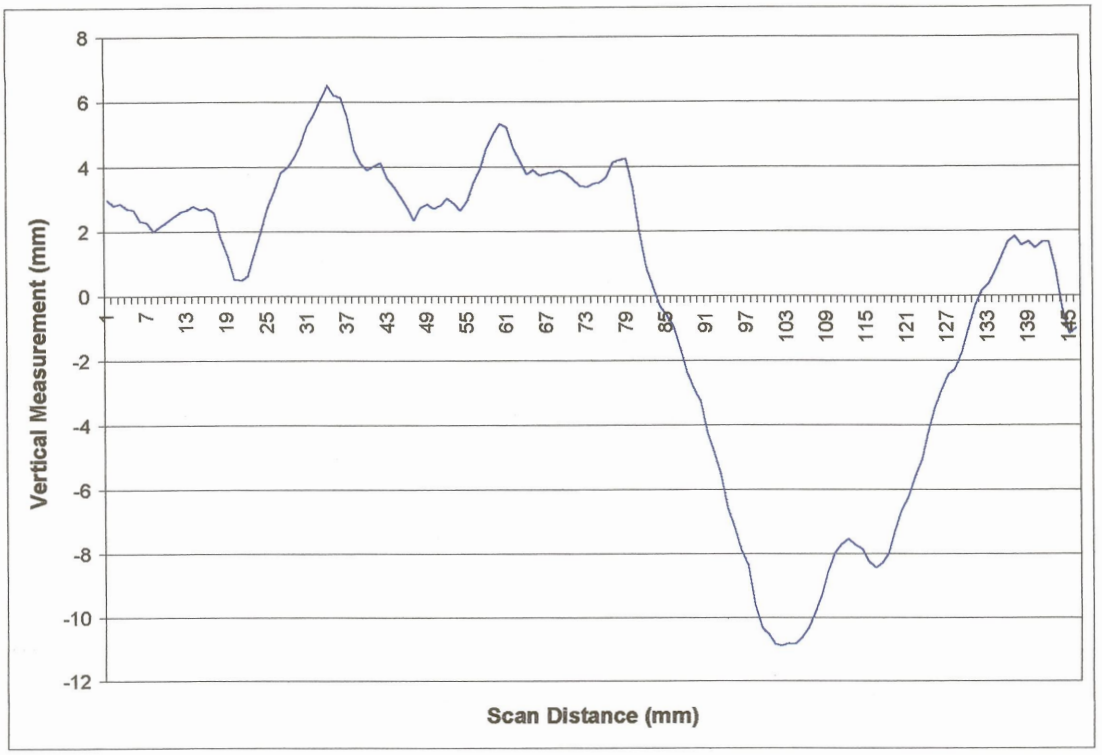

Figure F.2: Repeatability and/or accuracy of laser scans

The average measurement area in the study by Vandenbossche (1999) was about 161 cm^2 at an optimum grid of 3,18 mm (0,125 inch). The samples in this study were scanned on a 1 mm grid over a 100 mm x 100 mm (100 cm^2) area. By sub-dividing a block of data into four equal sized blocks, and calculating the average VSTR of the four blocks the effect of the smaller measurement area was determined. In each case the VSTR so calculated was less than the initial value. This indicated that the results would not be biased to give values larger than the comparative study.

The influence of the size of the grid was determined to verify whether the 3,18 mm grid used by Vandenbossche (1999) is indeed the optimum grid size. The VST of a sample at a grid of 1, 2, 3, 4, 5, 10, and 20 mm was measured, and the VSTR at each grid calculated. The results, with an exponential trend line fitted through the data points are shown on Figure F.3. The VSTR increased gradually with an increase in grid up to 4 mm, where after the increase was more marked, which confirmed that the smaller the grid, the more accurate the results. However, it is not clear from Figure F.3 whether the grid reported by Vandenbossche (1999) is indeed the optimum, as the VSTR of the 1, and 2 mm grid was less than for the 3 mm grid. On the other hand, the figure does show that the 1 mm grid used in this study will give a lower result for the area measured than for, for example if a 3 mm grid was used. A typical surface plot of a crack face, as measured with the laser is shown on Figure F.4.

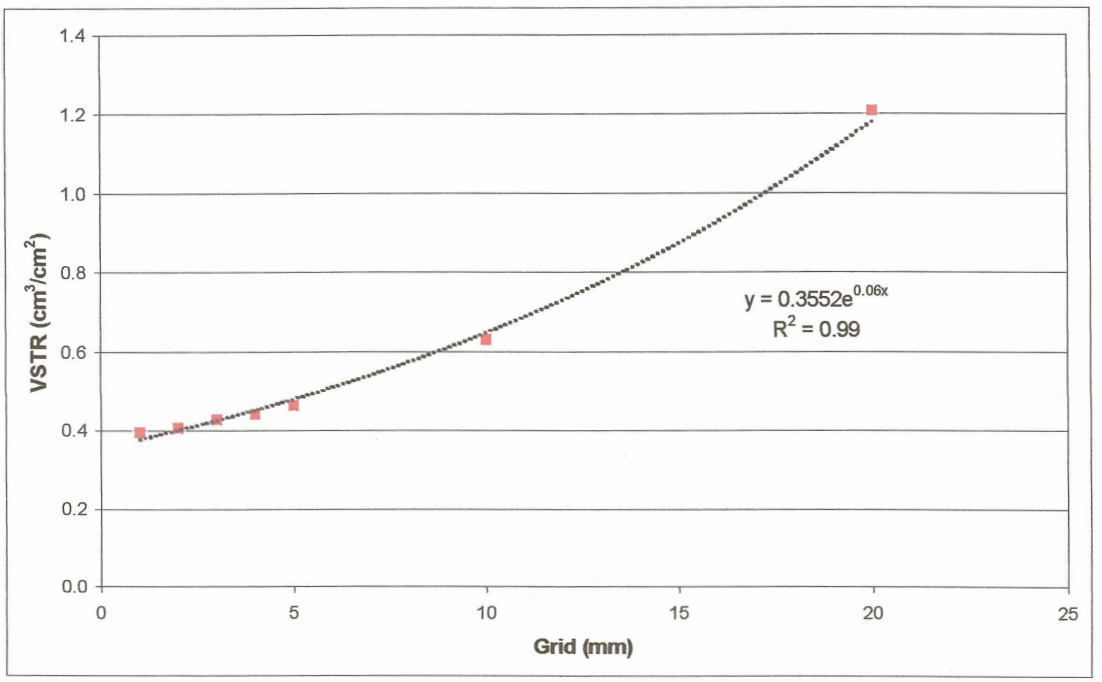

Figure F.3: Verification of optimum grid size

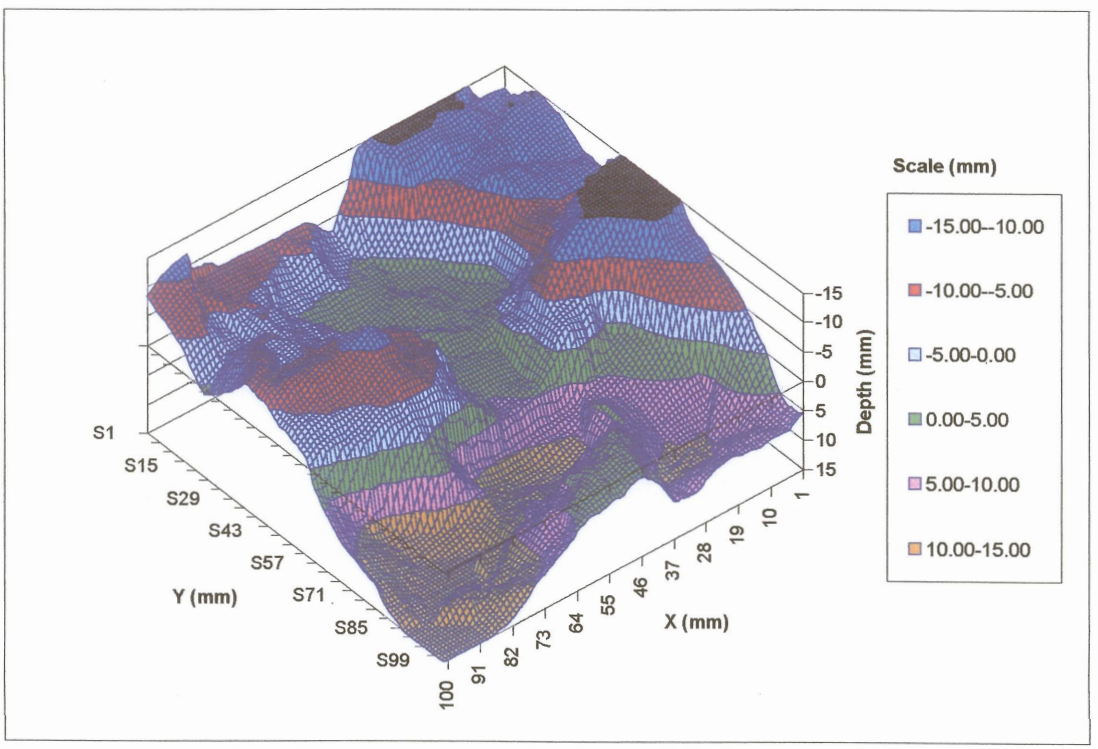

Figure F.4: Typical surface plot of VST data

The results published by Vandenbossche (1999) based on VSTR measurements made with cores from 16 different doweled joints are reproduced in Figure F.5, together with the results obtained in this study. Although the joints considered in this study were aggregate interlock joints, the volume of the aggregate interlock crack face itself could still be compared.

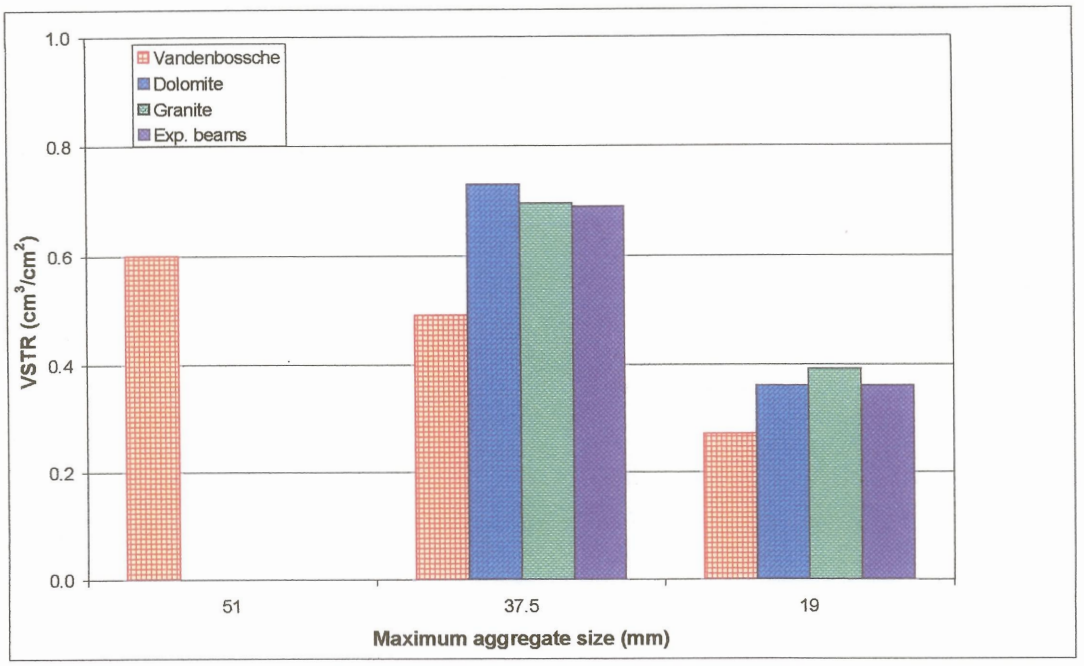

Figure F.5: Effect of maximum coarse aggregate size on VSTR - comparison between USA and South African aggregates

The objectives for determining the VST of the concrete samples were mentioned above. From Figure F.5 it is obvious that all the questions have been answered, as the VSTR of both the 19 mm granite and dolomite crack face volumes, as well as the 37,5 mm granite and dolomite crack face volumes differed less than 10% from each other. Furthermore, the VSTR of the crack faces of both the 19 mm and 37,5 mm coarse aggregate experimental beams were also approximately the same as the crack faces formed by breaking 28-day beams during modulus of rupture testing. It can therefore be assumed that the crack face formed when conducting modulus of rupture testing on test beams can be taken as representative of the VSTR of the crack inside the road pavement.

When comparing the VSTR results from this study with the results obtained from crack faces of concrete constructed with typical USA aggregates, published by Vandenbossche (1999), it is obvious that the South African aggregates have a far greater aggregate interlock potential. The VSTR results obtained for the concrete constructed with 19 mm and 37,5 mm coarse aggregate were 37% and 44%, respectively, higher then the USA results.

Although not shown on Figure F.5, the VSTR of the pre-deformed plastic joint was 0,63cm^3/cm^2. Bearing in mind that the "bubbles" in the plastic sheet were formed with a hot light bulb, with a circular radius of approximately 22 mm, the aggregate interlock size would then be approximately 44 mm. It could therefore be compared with the results obtained for 37,5 mm coarse aggregate concrete. The smooth surface finish, however, also influenced the VSTR value, which was only 89% of the average of the VSTR results for 37,5 mm coarse aggregate.

Although the VSTR was effective in determining the volume of the crack face, it could not quantify the smoothness of the surface of the pre-deformed plastic joint face. Various methods were investigated to quantify the smoothness of this surface. The simplest method of showing the smoothness of the pre-deformed plastic joint surface, was to plot an extract from the VST laser data, and compare it with the VST laser data obtained from a randomly selected aggregate interlock crack face. The obviously smoother pre-deformed plastic joint surface data is shown on Figure F.6 and the rougher aggregate interlock crack face data on Figure F.7. The shiny, smooth crack face created with the plastic sheet is also clearly visible on Photo G.24.

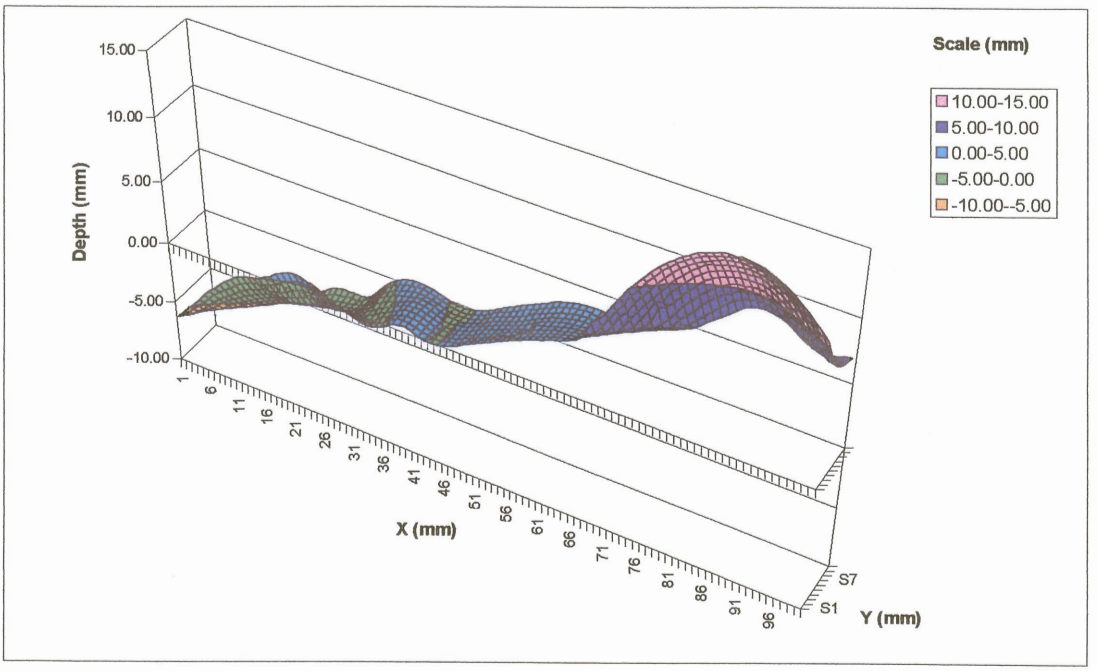

Figure F.6: Extract from pre-deformed plastic joint VST data

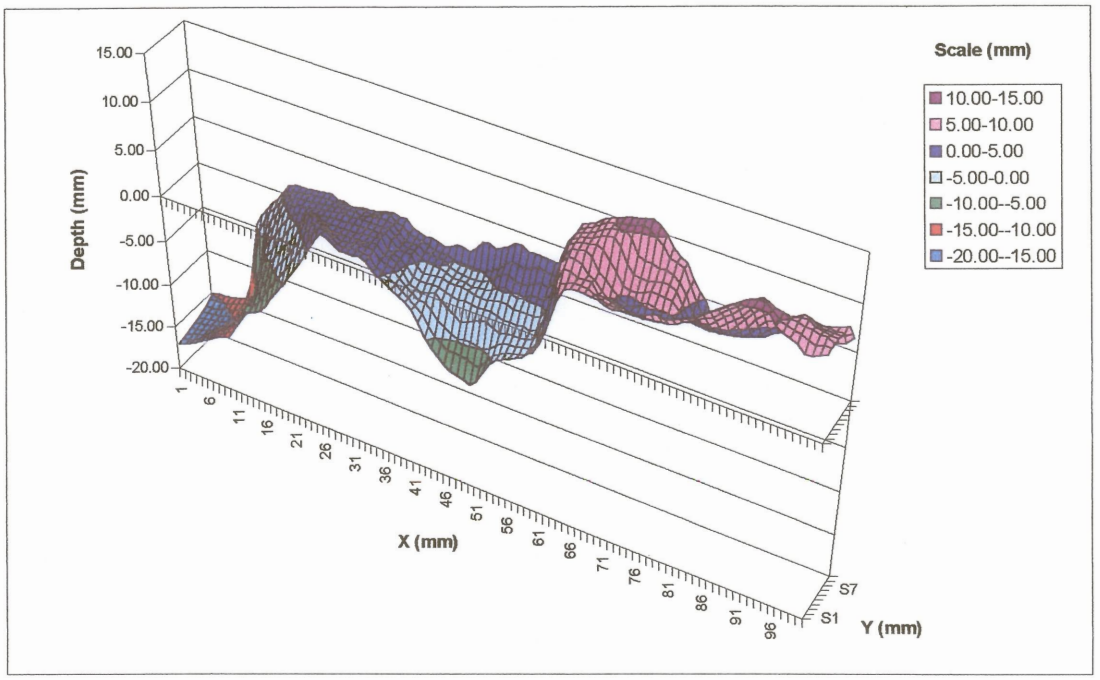

Figure F.7: Extract from randomly selected aggregate interlock joint VST data

APPENDIX G: PHOTOS

Photo G.1: Shuttering

Photo G.2: Casting concrete – crack inducer and crack former in place in mould

Photo G.3: Beam and air-cured cubes

Photo G.4: Forming crack within 24 hours after casting beam

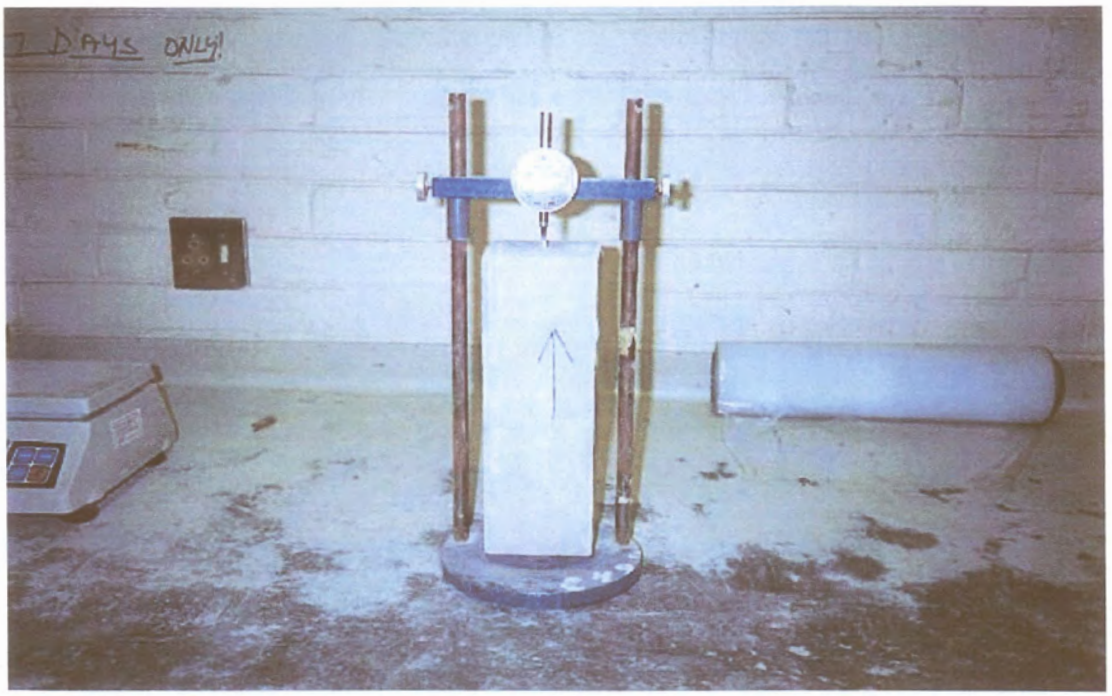

Photo G.5: Determining shrinkage of 100 x 100 x 300 mm beam

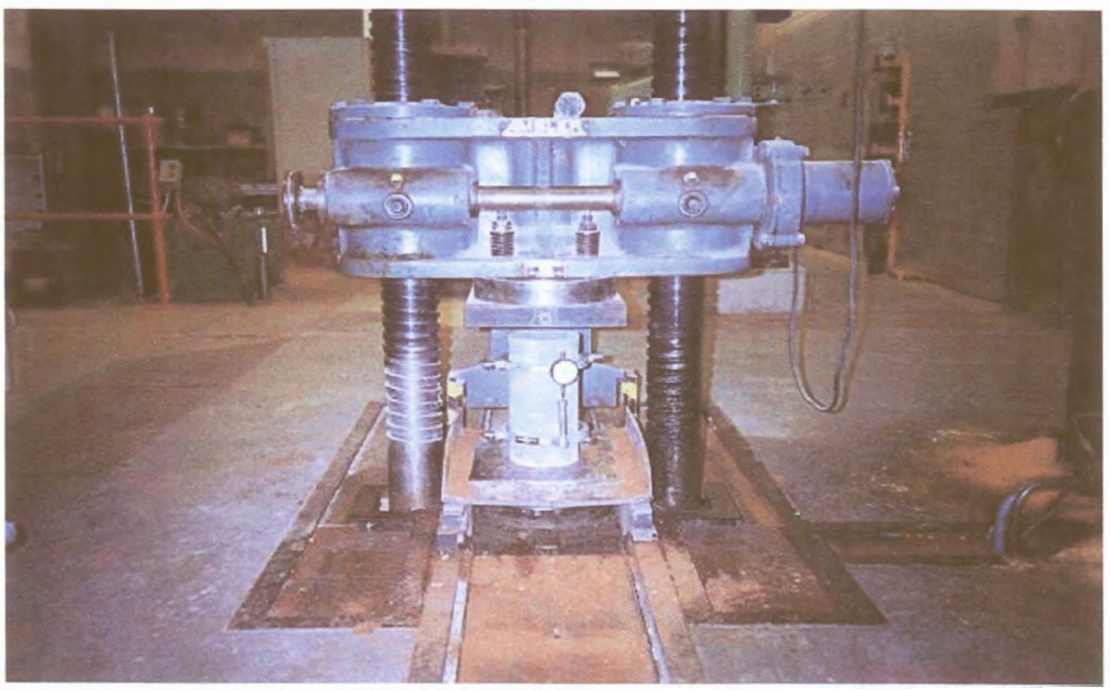

Photo G.6: Modulus of elasticity test on cylinder

Photo G.7: Determining compressive strength of concrete in cube press

Photo G.8: Determining modulus of rupture of concrete in two-point loading press

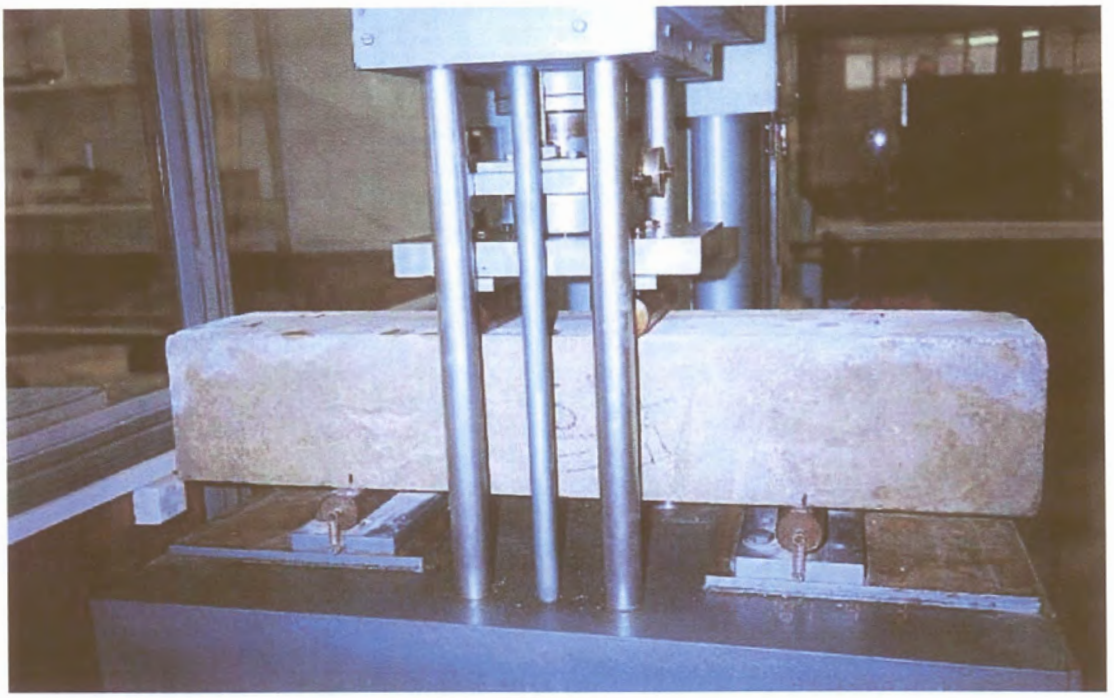

Photo G.9: Determining modulus of rupture of concrete in two-point loading press

Photo G.10: Crack face of modulus of rupture test beam - 37,5 mm dolomite aggregate

Photo G.11: Data logging equipment

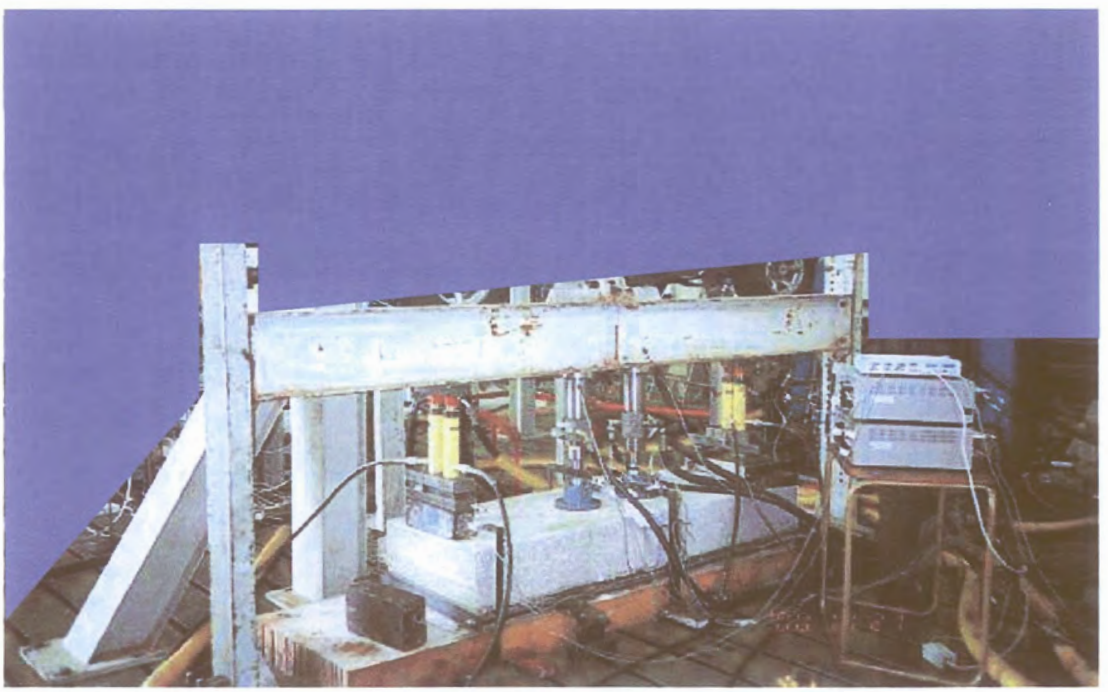

Photo G.12: Pressing down ends of beam to break aggregate interlock bond for testing at different crack widths – Experiment 1

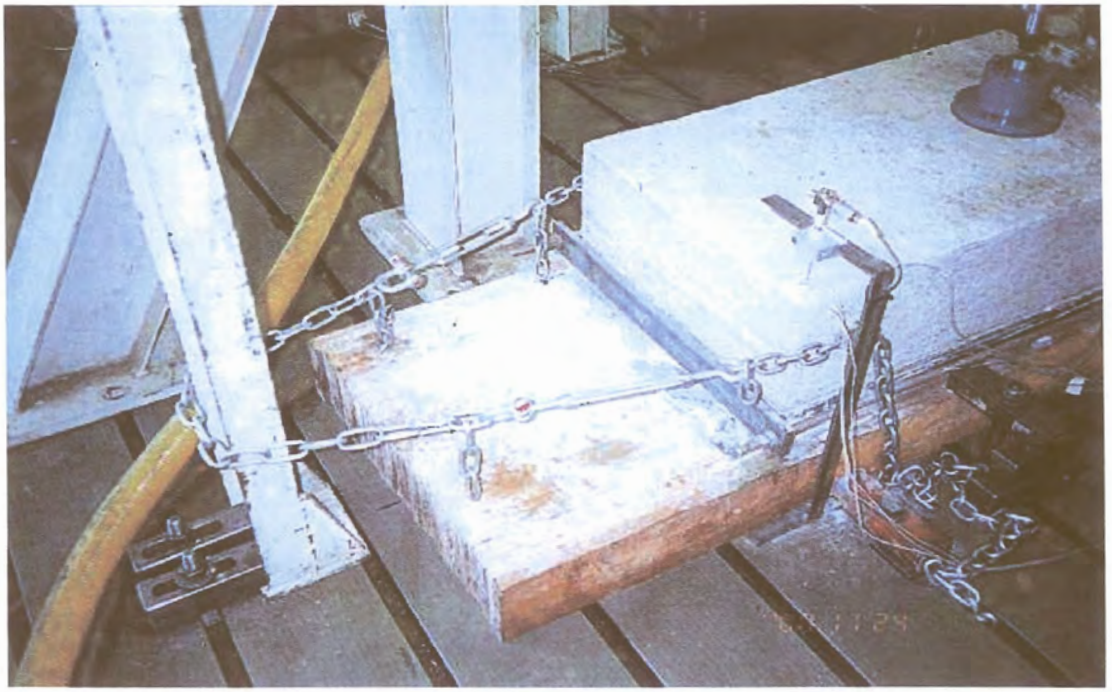

Photo G.13. : Initial crack opening/closing system

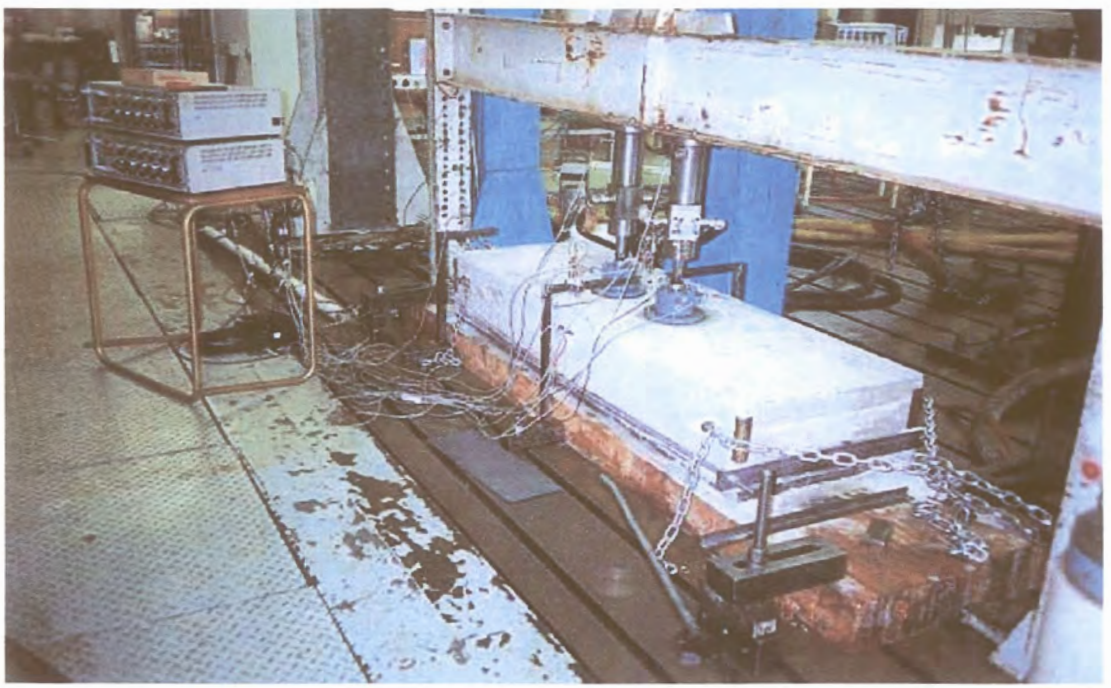

Photo G.14. : Dynamic loading and crack opening/closing system – Experiment 2

Photo G.15: Pressing down ends of beam to break crack open for testing at different crack widths – Experiment 3

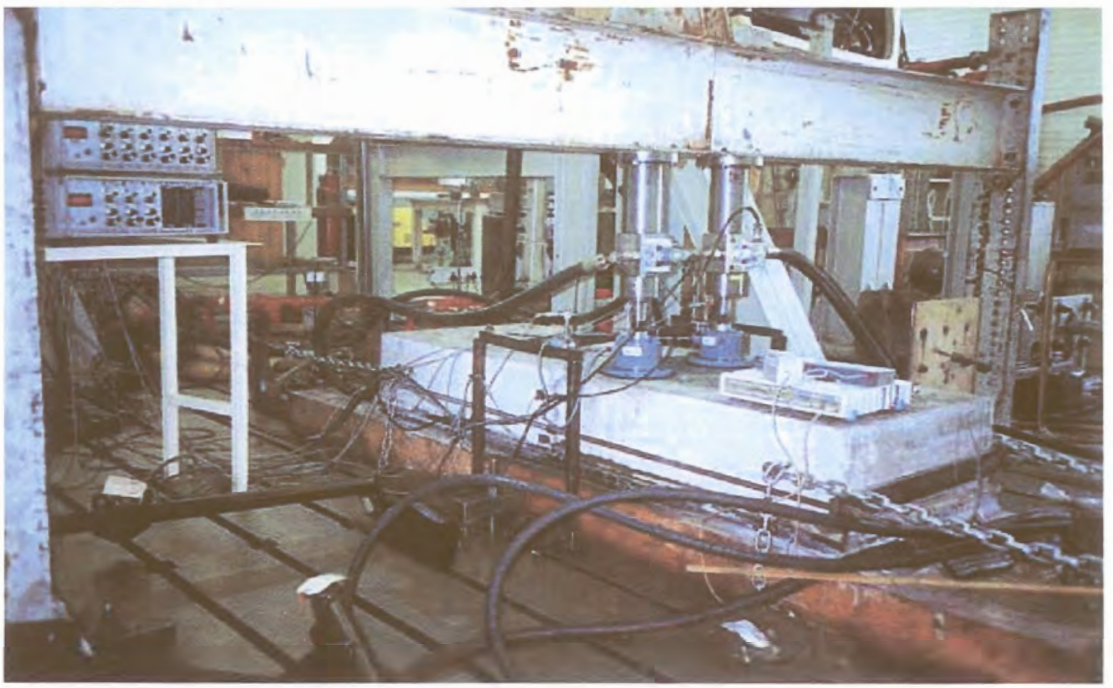

Photo G.16: 40 kN static loading with two actuators at one side of joint (Spider measuring temperature in beam in foreground) – Experiment 3

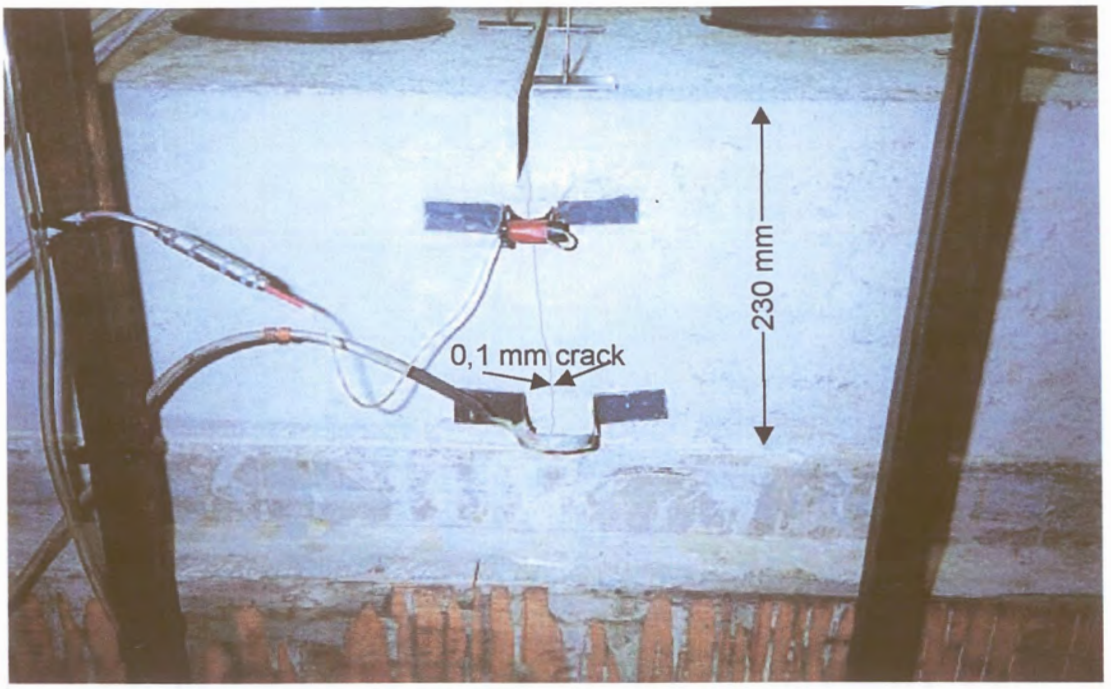

Photo G.17: Thin, 0,1 mm crack at start of testing

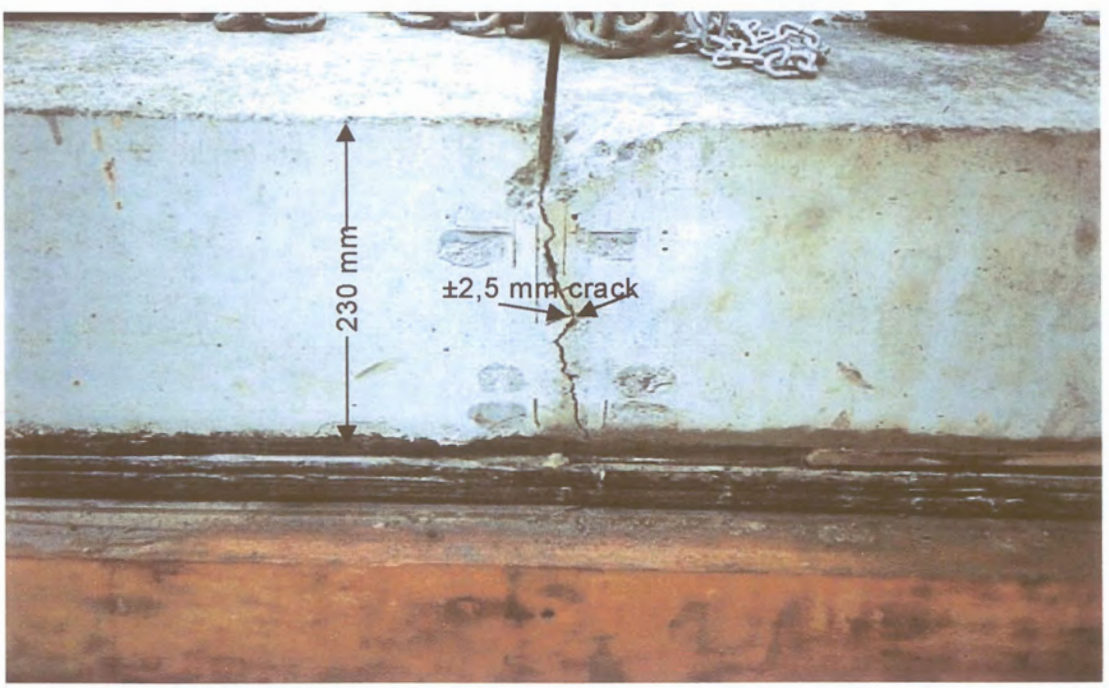

Photo G.18: Clearly visible crack after completion of testing

Photo G.19: Crack face of 19 mm granite aggregate test beam – Experiment 1

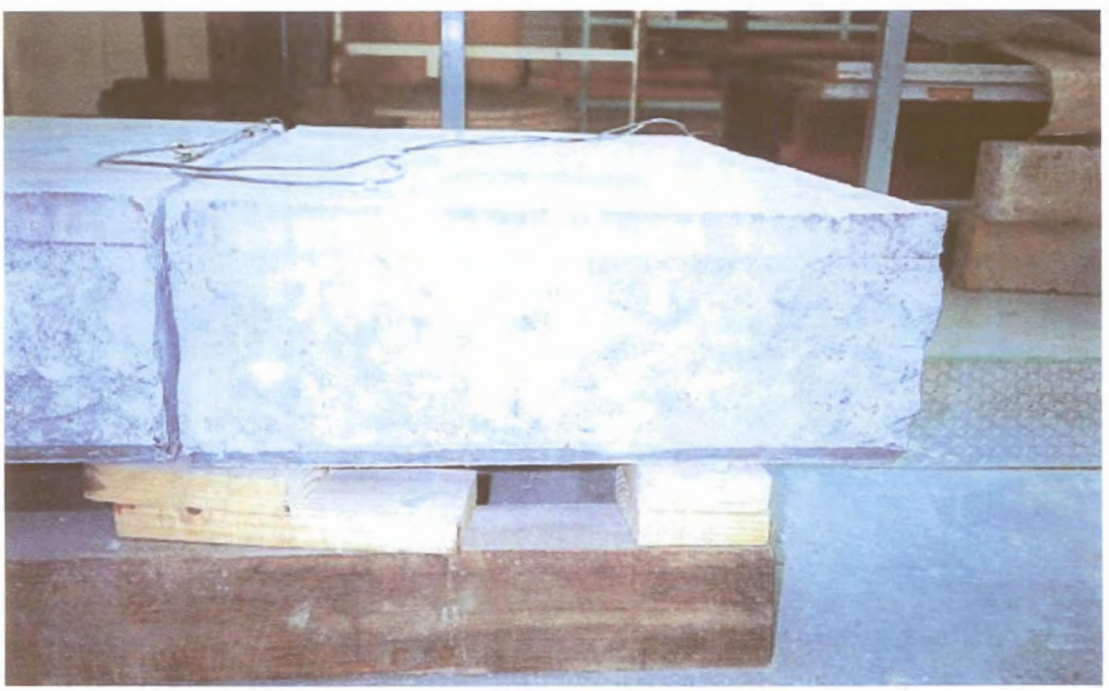

Photo G.20: Crack face of 37,5 mm granite aggregate test beam – Experiment 2

Photo G.21: Crack face of 19 mm dolomite aggregate test beam – Experiment 3

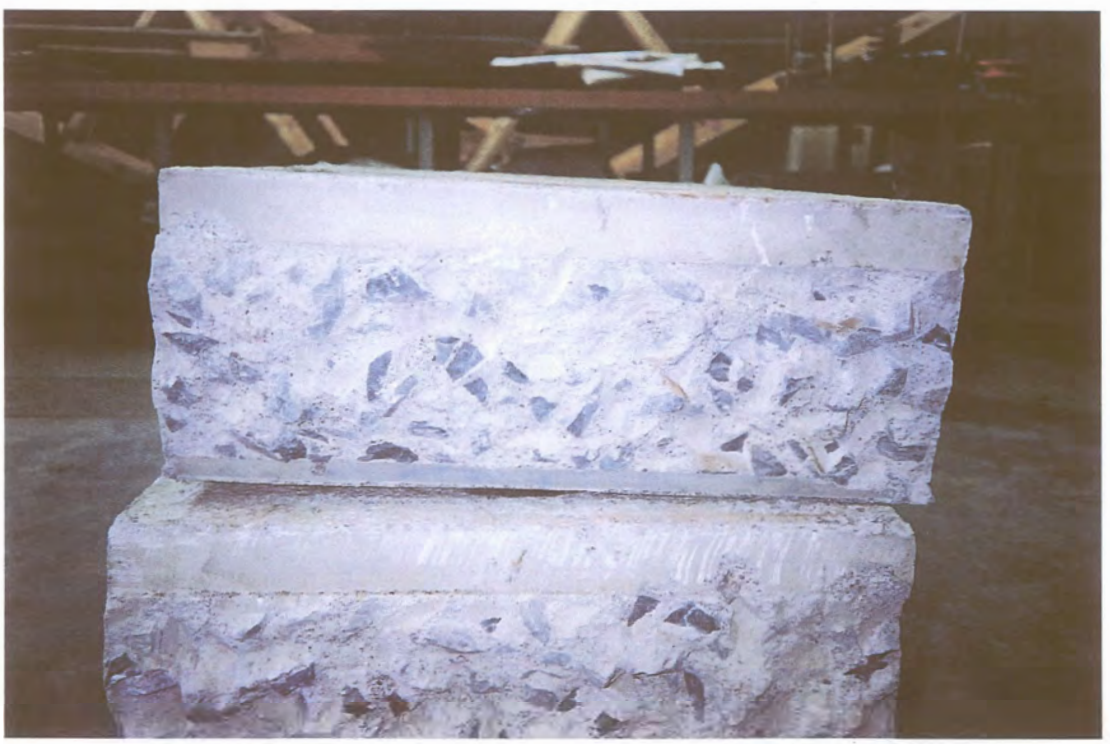

Photo G.22: Crack face of 37,5 mm dolomite aggregate test beam – Experiment 4

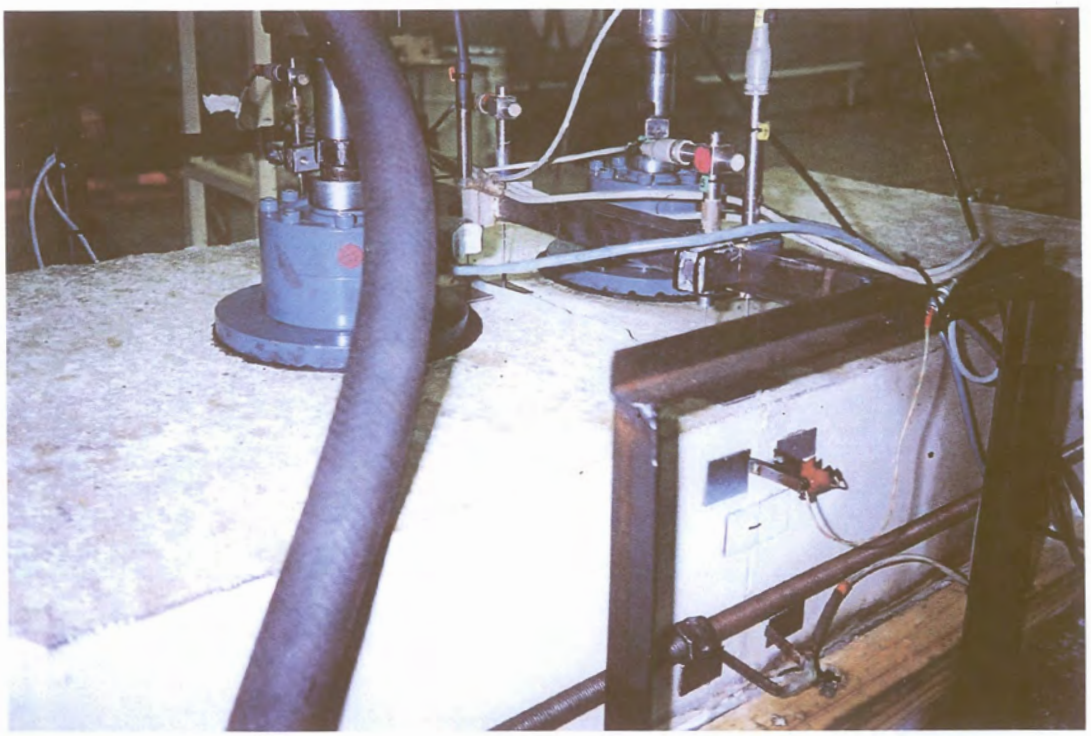

Photo G.23: Pre-deformed plastic joint with edge of plastic sticking out on top of concrete surface – Experiment 5

Photo G.24: Smooth face of pre-deformed plastic joint with plastic sheet in foreground – Experiment 5

Photo G.25: Laser measuring unit mounted on a milling machine to obtain Volumetric Surface Texture (VST) measurement of concrete sample